

SCHOLARLY PUBLICATIONS

*A CURRENT AWARENESS BULLETIN
OF RESEARCH OUTPUT*

@DTU

(39th Edition)

MARCH 2016

BY: CENTRAL LIBRARY

DELHI TECHNOLOGICAL UNIVERSITY

(FORMERLY *DELHI COLLEGE OF ENGINEERING*)

GOVT. OF N.C.T. OF DELHI

SHAHBAD DAULATPUR, MAIN BAWANA ROAD

DELHI 110042

PREFACE

This is the **Thirty Ninth** Issue of Current Awareness Bulletin started by Delhi Technological University, Central Library. The aim of the bulletin is to compile, preserve and disseminate information published by the faculty, students and alumni for mutual benefits. The bulletin also aims to propagate the intellectual contribution of Delhi Technological University (DTU) as a whole to the academia.

The bulletin contains information resources available in the internet in the form of articles, reports, presentations published in international journals, websites, etc. by the faculty and students of DTU. The publications of faculty and student which are not covered in this bulletin may be because of the reason that the full text either was not accessible or could not be searched by the search engine used by the library for this purpose.

The learned faculty and students are requested to provide their uncovered publications to the library either through email or in CD, etc to make the bulletin more comprehensive.

This issue contains the information published during **March 2016**. The arrangement of the contents is alphabetical. The full text of the article which is either subscribed by the university or available in the web is provided in this bulletin.

Central Library

CONTENTS

1. A Novel to Mode Converter Designed With Radially Loaded Dielectric Slabs, **7.1. Ashish Chittora**, Sandeep Singh, Archana Sharma, and Jayanta Mukherjee, electronics and communication engineering, DTU
2. Analysis of Surface Roughness in Turning Process Using Neural Network, **3.Ranganath M. Singari**, DTU
3. CFD Modeling of flow through S-Shaped Duct, Md. Nadim Shams, **3.Raj Kumar Singh**, **3.Md. Zunaid**, DTU
4. Challenges and Trends in Glucose Monitoring Technologies, Padma Batra, Reena Tomar, **3.Rajiv Kapoor**, DTU
5. **Dope** dyeing of polyacrylonitrile filaments with Ratanjot, Roli purwar, Priyadarshan Sahoo, Mehak Jain, Urvashi Bothra, Priya Yadav, Jigyasu Juneja and Chandra Mohan Srivastava, Applied Chemistry and Polymer Technology, DTU
6. Dynamical Behavior of A Stage Structured Eco–Epidemiological Model, **3.Shashi Kant** and **3.Vivek Kumar**, Applied Mathematics, DTU
7. Fault Immune Pico-Hydro Powered Base Station of Remote Telecommunication Tower, **3.Vishal Verma**, **3.Peeyush Pant** and Bhim Singh, Electrical engineering, DTU
8. Generalized power flow models for VSC based multi-terminal HVDC systems, **3.Shagufta Khan** and **3.Suman Bhowmick**, DTU

9. Green route synthesis of silicon/silicon oxide from bamboo **3.Vinay Kumar**, **3.Pranjala Tiwari**, **3.Lucky Krishnia**, **3.Reetu Kumari**, **3.Anshika Singh**, Arnab Ghosh, **3.Pawan k Tyagi**, Applied physics ,DTU
10. International Conference on Materials Science & Technology 2016 (Estimation of work function of thin layer graphene by probing with EFM, **3.Anshika Singh**, **3.Amrish K. Panwar**, **3.Pawan K. Tyagi** from page no 21-22), Applied physics, DTU
11. International Conference on Materials Science & Technology 2016 (Filled carbon nanotubes: Possess exotic magnetic properties, **3.Pawan k Tyagi**, from page no 6-7), Applied physics, DTU
12. International Conference on Materials Science & Technology 2016 (First principles study of fluorine adsorption on zigzag graphene nanoribbons, Neeraj K. Jaiswal, **3.Neha Tyagi** and Pankaj Srivastava from page no 3-4), Applied Physics, DTU
13. Journal of Integrated Science and Technology (Depolymerisation of Post-consumer PET Bottles using Waste Acid, **3.Stuti Sagar** and **3.Ram Singh**, from page no. 14-15), Applied Chemistry, DTU
14. Luminescence Spectral Studies of Tm³⁺ ions doped Lead Tungsten Tellurite Glasses For Visible Red and NIR applications, M.Venkateswarlu, Sk Mahamuda, K. Swapna, **3.A.Srinivasa Rao**, A. Mohan Babu, Suman Shakya, D.Haranath and G. Vijaya Prakash, Applied physics, DTU
15. Microstructural Indicators for Prognostication of Copper–Aluminum Wire Bond Reliability Under High-Temperature Storage and Temperature Humidity, **8.1.Pradeep Lall**, Shantanu Deshpande, Luu Nguyen, and Masood Murtuza, Mechanical Engineering, DTU

16. Mixing Enhancement by Degenerate Modes in Electrically Actuated Sessile Droplets, **8.1 Shubhi Bansal** and Prosenjit Sen, Applied physics, DTU
17. Ontologies for Software Engineering: Past, Present and Future, M.P.S.Bhatia, **3. Akshi Kumar** and Rohit Beniwal, Computer Engineering, DTU
18. Optimal AGC with redox flow batteries in multi-area restructured power systems, Yogendra Arya and **3. Narendra Kumar**, Electrical Engineering, DTU
19. Oxygen anion diffusion in double perovskite $\text{GdBaCo}_2\text{O}_{5-\delta}$ and $\text{LnBa}_{0.5}\text{Sr}_{0.5}\text{Co}_{2-x}\text{Fe}_x\text{O}_{5-\delta}$ ($\text{Ln} = \frac{1}{4} \text{ Gd, Pr, Nd}$) electrodes, Uzma Anjum, **3. Saumye Vashishtha**, Manish Agarwal, Pankaj Tiwari, Nishant Sinha d, Ankit Agrawal, S. Basu and M. Ali Haider, Applied Chemistry and Polymer Technology, DTU
20. Photonic crystal-based RGB primary colour optical filter, Brahm Raj Singh, Swati Rawal and **3. R.K. Sinha**, Applied Physics, DTU
21. Prediction of Surface Roughness in CNC Turning of Aluminum 6061 Using Taguchi Method and ANOVA for the Effect of Tool Geometry, **3. Ranganath M Singari**, **3. Vipin** and **3. Sanchay Gupta**, Mechanical, Production and Industrial Engineering, DTU
22. Pure orange color emitting Sm^{3+} doped BaNb_2O_6 phosphor for solid state lighting applications, **3. Amit K. Vishwakarma** and M. Jayasimhadri, Applied Physic, DTU
23. Recent Advances in Mycotoxins Detection, Ruchika Chauhan, **3. Jay Singh**, Tushar Sachdev, T. Basu and B.D. Malhotra, Applied Chemistry & Polymer Technology, DTU
24. Synthesis CNTs Particle Based Abrasive Media for Abrasive Flow Machining Process, Sonu Kumar, Q.Murtaza, R.S Walia, S. Dhull, **3. P. K. Tyagi**, Applied physics, DTU

25. Tailpipe emission from petrol driven passenger cars q, Abhinav Pandey, Govind Pandey, **3.Rajeev Kumar Mishra**, Environmental Engineering, DTU
26. Thermodynamic Analysis of Single-effect LiBr- H₂O Absorption Refrigeration System, **3.Rajesh Kumar** and **3.Ravindra Kannojiya**, Mechanical Engineering, DTU

1. Chancellor

2. Pro Vice Chancellor

3. Faculty

4. Teaching-cum-Research Fellow

5. Alumni

6. Research Scholar

7. PG Scholar

8. Undergraduate Student

2.1. Ex Pro Vice Chancellor

3.1. Ex Faculty

6.1. Ex Research Scholar

7.1. Ex PG Scholar

8.1. Ex Undergraduate Student

A new preparation method of a porous photocatalytic nanostructure containing lamellar graphene nanoparticles

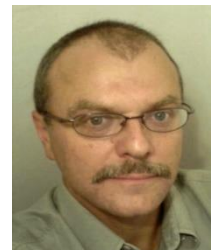
Richard Dvorsky^{1,2*}, Ladislav Svoboda³, Jiří Bednář¹, Pavel Mančík¹, Bruno Kostura³, Dalibor Matýsek⁴, Soňa Študentová³

¹Nanotechnology Centre, VŠB-Technical University of Ostrava, Ostrava, Czech Republic

²Department of Physics, VŠB-Technical University of Ostrava, Ostrava, Czech Republic

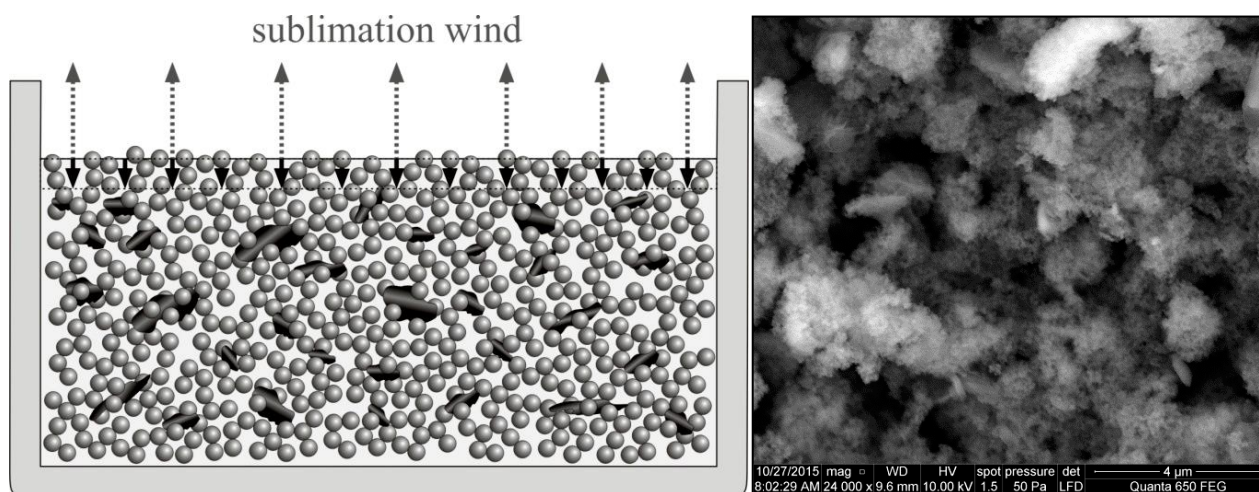
³Department of Chemistry, VŠB-Technical University of Ostrava, Ostrava, Czech Republic

⁴Institute of Clean Technologies for Mining and Utilization of Raw Materials for Energy Use, VŠB-Technical University of Ostrava, Ostrava, Czech Republic



**Corresponding author. Tel: (+420) 731186696

Table of contents



Scheme of sublimation extraction of the dispersion liquid and SEM micrograph of porous photocatalytic nanostructure

ABSTRACT

Currently, greater control for the level of pollutants in the environment is required. One of the remediation methods of chemical pollutants is their photocatalytic decomposition into non-toxic constituents. During the photocatalytic degradation reactions the initial phase of the process, in which the mechanism of zero-order reaction is predominant, plays often a very important role. In conditions of high concentration of pollutants the reaction rate is proportional only to the total area of the accessible surface of the photocatalytic particles. In this work we present a new preparation method of porous photocatalytic network nanostructure on silicate based Si-O-Zn which is doped by lamellar graphene nanoparticles. Such materials exhibit relatively very high values of specific surface area (about 300 m²/g) and porosity. Their photocatalytic activity is enhanced by admixture of the lamellar graphene nanoparticles which cause the relocation of electrons in exciton pairs and therefore prolong the lifetime of both charges in photocatalytic reactions.

Keywords: Nanoparticle; network silicate structure; photocatalysis; graphene; sublimation.

Acknowledgements

The research is supported by IT4Innovations Centre of Excellence project, reg. no. CZ.1.05/1.1.00/02.0070 and the project Regional Materials Science and Technology Centre - Feasibility Program (LO1203).

References

1. Pérez-Ramírez, J.; Kapteijn, F.; Schöffel, K.; Moulijn, J.A.; Appl. Catal. B: Environmental, 2003, 44, 2, 117-151 DOI: doi:10.1016/S0926-3373(03)00026-2
2. Dvorsky, R.; Praus, P.; Trojková, J.; Študentová, S.; Luňáček, J.; 4th International Conference NANOCON 2012, Brno, Czech Republic, Conference Proceedings Book 39-43 ISBN: 978-80-87294-35-2
3. Dvorsky, R.; PCT Patent: WO2013029576 Bibl. data: Espacenet

Designing of Corrosion Resistant Polymer Composite Coatings technology for protection of mild Steel in marine Environment

Pradeep Sambyal¹, Gazala Ruhi¹, Sundeep K. Dhawan^{1*}

¹Polymeric & Soft Materials Section, National Physical Laboratory, (CSIR), Dr. K.S. Krishnan Marg, New Delhi-110012, India

*Corresponding author. Tel: +91-11-4560940; Fax: +91-11-25726938; E-mail: skdhawan@mail.nplindia.ernet.in



Table of contents

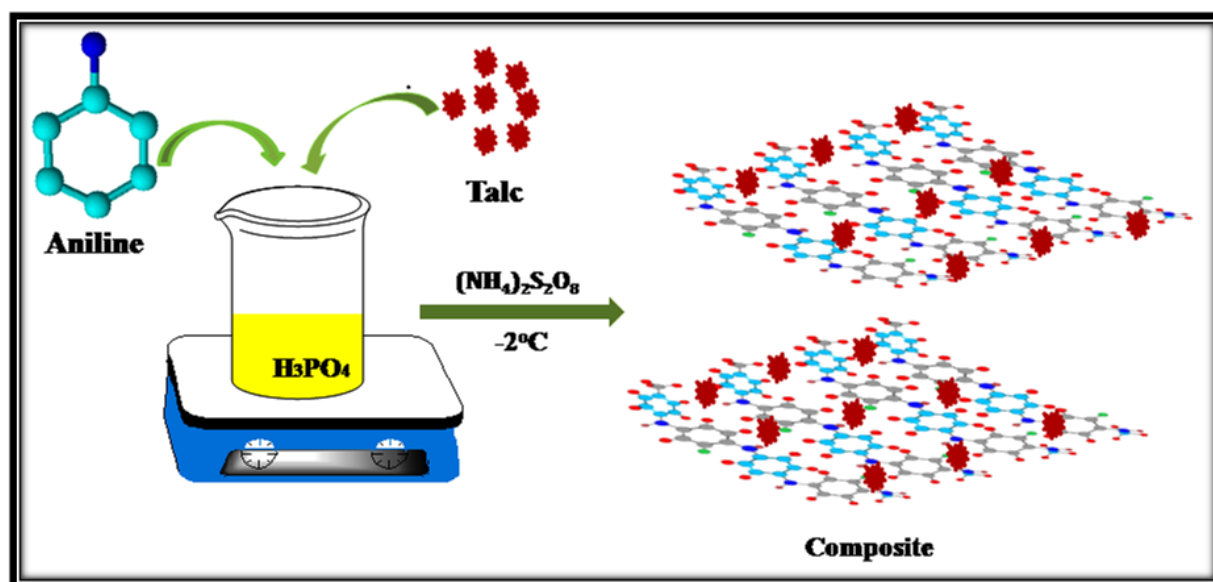


Figure 1 Schematic of the synthesis of polyaniline/talc composite by chemical oxidative polymerization process.

ABSTRACT

Present study focuses on the designing of talc reinforced polymer composite coatings for steel substrate. A facile one step in situ chemical oxidation emulsion polymerization of aniline is carried out in ortho-phosphoric solution. Talc powders are incorporated in the polymer matrix during polymerization process. Coatings were developed by loading of these polymer composite in epoxy resin. Polyaniline/talc composite coatings have demonstrated improvement in the corrosion resistance of mild steel substrate in 3.5% NaCl solution. Reinforcement of talc as filler in the conjugated polymer coating system is carried out to further improve the physical, thermal and corrosion properties of the coatings. The XRD and FTIR results exhibited a synergistic interaction between the filler and the polymer matrix. Scanning electron microscopy results confirms uniform distribution of talc in polymer matrix. All electrochemical studies of polymer composite coatings were done in 3.5% NaCl solution. The polymer composite coatings show remarkable results in electrochemical studies even after 30 days of immersion in 3.5% NaCl solution. The EIS parameters show high pore resistance and absence of under coating corrosion. A very low corrosion current is noticed for coatings with silica nanoparticles. The salt spray test results under accelerated conditions (as per ASTM B117 standards) of composite coatings revealed almost no extended corrosion and blistering along the scribe mark.

Keywords: Tafel plots; EIS; polymer coatings.

Acknowledgements

Authors thank Dr. K.N.Sood for doing SEM measurements and Dr. dinesh Singh for doing TEM measurements. Special thanks are extended to Mr. Brij Bisht for providing data on salt spray measurements.

Synthesis and characterization of vinyl carbazole functionalized silica polymer nanocomposites (SBA/VC) for the adsorption of dyes

Ankita Sharma and Amit Dubey*

Department of Chemistry, Maulana Azad National Institute of Technology (MANIT)-Bhopal (M.P.)-India

*Corresponding authot. Tel: (+91) 7554051655; E-mail: dramit.dubey@gmail.com

ABSTRACT

Ordered mesoporous silica (OMS) materials are superior substrates to generate organic/inorganic hybrid due to their remarkable properties such as large surface area, pore volume and flexible pore architecture [1]. Incorporation of different functional moieties on the surface of OMS improves the mechanical strength and controls the degree of hydrophilicity/hydrophobicity selectively on the surface for different applications in catalysis, sensors, adsorption, drug-delivery and energy storage etc. In order to generate the hydrophobicity on the surface, many researchers have directly incorporated the polymers but in most of the cases the structural order is either collapsed or becomes nonporous in nature [2]. In our previous reports, we have reported silica polymer nanocomposites via in-situ radical polymerization of the vinyl monomers for catalysis and adsorption applications [3, 4]. The dyes used in textile industries and pulp mills have been one of the main sources of severe water pollution which affect the marine life and human health. Synthetic dyes are highly toxic and carcinogenic. Therefore, it is very challenging to remove the dye from the wastewater. Many techniques have been applied for the removal of dye from wastewater such as adsorption on activated carbons, coagulation and flocculation, reverse osmosis, activated sludge, bacterial action, chemical oxidation, ozonation, and physical methods like membrane filtration, ion exchange and electrochemical techniques which are either expensive or ineffective [5]. In the present investigation, we report the synthesis and the characterization of vinyl carbazole (VC) functionalized silica polymer nanocomposites (SBA/VC) for the adsorption of different dyes such as methylene blue, methyl orange, eriochrome black-T, Phenol blue and congo red. Powder X-ray diffraction and N₂ adsorption isotherms showed the presence of mesoporous nature of the nanocomposites after functionalization with vinyl carbazole. Different adsorption parameters such as adsorption weight, adsorption time, pH etc. were optimized for adsorption of dyes ions under environmental friendly conditions.

Keywords: vinyl carbazole, mesoporous materials, adsorption

References

1. S. Inagaki, S. Guan, Y. Fukushima, T. Ohsuna, O. Terasaki, J. Am. Chem. Soc., 1999, 121, 9611.
2. N. Al-Haq, R. Ramnauth, S. Kleinebickel, D.L. Ou, A.C. Sullivan and J. Wilson, Green Chem., 2002, 4, 239.
3. D. Sachdev, A. Dubey, Catal. Commun., 2013, 39, 39
4. G.R. Wilson, A. Sharma, N.M. Srivastava, D. Sachdev and A. Dubey, J. Porous Mater., 2015, 22, 333.
5. B. Shi, G. Li, D. Wang, H. Feng and H.Tang, J. Hazard. Mater., 2007, 143, 567.

Graphene stacked SnS_2 nanoflakes for photocatalytic conversion of nitrobenzene and enhanced photocatalytic activity for degradation/reduction of various water polluting dyes and toxic Cr (VI)

Himani Chauhan¹, Kiran Soni¹ And Sasanka Deka^{1*}

¹Department of Chemistry, University of Delhi, North campus, Delhi-110007, India

*Corresponding author. E-mail: ssdeka@gmail.com



Table of contents

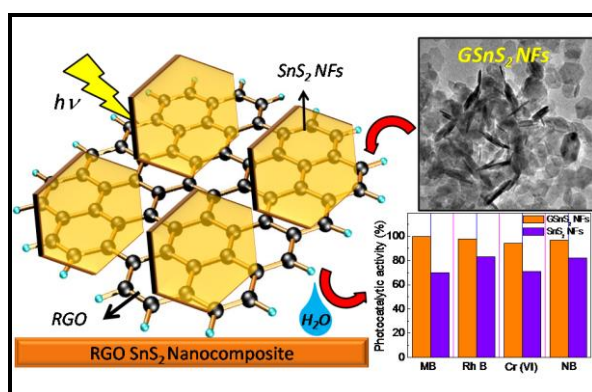


Figure 1: Schematic diagram showing enhanced photocatalytic activity of as-synthesised hexagonal nanoflakes of SnS_2 reduced graphene oxide nanocomposites (SnS_2/RGO)

ABSTRACT

2D SnS_2 hexagon nanoflakes and their graphene loaded nanocomposites (GSnS_2) were successfully synthesised by simple, economic, one pot hydrothermal approach on wider scale. Tin chalcogenides are optical semiconductor and has increasing interest in the fields of photocatalysis and photovoltaics. In terms of lower toxicity and wider spectral response, SnS_2 is becoming a superior layered metal sulphide for high photocatalytic activity. SnS_2 exist in CdI_2 can be synthesised in wide range of morphology¹, moreover due to the vast empty sites present in sandwiched structure of SnS_2 , it can be an important host material for various intercalation reaction. The layered structure, specific 2D morphology and enhance electron mobility of stacked graphene²⁻⁴ sheets due to small size, large specific surface area, microporosity and wider visible light absorption lead to excellent photocatalytic behaviour of catalyst. All these attractive features of simply synthesised low-cost and non-toxic GSnS_2 nanoflakes photocatalyst makes them to serve as sort of efficient visible light driven photocatalyst for industrial waste water treatment and organic nitro compounds conversion. The as-synthesised nanoparticles and nanocomposites were thoroughly characterised by XRD, Raman, FT-IR, TEM, HRTEM, SEM, EDS, BET and finally the excellent photocatalytic activity of graphene oxide- SnS_2 nanocomposites under visible light irradiation were analysed by UV-Vis spectroscopy where concentrations of reaction mixture was measured in supernatant solution by recording absorption spectra and noting down the gradual decrease in characteristic absorption peak at 655 nm (MB), 554 nm (Rh B), 372nm (Cr(IV)) and 267 nm (NB). We

observed photocatalytic synthesis of aniline from nitro-benzene with complete conversion and absolute selectivity. Furthermore, efficient photocatalytic application of graphene stacked SnS₂ nanoflakes under visible light illumination in the reduction of toxic Cr (VI) to nontoxic Cr(III) and degradation of mutagenic organic dyes are observed with 99% reduction/degradation and good recyclability.

Keywords: Chalcogenides; nanocomposite; photocatalysis

Acknowledgements

H.C. thanks UGC-India and K.S. thanks to CSIR for providing research fellowship. The authors thank USIC-DU and AIIMS EM facility for characterization

Reference

1. Y. Lei, S. Song, W. Fan, Y. Xing, H. Zhang. J. Phys. Chem. C, 113, 1280–1285, 2009.
2. A.K. Geim, Science, 324, 1530–1534. 2009
3. K. s. Novoselov, A.K. Geim, S. V. Morozov, D. Jiang, Y. Zhang, S.V. Dubonos, I.V. Grigorieva, A. A. Firsov, Science, , 306, 666–669, 2004.
4. Y. Jing , C.Y Xu, F.X Ma, S. P. Hu, Y.W. Zhang, L. Zhen, ACS Appl. Mater. Interfaces, 6, 22370–22377, 2014

Self assembly of functionalised graphene nanostructures by one step reduction of graphene oxide using aqueous extract of *Artemisia vulgaris*

Prajwal Chettri¹, V. S. Vendamani², Ajay Tripathi¹, Anand P. Pathak² and Archana Tiwari^{1**}

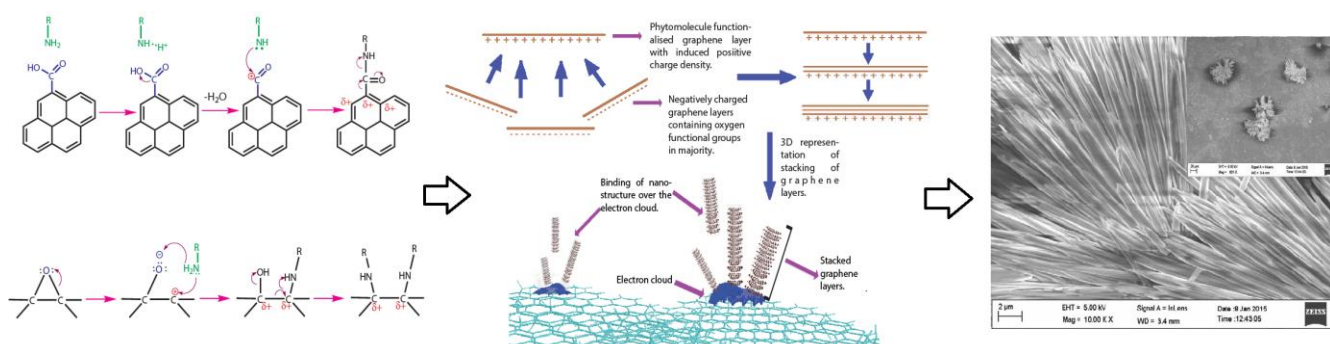
¹Department of Physics, School of Physical Sciences, Sikkim University, Gangtok 737102, India

²School of Physics, University of Hyderabad, Hyderabad 500046, India

*Corresponding authot. Tel: (03592) 232080; Fax: +91-3592-251067; E-mail: archana.tiwari.ox@gmail.com



Table of contents



Proposed mechanism for the formation of "Hedgehog" like nanostructure of graphene layers with a highly ordered crystallographic structure in the (002) direction.

ABSTRACT

We report template/substrate free approach for the synthesis of 3D graphene architecture via hydrothermal reduction. Aqueous extract of dry leaves of *Artemisia vulgaris* is used for de-oxygenation of graphene oxide as well as self assembly and organisation of graphene sheets to form a macroscopically ordered array of graphene layers. The reduced graphene oxide samples are investigated for two different reflux times viz. for 6 hours and 12 hours. It is found that for an efficient reduction of graphene oxide and for the minimal damage to the crystal structure 6 hours of reflux is the most favourable. Besides reducing graphene oxide, the phytomolecules also functionalise the graphene layers with electron withdrawing groups which become a hotspot for attracting negatively charged graphene layers. These layers restack themselves in an ordered fashion with a d spacing of 0.32 nm which is less than that of the parent graphite indicating increased van der Waal's force between the layers as a result of induced charge via functionalisation. The reduced graphene oxide sample showed activation of ferromagnetic ordering at room temperature indicating presence of unpaired spin units in sp³ bonded carbon atoms. The dominance of diamagnetic behaviour of graphene oxide which is an inherent characteristic is altered as a result of functionalisation by phytomolecules and instead ferromagnetic ordering is observed. In addition various bright quantum dots are also observed with diameters ranging between 3-20 nm.

Keywords: Reduced graphene oxide; nanosheets; *Artemisia vulgaris*; self assembly; ferromagnetic.

Acknowledgements

The authors would like to thank Department of Science and Technology, Government of India for financial support under DST-INSPIRE scheme. VSV thanks CSIR New Delhi for SRF (Extended) in the Emeritus Scientist project awarded to APP.

Reference

1. S. Thakur, N. Karak, *Carbon*, 50, 5331-5339, 2012.
2. X. Xin, X. Zhou, F. Wang, X. Yao, X. Xu, Y. Zhu, Z. Liu, *J. Mater. Chem.*, 22, 7724-7730, 2012.
3. B. Ivanescu, L. Vlase, A. Corciova, M. I. Lazar, *Chem. Nat. Compd.*, 46(3), 468-470, 2010.
4. A. B. Bourlinos, D. Gournis, D. Petridis, T. Szabo, A. Szeri, I. Dekany, *Langmuir*, 19, 6050-6055, 2003.
5. P. K. Sahoo, B. Panigrahy, D. Li, D. Bahadur, *J. Appl. Phys.*, 113(17B525), 1-3, 2013.

Fullerene grafted graphene oxide

Rachana Kumar,* Saba Khan, Kumar Gaurav, Samya Naqvi, Neha Gupta, Suresh Chand

Physics of Energy Harvesting Division, National Physical Laboratory, Dr. K. S. Krishnan Marg, New Delhi-110012, India

*Corresponding author. Tel: (+91) 45608577; Fax: (+91) 45609310;
E-mail: rachanak@nplindia.org

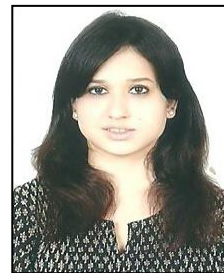
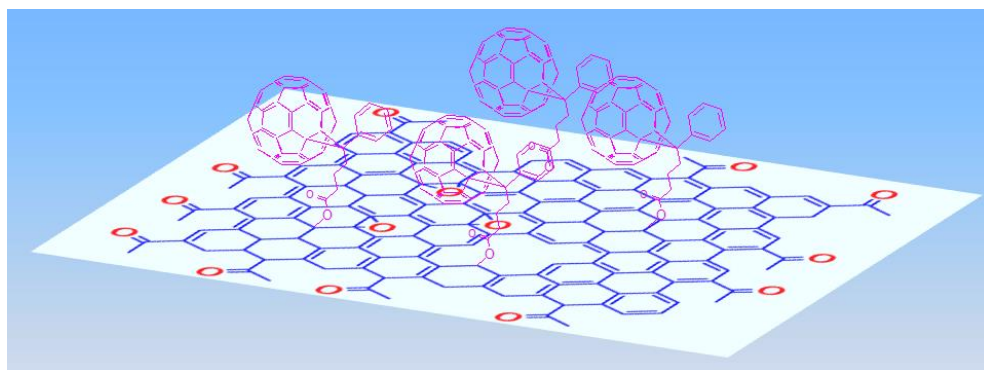


Table of contents



Fullerene grafted graphene oxide

ABSTRACT

The two dimensional monolayer of carbon atoms, graphene, has found special commercial and academic research interest. Graphene possesses outstanding electrical, mechanical, thermal and optical properties,ⁱ while graphene derivatives like, graphene oxide or other types of functionalized graphene have shown remarkable catalytic, mechanical, sensing and electronic properties offering broad range of nanotechnological applications.ⁱⁱ Attachment of small/large functional molecules like, diazonium salts, alkyl isocyanates, polymers, porphyrin and also bulky fullerene via substitution or additions reactions on GO have been reported to exploit the advantages by altering its properties and finding applications in several areas.ⁱⁱⁱ In the present work a comprehensive study has been performed on synthesis and characterization of functionalized highly conducting graphene oxide (GO)^{iv} with fullerene derivative i.e., Phenyl[6,6]butyric acid methyl ester (PCBM), the most conventional acceptor material in organic solar cell. PC61BM molecules have been attached covalently on the graphene oxide sheets resulting in formation of Donor-Acceptor Dyad type of structure (PCBGO) showing high charge transfer interaction between graphene sheets and fullerene ball. PCBGO has been characterized using different characterization tools like, FTIR, Raman spectroscopy, UV-vis absorption and XRD and charge transfer phenomenon has been established by photoluminescence and EPR analysis. Much broader peak to peak EPR line width, substantial quenching and red shifting of emission bands in fullerene-graphene dyad is attributed to strong electron transfer interactions between graphene sheets and grafted fullerene molecules.

Keywords: Graphene; fullerene; charge transfer.

Acknowledgements

Authors acknowledge DST APEX program for funding.

Reference

1. M. J. Allen, V. C. Tung, and R. B. Kaner, Chem. Rev., 110, 132-145, 2010.
2. K. S. Mali, J. Greenwood, J. Adisoejoso, R. Phillipson and S. DeFeyter, Nanoscale, 7, 1566-1585, 2015; (b) Y. Shen, Q. Fang and B. Chen, Environ. Sci. Technol., 49, 67-84, 2015.
3. R. Kumar, P. Kumar, S. Naqvi, N. Gupta, N. Saxena, J. Gaur, J. K. Maurya and S. Chand, New J. Chem., 38, 4922-4930, 2014; (b) Z. B. Liu, Y. -F. Xu, X. -y. Zhang, X. -L. Zhang, Y. -S. Chen and J. -G. Tian, J. Phys. Chem. B 113, 9681-9686, 2009.
4. R. Kumar, S. Naqvi, N. Gupta, K. Gaurav, S. Khan, P. Kumar, A. Rana, R. K. Singh, R. I. Bharadwaj and S. Chand, RSC Adv., 2015, 5, 35893-35898.

Reduced graphene oxide supported yolk type Ag@Cu₂O core-shell nanoparticles as a highly efficient multifunctional photocatalyst

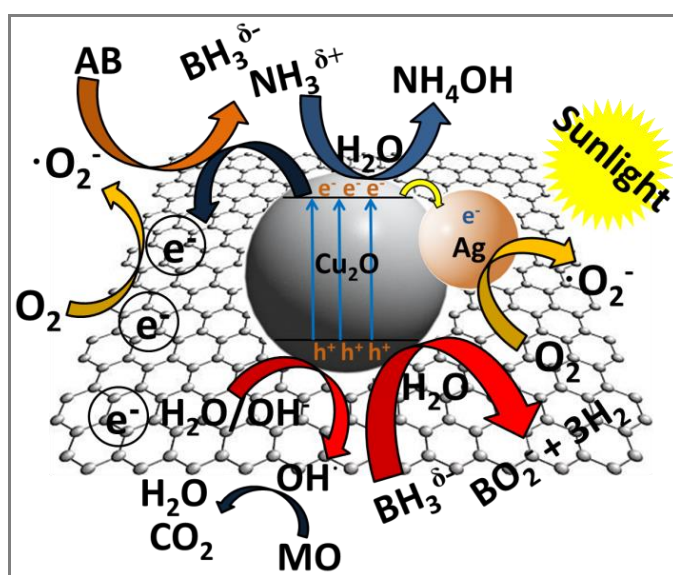
Mukesh Kumar, Sasanka Deka*

Ph.D. student, New Delhi, 110007, India

*Corresponding author. Fax: (+) 91-11-27667206;
E-mail: sdeka@chemistry.du.ac.in; ssdeka@gmail.com



Table of contents



Schematic illustration of photocatalytic charge separation, dye degradation and AB hydrolysis

ABSTRACT

Cu₂O is one of the important p-type semiconductor having nontoxicity, large abundance, low cost and have a narrow band gap (~2.0-2.2 eV) which matches well with solar visible spectrum and hence act as a visible light photocatalyst. However quantum efficiency of Cu₂O photocatalyst can be enhanced by making a hybrid material with noble metal which will decrease the electron hole pair recombination rate and enhance the light harvesting property of nanomaterials. In present work, yolk type Ag@Cu₂O core-shell hybrid nanostructures were insitu synthesized on graphene sheets for the first time under one pot mild reaction conditions. Nanocomposites were well characterized by XRD, TEM, HRTEM, FTIR, RAMAN and XPS techniques. Moreover the present nanocatalysts showed complete degradation of environmentally polluting methyl orange (MO) dye with 0.167 min⁻¹ apparent rate constant (k_{app}) in direct sunlight just in 20 minutes. Recently AB has drawn attention as a hydrogen reservoir due to high hydrogen capacity (19.6 wt %), good stability and non-toxicity. The catalytic activity of Ag@Cu₂O/RGO nanohybrids was further studied in hydrolysis of AB at 25±2 °C which showed much enhanced photocatalytic H₂ production compared to dark conditions with a rate of 514.28 mmol h⁻¹g⁻¹. This enhanced activity of present nanocatalyst can be ascribed to better charge separation resulting easy generation of radical species under ambient conditions.

Keywords: Cu₂O-Ag nanoparticles, nanocomposites, Ammonia borane hydrolysis, photocatalytic dye degradation;

Acknowledgements

MK thanks CSIR-India for providing research fellowship. SD thanks DST-DAAD. We thank SAIF-AIIMS and USIC, DU for instrumentation facility.

Reference

1. M. Kumar and S. Deka, *ACS Applied Materials & Interfaces*, 2014, **6**, 16071-16081.
2. P. Kush, K. Deori, A. Kumar and S. Deka, *Journal of Materials Chemistry A*, 2015, **3**, 8098-8106.

Effect of graphene on proton conductivity of B2SA grafted PVA-TEOS hybrid membrane for Fuel cell applications

Monisha R Tungal¹, Ashok M Sajjan^{*2}, Nagaraj R Banapurmath^{**2}.

¹ Automobile Engineering (7th sem), B.V.Bhoomaraddi College of Engineering and Technology, Hubli, 580032, India..

² Centre for Material Science, B.V.Bhoomaraddi College of Engineering and Technology, Hubli, 580032, India.

^{**}Corresponding author. Tel: (+91) 9880726748; E-mail: nr_banapurmath@bvb.edu



ABSTRACT

Proton exchange membrane fuel cells (PEMFC) is a promising energy source as they have high power density and good energy efficiency per unit volume. Graphite because of its corrosion resistance, electronic mobility and ballistic transport, is the preferred material in the fuel cell application. Thermo-chemical method is utilized to synthesize the polymer membrane. In order to achieve this, a Benzaldehyde 2 sulphonic sodium salt acid (B2SA) grafted with Poly Vinyl Alcohol(PVA) – Tetra Ethyl Ortho Silicate (TEOS) hybrid membrane was developed using casting technique by varying different mass percentage of TEOS in Polymer matrix. Graphene is embedded with this composition for better proton conductivity. Crosslinking in membranes was achieved by addition of TEOS. Developed membranes were subjected to spectroscopic and thermal investigations using FTIR, TEM, WXD, DSC, TGA and SEM. Effect of grafting was observed through swelling and conductivity of the membranes.

Keywords: Graphene ; Hybrid membrane ; B2SA ; Proton exchange membrane; Fuel cell application ;

Development of Functionalize Graphene – PDMS Nanocomposite Materials for Flexible Electronics and MEMS applications

Gunda Rajitha^{1*} and Raj Kishora Dash^{1**}

*1School of Engineering Sciences and Technology, University of Hyderabad,
Hyderabad, TS, India, 500046*

* Tel: +91 9985878458; E-mail: gundarajitha2006@gmail.com

**Tel: 040-2313-4460 ; E-mail: rkdse@uohyd.ernet.in



ABSTRACT

Polydimethylsiloxane (PDMS) are excellent materials for development of sensors, flexible electronics, MEMS devices due to their properties such as good flexibility, thermal stability, electrical resistance and dielectric strength due to the cross-linking density and degree of polymerization [1]. However due to their poor electrical properties such materials are not utilized for these applications. Now a days due to the development of nanomaterials such as nanoparticles, nanorods, CNTs, and graphene, such highly conductive nanomaterials filled polymer matrix composites are a rapidly developing field in switchable and flexible microelectronics technology [2, 3]. Out of several nanomaterials, graphene, a two-dimensional, single-atom-thick structure of sp² bonded carbon atoms are more promising material and has attracted tremendous research interest due to their excellent reinforcement, electrical properties, unique physical characteristics and high mechanical properties [4]. Hence, development of polymer nanocomposite based on such 2D nanomaterials can significantly improve the polymer electrical and mechanical properties for several applications such as in MEMS, NEMS, flexible electronics devices, anti-static materials, electromagnetic interference (EMI) shielding, chemical sensor, actuators and bipolar plates for fuel cells etc. [5].

However, still graphene cannot be uniformly dispersed in PDMS matrix due to agglomeration and formation larger aggregates of reduced graphene oxide (rGO) and therefore, the properties of such nanocomposite are degraded. The main focus of this research is to develop a functionalized rGO in PDMS based nanocomposite. In this present paper, we will discuss the fabrication of more uniform f-graphene-PDMS (Polydimethylsiloxane) nanocomposites by using different functionalized rGO dispersed in PDMS matrix. The morphology, structure, bonding characteristics were analysed by using AFM, FESEM, TEM, XRD and Raman spectroscopy for formation of more uniform f-graphene-PDMS nanocomposite. Finally, the effects of different functionalized methods to obtain more uniform f-rGO/PDMS nanocomposite on the structure, morphology and properties will be presented.

Key words: Nanocomposite, Graphene, PDMS, Flexible electronics, MEMS.

Reference

1. S. Sagar, N. Iqbal et. al., J. of Physics: Conference Series 439 (2013), 12024.
2. G. Eda and M. Chhowalla, Nano Letters, (2009), 9,2, 814-818.
3. S. H, Xie and et. al., Applied Physics Letters, **92**, 243121, 2008.
4. Liqiang Ren and et al., Smart Mater. Struct. 21 (2012) 105032.
5. Sasha Stankovich¹, Dmitriy A. Dikin et al., Nature, Vol. 442, 2006.

Green, economical, and scalable method for the preparation and transfer of high quality graphene

R. Brajpuriya^{1*}, T. Dikonimos², F. Buonocore² and N. Lisi²

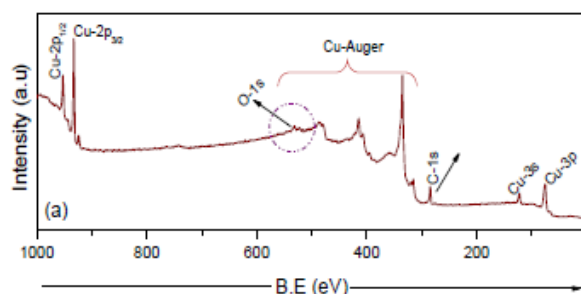
¹Department of Physics, Amity University Haryana, Manesar-122413, Gurgaon, India

²Surface Technology Laboratory, Materials Technology Unit, Casaccia Research Centre, ENEA, 00123 Roma, Italy

**Corresponding author. Tel: (+91) 8527769007; E-mail: ranjeetbjp@yahoo.co.in



Table of contents



XPS survey scans of graphene film grown on Cu foil.

ABSTRACT

Since the first report of the noteworthy features of graphene, two dimensional sheet of hexagonally arrayed sp^2 hybridized carbon atoms, the research areas of graphene has progressed exceedingly from the field of fundamental physics to the low-cost flexible transparent electronics, photovoltaics, or microelectronics devices [1-6]. These properties derive from graphene's unique electronic band structure and arrangement and symmetry of carbon atoms. However, for graphene to attain these promises and become a material for the large-scale electronic device, the sustainable fabrication of low cost, large-area, high-quality graphene on substrates susceptible to electrical device operation is needed, which is still a significant challenge. The key to solving this challenge requires us to develop synthesis and transfer methods to employ in the fabrication and the transfer of single layer graphene films with an optimal degree of control. Here we report on the growth and transfer of uniform and continuous large-sized thin-films composed of single- and few-layered graphene. The foils were grown by chemical vapor deposition (CVD) on polycrystalline copper (Cu) foils at low pressure using ethanol and were transferred onto the destination substrates using a cyclododecane supporting layer. Structural and optical characterizations indicate that the graphene films are composed of single or few layers depending on the growth conditions and exhibit low defect density. The graphene films can be transferred to arbitrary substrates with the help of a green transfer method based on an organic molecule, cyclododecane.

Keywords: Graphene; CVD; cyclododecane;

Acknowledgements

The author (R. B) would like to acknowledge ENEA for providing the International Research Fellowship.

5. A. Capasso, et. al., *Applied Physics Lett.* **105**, 113101 (2014).

6. X. Liang, et. al. *ACS Nano*, **5**, 9144 (2011).

Reference

1. K. S. Novoselov, et. al., *Science*, **306**, 666 (2004).
2. N. Tombros, *Nature*, **448**, 571 (2007).
3. G. Faggio, et. al., *J. Phy. Chem. C*, **117**, 21569 (2013).
4. X. Li, et. al. *Science*, **324**, 1312 (2009).

A review of graphene sheets: properties and applications

Karamveer Singh¹, Milanpreet Kaur², Simreet Kaur³, Harmandeep Singh⁴, Paras Dogra⁵

¹karamveersandhu132@gmail.com, ²mkb1313@yahoo.com, ³simreetsandhu8@gmail.com,

⁴harmanbhangu84@gmail.com, ⁵parasdogra21@gmail.com

^{1,2,3,4,5}Guru Nanak Dev University

G.T Road, Amritsar, Punjab-143001

Abstract: In this paper we present a review work on graphene sheet. Graphene is mainly one atom-thick layer of carbon atoms arranged in a hexagonal lattice. The review work has been divided into three parts. First, the preparation procedure of graphene sheets is discussed. Second, the properties of three types: single layer, bi-layer and few layer graphene are explained. Third, the various applications of graphene sheets have been mentioned. Two main applications: Graphene as Field Effect Transistor and transparent electrodes elucidated in this review paper.

Keywords: Graphene, carbon,

RGO-AuNP electrodeposited interdigitated chain electrode for cell growth analysis

Ajay Kumar Yagati^{1,2}, Jinsoo Park², Alexandra Zakharova¹, Sungbo Cho^{1,2}**

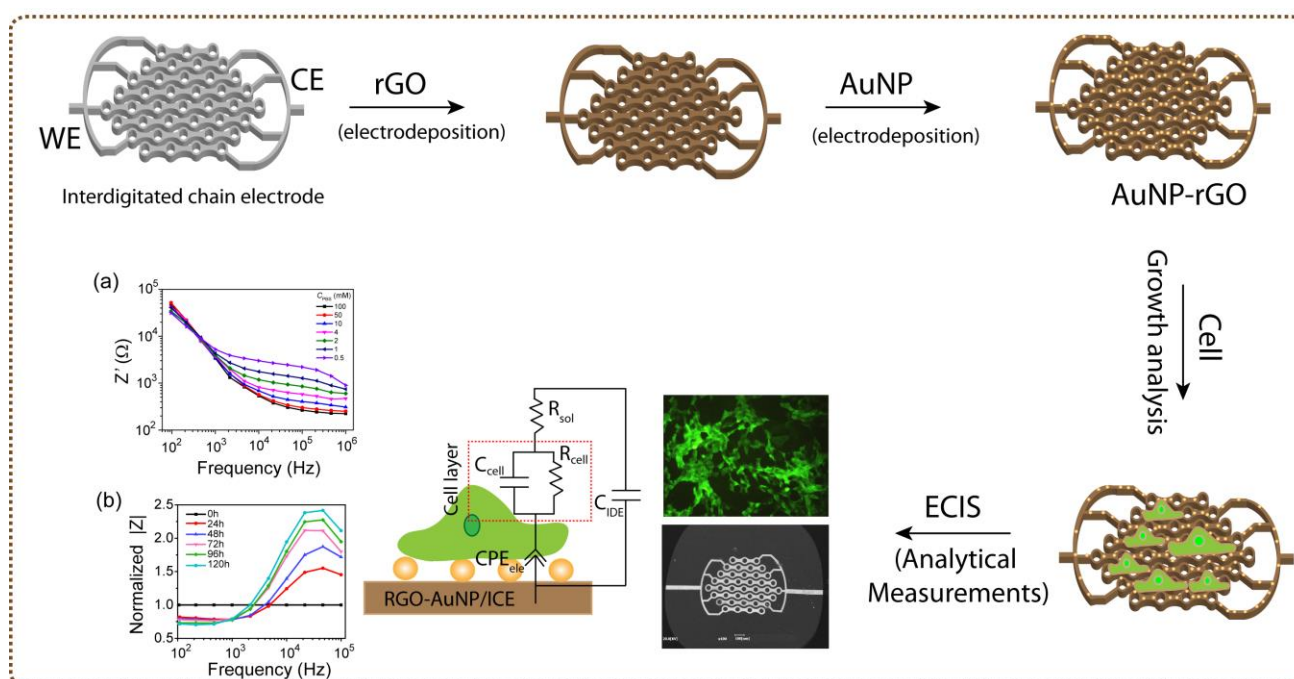
¹ Department of Biomedical Engineering, Gachon University, 191 Hambakmoe-ro, Yeonsu-gu, Incheon, 21936, Republic of Korea

² Gachon Advanced Institute for Health Science & Technology, Gachon University, 155 Get-Pearl-ro, Yeonsu-gu, Incheon, 21999, Republic of Korea

**Corresponding author. Tel: (+82) 328204433; Fax: (+82) 328204449; E-mail: sbcho@gachon.ac.kr



Table of contents



Schematic representation for the formation of reduced graphene oxide-Au nanoparticle deposited interdigitated electrode for electrical cell substrate impedance monitoring and its characterization.

ABSTRACT

Investigation of a particular type of cells can provide valuable information about related diseases in human body. Therefore, it is necessary to evaluate the properties of various type cells for developing early cancer diagnosis and therapy systems. In the present work, we demonstrate the development of reduced graphene oxide (RGO)-gold nanoparticle (AuNP) modified interdigitated chain electrode (ICE) for real time impedance monitoring of HEK 293 cells. Indium tin oxide (ITO) based ICE electrodes on glass substrate were fabricated through standard electrode fabrication methods and their deposition of RGO and AuNP was achieved by electrochemical deposition on both arms of ICE. The developed RGO-AuNP/ICE morphology was characterized by using scanning electron microscopy (SEM). The SEM analysis clearly showed that, RGO-AuNP hybrid nanocomposite layers are well formed on ICE electrode without causing any damage to the ICE structure. The impedance measurements were performed on each

deposition process to evaluate the conductivity of the electrode and found that the impedance was decreased 10 fold after deposition with composite material on ICE electrode. The electrical characteristics of the fabricated circular ICE and subsequent depositions were modeled as an equivalent circuit, and the values of the circuit parameters extrapolated from the fitting to the measured spectra in different concentrations of PBS were analysed. Electrical cell substrate impedance sensing (ECIS) was performed to achieve the cellular behavior such as adhesion, spreading and proliferation on the fabricated RGO-AuNP/ICE electrode. During cell growth the normalized impedance ($|Z|$) was increased and the maximum change in $|Z|$ was occurred at 24 kHz was found to be linearly increasing with increasing number of cells on the RGO-NP/ICEs. In comparison with the bare ICE, the deposited ICE showed higher sensitivity of $|Z|$ and provided biocompatible environment during cell growth analysis. Furthermore, the fluorescence imaging of cellular growth also confirmed that the proliferation of cells were high at modified ICE electrode in comparison with cells on bare ICE electrode. Therefore, the proposed sensor is feasible for label-free and real-time measurements of the various cell based applications in cancer diagnostic systems.

Keywords: graphene oxide; nanoparticle; interdigitated electrode; cell growth; impedance spectroscopy.

Acknowledgements

The work was supported by the National Research Foundation of Korea (No. 2015-022008, 2015-037739) and by the Korean Ministry of Trade, Industry & Energy (Industrial Convergence Promotion Business No. 10053803).

Reference (Not more than 5, please follow the below reference style if any).

1. G.H. Lee, J.C. Pyun, S. Cho, *J.Nanosci.Nanotechnol.*, 14(11), 8342-8346, **2014**.
2. T.B. Tran, S. Cho, J. Min, *Biosens. Bioelectron.*, 50, 453-459, **2013**.
3. A.K. Yagati, J.C. Pyun, J. Min, S. Cho, *Bioelectrochemistry*, 107, 37-44, **2016**.
4. A.K. Yagati, J. Min, S.Cho, *J. Electrochem. Soc.*, 161(14), G133-G140, **2014**.

Estimation of work function of thin layer graphene by probing with EFM

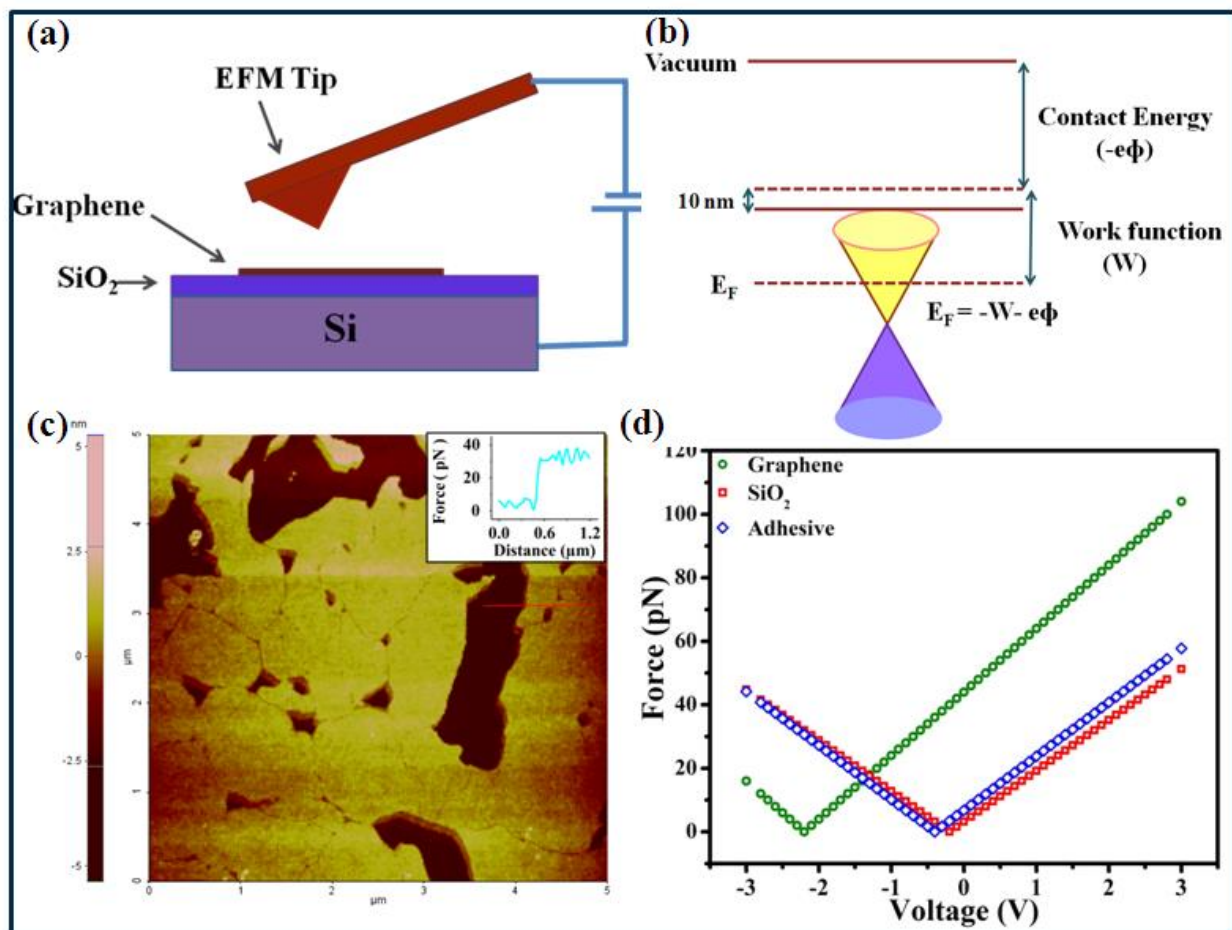
Anshika Singh¹, Amrish K. Panwar¹, Pawan K. Tyagi^{1*}

¹Department of Applied Physics, Delhi Technological University, Delhi, 110002

**Corresponding author: Tel:+91-11-27852212; Fax: +91-11- 27871023 E-mail address: pawan.phy@dce.edu (Pawan K Tyagi)



Table of contents



(a) Schematic of Electrostatic force microscopy, (b) Energy band diagram, (c) AFM topography and electrostatic force distance curve at -1 V tip sample voltage along the red line in topography image and (d) Electrostatic Force experienced by EFM tip as a function of tip sample voltage.

ABSTRACT

Graphene, a two dimensional sheet of carbon atoms has all the atoms at the surface. Due to un-saturated π -bonds and dangling bonds, electronic property of graphene is easily affected by unwanted adsorbed atoms. Electrostatic Force Microscopy (EFM) has been demonstrated as an appropriate tool to probe the work function. In present study, EFM is used to probe the work function of pristine few layer graphene (FLG) transferred on SiO₂ (300nm)/Si (500 μ m) substrate. FLG has been prepared by using the mechanical exfoliation technique. In our EFM measurement, a two pass scan is proceed in which first the topography is recorded in non-contact mode then the EFM tip is lifted to some height in order of nanometer and a bias is applied to tip and Si substrate. The electrostatic force between EFM tip and graphene layer changes according to the potential difference between them. The potential which minimize the electrostatic force represent the contact potential and determines work function of the graphene layer. The presence of adhesive residues left from scotch tape on graphene and SiO₂ substrate also modifies this work function which is due to the deposition of dipoles on the surface. Detailed analysis has been performed taking into account the effect of adhesive for comparison and precisely estimated the value observed from probing. The work function of FLG has been calculated from the analysis to be 4.58eV.

Keywords: Electrostatic Force Microscopy, surface potential, few layer graphene, mechanical exfoliation.

Reference

1. J. Moser, A. Verdaguer, D. Jimenez, A. Barreiro, A. Bachtold, *Applied Physics Letters*, 92(12), 123507-1-3, **2008**.
2. P Bergveld, J Hendrikse ,W Olthuis, *Measurement of Science And Technology*, 9(11), 1801–1808, **1998**.

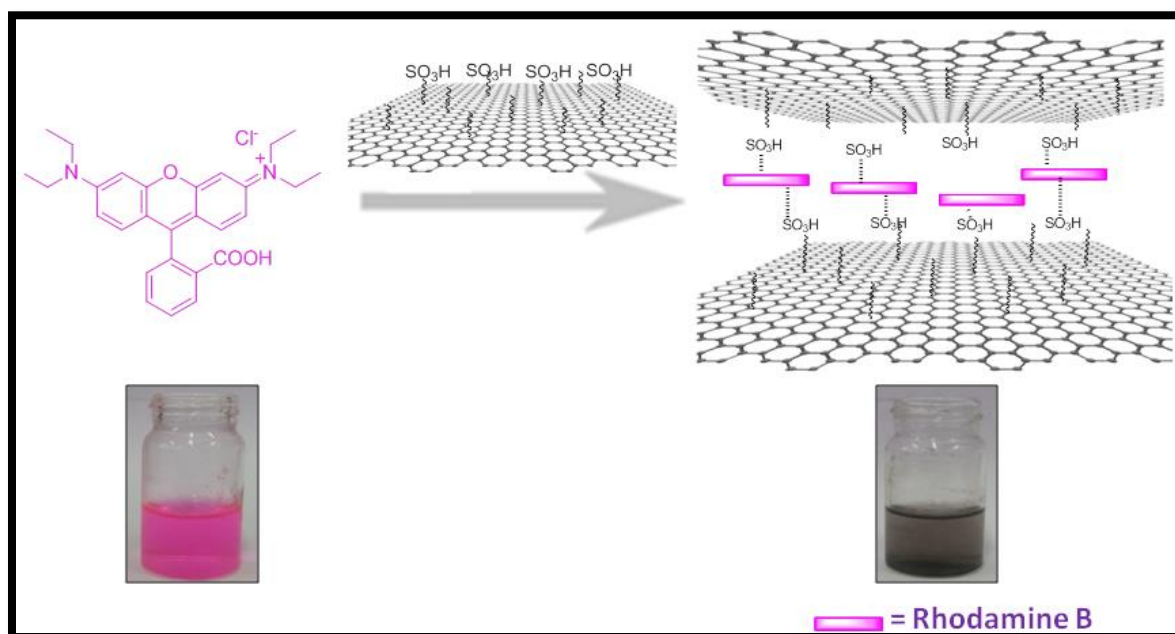
Sulphonated graphene – an efficient catalyst for waste water treatment

Smriti Arora¹, Ritika Nagpal, SMS Chauhan^{}**

¹ *Bioorganic Laboratory, Department of Chemistry, University of Delhi, Delhi-110 007, India*
Fax: +91-11-27666605; Tel: +91-11-27666845; E-mail: smschauhan@chemistry.du.ac.in



Table of contents



SGO composite material for wastewater treatment as well as removal of harmful dye

ABSTRACT

Nowadays, toxic organic dyes and their effluents have become one of the main sources of water pollution because of the greater demand in industry. Many semiconductors, such as TiO_2 , Ti_2O , ZnO , CdS , ZnS and Ag_3PO_4 can act as photocatalyst to decompose organic pollutants in waste water. However, they are not applied into practice because of such disadvantages or drawbacks as toxicity or low efficiency. There is an urgent need to develop highly efficient and environmentally friendly catalyst to degrade organic pollutants. Novel materials such as graphene enhance the degradation efficiency because of its large surface area and high intrinsic electron mobility. We report on a fast, sensitive, label-free, and general dye-sensor platform for synthetic organic cationic dye detection on sulfonated graphene oxide (rGO) against rhodamine B dye. Sulphonated graphene SGO has been obtained by thermal sulphonation of reduced graphene oxide at 180°C under pressure in autoclave, which consists of hexagonal ring based carbon network with both sp^2 - and sp^3 -hybridized carbon atoms, bearing $-\text{SO}_3\text{H}$ groups on each side of graphene sheet. The presence of sulphonated groups render strong hydrophilicity and good dispersibility in water. Interestingly, the as-prepared catalytic material serves as a good catalyst for dye mixture, suggesting the potentially real applications of the SGO composite materials for wastewater treatment as well as the removal of harmful dyes. The dye removal process is followed using UV-Visible spectroscopy, while the material before and after dye removal has been characterized using physicochemical and spectroscopic techniques. Raman and FT-IR spectroscopic data yield information on the interactions of dyes with the material.

Keywords: Sulphonated graphene oxide; Rhodamine B dye; Waste water treatment

Acknowledgements

We are grateful to acknowledge the Council of Scientific and Industrial Research (CSIR), New Delhi, University Grants Commissions (UGC), New Delhi, for financial assistance and USIC, University of Delhi.

Reference

1. T. Jiao, H. Zhao, J. Zhou, Q. Zhang, X. Luo, J. Hu, Q. Peng, and X. Yan, *ACS Sustainable Chem. Eng.*, 3, 3130-3139, **2015**.
2. G.K. Ramesha, A. Vijaya Kumara, H.B. Muralidhara, S. Sampath *Journal of Colloid and Interface Science*, 361, 270-277, **2011**.
3. N. A. Travlou, G. Z. Kyzas, N. K. Lazaridis, and E. A. Deliyanni, *Langmuir*, 29 (5), 1657–1668, **2013**.

A Novel TM_{01} to TE_{11} Mode Converter Designed With Radially Loaded Dielectric Slabs

Ashish Chittora, *Graduate Student Member, IEEE*,
Sandeep Singh, Archana Sharma, and Jayanta Mukherjee, *Senior Member, IEEE*

Abstract—A novel linear shaped TM_{01} to TE_{11} mode converter having high efficiency and wide bandwidth is proposed. The design consists of a circular waveguide sectored by a horizontal metallic plate partition, and dielectric slabs radially attached in the lower semicircular waveguide. The mode converter is designed and simulated at an operating frequency of 3 GHz. A maximum bandwidth of 504 MHz (2.81–3.35 GHz) with conversion efficiency greater than 90% is achieved when three Polytetrafluoroethylene (PTFE/Teflon) slabs are placed radially in the mode converter. The mode converter was fabricated and experiments were performed with PTFE as the dielectric slab material. The mode conversion was verified by measuring the far-field radiation pattern. The proposed mode converter is symmetric, compact, linear, and easy to fabricate. It can be used for S-band high-power microwave applications where wide bandwidth of mode conversion is required.

Index Terms—Dielectric materials, high-power microwaves (HPMs), mode converters, mode transducers, waveguide mode matching.

I. INTRODUCTION

HIGH-POWER microwave (HPM) sources emit axially symmetric modes (TEM or TM_{01}) as output, and cannot radiate the microwave power along the axis. Direct radiation of TM_{01} mode through horn antenna results in a minimum along the propagation axis (or boresight) at far-field distance. For efficient radiation there should be a maximum along the axis, hence it is necessary to convert the TM_{01} mode to TE_{11} mode before being launched into the free space. A mode converter is the device used for this purpose. Serpentine shaped mode converter designs (symmetric [1]–[5] and asymmetric [6]–[8]) have been extensively reported in the literature, but linearly shaped designs are more convenient in terms of compactness and ease of fabrication. Bandwidth of mode conversion is also an important factor due to the instability in the frequency of operation of the HPM sources [9]. A tapered baffle at the center of a linear

profile waveguide is reported in [10] for the mode conversion. There are no clearly defined intermediate modes in these mode converters.

In addition to the dual-bend mode converters, many linear shaped mode converters [11]–[13], [20] are reported and they employ intermediate modes (e.g., TEM , TE_{10} , and sectoral) for TM_{01} to TE_{11} mode conversion. In recent literature [13]–[21], a different approach, based on 180° phase shift in half of the TM_{01} mode pattern, is reported for mode conversion. Metallic plates of different lengths are loaded in [13]–[16] to provide the phase shift for TM_{01} – TE_{11} (circularly polarized) mode conversion. A dielectric lens at the end of a horn is employed in [17] and [18] for the mode conversion and gives TE_{11} (circularly polarized) as the output mode. A metallic photonic crystal loading is used in one half of the waveguide for the mode conversion [19]. A cross-shaped mode converter is reported in [20], which employs rectangular waveguide sections of different path lengths around the center conductor to convert the modes. The output is a circularly polarized TE_{11} mode. Uniform loading of the dielectric in the lower part of the coaxial section of waveguide for mode conversion is also reported in [21].

The mode converter proposed in this paper is a novel and compact solution for HPM applications (designed at 3 GHz), which require a linear profiled mode converter for compactness and wide bandwidth of mode conversion. In Section II, design and configuration of the proposed mode converter is explained along with the principle of operation. In Section III, simulation and experimental results are presented in detail.

II. DESIGN AND CONFIGURATION

The mode pattern of the TM_{01} mode consists of a radially diverging electric field (E_r) from the waveguide axis towards the wall. A phase shift of 180° in one half section of the TM_{01} mode pattern with respect to the other half section, results in a TE_{11} -like mode pattern [13], [21]. The dielectric slab loading is an effective way to provide the phase shift in a waveguide [22], [23]. A similar concept of dielectric slab or septum loading for phase shift is also reported in [24] and [25] to design a circular waveguide (CWG) polarizer. A CWG is partitioned with a metallic plate into two halves or semicircular waveguides (SWGs). Placing the dielectric slab in one SWG section (in our case, the lower one) with the slab plane parallel to the radial electric field (E_r) will result in strong perturbation in the propagation constant (β_d) of the lower SWG. On the other hand, there is no change in the propagation constant (β_0) of the upper SWG, as there is no dielectric loading in the upper half. Let the length traveled by the wave in upper and lower SWGs be L_0

Manuscript received May 16, 2015; revised August 11, 2015 and January 08, 2016; accepted February 13, 2016. This work was supported by the Board of Research in Nuclear Sciences (BRNS), Board of Research in Nuclear Sciences (DAE), Department of Science and Technology (DST), Indian Space Research Organisation (ISRO), and Tata Center, Indian Institute of Technology (IIT) Bombay.

A. Chittora and J. Mukherjee are with the Department of Electrical Engineering, Indian Institute of Technology Bombay, Powai, Mumbai 400076, India (e-mail: ashish.chittora22@gmail.com).

S. Singh and A. Sharma are with the Accelerator and Pulse Power Division (APPD), Bhabha Atomic Research Centre (BARC), Mumbai 400085, India.

Color versions of one or more of the figures in this paper are available online at <http://ieeexplore.ieee.org>.

Digital Object Identifier 10.1109/TMTT.2016.2536031

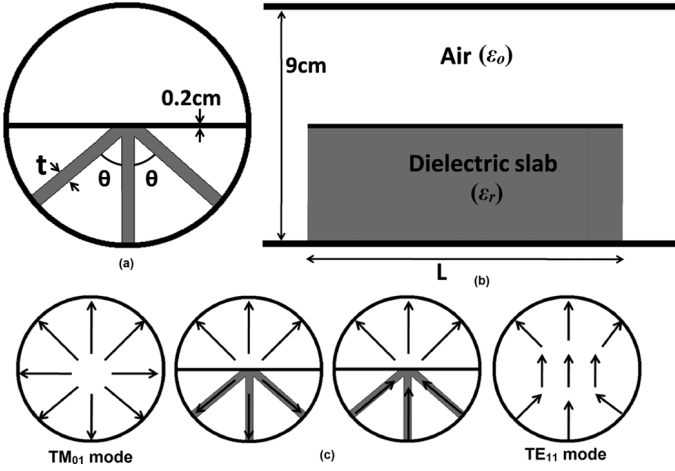


Fig. 1. Design of the proposed mode converter with three dielectric slabs: (a) front view, (b) side view, and (c) process of mode conversion.

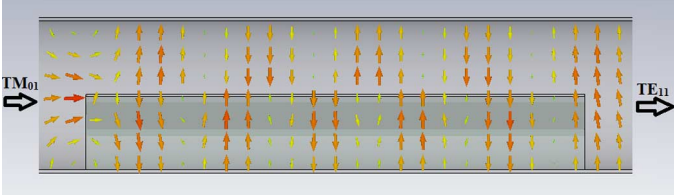


Fig. 2. Propagation of E -field through the mode converter.

and L_d , respectively. If the length ($L_0 = L_d = L$) of the dielectric slabs is chosen such that 180° phase shift is provided in the lower SWG with respect to the upper SWG, then the electric field lines will meet in phase at the end of the metallic partition (or SWG section). The output will be a TE_{11} like mode of the CWG, as shown in Figs. 1(c) and 2. If the lower SWG is loaded with symmetrically placed dielectric slabs of dielectric constant ϵ_r , then the length L of the mode converter section (or dielectric slabs) can be calculated using the following relation:

$$L = \frac{\pi}{(\beta_d - \beta_0)}. \quad (1)$$

The input CWG- TM_{01} mode is divided by metallic partition into two halves and enters into upper and lower SWGs as out-of-phase SWG- TE_{11} modes. Dielectric slabs of length (L), calculated from (1), in the lower SWG provides the necessary phase shift of 180° for mode conversion. Since the lower SWG is inhomogeneously filled with the dielectric, the propagating wave does not retain its pure TE character and takes the form of a hybrid mode. The hollow SWG- TE_{11} mode is one half of the pattern of the hollow CWG- TE_{11} mode, and the propagation constant of the two modes are equal [26]. With the increase in the number of slabs in the lower SWG, the effective dielectric constant and the propagation constant (β_d) of the lower SWG also increases and, therefore, the length (L) calculated from (1) decreases. This effect and corresponding results are discussed in Section III.

III. SIMULATIONS AND EXPERIMENTAL RESULTS

The parameters that affect the performance of the proposed mode converter are the number, length, thickness, mutual orien-

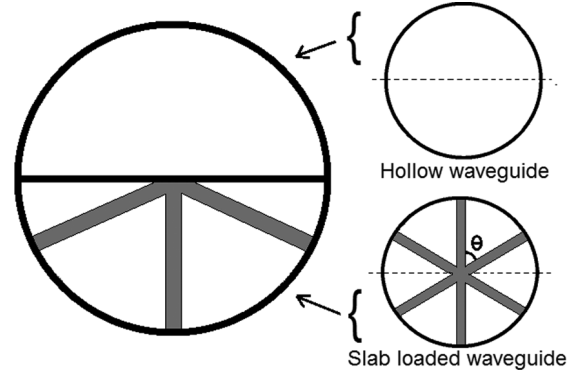


Fig. 3. Configuration of the mode converter from hollow and dielectric slab (symmetrically) loaded waveguide sections.

tation (angle θ), and material of the dielectric slabs. The mode conversion efficiency (defined as $|S_{21}|^2$), bandwidth, reflection at input port, and power-handling capability are the measures of performance of the mode converter. The proposed mode converter is designed and simulated in CST Microwave Studio at the operating frequency of 3 GHz. Diameter of the CWG is taken as 9 cm so that only the first two modes (TE_{11} and TM_{01}) can propagate through the waveguide and the next higher modes are attenuated [27]. A metal plate of thickness 0.2 cm is inserted horizontally to divide the CWG into two SWGs, as shown in Fig. 1. Dielectric slabs of PTFE/Teflon ($\epsilon_r = 2.1$), each of thickness $t = 0.5$ cm, are placed radially in the lower SWG. Due to the mathematical difficulties in obtaining an exact theoretical solution of the proposed design, the propagation constant of the dielectric slab loaded lower SWG is calculated at 3 GHz using the time-domain solver of CST Microwave Studio. With an increasing number of slabs, the fraction of dielectric in the lower SWG increases, which results in smaller length of the mode converter according to (1). The corresponding length (L) of the slabs is calculated using (1) and simulations are performed for the mode converter design.

A. Effect of the Number of Dielectric Slabs

A dielectric slab in a waveguide introduces phase shift in the propagating E -field components parallel to the slab plane, as in the case of polarizer design [25]. The TM_{01} mode has an azimuthally symmetric E -field equally distributed in the azimuth direction. The dielectric slab loaded in the lower SWG in the proposed mode converter can be considered as the one half taken from a CWG symmetrically ($\theta = 360^\circ/2N$) loaded with N -dielectric slabs, as shown in Fig. 3. The propagation constant of the slab loaded waveguide is higher than the hollow waveguide. Using (1), the appropriate length of the slab loaded waveguide section can be calculated to design the mode converter.

The effect of the number of slabs in the lower half of the mode converter is presented in Table I and Fig. 4. In the final design, the number of slabs is chosen taking into consideration the mode conversion bandwidth, maximum efficiency, compactness, dielectric losses, and ease of fabrication.

Maximum mode conversion efficiency (98.9%) and bandwidth (2.81–3.35 GHz) is observed with three slabs (and angle

TABLE I
EFFECT OF THE NUMBER OF SLABS ON MODE CONVERSION BANDWIDTH

Number of slabs (N)	Angle ($\theta=360^\circ/2N$)	Prop. constant β_d (rad/m)	Length L (cm)	Bandwidth (MHz)	Maximum Efficiency
One	-	52.96	60.41	440	98.1%
Two	90°	54.48	46.74	460	98.7%
Three	60°	57.43	32.48	504	98.9%
Four	45°	60.00	25.67	501	97.2%
Five	36°	62.87	20.79	580	98.4%

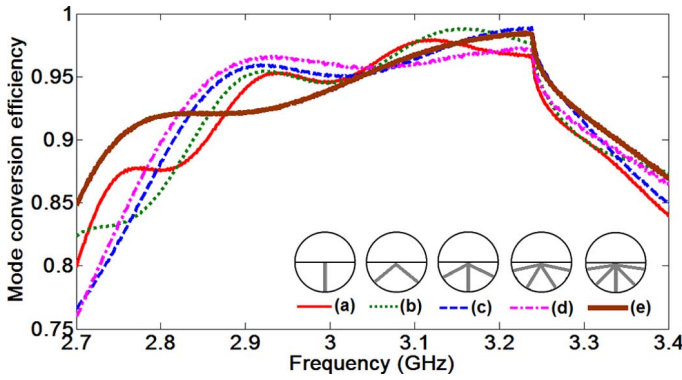


Fig. 4. Effect of the number of dielectric slabs on the simulated mode conversion efficiency.

60° between them) in the lower half of the mode converter, therefore triple slab loading is used in the fabricated design of the mode converter. The corresponding simulated insertion loss is below 0.5 dB in the operating bandwidth.

B. Simulation and Experiment With Triple PTFE-Slabs Loading

PTFE/Teflon is chosen as the slab material with angle $\theta = 360^\circ/(2N) = 60^\circ$ between the consecutive slabs ($N = 3$). Propagation constants are calculated at 3 GHz separately for the hollow and slab loaded SWGs as $\beta_0 = 47.76$ rad/m and $\beta_d = 57.43$ rad/m, respectively. Using these values in (1), the longitudinal length of dielectric slabs is calculated to be $L = 32.48$ cm. The conversion efficiencies from the input TM₀₁ mode to different modes for the optimized mode converter are shown in Fig. 5. It is observed that efficiency of transmission of the TM₀₁ mode and conversion to the TE₂₁ mode are less than 0.02% and 0.01%, respectively, in 2.81–3.35-GHz band. Thus, there is little possibility that the TE₂₁ mode will be generated at the output. On the other hand, the TE₂₁ mode may be excited at the input side and contaminate or transmit through the mode converter. Therefore, for the mode converter to work properly, the input mode should be a pure TM₀₁ mode. The monotonic decline after the discontinuity (at 3.24 GHz) in the TM₀₁–TE₁₁ conversion efficiency is due to the increase in conversion and transmission to TE₂₁ and TM₀₁ modes, respectively.

The size (length and diameter) and bandwidth of the proposed mode converter is compared with the reported work in the literature and summarized in Table II. The first reference (Lee *et*

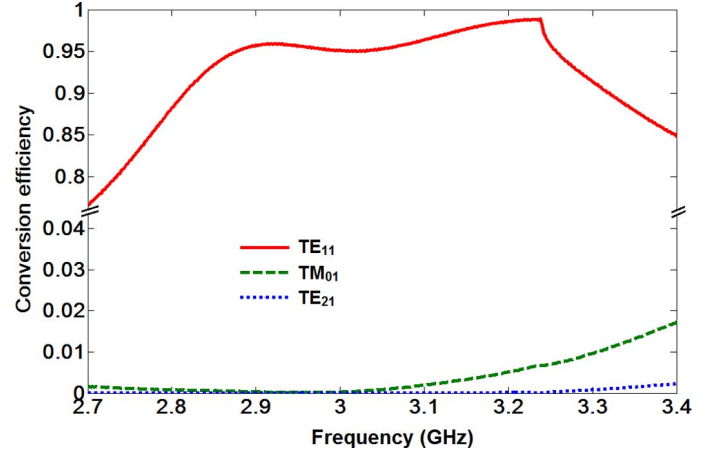


Fig. 5. Simulated conversion efficiency of the mode converter for TM₀₁ mode as the input excitation signal.

TABLE II
COMPARISON OF TM₀₁–TE₁₁ MODE CONVERTERS

Paper	Length λ	Diameter λ	Bandwidth	High Power Capability
Lee <i>et al.</i> [2]	6.66	3.06 ^s	33%	GW level
Eisenhart [11]	2.75	1.33	30.0%	5 MW
Yuan <i>et al.</i> [13]	2.53	1.14	10.0%	GW level
Yuan <i>et al.</i> [14]	4.67	1.73	12.5%	N.P. [#]
Yuan <i>et al.</i> [15]	2.06	1.02	Narrowband	2.4 GW
Yuan <i>et al.</i> [16]	2.95	1.06	11.7%	N.P. [#]
Jung <i>et al.</i> [18]	0.91	16.66	Narrowband	GW level
Wang <i>et al.</i> [19]	1.20	1.16	4.1%	4.05 GW
Peng <i>et al.</i> [20]	-	1.01	18.6%	1.75 GW
Chittora <i>et al.</i> [21]	1.43	0.96	20.3%	0.2 GW
Chittora <i>et al.</i> [10]	2.32	0.96	9.1%	1.0 GW
P.S.* (3 slabs)	3.25	0.90	16.8%	0.3 GW
P.S.* (4 slabs)	2.57	0.90	16.7%	0.3 GW
P.S.* (5 slabs)	2.08	0.90	19.3%	0.3 GW

*Proposed structure, [#]Not provided, ^smaximum transverse length

al. [3]) in Table I is a dual bent waveguide mode converter and others are linear profile CWG mode converters.

The mode converter with optimized design parameters is fabricated with PTFE as the slab material, as shown in Fig. 6. Metallic parts of the mode converter are made of aluminium for light weight, low cost, and ease of fabrication. Low-power experiments are performed by exciting the input port with a TM₀₁ mode signal. To excite a narrowband TM₀₁ mode signal, a probe is applied at the axis of the waveguide input port [28]. In our case, the TM₀₁ mode excitation is needed over a wide bandwidth (2.5–4 GHz).

The TM₀₁ mode is generated for wide bandwidth by extending the center conductor of a coaxial line as a monocone [29], [30], as shown in Fig. 7(a). The simulated and measured S-parameters for the TM₀₁ mode feed are shown in Fig. 7(b). The TM₀₁ mode feed is applied at the input port of the fabricated mode converter to measure the reflection coefficient. The corresponding simulated and measured results are shown in

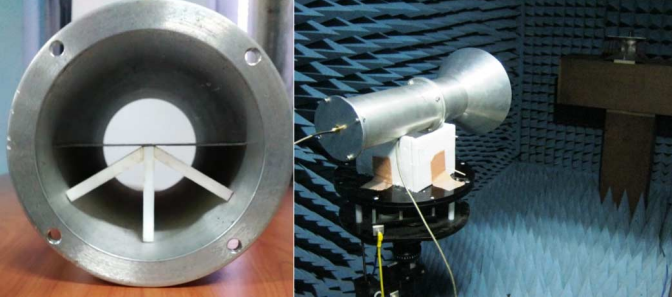


Fig. 6. Fabricated mode converter and radiation pattern measurement setup.

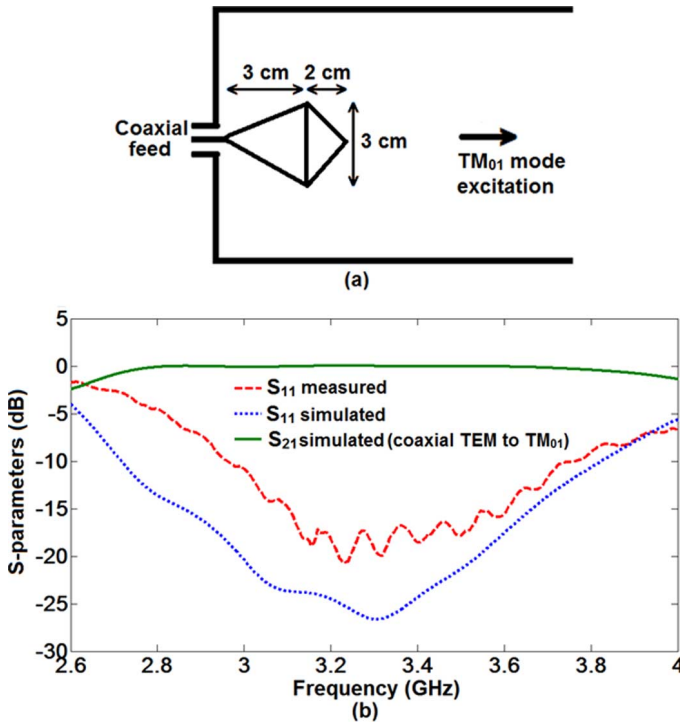


Fig. 7. (a) Monocone (with inverted cone on top) feed designed for TM_{01} mode excitation and (b) corresponding simulated and measured S-parameters.

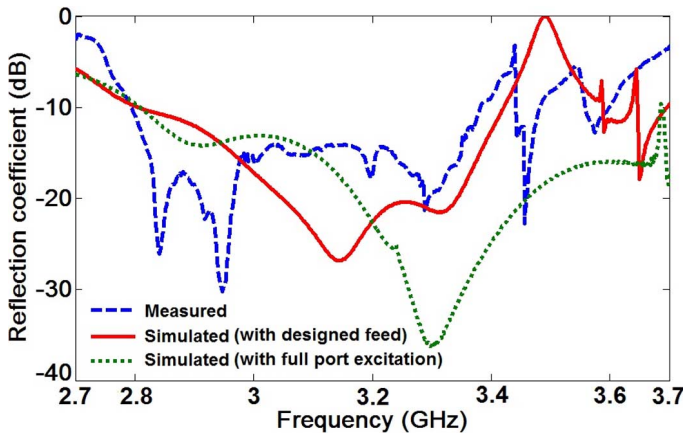


Fig. 8. Reflection coefficient at the input port of the mode converter.

Fig. 8. Both the simulated and measured reflection coefficients are below -10 dB over 2.80–3.38-GHz bandwidth.

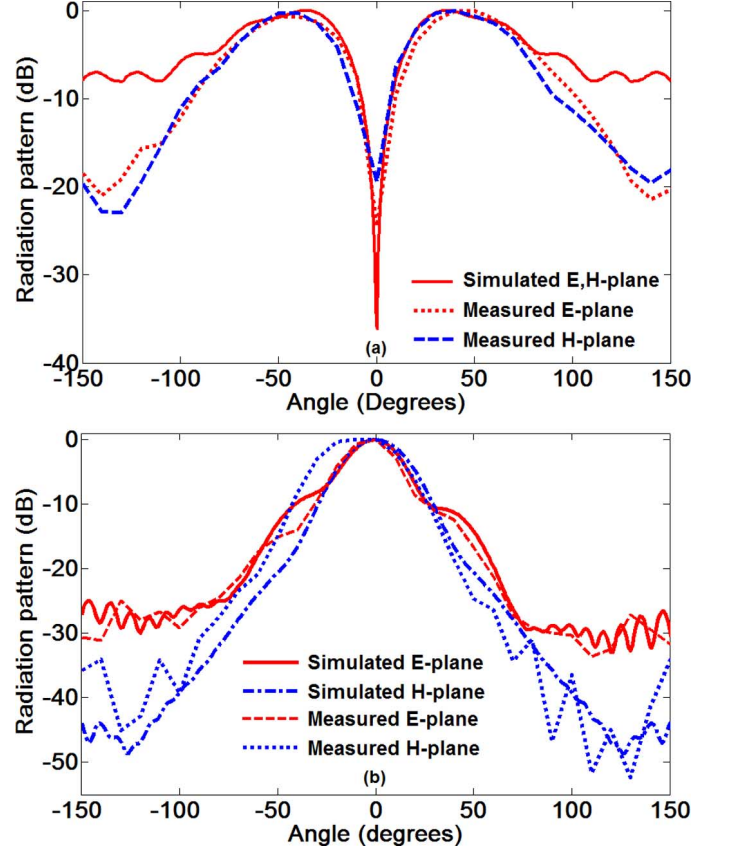


Fig. 9. Radiation pattern: (a) without mode converter section and (b) with mode converter section for input TM_{01} mode at the frequency of 3 GHz.

The mode conversion is verified by measuring and plotting the far-field radiation pattern [2]. First the TM_{01} mode feed is applied at the input of a hollow waveguide with a horn antenna and the radiation pattern is measured in an anechoic chamber. The measured radiation pattern has a minimum below -20 dB at the center, as shown in Fig. 9(a). The TM_{01} mode feed is then applied at the axis of the mode converter with a horn connected at the output, as shown in Fig. 6. The simulated and measured radiation patterns are shown in Fig. 9(b). A maximum is observed at the center of the radiation pattern, therefore it is verified that the input TM_{01} mode signal is successfully converted to the TE_{11} mode at the output aperture of the mode converter.

C. Power-Handling Capability and Dielectric Losses

Power-handling capability is calculated by exciting a megawatt-level microwave signal at the input port of the mode converter. If dry air at 1-atm pressure is used as a medium, maximum electric field inside the mode converter is 93 kV/cm on a metal surface and 20 kV/cm on a dielectric (PTFE) surface for the 100-MW input signal. These field values are within the breakdown limits of air and dielectric (PTFE), respectively [31]–[33]. Therefore, the proposed mode converter can be used in HPM systems [34]–[37], which require power-handling capability up to 100-MW peak power.

In order to improve the breakdown strength, an SF_6 medium can be used in the waveguide. This analysis is also performed and shown in Fig. 10. A maximum electric field of 195 kV/cm



Fig. 10. Simulated electric field inside the mode converter with SF_6 medium in place of air and the corresponding color map.

on the metal surface and 88 kV/cm on the dielectric surface is observed for 300-MW input power. The observed fields are smaller than the breakdown limits for the air and dielectric [31]–[33]. Therefore, using SF_6 instead of air as the medium in the mode converter increases the power-handling capability by almost three times. Other materials with high dielectric strength can also be used for the slab to improve the power-handling capability, while taking care of the tradeoff between bandwidth, breakdown strength, and compactness.

Dielectric loss is also an important factor to consider while using the dielectric in the waveguide as loading. These losses can vary with the frequency of operation, material type, dielectric constant, loss tangent, filling fraction, shape, and size. The advantages with dielectric loading are compactness and increased bandwidth [38]. Analysis of dielectric losses in a waveguide is reported in [39]. The loss tangent decreases as the frequency of operation is reduced. The loss tangent of PTFE (0.0002) is relatively smaller than other materials, e.g., Nylon (0.0027) and quartz (0.0004) for the frequency range of operation. The calculated attenuation factor is below 0.01 dB/cm due to the dielectric loading (assuming uniform PTFE loading). The dielectric losses are already taken into account in the simulated results (Figs. 4 and 5) for the mode converter. In the mode converter, dielectric loading is in the form of slabs and exists only in the lower SWG. The total length of the dielectric material ($L = 32.48$ cm) is also small, total dielectric losses will also be small and within an acceptable limit. Therefore, PTFE is a suitable choice for slab material due to its high power-handling capability and low dielectric losses.

IV. CONCLUSION

A novel design of a TM_{01} – TE_{11} mode converter with radial loading of dielectric slabs has been proposed in this paper. Analysis is presented for a different number of dielectric slabs for designing the mode converter. With an increase in the number of slabs, longitudinal length of the mode converter decreases. However, an optimum mode conversion efficiency and bandwidth is achieved in simulation when three dielectric slabs are used. The mode converter is fabricated with the loading of three PTFE slabs and experiments are performed to verify the mode conversion and input reflection coefficient. The mode conversion bandwidth is 16.8% at the operating frequency of 3 GHz and power-handling capability is up to 300 MW. The structure has aligned ports, is symmetric, is compact in terms of length (32.48 cm) and diameter (9 cm), and no bend is required in the waveguide. Therefore, it is easy to fabricate. Therefore, the proposed mode converter is useful for the HPM systems, where

wide bandwidth with a comparatively compact-linear structure is essential.

REFERENCES

- [1] W. S. Lee, K. S. Park, B. M. Lee, Y. J. Yoon, J. H. So, and W. Y. Song, “X-band TM_{01} – TE_{11} mode converter,” in *IEEE Antennas Propag. Soc. Int. Symp.*, 2004, vol. 2, pp. 1531–1534.
- [2] B. M. Lee, W. S. Lee, Y. J. Yoon, and J. H. So, “X-band TM_{01} – TE_{11} mode converter with short length for high power,” *Electron. Lett.*, vol. 40, no. 18, pp. 1126–1127, 2004.
- [3] S. H. Lee, B. M. Lee, J. Ahn, Y. J. Yoon, and J. H. So, “The design of X-band non-constant serpentine TM_{01} – TE_{11} mode converter with short length,” in *Proc. Asia-Pacific Microw. Conf.*, 2005, vol. 1, pp. 4–7.
- [4] C. W. Yuan, H. H. Zhong, and B. L. Qian, “Tri-bend TM_{01} – TE_{11} mode converter with input and output aligned on the same axis,” *High Power Laser Part. Beams*, vol. 18, no. 11, pp. 1864–1868, 2006.
- [5] Q. Zhang, C. W. Yuan, and L. Liu, “A dual-band coaxial waveguide mode converter for high-power microwave applications,” *Chin. Phys. Lett.*, vol. 28, no. 6, pp. 068401-1–068401-3, 2011.
- [6] G. S. Ling and J. J. Zhou, “Converters for the TE_{11} mode generation from TM_{01} vircator at 4 GHz,” *Chin. Phys. Lett.*, vol. 18, pp. 1285–1285, 2001.
- [7] G. S. Ling and J. J. Zhou, “Design of mode converters for generating the TE_{11} mode from TM_{01} vircator at 4 GHz,” *Int. J. Electron.*, vol. 89, no. 12, pp. 925–930, 2003.
- [8] K. S. S. Prasad, S. A. Singh, S. S. Shanmukha, R. Seshadri, and M. V. Kartikeyan, “Design of a TM_{01} – TE_{11} circular bend mode converter operating at 3 GHz,” in *IEEE Int. Vacuum Electron. Conf.*, 2011, pp. 177–178.
- [9] A. Roy *et al.*, “Oscillation frequency of a reflex-triode virtual cathode oscillator,” *IEEE Trans. Electron Devices*, vol. 58, no. 2, pp. 553–561, Feb. 2011.
- [10] A. Chittora, S. Singh, A. Sharma, and J. Mukherjee, “A tapered metallic baffle TM_{01} to TE_{11Y} mode converter with TE_{11X} mode transmission capability,” *IEEE Microw. Wireless Compon. Lett.*, vol. 25, no. 10, pp. 633–635, Oct. 2015.
- [11] R. L. Eisenhart, “A novel wideband TM_{01} to TE_{11} mode converter,” in *IEEE MTT-S Int. Microw. Symp. Dig.*, 1998, vol. 1, pp. 249–252.
- [12] A. Tribak, J. Zbitou, A. Mediavilla, and N. A. Touhami, “Ultra-broad-band high efficiency mode-converter,” *Progr. Electromagn. Res. C*, vol. 36, pp. 145–158, 2013.
- [13] C. W. Yuan, Q. X. Liu, H. H. Zhong, and B. L. Qian, “A novel TEM– TE_{11} mode converter,” *IEEE Microw. Wireless Compon. Lett.*, vol. 15, no. 8, pp. 513–515, Aug. 2005.
- [14] C. W. Yuan, H. H. Zhong, Q. X. Liu, and B. L. Qian, “A novel TM_{01} to TE_{11} Circularly Polarized (CP) mode converter,” *IEEE Microw. Wireless Compon. Lett.*, vol. 16, no. 8, pp. 455–457, Aug. 2006.
- [15] C. W. Yuan, Y. W. Fan, H. H. Zhong, Q. X. Liu, and B. L. Qian, “A novel mode-transducing antenna for high-power microwave application,” *IEEE Trans. Antennas Propag.*, vol. 54, no. 10, pp. 3022–3025, Oct. 2006.
- [16] C. W. Yuan and Q. Zhang, “Design of a TM_{01} – TE_{01} transmission line for high-power microwave applications,” *IEEE Trans. Plasma Sci.*, vol. 37, no. 10, pp. 1908–1915, Oct. 2009.
- [17] S. H. Min *et al.*, “Mode conversion of high-power electromagnetic microwave using coaxial-beam rotating antenna in relativistic backward-wave oscillator,” *IEEE Trans. Plasma Sci.*, vol. 38, no. 6, pp. 1391–1397, Jun. 2010.
- [18] H. C. Jung *et al.*, “Transmission of gigawatt-level microwave using a beam-rotating mode converter in a relativistic backward wave oscillator,” *Appl. Phys. Lett.*, vol. 96, 2010, Art. no. 131502.
- [19] D. Wang, F. Qin, S. Xu, and M. Shi, “A metallic photonic crystal high power microwave mode converter,” *Appl. Phys. Lett.*, vol. 102, no. 24, pp. 244107–244107-3, 2013.
- [20] S. Peng, C. Yuan, H. Zhong, and Y. Fan, “Design and experiment of a cross-shaped mode converter for high-power microwave applications,” *Rev. Sci. Instrum.*, vol. 84, no. 12, pp. 124703–124703-6, 2013.
- [21] A. Chittora, S. Singh, A. Sharma, and J. Mukherjee, “Dielectric loaded TM_{01} to TE_{11} mode converter for S-band applications,” *IEEE Trans. Dielectr. Electr. Insul.*, vol. 22, no. 4, pp. 2057–2063, Aug. 2015.
- [22] F. Arndt, F. Andreas, W. Manfred, and W. Rainer, “Double dielectric-slab-filled waveguide phase shifter,” *IEEE Trans. Microw. Theory Techn.*, vol. MTT-33, no. 5, pp. 373–381, May 1985.

- [23] F. Arndt, J. Bornemann, and R. Vahldieck, "Design of multisection impedance-matched dielectric-slab filled waveguide phase shifters," *IEEE Trans. Microw. Theory Techn.*, vol. MTT-32, no. 1, pp. 34–39, Jan. 1984.
- [24] W. Che and E. K. N. Yung, "90° dielectric polariser in circular waveguide," *Electron. Lett.*, vol. 36, no. 9, pp. 794–795, 2000.
- [25] S. W. Wang, C. H. Chien, C. L. Wang, and R. B. Wu, "A circular polarizer designed with a dielectric septum loading," *IEEE Trans. Microw. Theory Techn.*, vol. 52, no. 7, pp. 1719–1723, Jul. 2004.
- [26] A. Elsherbeni, D. Kajfez, and S. Zeng, "Circular sectoral waveguides," *IEEE Antennas Propag. Mag.*, vol. 33, no. 6, pp. 20–27, Dec. 1991.
- [27] D. M. Pozar, *Microwave Engineering*, Third ed. New York, NY, USA: Wiley, 2004.
- [28] R. H. MacPhie, M. Opie, and C. R. Ries, "Input impedance of a coaxial line probe feeding a circular waveguide in the TM_{01} mode," *IEEE Trans. Microw. Theory Techn.*, vol. 38, no. 3, pp. 334–337, Mar. 1990.
- [29] S. S. Sandler and R. W. P. King, "Compact conical antennas for wide-band coverage," *IEEE Trans. Antennas Propag.*, vol. 42, no. 3, pp. 436–439, Mar. 1994.
- [30] J. L. McDonald and D. S. Filipovic, "On the bandwidth of monocone antennas," *IEEE Trans. Antennas Propag.*, vol. 56, no. 4, pp. 1196–1201, Apr. 2008.
- [31] R. J. Barker and E. Schamiloglu, *High Power Microwave Sources and Technologies*. Piscataway, NJ, USA: IEEE Press, 2001.
- [32] Q. Zhang, S. Peng, C. Yuan, and L. Liu, "Waveguide-based combining S-band high power microwaves," *IET Microw., Antennas, Propag.*, vol. 8, no. 10, pp. 770–774, 2014.
- [33] L. K. Warne, R. E. Jorgenson, J. M. Lehr, Z. R. Wallace, and K. C. Hodge, "Surface interactions involved in flashover with high density electronegative gases," U.S. Dept. Energy, Sandia Nat. Lab., Rep. SAND2010-0268, Jan. 2010.
- [34] D. M. Goebel, R. W. Schumacher, and R. L. Eisenhart, "Performance and pulse shortening effects in a 200-kV PASOTRON™ HPM source," *IEEE Trans. Plasma Sci.*, vol. 26, no. 3, pp. 354–365, Jun. 1998.
- [35] Y. Ziqiang, G. Chengliang, and L. Zheng, "An unmagnetized plasma-loaded relativistic backward-wave oscillator: Experiment and simulation," *Int. J. Infrared Millim. Waves*, vol. 21, no. 11, pp. 1887–1896, 2000.
- [36] D. M. Goebel, J. M. Butler, R. W. Schumacher, J. Santoru, and R. L. Eisenhart, "High-power microwave source based on an unmagnetized backward-wave oscillator," *IEEE Trans. Plasma Sci.*, vol. 22, no. 5, pp. 547–553, Oct. 1994.
- [37] J. T. Krile, L. McQuage, G. F. Edmiston, J. Walter, and A. Neuber, "Short-pulse high-power microwave surface flashover at 3 GHz," *IEEE Trans. Plasma Sci.*, vol. 37, no. 11, pp. 2139–2145, Nov. 2009.
- [38] W. P. Ayres, P. H. Vartanian, and A. L. Helgesson, "Propagation in dielectric slab loaded rectangular waveguide," *IRE Trans. Microw. Theory Techn.*, vol. MTT-6, no. 2, pp. 215–222, Feb. 1958.
- [39] P. J. B. Clarricoats, "Propagation along unbounded and bounded dielectric rods," *Proc. Inst. Elect. Eng., C: Monographs*, vol. 108, no. 13, pp. 170–176, 1961.



Ashish Chittora (GSM'14) received the B.E. degree in electronics and communication engineering from the Engineering College, Kota, India, in 2009, the M.E. degree in electronics and communication engineering from the Delhi College of Engineering, Delhi, India, in 2011, and is currently working toward the Ph.D. degree at the Indian Institute of Technology Bombay, Mumbai, India.

He was an Assistant Professor with Amity University, Noida, India. His research interests include high-power microwave passive devices.



Sandeep Singh received the B.Tech. degree in electronics engineering from the Harcourt Butler Technological Institute (HBTI), Kanpur, India, in 2004, and the M.Tech. degree in RF and microwave engineering from the Indian Institute of Technology (IIT) Kharagpur, Kharagpur, India, in 2012.

He is currently a Scientific Officer with the Accelerator and Pulse Power Division (APPD), Bhabha Atomic Research Centre (BARC), Mumbai, India. His research interests include high-power microwave diagnostics, antenna design, electro-

magnetic interference–electromagnetic compatibility (EMI–EMC), and pulse power systems.



Archana Sharma received the B.E. degree in electrical engineering from the Regional Engineering College, Bhopal, India, in 1987, and the M.Sc. (Engg.) and Ph.D. degrees from the Indian Institute of Science, Bangalore, India, in 1994 and 2003, respectively.

She is currently a Senior Scientific Officer with the Accelerator and Pulse Power Division (APPD), Bhabha Atomic Research Centre (BARC), Mumbai, India. Her specialization is in the design and development of single shot and repetitive pulsed electron

beam generators based on Marx generator and linear induction accelerators. Her research interest also includes compact pulse power systems for HPM, FXR, and industrial applications.



Jayanta Mukherjee (M'07–SM'13) received the B.Eng. degree in electrical and electronics engineering from the Birla Institute of Technology, Mesra, India, and the M.S. and Ph.D. degrees from The Ohio State University, Columbus, OH, USA.

He is currently an Associate Professor with the Department of Electrical Engineering, Indian Institute of Technology, Bombay, India. From 2001 to 2004, he was a Fellow with Texas Instruments Incorporated. From 2002 to 2003, he was an Intern with Thomson Multimedia, Princeton, NJ, USA. He has authored or coauthored more than 50 research papers in peer-reviewed journals and conferences. He also authored three books on RF oscillators and antennas. His research interests include antennas, RF integrated circuit (RFIC) design, and biomedical very large scale integration (VLSI) circuits.

Dr. Mukherjee was the recipient of the Gold Medal on the basis of the order of merit from the Birla Institute of Technology.



Role of Analytical Sciences in Sustainable Development

Organized by: ¹Department of Chemistry, Hansraj College, University of Delhi, India in collaboration with ²Indian society of Analytical Scientists- Delhi Chapter (ISAS-DC) and **Petrotech Society**

Dates: 4-5 March 2016.

ORAL PRESENTATIONS

Cu (II) Removal From Waste Water by *Bacillus subtilis*

Kishor Kumar Singh¹ and Shailendra Kumar Singh²

¹Department of Chemistry, Govt. Post Graduate College, Obra, Sonbhadra (U.P.), India ²Department of Chemistry, Hansraj College, Delhi, India

The increase in environmental pollution caused by toxic heavy metals is of great concern because of their carcinogenic properties, non-biodegradability and bio-accumulation. In order to minimize this problem, biosorption of toxic metals by bacterial fungal or algal biomass (live or dead cells) and agricultural waste biomass can be part of the solution. For metal removal applications, the use of dead biomass or agricultural waste may be preferable as large quantities are readily and cheaply available as a byproduct of various industries. Therefore, it is proposed to use dead biomass of *Bacillus subtilis* for the removal of Cu (II) from wastewater, because it is cheap, easily available and mostly biodegradable.

The dead biomass of *Bacillus subtilis* has been used for the removal of Cu (II) from wastewater. The effects of different parameters such as contact time, adsorbate concentration, pH of the medium and temperature were examined. Optimum removal at 20°C was found to be 98.6 % at pH 6.5, with an initial Cu (II) concentration of 100 mg

L⁻¹. Dynamics of the sorption process and mass transfer of Cu (II) to dead biomass of *Bacillus subtilis* were investigated and the values of rate constant of adsorption, rate constant of intraparticle diffusion and the mass transfer coefficients were calculated. Different thermodynamic parameters viz., changes in standard free energy, enthalpy and entropy were evaluated and it was found that the reaction was spontaneous and exothermic in nature. The adsorption data fitted the Langmuir isotherm. The data were subjected to multiple regression analysis and a model was developed to predict the removal of Cu (II) from wastewater which is given as follows

$$Y = 6.5592 + 0.6389a_1 + 0.5169a_2 - 0.4691a_3 + 0.2830a_4 - 0.0972a_5$$

Where, Y is the predicted value of Cu (II) removal, a₁, concentration of adsorbate, a₂, contact time; a₃, temperature; a₄, pH; a₅, agitation rate of the system.

Preparation and Characterization of Biodegradable Nanoparticles for Oral Delivery of Epirubicin

Talegaonkar Sushama

¹Department of Pharmaceutics, F/O Pharmacy, Jamia Hamdard, New Delhi, India

Oral delivery of EPI, which elicits poor bioavailability, is highly challenging as it is a substrate for both P-gp and CYP450 which are widely distributed in the intestine and liver [1-3]. Oral bioavailability of Epirubicin (EPI) is very poor and it is commercially available for intravenous administration only (Elevance, Pfizer). Intravenous administration of the drug leads to its sudden rise and rapid fall in blood, often lead to sub-therapeutic level hence prompting frequent dosing which is often associated with cumulative adverse effects. In this perspective, present investigation was aimed to develop biodegradable nanoparticles of EPI (EPI-NPs) that could enhance the absorption via endocytic uptake across enterocytes as well as M cells of intestinal epithelium thus evading the first pass metabolism and P-gp mediated efflux. The particle size zeta potential and drug content were found to be 235.3 ± 15.12 nm, -27.5 ± 0.7 mV and (39.12 ± 2.13g/mg) respectively. SEM study showed prepared nanoparticles exhibited

Convener /Coordinator

Dr. Renu Parashar
Associate Professor of Chemistry
Hansraj College
University of Delhi
Email: renu.hrc@gmail.com
Tel: +91-9968977434

© IS Publications JIST
<http://pubs.iscience.in/jist>

ISSN 2321-4635

spherical shape and smooth surface. studyIn vitro release profiles of EPI demonstrated a cumulativepercentage release of $96.23 \pm 2.6\%$ from EPI-S in first hour and $80.94 \pm 6.39\%$ from EPI-NPs in 48 h. Cytotoxicity studies conducted on human breast adenocarcinoma cell lines (MCF-7) confirmed the superiority of epirubicin loaded poly-lactic-co-glycolic acid nanoparticles (EPI-NPs) over free epirubicin solution (EPI-S). Transport study accomplished on human colon adenocarcinoma cell line (Caco-2) showed 2.76 fold improvement in permeability for EPI-NPs as compared to EPI-S ($p < 0.001$).

1. W.T. Bellamy, Annu. Rev. Pharmacol. Toxicol. 36 (1996) 161.
2. L.J. Goldstein, H. Galski, A. Fojo, M. Willingham, S.L. Lai, A. Gazdar, R. Pirker, A.Green, W. Crist, G.M. Brodeur, et al., J. Natl. Cancer Inst. 81 (1989) 116.
3. D.R. Nelson, Biochim. Biophys. Acta 1814 (2011) 14.

An Eco-friendly synthesis of 7-hydroxyflavones under solvent free conditions using grinding technique

Dinesh K. Sharma¹, Surender Kumar²

¹Department of Chemistry, Kishan Lal Public College, Rewari-123401, India, ²Department of Chemistry, Technological Institute of Textile & Sciences, Bhiwani-127 021 (Haryana) India

An efficient and eco-friendly procedure for the synthesis of 7-hydroxyflavones by cyclisation of corresponding 2',4'-dihydroxychalcones in the presence of molecular iodine moistened with water at room temperature under solvent free conditions using grinding technique has been described. The structures of these compounds were identified from their spectral data (FT IR, ¹H NMR). This protocol avoids the use of hazardous chemicals and organic solvents at any stage of the reaction.

Seasonal trend in composition of n-alkanes in ambient aerosols at a traffic site, Delhi

Sarika Gupta^a, Ranu Gadi^b, T.K. Mandal^c

^aGuru Gobind Singh Indraprastha University, Delhi-110078, India, ^bIndira Gandhi Delhi Technical University for Women, Delhi-110006, India, ^cNational Physical Laboratory, Dr. K. S. Krishnan Marg, New Delhi, India

Delhi is one of the most polluted cities in the world. The generation of aerosols in the lower atmosphere of the city is mainly due to large amount of natural dust advection and sizable anthropogenic activities. The compositions of organic compounds in aerosols are highly variable in this region, and need to be investigated thoroughly. Twenty four hours sampling to assess concentrations of n-alkanes (ng/m³) in PM₁₀ was carried out during January 2015 to June 2015 at IGDTUW, University Campus, Delhi; India with the help of Respirable Dust Sampler. Quantitative estimation of n-alkanes was done by using Thermal Deposition-Gas Chromatography/ Mass spectrometry (TD-GC/MS). The mean concentration of n-alkanes along with the diagnostic tools like C_{max} (most abundant carbon number) and Carbon

Preference Index (CPI) has been calculated. The values of the CPI: 1.00 and C_{max} at C₂₅ & C₂₇ indicated the dominant inputs of n-alkanes to be from pathogenic emissions, with lower contribution of biogenic emissions. Significant seasonal variations were observed in average concentrations of n-alkanes; which is comparatively higher in winter than in the summer season.

Quantitative Estimation of Berberin using TLC and HPLC in *Tinosporacordifolia*, *T. sinensis* and *T. crispa*

Vijay Rani Rajpal^{1*}, Rakesh Thakur², S. N. Raina²

¹Associate Professor, Department of Botany, Hansraj College, Delhi University, Delhi, ²Department of Biotechnology, Amity University, Noida, Uttar Pradesh

Tinospora belonging to family Menispermaceae is represented by three species namely *T. cordifolia*, *T. sinensis* and *T. crispa* in India. The species are unisexual bearing male and female flowers on separate, morphologically distinct plants. *T. cordifolia* commonly known as Giloy is medicinally very important and is used as an immunomodulator in all the Ayurvedic Rasayanas. *T. sinensis* and *T. crispa* are also used for the same purposes, many a times, as a replacement of *T. cordifolia*. The medicinal properties of *Tinospora* are due to the presence of alkaloids, glycosides, diterpenoids, lactones, lignans and other miscellaneous compounds largely in the stem of the plants. Among alkaloids, Berberin, Tinosporin and Palmatine are found to be most abundant. We have tried to quantitatively estimate Berberin content in male and female genotypes in the above 3 *Tinospora* species by TLC and HPLC using different solvents for extraction. The investigations have helped identify the genotypes with the highest concentration of 0.2 % Berberin in methanolic extracts of dried stems in the female plants of *T. cordifolia*. Further, the identified high alkaloid containing genotypes have been utilized in the induction of polyploidy using colchicine with an aim to increase the alkaloids content in this important medicinal plant species.

Micro plastic a risk to our Health & Environment

Guncha Sharma¹, Chirashree Ghosh¹

Department of Environmental Studies, University of Delhi, India.

Water being an universal solvent has prominence and great vitality associated with it. Day by day water available for human consumption is getting polluted due to tallying of various solid waste constituents like plastic, glass, metal, rubber and wood etc. Plastic being widely used and highly resistant to degradation ends up into water in the form of plastic debris.[1] This due to various external forces and photo degradation leads to development of micro and nano size plastic particles. Micro plastic (size < 5mm) [2] is ubiquitous and resembles food for aquatic organism and further gets accumulated releasing toxic chemicals into the

aqua-terrestrial environment. Globally research on micro plastic is subsequently increasing and already considered it as an alarming threat for the aquatic biota; but on national level there exist a knowledge gap which needs to be filled. So there is a necessity to reminisce the associated micro plastic sources either through identification, quantification, fate analysis or potential impact assessment on aquatic organisms.

1. Barnes, D. K. a, Galgani, F., Thompson, R. C., & Barlaz, M. (2009). Accumulation and fragmentation of plastic debris in global environments. *Philosophical Transactions of the Royal Society of London. Series B, Biological Sciences*, 364(1526), 1985–1998. <http://doi.org/10.1098/rstb.2008.0205>
2. Ryan, P. G., Moore, C. J., van Franeker, J. a, & Moloney, C. L. (2009). Monitoring the abundance of plastic debris in the marine environment. *Philosophical Transactions of the Royal Society of London. Series B, Biological Sciences*, 364(1526), 1999–2012. <http://doi.org/10.1098/rstb.2008.0207>

Review on Municipal Waste Disposal and Management in India

Sagar Kumar, and Priyanshu Idnani

Department of Chemistry, Hansraj College, University of Delhi, Delhi.

Rapid industrialization and population explosion in India has led to the migration of people from villages to cities, which generate thousands of tons of Municipal Solid Waste(MSW) daily. The MSW amount, which has become one of the major environmental problems of Indian cities, is expected to increase significantly in the near future as the country strives to attain an industrialized nation status by the year 2020. With increasing urbanization and changing life styles, Indian cities now generate eight times more MSW than they did in 1947. Presently, about 90 million tons of solid wastes are generated annually as byproducts of industrial, mining, municipal, agricultural and other processes. The amount of MSW generated per capita is estimated to increase at a rate of 1–1.33% annually. Most of the MSW in India is dumped on land in an uncontrolled manner. Such inadequate disposal practices lead to problems that will impair human and animal health and result in economic, environmental and biological losses. The current regulations (MSW management rules, 2000) are very stringent. Norms have been developed to ensure a proper MSW management system. Unfortunately, clearly there is a large gap between policy and implementation. Improper management of MSW causes hazards to inhabitants. Various studies reveal that about 90% of MSW is disposed of unscientifically in open dumps and landfills, creating problems to public health and the environment. There is a need to provide a comprehensive review of the characteristics, generation, collection and transportation, disposal and treatment technologies of MSW practiced in India. This presentation focuses on MSW management for Indian cities, its status as described in scientific literatures and identify the major problems. Various adopted treatment technologies for MSW are critically reviewed, along with their advantages and limitations. The need to encourage the competent authorities/researchers to work towards further improvement of the present system is highlighted in this presentation work.

Eco-friendly Disposal and Recycling of Wastes and Green Chemistry

Anshul Joshi

B.Sc Life Sciences, Ramjas College, University Of Delhi

With the rampant increase in environmental pollution, solid & radioactive wastes and various environmental hazards, especially in urban and sub-urban populations affecting almost every section of society, The Green Chemistry & Proper Disposal has become the need of the hour. Young children & new born babies are facing a lot of medical complications and birth defects due to fragile condition of air quality and polluted environment. Respiratory problems have become common in the young children too. The poor air quality and the inefficient machinery of proper disposal of Radioactive and solid wastes are posing a great threats to the nation's youth.

Here in this presentation we are going to discuss that how we can reduce the burden of solid and radioactive wastes in our environment and improve the quality of environment. Today urban solid waste management program needs to be reviewed by separation of different kinds of wastes through screening, air classifying and magnetic separators. Controlled Incineration and Pyrolysis of wastes need to be done. Wastes from atomic power plants come in the form of fuels of uranium and plutonium, which needs to be properly disposed off to prevent the effects of harmful radiations. The biomedical wastes needs to be treated properly in incinerators, autoclave ,microwaves because they pose very dangerous threats when disposed untreated.

Apart from that *Biofuels play an essential role in reducing the carbon emissions from transportation and maintain air quality. The development of 'drop in' fuels produced from lignocellulosic raw materials will increase both the availability of biofuels and the sustainability of the biofuel industry. They can be produced from any source that can be replenished rapidly, e.g. plants, agricultural crops and municipal waste. Current biofuels are produced from sugar and starch crops such as wheat and sugar cane.*

Waste Disposal and Recycling

Srishti Jaiswal¹, Dhanu Saroha¹

¹Department of chemistry , Hansraj College ,University of Delhi - 110007

We live in a time of throw away consumerism- A time where waste stream grows in volume and toxicity. Thus making waste disposal a major issue in recent years. India alone generates about 60 million tonnes of trash every year. The landfills of most cities are already overflowing. "Instead of constructing new landfills we need innovative methods" , said an expert of CSE. But the governments are so pressured to dispose waste that they rely on short sighted quick fix solutions.

The prominent 3 ways of waste disposal include landfills, incineration and recycling, where the former two have their

flaws but recycling has morphed into a new concept 'ZERO GARBAGE'.

"Zero Garbage has potential to motivate people to change their lifestyles and incite corporations to behave in new ways", Peter Montague ,director ERF. Therefore in the presentation we will focus on waste disposal an issue , prevelant methods and its drawback , recycling an interesting development ,waste a potential resource , Zero Garbage (Elimination of waste rather than management), waste industry (commercial business) and contribution/awareness of society and government.

1. <http://toxicsaction.org/problems-and-solutions/waste>
2. <http://zerowaste.org/>
3. <http://www.eprint.iitd.ac.in/bitstream/2074/1494/1/agarwalmun2004.pdf>

Importance of Advanced Sensing in Smart Cities

Pratibha Singh¹, Ayushi Saxena¹, Ashima Srivastava¹

¹Department of chemistry, JSS Academy of Technical Education, Noida, U.P, India

Today's world where resources are scarce and urban areas consume the vast majority of these resources, it is vital to make cities greener and more sustainable. Advanced systems are required to improve and automate processes within a city for leading them into smart cities. Some smart design of buildings, like capturing rain water for later use, to intelligent control systems, which can monitor infrastructures autonomously, the possible improvements enabled by sensing technologies are immense. Ubiquitous sensing poses numerous challenges, which are of a technological or social nature. A smart city is a city which functions in a sustainable and intelligent way, by integrating all its infrastructures and services into a cohesive whole and using intelligent devices for monitoring and control, to ensure sustainability and efficiency.

This paper presents an overview of the state of the art with regards to sensing in smart cities. Topics include sensing applications in smart cities, sensing platforms and technical challenges associated with these technologies. In an effort to provide a holistic view of how sensing technologies play a role in smart cities, a range of applications and technical challenges associated with these applications are discussed. As some of these applications and technologies belong to different disciplines, the material presented in this paper attempts to bridge these to provide a broad overview, which can be of help to researchers and developers in understanding how advanced sensing can play a role in smart cities.

Waste Disposal and Recycling

Pallavi Babbar, Shagun Kushwaha

Chemistry Department, Hansraj College, India,

Wastes are the materials which are not prime products for which the generator has no further use. There are also many problems faced during their disposal such as threat to public

health, loosening our non-renewable resources, etc. So, it is necessary to dispose it properly.

Mainly 3 types of waste need proper disposal: solid waste, liquid waste and radioactive waste. Solid waste, can be disposed by composting, sanitary landfill, etc. Liquid waste, disposed through secure landfill and deep well disposal methods. Radioactive wastes are the most harmful waste and requires proper treatment involving storage, disposal or transformation of waste into non toxic form.

Simplest method of waste management is by reusing, reducing, recycling (3R's). Solid waste can be recycled. **Recycling** simply involves collecting, processing and selling products made from old materials. Radioactive wastes are also recyclable. Once reactor fuel is used in a reactor, it can be treated and put into another reactor as fuel.

Some of government initiatives and policies:

- 1). Self Employment Programme for Urban Poor (SEPUP) was introduced in 1986 and Nehru Rozgar Yojna was introduced in 1989.
- 2). Waste to Energy Policy as promoted by the ministry, of Non Conventional Energy sources (MNES), 1995, etc.

1. https://en.m.wikipedia.org/wiki/Waste_management
2. <https://en.m.wikipedia.org/wiki/Recycling>
3. <http://www.yourarticlelibrary.com/waste-management/solid-waste-management-types-sources-effects-and-methods-of-solid-waste-management/9949/>

Socioeconomic and Environmental Impact of Electronic Waste

Satyam Bansal¹, Harsh Chaudhary¹, Prashant Singh¹, Pratibha Singh¹

¹Department of chemistry, JSS Academy of Technical Education, Noida, U.P, India

In today's world, most of us have the luxury of not having to face the daily realities of all the damage humans do to the planet. It is difficult to understand the devastation created by human beings unless you travel to a developing nation or actively try to find it in our own country -- pictures or words will never do it justice. E-Waste (Electronic Waste) is the rapidly growing stream of waste from discarded electronics and appliances. These items include anything from computers, TVs and phones to washing machines and refrigerators to everything else in between. Most of these electronics appliances are often not trash, but simply outdated and traded up for the latest version on the market. To manufacture one computer and its monitor it takes 530lbs of fossil fuels, 48 pounds of chemicals, and 1.5 tons of water. Toxic substances when burnt at low temperature create additional toxins such as halogenated dioxins and furans- harmful to mankind. According to the most recent report released by the United Nations University (UNU) on the matter, findings show that globally we produced 41.8 million tons of e-waste in 2014. Even more startling -- it is believed that less than one-sixth is properly recycled or reused.

While the negative impact of e-waste is vast and growing, most people are probably unaware of its reach. The lack of proper recycling leads to harmful toxins like lead and mercury leaching into the environment. Harmful materials

like these and many others found in e-waste, cause all sorts of health issues like neurological damage, kidney damage and some cancers, to name a few. And let's not forget about the ozone-depleting chlorofluorocarbons left behind. Maybe the worst part of this issue is that most e-waste from developed countries is exported to developing countries like India, Africa and China. Often the pits of discarded computers and other electronics are picked over by locals who attempt to mine profitable materials like copper and gold from them. The improperly performed recovery methods like acid baths and burning of electronics are extremely harmful and are often performed by local women and children.

These issues are environmental as well as social and related to mankind. So, it is for us to choose, whether we want to choose life of doomsday by the invasion of machines and radiations over us completely so as we loose humanity and mankind from this planet completely and forever.

Research in Chemistry to Generate Green Energy

Harmeet Singh, Puneet Goel

Chemistry Department, Hansraj College, India

Green Energy refers to the environmental benign source of energy and it does not take into account the process of extracting and refining the energy. When extraction of green energy from a renewable source is processed, very often, it requires a fossil input which adversely affects the environment and consequently the sustainability of the process. The environmental sustainability of green energy production is expressed in energy returned on energy invested, carbon footprints and eco-footprints. Various modifications made in the process of producing green energy are: **1.** Production of hydrogen (H_2) gas (a great source of modern fueling) from supercritical water gasification of biomass. **2.** Nuclear routes for the production of H_2 gas-Electrolyzer is coupled to a nuclear reactor to produce oxygen (O_2) and H_2 gas. **3.** UNIST and KAIST have developed gold nanoparticles modified with titanium dioxide (Au -NPs/ TiO_2) photoelectrodes that could boost the ability of water splitting to produce H_2 . **4.** Solar water oxidation- $Ta:TiO_2$ and $BiVO_4$ used as photoanodes. **5.** P_{22} Hyd-This is a biomaterial made by *E. coli* in hydrogenase (Nitrogen-iron hydrogenesis).The resultant capsid produces P_{22} Hyd which can split water. **6.** Dubbed Combined Algae Processing (CAP)-A method used to produce ethanol from algae (*Chlorella* and *Scenedismus*). **7.** Camelina usage-Kansas State University engineered Camelina saliva, a non food oilseed crop, to produce high levels of acetyl triacyl glycerols. Camelina is a transgenic plant. These are some of the researches in chemistry in an effort to generate green energy that too via green routes which will be discussed in brief. Green synthesis will limit the emission of green house gases and usage of fossil fuels.

1. Applied Energy, **2016**, Volume 162, 131-138.

2. Green Car Congress.

3. Algal Research Doi, Algal **2015**, 12:02.

4. Industrial Crops and Products, Volume 65, 259-268.

Exploring the origin of nanocatalysis

Jyoti Yadav, Sangeeta Saini

Kurukshetra University, Kurukshetra, Haryana- 136119

Gold at bulk level is inert material however, at nanoscale it is found to catalyze reactions. To explore the origin of this catalytic activity, we selected to theoretically investigate a simple chemical reaction that is, oxidation of carbon monoxide catalysed by Au_5 clusters (neutral, positively and negatively charged). We have studied the reactivity of gold clusters towards dioxygen in terms of binding energy of O_2 . The binding energy is described in terms of various descriptors for example, d-band centre of metals, coordination number of binding sites, strain in the cluster i.e. bond lengths, angles etc. Such relationships are shown to successfully predict the catalytic activity of metals. We used regression analysis to quantify the dependence of binding energy on above said reactivity descriptors.

Partial Redundancy for a Sustained Future-The Carbon Case

Chakraborty, Ranabir

Department of Zoology, Hans Raj College, University of Delhi, India

What differentiates humans from other animals lies in the literal meaning of the term associated with describing us, 'Social'; needing companionship. This makes us suitable to integrate, as individual entities come and live together and develop not only the present, but laying a foundation for the future generations, what is known as 'Sustainable Development'. However, the emotion of greed got the better off us, and a lot off the future.

Analytical Sciences has, over the years, helped immensely in understanding the severity of the ill environmental health, by estimating the levels of Greenhouse Gases (GHGs) in the environment, 'Carbon Footprint'. A crude estimation of gases like Carbon di-oxide (CO_2) or Methane (CH_4) supports in developing strategies to reduce their levels, thus taking the present, with the future tagged along, a step closer towards efficient development and sustained living at both community and global level.

Reducing Carbon Footprint

Kriti Kapil

Department of Chemistry, Miranda House, University of Delhi, India

Essentially, the Ecological Footprint shows us how carbon emissions compare and interact with other elements of human demand. The carbon Footprint is 54 percent of humanity's overall Ecological Footprint and its most rapidly growing component. Humanity's carbon Footprint has increased 11-fold since 1961^[2]. Reducing humanity's carbon Footprint is the most essential step we can take to end overshoot and live within the means of our planet.

The Footprint framework also shows climate change in a greater context one which unites all of all the ecological threats we face today. Climate change, deforestation, overgrazing, fisheries collapse, food insecurity and the rapid extinction of species are all part of a single, over-arching problem: Humanity is simply demanding more from the Earth than it can provide. By focusing on the single issue, we can address all of its symptoms in a comprehensive way, rather than shifting the burden from one natural system to another.

1. How to reduce your carbon footprint - Green Wiki - Wikia
2. 25+ Tips to Reduce Carbon Footprint from COTAP.org

Waste Disposal and Recycling

Nikunj Kumar, Ashish Raghav

Chemistry department, Hansraj college, University of Delhi, India

In this era, where we are mainly focusing ourselves to progress and development, we are unknowingly increasing the consumerism and thus the waste produced, which includes every kind of waste whether it is solid waste which is mainly classified into electronic waste, unincinerated hospital waste and other kind of non-biodegradable waste. This will now or later will surely lead to havoc, thus we must indulge our chemistry oriented scientific minds to overcome it. As it is chemistry which can replace polythene with PHBV (Poly-Hydroxy butyrate – co - b-Hydroxy valerate) like organic degradable polymers, it is chemistry which can synthesis products which will not release free radicals like CFC's and can prevent the major Kyoto protocol problems called ozone depletion. Thus we are here to depict our analytical knowledge about chemistry so as to explain less waste production and its management.

1. R. Cossu, International Journal of Integrated Waste Management, Science and Technology, **2014**, www.journals.elsevier.com
2. NCERT chemistry class 12th

Strategies Involved in Treatment and Disposal of Pulp and Paper Mill Effluent

Noopur Srivastava¹, Pratibha Singh²

¹Department of Chemistry, Bhagwant university, Ajmer, Rajasthan, India, ²Department of Chemistry, JSS Academy of Technical Education, Noida, U.P, India

Pulp and paper industry is considered as one of the most polluted industry in the world due to its toxic effect on environment. Pulp and paper industry uses large quantity of freshwater and lignocelluloses materials in the process of production of paper and it generates large quantity of effluents. The problems associated with pulp and paper mill effluents are pH, colour, and high levels of biochemical oxygen demand (BOD), chemical oxygen demand (COD), suspended solids (SS), Absorbable Organic halides (AOX) etc. Paper manufacturing process release chlorinated lignosulphonic acids, chlorinated resin acids, chlorinated phenols and chlorinated hydrocarbon in the effluent. The high chlorine content of bleached plant reacts with lignin and its derivatives to form highly toxic and recalcitrant

compounds, which are responsible for high biological & chemical oxygen demand.

The most important problem which the pulp & paper industry is facing today is the disposal of tremendous volumes of waste water. This waste water is rich in dissolved solid such as chlorides & sulphates of Na, Ca & varying amounts of suspended organic materials. In addition to these constituents, effluents also contain some trace metals like Hg, Pb & Cr etc. The effluents are generally alkaline in reaction, thus the effluents discharge into the water systems make the water unfit for irrigation & potable use & create health hazards. Physical & Chemical methods undertaken to study colour removal from the effluent is not found to be cost effective. Hence, biological treatment has been applied for the decolourization of effluent of pulp & paper mills. The biological colour removal process is particularly attractive since in addition to colour & COD it also reduces BOD & low molecular weight chlorolignins. Additionally, some fungi species are used to remove color & AOX from the effluents. Several studies have been carried out with the final purpose of reduction in the pollution load during the pulp & paper making process. In this paper, waste characterization of this industry in terms of type and source with management approaches will be discussed with exemplary applications.

Algal Biofuel: A Boon for Society in Future to Solve Energy Crisis

Prashant Singh¹, Satyam Bansal¹, Pratibha Singh¹, Roli Verma¹, R. S. Jagadish¹

¹Department of Chemistry, JSS Academy of Technical Education, Noida, U.P, India

Our fossil fuel based energy resources (petroleum, coal and natural gas) are vanishing at a very faster rate to fulfill the demand of energy for growing population worldwide. So depletion of these resources will lead us to the chains of problems which may occur due to fuel shortage. It has been estimated that as per present uses, our coal reserves will be exhausted in 200 years and if we increase the use by 2%, then it will be vanished in 165 years. Therefore in such a condition sustainable and renewable energy resources are beneficial to solve the problem of energy crisis. Fortunately, our scientists have developed different categories of biodiesel as an alternative fuel to meet growing energy demands. In recent scenario, they are focused on the algae as a raw material for biodiesel and which may be proved as a boon for the society in future. Biofuels play a vital role in mitigating CO₂ emission, reducing global warming and bringing down the hike in oil prices. The biodegradable, renewable and non toxic nature of biodiesel has made it a recent attraction. The objective of the paper is to study the potential of microalgae as an alternative raw material for biodiesel generation that can be converted into fuel. Its easy availability, high mass productivity and faster lipid production have made it prior to all other alternatives for the raw material of biodiesel. Production of biodiesel from microalgae would be a greater alternative to oil crops due to economical instability, jeopardizing agricultural lands and insufficient oil crops. This paper provide holistic review to

enhance the production and commercialization of biodiesel by improving cultivation of different microalgal species, lipid content in various algal species, modes and efficiency of harvesting and trans-esterification methods.

Saviour of Earth: Carbon Footprint Reduction

Sakshi¹, Shubhi¹, Shyamali¹, Riya¹ and Shiksha¹

¹Darshan Singh¹, Ritu Gupta¹ Assistant professor¹, B.Sc (H) Chemistry², Department of chemistry, Daulat Ram College, University Of Delhi.

'Carbon footprint' has become a widely used term and concept in the public debate on responsibility and abatement action against the threat of global climate change. With climate change high up on the political and corporate agenda, carbon footprint calculations are in strong demand. **"The carbon footprint is the amount of carbon dioxide emitted due to your daily activities – from washing a load of laundry to driving a carload of kids to school"**[1]. It is proposed that landscaping works should focus on reduction of hidden carbon footprint in planning, design and construction and reduce dominant carbon footprint in the 3 stages through reasonable selection of planted vegetation, shortened long distance transport and reducing high fuel consumption of machineries [2]. The carbon handprint movement emphasizes individual forms of carbon offsetting, like using more public transportation or planting trees in deforested regions, to reduce one's carbon footprint and increase their "handprint." The carbon footprint is a very powerful tool to understand the impact of personal behaviour on global warming. If you personally want to contribute to stop global warming, the calculation and constant monitoring of your personal carbon footprint is essential.

1. ISA-UK Report 07-01: carbon foot printing final.
2. IEEE XPLORE : carbon foot printing research of landscaping works based on life cycle analysis

Reducing Carbon Footprints

Shivani, Anuj Pundir

¹Chemistry Department, Hansraj college, University of Delhi

Carbon emissions provide one of the most fatal grounds for acceleration of global warming which is a major threat to mankind. An individual's, nation's, or organisation's carbon emissions can be counted by taking in account GHG emissions assessment or other calculative activities referred as 'carbon accounting'. Carbon footprints is the amount of carbon produced by a person or an entity via direct emissions, resulting from fossil fuels combustion in transportation and manufacturing as well as emissions associated with production of electricity in goods and services consumed. This presentation focuses on elementary measures that can derogate the influence of green house gases (especially CO₂) on environment. A comparative study of various carbon footprint assessments standards, its causes and reduction techniques was carried out to identify their differences, similarities, deficiencies and advantages. We

focused on alternative sources of energy such as solar, wind etc to mitigate carbon footprints. Furthermore, various innovative and lyrical ideas will be shared helping in the reduction of carbon footprint. Several guidelines have been made on this issue but further improvement is still needed.

Waste management and disposal

Ria Miglani, Priya Bhatia

Department of Chemistry, Hansraj College, New Delhi, India

Waste Management and Disposal are All Those Activities and Action Required to Manage Waste from Its Inception to its Final Disposal. The Central Principles of Waste Management include Waste Hierarchy; Life Cycle of Product, Resource Efficiency and Polluter pays Principle. The Disposal Solutions are Landfill and Incineration.

Recycling is a Resource Recovery Practice that Refers to the Collection and Reuse of Waste Materials such as Empty Beverage Containers, Steel Cans etc. Methods of Reuse include Biological Reprocessing, Energy Recovery, Pyrolysis, Resource Recovery and Sustainability. The Methods of Plastic Recycling that is Physical Recycling, Chemical Recycling and Water Recycling will be taken into Account and the Economic Impact of Recycling will be explained.

1. Glossary of Environment Statistics : Series F, No. 67 / Department for Economic and Social Information and Policy Analysis, United Nations. New York: UN, 1997.
2. Waste Management (2013). "Editorial Board/Aims & Scopes". Waste Management 34: IFC.doi:10.1016/S0956-053X(14)00026-9.
3. Davidson, G. (2011). "Waste Management Practices". Retrieved from [http://www.dal.ca/content/dam/dalhousie/pdf/sustainability/Waste%20Management%20Literature%20Review%20Final%20June%202011%20\(1.49%20MB\).pdf](http://www.dal.ca/content/dam/dalhousie/pdf/sustainability/Waste%20Management%20Literature%20Review%20Final%20June%202011%20(1.49%20MB).pdf).
4. United Nations Environmental Programme (2013). "Guidelines for National Waste Management Strategies Moving from Challenges to Opportunities." (PDF). ISBN 978-92-807-3333-4.
5. Barbalace, Roberta Crowell (2003-08-01). "The History of Waste". EnvironmentalChemistry.com. Retrieved 2013-12-09.

Photogalvanic Cell : A Green Approach in Conserving Energy using Lawsone as Photosensitizer

Mahaveer Genwa¹, Chetna Angrish¹, Ayesha Seth¹, Umesh¹ and P. L. Meena^{2,*}

¹Department of Chemistry, Deen Dayal Upadhyaya College, University of Delhi, Shivaji Marg, Karampura, New Delhi - 110015, ²Department of Physics, Deen Dayal Upadhyaya College, University of Delhi, Shivaji Marg, Karampura, New Delhi - 110015

Photogalvanic cells were made using natural dyes extracted from *Lawsonia inermis* in a photogalvanic cell which was an H shaped tube. Various factors affected the natural dye extract like pH of the dye and the solvent used for dye preparation. We successfully attempted to isolate and purify Lawsone from the leaves of henna. The progress of the isolation of Lawsone was characterized by Ultra Violet-Visible spectroscopy done by Chemito UV 2100 and Thin Layer Chromatography (TLC) on silica gel. We got the maximum absorbance at λ_{max} (Experimental) = 440-460nm

in visible range and spot on the TLC plate when the solvent system taken was ethyl acetate and ethanol (2:1). Fabric block prints of Lawsone dye were taken to show excellent dyeing ability of lawsone. We studied solar energy conversion through photogalvanic effect of the cell using Lawsone dye, glucose and NaOH system (Glucose as reductant, Lawsone as sensitized dye and NaOH aqueous solution). The photopotential generated was 250 mV which was measured by Keithley 2450 Source Meter and the observed power of the cell being 8 μ W at room temperature [Solvent Ratio=6.5:6:7 (glucose: lawsone:NaOH)]. The effects of different parameters on the electrical output of the cell and other potential characteristics of the cell were studied.

By the different setups performed we conclude that these cells are the most promising cost effective photovoltaic technologies which are secure, clean and excellent in solar energy conversion. This kind of power management solution exemplified by this innovative project of ours is beneficiary for the living environment and for the booming industrial sector. We thus present our view on future prospects in the development of Lawsone dye as a photosensitizer.

Research in Chemistry to Generate Green Energy

Kritika Jha

Department of Chemistry, Kirorimal College, Delhi University

Green energy or Sustainable energy is derived from non-conventional energy which is continuously replenished by natural processes. If we see the electricity requirements of world including India are increasing at alarming rate and the power demand has been running ahead of supply. It is also now widely recognized that the fossil fuels and other conventional resources presently being used for generation of electrical energy, may not be either sufficient or suitable to keep pace with ever increasing demand of electrical energy of the world.

Chemists could smooth out the patchy supply of sun and wind power by developing fuels and batteries that can store energy during peak times. Various forms of green energy include solar energy, wind energy, hydroenergy, geothermal energy, wave and tidal energy. Renewable power is effective, reliable, sustainable, and environment friendly which we strongly need to cut our use of fossil.

Electrochemical Synthesis of Organic Light Emitting Diode(OLED) and Characterizations by X-ray Diffraction Techniques

Kalawati Saini¹, Raghendra Swarup²

¹ Miranda House, Chemistry Department, University of Delhi, New Delhi-110007, ²Chemistry Department, Indian Institute of Technology, Hauz Khas, New Delhi-110016

A facile and sustainable electrochemical approach towards the synthesis of tris-(8-hydroxyquinoline)

aluminium(III) (Alq3) using 8-Hydroxy quinoline as a ligand is presented. The synthesis has been done at three different conditions (a) 0.015M of 8-Hydroxy quinolin in 50% methanol, at pH7 for 24 hours (b) 0.0303M of 8-Hydroxy quinolin in 40% methanol at pH1 for 48 hours (c) 0.0317M of 8-Hydroxy quinolin in 50% methanol at pH2 for 24 hours at 1.5 V and 12V respectively. Simple room temperature electrolysis method has been employed, wherein Al wire as well as Al foil were used as a sacrificial anode for Al³⁺ ion source and platinum wire as a cathode. Tris-(8-hydroxyquinoline) aluminium (III) (Alq3) was synthesized for the first time by direct dissolution of Al³⁺ into the solution of 8-Hydroxy quinoline from Al electrode in the electrochemical cell. The structural characterizations have been done by using Single X-ray diffraction and Powder X-ray diffraction (XRD) techniques. Complexes of Aluminium with 8-Hydroxyquinoline have a wide applications to material science as organic light emitting diode (OLED).

Bio-Sustainable fertilizers: An overview

Nakul Sharma, Nitika Garg, Vibha Sharma, Ekta Kundra

The Chemistry Department, St.Stephen's College, University of Delhi, Delhi-110007

Synthetic fertilizers have been a cause of concern since many years. The problems related to their absorption by the land, their non-biodegradable nature (some are potential carcinogens), water polluting aspect make them ever-more dangerous to use. It leads to biological magnification too, which means they get accumulated in our bodies over time and cause various problems. Furthermore, recent studies show that increase in fertilizer use has led to a rise in Nitrous Oxide emissions having serious climate change impact. This leads us to look for a better alternative that contributes less to climate change and augment our goal of sustainable development. Bio-fertilizers show the way ahead. Bio-fertilizers consist of micro-organisms that increase the availability of essential nutrients such as nitrogen and phosphorus to the plants and act as 'potential fertilizers'. In our presentation we would discuss Bio-fertilizers in detail covering its production, usage and impact ; and how it appears promising to control climate change and promote sustainable development.

The Garbage Dump Can't Solve it Any More

Hemani Chhabra and Monika Rao

St. Stephen's College, New Delhi

Waste Management has been a major concern for environmentalists since the last few decades due to increased population and over consumption. Ample of researches have focused on methods of waste disposal, recycling, reuse and reduction in production of waste via sustainability. There are certain places all over the world where waste is efficiently disposed and recycled eg: Zabbaleen community in Cairo

recycles 80% of the waste collected which is 4 times the average rate of recycling in any part of the world. The other methods include **Plasma Gasification, Waste to energy process, Incineration, Composting, recycling, reusing** etc.

But how can a scientist reduce the production of waste in his lab? With the advancement of science and technology, a number of computational methods enable theoretical studies of processes which decades back could only be done practically. Resorting to theoretical studies can turn out to be a long term solution to minimize chemical waste which is not only difficult to dispose but also harmful for the mankind.

A Theoretical Proposal for Conversion of Polythene Waste to Ethanol

Amisha Gautam¹ and Shivendra Tiwari²

²Undergraduate Student (First Year), Indraprastha College for Women, University of Delhi, India, ¹Independent Researcher, Lucknow, India

Polythene waste is a stagnant menace in the society with no long-term solutions in sight. The present research proposes the conversion of waste polythene into ethanol and other hydrocarbons with high commercial value.

The conversion includes a two-step process. In the first step, solid polythene waste will go through thermal cracking at about 350°C-750°C. In the second step, the formed ethene gas will be hydrated in a cyclic process in the presence of an acid catalyst like phosphoric acid. The formed gases will be passed through a multilayered mesh coated with solid phosphoric acid catalyst producing ethanol as a major product [1]. The gaseous components can be cooled and dissolved inside a scrubber to yield ethanol and some lower alcohols. Ethanol can be distilled from this mixture using fractional distillation.

The aforementioned is theoretically proposed after literature survey and once analytically verified, can lead to commercial production of ethanol from waste polythene.

1. Morrison, R.T., Boyd, R.N. and Boyd, R.K. 1992, *Organic Chemistry*, 6th edn. p. 110, Benjamin Cummings Publications

Reducing the Carbon Footprint

Harshita Khurana

Department of Chemistry, Hansraj College, New Delhi

Carbon footprint refers to the total amount of greenhouse gases in the atmosphere caused by an individual, event or organization. The carbon footprint is 54 % of humanity's overall ecological footprint and its most rapidly growing component.

The total amount of carbon footprint is not easy to calculate because of large amount of data required and the fact that carbon dioxide can also be produced by natural occurrences. The average household carbon footprint is 50 tonnes per years.

Developed countries are contributing most to the carbon emissions with USA as the largest contributor. Most of the carbon emissions come from burning of fossil fuels. The drastic effects include global warming & global climate

change. Each one of us can contribute our part towards reduction of carbon footprint. Reduce, reduce & recycle should be the principle of our life. After all, it is our duty to give our future generations a healthier earth to live in.

1. <http://articles.economictimes.indiatimes.com/keyword/carbon-footprint>
2. <https://www.gov.uk/government/statistics/uk-carbon-footprint>
3. <http://www3.epa.gov/climatechange/ghgemissions/gases/co2.html>

Research in Chemistry to Generate Green Energy

Amisha Verma

1997.vermaamisha@gmail.com

As global supplies of oil, coal and natural gas shrink and as climate change becomes an increasingly important environmental concern, green energy is clearly a way for future. Difference between renewable energy and green energy can be made by saying that renewable energy comes from natural resources whereas green energy includes natural energetic processes that can be harnessed with little pollution.

Types of green energy are; anaerobic digestion, geothermal power, wind power, small scale hydropower, solar energy, biomass power, tidal power, wave power, CHP (combined heat and power) and some forms of nuclear power. In the case of nuclear power some say that it's a form of green energy but others claim problems associated with radioactive waste.

Information regarding need of harnessing green energy and the ways will be explained further by taking into account the types of green energy. Points will be taken into consideration by how we can go for green energy production and usage. This can include usage of solar energy, heat pumps, LED lighting, various other energy saving ideas.

There has been a lot of research in the photovoltaic market:

- 1) first generation-using multi crystalline silicon wafers,
- 2) using thin film solar cells based on amorphous silicon-hydrogen alloys.

We can too have thermoelectric power generation using waste- that is using heat energy as an alternative for green technology.

Pseudocapacitive Properties of Symmetry and the Asymmetry Two Electrode Type Supercapacitor Cells Made from Polyaniline-Hybrid carbon assemblage composites

Ashok K. Sharma^{1*}, Preetam Bhardwaj¹ and Sundeep K. Dhawan²

¹Department of Materials Science & Nanotechnology, D.C.R. University of Science & Technology, Murthal (India), ²Conducting Polymers Group, CSIR-National Physical Laboratory, New Delhi (India)

Pseudocapacitive properties of synthesised polyaniline integrated with hybrid carbon assemblage in a two-electrode

cell type supercapacitor were investigated. Successful formation of the composites was confirmed with techniques such as transmission electron microscopy (TEM), scan electron microscopy (SEM), electron dispersive X-ray spectroscopy (EDX) and X-ray diffraction spectroscopy (XRD). The pseudocapacitance behaviour of both the symmetry and the asymmetry PANI and PANI-HC based supercapacitor in 1 M H₂SO₄ electrolyte was evaluated using cyclic voltammetry (CV), electrochemical impedance spectroscopy (EIS) and galvanostatic constant current charge-discharge (CD) techniques. There was a good correlation between the CV and the GCD specific capacitance (SC) values for the symmetry and asymmetry supercapacitor. The symmetric and asymmetric configuration of 025PANI-HC cell approaches specific capacitance, energy density and power density of 194 F/g, 107 Wh/Kg, 873 W/Kg and 257 F/g, 142 Wh/kg, 978 W/kg at 1 A/g current density in 1mol/L H₂SO₄, respectively, indicate usefulness of electrode material for supercapacitor application.

Chromium speciation in water samples using various solid phase extractants and determination by Hyphenated Flow Injection Flame Atomic Absorption Spectrometry (FI-FAAS)

Shelja Tiwari, Niharika Sharma and Reena Saxena

Department of Chemistry, Kirori Mal College, University of Delhi, Delhi, India

The chemistry of Cr (III) and Cr (VI) is entirely contrasting to each other. Cr(III) is essential for glucose and lipid metabolism in mammals, whereas Cr(VI) is a carcinogen with strong oxidizing properties. Thus, selective determination of both species in environmental samples is of prime importance. In the last decade, solid phase extraction (SPE) was the method of choice and solid sorbents were used with and without chemical modification. In speciation analysis SPE offers many advantages the most important can be listed as selectivity, stability etc. One of the most widely used spectroscopic detection techniques is FAAS. It can be easily hyphenated to flow injection (FI) systems which makes the system automated and fast. The hyphenation of FI system to FAAS along with SPE has proven to be an excellent method for the speciation of chromium at ultra trace levels. Recent trends and futuristic aspects of the SPE to be used for speciation analysis are highlighted.

1. R. Saxena, S. Tiwari and N. Sharma, *RSC Adv.*, 2015, **5**, 69196.
2. R. Saxena, N. Sharma and S. Tiwari, *Anal. Sci.*, 2015, **31**, 1303.
3. S. Tiwari, N. Sharma and R. Saxena, *New J. Chem.*, 2016, **40**, 1412.

Waste Disposal and Recycling

Mohit Sheokand

Department of Chemistry, Hansraj College, Delhi University

Waste management is one of the most important topic in the contemporary times. Waste is basically the unwanted or useless materials. In biology, waste is any unwanted

substance expelled from living organisms, metabolic waste such as urea and sweat. In this presentation i will be focusing on the types of wastes and its health impacts. Further, waste treatment processes and types will be discussed covering their advantages and disadvantages. Also some statistical data will be shared. Various research in the field of waste management has been done but further improvement is required for mitigation of waste.

Integrated Applications of Algal Biomass for Textile Effluent Treatment and Biodiesel Production

Bhawna Rana, Kannikka Behl, Surbhi Sinha, Subhasha Nigam

Amity Institute of Biotechnology, Amity University, Noida, Uttar Pradesh

Releasing of textile dyes into water bodies is a major environmental issue. Sustainable, eco-friendly bioremediation of azo-dye still remains a challenge to save the aquatic ecosystem. The focus has now shifted to the use of biological techniques for the treatment of textile dyes. This study was directed towards evaluating the potential of microalga (*Chlorella pyrenoidosa*) for simultaneous treatment of textile wastewater and lipid biosynthesis for the production of biodiesel. [1] *Chlorella pyrenoidosa* shows superior results in terms of maximum specific growth rate of 416 mg/m³(glycerol)and 867mg/m³(sodium acetate), biomass yield of 121 mg/m³/d and total lipid content of 17.3% (glycerol). The FAME (Fatty Acid Methyl Ester) composition of *Chlorella pyrenoidosa* lipid was found to be encouraging for biodiesel application and saturated: unsaturated fatty acid was favourable to about 3.82:1.[2] The study indicates that *Chlorella pyrenoidosa* can effectively utilize textile wastewater instead of using synthetic culture medium for its growth and can produce a significant amount of biomass for biodiesel production.

1. Sinha S., Singh R., Chaurasia AK and Nigam, *Journal of Hazardous Materials*, 2016, vol 306, Pg no. 386-394
2. Nigam S, Rai M.P., Sharma R, *Biomass and Bioenergy* 2013, vol 58. Pg no. 251-257

Waste disposal and recycling

Shubh Narayan, Lakshya Bajaj

¹Chemistry Department, Hansraj College, University of Delhi

Recycling is the process of converting waste materials into reusable objects to prevent waste of potentially usefull materials, reduce the consumption of fresh raw materials, energy usage, air pollution (from incineration) and water pollution (from land filling) by decreasing the need for "conventional" waste disposal and lowering greenhouse gas emissions compared to plastic production. Recycling is a key component of modern waste reduction and is the third component of the "Reduce, Reuse and Recycle" waste hierarchy.

Waste management is all those activities and action required to manage waste from its inception to its final

disposal. This includes amongst other things, collection, transport, treatment and disposal of waste together with monitoring and regulation. It also encompasses the legal and regulatory framework that relates to waste management encompassing guidance on recycling etc.

The term usually relates to all kinds of waste, whether generated during the extraction of raw materials, the processing of raw materials into intermediate and final products, the consumption of final products, or other human activities, including municipal (residential, institutional, commercial), agricultural, and special (health care, household hazardous wastes, sewage sludge). Waste management is intended to reduce adverse effects of waste on health, the environment or aesthetics.

Green Chemistry

Niharika and Anjali

Shyam Lal College (D.U.)

Green chemistry is the utilization of a set of principles that reduces or eliminates the use or generation of hazardous substances in the design, manufacture and application of chemical products. This is a new philosophical approach that through application and extension of the principles of green chemistry can contribute sustainable development. Green chemistry is essential in developing the alternative for energy generation by technologically and economically (hydrogen cell, solar energy, bio-fuels).

Why to approach green chemistry to produce green energy- in case of traditional chemistry the chemical industry relies almost entirely non renewable petroleum as the primary building block to create chemicals. This type of chemical is very intensive inefficient and toxic resulting in significant energy used and generation of hazardous waste. But in case of green chemistry it is to prioritize the use of alternative and renewable materials include use of agricultural waste, biomass and non-food related products and chemical reactions with these materials with less hazardous than when conducted with petroleum products. And this method focused the safely degrade in environment, efficiency and simplicity in chemical processes.

Method of preparation of green energy through green chemistry-(a) production of bio-diesel from vegetable oil with batch method - take a waste and virgin vegetable oil and methanol and KOH catalyst at 55 degree Celsius. This process with KOH catalyst produce bio-diesel as well as soap and glycerol that have to be removed before use. Wash with water to remove soap and separate glycerol from bio-diesel test of presence and quality of bio-diesel by mass spectrometrically. (b) preparation of solar cell of green energy from green method-solar energy is only renewable resource that have enough terrestrial energy potential to satisfy a 10-20 TW carbon-free supply supply constraint 2050. The solar energy is a technology intended to reduce both air pollution and CO₂ emission is the use of photo voltaic cell to generate electricity (electrons) from photons emitted by sun. For example through the use of nanotechnology the light and energy generation of crystalline silicon solar cells or organic solar cells can be

enabled significantly increased. Their manufacturing also requires less material and is more efficient.

Advantage and disadvantage of green energy-. The advantage of using green energy sources is that they are cleaner so they do not emit as many harmful pollutants into the air, which creates a lesser impact on the environment. Green energy sources are also renewable which means we will never run out of them. The disadvantage is the fact that some of the green energy sources cannot be installed in certain areas of the planet. For instance, wave energy can only be utilized if ocean waves reach at least 16 feet. The use geothermal energy can only be done in geologically unstable parts of the planet.

Conclusion: chemicals and much more satisfactory pouring into the environment. Green research areas and their applicably appropriately provide safer specialty chemicals and much more satisfactory processes for the chemical industry.

Reducing carbon footprints

Aishwarya Rai, Joy Bhattacharya

Department of Chemistry, Hansraj College, University of Delhi, Delhi

Of all the potential threats faced by the present world, carbon footprint tops the index. When talking about climate change, footprint is a metaphor for the total impact that something has. And carbon is a shorthand for all the different green house gases that contribute to global warming. The term carbon footprint, is a shorthand to describe the best estimate that we can get of the full climate change of the impact of something. That something could be anything-an activity, an item, a lifestyle or even the whole world.

In our presentation we'll be dealing with the factors that are accountable for the increased levels of greenhouse gases primarily carbon. On the basis of studies conducted by us we'll also be discussing about the efforts that can be made on the grassroot level for dealing with the perils of carbon footprint. A lot have been done and so much more is yet to be if we want this earth to be a better place to live in.

POSTER PRESENTATIONS

Preparation of Biodiesel from Used Olive Oil

Meenakshi Garg, Deeksha, Vandana Batra and
Susmita Dey Sadhu

*Department of Food Technology, Department of Physics
Department of Polymer Sciences, Bhaskaracharya College of
Applied Sciences, University of Delhi, Dwarka, New Delhi-110 075*

In today's world, our life is highly dependent on energy. Due to high consumption of the natural fuel and gases the resources for the same are going to finish at a very high rate. The world is now looking for a sustainable alternative of energy. Bio diesel is one of the promising area coming up where the bio resources like oil, vegetables and fatty acids may be used as an alternative to mineral oil and gases. For this reason, in this work bio diesel have been prepared from waste oil sources by green chemistry method. This way, the work process also is useful from environmental point of view where waste is being reused and also because of green technology the process is safe and environmentally safe. The percentage yield of the biodiesel is about 70%. The calorific values of the bio diesel(8Kcal/gm) suggests that it can be used in place of mineral oil and also does not require the replacement or alternation of the car engines. The Fourier Transform Infrared Technique (FTIR) studies reveal that the structure of the biodiesel has the presence of ester groups.

Fruits Peels Get a Second Life as Water Purifiers

Nandini Dixit, Anjali Jain

Deshbandhu College, University of Delhi

Access to clean drinking water is a worldwide problem. Each year, waterborne pathogens make tens of millions of people sick and lead to 1.8 million deaths. And all of these are preventable. By using peels of fruits it was believed that it make water safe to drink, so for this....Banana and orange – a versatile biomass for water purification. Highly colored industrial waste water is a serious environment problem as it seriously discolors waterways as well as blocking sunlight for photosynthesizing plant species in the water. Mining process, run off from farms and industrial waste can all put heavy metal such as lead and copper which can be treated by solid phase extraction using banana peels for waterways. Orange peels is used as absorbent for removal of acid dyes from industrial effluent which are highly colored, and disposal of these waste into the environment can be extremely deleterious. Using of fruit peels for the purification of water has many advantages such as it is eco-friendly, low cost, natural and abundant source for removal of harmful or undesirable species in the water effluent, it is been alternative to most costly materials.

Phytoremediation: Green Therapy to Cure Polluted Environment

Mithlesh Kumar Temre, Thaleswar Verma,
Deepak Kumar Dubey and Rajeev Kumar Jain

*Department of Education in Science and Mathematics, Regional
Institute of Education, NCERT, Bhopal-462013, India*

Human population is increasing continuously and simultaneously requirement for various human need rising. Growing industrialization to fulfill human need increases various types of pollutions on our planet. The rapid build-up of toxic metal and other pollutants not only affects natural resources, but also causes major strains on ecosystems. Phytoremediation as a method to solve environmental contamination has been growing rapidly in recent years. In this green therapy, tolerant plant has been utilized in a contaminated matrix to remove environmental contaminants by facilitating detoxification of the pollutants. Plants are unique organisms equipped with remarkable metabolic and absorption capabilities, as well as transport systems that can take up nutrients or contaminants selectively from the growth matrix, soil or water. Phytoremediation is an ideal, cost effective, solar energy driven cleanup technology which can be used to clean our environment. In this poster presentation, phytoremediation technology will be explained briefly.

Waste Disposal and Recycling

Aditi Singh, Maansi Khanna

Chemistry, Hansraj College ,University of Delhi, INDIA ,

Over 6 billion people live on Earth. Every person creates waste such as food packages, made of cardboard and plastics, aluminium cans, worn out tires, used paper, broken down cars, bent bicycle, old toothbrushes, grass clippings, leftover food, old movie tickets, etc. Whatever we throw away. Where Does It All Go?

In towns and cities all over the world, trash is put into a dump. A dump is a place where trash is left in one spot on top of the ground or in deep holes in the earth. The holes are filled with trash. This is done year after year, until there is no room at the dump. Then, a new dump is begun. In some towns, there is no room left for the dump. Trash has to be moved to the dumps in other towns.

One of the worst problems with older dump is that polluting chemicals were dumped there before any rules were made about how to handle it. Those chemicals seep into the soil and into the water, polluting that also.

In some towns and cities where the space for dumps is running out, laws have been passed that make people recycle. Using something again is called Recycling. For example, a lot of used plastic and glass can be melted and reshaped into new containers, carpeting, play ground equipment, and a lot of other useful items. Paper can be cleaned, soaked in water and turn into new paper.

3. <http://www.kidsecologycorps.org/our-environment/natural-cycles/waste-disposal>

Development Of Theranostics Based Product With Curcumin-Oligonucleotid-Rare Earth Metal based Nanoparticle Probes As MRI Contrast Agent

Dr. MeenuS. Shrivastava¹, Anshula Dhiman²

¹Department of Chemistry, Hindu College, ² Department of Zoology, Hindu College

Target-specific drug delivery and early diagnosis in cancer treatment is one of the priority research areas in which nanomedicine plays a vital role. Nanotheranostics aims at formulation of the therapeutic and diagnostic agents in nanomedicine as a single theranostic platform, which can then be further conjugated to biological ligand for targeting. Potential applications of theranostic nanomedicine formulations range from the noninvasive assessment of the bio distribution and the target site accumulation of low-molecular-weight drugs, and the visualization of drug distribution and drug release at the target site, to the optimization of strategies relying on triggered drug release, and the prediction and real-time monitoring of therapeutic to diagnose and treat the disease at cellular and molecular level. In particular gadolinium based compounds have the ability to enhance the contrast in MRI for better in vivo visualization. Lipid based formulations, liposomes loaded with curcumin conjugate and a gadolinium based contrast agents have been developed as new modalities for better theranostic effects with fewer side effects in cancer treatment. The fruition of nanotheranostics with highly suitable systems for (pre-) clinical implementation will also be able to provide personalized therapy with bright prognosis and less toxic treatment regimens for individual patients of cancer.

Analytical study of morphological and economically important traits of *Garcinia indica*

Romila Rawat Bisht,¹ A.K. Bhatnagar²

¹Department of Botany, Hansraj College, University of Delhi.
²Professor Emeritus, IGNOU, Delhi

Garcinia indica, an endemic tree species of Western Ghats in India, has been exploited throughout world for its property to regulate obesity. The fruit rind is an important source of stereoisomer of hydroxycitric acid (HCA). HCA triggers signals in brain to suppress appetite. Chemically it inhibits the oxidation of fat. The study of diversity in morphological and economically important traits of a species can help to locate and collect the best germplasm. Keeping this as a major objective, fruit samples from five different sites in Western Ghats were collected. These were statistically analyzed for their size, rind thickness, fatty acid and ascorbic acid content, seed protein and oil, and HCA content. High Performance Liquid Chromatography (HPLC) was carried out for HCA content. The samples were significantly different most of their economically important traits. The differences in these traits are probably because of

the habitat, topography and climate. The conservation of germplasm from specific location should be the priority of environmentalist and pharmaceutical scientist.

Synthesis and Characterization of Transition metal doped Polymer/Carbon Nanotubes composite for Supercapacitor Electrode

Ashok. K. Sharma, Gunjana Chaudhary

Thin Film Lab, Department of Materials Science & Nanotechnology, D.C.R. University of Science & Technology, Murthal (India)

A facile in-situ chemical oxidative route for synthesizing transition metal doped polymer/Carbon nanotubes composite has been reported. The possible interactions between transition metal ions and PANI/CNTs were analysed by FTIR spectroscopy and UV-Visible spectroscopy. The X-Ray diffraction technique revealed the crystalline nature of the composite and indicates successful incorporation of metal ions in the composite structure. The morphological characteristics of the electrode materials were investigated by field emission scanning microscopy (FESEM). It is observed that composite has uniform coating of polymer onto CNTs surface. Composite possess the benefits of pseudoactive species and high surface area of CNT which make them promising candidate for applications in supercapacitor.

Design, Synthesis, Spectral Characterization and Molecular Docking of Pyrazole Derivatives as Selective Cox-II Inhibitors and Anticancer Agents

Ozair Alam, Md.Jahangir Alam, Md. Javed Naim and Neelima Srivastava

Dept. of Pharmaceutical Chemistry, Faculty of Pharmacy, Jamia Hamdard, New Delhi-110062

A novel series of pyrazole bearing methyl amine derivatives (**8a-p**, &**11a**, **11b**) were characterized by IR, NMR and Mass spectral data and evaluated for *in-vivo* anti-inflammatory, analgesic, *in-vitro* COX-II and TNF- α inhibition activities. Compounds **8b**, **8d**, **8i**, **11a** and **11b** exhibited potent anti-inflammatory activity along with analgesic activity and it also exhibited optimal COX-II inhibitory potency with (IC₅₀= 1.90, 2.99, 2.87, 2.24, 2.60 and 3.11 μ M respectively) along the selectivity index (SI) in range of 14-72. Structure activity studies revealed that compounds **8i** and **11a** are highly potent anti-inflammatory agents and selective COX-II inhibitors (IC₅₀ -2.99 and 2.60 μ M, SI=64.40 and 72.73 respectively) which is comparable to celecoxib (IC₅₀- 0.31 μ M; SI-78.06). The results of *in-vivo* and *in-vitro* studies prove that pyrazole ring attached with benzene sulphonamide groups could generate more potent anti-inflammatory and anticancer agents and it was also ascertained by docking analysis.

Green Energy through green synthesis of zero valent iron nanoparticles

Diksha Changulani, Pratishtha Khurana, Priti Malhotra, Avneet Kaur

Daulat Ram College, University of Delhi, Delhi-110007, India

Iron nanoparticles (Fe NP) have been receiving ample attention by researchers due to their wide range of applications in various fields. Owing to their high intrinsic reactivity on their surface sites, they have been successfully employed for remediation of heavy metals from soil. Earlier methods of synthesis of Fe NP were based on using sodium borohydride as the reducing agent which incurred high cost and were toxic to the environment. To overcome these factors, the proposed green synthesis of Fe NP from biorenewable natural sources are bound to attract a great deal of attention. The green extracts are not only non-toxic and biodegradable but also act as both a dispersing and capping agent which also help to minimize the oxidation and agglomeration of zero valent Fe NP. FeNP obtained can be used in the remediation of waste ground water *e.g.* for removal of Ni(II), As(III), Cd(II), Pb(II) etc. Also, they can be used for the catalytic elimination of various environmental pollutants using bimetallic Fe NPs. Their strong reducing ability can be used to remove numerous pollutants (*e.g.* heavy metals, halogenated organic compounds, nitro and azo compounds and oxyanions). The technique for obtaining nanoparticles using naturally occurring reagents like plant extracts as reductants and capping agents could be considered as significant and attractive.

1. W.Wu, Q.He, and C. Jiang, *Nanoscale Research Letters*, vol. 3, no. 11, pp. 397–415, 2008.
2. Abhilash, K. Revati, and B. D. Pandey, *Bulletin of Materials Science*, vol. 34, no. 2, pp. 191–198, 2011.
3. G. E. Hoag, J. B. Collins, J. L. Holcomb, J. R. Hoag, M. N. Nadagouda, and R. S. Varma, *Journal of Materials Chemistry*, vol. 19, no. 45, pp. 8671–8677, 2009.
4. M. N. Nadagouda, A. B. Castle, R. C. Murdock, S. M. Hussain, and R. S. Varma, *Green Chemistry*, vol. 12, no. 1, pp. 114–122, 2010.
5. T. Shahwan, S. Abu Sirriah, M. Nairat et al., *Chemical Engineering Journal*, vol. 172, no. 1, pp. 258–266, 2011.

Extraction of Algal Lipids for Use in Biodiesel Production

Sumit Dhanda and Bharat Meena

Chemistry Department, Hansraj College, University of Delhi

Due to limited fossil fuel supplies and global climate change, alternative energy sources must be found. Biodiesel produced from algae shows great potential to sustainably replace petroleum-based transport fuel, but technological hindrances, including inefficient lipid extraction, have prevented their implementation.

Approach: In order to improve upon the current extraction methods, cell disruption, greener solvent systems, selective extraction, and simplified extraction-fuel conversion processes will be evaluated for their ability to increase efficiency and decrease hazard associated with lipid

extraction. In particular, supercritical carbon dioxide (scCO₂) will be used as a non-polar solvent to solubilize the algal lipid. The supercritical extraction conditions will be modified by varying pressure, temperature, and co-solvent use, in order to find the most effective conditions in terms of efficiency and selectivity. The efficiency of extraction can be evaluated by assessing the fatty acid methyl ester (FAME) content of the lipid extraction and thus the algal biodiesel production potential. Further, the selectivity of each variation can be quantified by also assessing the full lipid profile of the extract, including triglyceride and phospholipid content.

Supercritical carbon dioxide (scCO₂) was used to extract components of interest from *Scenedesmus dimorphus*, a microalgae species, under varied algal harvesting and extraction conditions. Liquid chromatography-mass spectrometry (LC-MS) was used to quantify the concentration of fatty acid methyl esters (FAME) and the FAME profile of transesterified lipids, phospholipids and pigments extracted under varied supercritical temperatures and pressures. The scCO₂ extraction results are compared with conventional solvent extraction to evaluate differences in the efficiency and nature of the extracted materials. Algae harvested by centrifugation (*vs.* lyophilization) demonstrated a similar extraction efficiency in scCO₂, indicating potential energy benefits by avoiding conventional algal mass dehydration prior to extraction. Centrifuged algae and optimized extraction conditions (6000 psi; 100 °C) resulted in comparable FAME yields to conventional processes, as well as increased selectivity, reflected in the decreased pigment, nitrogen and phospholipid contamination of the FAME. Cell pre-treatments—sonication, microwave, bead beating and lyophilization—showed an enhancement in extraction yield in both conventional solvent and scCO₂ extraction, allowing for improved extraction efficiencies. This study suggests that scCO₂, a green solvent, shows great potential for algal lipid extraction for the sustainable production of biodiesel.

Depolymerisation of Post-consumer PET Bottles using Waste Acid

Stuti Sagar and Ram Singh

Department of Applied Chemistry, Delhi Technological University, Delhi – 110 042, India

Poly(ethylene terephthalate) [PET] is widely used in the manufacture of high strength fibres, soft drink bottles and photographic films. With increasing PET consumption as packaging material, the effective utilization of PET wastes has received wide attention for the preservation of resources and protection of the environment. A study conducted in Mumbai indicated that an average 25,03,334 virgin PET bottles were used for packing carbonated soft drink and water bottles per month in Mumbai only. Average consumption of Hotels, Airline and Caterers was 7.5 kg/day, 70.25 kg/day and 11.75 kg/day respectively there. Also, along with the other application of PET, these accounts for 8% by weight and 12 by volume of the World's solid waste (www.plasticsnews.com; www.plasticseurope.org; accessed on December 5, 2015). Taking a closer look on the world

statistics, the observed facts includes the waste PET generation of 2.67 million tons, or 1.1% of municipal solid waste (MSW) by weight and 17.28 pounds of PET bottles per person per year.

Depolymerization is an important method for utilization of the waste PET. In the present work, we are using the waste acid to depolymerise the post-consumer PET bottles.

Waste-No More a Nuisance

Apoorva Grewal and Shaili Singh

Department of Chemistry, HansRaj College, Delhi University

This poster presents an overview on the history of waste, its types, and the methods of its disposal and recycling. It focuses on the problems posed by solid waste, radioactive waste and waste from Electric and Electronic Equipments (WEEEs) which are currently considered to be some of the fastest growing waste streams in the world with huge impact on health and environment. Mountains of hazardous waste have been created on the outskirts of mega cities. Various methods like land filling, incineration and composting have been used for waste management, but none of them fully satisfy the growing need of waste management in major cities.

The poster throws light on new research in the field of waste management like Steam Pyrolysis of Amides as a Waste Solvent Management Method [1], Solid Waste Management through Plasma Arc Gasification [2], Greenhouse gas emission factors for recycling of source-segregated waste materials [3], etc.

1. Deepak D. Dicholkar, Vilas. G. Gaikar and Shekhar Kumar. Energy Procedia, 2011, 7, 534–539
2. Anubhav Ojha, Abhishek Clement Reuben, Durgesh Sharma. APCBEE Procedia, 2012, 1, 193 – 198
3. David A. Turner, Ian D. Williams, Simon Kemp. Resources, Conservation and Recycling., 2015, 105, 186–197

Waste Disposal and Recycling

Tanushree Gupta, Alisha Debas

Chemistry Department, Hansraj College

Waste management is all those activities and action required to manage waste from its inception to its final disposal. This include amongst other things, collection, transportation, treatment and disposal of waste together with monitoring and regulation. It also encompasses the legal and regulatory framework that relates to waste management encompassing guidance on recycling etc. For example- land fill trash in grey or black bins. Recyclable waste in blue colored bins and organic waste in green colored bins. There are number of concepts about waste management which vary in their usage between countries or regions.

E-waste or Electronic waste is also called universal waste. E-waste is the waste which includes electronic equipment, mercury containing equipment, LED, etc. all these contains a lot of heavy metals and toxic material that can seep into the water supply or poison ground. All of these materials can be contained and most can be reused, if they are properly disposed off.

There are 3R's of waste management. These are Reduce, Reuse and Recycle. It is the order of priority of actions to be taken to reduce the amount of waste generated and to improve the overall waste management processes and programs.

Research in chemistry to generate green energy

Karan Ghelot, Ridhima Jain

Department of Chemistry, Hansraj College

Biofuels play an essential role in reducing the carbon emissions from transportation. Current biofuels, such as ethanol, have a lower energy content compared with conventional hydrocarbon fuels, petroleum and natural gas. The aim is to produce fuels that have a high carbon content and therefore have a higher volumetric energy density. This can be achieved by chemical reactions that remove oxygen atoms from biofuel chemical compounds. This process produces a so called 'drop-in biofuel', i.e. a fuel that can be blended directly with existing hydrocarbon fuels that have similar combustion properties.

Levulinic acid and furfural are examples of potential 'platform molecules', i.e. molecules that can be produced from biomass and converted into biofuels. Levulinic acid can be produced in high yield (>70%) from inedible hexose bio-polymers such as cellulose, which is a polymer of glucose and the most common organic compound on Earth. Furfural has been produced industrially for many years from pentose-rich agricultural wastes and can also act as a platform molecule.

1. Q Bond, D M Alonso, D Wang, R M West and J A Dumesic, Science, 2010, 327, 1110
2. A Corma, O de la Torre, M Renz and N Vollandier, Angew. Chem. Int. Ed., 2011, 50, 2375

Synthesis and biological screening of 1,3,4-oxadiazole clubbed quinoxaline Derivatives as potential anti-inflammatory Agents.

Mohammad Shahar Yar, Zulphikar Ali, Md Jawaid Akhtar, Ahsan Ahmed Khan, Md Rafi Haider

Department of Pharmaceutical Chemistry, Faculty of Pharmacy, Hamdard University, Hamdard Nagar, New Delhi-110062, India

A new series of substituted 2-(phenyl)-5-(quinoxalin-2-yl)-1,3,4-oxadiazole derivatives (**5a-l**) were designed and synthesized from the key intermediate Quinoxaline-2-carbohydrazide (**4**). Cyclization of (**4**) with substituted aromatic acids in the presence of phosphorous oxychloride (POCl₃) afforded 1, 3, 4-oxadiazole derivatives (**5a-l**). The structure of synthesized derivatives was confirmed by ¹H NMR, ¹³C NMR, IR and mass spectrometry. All the compounds were evaluated for anti-inflammatory activity by carrageenan induced rat paw edema method. Among the synthesized derivatives, compound **5d** was found to be most

active (**81.95 %**) and equipotent to indomethacin (**86.30 %**). The compound **5d** exhibited lower ulcerogenic activity probably due to the inhibition of lipid peroxidation in the gastric mucosal wall. Furthermore, compound **5d** was found to be potent COX-2 inhibitor, having a selectivity index (SI) of 115.3, as compared to the standard COX-2 inhibitor Celecoxib (SI = 117.5). Docking studies of the compound **5d** revealed that interaction with key amino acid residues Arg120 and Tyr355 is responsible for COX 1 and COX 2 inhibition.

Optimization of Parameters for *In-situ* Hydrolysis and Extraction of Solasodine from Fruits of *Solanunvirginianum* L.

Showkat R. Mir, AnzarAlam, Md. Munawwar Alam, Saima Amin

Phytopharmaceuticals Research Laboratory, Faculty of Pharmacy, HamdardUniversity, PO Hamdard Nagar, New Delhi, India

Solasodine is a potential alternative to diosgenin which is used in the synthesis of steroidal drugs through the formation of 16-dehydropregnelone. The biggest problem, however with the extraction of solasodine from the plant materials is the formation of hydrolysis intermediates of glycoalkaloids as precipitates resulting in its low yield as well as low purity.

The present study was performed with the aim of optimizing the solasodine extraction from fruits of *Solanumviriginianum* L. Initial extraction studies were carried out in two hydro-alcoholic solvent systems *viz.*, methanol-water and 2-propanol-water with a solid-to-solvent ratio of 1: 8 w/v. The yield of crude solasodine was selected as the basis for assessment. The methanol-water solvent system was found to give higher yield than 2-propanol-water combination. Therefore, methanol-water was used as solvent for extraction in further studies.

The optimization of parameters was carried out in two stages. In single factorial design, one parameter was varied keeping the other parameters constant. The parameters such as acid concentration, reflux time and solvent system for *in-situ* hydrolysis and extractions were optimized. The assessment of these studies was done on the basis of solasodine content in the extractives by HPTLC densitometry at 510 nm. Ascending development on pre-coated silica gel plates using chloroform-methanol (5:1, v/v) as mobile phase was followed by derivatization with 10 % sulphuric acid and heating at 100° C for 20 min. Methanol content, acid concentration and reflux time were found to have significant effect on solasodine extraction. In further optimization more than one variable were simultaneously varied in order to study the interaction between variable. The optimum condition for *in-situ* hydrolysis extraction of solasodine was found to be: extraction with methanol-water (80:20, v/v) containing 5% HCl with a solid-to-solvent ratio of 1:8 w/v and refluxed for 4 hours.

Arsenic Bioremediation by Arsenite Oxidase from *Pseudomonas Stutzeri* TS44: An In-Silico Approach

Apeksha Shrivastava¹, Mymoona Akhter¹, M.Mumtaz Alam¹, M. S. Zaman¹, Shakir Ali¹

¹*Drug Design and Medicinal Chemistry Lab, Department of Pharmaceutical Chemistry, Faculty of Pharmacy, Jamia Hamdard, New Delhi-110062; 2 Bioinformatics facility, Jamia Hamdard, New Delhi-110062; 3 Department of Biochemistry, Faculty of Science, Jamia Hamdard, New Delhi-110062*

Bioremediation techniques using microorganisms especially bacteria have been a promising alternative technique for the removal of toxic metals like arsenic because of their low cost and eco-friendly nature. This article tries to find a bioremediation of arsenic using bacterial enzyme. We herein present the 3D models of arsenite oxidase of *Pseudomonas stutzeri* TS44 by homology modelling using BioPredicta module of the software VLifeMDS. BLASTp, ProtParam tool and CFSSP server were used to identify the conserved regions, to determine physicochemical properties and to predict the secondary structure of protein of the arsenite oxidase of *P. stutzeri* TS44 against the existing database respectively. The 3D structure of arsenite oxidase was modelled, validated and used as a target macromolecule for docking to find the chain having the best binding efficiency to accomplish bioremediation of arsenic. The results showed that arsenite oxidase Rieske subunit's chain D and Mo-pterin subunit's chain A of *P. stutzeri* TS44 are potential to be developed for the enzymatic bioremediation of arsenic

1. Rehman, A., A.S. Butt and S. Hasnain: Isolation and characterization of arsenite oxidizing *Pseudomonas lubricans* and its potential use in bioremediation of wastewater. *Afr. J. Biotechnol.*, 9, 1493-1498 (2010).
2. Nies, D.H. Microbial heavy metal resistance. *Appl. Microbiol. Biotechnol.* 1999, 51, 730-750.

Sustainable approach in denim production: handloom denim

Neha Arora¹, Seema Sekhri²,

¹*Department Of Fabric & Apparel Science, Lady Irwin College, University Of Delhi, New Delhi, India, ²Associate Professor, Department Of Fabric & Apparel Science, Lady Irwin College, University Of Delhi, New Delhi, India*

The issue of sustainability with regard to denim (fabrics) has for many years been a matter of concern to environmentally-concerned garment consumers as well as retailers. Also increased awareness among consumers and regulatory standards has increased the importance for sustainable clothing. They are gradually getting into mainstream fashion and consumer preferences. This trend, rather a necessity, has influenced the making of denims also. Denim is one of the oldest known fabrics in the recorded history of modern textiles. Its qualities like durability and comfort make it popular amongst all age group. Although it is very popular but it is the most pollution causing fabric

amongst all. Its manufacturing process consumes a lot of water and chemicals, it also discharges huge quantities of waste-water mixed with strong chemicals. The industrial production of denim, consumes a lot of electricity and steam, thereby consuming a lot of fuel. There is a very strong need to turn-around and look at the eco-friendly options available to us.

A recent development in the making of denim fabrics is handloom denim which is an ecofriendly method of denim production. It is both innovative and sustainable method of denim production. Denim made on handlooms is softer than mill made denim, has a unique texture, breathes well, helps feel cool in summer and retain body warmth in winter. It has negligible carbon footprint. The entire process of making fabric from yarn is hand-based. The handloom denim is made out of 100% cotton yarn.

The aim of present study is to understand the manufacturing process of handloom denim and problems encountered during manufacturing of handloom denim.

Arsenic toxicity in the environment

Pooja Gupta¹ and A.K.Bhatnagar²

²*Environmental Biology Laboratory, Department of Botany, University of Delhi, Delhi – 110 007, ¹Current Address- Department of Botany, Ramjas College, University of Delhi, Delhi – 110 007*

Arsenic (As) is ubiquitous in the environment originating from both natural and anthropogenic sources, and both may pose a threat to human health. Arsenic contamination of the environment is of particular interest among the various toxic elements because of its high toxicity and carcinogenicity of the inorganic redox species. Various As species get accumulated in living organisms and exert different toxicological impacts. Arsenic has been shown to be a non-essential element for plants; though it is considered to be essential for animals at low concentrations. It may be toxic to plants even at low concentrations, though at very low concentrations it has been reported to be beneficial for plant growth. At higher concentrations, As becomes toxic for all plants as it interferes with plant metabolic processes causing chlorosis, necrosis, inhibition of growth, often leading to death.

Although there are various settings of As exposure, ingestion of contaminated ground-water is more widespread. Arsenic exposure occurs to the greatest extent from contaminated drinking water with dissolved inorganic forms and secondarily from contaminated foods. However, As ingestion might also occur locally from air. In recent years, bioaccumulation of As in crops grown in areas with elevated atmospheric deposition, contaminated lands, and areas irrigated with contaminated ground-water has emerged as an issue of great concern.

Arsenic is well known to be poisonous to organisms. However, the toxic effect of As is highly dependent on its chemical form. Inorganic As species are generally considered to be more toxic than organic species. Arsenic is identified as a human metallic carcinogen by the US Environmental Protection Agency, World Health Organization and the International Agency for Research on Cancer. The adverse effects from exposure to this metalloid

are considered among the top priority health hazards in the world. Various carcinogenic, teratogenic and mutagenic effects of As have been recognized. Inorganic As is a general cellular poison causing arsenicosis that produces a variety of effects in different organ systems. It is known to cause cancers of several organs including skin, lung, liver, bladder and kidney.

The "Dark World" of Cosmetics

Akshat Verma¹, Vinay Gupta¹, Dileep Kumar Ojha¹, Pradeep Pratap Singh¹ and Ambika²

¹*Department of Chemistry, Swami Shraddhanand College, University of Delhi, Delhi-110036, ²Department of Chemistry, Hans Raj College, University of Delhi, Delhi-110007.*

Cosmetics are substances used to enhance the 'appearance' of the human body. Cosmetics include skin-care creams, lotions, powders, perfumes, lipsticks, nail polish, eye and facial makeup, hair colours and gels, toothpastes, dental care products, deodorants, personal hygiene products and many others. Millions of consumers use cosmetic and their ingredients on a daily basis. The cosmetics industry has traditionally relied on convincing people that they are incomplete without a particular product. In a country such as India, the dominance of fair skin has both a colonial and a caste legacy and the global narrative is that those at the top of society have fair skin. With issues such as employment and relationships often resting on skin tone, people invest in skin-whitening creams in the hope of a better existence. In addition, natural and synthetic substances may produce local effects in human skin, such as irritation, sensitization or photoreactions. Some of the chemicals used in the preparation of cosmetics are harmful and can even cause serious threatening diseases. Given the significant and relatively uncontrolled human exposure to cosmetics, these products must be thoroughly evaluated for their safety. This presentation will provide an overview of the dark world of cosmetics.

1. E. Antignac, G.J. Nohynek, T. Re, J. Clouzeau, H. Toutain. Safety of botanical ingredients in personal care products/cosmetics. *Food Chem. Toxicol.*, **2011**, 49, 324–341.

2. P. K. Nigam. Adverse reactions to cosmetics and methods of diverse reactions to cosmetics and methods of testing. *Indian J. Dermatol. Venereol. Leprol.*, **2009**, 75, 10–19.

Nanomaterials in waste water treatment

Ashish Tiwari¹, Liyaqat Ali Kamran¹ and Pradeep Pratap Singh¹

¹*Department of Chemistry, Swami Shraddhanand College, University of Delhi, Delhi-110036.*

Water is the most important and essential component on Earth for vital activities of living beings. As there are limited sources of drinking water and due to geometrical growth of population, industrialization and environmental changes quality of our water resources is deteriorating continuously [1]. Therefore there is an urgent need to conserve and purify this valuable resource. Air pollutants, litter, agriculture waste, sewage etc. are the major contributors of the

pollutants in water. A large number of organic, inorganic, and biological pollutants have been reported as water contaminants, such as heavy metals, organic pollutants, and many other complex compounds [2]. Some of these pollutants are highly toxic with a few being lethal and carcinogenic. Consequently, treatment of contaminated waste water is essential for a healthy life. The rapid and significant progress in waste water treatment has been made, including photo-catalytic oxidation, adsorption/separation processing and bioremediation. However, their application has been restricted by many factors, such as processing efficiency, operational method, energy requirement, and economic benefits. In this poster, an overview on the history of waste and its types, and methods remediation has been discussed.

1. L.B. Franklin. Waste water engineering: Treatment, disposal and reuse, McGraw Hill Inc., New York, 1991.
2. K.D. Fatta, I.K. Kalavrouziotis, P.H. Koukoulakis, M.I. Vasquez. Science of the Total Environment, 2011, 409, 3555.

Biodiesel: A Sustainable fuel Alternative

Kanika and Ambika

Department of Chemistry, Hansraj College, University of Delhi, Delhi-110036.

The world is confronting the energy crisis due to the excessive utilization of the world's depleting oil reserves. The world's economy is largely dependent on the transportation of goods and services, which is mainly dependent on energy from petroleum products. The utilisation of these fuels led to increasing prices, deteriorating health and environmental degradations. These concerns have led to the search for sustainable biofuel alternatives. Therefore, the research is aimed at retarding the risk of climate changes with reduced health problems. A renewable and sustainable fuel currently receiving renewed interests and intensive experimentations is biodiesel. It is increasingly becoming attractive as an alternative to petrodiesel. It is worthy to note that biodiesel is considered the fastest growing industry worldwide. The key focus of this presentation is to highlight the potential of biodiesel and its applications.

1. J.J. Cheng, G.R. Timilsina. *Renewable Energy*, **2011**, 36, 3541-3549.
2. F. Zhang, D.M. Johnson, M.A. Johnson. *Renewable Energy*, **2012**, 44, 380-391.

Gentle footprint today will ensure a path for tomorrow

Riya, Shiksha, Shyamali, Sakshi and Shubhi

Mentor: Darshan Singh, Ritu Gupta

Department of chemistry, Daulat Ram College, University Of Delhi.

Carbon footprint is a new buzzword that has gained tremendous popularity over the last few years. Carbon footprinting is actually a measure of the total amount of carbon dioxide and methane (greenhouse gases) emissions of a defined population system or activity considering all relevant sources [1]. Once the size of carbon footprint is

known, a strategy can be devised to reduce it by technological developments product management, carbon capture and changed green public. Everyone has a responsibility to reduce their individual carbon footprint and there are lots of ways to do so. We encourage everyone to think about their lifestyle decisions and find opportunities to reduce their climate impact. Basically, we should focus on the reduction of carbon footprint of cars, travel, air travel, home, office and your life [2]. Carbon footprints are much more specific than ecological footprints since they measure direct emissions of gases that cause climate change into atmosphere.

1. Wright, L., Kemp, S., Williams, I. (2011) 'Carbon footprinting': towards a universally accepted definition. Carbon Management.
2. Carbonfund.org (reduce what you can, offset what you can't).

Gentle Footprint Today will Ensure a Path for Tomorrow

Niharika Sharma

Chemistry, Hansraj College, University of Delhi, India

A carbon footprint is defined as the total set of greenhouse gas emissions caused by an individual, event, organization and is expressed as CO₂. The carbon footprint is 54% of humanity's overall ecological footprint and its most rapidly growing component.

The total amount carbon footprint cannot be calculated because of large amount of data required and the fact that carbon dioxide can be produced by natural occurrences. The average U.S. household carbon footprint is about 50 tons CO₂ per year.

Most of the carbon emissions come from fuel burned to produce goods far away from final consumer and deforestation, burning fossil fuels, over exploitation of natural resources. The most common ways to reduce the carbon footprint of human is to reduce, reuse, recycle, refuse. This can be done by recycling the packing materials, by using reusable items, by driving less, by using less air conditioning and heating in home, by optimizing the supply chain.

1. <http://articles.economictimes.indiatimes.com/keyword/carbon-footprint>
2. <https://www.gov.uk/government/statistics/uks-carbon-footprint>
3. <http://www3.epa.gov/climatechange/ghgemissions/gases/co2.html>

Reducing the Carbon Footprint

Vicky Khandelwal, Arushi Anand

Department of Chemistry, Hansraj College, New Delhi

A carbon footprint is defined as the total amount of greenhouse gases produced to directly and indirectly support human activities usually expressed in equivalent tons of carbon dioxide. It is the sum of two parts namely primary footprints and secondary footprints. Primary footprints is a measure of direct emissions of CO₂ from burning of fossil fuels. Secondary footprint is a measure of indirect CO₂ emissions from the whole lifecycle of products we use. The cause of carbon footprints is driving cars and other transportational vehicles that emit large amount of carbon dioxide into the air. Use of electricity, coal, gas also create

large carbon footprints. The ways to reduce carbon footprints are: alternative to driving, driving a low carbon vehicle etc, insulating and sealing your home, using more and more renewable resources such as wind power and solar power that emit no carbon. The 3R's principle is the most common way to reduce carbon footprints. Various acts and agreements were also passed in the world to reduce carbon footprints like climate change act 2008, global warming pollution act 2007, federal act, US-Canada air quality agreement.

1. <http://www.livestrong.com/article/152797-what-are-the-causes-of-a-large-carbon-footprint/>
2. <http://cotap.org/reduce-carbon-footprint/>

Conservation of some endangered and economically important medicinal plants of India – A sustainable approach

Neeti Yadav

Department of Botany, Daulat Ram College, University of Delhi, Delhi-110007

India has a great wealth of medicinal plant biodiversity which is used by various tribal's and local people to cure different ailments. Unchecked commercialization, habitat loss and habitat degradation have placed many medicinal plant species at a risk of extinction. Therefore there is an immense need for their conservation. There are two basic methods of biodiversity conservation: *in situ* (on site) and *ex situ* (off site), both are complementary to each other. *In situ* methods allow conservation to occur at gradual rate with natural evolutionary processes while *ex situ* conservation involves conservation outside the native habitat. *Ex situ* conservation via tissue culture technology helps in achieving the objective at a faster rate. The present paper discusses the various *in vitro* protocols developed for some of the selected endangered and economically important medicinal plants of India such as *Tinospora cordifolia*, *Pterocarpus santalinus*, *Stevia rebaudiana*, *Tylophora indica* and *Aquilaria malaccensis*.

Determination of Amoxicillin in Plasma by Liquid Chromatography Tandem Mass Spectrometric Detection

Saima Amin¹, Babar Ali¹, Showkat R. Mir¹

Faculty of Pharmacy, Hamdard University, PO Hamdard Nagar, New Delhi, India

The aim of this work was to develop a simple, sensitive and selective UPLC/MS/MS method for the estimation of amoxicillin in rat plasma. A protein precipitation followed by liquid-liquid extraction method was developed to isolate amoxicillin from rat plasma. Separation was performed on an Acquity UPLC BEH C₁₈ column (2.1 mm × 100 mm, 1.7 µm), using acetonitrile-1 mM ammonium acetate (85:15, v/v) as mobile phase. Amoxicillin was detected by Waters Q-TOF Synapt mass spectrometer when operated in positive mode with 1.0 min scan time and 0.02 s inter-scan delay.

Calibration curve with good linearity $r \geq 0.995$ was obtained in the range of 100-2000 ng/mL for amoxicillin. The mean recovery from plasma was 88.87% (± 5.89 SD, $n = 3$) for amoxicillin and 80.37% (± 6.21 SD, $n = 3$) for ampicillin (Internal Standard). The method provided a simple and selective procedure that can be easily used for the evaluation of pharmacokinetic profile of amoxicillin in plasma. The method was successfully applied to a bioavailability enhancement study of amoxicillin with oleic acid in rats.

Modified chelating sorbents in flow injection-SPE systems coupled to FAAS – A study of chromium speciation in industrial water samples

Niharika Sharma, Shelja Tiwari and Reena Saxena

Department of Chemistry, Kirori Mal College, University of Delhi, Delhi – 110007

Chromium exists in two chemically stable forms – trivalent and hexavalent. While Cr(III) is an essential component of the glucose tolerance factor, Cr(VI) exhibits carcinogenic activity and causes oxidative stress. Though singular analytical techniques such as flame atomic absorption spectrometry (FAAS) can determine the amount of total chromium, chromium speciation is important due to opposing biological behavior of the two forms. Solid phase extraction (SPE) is a sample preconcentration step required before speciation analysis due to the low concentration of chromium in environmental samples, especially water. SPE leads to reduction in solvent usage and extraction time, while removing interferences. Flow-injection SPE coupled with FAAS simultaneously preconcentrates and detects the chromium species. This coupled technique is advantageous as it offers high preconcentration factor, enhanced detection and quantification limits with high reproducibility. The application of different chemically modified chelating sorbents in chromium speciation in industrial water samples by preconcentration using flow injection-SPE and determination using FAAS has been explored.

1. N. Sharma, S. Tiwari and R. Saxena, RSC Adv., 2016, 6, 10775.
2. R. Saxena, N. Sharma and S. Tiwari, Anal. Sci., 2015, 31, 1303.
3. R. Saxena, P. L. Meena and S. Tiwari, Instrum. Sci. Technol., 2016, 44(2), 210.

Preparation and Characterization of Polymer Gel Electrolytes

Roshan Lal Sharma¹, Mohd. Abuzar, Kumar Gaurav² and Richa Srivastava¹

¹Department of Applied Chemistry, Delhi Technological University, Delhi – 110 042, ²Amity Institute of Biotechnology, Amity University, Gurgaon, Haryana 122413

Electrolyte, that separates cathode and anode, is one of the key components of a battery. It plays an important role in deciding charging/discharging capacity and current density

of a battery. Polymer gel electrolytes (PGE), comprising a polymer matrix plasticized with an electrolyte solution is of practical interest for the various types of fuel cell applications.^{1,2} They have several advantages over solid and liquid electrolytes. In recent years, a variety of polymers has been used to prepare such polymer gel electrolytes. PGEs have been given much attention due to their possible applications in various electrochemical devices such as fuel cells, humidity sensors etc. The most commonly available polymeric membrane is fluorinated membrane, known by its trade name, Nafion. It has shown good electrochemical property and mechanical stability. But still, its wide application is hampered by its high cost and difficulty in synthesis and processing.

The present work deals with the synthesis and characterization of PGE by using polyvinylalcohol (PVA) with an aim to get the high conducting membrane.

1. J. Qiao, T. Hamaya, T. Okada. *Polymer*, **2005**, 46, 10809–10816.

2. J.-W. Rhim, H.B. Park, C.-S. Lee, J.-H. Jun, D.S. Kim, Y.M. Lee. *Journal of Membrane Science*, **2004**, 238, 143–151.

Effects of 10 GHz microwave radiation in male infertility and its amelioration by melatonin

Geetika Bhalla, Saina Dhingra

Department of Chemistry, Hindu College, University of Delhi, India

Microwave at X-band (8-10 GHz) is widely used in communication systems for civil and military application devices such as aircraft, weather forecast system and various types of radars. Increased usage of such radiation in occupational environment poses a threat to human health. Our study aims to investigate the detrimental and deleterious effects of microwave radiation on reproductive system of male Swiss albino mice. The study also aims at investigating the ameliorating properties of Melatonin against the detrimental effects of these radiations on male reproductive system. A comparative analysis of the physiological and biochemical parameters of control group v/s radiation exposed group of animals will help us to explore the detrimental effects of harmful radiation on the reproductive system of mammals.

Research in Chemistry to Generate Green Energy

Kritika Jha

Department of Chemistry, Kirori Mal College

Green energy or Sustainable energy is derived from non-conventional energy which is continuously replenished by natural processes. If we see the electricity requirements of world including India are increasing at alarming rate and the power demand has been running ahead of supply. It is also now widely recognized that the fossil fuels and other conventional resources presently being used for generation of electrical energy, may not be either sufficient or suitable to keep pace with ever increasing demand of electrical energy of the world.

Chemists could smooth out the patchy supply of sun and wind power by developing fuels and batteries that can store energy during peak times. Various forms of green energy include solar energy, wind energy, hydroenergy, geothermal energy, wave and tidal energy. Renewable power is effective, reliable, sustainable, and environment friendly which we strongly need to cut our use of fossil.

Power Production from Waste Materials: A Review

Mahaveer Genwa¹, Alka Singh¹, Ankita¹, and P. L. Meena²

¹*Department of Chemistry, Deen Dayal Upadhyaya College (University of Delhi), Shivaji Marg, Karampura, New Delhi 110015, India*, ²*Department of Physics, Deen Dayal Upadhyaya College (University of Delhi), Shivaji Marg, Karampura, New Delhi 110015, India*

In today's world we are facing two major problems; one is energy crises and another is disposal of waste. This review aims to study the wide research field that has become a necessity for the sustainable development. The review has been brought out to study various types of wastes that are produced worldwide in the form of solid, liquid, gas, and heat and various techniques that have been evolved over due course of time from incinerators to modern waste-to-energy plants. Various pathways are studied in the review to convert the industrial waste to electrical energy that can be used easily. These include thermo-chemical, bio-chemical and physio-chemical conversion pathways for power production from industrial waste depending upon the nature of the waste. It also depicts the various factors affecting the energy recovery from waste which includes quality, quantity and physio-chemical parameters of waste. The review also includes efficiency of various techniques and various countries which are making best use of waste in power generation.

Waste Disposal and Recycling

Harsh Sharma

Department of Chemistry, Hansraj College, University of Delhi

"If it can't be reduced, reused, repaired, rebuilt, refurbished, refinished, resold, recycled or composted then it should be restricted, redesigned or removed from production."

Given the growth in population, the changing patterns of consumption and expansion of urban living, the need to properly manage waste is becoming a challenge throughout the world.

Evolution of Waste Management: The evolution in the waste management industry dictates change in the environmental well-being, decrease in the number of diseases, and reduction in the number of pest infestations. Waste Management solely focuses on ways to reduce risks of pollution produced from the waste generated from domestic, commercial, manufacturing, municipal consumption and disposal. Keeping all these factors in view,

how are we progressing in the field of waste management so that we can rely on some substantial efforts in the present and future?

Anaerobic Breakdown of Organic Waste: Initially bio waste was being composted in open air to be used as fertilizer. Later, in vessel compost plants were created to get rid from problems like odor. Through research and development in vessel waste treatment eventually evolved to Anaerobic Digestion. This new advancement utilizes microorganisms, kept in an environment without oxygen. Air tight reactors, known as anaerobic biogas digesters are used to transform this decomposed waste into bio gas. is utilized as energy and is adapted to fuel low-tech set ups in many developing countries today.

Zero Waste: According to the Zero Waste Alliance, “A future without waste and toxics is not just a dream; it’s a necessity. Waste reduces the effectiveness of our businesses, increases pressures on the natural environment and harms the vitality of our communities. It does not have to be this way; waste is the result of a broken process. Fortunately, this is a process that can be fixed.”

- Create and handling the overall process through a systematic approach; in order to, avoid and eradicate the harmfulness of waste.
- Protect and reuse energy that can be attained from waste resources.
- Eliminate discharge of toxic elements to water, air, land or those which are threatening quality of life, in any way.

The core principles of zero waste are quite identical to that of waste to energy as it emphasizes on utilizing waste to its core and transforming all to energy.

Waste Disposal and Recycling

Aditi Singh, Maansi Khanna

Chemistry, Hansraj College ,University of Delhi, INDIA

Over 6 billion people live on Earth. Every person creates waste such as food packages, made of cardboard and plastics, aluminium cans, worn out tires, used papers, broken down cars, bent bicycle, old toothbrushes, grass clippings, leftover food, old movie tickets, etc. Whatever we throw away. Where Does It All Go?

In towns and cities all over the world, trash is put into a dump. A dump is a place where trash is left in one spot on top of the ground or in deep holes in the earth. The holes are filled with trash. This is done year after year, until there is no room at the dump. Then, a new dump is begun. In some towns, there is no room left for the dump. Trash has to be moved to the dumps in other towns.

One of the worst problems with older dump is that polluting chemicals were dumped there before any rules were made about how to handle it. Those chemicals seep into the soil and into the water, polluting that also.

In some towns and cities where the space for dumps is running out, laws have been passed that make people recycle. Using something again is called Recycling. For example, a lot of used plastic and glass can be melted and reshaped into new containers, carpeting, play ground equipment, and a lot of other useful items. Paper can be cleaned, soaked in water and turn into new paper.

Research in Chemistry to Generate Green Energy

Sagarika Taneja

Department of Chemistry, Daulat Ram College, University of Delhi

The aim of this study is to highlight some of the revolutionary work that is being undertaken by scientists across the globe in generation of green energy. The ever-increasing demand for energy has put up great pressure on the energy sector to come up with a solution with little or no usage of exhaustible resources. Generation of side product should be low and our method should not leave much carbon footprint behind. Development of 'Spherical sun power generator' which can “squeeze more juice out of the sun” is commendable. Scientists at University of Arizona developed way to generate energy out of heat which until now used to be total waste. Organic Rankine Cycle converts low temperature heat into electricity. Scientists at MIT have developed thermo-chemical technology to convert solar energy into electrical energy. Nanotechnology has been utilized in generation of hydrogen as fuel and algae for production of butanol to replace ethanol.

Synthesis and characterization of Tin Doped MnO₂/CNT composites as electrode materials for supercapacitor

Ashok K. Sharma and Indu Kaushal

Thin Film Lab, Department of Materials Science & Nanotechnology, D.C.R. University of Science & Technology, Murthal (India)

Tin doped MnO₂/carbon nanotubes composite was synthesized by chemical co-precipitation method to be used as an electrode material for supercapacitors. The structural features of composite was characterized by FTIR spectroscopy and UV-Visible spectroscopy. The spectral peaks obtained indicate the presence of Sn doped MnO₂ and CNT in the composite. The X-Ray diffraction pattern revealed crystalline nature of the composite and successful incorporation of metal oxide in the composite structure. The morphology of the composite studied by scanning electron microscopy (SEM) confirms that the composite had a nanofiber mesh like structure. The resulting composite combine the advantages of pseudo active species and the high surface area of CNT providing a conductive network of amorphous composite, which shows good conductive behaviour.

Catalytic Reductive Degradation of Methyl Orange Using Copper Nanostructures

Ankur, Jyoti Yadav, Urvashi Bhatia, Narender Singh, Kalpa Mandal, Devraj Singh, Seema Trama, Alka Gupta

Department of Chemistry Dyal Singh College, University of Delhi, Lodhi Road, New Delhi 110003, Department of physics, Dyal Singh College, University of Delhi, Lodhi Road, New Delhi – 110003.

The textile industry and its waste water have been increasing proportionally, making it one of the main sources of severe water pollution. In particular dyes comprise a major section of industrial waste water effluents as they are released in abundance, upto 50% of the dyes may be lost in directly into the water ways due to inefficient and uneconomic dyeing techniques. The release of these dyes in aquatic systems is of environmental concern due to their carcinogenic, persistent, and recalcitrant nature. Dyes released in waste water may also undergo incomplete anaerobic degradation, inducing additional toxicity caused by mutagenic end products. Besides this the coloring decreases sunlight penetration and oxygen dissolution in water which is also a considerable threat to ecosystem. In order to cope with increasingly strict legislations and regulations concerning waste water management, the associated industries are required to find green, efficient and economically viable solutions for waste water treatment. The conventional routes include adsorption, biological, coagulation routes, and ozonation. However these methods are expensive, time consuming and inefficient resulting in secondary pollution with overall increase in method cost because of extra disposal procedures.

Advanced oxidation processes employing metal oxides are being adopted as technically feasible degradation processes but are proving to be inefficient and impractical. Among such processes reductive degradation of organic dyes with metal nanostructures is a convenient degradation model system which is not only viable in terms of efficiency and costliness but also greener as it provides biodegradable end products like aromatic amines, which are readily and easily degraded by microorganisms.

Present study is targeted towards the application of oxidation resistant copper nanoparticles as a catalyst for waste water remediation, particularly water from water bodies near dyeing and printing industries. Cu nanoparticles capped with an organic protecting group, sodium dodecyl sulphate were synthesized via an aqueous reduction route. The obtained Cu nanoparticles were characterized for their size and charge using DLS measurements and also by UV spectroscopy. These surfactant capped Cu nanoparticles have been used as a heterogeneous catalyst for the comparative reductive degradation of commercial azo dye, Methyl Orange in the presence of sodium borohydride, used as a potential reductant.

Design & Development of Optimized Vibration Isolation Systems for High Resolution Analytical Instruments in Industrial Environment

S.N.Bagchi,

Design section, Vibration & Seismic Engineering Dept., Corporate Office, Resistoflex Group of Industries, B-103, Sec.5, Noida - 201301, India.

This is an Industry-Academia oriented presentation highlighting the design and application aspects of Vibration Isolation Systems focusing the high resolution analytical instruments like Atomic Force Microscopes (AFM), Laser Confocal Microscopes, Photo-Acoustic Spectrometers will be highlighted. The performance of these instruments are affected by various types ground disturbances of micro-seismic nature induced by the rail & roads traffic in the vicinity of the test laboratory. With the development of Micro-Electro Mechanical Systems (MEMS) and VLSI the demand for Nano-Dimensional metrology has increased in QC lab located in Micro-Electronic Component fabrication workshop situated in industrial area, the micro-seismic disturbances in the environment require vibration isolation systems for the accurate and repeatable results. In introduction the Fundamental Forces of nature inducing vibrations and oscillations in Atoms & molecules to machines and mechanisms, buildings & structures and its related frequency spectrum will be focused. An analogy of Molecular Vibration and Machine Vibration spectrum will be presented. The other industrial application areas include Earthquake protection of Buildings and plant machineries, isolation of sensitive electronic equipments in aircraft & aerospace vehicles, automobiles, railways, naval ships & Submarines.

Green Odorants

Sajal Pramanik

Odorants are added in Petroleum Gases and Liquefied Petroleum Gases and its products for its proper identification in atmosphere. Since long the organic synthesized product as Thioether, Thiopenes or Thioal are being used for the purpose. In order to detect if presence and prevent an explosion from a buildup of propane gas, odorant (almost always ethyl mercaptan) is added to liquid LP-Gas. Ethyl mercaptan has a distinctive odor and has a high odor impact. Propane is occasionally odorized with something other than ethyl mercaptan and it may smell different.

In India these odorants are used in domestic LPG product for its quick identification in case of any leak. As per IS 4576, a minimum 20ppm has been recommended for the said purposes. Moreover, it has been very popular in Indian community of domestic LPG users. These synthetic products are highly carcinogenic and dangerous for marine species. Everyone handling or using LP-Gas should realize that the odorant used to give propane a distinctive smell may not be detected by all people under all circumstances. Certain

individuals (especially the elderly) can have an impaired sense of smell. Environmental conditions also may exist which diminish odor detection. For example: 1. the odorized gas may be masked or covered up by other odors such as musty basements, cooking odors and certain foods, or 2. high concentrations of odor can shock or diminish the sense of smell which can also occur from prolonged exposure to the odor of LP-Gas.

Extracts of Herbs present in India, Sri Lanka, Thailand does the same purpose without affection the ecology, flora and fauna. Easy available leaves of herbs alcoholic extracts have been tested mixing in a stoichiometry ratios gives a successful results.

Advantages :

1. Easily available green product
2. Easy Process

Microwave Assisted Synthesis, Characterization and Antibacterial Activity of Some Arsenic (III) Derivatives of O-Alkyl or O-Aryl Trithiophosphates

Sankhala K. and Chaturvedi A.*

Synthetic and Surface Science Laboratory, Dept. of Chemistry, Govt. College, Ajmer (Raj.) 305001, INDIA

Arsenic (III) O-alkyl or O-aryl trithiophosphate of the type $\text{ClAs}[\text{S}_2(\text{S})\text{P}(\text{OR})]$ and $\text{ROP}(\text{S})[\text{SAsS}_2\text{P}(\text{S})\text{OR}]_2$ ($\text{R}=\text{Me}$, Et , Pr^i , Bu^i , Ph , CH_2Ph) have been synthesized by solvent free microwave assisted procedure from the reaction of arsenic trichloride with potassium salts of O-alkyl or O-aryl trithiophosphate in 1:1 and 2:3 molar ratio respectively. These derivatives have been characterized by elemental analysis, molecular weight determinations and spectroscopic (IR, ^1H and ^{31}P NMR) studies. On the basis of them distorted tetrahedral geometry has been proposed for these derivatives. The newly synthesized derivatives show good activity against gram positive and gram negative bacteria and a comparative study of antibacterial effect has also been made with standard drugs.

Study of Different Varieties of Holy Basil as Potential Corrosion Inhibition on Tin in Inorganic Acid

Nutan Kumpawat , Alok Chaturvedi *, R.K. Upadhyay

Synthetic and Surface Science Laboratory, Department of Chemistry, Govt. College, Ajmer (Raj.) - INDIA

The study of corrosion inhibition of three different varieties of Holy basil viz. *ocimum canum* (E_C), *ocimum*

basilicum (E_B) and *ocimum sanctum* (E_S) in controlling corrosion of tin immersed in nitric acid solution in absence and presence of inhibitor has been evaluated by weight loss and thermometric methods. Maximum efficiency was found up to 97.45 % for tin in 2.5N HNO_3 solution. Inhibition efficiency of all inhibitor increases with increasing concentration of inhibitor as well as acid strength. In thermometric method inhibition efficiency also increases with increasing concentration of acids. Results show that all varieties under study are good corrosion inhibitors, among which (E_C) is most effective.

Synthesis and Spectroscopic Studies of Some Biologically Important Esters of o-Alkyl Trithiophosphates

Alok Chaturvedi¹, Sudhanshu Khichi²

Synthetic and Surface Science Laboratory, Department of Chemistry, SPC Govt. College, Ajmer

A series of substituted organic esters of the type $\text{ROPS}_3(\text{C}_6\text{H}_4\text{CH}_2)_2$ and $\text{ROPS}_3(\text{RCO})_2$ have been synthesized by the reaction of dipotassium salts of o-alkyl trithiophosphate with acetyl, benzyl and benzoyl chloride. The newly synthesized complexes are white crystalline solids, insoluble in common organic solvent but soluble in coordinating solvent like DMSO. The compounds are characterized by elemental analysis, molecular weight measurement and spectroscopic (IR, ^1H NMR, ^{31}P NMR) studies and tested for antibacterial activity. On the basis of physico-chemical as well as spectral studies distorted tetrahedral geometry of molecule has been established.

Inhibitive Effect of Some Schiff Bases on Corrosion of Mild Steel in Hydrochloric Acid Solution

S.Sahu^{*1}, S.K.Arora², Kiran Kumari³

¹. Department of Chemistry, Govt. Engineering College Ajmer,

^{2,3}Material Research Laboratories, Govt. College Ajmer

Mass loss method and thermometric methods have been employed to study the corrosion inhibition of Mild steel in acidic media (HCl). Three Schiff's bases viz; N(vanillidine)-4-methyl-1-phenylimine(SB₁), N(vanillidine)-4-methoxy-1-phenylimine(SB₂), N(anisidine)-1-naphthylimine(SB₃). Values of inhibition efficiency obtained from two methods are in good agreement and dependent upon the concentration from the mass loss data, it is concluded that the inhibition efficiency increases with the increase in concentration of inhibitor.

See discussions, stats, and author profiles for this publication at: <https://www.researchgate.net/publication/292604597>

Analysis of Surface Roughness in Turning Process Using Neural Network

CONFERENCE PAPER · JANUARY 2016

READS

18

1 AUTHOR:



Ranganath M Singari

Delhi Technological University, Formerly Del...

56 PUBLICATIONS 105 CITATIONS

SEE PROFILE

Analysis of Surface Roughness in Turning Process Using Neural Network

Ranganath M. Singari

Delhi Technological University, Delhi, India
ranganathdce@gmail.com

Abstract: Machine parts are significantly influenced by surface roughness quality. For efficient use of machine tools, optimum cutting parameters are required. Therefore it is necessary to find a suitable optimization method which can find optimum values of cutting parameters for minimizing surface roughness. The turning process parameter optimization is highly constrained and nonlinear. Many researchers have used an artificial neural network (ANN) model for the data obtained through experiments to predict the surface roughness. In this study two experimental data are analysed through Neural Network fitting tool using MATLAB software. The results obtained, conclude that ANN is reliable and accurate for solving the cutting parameter optimization.

Keywords: Neural Network, MATLAB, Turning, Surface Roughness

1. INTRODUCTION

Surface roughness quality of a machine part ensures its performance and fatigue life. It depends on various factors such as cutting speed, Feed rate, Depth of cut. Vibrations, tool wear, tool life, surface finish and cutting forces etc. Hence to improve the efficiency of process and quality of the product it is necessary to control the process parameters. Therefore it is necessary to find a suitable optimization method which can find optimum values of cutting parameters for minimizing surface roughness. It is necessary to find a suitable optimization method which can find optimum values of cutting parameters for minimizing surface roughness. ANN is found to be very useful with simulations tasks which have complex and explicit relation between control factors and result of process. Neural network is one of the important components in Artificial Intelligence (AI). It has been studied for many years in the hope of achieving human-like performance in many fields, such as speech and image recognition as well as information retrieval. Artificial Neural Network can be created using feed forward back propagation technique for simulation of the process. With assurance of accuracy of the predictive capabilities of the neural network; it may be then used for optimization.

Artificial Neural Network Analysis—A Brief Review

A neural network model (or neural model) is an interconnected assembly of simple processing elements, units or nodes, whose functionality is based on the biological neuron. It resembles the brain in two respects:

- Knowledge is acquired by the network from its environment through a learning process;
- Interneuron connection strengths, known as synaptic weights, are used to store the acquired knowledge.

An Artificial Neural Network has three components: network architecture, an activation function and a learning rule.

- Network architectures
- Activation function
- Learning rules
- Training methods

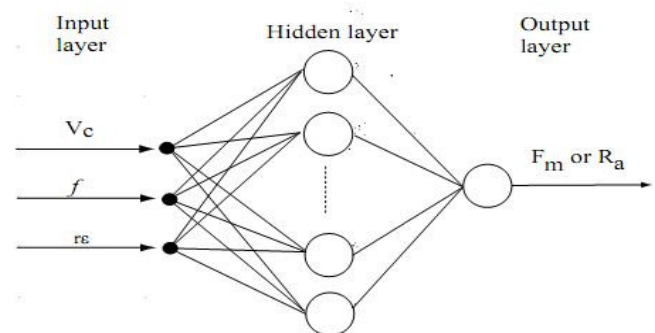


Fig. 1. Architecture of multilayer feed forward neural network

There are different types of Neural Network

1. Perceptron
2. Back propagation networks
3. Associative memory neural networks
4. Radial basis function networks (RBFN)

5. Adaline networks
6. Probabilistic networks

There are many applications of ANN such as in arts, bioinformatics, forecasting, health care, intrusion detection, communication, robotics, control, pattern recognition etc.

1.1 NEURAL NETWORK FITTING TOOL

The Neural Network Fitting Tool helps us select data, create and train a network, and evaluate its performance using square error and regression analysis. In fitting problems, we want a neural network to map between a data set of numeric inputs and a set of numeric targets. A two layer feed-forward network with sigmoid hidden neurons and linear output neurons (fitnet), can fit multi-dimensional mapping problems arbitrarily well, given consistent data and enough neurons in its hidden layer. The network will be trained with Levenberg-Marquardt backpropagation algorithm (trainlm), unless there is not enough memory, in which case scaled conjugate gradient backpropagation (trainscg) will be used.

1.2 MATLAB

MATLAB (matrix laboratory) is a multi-paradigm numerical computing environment and fourth-generation programming language. Using MATLAB, we can analyze data, develop algorithms, and create models and applications. The language, tools, and built-in math functions enable us to explore multiple approaches and reach a solution faster than with spreadsheets or traditional programming languages, such as C/C++ or Java. We can use MATLAB for a range of applications, including signal processing and communications, image and video processing, control systems, test and measurement, computational finance, and computational biology. More than a million engineers and scientists in industry and academia use MATLAB, the language of technical computing.

Its various key features are:

- High-level language for numerical computation, visualization, and application development
- Interactive environment for iterative exploration, design, and problem solving
- Mathematical functions for linear algebra, statistics, Fourier analysis, filtering, optimization, numerical integration, and solving ordinary differential equations
- Built-in graphics for visualizing data and tools for creating custom plots
- Development tools for improving code quality and maintainability and maximizing performance
- Tools for building applications with custom graphical interfaces
- Functions for integrating MATLAB based algorithms with external applications and languages such as C, Java, .NET, and Microsoft Excel.

Neural Network Toolbox supports a variety of training algorithms, including several gradient descent methods, conjugate gradient methods, the Levenberg-Marquardt algorithm (LM), and the resilient backpropagation algorithm (Rprop). The toolbox's modular framework let us quickly develop custom training algorithms that can be integrated with built-in algorithms. While training neural network, we can use error weights to define the relative importance of desired outputs, which can be prioritized in terms of sample, time step (for time-series problems), output element, or any combination of these. We can access training algorithms from the command line or via apps that show diagrams of the network being trained and provide network performance plots and status information to help us monitor the training process.

2. LITERATURE REVIEW

Diwakar Reddy V. et al, "ANN Based prediction of Surface Roughness in Turning", December 2011[3] have carried out machining process on Mild steel material in dry cutting condition in a lathe machine and surface roughness was measured using Surface Roughness Tester. To predict the surface roughness, an artificial neural network (ANN) model was designed through back propagation network for the data obtained. Comparison of the experimental data and ANN results showed that there is no significant difference and ANN was used confidently. Three cutting parameters speed, feed, depth of cut have been considered. The machining tests have been carried out by straight turning of medium carbon steel (mild steel) on a lathe by a standard HSS uncoated and carbide insert with ISO designation-SNMG 120408 at different speed-feed and depth combinations. By using the MATLAB command 'postmnmx' the network values have been predicted, regression analysis was adopted to find the coefficient of determination value (R^2) for both training and testing phases to judge performance of each network. The multilayer feed forward network consisting of three inputs, 25 hidden neurons (tangent sigmoid neurons) and one output (network architecture represented as 3-25-1) was found to be the optimum network for the model developed in their study. They concluded from their results obtained that ANN is reliable and accurate for solving the cutting parameter optimization. TugrulOzel et al, [17] studied the effects of tool corner design on the surface finish and productivity in turning of steel parts. Surface finishing has been investigated in finish turning of AISI 1045 steel using conventional and wiper (multi-radii) design inserts. Multiple linear regression models and neural network models have been developed for predicting surface roughness, mean force and cutting Power. The Levenberg-Marquardt method was used together with Bayesian regularization in training neural networks in order to obtain neural networks with

good generalization capability. Neural network based predictions of surface roughness were carried out and compared with a non-training experimental data. These results showed that neural network models are suitable to predict surface roughness patterns for a range of cutting conditions in turning with conventional and wiper inserts.

Ilhan Asiltürk a, Mehmet Çunkas [5] used Artificial neural networks (ANN) and multiple regression approaches to model the surface roughness of AISI 1040 steel. Full factorial experimental design is implemented to investigate the effect of the cutting parameters (i.e. cutting speed, feed rate, and depth of cut) on the surface roughness. The multiple regression models are tested by aiding the analysis of variance (ANOVA). The data have been used to build the multiple regression model. Multilayer perception (MLP) architecture with back-propagation algorithm having two different variants is used in neural network. The performances of multiple regression and neural network-based models are compared by means of statistical methods. The back-propagation learning algorithms such as scaled conjugate gradient (SCG) and Levenberg–Marquardt (LM) were used to update the parameters in feed forward single hidden layers. The cutting speed (V), feed (f), and depth of cut (d) were considered as the process parameters. The input layers of the neural network consist of three neurons whereas the output layer had a single neuron that represents the predicted value of surface roughness. The logsig processing function and single hidden layer had been used. They concluded that ANN is a powerful tool in predicting surface roughness. Ranganath M S, et al, [11] analyzed surface roughness of Aluminium (6061) through neural network model. To predict the surface roughness, neural network model was designed through Multilayer Perceptron network for the data obtained. The predicted surface roughness values computed from ANN, were compared with experimental data and the results obtained showed that neural network model is reliable and accurate for solving the cutting parameter optimization. They concluded that the appropriate cutting parameters can be determined for a desired value of surface roughness.

Durmus Karayel [4], has used neural network approach for the prediction and control of surface roughness in a computer numerically controlled (CNC) lathe. A feed forward multilayered neural network was developed and the network model was trained using the scaled conjugate gradient algorithm (SCGA), which is a type of back-propagation. The adaptive learning rate was used. He concluded that the appropriate cutting parameters can be determined for a desired value of surface roughness.

Anna Zawada- Tomkiewicz [2], have estimated the surface roughness parameter with use of a neural network (NN). The optical method suggested in this paper is based on the vision system created to acquire an image of the machined surface during the cutting process. The acquired image is analyzed to correlate its parameters with surface parameters.

In the application of machined surface image analysis, the wavelet methods were introduced. A digital image of a machined surface was described using the one-dimensional Digital Wavelet Transform with the basic wavelet as Coiflet. The increment of machined surface image parameters was applied as input for the neural network estimator. Five cross-sections of the image were loaded, from which six statistical parameters of the six levels of wavelet decomposition were computed. These six parameters were chosen via the Optimal Brain Surgeon Method. They found that by applying the increments of these parameters and of the estimated value in a given time, it made possible to establish the *Ra* estimator for the points in time when the surface roughness parameters were unknown. Ranganath M S et al., [8, 10, 14], have reviewed the works related to Artificial Neural Networks ANN, in predicting the surface roughness in turning process. They studied in papers that some of the machining variables, that have a major impact on the surface roughness in turning process, such as spindle speed, feed rate and depth of cut were considered as inputs and surface roughness as output for a neural network model. They found that the predicted surface roughness values computed from ANN, were compared with experimental data and the results obtained. These results showed that the neural network model is reliable and accurate for solving the cutting parameter optimization.

Ruturaj Kulkarni et al, [15], carried out tests on AISI 4140 steel. 12 speed Jones and Lamson Lathe model was used for turning operation. The specimen with a diameter of 60mm, 500mm length and hardened 35 HRC is used. The operating parameters that contribute to turning process are cutting speed, Feed rate, Depth of cut, Vibrations, tool wear, tool life, surface finish and cutting forces. These readings were used to train and validate the Neural Network. They found ANN to be very useful with simulations tasks which have complex and explicit relation between control factors and result of process. They created Neural Network using feed forward back propagation technique for simulation of the process using the Matlab Neural network toolbox. With assurance of accuracy of the predictive capabilities of the neural network, it was then used for optimization. Particle Swarm Optimization Algorithm, an evolutionary computation technique is used to find out the optimum values of the input parameters to achieve the minimum surface roughness. The objective function used here is to minimize the surface roughness. Limits of the operational variables are used as constraints for developing the code for optimization algorithm.

3. DATA AND ANALYSIS

For surface roughness analysis, data from two experiments values has been taken. Data 1 is taken from the paper “Neural Network Process Modelling for Turning of Aluminium (6061) using Cemented Carbide Inserts, [16]” and Data 2 is taken from the paper “Optimization of surface

roughness and material removal rate on conventional dry turning of aluminium (6061)". Software used is MATLAB R2011b(7.13.0.564). In this software Neural network fitting tool is used in which cutting speed, Feed rate, Depth of cut are taken as inputs and measured surface roughness values are taken as output and 10 is entered as number of hidden neurons. The following observations are obtained by running NN fitting tool: Data 1 is explained with tables 1 and 2.

TABLE 1. Neural Networks Multilayer Perceptron predicted values [11] : 27 readings

S	f	d	Ra	MLP_PredictedValue
1700	0.1	0.2	0.82	0.83
1700	0.1	0.3	0.94	0.86
1700	0.1	0.4	0.96	0.87
1700	0.13	0.2	1.12	0.99
1700	0.13	0.3	1.06	1.09
1700	0.13	0.4	1.1	1.1
1700	0.15	0.2	1.44	1.38
1700	0.15	0.3	1.54	1.44
1700	0.15	0.4	1.5	1.45
1900	0.1	0.2	0.86	0.84
1900	0.1	0.3	0.92	0.88
1900	0.1	0.4	0.76	0.88
1900	0.13	0.2	1.04	1.01
1900	0.13	0.3	1.2	1.12
1900	0.13	0.4	1.1	1.13
1900	0.15	0.2	1.44	1.4
1900	0.15	0.3	1.6	1.46
1900	0.15	0.4	1.5	1.46
2100	0.1	0.2	0.88	0.84
2100	0.1	0.3	0.78	0.88
2100	0.1	0.4	1.16	0.89
2100	0.13	0.2	1.08	1.03
2100	0.13	0.3	1.14	1.14
2100	0.13	0.4	1.26	1.15
2100	0.15	0.2	0.58	1.41
2100	0.15	0.3	1.42	1.46
2100	0.15	0.4	1.86	1.47

DATA 1 RESULTS

TABLE 2: Neural Network fitting tool result

MLP_PredictedValue	Matlab result	error
0.83	0.748016	0.081984
0.86	0.924706	-0.06471
0.87	0.734418	0.135582
0.99	1.113399	-0.1234
1.09	1.054578	0.035422
1.1	1.811298	-0.7113
1.38	1.397261	-0.01726
1.44	1.514902	-0.0749
1.45	1.496657	-0.04666
0.84	1.326844	-0.48684
0.88	0.90934	-0.02934
0.88	0.777333	0.102667
1.01	0.866078	0.143922
1.12	1.180717	-0.06072
1.13	1.113354	0.016646
1.4	1.457345	-0.05735
1.46	1.34779	0.11221
1.46	1.729337	-0.26934
0.84	0.871308	-0.03131
0.88	0.838522	0.041478
0.89	1.162115	-0.27212
1.03	1.098007	-0.06801
1.14	1.19385	-0.05385
1.15	1.268647	-0.11865
1.41	0.558813	0.851187
1.46	1.477801	-0.0178
1.47	1.446139	0.023861

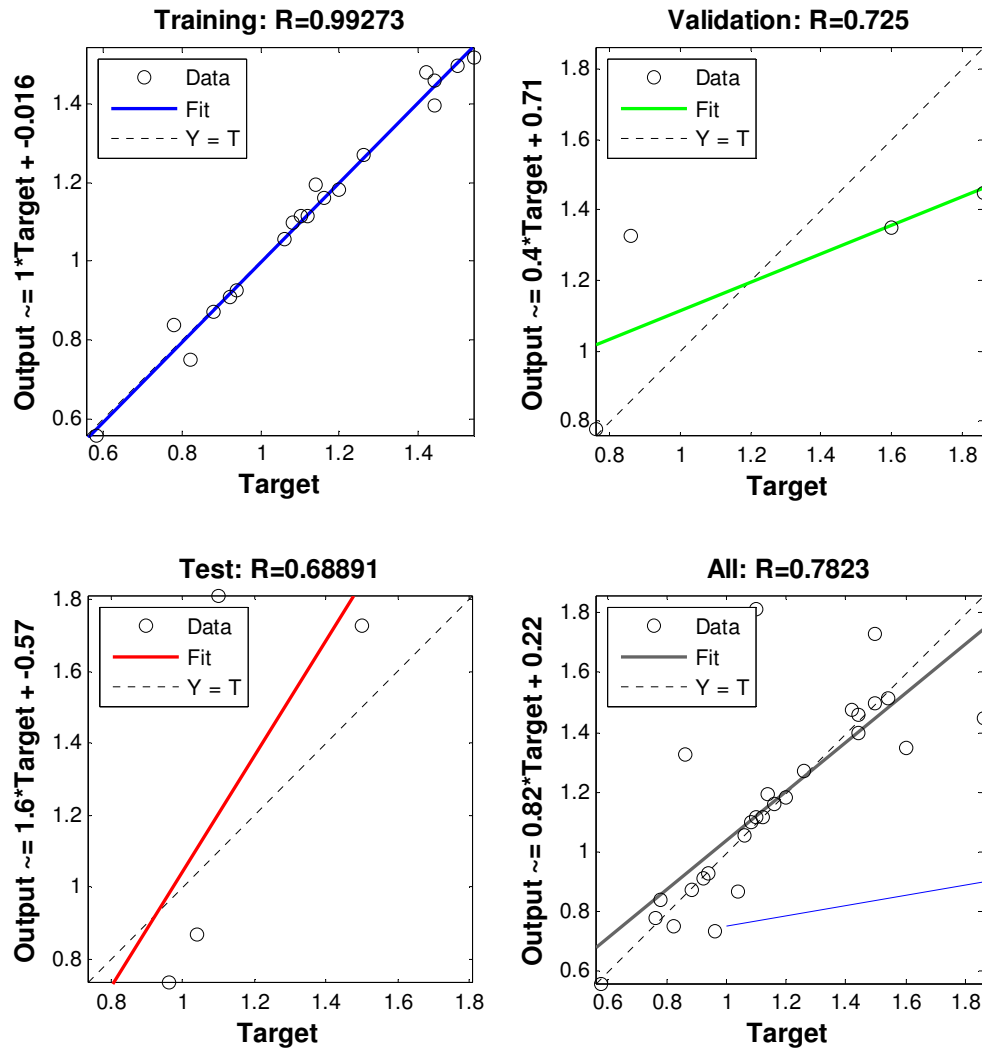


Fig. 2. Regression plot for Data 1

DATA 2

TABLE 3: Machine readings and calculations of Roughness [17]: 27 readings

Speeds (s) (Rev/min.)	Feed (f) (mm per rev.)	Depth of cut (mm)	Measured Ra (μm)	MRR mm ³ /min	MRR mm ³ /sec
180	0.2	0.2	1.04	113.927	8.56545
180	0.2	0.4	0.98	212.018	6.86697
180	0.2	0.6	2.2	261.698	4.36163
180	0.315	0.2	2.44	672.129	7.86882
180	0.315	0.4	3.84	333.569	5.55948
180	0.315	0.6	2.4	897.738	1.62897
180	0.4	0.2	2.06	22.443	3.70738
180	0.4	0.4	2.3	953.491	5.89151
180	0.4	0.6	3.66	901.732	8.3622

Analysis of Surface Roughness in Turning Process Using Neural Network

Speeds (s) (Rev/min.)	Feed (f) (mm per rev.)	Depth of cut (mm)	Measured Ra (μm)	MRR mm ³ /min	MRR mm ³ /sec
450	0.2	0.2	0.9	780.859	6.34764
450	0.2	0.4	0.94	528.915	2.14858
450	0.2	0.6	2.9	145.761	35.7627
450	0.315	0.2	1.42	176.76	9.61266
450	0.315	0.4	3.38	303.637	38.3939
450	0.315	0.6	1.34	2263.05	4.3842
450	0.4	0.2	1.74	40.271	4.00451
450	0.4	0.4	1.94	890.513	64.8419
450	0.4	0.6	2.88	4822.2	47.0366
710	0.2	0.2	0.86	130.586	8.84311
710	0.2	0.4	0.92	744.814	45.7469
710	0.2	0.6	1.98	2862.91	14.3818
710	0.315	0.2	1.14	592.809	9.8802
710	0.315	0.4	1.22	3098.48	18.308
710	0.315	0.6	1.16	9365.24	22.7539
710	0.4	0.2	1.2	948.858	32.481
710	0.4	0.4	1.38	5658.57	60.9762
710	0.4	0.6	2.68	3305.82	88.4304

TABLE 4: NN fitting results for data 2

Matlab Ra output	Result error	Matlab mm ³ /min output	Result Error	Matlab mm ³ /sec Output	Result Error
0.913232	0.126768	107.8126	6.11437	10.88436	-2.31891
0.644669	0.335331	216.477	-4.45896	7.334996	-0.46803
2.367982	-0.16798	261.7513	-0.05331	34.48975	-30.1281
2.384893	0.055107	-1652.66	2324.79	5.929252	1.939568
3.770516	0.069484	329.0229	4.546104	7.357375	-1.79789
2.591715	-0.19171	364.3161	533.4219	1.568322	0.060648
2.824479	-0.76448	25.46908	-3.02608	-0.48595	4.19333
2.260763	0.039237	-1211.21	2164.706	6.226291	-0.33478
3.793547	-0.13355	880.8359	20.89612	8.48437	-0.12217
1.683223	-0.78322	777.9455	2.913516	6.58626	-0.23862
0.656883	0.283117	523.8659	5.049055	26.42648	-24.2779
2.467942	0.432058	147.6897	-1.92866	35.11149	0.651206
1.651251	-0.23125	169.1197	7.640342	9.45825	0.15441
3.350995	0.029005	288.2407	15.39625	38.49349	-0.09959
1.538269	-0.19827	2243.545	19.5049	4.386742	-0.00254
1.712336	0.027664	462.1214	-421.85	6.840818	-2.83631

Matlab Ra output	Result error	Matlab mm3/min output	Result Error	Matlab mm3/sec Output	Result Error
2.356691	-0.41669	880.1073	10.40575	58.94161	5.900295
3.011701	-0.1317	5083.391	-261.191	25.1766	21.86
0.934006	-0.07401	1690.157	-1559.57	15.71471	-6.8716
-0.06489	0.984886	744.4401	0.373851	26.52107	19.22583
0.936604	1.043396	2878.882	-15.9723	9.494034	4.887766
1.149902	-0.0099	561.6668	31.14223	10.48262	-0.60242
1.125381	0.094619	3088.285	10.19504	18.30693	0.00107
0.972137	0.187863	9340.405	24.83477	22.72939	0.024506
1.095317	0.104683	958.3188	-9.46083	33.28007	-0.79907
1.179694	0.200306	5660.588	-2.01829	62.16878	-1.19258
2.149931	0.530069	9161.016	-5855.2	87.32237	1.108029

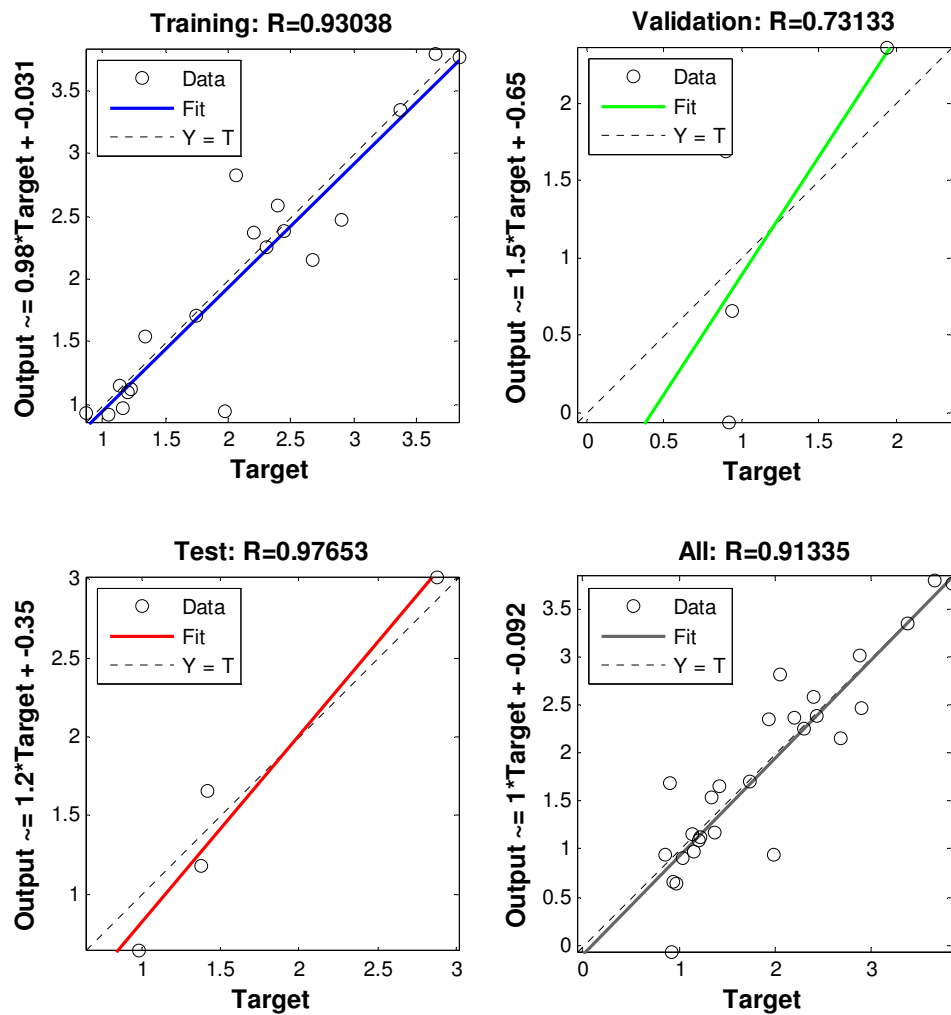


Fig. 3. Regression plot for surface roughness analysis for data 2

4. CONCLUSIONS

Increase in cutting speed improves the surface finish, thus the average surface roughness value decreases. Increase in depth of cut affects the surface finish adversely to a small extent, but as depth of cut increases beyond a certain limit, surface finish deteriorates to a large extent. Small increase in feed rate deteriorates surface finish to a large extent. ANN is reliable and accurate for solving the cutting parameter optimization. Data analysed also showed that there is very minimum error between the MLP/ measured value and the MATLAB values.

REFERENCES

- [1] Jameel, A.; Minhat, M.; Nizam, Md. Using genetic algorithm to optimize machining parameters in turning operation: A Review, International journal of scientific and research publications. 2013, 3.
- [2] Tomkiewicz, A.Z. Estimation of surface roughness parameter based on machined surface image. 2010, Metrol. Meas. Syst. XVII, 3, 493-504.
- [3] Reddy, V.; Krishnaiah, G.; Kumar, A.H.; Priya, S.H. ANN based predication of surface roughness in turning. International conference on trends in mechanical and industrial engineering Bangkok, 2011.
- [4] Karayel, D. Prediction and control of surface roughness in CNC lathe using artificial neural network. Journal of materials processing technology, 209, 3125–3137.
- [5] Çunkas, M.; Selçuk. Modeling and prediction of surface roughness in turning operations using artificial neural network and multiple regression method. Expert Systems with Applications, 2011, 38, 5826–5832.
- [6] Davim, J.P.; Gaitonde, V. N.; Karnik, S. R. Investigations into the effect of cutting conditions on surface roughness in turning of free machining steel by ANN models. Journal of materials processing technology, 2007.
- [7] Benardos, P.G.; Vosniakos, G.C. Optimizing feed forward artificial neural network architecture. Engineering Applications of Artificial Intelligence, 2007, 20, 365–382.
- [8] Ranganath, M.S.; Vipin. Measuring Effect of Machining Parameters on Surface Roughness with Turning Process- Literature Survey. International Journal of Advance Research and Innovation, 2014, 2, 313-318.
- [9] Ranganath, M.S.; Vipin. Effect of Cutting Parameters on MRR and Surface Roughness in Turning of Aluminium (6061). International Journal of Advance Research and Innovation, 2014, 2, 32-39.
- [10] Ranganath, M.S.; Vipin. Application of ANN for Prediction of Surface Roughness in Turning Process: A Review. International Journal of Advance Research and Innovation, 2013, 3, 229-233.
- [11] Ranganath, M.S.; Vipin. Neural Network Process Modelling for Turning of Aluminium (6061) using Cemented Carbide Inserts. International Journal of Advance Research and Innovation, 2013, 3, 211-219.
- [12] Ranganath, M.S.; Vipin. Optimization of surface roughness and material removal rate on conventional dry turning of aluminium (6061). International Journal of Advance Research and Innovation, 2014, 2, 62-71.
- [13] Ranganath, M.S.; Vipin. Optimization of Process Parameters in Turning Operation of Aluminium (6061) with Cemented Carbide Inserts Using Taguchi Method and Anova. International Journal of Advance Research and Innovation, 2013, 1, 13-21.
- [14] Ranganath, M.S.; Vipin; Maurya, S.; Yadav, S. Parametric Analysis of Surface Roughness Studies in Turning Using Artificial Neural Network. International Journal of Advance Research and Innovation, 2, 676-683.
- [15] Kulkarni, R.; Mounayri, H.A. Simulate turning process using ANN, predict optimum control factors to achieve minimum surface roughness
- [16] Sivanandam, S.N.; Sumathi, S.; Deepa, S.N. Introduction to Neural Networks using MATLAB 6.0. Tata McGraw Hill Education Private Limited, New Delhi.
- [17] Tugrulozel; EstevesCorreia, A.; Davim, J.P. Neural network process modeling for turning of steel parts using conventional and wiper inserts
- [18] Chaudhari, V.R.; Gohil, D.B. Predication of surface roughness using artificial neural network. International journal of Emerging trends in Engineering and development, 2012, 4.

CFD Modeling of flow through S-Shaped Duct

Md. Nadim Shams¹, Raj Kumar Singh², Md. Zunaid³

¹JK Laxmipat University, Jaipur, Rajasthan, India

^{2, 3} Delhi Technological University, Bawana Road, Delhi, India

Abstract : This Paper investigates the flow inside an S- Shaped square Duct. In this paper, a computational fluid dynamics (CFD) model of fully developed turbulent flow(k- ϵ model) is implemented with the help of FLUENT software and the variation of pressure along the length of bend with variation in Reynolds number is analyzed. The curvatures is investigated at Reynolds numbers $Re=4.73 \times 10^4$ and 1.47×10^5 . A non-dimensional parameter ω , defined as the total pressure loss coefficient is analyzed for finding out the total pressure loss in the duct. Cp Data obtained from the simulation of S-shaped ducts show that there is flow separation at the near side wall of the first bend and far side wall of the second bend. At high Reynolds number separation is more dominant near junction of bend as compare to low Reynolds number flow. To improve the flow in S-ducts, vortex generators as flow control methods is implemented. This methods shown to be effective in suppressing flow separation and reducing total pressure loss.

Keywords: CFD, FLUENT, Reynolds number, S- Shaped square Duct, Vortex generators

I. INTRODUCTION

The layout of any practical piping system necessarily includes bends and the accurate prediction of pressure losses, flow rate and pumping requirements demands knowledge of the character of curved duct flows, such wide applications in the industry have forced researchers to acknowledge the importance of study of flow in curved ducts.

Curved duct flows are common in aerospace applications. Many military aircraft have wing root or ventral air intakes and the engine is usually positioned in the Centre of the aircraft's fuselage. Air entering these intake ducts must be turned through two curves (of opposite sign) before reaching the compressor face. Such a configuration results in an S-shaped air intake duct and therefore the engine performance becomes a strong function of the uniformity and direction of the inlet flow and these parameters are primarily determined by duct curvature.

This chapter intends to present a review of the flows in curved ducts and S-shaped ducts. Discussion is based on the Flow Separation, mechanism of total pressure loss and duct's exit flow conditions.

II. LITERATURE REVIEW

The total pressure distribution was represented on the S-duct exit and the thickened boundary layer along the outside wall of the second bend. The boundary layer near that wall to thicken rapidly due to enhanced entrainment and accumulate into a region of low momentum fluid. Another variant is due to the combined effects of centrifugal forces and radial pressure gradient in S-duct flows. Due to the increasing cross sectional area, a stream-wise adverse pressure gradient is also present. The combined effects may result in increased flow non-uniformity

and total pressure loss at the duct exit as compared to a uniformed cross sectioned S-duct [1, 5]. Blowing and vortex generators are used to energize low momentum of fluid near the separation point to overcome adverse pressure gradient [11].

The development of longitudinal vortices near the wall is accompanied by the rapid thickening of the boundary layer at the outside wall of the second bend. Since a favorable longitudinal pressure gradient exists on the outside wall of the second bend, the flow near this wall is accelerating and hence these longitudinal vortices could undergo “vortex stretching”, thus intensifying vorticity. This causes the boundary layer near that wall to thicken rapidly due to enhanced entrainment and accumulate into a region of low momentum fluid. large scale, vertical structures exist along the outside wall of the second bend in both the circular [4, 12].

Flows can be used by flow visualization only and in a Dean number range of 25 to 350. Their results show that Dean vortices formed at $De = 101, 151, 201$ and 252 and at a turning angle of about 180° in the first bend. These vortices continue to grow until 225° within the first bend and with increasing asymmetric structure for the higher De 201, while the vortices stay relatively symmetric for lower De of 101 and 151. Upon entering the second bend, the curvature of the outer and inner wall changes and the direction of the centrifugal force also changes accordingly. At 45° there still exist some remnants of the Dean vortices on the inner wall of the second bend that was generated on the outer wall of the first bend. Flows at higher $De > 200$ seem to display complex and asymmetrical structures in the second bend. The improvements in performance of S-shaped ducts are thus a reduction in flow distortion at the duct exits, maximizing the flow rate and hence minimizing the total pressure losses and elimination of flow separation if it is present [5]. Separation control flow can be done by flow control devices which are placed on the side walls of the S-duct and slightly upstream of the separation point so that when Vortex generators “locally” mix the high momentum fluid in the free stream with the low momentum fluid near the wall and thus energizes the boundary layer to suppress flow separation [6].

Studies have done at the inlet of the duct, the high and low pressure side walls are respectively at the outer wall and inner wall of the first bend. The high and low pressure side changes in the second bend to reflect the change in duct curvature. The observation on swirl development in S-duct is generally true for both circular and non-circular geometry [7].

The marker-and-cell method is employed to allocate the parameters on the staggered mesh, and static pressure is calculated using the artificial compressibility approach. The effect of centrifugal force due to the curvature of the duct and the opposing effects of the first and second normal stress difference on the flow field are investigated. Based on the relations, the performance mechanism of centrifugal force and normal stress differences on the generation of secondary flows is considered [9].

Many numerical investigation for examining the secondary vortex motion and associated heat transfer process in fluid flow through curved passages taken place. For developing laminar fluid flow through curved rectangular ducts, the analysis performs a detailed parametric study involving the contours of helicity and outer duct wall pressure gradient for a range of flow rates, duct aspect ratios, duct flow curvatures and external wall heat fluxes. The flow conditions leading to hydrodynamic instability and Dean Vortex generation in curved passages are carefully analyzed, identifying the flow and geometrical parametric influences. Active interaction of buoyancy force on fluid motion

arising from wall heating is considered where aspects of boundary layer separation is used in recognizing thermal enhancement due to secondary flow [14].

It has been quoted that $0.4U_m$ versus $0.15U_m$ and $0.16U_m$ versus $0.12U_m$ for the corresponding thick and thin boundary layer cases. However, the details in flow topology within the second bend are dependent on whether flow separation is present. An increase in inlet boundary layer thickness led to a corresponding decrease in boundary layer thickness along the outer wall of the second bend. It has been also found that increasing inlet boundary layer led to a reduction in separation region in their S-duct study. The above review has concentrated mainly on S-duct with limited turning angle at relatively high Re (or De) where Dean vortices are not present [10, 15].

The vortex patterns of the secondary flow in a curved duct of square cross-section are numerically investigated. The flow is driven by the axial pressure gradient as well as the walls rotation of the duct except the outer wall around the center of curvature. When the rotation is in the same direction as the negative pressure gradient, the secondary flow shows complicated multiple patterns, which consists of two-vortex, four-vortex, eight-vortex or even non-symmetric secondary flow pattern [17].

III. RESULTS AND DISCUSSION

The optimum aerodynamic performance of S-shaped ducts (or aircraft air-intake ducts) demands that a relatively uniform flow with a smallest possible pressure loss. These requirements naturally lead one to consider the use of traditional flow control devices like vortex generators, blowing jets. Passive devices like vortex generators placed on the side wall eliminate flow separation if it is present. They “locally” mix the high-momentum fluid in the free stream with low-momentum fluid near the wall and thus suppress flow separation. In contrast to the passive means of flow control, blowing jets and vortex generator jets are active flow control devices for flow separation control, whereby mass addition near the separation point energizes the low momentum fluid close to the wall to overcome the adverse pressure gradient. To study the effects of flow control in square cross sectioned S-duct, vortex generator flow control method was studied. In this Chapter, the relative merit of vortex generators on the flow in a square cross sectioned S-duct. Suppression of flow separation, reduction of total pressure loss, and flow uniformity at duct exit are the chosen criteria. Investigation of (S-duct Fig: 1) has been carried out with help of FLUENT, a CFD tool to simulate the Effect of pressure is studied. The present work is conducted at higher $Re=4.73 \times 10^4$ and 1.47×10^5 and with square cross-sectioned, S- shaped ducts with sharper bends and larger turning angle. The geometry is made in solid works and imported on Ansys software for analysis. After analysis on FLUENT following graphs are plotted.

Case 1: Study of 3D S-Shaped Duct:

Mesh Independency Study:

The grid independency is studied for the k- ϵ model employing four size of grid to examine the sensitivity of grid. As we get result in the third column that is fine mesh size is independent of grid that's the optimum grid.

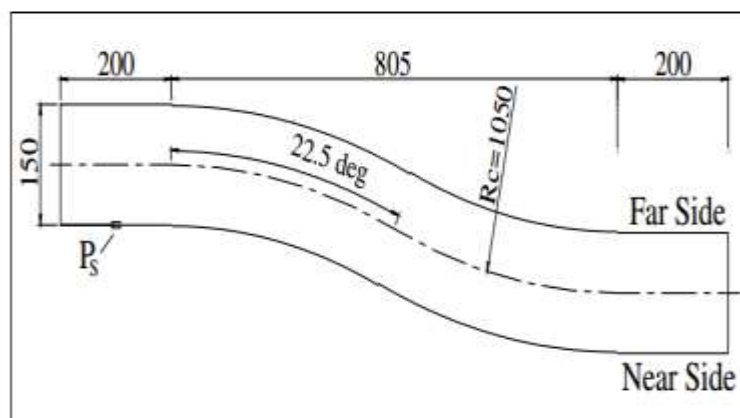


Fig: 1 S-duct configuration

Table: 1 Grid independency chart

	Maximum cell squish	Maximum aspect ratio	Pressure and static pressure (min and max.)	Pressure and pressure coefficient
coarse	5.05561×10^{-2}	2.03094	-1.37609, 3.683053	-2.246697, 6.013155
medium	6.5253×10^{-2}	2.16342	-1.553137, 3.96047	-2.535753, 6.466074
fine	9.28082×10^{-2}	2.18632	-1.585209, 4.26690	-2.5881, 6.966368
Mesh with sizing	9.28082×10^{-2}	2018632	-1.585209, 4.26690	-2.5881, 6.966368

On the study of 3d s-shaped duct we found that from Fig.2 and Fig.3 i.e. contour of static pressure there are two low pressure zones are create on the duct one at near side wall of the 1st bend and other on the far side wall of the second bend. On these two pocket of the bend there is a flow separation which is clearly seen by the Fig. no.4 i.e. contour of velocity vector. For suppressing this flow separation we can use different flow control techniques. From Fig. 2 and Fig. 3 it is clearly seen that the contour of static pressure is same for both the Reynolds number only there is difference in magnitude. Fig. 5 shows that the plot of static pressure vs. position.

Study of 3D S-Shaped Duct with Flow control Techniques:

Different flow control Techniques for improving the performance of S-Duct.

➤ Vortex generator

1. Study of 3D S-Shaped Duct with vortex generator:

Vortex generators “locally” mix the high momentum fluid in the free stream with the low momentum fluid near the wall and thus energies the boundary layer to suppress flow separation.

Graphs of Static Pressure Contours:

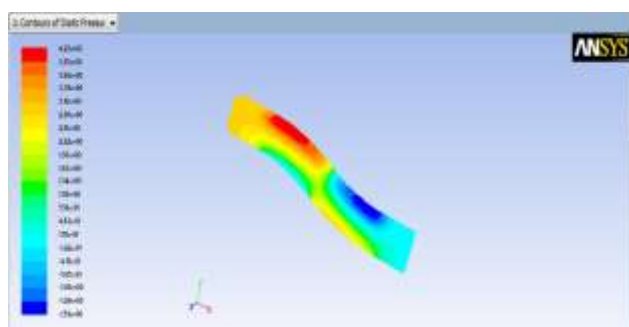


Fig: 2 Contour of Static Pressure at $Re=4.73 \times 10^4$

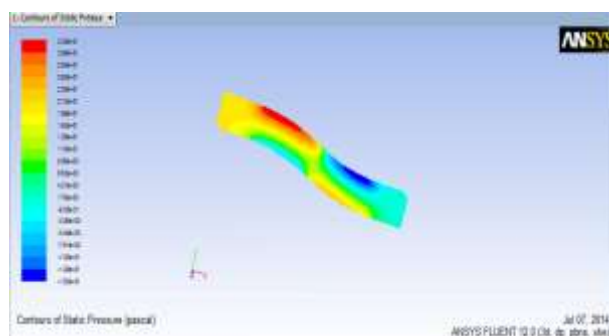


Fig: 3 Contour of static Pressure at $Re=1.47 \times 10^5$

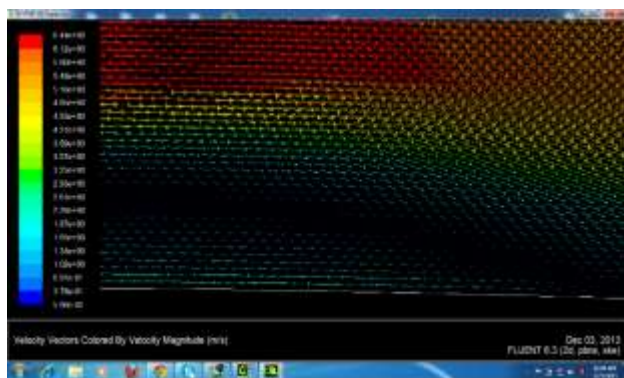


Fig: 4 Velocity vector showing flow separation.

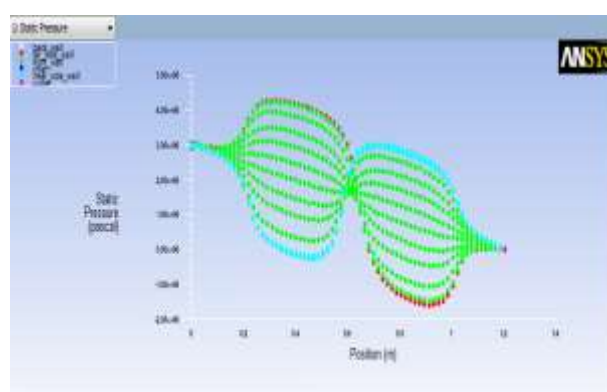


Fig: 5 Graph of static pressure v/s position

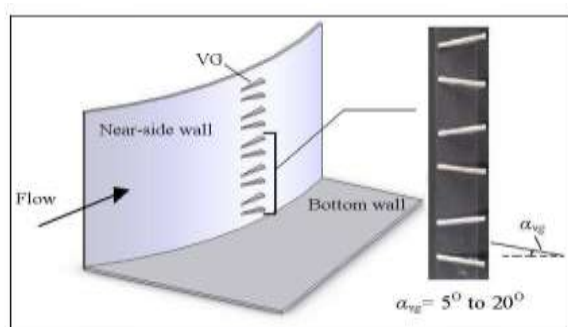


Fig: 6 Vortex generator on near side wall

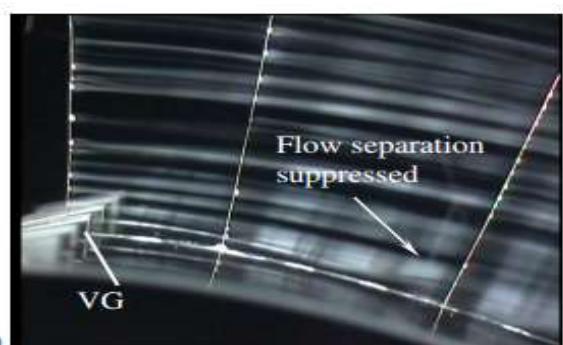


Fig: 7 Shows flow separation and suppressed flow [13]

On the study of 3d S-shaped duct with flow control technique i.e. with vortex generator we found that from Fig.9 and Fig.10 i.e. contour of static pressure there are no low pressure zones are create on the duct one at near side wall of the 1st bend and other on the far side wall of the second bend as found from the analysis from bare duct. From Fig. 9 and 10 it is clearly seen that the contour

of static pressure is same for both the Reynolds number only there is difference in magnitude. Fig 11 shows that the plot of static pressure vs. position .the trend obtained from Fig. 11 is clearly matched with the Fig. 13 i.e. practically result obtained by the Thye,N. Y., 2009.now from the different values obtained from the pressure graph we calculate value of C_p at different point of the duct which is shown on the Table no 2. Fig.12 shows graph obtained C_p v/s s/d by simulation which is matched by the practical result.

From the above simulation results following tables and graphs are plotted for surface pressure distribution C_p and total pressure loss coefficient.

Effects of Flow Control Devices:

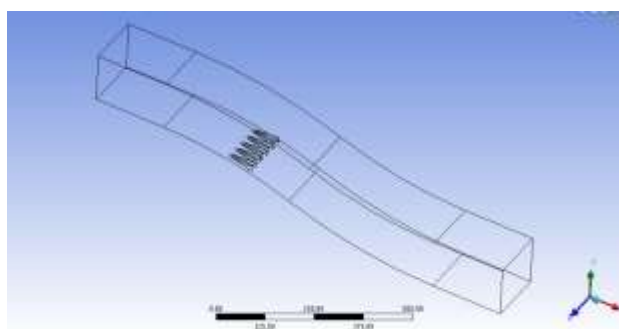


Fig: 8 S-duct with vortex generator

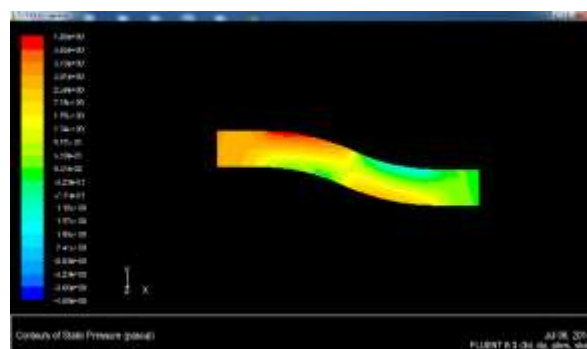


Fig: 9 Contour of static pressure v/s position for $Re=4.73 \times 10^4$

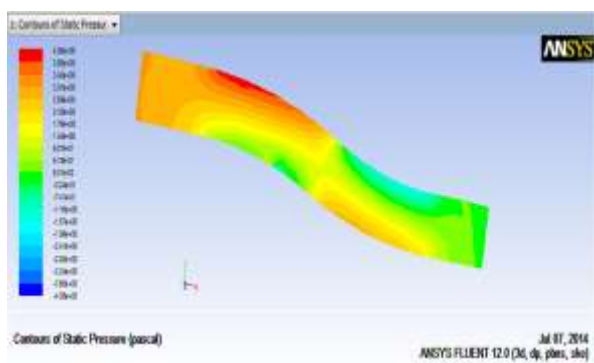


Fig: 10 Contour of static pressure v/s position for $Re=1.47 \times 10^5$

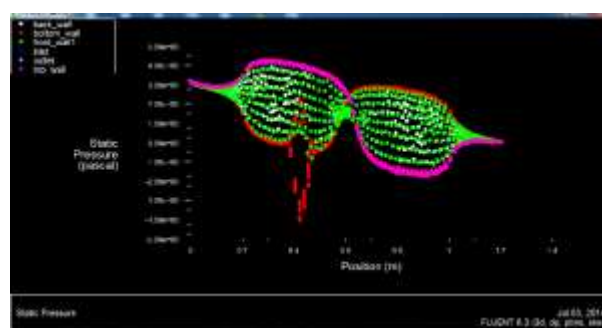


Fig: 11 Plot of static pressure v/s position

2. Table of surface pressure distribution on the side wall (far side wall and near side wall) for bare duct and duct with vortex generator at $Re=4.73 \times 10^4$

Table.2: Surface pressure distribution on the side wall at $Re=4.73 \times 10^4$

S/D	Cp far Side (bare)	Cp far Side (vg)	Cp Near Side (bare)	Cp Near Side (vg)
0	0.21	0.2	-0.3	-0.35
0.25	0.3	0.3	-0.45	-0.47
0.5	0.35	0.35	-0.52	-0.7
0.75	0.43	0.44	-0.55	-1
1	0.3	0.35	-0.45	-0.7
1.25	0.3	0.3	-0.5	-0.58
1.5	-0.25	-0.1	-0.5	-0.2
1.75	-0.4	-0.25	-0.2	0
2	-1.1	-0.8	-0.2	0.2
2.25	-1	-0.9	-0.01	0.25
2.5	-1.05	-0.9	0	0.25
2.75	-0.9	-0.8	0	0.25
3	-0.9	-0.7	0	0.15
3.25	-0.5	-0.6	0.2	0.2
3.5				

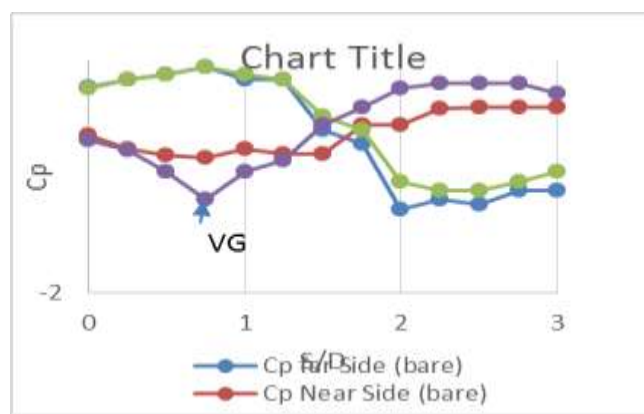


Fig: 12 Surface pressure distribution on the side wall at $Re=4.73 \times 10^4$

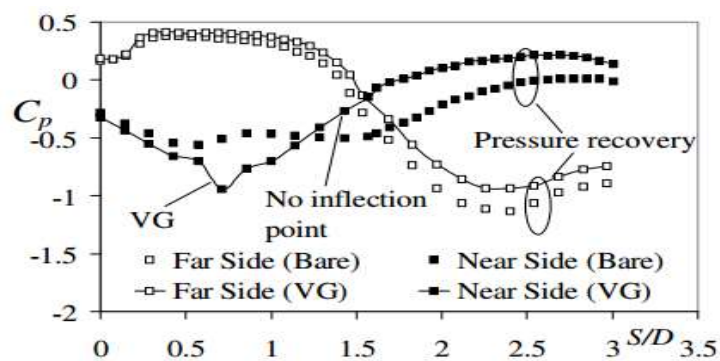


Fig: 13. Graph of C_p v/s S/D obtained practically by Thy, N. Y [13] at $Re=4.73 \times 10^4$

From above chart it is clearly seen that there is no point of inflection in case of duct with vortex generator as compare to bare duct so it can be concluded from above chart that flow separation is suppressed by use of flow control device i.e. vortex generator.

From Fig.12 and Fig.14 it is seen that there is no point of inflection in case of duct with vortex generator as compare to bare duct so it can be concluded from above chart that flow separation is suppressed by use of flow control device i.e. vortex generator and the pattern obtained by simulation is similar to the graph of C_p vs S/D obtained practically by Thyne, N.Y. i.e. Fig.13.

3. Table of surface pressure distribution on the side wall (far side wall and near side wall) for bare duct and duct with vortex generator at $Re= 1.47 \times 10^5$

Table 3: surface pressure distribution on the side wall at $Re=4.73 \times 10^4$

S/D	Cp far Side (bare)	Cp far Side (vg)	Cp Near Side (bare)	Cp Near Side (vg)
0	0.3	0.3	-0.35	-0.35
0.25	0.3	0.3	-0.45	-0.47
0.5	0.45	0.45	-0.65	-0.65
0.75	0.43	0.44	-0.55	-0.9
1	0.4	0.4	-0.6	-0.65
1.25	0.3	0.3	-0.5	-0.55
1.5	-0.1	-0.05	-0.05	0
1.75	-0.3	-0.25	0.28	0.3
2	-0.65	-0.6	0.25	0.25
2.25	-0.92	-0.9	0.35	0.4
2.5	-0.9	-0.9	0.35	0.3
2.75	-0.82	-0.8	0.25	0.25
3	-0.7	-0.7	0.25	0.2
3.25	-0.5	-0.6	0.2	0.2
3.5				

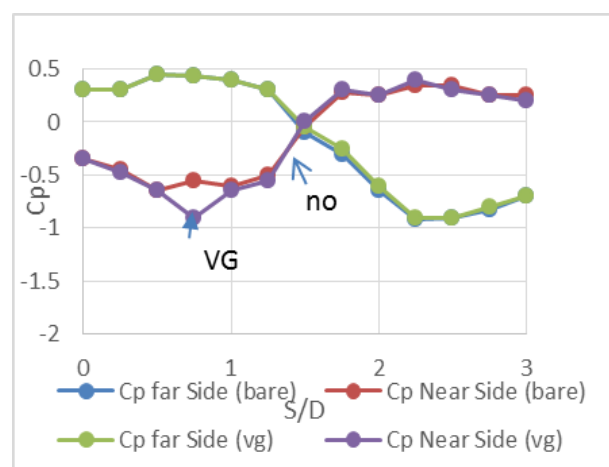


Fig: 14 surface pressure distribution on the side wall at $Re=1.47 \times 10^5$

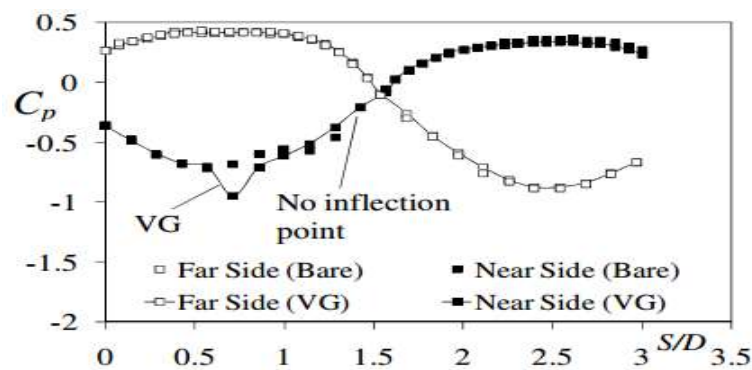


Fig: 15. Graph of C_p v/s S/D obtained practically by Thye, N. Y [13] $Re=1.47 \times 10^5$

From Fig.12 and Fig.14 it is seen that there is no point of inflection in case of duct with vortex generator as compare to bare duct at $Re=1.47 \times 10^5$ so it can be concluded from above chart that flow separation is suppressed by use of flow control device i.e. Tangential Blowing and the pattern obtained by simulation is similar to the graph of C_p vs S/D obtained practically by Thye, N.Y. i.e. Fig. 15.

Total Pressure Loss:

Table 4: Total pressure loss coefficient with respect to Reynolds number for bare and vortex generator duct.

Sr. No	Total pressure loss coefficient	Reynolds number 4.73×10^4		Reynolds number 1.47×10^5	
		simulation	Experimental[14]	Simulation	Experimental[14]
1.	Bare Duct	0.2	0.24	0.25	0.2
2.	VG	0.115	0.2	0.12	0.13
3.	Tangential Blowing $C_m=0.12$	0.15	0.16	0.15	0.14
4.	Tangential blowing $C_m=0.045$	0.12	0.13	0.125	0.12

Variation of total pressure loss coefficient 5° angle for VG configuration at $Re = 4.73 \times 10^4$ and Variation of total pressure loss coefficient at 5° angle for VG configuration at $Re = 1.47 \times 10^5$ it is found that there is reduction in total pressure loss coefficient by using vortex generator. As total loss coefficient is 0.25 and 0.2 for the bare duct for respective Reynolds number. In case of vortex generator it is 0.115 For $Re=4.73 \times 10^4$. For Reynolds number 1.473×10^5 for vortex generator it is 0.2.

IV. CONCLUSION

The optimum aerodynamic performance of S-shaped ducts (or aircraft air-intake ducts) demands that a relatively uniform flow with a smallest possible pressure loss. The contour of static pressure obtained from simulation of bare Duct, shows two low pressure zones are developed on the duct, one at near side wall of the 1st bend and other on the far side wall of the second bend. There is a flow separation in these two pockets of the bend which is clearly seen on the contour of velocity vector (Fig. 6). As we use two Reynolds number the effect is same, only difference in magnitude observed. Flow control techniques namely Vortex generator is used to suppress the flow separation there by reducing total pressure loss. The effectiveness of VGs to control flow separation, reduce total pressure loss is studied. The graph of C_p vs S/D (Fig.12) of simulation shows no point of inflection i.e. there is no flow separation on these walls. There is also reduction in total pressure loss coefficient by using vortex generator shown in table 4. As total loss coefficient is 0.25 and 0.2 for the bare duct for respective Reynolds number. In the case of vortex generator it is 0.115 and 0.2 for respective Reynolds number. The method vortex generator was shown to be effective in suppressing flow separation and reducing total pressure loss. Therefore the results indicates competing parameters for improving the performance of flow in S-ducts.

V. REFERENCES

- [1] B.H Anderson and J. Gibb, Vortex-Generator Installation Studies on Steady-State and Dynamic Distortion, *Journal of Aircraft*, 35(4), (1998), 513-520.
- [2] B.H Anderson, D.R. Reddy and K. Kapoor, Study on Computing Separating Flows Within a Diffusing Inlet S-duct, *Journal of Propulsion and Power*, 10(5), (1994), 661-667.
- [3] B.H Anderson, A.M.K.P Taylor, J.H Whitelaw and M. Yianneskis. Developing Flow in S shaped Ducts. In: *Proceeding of Second Symposium on the Application of LDA to Fluid Mechanics*, Lisbon, Portugal, 4.2, 1982, 17.
- [4] P. Bansod and P. Bradshaw, The Flow in S-Shaped Ducts, *Aeronautical Quarterly*, 23, (1972), 131-140.
- [5] K.C Cheng and L. Shi, Visualizations of Developing Secondary Flow and Measurements of Velocity Profiles in a Curved Square Duct with and without an Offset Bend. In: *Flucon '91, 3rd Triennial International Symposium on Fluid Control, Measurement, and Visualization*, San Francisco, USA, (1991), 415-422.
- [6] M. Gad-el Hak and D.M Bushnell, Separation Control: Review, *Transactions of ASME: Journal of Fluid Engineering*, 113(1), (1991), 5-30.
- [7] R.W Guo and J. Seddon, The Swirl in an S-duct of Typical Air Intake Proportions, *Aeronautical Quarterly*, 34(2), 1983, 99-129.
- [8] B.J. Kitchen and J.M. Jr. Bowyer, Towards the Optimization of a Non-diffusing Two Dimensional, S-shaped Duct, In: *Forum of Turbulent Flows*, ASME Fluid Engineering Division FED, San Diego, USA, 76, (1989), 85-92.
- [9] M. Norouzia, M.H. Kayhani, C. Shu, M.R.H. Nobari et al., Flow of second-order fluid in a curved duct with square cross-section, *Journal Non-Newtonian Fluid Mech.* 165, (2010), 323–339.
- [10] J. Rojars, J.H Whitelaw, and M. Yianneskis, Developing Flows in S-shaped Diffusers Part I: Square to Rectangular Cross Section Diffuser, *NASA Contractor Report 3631*, (1983), 50.
- [11] R.K. Sullerey, and A.M. Pradeep, Effectiveness of Flow Control Devices on S-Duct Diffuser Performance in the Presence of Inflow Distortion, *International Journal of Turbo and Jet-Engines*, 19(4), (2002), 259-270.
- [12] A.M.K.P Taylor, J.H. Whitelaw and M. Yianneskis, Developing Flow in S-shaped Ducts 2: Circular Cross-section Duct, *NASA Contractor Report 3759*, 1984, 60.
- [13] N.Y. Thye. A Thesis, Doctor of Philosophy, National University of Singapore, 2009.

- [14] T. Chandratilleke Tilak, NimaNadim, Ramesh Narayanaswamy et al , Vortex structure-based analysis of laminar flow behavior and thermal characteristics in curved ducts, *International Journal of Thermal Sciences* 59, (2012), 75e86.
- [15] J.H.Whitelaw and S.C.M Yu, Turbulent Flow Characteristics in an S-shaped Diffusing Duct, *Flow Measurement and Instrumentation*, 4(3),1993a, 171-179.
- [16] J.H Whitelaw and S.C.M Yu, S.C.M. Velocity Measurements in an S-shaped Diffusing Duct, *Experiments in Fluids*, 15(3-4), 1993b, 364-367.
- [17] Wu Xiaoyun , Sangding Lai, Kyoji Yamamoto, Shinichiro Yanase et al, Vortex Patterns of the Flow in a Curved Duct, *ICSGCE* 2011.
- [18] S.C.M Yu and E.L.Goldsmith. Some Aspects of the Flow in S-shaped Diffusing Ducts, *Aeronautical Journal*, 98(978), 1994, 305-310.



Challenges and trends in glucose monitoring technologies

Padma Batra, Reena Tomar, and Rajiv Kapoor

Citation: [AIP Conference Proceedings](#) **1715**, 020060 (2016); doi: 10.1063/1.4942742

View online: <http://dx.doi.org/10.1063/1.4942742>

View Table of Contents: <http://scitation.aip.org/content/aip/proceeding/aipcp/1715?ver=pdfcov>

Published by the [AIP Publishing](#)

Articles you may be interested in

[Dosimetry in Medical Exposures: Trends, Challenges and Next Steps](#)

AIP Conf. Proc. **1345**, 181 (2011); 10.1063/1.3576166

[New Trends in Forging Technologies](#)

AIP Conf. Proc. **1353**, 380 (2011); 10.1063/1.3589545

[Information technology challenges in passive acoustic monitoring of marine life.](#)

J. Acoust. Soc. Am. **128**, 2298 (2010); 10.1121/1.3508071

[CURRENT TRENDS AND CHALLENGES OF MODELING AND EXPERIMENTING ON TOXICITY OF NANOPARTICLES](#)

AIP Conf. Proc. **1229**, 23 (2010); 10.1063/1.3419686

[Interconnect Challenges in the Nanometer Technology](#)

AIP Conf. Proc. **929**, 32 (2007); 10.1063/1.2776684

Challenges and Trends in Glucose Monitoring Technologies

Padma Batra^{1,a)}, Reena Tomar², Rajiv Kapoor³

^{1,2}Krishna Institute of Engineering & Technology, Ghaziabad

³Delhi Technological University, Delhi

^{a)} Corresponding author: padmabatra61@gmail.com

Abstract. It is known that diabetes is a very serious disease as it may lead to heart attack, kidney failure and neuro diseases. The present study was aimed to review and compare various techniques useful for detecting diabetes or hypoglycemia in human body. In this paper we discuss the invasive and non-invasive techniques which are used for early detection of hypoglycemia or hyperglycemia and highlight their advantages as well as limitations. The use of bio impedance measurement technology has been described as it is an emerging non-invasive technique useful for the same purpose.

INTRODUCTION

Glucose is an essential component and the main energy carrier carbohydrate in human body. The appropriate range of glucose level in human blood should be from 89 mg/dL to 125 mg/dL under normal conditions. The imbalance of this component can cause very serious disease called diabetes. Therefore several techniques of glucose monitoring have been used for the past few decades. Diabetes is of two types- type 1 diabetes and type 2 diabetes; both are very dangerous to the patient's life. The long term excess of glucose may lead to type 1 diabetes. The diseases caused due to this type of diabetes are blindness, damaged nerves, kidney (renal) failure or even increase in the risk of heart stroke, birth defects, etc. On the other hand, the low intake of glucose leads to type 2 diabetes which may cause problems like confusion, coma or even death. Therefore, it is essential to monitor the glucose level in human body. Earlier, glucose monitoring was done through invasive techniques but these methods are painful and also have the risk of infection. Therefore, extensive research has been carried out to develop painless and noninvasive methods for measuring glucose level. Bio-impedance measurement is an area in which research has been successfully conducted for measurement of body fluid compartments [1], fat free mass [2], heart rate detection[3], detection of fake fingers in fingerprint systems by calculating electrical properties of epidermal skin [4], human prostate [5] etc. Other applications in which bio impedance measurement method has been investigated include myocardial ischemic injury [6], pulsatile blood flow through rigid tubes [7], breast cancer [8], liver tissue [9], preterm birth detection [10] and sleep apnea [11]. In this paper we have discussed various invasive and noninvasive methods (Fig.1) for measuring glucose level in blood; and a comparative analysis of these techniques as well as their limitations have been pointed out along with the future directions of research.

METHODS INVESTIGATED

Although point sample glucose sensors are found in the literature but due to their limited use, our discussion is focused only on continuous glucose sensing technologies.

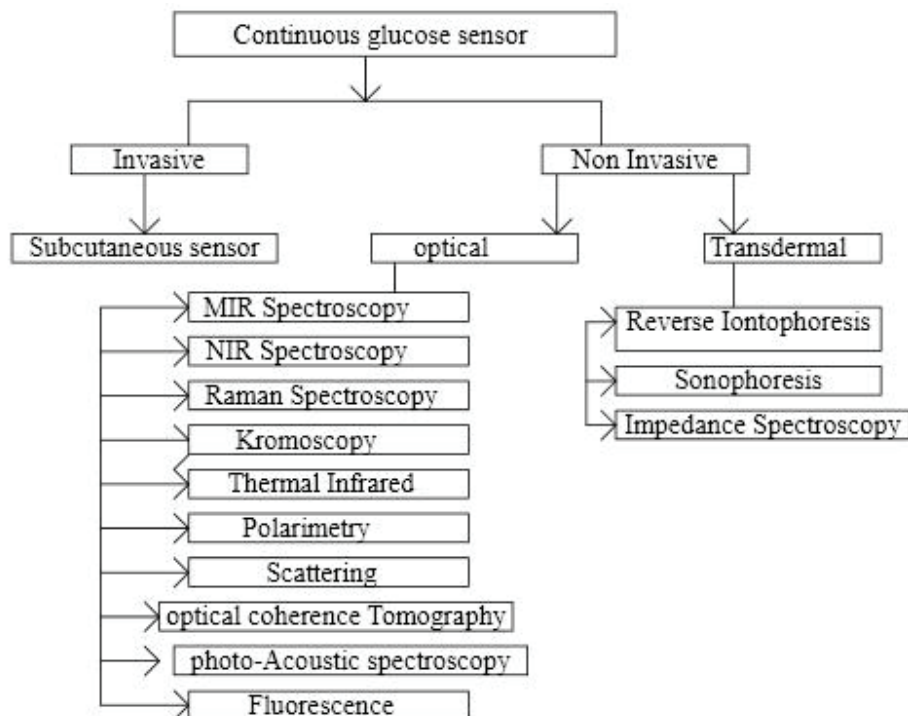


FIGURE 1. Various glucose sensing technologies.

A Invasive technology

The very first glucose monitor device was filed in 1971 in USA by Anton Clemes [12]. The device was named Ames reflectance meter which assessed the color change of enzyme based on reagent strip. The blood glucose was identified by reading the color change by eye from a chart. This method is improved by using subcutaneous needle type sensor. In this method, glucose may be sensed by the use of enzyme electrodes. These enzyme electrodes make use of enzyme which catalyzes redox reaction. During this process electrons can be accepted or donated. Due to the movement of electrons, current or voltage is produced which is measured using these electrodes.

B Noninvasive technologies

Spectroscopic Measurement Based on Optical Transducer

For detection of glucose level, optical transducer uses photons in variable frequencies which utilize multiple properties of light to collide with molecules of glucose, which is dependent on the concentration of glucose molecules. The amount of light transmitted, absorbed or reflected is analyzed by spectroscopic measurement which is considered to be an effective technique for measuring glucose level in human body as shown in (Fig 2).

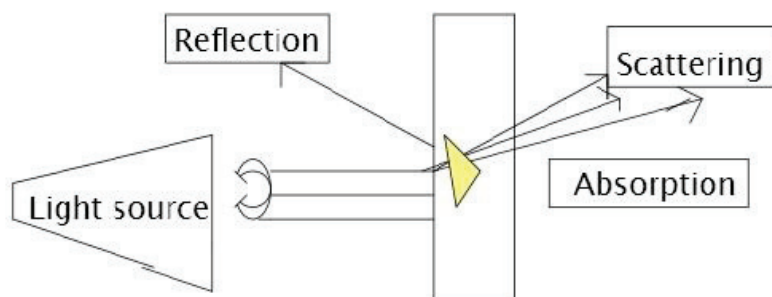


FIGURE 2. Use of properties of light for detection of glucose level.

i Mid infrared spectroscopy (MIR)

MIR light has a wavelength between 2.5 to 5 micro meters. In this type of spectroscopy light intensity is measured in two phases before and after it collides with matter. Because of stretching and bending of molecules absorption band is seen. While travelling through tissue MIR has short path length. In spite of this, glucose concentration is measured in blood with standard prediction error of 0.95mmol/l [13].

ii Near Infrared spectroscopy (NIR)

The wavelength of NIR light is limited between 0.7- 1.4 micro meters. Almost 90-95% of light passes through the stratum corneum and epidermis into the subcutaneous space independent of skin pigmentation [14]. The absorption of NIR light is based on molecular structure and the kinks of glucose absorption in this region are few. All spectroscopic technologies face several problems, even scattering reduces signal-to-noise ratio. Scattering is a random effect based on hydration temperature, blood flow, non-glucose metabolites. There are several heterogeneous specifications of absorption of light and scattering of light structure between singles and within singles over time period. Oral mucosa is used for measuring blood glucose by using NIR. Correlation is good i.e., $r=0.91$ but glucose specific absorption kinks vary with pressure includes saliva, different glucose concentration and residual food may contain interferences [15]. The standard prediction error is 3.5mmol/l caused by variability in tissue fat. Therefore accuracy of this technique is less as compared to MIR technique

iii Raman Spectroscopy

This technique is used to evaluate a single wavelength of light and has a light absorption band. It is dependent on vibrational and rotational energy states of molecules. In this technique the absorption band is highly specific. In comparison to other technologies the signal obtained in this technique is weaker therefore powerful detectors are required for measurement of glucose in human blood. As compared to MIR and NIR spectroscopy, this technique has the benefit of less interference from water [16]. Experimental studies with Raman spectroscopy have shown a good correlation of $r=0.91$ [17]

iv Kromoscopy technology

In this method there are four detectors which are used to record the spectrum of different wavelengths of NIR light. The output of these four detectors give responses which are overlapping. Kromoscopy technique helps us to identify the relative intensities of these overlapping responses.

v Thermal Infrared

Thermal Infrared is a measurement technique which is based on the principle that cutaneous microcirculation depends on glucose concentration in humans. This method is based on evaluating the MIR light scattering in the skin at various tissue depths. The authors in [18] studied 20 subjects and experimented on tympanic membrane and then calculated glucose concentration in all subjects. A good correlation was obtained which is $r=0.87$ and 100% points were in area A and B of the Clarke error grid. Error Grid Analysis (EGA) has been accepted as one of the standard methods for estimation of the accuracy of blood glucose meter.

vi Polarimetry

Polarimetry is a technique based on polarization of light. It measures the rotation of polarized light when it passes through an optically active fluid (Fig 3). By considering the measured rotation we can calculate value of solution concentrations like that of sugar, volatile oils and peptides. The rotation of polarized light depends on pH, temperature, path length of light, wavelength of light and other factors. It is very difficult to maintain polarization of light through skin, so this technology needs to measure milli degree rotation under conditions of greater than 95% retained polarization through tissue which is less than 4 mm thick. Therefore, blood glucose and interstitial fluid (ISF) glucose cannot be measured with this technology [19].

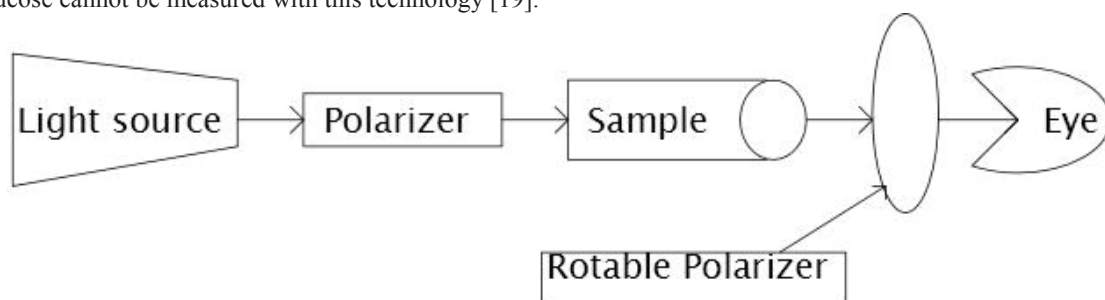


FIGURE 3. Principle of polarimetry

vii Scattering

Scattering is a process in which some form of radiation like light, sound or moving particles are forced to deviate from a straight path to multiple paths. The scattering properties (Fig 4) of tissues depend on relative refractive index of particles like cell membrane, collagen fiber, ISF, blood etc. When glucose concentration rises in the body, the refractive index of ISF falls but that of the surrounding medium remains constant resulting in the change in the degree of scattering of NIR light. The scattering is affected by many factors like temperature change, motion artifacts, change in parameters like water and protein [20].

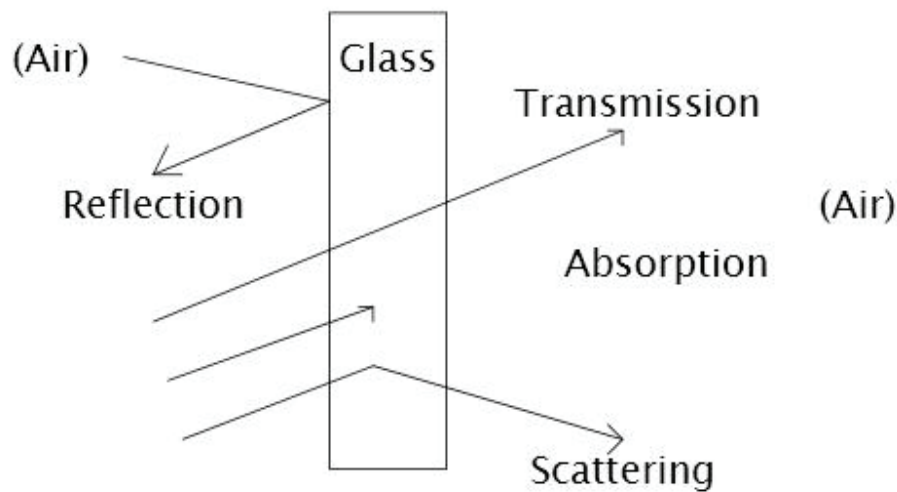


FIGURE 4. Properties of light in different media.

viii Optical coherence tomography (OCT)

Optical coherence tomography is a non-invasive technology which is used to measure blood glucose and hemoglobin. In this technology we use NIR spectroscopy along with occlusion principle. NIR sensor consists of two light sources such as 100 nm wavelength for detecting blood glucose level in the body and 870nm wavelength for detecting hemoglobin. An optical coherence tomography technique makes use of a low power laser source, a system for scanning in depth, a sampling device and a light detector. By using this technique glucose concentration in the dermis can be found. Optical coherence tomography is not affected by minerals which are present in the human body such as sodium chloride (NaCl), potassium chloride (KCl), or by temperature, pressure, heart rate etc.

ix Photo acoustic spectroscopy

Photo acoustic spectroscopy is the technique which measures the effect of absorbed electromagnetic waves by using acoustic detection. The absorbed energy causes local heating leading to increase in temperature which is dependent on specific heat capacity of tissue irradiated. Increasing glucose concentration in tissue reduces specific heat capacity of tissue and therefore, velocity of generated pulse increases. So, this is another method which can be used for measuring glucose level. In this technique, we make use of aqueous solution with gelatin based tissue simulations [21], [22]. No interference was noted from albumin cholesterol and NaCl. This technology was studied by considering 10 normal individuals which showed a good prediction of glucose level and resulted in the value $r=0.7$ and all points were falling in area A and B of Clarke error grid [23]

x Fluorescence spectroscopy

In fluorescence spectroscopy, first the molecular system absorbs and then emits light. During absorption, high energy of the light excites the molecules to transit from ground state to excited state. When in the year 1988, the concept was developed further for fluorescence resonance energy transfer (FRET) system. In this concept, energy is passed from fluorescent donor molecule to fluorescent acceptor molecule by dipole interaction, which leads to decrease in fluorescence and life-span of donor molecule. Due to dipole-dipole interaction FRET becomes sensitive to change in separation between donor and acceptor. FITC was used as a fluorescent donor molecule whereas

rhodamine was used as acceptor molecule. This rhodamine binds with concanavalin A and dextran was labeled with FITC [24]. The displaced label of glucose shows increase in dextran path between donor and acceptor which tends to decrease in FRET signal. Glucose detection was linear up to a concentration of 1.1 millimole/litre. Other fluorescence techniques which use enzyme catalyzed reaction to change fluorescence status are glucose oxidase and hexokinase. A molecule reaches to the excited state, it remains there for a few seconds and then emits its stored energy in the form of emitted photon and returns back to the ground state (Fig 5)

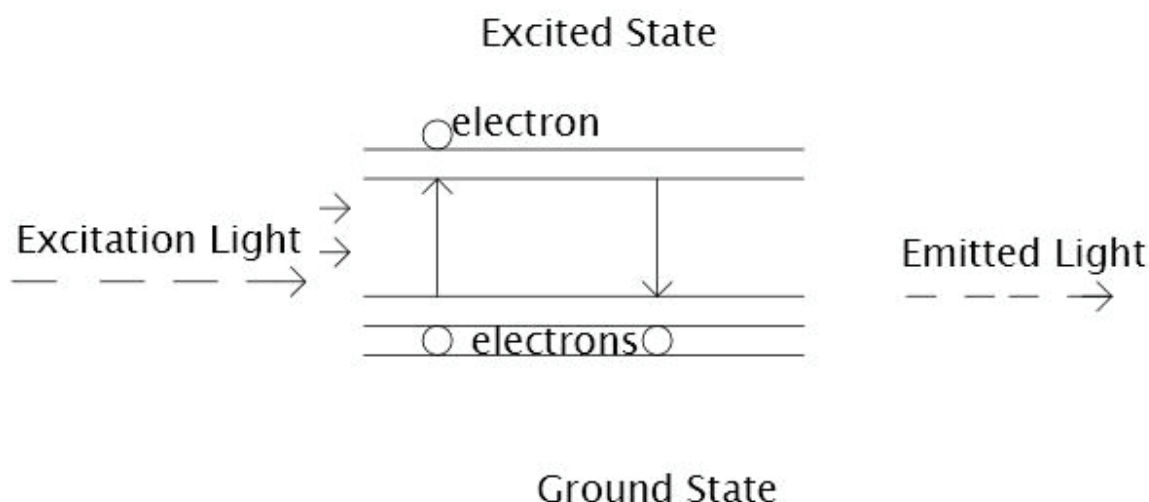


FIGURE 5. Excitation of electron and emitting of light

In the year 1988, the concept was developed further for fluorescence resonance energy transfer (FRET) system. In this concept, energy is passed from fluorescent donor molecule to fluorescent acceptor molecule by dipole interaction, which leads to decrease in fluorescence and life-span of donor molecule. Due to dipole-dipole interaction FRET becomes sensitive to change in separation between donor and acceptor. FITC was used as a fluorescent donor molecule whereas rhodamine was used as acceptor molecule. This rhodamine binds with concanavalin A and dextran was labeled with FITC [24]. The displaced label of glucose shows increase in dextran path between donor and acceptor which tends to decrease in FRET signal. Glucose detection was linear up to a concentration of 1.1 millimole/litre. Other fluorescence techniques which use enzyme catalyzed reaction to change fluorescence status are glucose oxidase and hexokinase.



Transdermal sensor

i) Reverse iontophoresis

It is a transdermal technique for measuring ISF. In this technique a low electric current is applied on the skin between two electrodes. These two electrodes initiate charged and uncharged species to pass across the skin at the rate significantly greater than passive permeability. Skin is negatively charged at normal pH level, so it is permeable to cations mainly Na^+ (Fig 6). Now, the flow is induced by reverse iontophoresis which carries neutral molecules along with glucose from anode to cathode. The glucose concentration by using reverse iontophoresis is 1000 times lower than ICF. The advantage of transdermal iontophoresis is that the concentration of glucose is low so O_2 supply is not a factor of limitation to glucose oxidase, also skin filters large molecules reducing electrode fouling etc. However low power current can cause mild to moderate erythema and system does not operate if sweat is present on the skin [25]

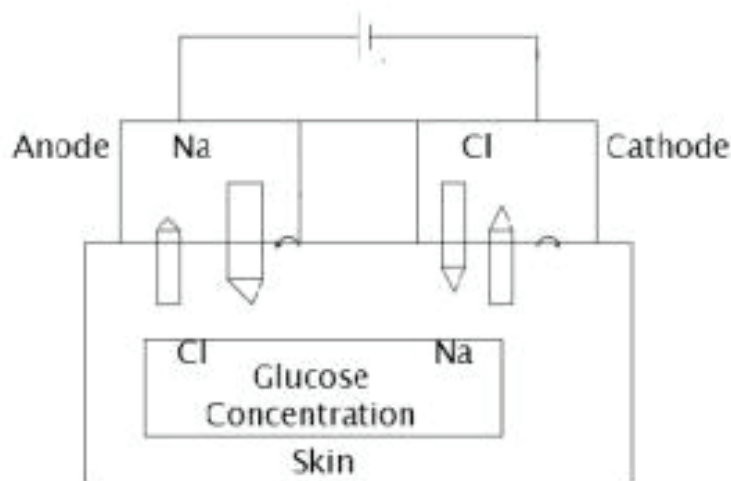


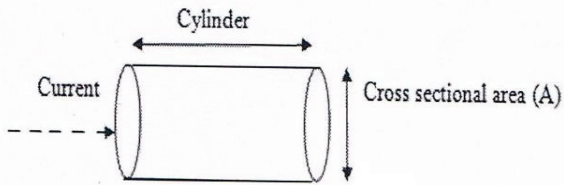
FIGURE 6. Reverse iontophoresis process showing movement of ions.

ii) Sonophoresis

It works on low frequency ultrasound to increase skin permeability. It increases absorption of compound into epidermis, dermis and skin. It occurs because ultrasound waves activate micro vibration within the skin dermis and all over kinetic energy of molecule increases. This technique is generally used in hospitals to give drugs through skin. In clinical analysis 2 min of ultrasound application is followed by 5 min period of vacuum to extract ISF at 25 $\mu\text{l}/\text{cm}^2/\text{h}$ which is almost greater than reverse iontophoresis. The analysis of extracted ISF shows main reactive error of 23 of result in area A and B of Clarke error grid and $r > 0.7$ [26]

iii) Impedance spectroscopy

It is a technology in which a small alternating current is injected in a segment of the human body and impedance is measured as a function of frequency. The human body can be assumed to be consisting of cylindrical segments (Fig 7) therefore, impedance Z of a segment is given by:



$$Z = \rho \frac{L}{A}$$

$$Z = \rho \frac{\text{Length}^2}{\text{Volume}}$$

$$V = \rho \frac{\text{Height}^2}{Z} \quad - (3)$$

FIGURE 7. Impedance of a human body segment

As we see in equation (3), the value of Z depends on resistivity (ρ). When the amount of glucose in the blood changes, the resistivity of blood will change. This change can be detected by measuring the impedance of blood and hence the glucose level can be sensed. Different components of human body have different values of permittivity and conductivity (Table 1).

TABLE 1. Values of permittivity and conductivity for different components of human body. [28], [30], [31]

Human Body Components	Permittivity (ϵ) F/m	Conductivity (σ) S/m
Skin	33-45	0.0000-0002
Bone	-	.06
Blood	64-70	0.43-0.7
Tissues	16	0.03
Muscles	23-32	-
Liver	20-25	2.8

In year 2012, Kuosheng Cheng et al., [27] have found that by measuring the bio impedance of the foot sole, it is possible to detect diabetes in humans. The foot of a diabetic patient is very crucial which may leads to disability, morbidity etc. The bio impedance measurement system consists of a hardware module and a software module (Fig 8). Hardware module consists of MCU C8051F060 which is used as control kernel. This is a 25 MIPS mixed signal 8051 with 2 channel (16 bit) A/D and 8 channel (10 bit) A/D converter. SPI and URTS are used to control sine wave generator and URTS helps in controlling transmitter and it also receives command and data to and from the PC.

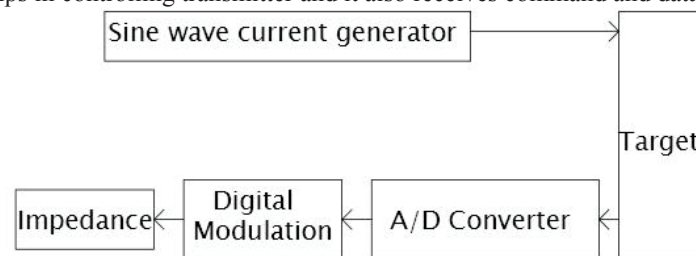


FIGURE 8. Block diagram of impedance measurement system

In year 2013, V.Pockevicius et al., [28] have found that the change in glucose level can be calculated by using inter digital electrode sensor by considering its two properties, i.e., permittivity and conductivity. The parameters required for computations using this method are assumed as skin thickness equal to 1.5 mm and diameter of blood vessels 3.2 mm. Modeling was done [29] under frequency range from 10 KHz to 100 KHz. The conductivity of blood is found to increase from 0.43 S/m to 0.7 S/m and permittivity is set to 68.5.

In year 2014, T.Mastantuono et al., [30] found that skin blood flow and total power spectral density was low in hypoglycemic patients as compared to normal subjects. The test was conducted on 17 normal female subjects and 16 hyperglycemic females of the age group 50-65 years. Their micro vascular blood flow was measured in supine position after 10 min of acclimatization in a temperature controlled room. The probe is connected to laser Doppler flow meter and a PC for recording blood flow using Perisoft software and data is analyzed by using ANOVA test and it is found that hyperglycemic patient have higher glycaemia compared to normal cases.

III Discussion

It can be easily understood that non – invasive techniques are preferable as compared to the invasive ones because they are simple to use and free from infections. In non-invasive technologies, we make use of different spectroscopy techniques. The accuracy of MIR is less as compared to NIR spectroscopy. MIR and NIR have poor interference from water whereas in polarimetry it is very difficult to maintain polarization of light through skin. The scattering is affected by many factors like temperature change, motion artifacts, water and protein. In reverse iontophoresis low power current can cause mild to moderate erythema and thus system does not operate if sweat is present on skin. The common disadvantage of all these spectroscopy techniques is the low value of signal- to- noise-ratio which

varies as a random effect. We found that a good correlation is obtained ($0.87 < r < 0.7$) and which falls in area A and B of the Clarke error grid. So many researchers are looking forward to impedance spectroscopy in which we measure impedance as a function of frequency. Table 2 describes correlation factor for all techniques and also the Clark error grid %.

TABLE 2. Comparison of different techniques

S.No	Technique			r value	% (A&B) area within Clarke error grid
1	Subcutaneous sensor	needle	type	0.85	96.6
2	NIR			0.91	99.3
3	Thermal Infrared			0.87	100
4	Raman spectroscopy			0.91	-
5	Polarimetry			0.99	-
6	OCT			0.8-0.95	-
7	Photoacoustic spectroscopy			0.7	100

CONCLUSION

In this paper we have discussed various currently used techniques as well as some emerging techniques used for monitoring of glucose level in human body. First, invasive technology has been analyzed and then various non-invasive technologies are discussed in detail. A comparative analysis of these methods has been done with reference to the correlation coefficient and the accuracy of these methods. Bioelectrical impedance method has numerous advantages as it is simple, non- invasive, inexpensive, fast, painless, radiation less and reproducible. The only drawback of this method is its less accuracy. Hence researchers are working in this field with the aim of increasing the accuracy of this method.

REFERENCES

1. Khan M, O' Hara R, PohlmanRL,Goldstein DG, Guha SK, JEP online Volume 8 Number 1 February 2005.
2. Ji-Jer Huang, Kuo-Sheng Cheng, and Cheau-Jane Peng, The Influence of Temperature Variation on Segmental Fat-Free Mass Estimation, IEEE Engineering In Medicine , November/December 2000.
3. Rafael Gonzalez-Landaeta et al., IEEE Transactions on Biomedical Engineering, Vol.55, No.3, March 2008.
4. Orjan G. Martinsen,Sigmund Clausen, Jon B. Nysaether, and SverreGrimnes, IEEE Transactions On Biomedical Engineering ,Vol.54, No.5 May 2007.
5. Ryan J. Halter, Alex Hartov, John A. Heaney, Keith D. Paulsen,, IEEE Transactions On Biomedical Engineering, Vol.54, No.7 July 2007.
6. Fritz Mellert , Kai Winkler, Christian Schneider, TarasDudykevych, Armin Welz, Markus Osypka, Eberhard Gersing, and Claus J. Preusse, [IEEE Transactions On Biomedical Engineering](#), Vol. 58, No. 6, June 2011.
7. R. L. Gaw, B. H. Cornish, and B. J. Thomas, [IEEE Transactions On Biomedical Engineering](#), Vol.55, No. 2 , February 2008.
8. GuofengQiao, Wei Wang, Wei Duan, Fan Zheng, Alison J. Sinclair, and Chris R. Chatwin, "Bio impedance Analysis for the Characterization of Breast Cancer Cells in Suspension", IEEE Transactions On Biomedical Engineering, Vol.59, No.8 August 2012.

9. W. H. Huang, C. K. Chui, S. H. Teoh, and S. K. Y. Chang, [IEEE Transactions on Biomedical Engineering](#), Vol.59, No. 6, June 2012.
10. Mozziyar Etemadi, Philip Chung, J. Alex Heller, Jonathan A. Liu, Larry Rand, and Shuvo Roy, “Towards Birth Alert—A Clinical Device Intended for Early Preterm Birth Detection”, [IEEE Transactions On Biomedical Engineering](#) Vol.60, No.12 December 2013.
11. Saif Ahmad, Izmail Batkin, Owen Kelly, Hilmi R. Dajani, Miodrag Bolic, Voicu Groza, [IEEE Transactions on Instrumentation and Measurement](#), Vol.62, No.10, October 2013.
12. The Diabetes Control and Complications Trial Research Group, [N Engl J Med](#) 1993; 329:977-986 September 30, 1993.
13. Shen YC, Davies AG, Linfield EH, Taday PF, Arnone DD, [Phys Med](#) 48: 2023–2032.
14. Nelson LA, McCann JC, Loepke AW, Wu J, Dor BB, Kurth CD, [J Biomed Opt](#) 2006; 11: 064022.
15. Burmeister JJ, Arnold MA, Small GW, [Diabetes Technol Ther](#) 2000; 2:5-16.
16. Dieringer JA, et. al., [Faraday Discuss](#) 2006; 132: 9–27.
17. Enejder A, Scecina T, Oh J, Hunter M, Shih WC, Sasic S, [J Biomed Optics](#) 2005;10:031114.
18. Malchoff CD, Shoukri K, Landau JI, Buchert JM, [Diabetes Care](#) 2002; 25: 2268–2275.
19. Cameron BD, Anumula H, [Diabetes Technol Ther](#) 2006; 8:156-164.
20. Heinemann L, Krämer U, Klötzer HM, Hein M, Volz D, Hermann, [Diabetes Technol Ther](#) 2000; 2: 211–220.
21. Spanner G, Niessner R, Fresenius J [Anal Chem](#) 1996; 355:327-328.
22. MacKenzie HA, Ashton HS, Shen YC, Lindberg J, Rae P, Quan KM, [OSA Trends in Optics and Photonics Series](#) 1998;22:156-159.
23. Raz I, Wainstein J, Argaman D, [Diabetes](#) 2003; 52: A98.
24. Reeke GN, Becker JW, Edelman GM, [A J Biol Chem](#) 1975;250:1525-1547.
25. Rao G, Glikfeld P, Guy RH, [Pharm Res](#) 1993; 10:1751-1755.
26. Kost J, Mitragotri S, Gabbay RA, Pishko M, Langer R, [Nat Med](#) 2000; 6: 347–350.
27. Kuo-Sheng Cheng, Yen-Fen Ko, Ting Wang, [Sixth International Conference on Genetic and Evolutionary Computing](#), 2012.
28. V. Pocekevicius¹, V. Markevicius¹, M. Cepenas¹, D. Andriukaitis¹, D. Navikas¹, [Studentu St, Kaunas, Lithuania](#), 50–438, LT-51368, ISSN 1392-1215, Vol. 19, No.6, 2013.
29. T. Mastantuono, E. Muscariello, T. Novellino, D. Lapi, M. Cesarelli, G. D’Addio, L. Iuppariello and A. Colantuoni, [8th conference of the European study group on cardiovascular oscillations \(ESGCO 2014\)](#).
30. Mark J Schroeder, Anupama Sadasiva, Robert M Nelson, [Journal of Biomechanics, Biomedical and Biophysical Engineering Volume 2, Issue 1](#), 2008.
31. Joseph D. Bronzino, “[Biomedical Engineering Handbook](#)” 2nd Ed, Vol 1, CRC Press and IEEE Press.

DYNAMICAL BEHAVIOR OF A STAGE STRUCTURED ECO-EPIDEMIOLOGICAL MODEL

SHASHI KANT AND VIVEK KUMAR

(Communicated by Jurang Yan)

Abstract. In this paper, a stage structured eco-epidemiological model with linear functional response is proposed and studied. The stages for both prey and predator have been considered. Infection occurs in the prey population only. The proposed mathematical model consists of five nonlinear ordinary differential equations to describe the interaction among juvenile prey, adult prey, infected prey, juvenile predator and adult predator populations. The model is analyzed by using linear stability analysis to obtain the conditions for which our model exhibits stability around the possible equilibrium points.

1. Introduction

Many of the 'old' mathematical equations resulting from the progress of mathematical ecology such as classical Volterra prey-predator model, Lotka-Volterra competition equations and logistic growth equations [1, 46], have imposed a huge amount of influence on the growth of theoretical and mathematical ecology. They provided the fundamental basis to many (if not almost) to the underlie subdisciplines of the subject. Without paying due credit to them is not possible to model any ecological problem. Truly speaking they are the father of the further development in the subject. The main motivation behind writing this paper is these old studies.

The basic goal in population dynamics is to study the dynamical relationship between predator and prey which has long been and will continue to be one of the important aspect in the subject. This relationship may be formulated by the term so called 'functional response', which means the change in the quantity of prey consumed by a single predator per unit time in relation to prey density. In literature there have been proposed number of functional responses. Few of them are enlisted for ready reference (without full detail):

- $g(x) = C(t)x$: Holling type I or linear function response [7, 8, 59].
- $g(x) = \frac{C(t)x}{m+x}$: Holling type II [7, 8, 59, 54].
- $g(x) = \frac{C(t)x^p}{1+mx^p}$, $0 < p \leq 1$: Generalized type II Holling functional response [9].

Mathematics subject classification (2010): 70Kxx, 34Cxx.

Keywords and phrases: Stage structured population, local stability.

- $g(x) = \frac{C(t)x^2}{m+x^2}$: Holling type III [7, 8, 59].
- $g(x) = \frac{C(t)x}{a+x+\frac{x^2}{m}}$: Holling type IV [59].
- $g(x,y) = \frac{xy}{ay+x}$: Ratio dependent [60, 53, 35].
- $g(x,y) = \frac{Cxy}{(1+ax)(1+by)}$: Crowley-Martin type functional response [32, 40].
- Hassell-Verley type functional response [25, 40].
- $g(x,y) = \frac{Cx}{1+k_1x+k_2y}$:Beddington-De Anglis type [11, 40, 18].
- Function response of the type $g(x) = k(1 - e^{-Cx})$ [Ivlev][15].

These functional responses has been extensively used. It is obvious that all the function responses convey their importance. It is also remarkable that Holling type functional responses are more frequently used as compare to other functional responses. Recently a very good study of Dawes JH and Souza MO (2013) [9] on Holling type functional responses is published. They derive Holling's type I,II,III responses and possible generalization of these responses. It is also important to mention that all these functional reponses somewhat generalize the Lotka-Volterra model (response).

A general prey-predator is of the form

$$\begin{cases} \frac{dx}{dt} = \alpha x - \beta g(x), \\ \frac{dy}{dt} = \delta g(x) - \gamma y, \end{cases} \quad (1)$$

where $x(t)$ and $y(t)$ are prey and predator populations respectively at any time t ; $\frac{dx}{dt}, \frac{dy}{dt}$ represents growth rate of two populations over time t and the constants $\alpha, \beta, \delta, \gamma$ govern interaction among two populations. Function $g(x)$ is the functional response.

If $g(x)$ follows the Holling type I functional response, then model (1) takes the form

$$\begin{cases} \frac{dx}{dt} = \alpha x - \beta xy, \\ \frac{dy}{dt} = \delta xy - \gamma y, \end{cases} \quad (2)$$

Holling type I is linear as used in Lotka-Volterra system, hence it is oldest among all the functional responses. Since the intake rate is constant in this case, hence the curve represented by the Holling type I functional response is linear, passing through origin and unbounded. In other words, the model (2) is the Lotka-Volterra functional response.

If $g(x)$ follows the Holling type II functional response, then model (1) takes the form

$$\begin{cases} \frac{dx}{dt} = \alpha x - \frac{\beta xy}{m+x}, \\ \frac{dy}{dt} = \frac{\delta xy}{m+x} - \gamma y, \end{cases} \quad (3)$$

this model may also written as

$$\begin{cases} \frac{dx}{dt} = \alpha x - \frac{\beta xy}{m+ahx}, \\ \frac{dy}{dt} = \frac{\delta xy}{m+ahx} - \gamma y, \end{cases} \quad (4)$$

or

$$\begin{cases} \frac{dx}{dt} = \alpha x - \frac{\beta xy}{1+ahx}, \\ \frac{dy}{dt} = \frac{\delta xy}{1+ahx} - \gamma y, \end{cases} \quad (5)$$

here a and h are attack rate and handling time of a predator respectively. In the case of Holling type II, the curve is rectangular hyperbola (for example Holling's disc equation) [7, 8]. Hence, it is clear that model (3-5) are more general as compare to (2). More detail about the Type I, II, III responses may be found in [7, 8].

Model (1) may be written by other functional responses as mentioned in the discussion above. For example;

Holling type IV model;

$$\begin{cases} \frac{dx}{dt} = \alpha x - \frac{\beta yx}{a+x+\frac{x^2}{m}}, \\ \frac{dy}{dt} = \frac{\beta yx}{a+x+\frac{x^2}{m}} - \gamma y, \end{cases} \quad (6)$$

Ratio dependent model;

$$\begin{cases} \frac{dx}{dt} = \alpha x - \frac{\beta xy}{ay+x}, \\ \frac{dy}{dt} = \frac{\delta xy}{ay+x} - \gamma y, \end{cases} \quad (7)$$

Crowley-Martin model;

$$\begin{cases} \frac{dx}{dt} = \alpha x - \frac{Cxy}{(1+ax)(1+by)}, \\ \frac{dy}{dt} = \frac{Cxy}{(1+ax)(1+by)} - \gamma y, \end{cases} \quad (8)$$

and so on.

Till now, we have mentioned two dimensional models. Three dimensional models have also been proposed by incorporating some more concepts. We mention two such concepts (i) infection in species (ii) stages of life. If infection occurs in prey species then model (2) becomes three dimensional model and takes the form;

$$\begin{cases} \frac{dx}{dt} = \alpha x - \xi xy, \\ \frac{dy}{dt} = \xi xy - d_1 y - pyz, \\ \frac{dz}{dt} = qpyz - d_2 y, \end{cases} \quad (9)$$

where x , y and z denote, respectively, the population densities of susceptible prey species, infected prey species and predator species. The model (9) with logistic growth term takes the form

$$\begin{cases} \frac{dx}{dt} = rx(1 - \frac{x+y}{K}) - \xi xy, \\ \frac{dy}{dt} = \xi xy - d_1 y - pyz, \\ \frac{dz}{dt} = qpyz - d_2 y. \end{cases} \quad (10)$$

The dynamical behavior of system (10) has been studied in [16]. For more studies wherein infection in prey have been considered, we refer [3, 10, 12, 27, 30, 37, 58, 39]. If we consider infection in predator population then again we have the three dimensional prey-predator system. For such systems, we refer reader to ([33, 48, 13] and references therein). Similarly, if one consider the stages of prey i.e. juvenile and adult, we have a

three dimensional model. For prey-predator system with stage-structured for prey, we cite ([23, 41] and references therein). If we consider the stages for predator, we have a three dimensional system. For such models, we refer reader to [24, 31, 36, 50, 61, 20].

For four dimensional models, in literature two situations (i) infection in both species (ii) stages for both species have been proposed. We can refer to [22, 43] for such four dimensional models. High dimensional models (dimension 5 and more) are rare. Five dimensional models evolved when infection and stages have been considered [44]. Motivated by this fact, in the present study, a five dimensional prey-predator model is proposed and analyzed.

Rest of the paper is organized as follows. The next Section is dealing with the model formulation. Stability results are presented in Section 3. Paper ends with a brief discussion in Section 4.

2. Mathematical model and basic dynamical results

In this paper, we proposed a new prey-predator model

$$\begin{cases} \frac{dx_1}{dt} = rx_1 - \beta x_1 - d_1 x_1 - ax_1 x_5, \\ \frac{dx_2}{dt} = \beta x_1 - d_2 x_2 - bx_2 x_5 - \gamma x_2 x_3, \\ \frac{dx_3}{dt} = \gamma x_2 x_3 - d_3 x_3, \\ \frac{dx_4}{dt} = k_1 ax_1 x_5 + k_2 bx_2 x_5 - \delta x_4 - d_4 x_4, \\ \frac{dx_5}{dt} = \delta x_4 - d_5 x_5, \end{cases} \quad (11)$$

subjected to the initial conditions;

$$x_1(0) > 0, x_2(0) > 0, x_3(0) > 0, x_4(0) > 0, x_5(0) > 0. \quad (12)$$

In system (11), $x_1(t), x_2(t), x_3(t), x_4(t)$ and $x_5(t)$ stand for juvenile prey, adult prey, infected prey, juvenile predator and adult predator densities, at time t respectively. The constants $r, \beta, d_1, a, d_2, b, \gamma, d_3, k_1, k_2, \delta, d_4, d_5$ are positive. That stand for

- r : birth rate of the juvenile prey;
- β : the transmission rate of juvenile prey to adult one;
- d_1 : death rate of juvenile prey;
- a : the capturing rate of juvenile prey by the adult predator;
- d_2 : death rate of adult prey;
- b : the capturing rate of adult prey by the adult predator;
- γ : infection coefficient of prey;
- d_3 : death rate of infected prey;
- k_1, k_2 : the coefficients of conversing prey to predator;
- δ : the transmission rate of juvenile predator to adult one;
- d_4 : death rate of juvenile predator;
- d_5 : death rate of adult predator.

The model (11) is derived under the following ecological assumptions.

(A1) We assume that $x(t)$ is the total prey density at any time t . Prey density is divided into three parts viz. juvenile prey ($x_1(t)$), adult prey ($x_2(t)$) and infected prey ($x_3(t)$). Hence, at any time t , we have,

$$x(t) = (x_1(t) + x_2(t) + x_3(t)). \quad (13)$$

It is assumed that birth and death rates of all the species are linear.

(A2) We assume that $y(t)$ is the total predator density at any time t . Predator density is divided into two parts viz. juvenile predator ($x_4(t)$) and adult predator ($x_5(t)$). Hence, at any time t , we have,

$$y(t) = (x_4(t) + x_5(t)). \quad (14)$$

(A3) We assume that infection occurs in prey species only. Infection is not communicable to predator population. To do so, we assume that predator consume juvenile and adult prey only (infected prey are safe from predation). The infected prey population neither recover nor immune. The infection process follows simple mass action law action $\gamma x_2 x_3$, γ is called the transmission rate.

(A4) We also assume that only adult predator can hunt the prey population. Juvenile predator population depend on adult predator population for food and safety etc. We also assume that predator predate the juvenile and adult prey at different rates.

LEMMA 1. *Solutions of model (11) corresponding to the initial conditions (12) are defined on the interval $[0, +\infty)$ and remain positive for all time $t \geq 0$.*

Proof. The system of equations (11) can be written in the vector notation

$$\frac{dX(t)}{dt} = \mathbb{A}(X(t)), \quad (15)$$

where,

$$X(t) = \text{col}(x_1, x_2, x_3, x_4, x_5) \in \mathbb{R}_+^5$$

$$X(0) = \text{col}(x_1(0), x_2(0), x_3(0), x_4(0), x_5(0)) \in \mathbb{R}_+^5$$

and

$$\begin{aligned} \mathbb{A}(X(t)) &= \begin{pmatrix} \mathbb{A}_1(X(t)) \\ \mathbb{A}_2(X(t)) \\ \mathbb{A}_3(X(t)) \\ \mathbb{A}_4(X(t)) \\ \mathbb{A}_5(X(t)) \end{pmatrix} \\ &= \begin{pmatrix} rx_1 - \beta x_1 - d_1 x_1 - ax_1 x_5 \\ \beta x_1 - d_2 x_2 - bx_2 x_5 - \gamma x_2 x_3 \\ \gamma x_2 x_3 - d_3 x_3 \\ k_1 ax_1 x_5 + k_2 bx_2 x_5 - \delta x_4 - d_4 x_4 \\ \delta x_4 - d_5 x_5 \end{pmatrix} \end{aligned}$$

with $\mathbb{A} : \mathbb{R}^5 \rightarrow \mathbb{R}_+^5$ and $\mathbb{A} \in C^\infty(\mathbb{R}^5)$.

It is clear that in the Eqs. (15), $\mathbb{A}_i(X_i) |_{X_i=0} \geq 0$, for $i = 1, 2, \dots, 5$. Due to the general classical theorem introduced by Nagumo[29], the solution of (15) with initial conditions $\mathbb{A}(0) \in \mathbb{R}^5$, say $\mathbb{A} = \mathbb{A}(t; \mathbb{A}_0)$, such that $\mathbb{A} \in \mathbb{R}^5, \forall t \geq 0$ that is for all finite time.

LEMMA 2. *Solutions of model (11) corresponding to the initial conditions (12) which initiate in R_+^5 are uniformly bounded within the region Ω .*

Proof. Case I. $k_1 = k_2 = 1$.

Let

$$W = x_1 + x_2 + x_3 + x_4 + x_5, \quad (16)$$

differentiation of (16) and using Eq. (11), we get

$$\frac{dW}{dt} = (r - d_1)x_1 - d_2x_2 - d_3x_3 - d_4x_4 - d_5x_5. \quad (17)$$

For a constant η , by Eq. (17), we have

$$\begin{cases} \frac{dW}{dt} + \eta W = (r - d_1 + \eta)x_1 - (d_2 - \eta)x_2 - (d_3 - \eta)x_3 \\ -(d_4 - \eta)x_4 - (d_5 - \eta)x_5. \end{cases} \quad (18)$$

If we choose $\eta = \min\{d_1, d_2, d_3, d_4, d_5\}$, Eq. (18) gives

$$\frac{dW}{dt} + \eta W \leq (r + \eta + \varepsilon), \varepsilon > 0, \quad (19)$$

If we denote $K' = (r + \eta + \varepsilon)$, we have

$$\frac{dW}{dt} + \eta W \leq K', \quad (20)$$

integrating both sides, due to [5, 14, 21, 42], the above inequality (20), we get

$$0 < \leq \frac{\eta W(0) - K'}{\eta} e^{-\eta t} + \frac{K'}{\eta}, \quad (21)$$

taking $t \rightarrow \infty$, we have from (21),

$$0 < W(x_1, x_2, x_3, x_4, x_5) \leq \frac{K'}{\eta}. \quad (22)$$

Hence, from Eq. (22) it can be concluded that, all the solutions of system (11), initiating from $\{R_+^5 \setminus 0\}$ are confined in the region $\Omega = \{(x_1, x_2, x_3, x_4, x_5) \in R_+^5, W = \frac{K'}{\eta} + \varepsilon_1\}$ for any $\varepsilon_1 > 0$ and $t \rightarrow \infty$, hence the proof completed.

The two cases viz. (i) $k_1 = k_2 \neq 1$ (ii) $k_1 \neq k_2$ may also be proceeded similarly.

2.1. Equilibria and their existence

Infection free equilibrium $(E_{x_1x_2x_4x_5})$ may be obtained by solving the following system;

$$\begin{cases} rx_1 - \beta x_1 - d_1x_1 - ax_1x_5 = 0, \\ \beta x_1 - d_2x_2 - bx_2x_5 = 0, \\ k_1ax_1x_5 + k_2bx_2x_5 - \delta x_4 - d_4x_4 = 0, \\ \delta x_4 - d_5x_5 = 0, \end{cases} \quad (23)$$

The components of equilibrium point $E_{x_1x_2x_4x_5}$ are given by

$$\begin{cases} x_1 = \frac{x_2(d_2+bx_5)}{\beta}, \\ x_2 = \frac{x_5}{\frac{(d_2+bx_5)k_1a}{\beta} + k_2b}, \\ x_4 = \frac{d_5(r-\beta-d_1)}{\delta a}, \\ x_5 = \frac{(r-\beta-d_1)}{a}, \end{cases} \quad (24)$$

Ecologically feasible co-existing equilibrium point may be obtained by solving the following system;

$$\begin{cases} rx_1 - \beta x_1 - d_1x_1 - ax_1x_5 = 0, \\ \beta x_1 - d_2x_2 - bx_2x_5 - \gamma x_2x_3 = 0, \\ \gamma x_2x_3 - d_3x_3 = 0, \\ k_1ax_1x_5 + k_2bx_2x_5 - \delta x_4 - d_4x_4 = 0, \\ \delta x_4 - d_5x_5 = 0, \end{cases} \quad (25)$$

in $R_+^5 = \{(x_1, x_2, x_3, x_4, x_5) \in R^5 : x_1 \geq 0, x_2 \geq 0, x_3 \geq 0, x_4 \geq 0, x_5 \geq 0\}$. Let co-existing equilibrium point(s) be $E^* = (x_1^*, x_2^*, x_3^*, x_4^*, x_5^*)$. Mathematically, components of interior equilibrium point $E^* = (x_1^*, x_2^*, x_3^*, x_4^*, x_5^*)$ are given by

$$\begin{cases} x_1^* = \left(\frac{(\delta+d_4)d_5}{\delta k_1 a} - \frac{k_2 b d_3}{\gamma k_1 a} \right), \\ x_2^* = \frac{d_3}{\gamma}, \\ x_3^* = \left(\frac{(\delta+d_4)\beta d_5}{d_3 \delta k_1 a} - \frac{k_2 b \beta}{\gamma k_1 a} - \frac{d_2}{\gamma} - \frac{b(r-\beta-d_1)}{\gamma a} \right), \\ x_4^* = \frac{d_5(r-\beta-d_1)}{\delta a}, \\ x_5^* = \frac{(r-\beta-d_1)}{a}, \end{cases} \quad (26)$$

It is also important to mention that, our model (11) has unique co-existing equilibrium point $E^* = (x_1^*, x_2^*, x_3^*, x_4^*, x_5^*)$. Hence, the co-existing equilibrium $E^* = (x_1^*, x_2^*, x_3^*, x_4^*, x_5^*)$ exists provided the following conditions are satisfied;

$$\begin{cases} (\delta + d_4)d_5\gamma > k_2b\delta d_3, \\ \left(\frac{(\delta+d_4)\beta d_5}{d_3 \delta k_1 a} - \frac{k_2 b \beta}{\gamma k_1 a} - \frac{d_2}{\gamma} - \frac{b(r-\beta-d_1)}{\gamma a} \right) > 0, \\ (r - \beta - d_1) > 0. \end{cases} \quad (27)$$

REMARK 1. Equilibrium points other than $E_{x_1x_2x_4x_5}$, E^* (as mentioned above) viz. $E_{x_2x_3x_4x_5}$, $E_{x_1x_3x_4x_5}$, $E_{x_1x_2x_3x_5}$, $E_{x_1x_2x_3x_4}$, $E_{x_3x_4x_5}$, $E_{x_1x_4x_5}$, $E_{x_1x_2x_5}$, $E_{x_1x_2x_3}$, $E_{x_2x_4x_5}$, $E_{x_2x_3x_5}$ etc. do not exist.

3. Stability Analysis

At any non zero point $(x_1, x_2, x_3, x_4, x_5)$, Jacobian matrix of Eq. (11) is given by

$$J = \begin{pmatrix} a_{11} & 0 & 0 & 0 & a_{15} \\ a_{21} & a_{22} & a_{23} & 0 & a_{25} \\ 0 & a_{32} & a_{33} & 0 & 0 \\ a_{41} & a_{42} & 0 & a_{44} & a_{45} \\ 0 & 0 & 0 & a_{54} & a_{55} \end{pmatrix}, \quad (28)$$

where, $a_{11} = (r - \beta - d_1 - ax_5)$, $a_{15} = -ax_1$, $a_{21} = \beta$, $a_{22} = -d_2 - bx_5 - \gamma x_3$, $a_{23} = -\gamma x_2$, $a_{25} = -bx_2$, $a_{32} = \gamma x_3$, $a_{33} = \gamma x_2 - d_3$, $a_{41} = k_1 ax_5$, $a_{42} = k_2 bx_5$, $a_{44} = -\delta - d_4$, $a_{45} = k_1 ax_1 + k_2 bx_2$, $a_{54} = \delta$, $a_{55} = -d_5$.

3.1. Infection free equilibrium $(E_{x_1 x_2 x_4 x_5})$

At the point $(x_1, x_2, 0, x_4, x_5)$, Jacobian matrix J (corresponding to $(E_{x_1 x_2 x_4 x_5})$) reduced to the following form

$$J = \begin{pmatrix} a_{11} & 0 & 0 & 0 & a_{15} \\ a_{21} & a_{22} & a_{23} & 0 & a_{25} \\ 0 & 0 & a_{33} & 0 & 0 \\ a_{41} & a_{42} & 0 & a_{44} & a_{45} \\ 0 & 0 & 0 & a_{54} & a_{55} \end{pmatrix}, \quad (29)$$

where, $a_{11} = (r - \beta - d_1 - ax_5)$, $a_{15} = -ax_1$, $a_{21} = \beta$, $a_{22} = -d_2 - bx_5$, $a_{23} = -\gamma x_2$, $a_{25} = -bx_2$, $a_{33} = \gamma x_2 - d_3$, $a_{41} = k_1 ax_5$, $a_{42} = k_2 bx_5$, $a_{44} = -\delta - d_4$, $a_{45} = k_1 ax_1 + k_2 bx_2$, $a_{54} = \delta$, $a_{55} = -d_5$. And x_1, x_2, x_4, x_5 are listed at Eq. (24). One eigenvalue of Eq. (29) is a_{33} and rest four are the eigen values of the matrix

$$\begin{pmatrix} a_{11} & 0 & 0 & a_{15} \\ a_{21} & a_{22} & 0 & a_{25} \\ a_{41} & a_{42} & a_{44} & a_{45} \\ 0 & 0 & a_{54} & a_{55} \end{pmatrix}, \quad (30)$$

the characteristic equation of Eq. (30) is given by

$$(\lambda^3 + A_1 \lambda^2 + A_2 \lambda + A_3) \lambda = 0, \quad (31)$$

where,

$$\begin{cases} A_1 = -[a_{11} + a_{22} + a_{44} + a_{55}], \\ A_2 = -a_{44}a_{54} + a_{11}a_{44}, \\ A_3 = (a_{45}a_{54})a_{11}. \end{cases} \quad (32)$$

Hence, characteristic equation of Eq. (29) is given by

$$(\lambda^3 + A_1 \lambda^2 + A_2 \lambda + A_3) \lambda (\lambda - a_{33}) = 0, \quad (33)$$

Therefore, '0' is an eigenvalue, hence, the infection free equilibrium point $(E_{x_1 x_2 x_4 x_5})$ is unstable.

3.2. The co-existing equilibrium point $E^* = (x_1^*, x_2^*, x_3^*, x_4^*, x_5^*)$

The Jacobian matrix corresponding to E^* is given by

$$J = \begin{pmatrix} a_{11}^* & 0 & 0 & 0 & a_{15}^* \\ a_{21}^* & a_{22}^* & a_{23}^* & 0 & a_{25}^* \\ 0 & a_{32}^* & a_{33}^* & 0 & 0 \\ a_{41}^* & a_{42}^* & 0 & a_{44}^* & a_{45}^* \\ 0 & 0 & 0 & a_{54}^* & a_{55}^* \end{pmatrix}, \quad (34)$$

where, $a_{11}^* = (r - \beta - d_1 - ax_5^*)$, $a_{15}^* = -ax_1^*$, $a_{21}^* = \beta$, $a_{22}^* = -d_2 - bx_5^* - \gamma x_3^*$, $a_{23}^* = -\gamma x_2^*$, $a_{25}^* = -bx_2^*$, $a_{32}^* = \gamma x_3^*$, $a_{33}^* = \gamma x_2^* - d_3$, $a_{41}^* = k_1 ax_5^*$, $a_{42}^* = k_2 bx_5^*$, $a_{44}^* = -\delta - d_4$, $a_{45}^* = k_1 ax_1^* + k_2 bx_2^*$, $a_{54}^* = \delta$, $a_{55}^* = -d_5$.

The characteristic equation of Eq. (34) is given by

$$\lambda^5 + B_1\lambda^4 + B_2\lambda^3 + B_3\lambda^2 + B_4\lambda + B_5 = 0, \quad (35)$$

where,

$$\begin{cases} B_1 = a_{11}^* + a_{22}^* + a_{33}^* + a_{44}^* + a_{55}^*, \\ B_2 = (a_{44}^*a_{55}^* - a_{45}^*a_{54}^*) + (a_{22}^*a_{33}^* - a_{23}^*a_{32}^*) + (a_{44}^* + a_{55}^*) \\ \quad + a_{11}^*(a_{44}^* + a_{55}^*) + a_{11}^*(a_{22}^* + a_{33}^*), \\ B_3 = (a_{44}^* + a_{55}^* - 1)(a_{22}^*a_{33}^* - a_{23}^*a_{32}^*) + (a_{22}^* + a_{33}^* - 1)(a_{44}^*a_{55}^*, \\ \quad - a_{45}^*a_{54}^*) - (a_{44}^* + a_{55}^*)(a_{22}^* + a_{33}^*) - a_{54}^*a_{15}^*a_{41}^*, \\ B_4 = a_{11}^*(a_{22}^* + a_{33}^*)(a_{44}^*a_{55}^* - a_{45}^*a_{54}^*) + a_{11}^*(a_{44}^* + a_{55}^*), \\ \quad (a_{22}^*a_{33}^* - a_{23}^*a_{32}^*) - (a_{44}^*a_{55}^* - a_{45}^*a_{54}^*)(a_{22}^*a_{33}^* - a_{23}^*a_{32}^*) \\ \quad - a_{25}^*a_{54}^*a_{42}^*a_{33}^* + a_{11}^*a_{25}^*a_{54}^*a_{42}^* - a_{15}^*a_{42}^*a_{21}^* + a_{15}^*(a_{22}^* + a_{33}^*)a_{41}^*, \\ B_5 = a_{54}^*a_{15}^*(a_{21}^*a_{33}^*a_{42}^* + a_{23}^*a_{41}^*a_{32}^* - a_{41}^*a_{22}^*a_{33}^*), \\ \quad - a_{25}^*a_{54}^*a_{42}^*a_{33}^* - (a_{44}^*a_{55}^* - a_{45}^*a_{54}^*)(a_{22}^*a_{33}^* - a_{23}^*a_{32}^*). \end{cases} \quad (36)$$

The co-existing equilibrium point $E^* = (x_1^*, x_2^*, x_3^*, x_4^*, x_5^*)$ for the system (11) is locally asymptotically stable (using the Routh-Hurwitz criteria) if the following conditions hold as follows:

$$\begin{cases} B_i > 0, i = 1, 2, 3, 4, 5, \\ B_1B_2B_3 > B_3^2 + B_1^2B_4, \\ (B_1B_4 - B_5)(B_1B_2B_3 - B_3^2 - B_1^2B_4) > B_5(B_1B_2 - B_3)^2 + B_1B_5^2. \end{cases} \quad (37)$$

REMARK 2. The existence of co-existing equilibrium point $E^* = (x_1^*, x_2^*, x_3^*, x_4^*, x_5^*)$ convey a message that all the five species viz. immature prey, mature prey, infected prey, immature predator and mature predator exist in the ecosystem. It means that existence of E^* implies that infection in the system also exists. Infection free equilibrium point $(E_{x_1x_2x_4x_5})$ is not stable. It means that once the infection occurs in the system, it can not remove. Because the co-existing equilibrium point E^* may be stable if the conditions listed in (37) are satisfied.

4. Discussion

In this paper, a stage structured prey-predator model is proposed and studied. Stages for prey and predator both have been considered, therefore the prey population is bifurcated into two populations viz. immature prey and mature prey and similarly predator population is also bifurcated into two classes viz. immature predator and mature predator. We also considered that infection occurs in the prey population only. By remark 1, it is observed that only two equilibrium points for the model (11) viz. infection free equilibrium ($E_{x_1x_2x_4x_5}$) and the co-existing equilibrium point $E^* = (x_1^*, x_2^*, x_3^*, x_4^*, x_5^*)$ exist. Local stability analysis have been investigated and results show that the infection free equilibrium point ($E_{x_1x_2x_4x_5}$) is not stable. The co-existing equilibrium point $E^* = (x_1^*, x_2^*, x_3^*, x_4^*, x_5^*)$ is conditionally stable i.e. it is stable provided the set of conditions listed in the Eq. (37) are satisfied. In real life situations the parameters are changing with time. Hence, models with time dependent parameters may be included in the future scope. As a matter of fact, this study is not a case study hence real data/parameters are not available. Real parameters investigation is also a concern of future study.

Acknowledgements. We are grateful to Prof. Edoardo Beretta, Instituto do Biomatemática, Universita di Urbino, I-61029, Urbino, Italy for valuable suggestions.

REFERENCES

- [1] A. Lotka, Elements of physical biology *Williams and Wilkins, Baltimore, 1925.*
- [2] Banshidhar Sahoo and Swarup Poria, Diseased prey predator model with general Holling type interactions, *Applied Mathematics and Computation*, **226**, (2014), 83 – 100.
<http://dx.doi.org/10.1016/j.amc.2013.10.013>.
- [3] B. Mukhopadhyaya and B. Bhattacharyya, Dynamics of a delay-diffusion prey-predator Model with disease in the prey, *J. Appl. Math and Comp.*, **17**, 12(2005), 361 – 377.
<http://dx.doi.org/10.1007/BF02936062>.
- [4] B. Liu et al, The effects of impulsive toxicant input on a population in a polluted environment, *J. Biol. Syst.*, **11**, 3(2003), 265 – 274. <http://dx.doi.org/10.1142/S0218339003000907>.
- [5] Birkhoff, G. , Rota, G.C.: Ordinary Differential Equations. *Ginn, Boston*, 1982.
- [6] Chao Liu et al, Dynamical behaviour in a stage-structured differential-algebraic prey-predator model with discrete time delay and harvesting, *J. Comp. Appl. Math.*, **231**, 2(2009), 612–625.
<http://dx.doi.org/10.1016/j.cam.2009.04.011>.
- [7] C.S. Holling, The components of predation as revealed by a study of small mammal predation of the European pine sawfly, *Canad. Entomologist*, **91**, (1959), 293–320.
- [8] C.S. Holling, Some characteristics of simple types of predation and parasitism, *Canad. Entomologist*, **91**, (1959), 385–395.
- [9] J.H. Dawes and M.O. Souza, A derivatiation of Holling's type I,II and III functional responses in predator-prey system, *J. Theor. Biol.*, **327**, (2013), 11–22.
<http://dx.doi.org/10.1016/j.thbi.2013.02.017>.
- [10] D. Greenhalgh and M. Haque, A predator-prey model with disease in the prey species only, *Math. Methods Appl. Sci.*, **30**, 8(2007), 911–929. <http://dx.doi.org/10.1002/mma.815>.
- [11] D.L. Deangelis et al, A model for trophic interaction, *Ecology*, **56**, (1975), 881–892.
- [12] Guang-Ping Hu and Xiao-Ling Li, Stability and Hopf bifurcation for a delayed predator-prey model with disease in the prey, *Chaos, Solitons and Fractals*, **45**, (2012), 229–237.
<http://dx.doi.org/10.1016/j.chaos.2011.11.011>.
- [13] M. Haque, E. Venturino, An ecoepidemiological model with disease in predator: the ratio-dependent case. *Math. Meth. Appl. Sci.*, **30**, (2007), 1791 – 1809.

- [14] M. Haque, E. Venturino, The role of transmissible diseases in Holling-Tanner predator-prey model. *Theor Popul Biol*, **70**, 3(2006), 273 – 88.
- [15] V.S. Ivlev, Experiment Ecology of the feeding of fishes (*Yale University Press, New Haven, C.T.*, 1961).
- [16] J. Chattopadhyay, O. Arino, A predator-prey model with disease in prey, *Non Linear Analysis*, **36**, (1999), 747 – 766.
- [17] Jian-Jun-Jiao, Permanence and global attractivity of stage-structured predator-prey model with continuous harvesting on predator and impulsive stocking on prey, *Appl. Math. Mech.(Engl. Ed.)*, **29**, 5(2008), 653–663. <http://dx.doi.org/10.1007/S10483-008-0509-X>.
- [18] J.R. Beddington, Mutual interference between parasites or predators and its effect on searching efficiency, *J. Animal Ecology*, **44**, (1975), 331–340.
- [19] J. Cui and X. Song, Permanence of predator-prey system with stage structure, *Discrete Contin. Dyn. Syst. Ser. B*, **4** 3(2004) 547–554. <http://dx.doi.org/10.3934/dcdsb.2004.4.547-554>
- [20] Jawdat Alebraheem, Yahya Abu Hasan, Dynamics of a two predator and one prey system, *Comp. Appl. Math*, (2014). <http://dx.doi.org/10.1007/s40314-013-0093-8>
- [21] T.K. Kar, S. Jana, A Theoretical study on mathematical modeling of an infectious disease with application of optimal control, *Biosystems*, (2012). <http://dx.doi.org/10.1016/j.biosystems.2012.10.003>
- [22] Litao Han et al, Four Predator Prey Models with Infectious Diseases, *Mathematical and Computer Modeling*, **34**, 7-8(2001), 849 – 858. [http://dx.doi.org/10.1016/S0895-7177\(01\)00104-2](http://dx.doi.org/10.1016/S0895-7177(01)00104-2).
- [23] Linfei Nie and Zhidong Ting, Singular perturbation method for global stability of ratio dependent predator-prey model with stage structure for the prey, *Electronic Journal of Differential Equations*, **86**, (2013) 1–9. <http://ejde.math.txstate.edu> or <http://ejde.math.unt.edu> <http://ejde.math.txstate.edu>
- [24] Liming Cai, Xinyu Song, Permanence and stability of a predator-prey system with stage structure for predator, *J. Comp. Appl. Math.*, **201**, (2007), 356–366.
- [25] M.P. Hassell and C.C. Varley, New inductive population model for insect parasites and its bearing on biological control, *Nature*, **223**, (1969), 1133–1137.
- [26] L. Maoxing et al, An Impulsive predator-prey model with communicable disease in the prey species only, *Non Linear analysis: Real World Applications*, **10**, (2009), 3098–3111. <http://dx.doi.org/10.1016/j.nonrwa.2008.10.010>.
- [27] M. Haque and E. Venturino, Increase of the prey may decrease the healthy predator population in presence of a disease in predator, *HERMIS* **7**, (2006), 38–59. www.aueb.gr/pympe/hermis-volume-7/DIFF-INTEGRAL-EQUATIONS/HAQUE-VENTURINO-1.pdf.
- [28] W.W. Murdoch, C.J. Briggs, R.M. Nisbet, Consumer-Resource dynamics *Princeton: Princeton University Press*, 2003.
- [29] M. Nagumo, Über die Lage der Integralkurven gew. onlicher Differentialgleichungen, *Proc. Phys. Math. Soc. Japan.*, **24**, (1942), 555.
- [30] D. Mukherjee, Persistence Aspect of a predator-prey model with disease in the prey, *Differ Equ Dyn Syst*, (2014). <http://dx.doi.org/10.1007/s12591-014-0213-y>.
- [31] Paul Georgescu and Ying-Hen Hsieh, Global dynamics of a predator-prey model with stage-structure for the predator, *SIAM J. Appl. Math.*, **67**, 5(2007), 1379–1395. <http://dx.doi.org/10.1137/06070377>.
- [32] P.H. Crowley and E.K. Martin, Functional responses and interference within and between year classes of a dragonfly population, *J. North American Benthological Soc.*, **8**, (1989), 211–221.
- [33] Pallav Jyoti Pal, Mainul Haque, Prashanta Kumar Mandal, Dynamics of a predator-prey model with disease in the predator *Math. Meth. Appl. Sci.*, (2013). <http://dx.doi.org/10.1002/mma.2988>.
- [34] Raid Kamel Naji and Kawa Ahmed Hasan, The dynamics of prey-predator model with disease in the prey, *J. Math. Comput. Sci.*, **2**, 4(2012), 1052–1072.
- [35] R. Arditi and L.R. Ginzburg, Coupling in predator-prey dynamics: Ratio-dependence, *J. Theor. Bio.* **139**, (1989), 311–326.
- [36] Rui Xu et al, Periodic solutions of a delayed predator prey model with stage structure for predator, *J. Appl. Math.*, **3**, (2004), 255–270. <http://dx.doi.org/10.1155/S1110757X04308090>.
- [37] G.P. Samanta, Analysis of a delay nonautonomous predator-prey system with disease in the prey. *Non Linear Analysis: Modeling and Control*, **15**, 1(2010), 97–108. www.lana.lt/journal/36/samanta.pdf.

- [38] S.A. Gourley, Y. Kuang, A stage structured predator-prey model and its dependence on maturation delay and death rate, *J. Math. Bio.*, **49**, 2(2004), 188–200.
<http://dx.doi.org/10.1007/s00285-004-0278-2>.
- [39] Soovoojeet Jana and T.K. Kar, Modeling and analysis of a prey-predator system with disease in the prey, *Chaos, Solitons and Fractals*, **47**, (2013), 42–53.
<http://dx.doi.org/10.1016/j.chaos.2012.12.002>.
- [40] Shengqiung Liu, Edoardo Beretta, A stage-structured predator-prey model of Beddington-DeAgelis type, *SIAM J. Appl. Math.*, **66**, 4(2006), 1101–1129. <http://dx.doi.org/10.1137/050630003>.
- [41] Swarnali Sharma and Samanta G.P., Dynamical behaviour of a two prey and one predator system, *Differ Equ Dyn Syst*, **22**, 2(2014), 125–145. <http://dx.doi.org/10.1007/s12591-012-0158-y>.
- [42] Sana SS, Purohit D, Chaudhury KS, Joint project of fishery and poultry- a bioeconomic model, *Appl Math Model.*, **36**, (2012), 72–86.
- [43] Santosh Biswas, Sudip Samanta and Joydev Chattopadhyay, A model based theoretical study on cannibalistic prey-predator system with disease in both populations, *Differ Equ Dyn Syst*, (2014).
<http://dx.doi.org/10.1007/s12591-014-0211-0>.
- [44] Tongqian Zhang et al, A stage-structured predator-prey SI model with disease in the prey and impulsive effects, *Mathematical Modelling and Analysis*, **18**, 4(2013), 505–528.
<http://dx.doi.org/10.3846/13926292.2013.840866>.
- [45] T. Zhang et al, The dynamics of a high dimensional delayed pest management model with impulsive pesticide input and harvesting prey at different fixed moments, *Nonlinear Dynamics*, **64**, 1(2011), 1–12. <http://dx.doi.org/10.1007/s11071-010-9840-1>.
- [46] V. Volterra, Variazioni e fluttuazioni del numero d individui in species animali conviventi, *Mem Accd. Lincei*, **2**, (1926), 31 – 113.
- [47] V. Lakshmikantham, D. Bainov and P. Simeonov, Theory of Impulsive Differential Equations, *World Scientific, Singapore*, 1989.
- [48] Venturino E., Epidemics in predator-prey models: disease in predators, *IMA J. Math Appl. Med. Bio.*, **19**, (2009), 185–205.
- [49] W.O. Kermack and A.G. McKendrick, Contributions to the mathematical Theory of Epidemics, Part 1, *Proc. Roy. Soc. A*, **115**, 5(1927), 700–721.
- [50] W. Wang and L. Chen, A predator-prey system with age structure for predator, *Comp. Math. Appl.*, **33**, 8(1997), 83–91. [http://dx.doi.org/10.1016/S0898-1221\(97\)00056-4](http://dx.doi.org/10.1016/S0898-1221(97)00056-4).
- [51] W.G. Aiello et al, A time-delay model of single species growth with stage structure, *Math. Biosci.*, **101**, 2(1990), 139–153. [http://dx.doi.org/10.1016/0025-5564\(90\)90019-U](http://dx.doi.org/10.1016/0025-5564(90)90019-U).
- [52] X. Meng and L. Chen, A stage structured SI eco-epidemiological model with time delay and impulsive controlling, *J. Syst. Sci. Complex*, **21**, 3(2008), 427–440.
<http://dx.doi.org/10.1007/S11424-008-9214-8>.
- [53] Xu et al, Persistence and global stability of a ratio dependent prey model with stage-structure, *Appl. Math. Comp.*, **158**, 3(2004), 729–744. <http://dx.doi.org/10.1016/j.amc.2003.10.012>.
- [54] Xiaohong Tian and Rui Xu, Global dynamics of a predator-prey system with Holling type II functional response, *Nonlinear Analysis: Modelling and Control*, **16**, 2(2011), 242–253.
www.lana.lt/journal/41/NA16210.pdf.
- [55] Xue Zhang et al, Bifurcations of a singular prey-predator economic model with time delay and stage structure, *Chaos Soliton and Fractals*, **42**, (2009), 1485–1494.
<http://dx.doi.org/10.1016/j.chaos.2009.03.051>.
- [56] Xinyu Song et al, A stage-structured predator-prey model with disturbing pulse and time delays, *Appl. Math. Modell.*, **33**, 1(2009), 211–223. <http://dx.doi.org/10.1016/j.apm.2007.10.020>.
- [57] X. Song and L. Chen, Optimal harvesting and stability for a two species competitive system with stage structure, *Math. Biosci.*, **170**, 2(2001), 173–186.
[http://dx.doi.org/10.1016/S0025-5564\(00\)00068-7](http://dx.doi.org/10.1016/S0025-5564(00)00068-7)
- [58] Yanni Xiao, Lansun Chen, Modeling and analysis of a predator-prey model with disease in the prey, *Math. Biosci.*, **171**, 1(2001), 59–82. [http://dx.doi.org/10.1016/S0025-5534\(01\)00049-9](http://dx.doi.org/10.1016/S0025-5534(01)00049-9).
- [59] Yonghui Xia et al, Multiple periodic solutions of a delayed stage-structured predator-prey model with non-monotonic functional responses, *Appl. Math. Modell.*, **31**, 9(2007), 1947–1959.
<http://dx.doi.org/10.1016/j.apm.2006.08.012>
- [60] Y. Kuang and E. Beretta, Global qualitative analysis of a ratio-dependent predator-prey system, *J. Math. Bio.*, **36**, (1998), 1319–1360.

- [61] Zhongui Xiang, A Lotka-Volterra model with impulsive effects on the prey and stage structure on the predator, *Appl. Math. Sci.*, **4**, 17-20(2010), 849–856.

www.m-hikari.com/ams/ams-2010/ams-17-20-2010/xiangAMS17-20-2010.pdf

(Received May 17, 2015)

Shashi Kant

Department of Applied Mathematics

Delhi Technological University

Delhi India 110042

e-mail: onlineskmishra@gmail.com

Vivek Kumar

Department of Applied Mathematics

Delhi Technological University

Delhi India 110042

e-mail: vivekkumar.ag@gmail.com

Fault Immune Pico-Hydro Powered Base Station of Remote Telecommunication Tower

Vishal Verma[†], Peeyush Pant[†], and Bhim Singh^{*}

[†]Department of Elect. Engg., Delhi College of Engineering (Now Delhi Technological Univ.), Delhi, India

^{*}Department of Electrical Engineering, Indian Institute of Technology, Delhi, India.

Abstract

This paper presents dynamic excitation control of Siphon-turbine coupled Pico-Hydro powered Cage-rotor Induction Generator and load matching for off-grid electricity generation. The proposed dual-role current controlled voltage source converter (VSC) enacting as STATIC synchronous COMPensator (STATCOM) and load-controller, dynamically controls both real and reactive power in decoupled manner with a self-supported its DC-bus. The proposed scheme employ minimum computation effort for ensuring draw of rated (set) capacity real-power. The scheme also embeds fault immune features for protection, enabling effective handling of constant power electrical load presented by the base telecom stations towers in remote locations. The performance of the system is evaluated under Matlab/Simulink and is experimented through developed hardware prototype. Presented simulation and experimental results show close conformity and validates the effectiveness of the proposed scheme.

Keywords: Isolated Base Telecom Station, Load Controller, Pico-Hydro, Siphon turbine, STATCOM

I. INTRODUCTION

Installation of additional telecom-towers is emerging and mandatory requirement for remote wireless communication. A typical base telecom station (BTS) tower requires three-phase, 50Hz supply and consumes power in 2-10kW range [1]. Remotely located telecom towers conventionally employs three-phase Diesel-Generator (DG) set(s)/ Hybrid supply systems, however, pollution, costly-maintenance, poor efficiency, difficult approach and higher recurring fuel cost are major issues. For sustainable solution, renewable resources presents low-cost and efficient solution with less carbon footprint and hence emerged as a solution to energy needs of remotely located telecom-tower(s) [2]. Popular renewable sources, like Solar Photovoltaic (PV) and wind turbine fall short, due to intermittency, costly storage, poor efficiency and needs routine maintenance [3].

For smaller capacity Pico-hydro generation (PHG), employing Cage-rotor Induction Generator (IG) coupled with Siphon-turbine is advocated suitable [4]. Since, smaller

capacity IG has low reactance-to-resistance ratio and low mechanical inertia it presents a weak source before the load. Moreover, when weak grid caters to perturbing loads issues such as voltage sag/swell, harmonics, unregulated frequency, voltage-collapse etc., poses problems for power supply [5]. Investigations reported so far address to only few of aforesaid issues viz, voltage regulation and harmonic compensation of Self-Excited Induction Generator (SEIG) by employing pulse-width modulation (PWM) rectifier and STATIC synchronous COMPensator (STATCOM) [6]. Further, the issue of unregulated frequency of SEIG amidst perturbing loads is addressed by employing Electronic Load Controller (ELC), and investigations are furthered aiming at size reduction and harmonics elimination [7]. However, due to presence of large fixed excitation capacitor several issues props up during sudden generator under-loading, load-controller malfunction, abnormal fault causing voltage sag/swells, excess winding stress, insulation failure/breakdown etc., in the weak off-grid power supply. Since, BTS often witness intermittent operation of fast acting linear and non-linear constant power load like Switched Mode Power Supply (SMPS) etc., it causes stabilization issues [1], [2]. Therefore, investigations are due to provide concrete solutions to an inherent self protection and a good voltage regulation even under perturbing and fast switching loads.

This paper proposes suitability of Siphon-turbine coupled

Manuscript received Month. Date, Year; acceptedMonth. Date, Year
Recommended for publication by ???????????.

[†]Corresponding Author: vishalverma@dce.ac.in

Tel: +91-11-27871018, Fax: +91-11-27871023, Delhi. Tech. University

[†]Dept. of Elect. Engg. Delhi College of Engineering (Now Delhi Technological Univ.), Delhi, India

^{*}Dept. of Elect. Engg. Indian Institute of Technology, Delhi, India

with IG to cater electricity requirements of remote BTS (Refer Fig.1) from Pico-Hydro source. The proposed control scheme forces to draw rated power from the IG making it optimally efficient, and easy to operate. Moreover, variable reactive power for requisite excitation of generator is dynamically supplied by current-controlled VSC with a tank capacitor at DC bus, and small fixed capacitor bank for ripple filtering and providing part excitation of IG. The operation of VSC pivots the generator voltage and frequency regulated amidst varying reactive power hungry loads, due to presence of VSC enacting as STATCOM in the circuit, and also realizing load matching by dumping excess energy on DC-bus which eventually is bled through chopper/bleeder avoiding the duplication of circuits. Further, the control scheme makes the supply system fault immune without installing additional costly hardware and offers fast self-protection by ceasing VSC pulses against any abnormality like over/under-voltages/current, load-controller mal-operation, instant load removal etc., which would not be possible if self excitation capacitor keeps the generator alive. The performance of the system is evaluated in Matlab/Simulink and the same is experimentally validated on developed hardware prototype (2.2kW, 415V, 50Hz). Presented simulation and experimental results show close conformity and validates the effectiveness of the proposed scheme.

II. SYSTEM CONFIGURATION

The proposed system shown in Fig.2 represents a remote PHG system employing Siphon -turbine enacting as prime mover duly coupled with IG. The combination of IG and small filter capacitor bank at its terminals is henceforth referred as a Pico-Hydro Generating Source (PHGS) connected at point of common-coupling (PCC) with self supported VSC. The three-phase VSC is integrated with load controller on DC-bus for providing both reactive power requirement of PHG and load with load matching. The VSC is connected through PCC by the interfacing inductors. The considered loads are intermittent constant power load (CPL) connected in parallel, emulating a remote telecom base-station when seen from PCC. The scheme operates in power decoupling mode to present voltage regulation and load matching at PCC.

III. ANALYSIS OF CONSTANT POWER LOAD

Electrical loads of a typical BTS often undergo intermittent operation of CPL before the PCC. The characteristic of CPL (capacity P_{load}) is depicted in Fig.3 (a), which is analyzed through piecewise linearizing the nonlinear supply perturbations of PCC. Loads intermittency in a weak-source often causes voltage sag ΔV (say) at PCC, which results in displacement of current ΔI of the current I_1 thus, disturbing the equivalent resistance perceived by PCC, which is

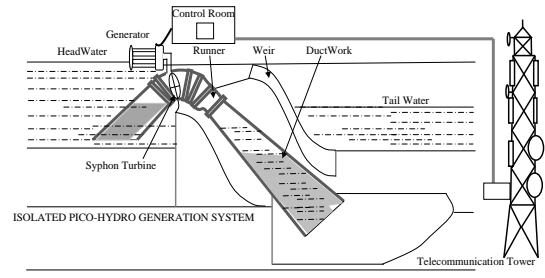


Fig.1 Schematic diagram of the Pico-Hydro powered BTS

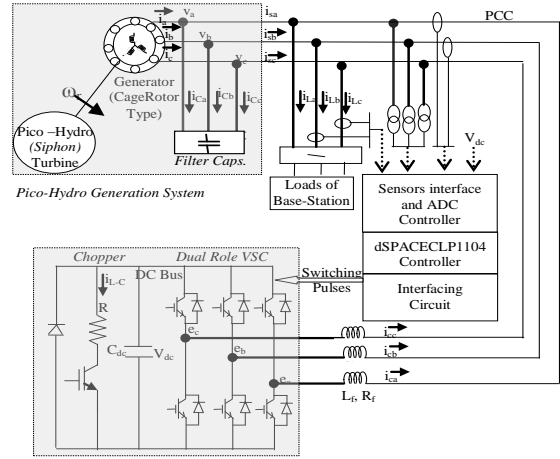


Fig.2. Schematic diagram of the proposed system.

expressed as:

$$R_e = \frac{P_{load}}{(I_1)^2} \quad \text{and} \quad R_{e1} = \frac{P_{load}}{(I_1 + \Delta I)^2} \approx \frac{P_{load} / I_1^2}{1 + \frac{2\Delta I}{I_1}} \quad (1)$$

From Taylor's series expansion and approximation in equivalent resistance in Equ.(1) becomes:

$$R_{e1} = R_e - 2.R_e \frac{\Delta I}{I_1} \quad (2)$$

As observed in Equ. (2), the net fall in R_e provokes escalation in current drawn by load furthering the fall in voltage at PCC. Such loading when connected at the terminal of self-excited IG produces cascading effect on PCC voltage (V_{PCC}) and would result in voltage collapse. Surface plot depicted in Fig. 3(b) presents voltage collapse phenomenon observed in PCC of SEIG fed weak-distribution grid in reference current with corresponding to real and reactive power. It may be observed in Fig. 3(b), that under nominal condition, the operating point lies in active region "A", where IG is magnetized by rated current with nominal voltage at its terminals, any voltage-droop (ΔV) by load intermittency at PCC of SEIG disturbs the operating point from "A" to a new operating point at "B" earlier to reduction in magnetizing currents, as it depends on voltage and is supplied by fixed capacitors installed at PCC. The voltage sag (ΔV) shall cause

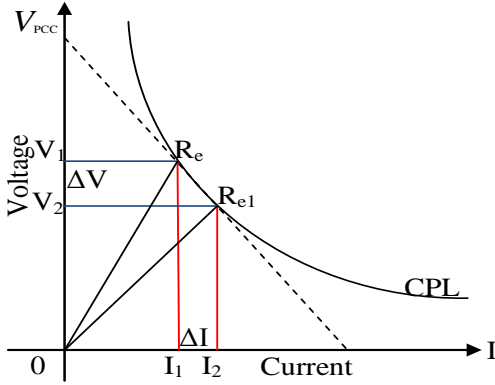


Fig. 3 (a). Dynamic behavior of CPL

under-excitation of IG, which shall further deepen the voltage-sag at PCC of weak distribution grid. It is clearly seen in the plot (Refer Fig. 3(b)) that point of operation follows the voltage diminishing path from B, C and D, which shall recursively push SEIG out of generation and leads to voltage collapse in weak distribution grid.

Dynamic compensation of real and reactive power through decoupled control by the proposed dual-role self supported VSC shall additionally supply the requisite reactive power keeping the magnetizing current nearly constant, thus preventing the further fall in voltage and prevents the voltage collapse of IG, particularly when it caters intermittent CPL loads at PCC. The process of such compensation can be understood by operation of VSC in decoupled mode. The decoupled control of real and reactive power facilitates voltage regulation and frequency at PCC respectively. The reference can command currents (I_d and I_q) of VSC. Mathematically it may be expressed as :

$$\Delta V = \xi(\Delta I_q) \quad \text{and} \quad \Delta f = \gamma(\Delta I_d) \quad (3)$$

$$\text{and, } P_{IG} = P_{load} + P_{LC} + \frac{1}{2} J \omega^2 \quad (4)$$

Where, P_{IG} is the rated capacity of IG, P_{load} is real-power drawn by CPL, P_{LC} is power dispensed to load controller and J is moment of inertia of IG.

In order to regulate source frequency, real power extraction

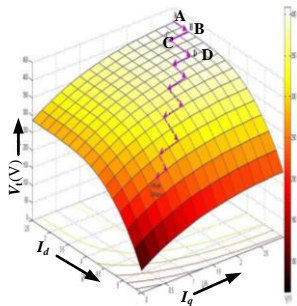


Fig. 3(b) Surface plot depicting voltage collapse when IG (excited by fixed capacitors) feeds Constant power loads

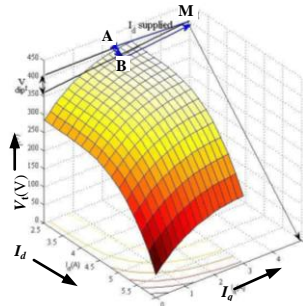


Fig. 3(c) Surface plot depicting voltage recovery at IG terminals by proposed decoupled control of real and reactive power.

from PHG terminals (P_{IG}) shall be maintained fixed. CPL demands real-power and causes voltage-sag (ΔV) at PCC. For voltage and frequency regulation, proposed decoupled control of real and reactive power is observed in surface plot depicted in Fig. 3(c). Since, voltage-sag shifts operating point from “A” to point “B”, therefore in proposed scheme reactive power is dynamically supplied by current-controlled STATCOM, and magnetization of IG is maintained intact during the voltage sag (Refer Equ.3). To compensate the voltage-sag (ΔV), reactive power is dynamically supplied by STATCOM, which lets the swift recovery of the voltage sag at PCC, and pushes the operating point towards “M” (Refer Fig. 3(c)). Further, the real-power supply is instantly made by fast extraction of kinetic energy from rotor inertia, followed by load matching provided by load controller action. Intermittent real-power demand (ΔP) met by trapping stored energy from rotor-inertia, trim down the frequency, however, follow up action of load controller, steadily matches real-power (ΔP), corresponding to raised current margin (ΔI) and restricts the margin of real-power (ΔP). Load controller current (ΔI) corresponding to match the intermittency is given as-

$$\Delta I = \frac{\delta V_{dc}}{R} \quad (5)$$

$$\Delta P = \frac{(\delta V_{dc})^2}{R} \quad (6)$$

Where δ = duty cycle, V_{dc} = DC bus voltage and R = Load controller resistance. The net effect of dynamic reactive power control and load matching (Eqs.(3)-(6)) by the proposed VSC addresses the voltage recovery in weak PHG system, and as depicted in Fig.3(c) the real-power restores back to the operating point of IG near to point “A” (active region for IG operation). This keeps the operation of IG live even under intermittency amidst CPL loads connected at PCC. The validation of proposed analysis is made through simulation and experimentation on developed prototype in forthcoming section of the paper.

IV. CONTROL STRATEGY

The schematic diagram of control scheme employed for dual role converter control to regulate STATCOM and load controller at DC bus to support loads emulating CPL of BTS is shown in Fig.4. The proposed control scheme assures VSC supplies requisite amount of reactive power demanded by IG and connected loads at PCC, besides damping real power under light load condition for power matching. The scheme respects the limits of the presented control to draw always the rated current through the IG and the load perturbations are maintained by energy transfer across DC-bus. The control relies on the fact that any rise in DC-bus voltage in turn transfers real power to the load controller connected at DC-bus to match the load to the rated value by keeping the

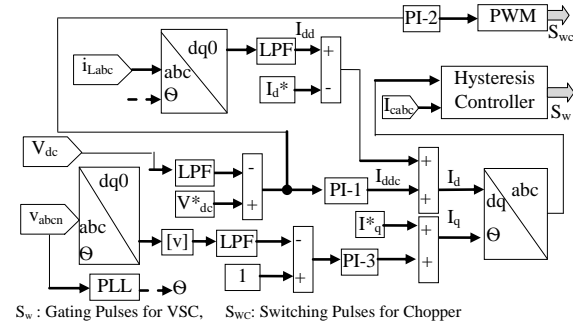


Fig.4. Proposed control scheme for dual-role VSC.

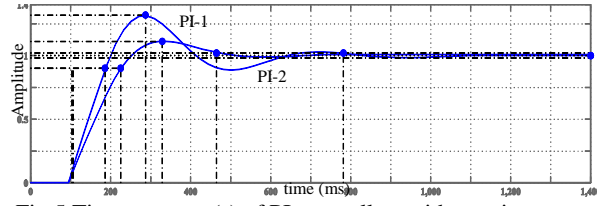


Fig.5 Time response(s) of PI-controllers with step input.

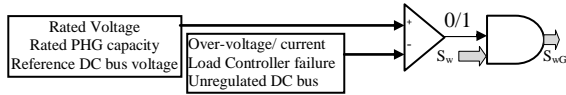


Fig.6. Protection scheme for Fault Immune PHG System.

DC-bus voltage constant. This makes the current at source terminal sinusoidal, along-with regulation of voltage and frequency at its terminals. Current control of VSC effectively compensates the perturbing real and reactive power demand for low capacity IG. The control strategy is realized in following parts:

- DC Bus Control:** Computation of VSC Current I_d .
- Voltage Regulation:** Computation of VSC Current I_q
- Determination of Synchronization Angle.**
- Frequency Control: Load Control Implementation.**

The control strategy is implemented through three PI-controllers for different components of control as aforesaid. The sensed DC-bus voltage is processed through low pass filter (LPF) and compared with a reference DC-bus voltage. The error is processed through controller PI-1, which estimates the real current (I_{ddc}) component required to maintain the DC bus voltage at the reference value, whereas, the deviation of loading from rated value on generator simultaneously affects the DC bus voltage, as the energy to be transferred across DC bus plays a vital role. Thus other component corresponds to real power component of the load current (I_{dd}) is estimated through Park's transformation of load currents and added to the current determined from PI-controller (PI-1) responsible for voltage regulation of DC-bus and transfer the power deviation for rated value of PHG source. Thus, sum of the two currents components i.e. I_{ddc} and ΔI_d gives net estimation of reference real-current which in turn maintains DC-bus voltage and operates the PHG source at rated value by extracting equalizing power from VSC on DC bus.

The net estimation of current correspond to reactive power

I_q , is made through the accumulation of fixed reactive current from component of required by IG and the current corresponds to reactive power which is required for voltage regulation at PCC. The estimation of the said component is derived from per unit rms value of the sensed voltage, and is compared with unit reference voltage to regulate reactive power through the PI-controller (PI-3).

To attain fast and simplified control utilizing minimal computation for estimation of reference currents, I_d^* and I_q^* are decided using the rated parameters of Induction machine, and are derived from mathematical expressions as-

$$I_d^* = \sqrt{2} \eta_{pu} \frac{kW}{\sqrt{3} V_L \cos \phi}, \text{ and } I_q^* = \sqrt{2} I_{m0} \quad (7)$$

Where, η_{pu} , kW and $\cos \phi$ are efficiency, rated capacity and full load power-factor respectively. I_{m0} represents rms value of no-load magnetizing current. Predetermined values of I_q^* shall make controller action fast or to reach the exact requirement of current for attaining fast dynamic compensation of reactive power. Estimated reference currents as aforesaid are reverse transformed and compared with sensed VSC currents and the error is fed to a hysteresis current controller to forces the VSC currents to follow the reference currents, to pose required real and reactive power transaction at PCC. Such action matches the loading of IG to the rated value and also automatically offsets the fluctuation in the ac-side voltage to pose ideal rated condition before generator. The proposed direct current control scheme successfully regulates the voltage and frequency directly by proper compensation of reactive power and effective load control across the source and facilitates the source to supply only real power to any type of connected load. The control is knitted through three PI-controllers which are tuned such that power flow across the VSC is regulated to suit the laid out objectives as aforesaid. The PI controller (PI-1) regulating the DC bus is acting fast to keep the DC bus voltage constant by dumping excess power into the load, while the slow PI-controller (PI-2) used by VSC for estimation of control component of I_d current leaves the margin of time to favor the process of transfer of power rapidly across the VSC to enable the system reach steady state quickly. The time response against step input for the deployed PI-1 and PI-2 controller is depicted in Fig.5.

The various sections of control as aforesaid are depicted in the comprehensive block diagram of control scheme (Refer Fig.4). A fast digital Phase locked loop is used for producing the synchronizing signals used by Park, and Inverse Park transform. Further, as depicted in Fig.6, VSC gating pulses are embedded with comparator(s) output to safeguards PHG system against abnormal PCC voltage, source/load current, DC-bus voltage and presents the proposed PHG system fault immune.

V. SIMULATION SCHEME

The proposed control scheme is simulated in Matlab/Simulink. The machine parameters are kept at measured values to enable correct modeling assessment of control parameters and interface hardware through real time system (Refer Table I). The model is simulated with VSC and load controller supporting IG, which feeds the load emulating BTS. The simulation result depicts decoupled power control with VSC to operate with constant voltage and constant frequency for feeding the load along-with maintenance of DC-bus voltage.

100Hz to offer low pass filtering of V_d and V_q voltages the reverse transformed samples of voltage at PCC and the I_d current derived from current of connected load. A similar moving average filter is also used with samples of voltage at DC bus. The hysteresis band switching with 0.1A enables the control of VSC in current control mode. The high frequency switching is automatically avoided due to fixed frequency operation of real time controller preventing the circuit entering into limit cycles. PCC voltages are sensed through three LEM LV-25P Hall Effect voltage sensors and one LEM

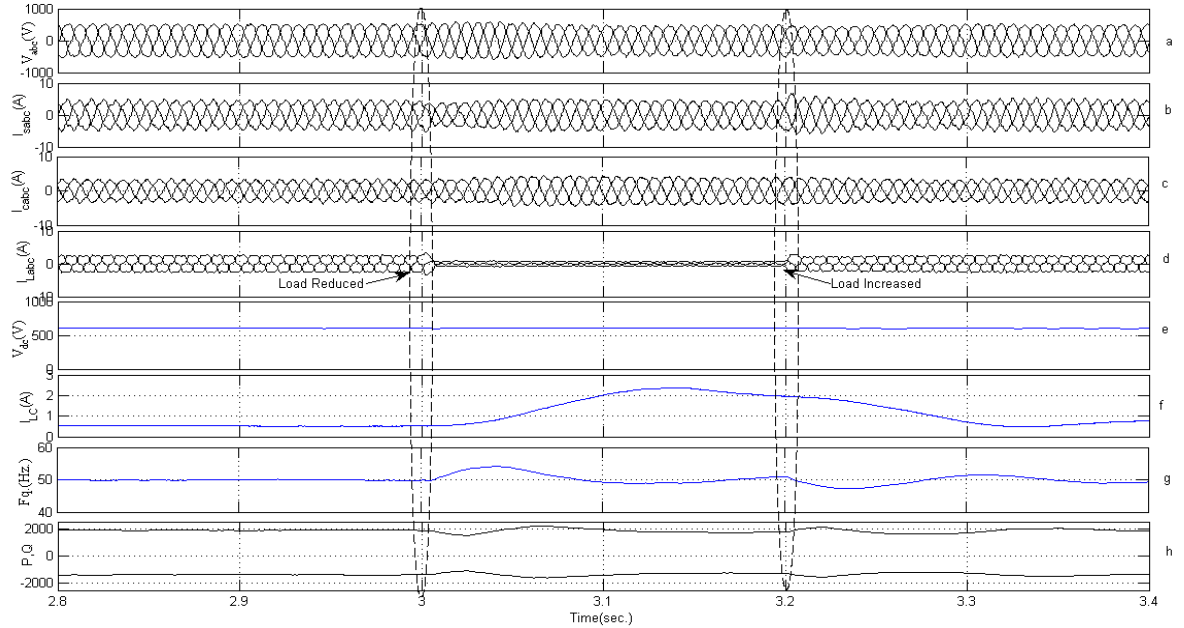


Fig.7(a-h) Simulated Performance of CC-VSC Supported PHG System Feeding Loads Presented in Base Station of Remote Telecom-Tower. (a) PCC voltage (b) Source current (c) VSC Current (d) load current (e)DC-Bus voltage (f) Source frequency (g) Load controller current(h) Real/ Reactive power of source.

VI. HARDWARE IMPLEMENTATION

The prototype hardware of the proposed system is developed by the integration of electrical system with electronic and power electronic system interfacing with dS1104 real time controller, voltage/ current sensors and interfacing circuits. The control scheme is implemented in the laboratory environment for experimental validation of the simulation results. The parameters of PHG system is presented in Table-I. V/f controlled electric drive emulates a pico-hydel based Siphon-turbine run system delivering constant power to the generator. The control scheme is realized through dS1104 real time controller for providing switching pulses for VSC, and load controller gating circuits. The controller is run in closed loop at 12.8 kHz to enable collections of 256 samples per cycle of different voltage and current through voltage and current sensors. The loop is closed at each analog to digital converter (ADC) timer interrupt to sequentially sample the aforesaid voltage and current values. The choice of 256 samples per cycle enables the easy realization of moving average filter operating at

LV-25PSP5 Hall Effect voltage sensor is used to sense DC link voltage ranging between 0-800V. TELCON HTP-25 Hall

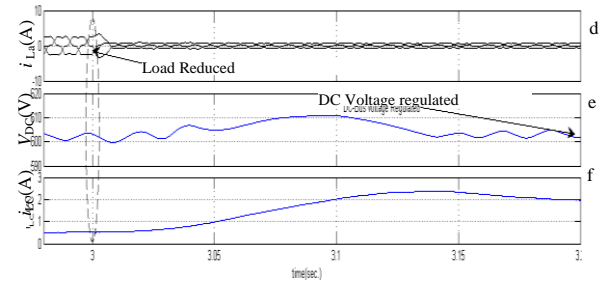


Fig.8. Dynamics of V_{dc} and current in load-controller (i_{Lc})

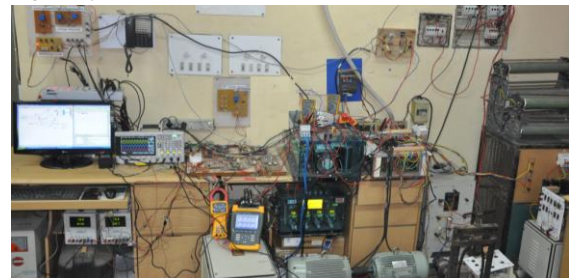


Fig.9. Photograph of prototype experimental setup.

effect current sensors are used to sense currents in two phases of VSC. The switching signals are fed to the SKYPER-32 drivers, which provide gate signals to IGBT module (Semikron GB 128DN) and chopper switch on the DC-bus. Test results are recorded using Agilent make DSOX-2014A digital storage oscilloscope, and Fluke 434 Power Quality analyzer, to evaluate both steady-state and transient state of

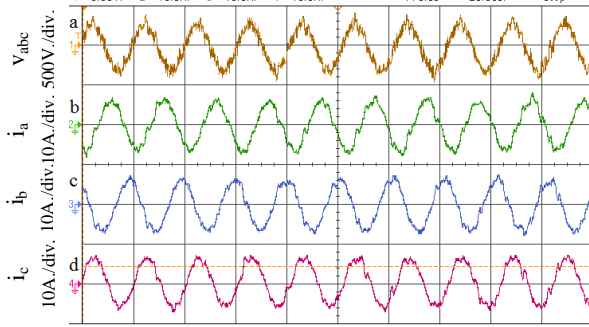


Fig.10. Oscilloscope traces showing voltage/ph., at PCC of PHG source currents at steady state operation. Observed condition- current near balanced, voltage and frequency regulated. [Time scale= 20ms./div]

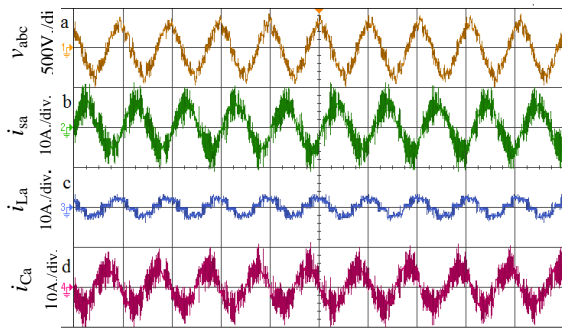


Fig.11. Oscilloscope traces (a) PCC voltage/ph. (b) source current (c) Load current (d) STATCOM current at steady state operation. Observed condition- Source current near in phase opposition(lag), Load current in phase; STATCOM current phase quadrature with voltage.

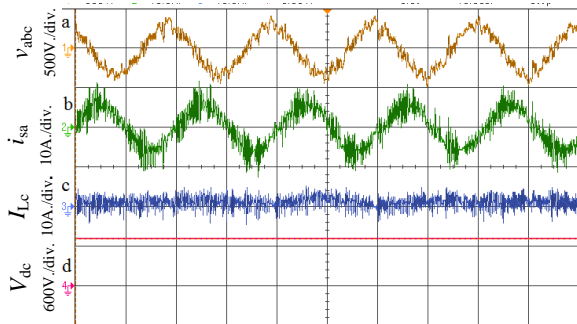


Fig.12. Oscilloscope traces showing (a)PCC voltage (b)source current (c) Current in DC Bus(d) DC bus voltage at steady state operation. Observed condition- Source current near in phase; deficit source load is transferred to load controller via DC bus, DC bus voltage is maintained at set value. the system.

VII. PERFORMANCE EVALUATION

To evaluate the effectiveness of the proposed scheme both, simulation studies are performed on Matlab/Simulink and experimental testing is done for validation of results on developed prototype hardware. The performance of the proposed system is verified in terms of-

- 1) Steady-state Operation of dual-role VSC.
- 2) Dynamic operation of dual-role VSC under load perturbations.

A. Simulation Studies- To verify the feasibility of the proposed scheme, Matlab simulations are performed on PHG system. The performance of STATCOM supported PHGS with intermittent CPL at PCC is simulated and analysis is performed on observed steady- state and dynamic waveforms for PCC voltage, source currents, STATCOM current, load current, DC-bus voltage etc. shown in Fig. 7(a-h). The results are analyzed in three time duration (i) $t=2.8s$ to $3.0s$: Operation of PHG system during steady-state operation with balanced load at PCC. (ii) $t=3s$ to $3.2s$: Load reduction at PCC and, (iii) $t=3.2s$ onwards, load re-insertion at PCC.

As depicted in Fig.7 (a, b) during $t=2.8s$ to $t=3s$, both PCC voltage and source currents are regulated and maintained. In this duration, as observed in Fig.7(c) VSC supplies leading current in quadrature with PCC voltage, presenting it as a VAR generator. Fig.7(f) depicts current drawn by load controller action, to ensure extraction of rated capacity power from PHGS, and as observed in Fig.7(g) PHGS frequency is well regulated under limits. Further, Fig.7(e) depicts regulated DC bus voltage (600V) validating effectiveness of proposed control during steady-state operation.

The magnified portion of Fig.7(d-f) portraying perturbing load current, DC-bus voltage and load controller current is depicted in Fig.8. It may be observed at $t=3s$, that the load is drastically reduced at PCC. Light loading at PCC forces the DC-voltage to increase at a longer pace with small oscillation due to delayed response of PI-control corresponding to load controller, since excess power starts accumulating in the capacitor at DC bus of VSC. However, it may be clearly seen that load-controller follows suitably dumping excess power, and the current (I_{LC}) starts rising, this leads to decrease in DC-bus voltage and thus assigning the controller to stabilize the DC-bus voltage quickly. Therefore, the coordinated action of controllers for DC-bus regulation and load controller maintains DC-bus voltage quickly and maintain the constant real-power extraction from the source, sticking to near steady-state condition. Performance of system during intermittent loading at PCC is explained in forthcoming section through experimental results under same conditions as the simulations.

B. Experimental Results

The experimental evaluation of the proposed control scheme is made on the developed prototype of 2.2kW PHG system. The photograph of the experimental setup is shown in Fig.9. The performance of the PHG system is evaluated

experimentally with current controlled VSC feeding three-phase balanced load in local distribution grid. The results are depicted in Figs.(10–20). The results are analyzed and depicted through operation of dual-role VSC as STATCOM and load controller to cater the reactive power requirement of IG and to provide load matching for remote telecom-towers amidst intermittent operation of CPL connected in parallel at PCC by importing the load deviation from rated condition to DC bus, maintaining the self supported DC bus voltage under rated loading condition, load matching by load controller through dissipation of power imported by VSC on DC bus.

1) STATCOM Operation Under Steady- State CPL -

The performance of STATCOM operation under steady-state conditions with balanced and rated connected load at PCC is analyzed through results depicted in Figs. (10-12). A CPL of 0-2kW, 600V is connected at PCC, Oscilloscope traces of phase-voltage and generator source-currents are depicted in Fig.10(a) and Fig.10(b-d) respectively. It is observed as PCC voltage and generator source-currents are balanced and well regulated. The frequency is also maintained at rated value upon rated loading of IG terminals with 20ms division of the oscilloscope trace the voltage and current complete their full cycle in one division.

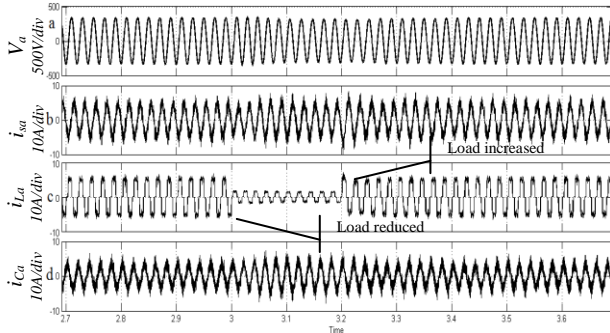


Fig.13. Simulation results showing (a) source voltage (b) source current (c) Load current (d) STATCOM current: Observed condition- PCC voltage is regulated and Source current is maintained fixed perturbing load.

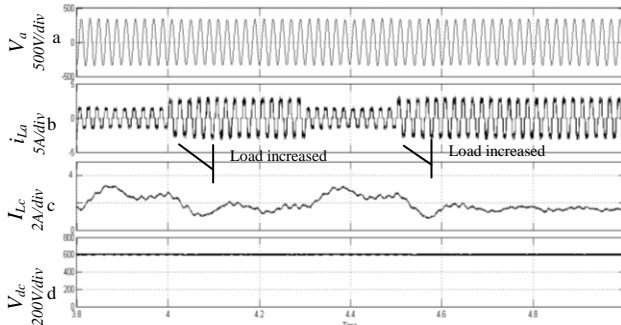


Fig.14. Simulation Results during load perturbations (a) PCC voltage (b) Load current (c) Load controller current (d) DC bus voltage: PCC voltage is maintained on perturbing load and deficit/ excess load current at PCC is transferred to load controller.

Fig.11 (a-d) depicts the waveform for PCC phase voltage, source current, load current and STATCOM current respectively during steady state conditions. It may be observed that source current is slightly leading and nearly 180° opposite to PCC voltage waveform affirming that the real power is supplied by a generator but at the same time it also shows that the generator is also absorbing negative VAR's. Load current is absolutely in-phase and STATCOM current is in perfect quadrature and leading with voltage at PCC showing it as VAR generator. It may also be observed that applied load is slightly lesser than 2.0kW than IG capacity 2.2kW, however it is effectively equalized through load controller, maintaining constant power withdrawal from the source.

Fig.12 (a-d) depicts source voltage (voltage/ph.), source current, load-current and voltage in DC-bus for similar loading conditions. It may be clearly observed that the net power corresponding to connected load lesser than rated value is absorbed at DC bus through VSC by the load controller. The traces of Fig.12(c) also clearly show the current in DC bus depicts the absorption of power by load controller, while the DC bus voltage (Fig.12(d)) is maintained constant at 600V. DC bus voltage is self supported and maintained at set value throughout the experiment justifying the effectiveness of the proposed scheme.

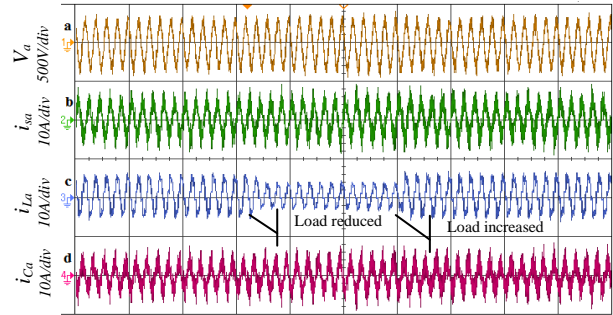


Fig.15. Experimental results showing (a) source voltage (b) source current (c) Load current (d) STATCOM current: Observed condition- PCC voltage is maintained on perturbing load, and source current maintained fixed.

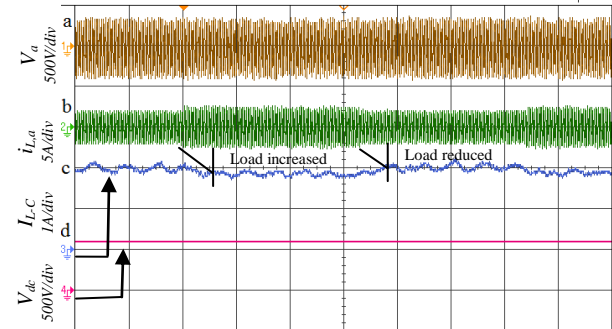


Fig.16. Experimental results showing (a) source voltage (b) Load current (c) DC Bus current (d) Load controller voltage during load perturbations at PCC: Observed condition- voltage is regulated; DC bus is regulated on dynamic load operation.

2) VSC Operation During Intermittent Loading at PCC-

Both Simulation and experimental results depicting load

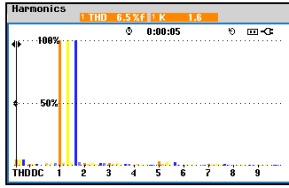


Fig.17. Harmonic spectrum of PHG source.

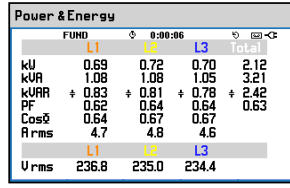


Fig.18. Power, current and phase-voltage of PHG.

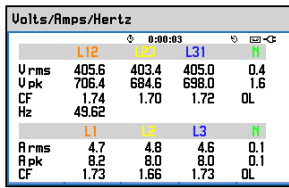


Fig.19 Screen shots of PQA showing Line voltage, frequency and source current.

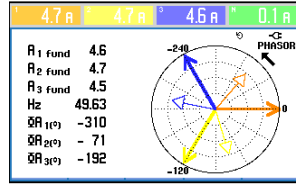


Fig.20. voltage and current phasors at source terminals.

perturbations at PCC are shown in Fig.(13,14) and Fig.(15,16) respectively. Performance of PHG system through simulation study during dynamic load perturbations by sudden partial load removal and its re-insertion is depicted in Fig. 13(c) at $t=3$ and at 3.2s respectively. As observed, proposed decoupled control action assist to load matching and voltage recovery through reactive power compensation, as a result it may be observed in Fig. 13(a) that PCC voltage is regulated throughout the operation. It may also be observed in Fig.13 (b), the current withdrawal from IG is maintained fixed and VSC supplies requisite leading current in phase quadrature.

Experimental results depicting performance of the system amidst perturbation in load at PCC is shown in Fig.15 (a-d). The three-phase balance load at PCC (Refer Fig. 15(c)) is reduced after 3rd division and the same is increased after 6th division. It is clearly observed in Fig.15 (a) that PCC voltage is regulated during load perturbations. Also, IG current depicted in Fig.15 (b) is maintained fixed. It may also be observed in Fig. 15(d) that STATCOM supplies requisite leading current in phase quadrature showing close matching with simulation results.

To have further insight of the action of load controller and dissemination of power on DC-bus the waveform of current processed by load controller and DC-bus voltage is observed amidst perturbing load both through simulations and experimentations presented in Fig.14(a-d) and Fig.16(a-d) respectively. It may be observed both in simulations and experimental results the DC-bus voltage only change marginally due to tight control invoked by the load controller. This validates the effective operation of the load controller to realize load matching for PHG source. It may also be seen that DC-bus voltage is well regulated throughout operation. Test results validate regulated voltage and frequency at

source terminals and load matching for IG under load perturbations and thus justify the effectiveness of the

TABLE I

PARAMETERS OF THE CONSIDERED PHG SYSTEM

System Parameters-	
V/f Drive	Delta, e series, 5kW
Prime-Mover	IM, 3-Φ, 3.5kW, 415V, 50Hz., Y, CG
IG	3-Φ, 2.2kW, 415±10V 50Hz, Y, CG
Filter Cap.	4μF, 440V, Y, Epcos
Load	0-2.2kW at 415±10% V
DC-Bus(VSC), V_{DC}^*	3000μF/ 1200V, 600V
Line Reactor	6.4mH, 10A
Bleeder	600V, 175ohm(R)
Control Parameters- Simulation Parameters-	
PI-1(K_p, K_i); 0.09,0.001	R_s, I_{ls} ; 0.035, 0.045
PI-2(K_p, K_i); 0.08, 0.001	R_r, L_{lr} ; 0.034, 0.045
PI-3(K_p, K_i); 0.1, 0.01	L_m (pu), J,P; 1.352, 0.0404,2
Swit. fq.; 12.8kHz	Hysteresis Band 0.1A

proposed scheme.

To evaluate further the effectiveness of the proposed scheme for control of PHG based low capacity pico-hydro system, "Fluke-434 Power Quality Analyzer" (PQA) is used for assessment of Power-quality of the PHG system. The screenshots are depicted in Figs. (17-20) for assessment of generated power by the IG system, supported by STATCOM and load controller. It may be seen from snapshot on Fig.17 that Total Harmonic distortion (THD) of source current is 6.5%, which is under acceptable limits for low capacity based generation system for such applications. The distortion near switching frequency can be mitigated easily by employing filters for further improvement in power quality. Moreover, it may be seen in Figs. (18, 19) that IG as source effectively supplies real-power equivalent to its capacity, and STATCOM supplies reactive-power for IG magnetization and voltage regulation. Test results obtained on PQ-Analyzer reaffirm that voltage and frequency are well regulated. Fig.20 depicts phasor representation of PCC voltage and PHG source current. It may be observed that source current, frequency and phasor are fairly under control and balanced. The system is stable under all limits and caters the rated capacity loads in continuous duty operation without any overload/ overheating.

VIII. CONCLUSIONS

The performance of PHG system with self supported dual role VSC enacting as STATCOM and load controller is studied through simulation and is experimentally validated on a prototype setup. It is seen that the proposed control scheme effectively regulates voltage and frequency of local distribution grid when it caters intermittent loads in parallel employed in base station of remote telecom towers. It is validated through results that proposed scheme is effective to meet the desired conditions. The scheme also assure that STATCOM meets reactive power demand of the system and

PHG meets real power demand of the system in power decoupling manner. Load controller at DC bus effectively equalizes power flow through source and maintains constant real power extraction from the source. It is seen that the proposed control scheme is easy, effective and requiring less number of sensors, and is immune to faults in distribution system through embedded auto protection. It is found that proposed scheme is effective to generate quality electricity through Pico-hydro source for telecom-tower applications.

REFERENCES

- [1] W.Balshe, "Power System Considerations for Cell Tower Applications," in *Proc. Technical Information from Cummins Power Generation*, Vol. Power Topic, No. 9019, 2011.
- [2] D.Li, W. Saad, I. Guvenc, A. Mehbodniya, and F. Adachi, "Decentralized Energy Allocation for Wireless Networks with Renewable Energy Powered Base Stations," *IEEE Trans. on Comm.*, Vol.63, No. 6, pp.2126-2142, June 2015.
- [3] G. M. Dousoky, A. M. El-Sayed, and M. Shoyama, "Improved Orientation Strategy for Energy-Efficiency in Photovoltaic Panels," *Journal of Power Electronics*, Vol. 11, No. 3, pp.335-341, May 2011.
- [4] J.T.Carter, "Siphon Pump Technology and Apparatuses," U.S. Patent 8763625, July 1, 2014.
- [5] A. V. Braga, A. J. Rezek, V. F. Silva, A. N. C. Viana, E. C. Bortoni, W. D. C. Sanchez, and P. F. Ribeiro, "Isolated induction generator in a rural Brazilian area: Field performance tests," *Renewable Energy*, Vol. 83, pp.1352-1361, Nov. 2015.
- [6] Li Wang, and Dong-Jing Lee, "Coordination Control of an AC-to-DC Converter and a Switched Excitation Capacitor Bank for an Autonomous Self-Excited Induction Generator in Renewable-Energy Systems," *IEEE Trans. Ind. Appl.*, Vol.50, No. 4, pp.2828-2836, Aug. 2014.
- [7] B.Singh, and V.Rajagopal, "Battery energy storage based voltage and frequency controller for isolated pico hydro systems," *Journal of Power Electronics*, Vol. 9, No. 6, pp. 874-883, Nov. 2009.



Vishal Verma received the B.Tech. degree in Electrical Engineering from the G. B. Pant Univ. of Agr. & Technology, Pantnagar, India, in 1989, and the M.Tech. and Ph.D. degrees from the Indian Institute of Technology Delhi, New Delhi, India, in 1998 and 2006, respectively. In 1991, he became an Assistant Professor in the Dept. of Electrical Engineering, G. B. Pant University of Agr. & Technology, Pantnagar. He joined as Assoc. Prof. at Delhi College of Engineering, Delhi in 2004. He became full Professor in 2009. Currently Dean Academic in the University. His fields of interest include power electronics, drives, active filters, and power quality issues. Dr.Verma is a member of the Indian Society for Technical Education and a Life Member of the Continuing Education Society of India.

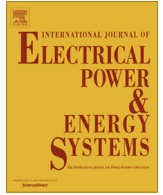


Peeyush Pant received the B.Tech. degree in Electrical Engineering from the Kamla Nehru Institute of Technology, Sultanpur, India, in 1999, and the M.Tech. degree from the Indian

Institute of Technology Delhi, New Delhi, India in 2005. He is currently a Research Scholar in the Department of Elect. Engg., Delhi College of Engineering (Now Delhi Technological Univ.), Delhi, India. His research interests include renewable energy, power electronics, Electric machines and drives.



Bhim Singh received the B.E. (Electrical) degree from the University of Roorkee, Roorkee, India, in 1977 and the M.Tech. (Power Apparatus & Systems) and Ph.D. degrees from the Indian Institute of Technology (IIT) Delhi, New Delhi, India, in 1979 and 1983, respectively. In 1983, he joined the Department of Electrical Engineering, University of Roorkee, as a Lecturer. He became a Reader there in 1988. In December 1990, he joined the Department of Electrical Engineering, IIT Delhi, as an Assistant Professor, where he became an Associate Professor in 1994 and a Professor in 1997. He has guided 59 Ph.D. dissertations and 156 M.E./M.Tech. theses. He has been granted one U.S. patent and filed 17 Indian patents. He has executed more than 75 sponsored and consultancy projects. Prof. Singh is a Fellow of the Indian National Academy of Engineering, the National Science Academy, the Indian Academy of Science, the Institute of Engineering and Technology, U.K., the Institution of Engineers (India), the World Academy of Sciences (FTWAS), the Indian National Science Academy, and the Institution of Electronics and Telecommunication Engineers. He has also received Shri Om Prakash Bhasin Award-2014 in the field of Engineering including Energy & Aerospace.



Generalized power flow models for VSC based multi-terminal HVDC systems



Shagufta Khan*, Suman Bhowmick

Department of Electrical Engineering, Delhi Technological University, Delhi 110042, India

ARTICLE INFO

Article history:

Received 5 September 2015

Received in revised form 24 February 2016

Accepted 9 March 2016

Keywords:

Newton Raphson

M-VSC-HVDC

BTB

PTP

PWM

Control strategies

ABSTRACT

This paper presents a generalized Newton Raphson (NR) power flow model for voltage source converter (VSC) based multi-terminal HVDC (M-VSC-HVDC) systems. This model is applicable to both the back to back (BTB) and the point to point (PTP) M-VSC-HVDC configurations. The amplitude modulation indices of the PWM scheme and the converter DC voltage(s) appear as unknowns in the generalized model, which is developed from first principles. While the master converter controls the voltage magnitude at its AC terminal bus and maintains the converters' active power balance, the slave converters operate their terminal buses in the PV or PQ control modes. This model offers the flexibility of controlling either the DC voltage or the modulation index for the master converter. Numerous case studies carried out by applying different control strategies to various topologies of MTDC networks incorporated in the IEEE-118 bus test system validate the model.

© 2016 Elsevier Ltd. All rights reserved.

Introduction

Over the years, ever increasing electricity demand has necessitated the requirement of increased transmission capacities by power utilities worldwide. This has been made possible by the development of voltage sourced converter (VSC) based HVDC technology with PWM control technique, employing IGBTs and GTOs. VSC based HVDC transmission systems facilitate the interconnection of asynchronous AC grids along with integration of renewable energy sources like offshore wind farms. PWM-VSC based HVDC transmission leads to fast and independent control of both active and reactive powers along with reduction in size and cost of harmonic filters [1–4]. Moreover, they are immune to the problems of commutation failure.

Depending on the locations of the converters, a VSC-HVDC system can have a Back to Back (BTB) or a point to point (PTP) configuration. In the Back to Back (BTB) scheme, the converters usually exist at the same location. On the other hand, in a point to point (PTP) scheme, the DC link is used to transmit the bulk power between converters which are at different locations [1–4].

The first 3-MW, VSC-HVDC link was commissioned at Hellsjön in Sweden in 1997. Subsequently, several VSC-HVDC projects have been installed in the U.S., Mexico, Australia, Sweden and Norway.

This has led to increased interest in VSC-HVDC systems from both the academia and the utilities, worldwide. Although most of these VSC-HVDC interconnections are two-terminal, their modus operandi can also be extended to multi-terminal HVDC (MTDC) systems. Unlike a two-terminal HVDC interconnection, a MTDC system is more versatile and better capable to utilize the economic and technical advantages of the VSC HVDC technology. It is also better suited if futuristic integration of renewable energy sources are planned. A meshed HVDC interconnection between offshore wind farms and three asynchronous AC grids of the European Network of Transmission System Operators for Electricity (ENTSO-E) is being envisaged in the North Sea region [5–6].

For MTDC operation, one of the terminals is considered as a slack bus at which the DC voltage is specified. Depending on the control specifications adopted, a converter may be termed 'master'/'slave' or 'primary'/'secondary' [7]. While a master or primary converter operates in the voltage control mode, a slave or secondary converter operates in the PQ or PV control mode. Refs. [8–11] present some excellent research works in the area of VSC-HVDC system controls.

Now, for planning, operation and control of a power system with multi-terminal VSC-HVDC (M-VSC HVDC) links, power flow solution of the network incorporating them are required. Thus, the development of suitable power flow models of M-VSC-HVDC systems is a fundamental requirement. Refs. [12–18] present some comprehensive research works in the area of Newton power-flow modelling of VSC-HVDC systems. Angeles-Camacho et al. [12]

* Corresponding author.

E-mail addresses: khan.shagufta7@gmail.com (S. Khan), suman.bhowmick@dcu.ac.in (S. Bhowmick).

Nomenclature

V_{dc}, I_{dc}	DC voltage and current, respectively	R_{sh}, X_{sh}	resistance and leakage reactance of the coupling transformer, respectively
$V_{dci}, V_{dcj}, V_{dck}$	DC voltages of converters connected to buses “i”, “j” and “k” respectively	V_i, V_j, V_k	AC bus voltage magnitudes (rms) at buses “i”, “j” and “k” respectively
$I_{dci}, I_{dcj}, I_{dck}$	DC currents of converters connected to buses “i”, “j” and “k” respectively	$\theta_i, \theta_j, \theta_k$	phase angles (degree) of AC voltages at buses “i”, “j” and “k” respectively
$P_{dci}, P_{dcj}, P_{dck}$	DC powers of converters connected to buses “i”, “j” and “k”, respectively	$V_{shi}, V_{shj}, V_{shk}$	output voltage magnitudes (rms) of converters connected to AC terminal buses “i”, “j” and “k”, respectively
m_i, m_j, m_k	modulation indices of the converters connected to buses “i”, “j” and “k” respectively	$\theta_{shi}, \theta_{shj}, \theta_{shk}$	phase angles (degree) of output voltages of converters connected to AC terminal buses “i”, “j” and “k”, respectively
Y_{ij}	magnitude of element in the i th row and j th column of the bus admittance matrix	$P_{shi}, P_{shj}, P_{shk}$	active powers in the lines connecting buses ‘i’, ‘j’ and ‘k’ to the corresponding converters respectively
ϕ_{ij}	phase angle of element in the i th row and j th column of the bus admittance matrix	$Q_{shi}, Q_{shj}, Q_{shk}$	reactive powers in the lines connecting buses ‘i’, ‘j’ and ‘k’ to the corresponding converters respectively
R_{dc}	resistance of the DC link	NI	number of iterations
\mathbf{Y}_{dc}	admittance matrix of the DC grid		
Y_{dcij}	element in the i th row and j th column of the admittance matrix of the DC network		
\mathbf{Z}_{sh}	impedance of the converter coupling transformer		

presents a VSC-HVDC mathematical model suitable for direct incorporation into existing Newton–Raphson power flow programs. However, the analysis of [12] is limited to a two terminal HVDC system. A multi-terminal VSC-HVDC power flow model suitable for both the BTB and the PTP configurations is presented in [13]. However, it does not explicitly address the inclusion of the modulation index as an unknown. Although [14,15] extend the realm of VSC-HVDC modelling to optimal power flow, the analyses are again limited to two terminal systems. A steady-state VSC MTDC model including DC grids with arbitrary topologies is reported in [16]. However, due to the adoption of the sequential power flow algorithm, Beerten et al. [16] fails to exploit the quadratic convergence characteristics of the Newton–Raphson method. Acha et al. [17] presents a comprehensive VSC-HVDC Newton power flow model which treats the VSCs as compound transformer devices and takes into account the phase shifting and scaling nature of PWM control, inclusive of VSC inductive and capacitive power design limits along with switching and ohmic losses. However, this paper does not address exclusively the modelling of multi-terminal VSC-HVDC systems. Wang and Barnes [18] presents a novel power flow approach for MTDC systems with different network topologies incorporating different DC voltage strategies. However, this model does not address exclusively the treatment of the converter modulation indices as unknowns. Also, the quadratic convergence characteristics of the unified AC/DC Newton–Raphson algorithm is sacrificed due to the sequential iterative solution adopted.

This work discusses the modelling of a M-VSC-HVDC system with arbitrary DC grid topologies for incorporation in an existing AC power flow model. In this model, the amplitude modulation indices of the PWM scheme along with the DC side voltages of the converters appear as unknowns. This is an advantage over most of the existing models [12,13,15,16,18] as the modulation index ‘ m ’ is an important parameter for VSC operation. While a low ‘ m ’ limits the maximum fundamental VSC AC side voltage, over modulation ($m > 1$) results in low-order harmonics in the AC voltage spectrum [19,20]. Additionally, this model offers the flexibility of controlling either the modulation index or the DC side voltage for the master converter. Two mathematical models for the M-VSC HVDC are presented in this work. While the first model represents a Back to Back (BTB) M-VSC-HVDC system, the second one pertains to a point to point (PTP) M-VSC-HVDC system. In both the models, for control of the DC links, multiple control modes are implemented. Numerous case studies carried out by applying different control strategies

to varying topologies of MTDC networks incorporated in the 118-bus test system validate the proposed model.

The remainder of this paper is organized as follows: In Section ‘Modelling of a BTB M-VSC HVDC system’, the mathematical modelling of the Back to Back M-VSC-HVDC is presented. Section ‘Newton power flow equations of the BTB M-VSC-HVDC system’ details the Newton power flow equations for the BTB M-VSC-HVDC. In Section ‘Modeling of the PTP-M-VSC HVDC system’, the mathematical modelling for the point to point (PTP) M-VSC-HVDC is presented. Section ‘Newton power flow equations of the PTP M-VSC-HVDC system’ details the Newton power flow equations for the PTP M-VSC-HVDC system. The case studies and results are presented in Section ‘Case studies and results’. The conclusions are presented in Section ‘Conclusions’.

Modelling of a BTB M-VSC HVDC system

For the power flow modelling of a M-VSC-HVDC system, the following assumptions have been adopted [1–3].

- The supply voltages are sinusoidal and balanced (contain only fundamental frequency and positive sequence components).
- The harmonics generated by the converters are neglected.
- The switches are assumed to be ideal.

In the rest of the paper, bold quantities represent complex variables and matrices while regular variables denote scalar variables. All the transmission lines are represented by their equivalent- π models.

The schematic representation of a BTB M-VSC-HVDC system is shown in Fig. 1. From Fig. 1, it can be observed that three converters are shown connected to three AC buses ‘i’, ‘j’ and ‘k’ via three converter transformers. All the converters are located at the same site and are interconnected through a common DC link. Fig. 2 shows the equivalent circuit of the network shown in Fig. 1. The converter connected to bus ‘i’ is considered as a master converter, while the converters connected to buses ‘j’ and ‘k’ are considered slave converters. The master converter controls the terminal voltage of its AC bus i.e. bus ‘i’ and also balances the active power exchange among the converters.

In Fig. 2, let $\mathbf{Z}_{shn} = R_{shn} + jX_{shn}$ ($n = i, j, k$) be the impedance of the converter coupling transformer, where R_{shn} and X_{shn} represent its resistance and leakage reactance, respectively. Then, from Fig. 2, the current in the line connecting the AC terminal bus ‘n’ ($n = i, j, k$) to its respective converter can be computed to be

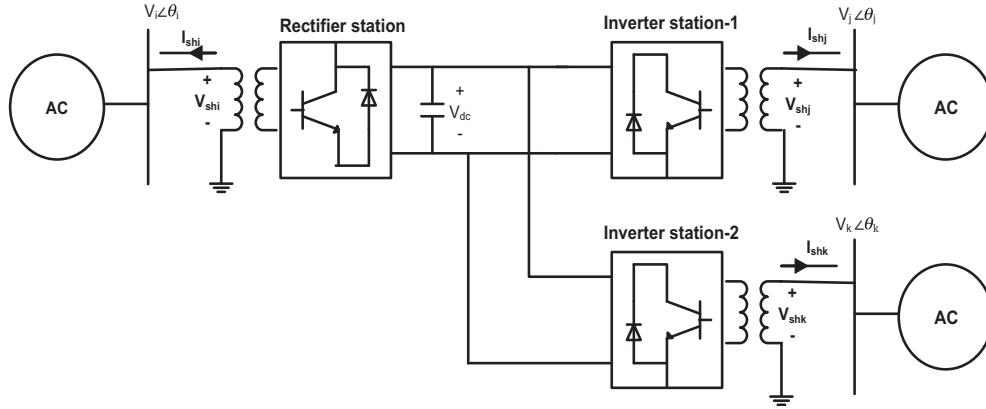


Fig. 1. Schematic diagram of a three terminal BTB M-VSC-HVDC network.

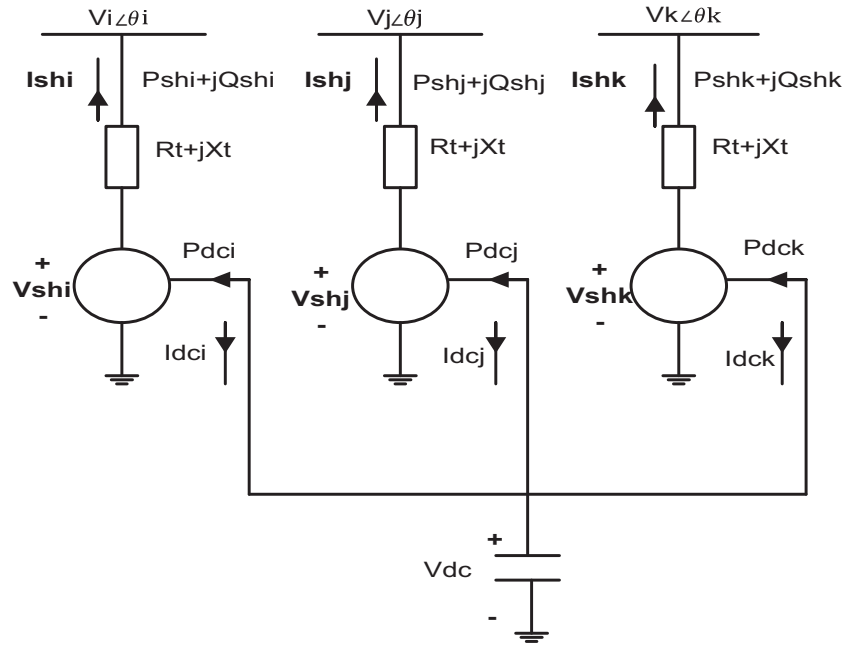


Fig. 2. Equivalent circuit of the three terminal BTB M-VSC-HVDC network.

$$\mathbf{I}_{shn} = \mathbf{Y}_{shn}(\mathbf{V}_{shn} - \mathbf{V}_n) \quad (1)$$

where $\mathbf{Y}_{shn} = 1/\mathbf{Z}_{shn}$.

The output voltage of each voltage source converter is represented by the voltage phasor $\mathbf{V}_{shn} = V_{shn} \angle \theta_{shn} = m_n c V_{dc} \angle \theta_{shn}$, where ' m_n ' ($n = i, j, k$) is the modulation index of the converter and ' c ' is a constant which depends on the type of converter [14]. The AC terminal bus voltage is represented by the phasor $\mathbf{V}_n = V_n \angle \theta_n$ ($n = i, j, k$).

Hence from Fig. 2, the net current injection at the AC terminal bus ' n ' ($n = i, j, k$) can be written as

$$\mathbf{I}_n = [\mathbf{Y}_{nn}^{old} + \mathbf{Y}_{shn}] \mathbf{V}_n + \sum_{g=1, g \neq n}^p \mathbf{Y}_{ng} \mathbf{V}_g - \mathbf{Y}_{shn} \mathbf{V}_{shn} \quad (2)$$

where $\mathbf{Y}_{nn}^{old} = \mathbf{y}_{n0} + \sum_{g=1, g \neq n}^p \mathbf{Y}_{ng}$ is the self admittance of bus ' n ' for the original ' p ' bus AC system without any converter and ' \mathbf{y}_{n0} ' accounts for the shunt capacitances of all the transmission lines connected to bus ' n ' ($n = i, j, k$).

Substituting Eqs. (1) in (2) and manipulating, we get

$$\mathbf{I}_n = \sum_{g=1}^p \mathbf{Y}_{ng} \mathbf{V}_g - \mathbf{Y}_{shn} \mathbf{V}_{shn} \quad (3)$$

where $\mathbf{Y}_{nn} = \mathbf{Y}_{nn}^{old} + \mathbf{Y}_{shn}$ is the new value of self admittance for the bus ' n ' ($n = i, j, k$) with its converter connected.

Subsequently, the net injected active power at AC terminal bus ' n ' ($n = i, j, k$) can be written as

$$P_n = \text{Re}\{\mathbf{V}_n \mathbf{I}_n^*\} = \sum_{g=1}^p V_n V_g Y_{ng} \cos(\theta_n - \theta_g - \phi_{ng}) - V_n V_{shn} Y_{shn} \cos(\theta_n - \theta_{shn} - \phi_{shn}) \quad (4)$$

$$\text{or, } P_n = \sum_{g=1}^p V_n V_g Y_{ng} \cos(\theta_n - \theta_g - \phi_{ng}) - m_n c V_{dc} V_n Y_{shn} \cos(\theta_n - \theta_{shn} - \phi_{shn})$$

In a similar manner, the net injected reactive power at bus ' n ' can be written as

$$Q_n = \sum_{g=1}^p V_n V_g Y_{ng} \sin(\theta_n - \theta_g - \phi_{ng}) - m_n c V_{dc} V_n Y_{shn} \sin(\theta_n - \theta_{shn} - \phi_{shn}) \quad (5)$$

Also from Fig. 2, the terminal active and reactive power flows in the line connecting bus 'n' ($n = i, j, k$) to its converter can be written as

$$P_{shn} = \text{Re}[\mathbf{V}_n \mathbf{I}_{shn}^*] \\ = V_n m_n c V_{dc} Y_{shn} \cos(\theta_n - \theta_{shn} - \phi_{shn}) - V_n^2 Y_{shn} \cos \phi_{shn} \quad (6)$$

$$Q_{shn} = \text{Im}[\mathbf{V}_n \mathbf{I}_{shn}^*] \\ = V_n m_n c V_{dc} Y_{shn} \sin(\theta_n - \theta_{shn} - \phi_{shn}) + V_n^2 Y_{shn} \sin \phi_{shn} \quad (7)$$

Again, from Fig. 2, let the power exchange of the n th converter with the DC link ($n = i, j, k$) be expressed as

$$P_{dcn} = \text{Re}(\mathbf{V}_{shn} \mathbf{I}_{shn}^*) = (m_n c V_{dc})^2 Y_{shn} \cos \phi_{shn} \\ - m_n c V_{dc} V_n Y_{shn} \cos(\theta_{shn} - \theta_n - \phi_{shn}) \quad (8)$$

Then, from Fig. 2, it can be observed that

$$-(P_{dci} + P_{dcj} + P_{dck}) = P_{\text{loss}} \quad (9)$$

where P_{loss} represents the losses in the converters.

If the converters are assumed lossless, Eq. (9) can be expressed as

$$f = 0 \quad (10)$$

where $f = P_{dci} + P_{dcj} + P_{dck}$.

Eq. (10) represents an independent equation. For the three converter system, four more independent equations are obtained for the power flow equations at the AC terminal buses corresponding to the two slave converters. Since converters 'j' and 'k' are considered as slave converters, these four equations are

$$P_{shj}^{sp} - P_{shj}^{cal} = 0 \quad (11)$$

$$Q_{shj}^{sp} - Q_{shj}^{cal} = 0 \quad (12)$$

$$P_{shk}^{sp} - P_{shk}^{cal} = 0 \quad (13)$$

$$Q_{shk}^{sp} - Q_{shk}^{cal} = 0 \quad (14)$$

where P_{shj}^{sp} , P_{shk}^{sp} , Q_{shj}^{sp} and Q_{shk}^{sp} are the specified line active and the reactive powers respectively at buses 'j' and 'k', respectively, while P_{shj}^{cal} , P_{shk}^{cal} , Q_{shj}^{cal} and Q_{shk}^{cal} are their calculated values which can be obtained using Eqs. (6) and (7).

Since converter 'i' is considered as a master converter, it can be used to control the voltage magnitude of its AC terminal bus. This provides one more independent equation as

$$V_i^{sp} - V_i^{cal} = 0 \quad (15)$$

where V_i^{sp} is the bus voltage control reference and V_i^{cal} is the calculated value of the voltage magnitude at the i th bus.

It may be noted that the slave converters at buses 'j' and 'k' may be used to control the bus voltage magnitudes rather than the line reactive powers, in which case Eqs. (12) and (14) become

$$V_j^{sp} - V_j^{cal} = 0 \quad (16)$$

$$V_k^{sp} - V_k^{cal} = 0 \quad (17)$$

Newton power flow equations of the BTB M-VSC-HVDC system

From the analysis made in the last section, it is observed that for the AC–DC system considered, several new variables enter into the picture. These include the phase angles of the three VSCs namely, θ_{shn} and their modulation indices m_n ($n = i, j, k$), along with the DC link voltage V_{dc} . Corresponding to these, a total of five independent

equations exist comprising the line active and reactive powers of the two slave converters and one active power balance equation. In addition, the master converter controls the voltage magnitude at bus 'i', thereby making available the reactive power injection equation thereof, as an independent equation, which can be written as

$$Q_i^{sp} - Q_i^{cal} = 0 \quad (18)$$

where Q_i^{cal} is given by Eq. (5).

Now, if the number of voltage control buses in the AC system is ' $q - 1$ ', the power flow problem for the ' p ' bus AC system incorporated with the M-VSC-HVDC can be formulated as

Solve $\theta, \mathbf{V}, \theta_{sh}, \mathbf{m}$
Specified $\mathbf{P}, \mathbf{Q}, \mathbf{R}$

where $\theta = [\theta_2 \dots \theta_p]^T$, $\mathbf{V} = [V_{q+1} \dots V_p]^T$, $\theta_{sh} = [\theta_{shi} \ \theta_{shj} \ \theta_{shk}]^T$, $\mathbf{m} = [m_i \ m_j \ m_k]^T$, $\mathbf{P} = [P_2 \dots P_p]^T$, $\mathbf{Q} = [Q_{q+1} \dots Q_p]^T$, $\mathbf{R} = [\mathbf{P}_{sh}^T \ \mathbf{Q}_{sh}^T \ V_i f]^T$ with $\mathbf{P}_{sh} = [P_{shj} \ P_{shk}]^T$ and $\mathbf{Q}_{sh} = [Q_{shj} \ Q_{shk}]^T$.

In the above analysis, it is assumed that, without any loss of generality, there are ' q ' generators connected at the first ' q ' buses of the AC system with bus 1 being the slack bus. Subsequently, the Newton power flow equation [21] may be written as

$$\mathbf{J} \begin{bmatrix} \Delta \theta \\ \Delta \mathbf{V} \\ \Delta \theta_{sh} \\ \Delta \mathbf{m} \end{bmatrix} = \begin{bmatrix} \Delta \mathbf{P} \\ \Delta \mathbf{Q} \\ \Delta \mathbf{R} \end{bmatrix} \quad (19)$$

where $\mathbf{J} = \begin{bmatrix} \mathbf{J}_{old} & \frac{\partial \mathbf{P}}{\partial \theta_{sh}} & \frac{\partial \mathbf{P}}{\partial \mathbf{m}} \\ \frac{\partial \mathbf{Q}}{\partial \theta} & \frac{\partial \mathbf{Q}}{\partial \mathbf{V}} & \frac{\partial \mathbf{Q}}{\partial \theta_{sh}} \\ \frac{\partial \mathbf{R}}{\partial \theta} & \frac{\partial \mathbf{R}}{\partial \mathbf{V}} & \frac{\partial \mathbf{R}}{\partial \theta_{sh}} \end{bmatrix}$ is the Jacobian matrix. In Eq. (19),

' \mathbf{J}_{old} ' is the conventional power flow Jacobian sub-block corresponding to the ' p ' bus AC system. Also, in Eq. (19), ' $\Delta \mathbf{R}$ ' is the vector comprising the mismatches of the control specifications of the VSC-HVDC. In the above formulation, it is assumed that both the slave converters connected to the buses 'j' and 'k' operate in the PQ control mode. However, it may be noted that if they are made to operate in the PV control mode, the corresponding elements of the correction and mismatch vectors have to be modified accordingly.

Modeling of the PTP-M-VSC HVDC system

Unlike a BTB scheme, in a point to PTP scheme, converters exist at different locations, with the DC terminals interconnected by DC overhead lines or cables. Fig. 3 shows a schematic diagram for a three terminal point to point VSC-HVDC system. It consists of three converters which are connected to three AC buses 'i', 'j' and 'k'. The converter connected at bus 'i' is considered as a master converter, while the converters connected to the AC buses 'j' and 'k' are considered as slave converters. Fig. 4 shows the equivalent circuit for the network shown in Fig. 3.

In a ' r ' terminal DC system, the net current injection at the n th DC node ($n = i, j, k$) is given as

$$I_{dcn} = \sum_{g=1}^r Y_{dcng} V_{dcg} \quad (20)$$

where $Y_{dcng} = -\frac{1}{R_{dcng}}$, with ' R_{dcng} ' being the DC link resistance between DC buses ' n ' and ' g ' ($n = i, j, k$).

Now, from Fig. 4, for the n th ($n = i, j, k$) converter, it can be observed that

$$P_{dcn} = \text{Re}(\mathbf{V}_{shn} \mathbf{I}_{shn}^*) = V_{dcn} (-I_{dcn}) = -\sum_{g=1}^r V_{dcn} V_{dcg} Y_{dcng} \quad (21)$$

which yields

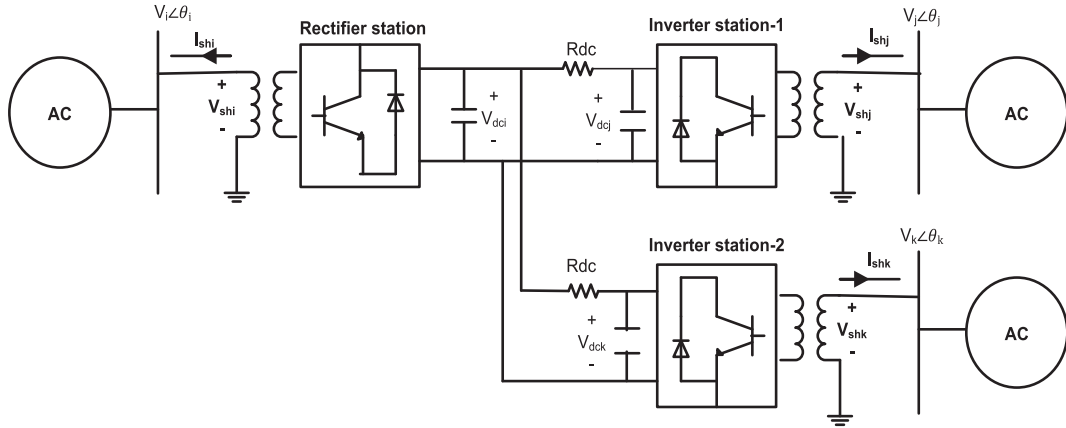


Fig. 3. Schematic diagram of a three terminal PTP M-VSC-HVDC system.

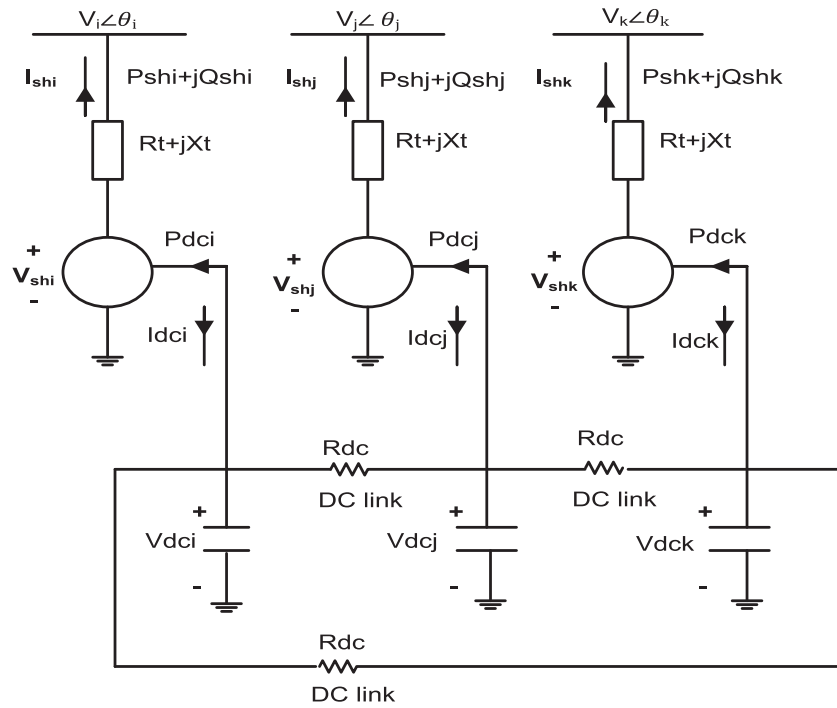


Fig. 4. Equivalent circuit of the three terminal PTP M-VSC-HVDC system.

$$(m_n c V_{dcn})^2 Y_{shn} \cos \phi_{shn} - m_n c V_{dcn} V_n Y_{shn} \cos(\theta_{shn} - \theta_n - \phi_{shn}) + \sum_{g=1}^r V_{dcn} V_{dng} Y_{dng} = 0$$

or, $f_n = 0$

(22)

where $(n = i, j, k)$.

Thus, three independent equations are obtained.

In addition, as shown in Section 'Modelling of a BTB M-VSC HVDC system', four more independent equations {Eqs. (11)–(14)} are obtained for the power flow equations at the AC terminal buses corresponding to the two slave converters.

Now, similar to AC power flow, a slack bus is chosen for the DC power flow and its voltage is kept constant. It also serves the dual role of providing the DC voltage control and balancing the active power exchange among the converters via the DC network. In the three terminal DC system considered, bus 'i' is chosen as the DC slack bus. This is represented as

$$V_{dci}^{sp} - V_{dci}^{cal} = 0 \quad (23)$$

Instead of specifying V_{dci} , the modulation index m_i can also be specified as

$$m_i^{sp} - m_i^{cal} = 0 \quad (24)$$

Newton power flow equations of the PTP M-VSC-HVDC system

Due to the composite AC–DC system, the phase angles of the three VSCs i.e. θ_{shn} , their modulation indices m_n and the DC side voltages V_{dcn} ($n = i, j, k$) constitute the new variables. Now, similar to the BTB model, five independent equations comprising the line active and reactive powers of the two slave converters and the reactive power injection equation at bus 'i' (due to the voltage control by the master converter) are available. In addition, three more independent equations are made available from the AC–DC power balance at the individual converter terminals. Also, at the DC slack bus, either the DC voltage or the modulation index is specified. Thus, similar to the BTB model, the Newton power flow equation can be written as

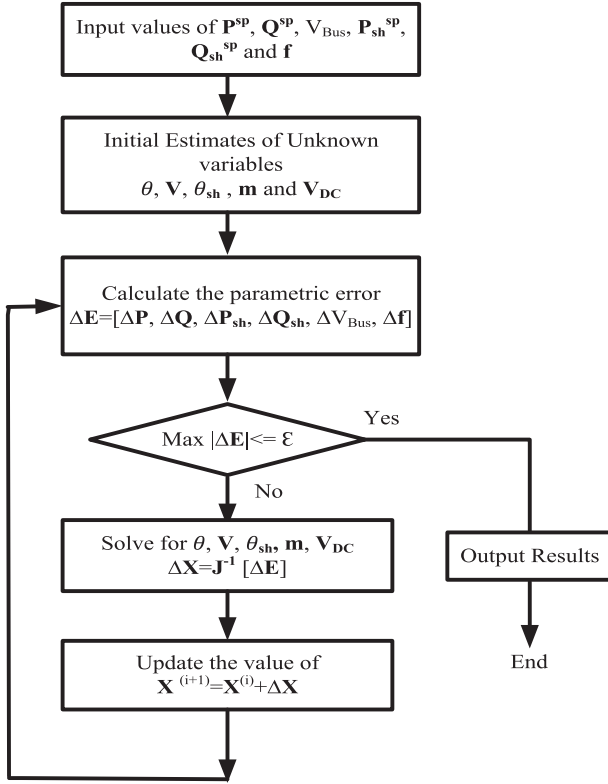


Fig. 5. Flow chart of the NR method for PTP-M-VSC-HVDC power flow.

case the elements of \mathbf{J} would be modified accordingly. Fig. 5 depicts the flow chart of the NR power flow method for the PTP M-VSC-HVDC system.

Case studies and results

For validation of the proposed BTB and PTP models, numerous case studies are carried out in the IEEE-118-bus test system [22]. All computations were carried out in MATLAB on a 2.4 GHz, 4 GB RAM Intel Core (TM) Machine with i3-3110 M CPU. In each case, the converters are connected to their respective AC buses through converter transformers. The resistances and the leakage reactances of all the converter transformers are taken as 0.001 p.u. and 0.1 p.u. respectively, for all the case studies. The resistance of each DC link is taken as 0.01 p.u. for all the case studies. In addition, the value of 'c' for the VSC based converters is uniformly chosen to be $\frac{1}{2\sqrt{2}}$ [14]. A convergence tolerance of 10^{-10} p.u. was uniformly adopted for all the case studies.

Case Study-I: In this case study, a three terminal BTB VSC-HVDC network is incorporated in the IEEE-118 bus test system between buses 82, 93 and 94. The master converter is connected to bus no. 82. On the other hand, both the slave converters are connected to buses 93 and 94 which operate in the PQ control mode. The specified values are given in the columns 1–4 of Table 1. The power flow solution is shown in the columns 5–7 of Table 1. From Table 1 it is observed that the power flow converges in five iterations, similar to the base case power flow (without HVDC network incorporated). Also, the power-flow solution directly yields the VSC modulation indices, unlike existing models [12,13,15,18]. The convergence characteristic plots for the power flows of the base case and the BTB VSC-HVDC are shown in Figs. 6 and 7, respectively. From Figs. 6 and 7, it is observed that similar to the base case, the proposed VSC-HVDC model demonstrates the quadratic convergence of the Newton–Raphson method.

The bus voltage profile for the case study corresponding to Table 1 is shown in Fig. 8. From Fig. 8, it is again observed that the bus voltage profile does not change much except for the AC terminal buses at which the VSCs are installed.

Case study II: In this case study, a three terminal PTP VSC HVDC network is incorporated in the IEEE-118 bus test system. The converters are connected between buses 82, 93 and 94. The master converter is connected to bus no. 82 while both the slave converters are connected to buses 93 and 94 and are operated in the PQ control mode. The specified values are given in the columns 1–4 of Table 2. The power flow solution is shown in the columns 5–7 of Table 2. The convergence characteristic plot for this power flow is shown in Fig. 9. From the power flow solution and by comparing the convergence characteristic plot (Fig. 9) with that of the base

$$\mathbf{J} \begin{bmatrix} \Delta\theta \\ \Delta V \\ \Delta\theta_{sh} \\ \Delta m \\ \Delta V_{dc} \end{bmatrix} = \begin{bmatrix} \Delta P \\ \Delta Q \\ \Delta R \end{bmatrix} \quad (25)$$

$$\text{where, } \mathbf{J} = \begin{bmatrix} \mathbf{J}_{old} & \frac{\partial P}{\partial \theta_{sh}} & \frac{\partial P}{\partial m} & \frac{\partial P}{\partial V_{dc}} \\ \frac{\partial Q}{\partial \theta} & \frac{\partial Q}{\partial V} & \frac{\partial Q}{\partial \theta_{sh}} & \frac{\partial Q}{\partial m} \\ \frac{\partial R}{\partial \theta} & \frac{\partial R}{\partial V} & \frac{\partial R}{\partial \theta_{sh}} & \frac{\partial R}{\partial m} \end{bmatrix},$$

$$\Delta \mathbf{m} = [\Delta m_i \ \Delta m_j \ \Delta m_k]^T; \quad \Delta \mathbf{V}_{dc} = [\Delta V_{dc_i} \ \Delta V_{dc_j} \ \Delta V_{dc_k}]^T; \quad \Delta \mathbf{f} = [\Delta f_i \ \Delta f_j \ \Delta f_k]^T$$

$$\Delta \theta_{sh} = [\Delta \theta_{shi} \ \Delta \theta_{shj} \ \Delta \theta_{shk}]^T \quad \text{and} \quad \Delta \mathbf{R} = [\Delta P_{sh}^T \ \Delta Q_{sh}^T \ \Delta V_i \ \Delta V_{dc_i} \ \Delta \mathbf{f}^T]^T$$

In Eq. (25), ' $\Delta \mathbf{R}$ ' represents the control specification mismatch vector. It may be noted that ' Δm_i ' may replace ' ΔV_{dc_i} ' in ' $\Delta \mathbf{R}$ ', in which

Table 1
Study of IEEE-118 bus system with a three terminal BTB VSC-HVDC network.

HVDC link		HVDC link specification		Power flow solution		
Primary converter	Secondary converters	Primary converter	Secondary converters	AC terminal buses	HVDC variables	
					Primary converter	Secondary converters
i	j, k	$V_{dc} = 3;$ $V_i = 0.99$	$P_{shj} = 0.5;$ $Q_{shj} = 0.2;$ $P_{shk} = 0.3;$ $Q_{shk} = 0.1$	$\mathbf{V}_j = 1.007 \angle 1.1077;$ $\mathbf{V}_k = 1.006 \angle -1.213;$ $\theta_i = -3.6804$	$\mathbf{V}_{shi} = 1.0239 \angle -8.231;$ $m_i = 0.9654;$	$m_j = 0.9697;$ $m_k = 0.9535;$ $\mathbf{V}_{shj} = 1.0285 \angle 3.8639;$ $\mathbf{V}_{shk} = 1.0113 \angle 0.4798$

NI = 5

Note: For the above case study, $i = 82, j = 93$ and $k = 94$; values of voltage magnitudes and phase angles are in p.u. and degrees, respectively

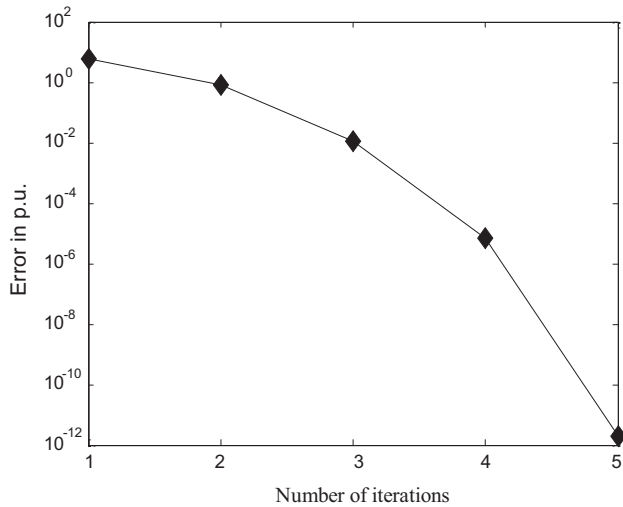


Fig. 6. Convergence characteristics for the base case power flow in IEEE-118 bus system.

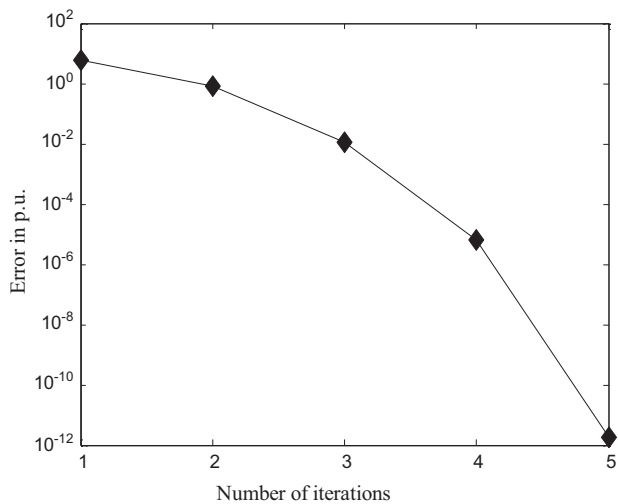


Fig. 7. Convergence characteristics for the case study of Table 1.

case (Fig. 6), the excellent convergence characteristics of the proposed VSC-HVDC model can be observed.

From the plot of the bus voltage profile for the case study corresponding to Table 2, it was observed that it does not change much except for the AC terminal buses at which the VSCs are installed. However, the bus voltage profile plot could not be accommodated due to an upper limit on the number of figures.

Case study III: This case study demonstrates the versatility of the proposed VSC-HVDC model. In this case study, a three terminal PTP VSC-HVDC system is incorporated in the IEEE-118 bus test system between buses 88, 117 and 118. The master converter connected to bus no. 88 operates in the voltage control mode while both the slave converters connected to buses 117 and 118 are now operated in the PV control mode, unlike earlier cases. Similar to the earlier cases, the voltage at the DC slack bus is also specified.

Case study IV: In this case study, another three terminal PTP VSC-HVDC system is incorporated in the IEEE-118 bus test system between buses 82, 93 and 94. The master converter is connected to bus no. 82 operates in the voltage control mode while both the slave converters connected to buses 93 and 94 again operate in the PQ control mode. This is the special case in which the modulation index of the master converter is specified instead of the voltage at the DC slack bus. This is an additional advantage of the proposed model over existing ones.

The specified values for Case studies III and IV discussed above are given in the first and second rows, respectively and columns 1–4 of Table 3. The power flow solutions corresponding to Case studies III and IV are shown in the first and second rows respectively and columns 5–7 of Table 3. From Table 3 it can be observed that the number of iterations to attain convergence does not depend upon the HVDC control mode (PQ or PV) or the location of the DC network in the AC system (the VSC-HVDC network can be connected to different AC buses). This demonstrates the versatility and the robustness of the proposed model.

It was observed that the convergence characteristic plots for the power flows of Case studies III and IV retained the quadratic convergence characteristics of the Newton's method, similar to the base case. However, they could not be accommodated due to an upper limit on the number of figures.

In above studies, a generalized M-VSC-HVDC model with different operating modes has been proposed for power flow analysis. A comparison of the different case studies is shown in Table 4.

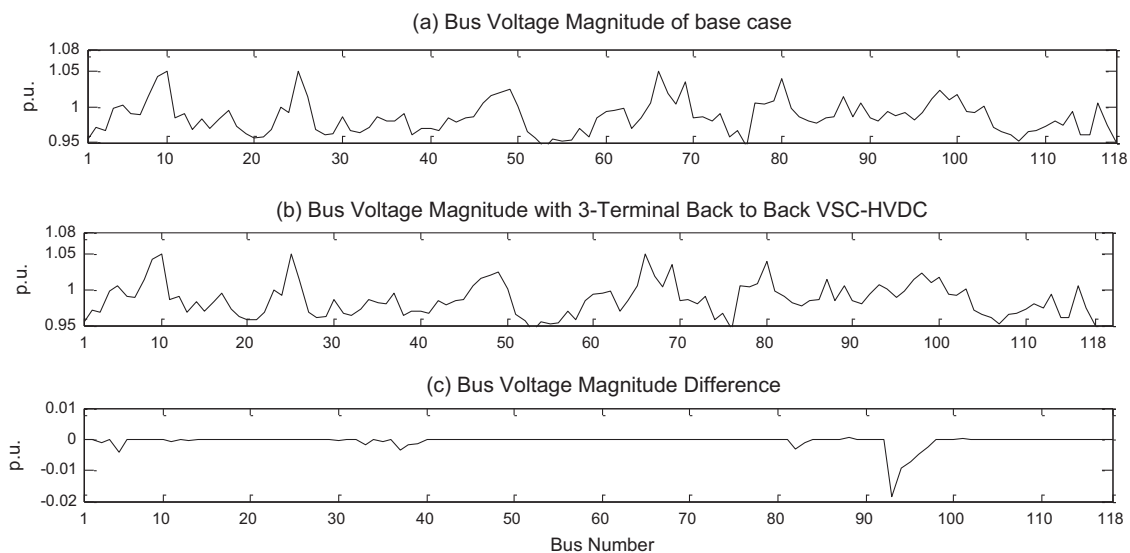


Fig. 8. Bus voltage profile for the case study of Table 1.

Table 2
Study of IEEE-118 bus system with a three terminal PTP VSC-HVDC network.

HVDC link		HVDC link specification		Power flow solution		
Primary converter	Secondary converters	Primary converter	Secondary converters	AC terminal buses	HVDC variables	
i	j, k				Primary converters	Secondary converter
		$V_{dci} = 3;$ $V_i = 0.99$	$P_{shj} = 0.5;$ $Q_{shj} = 0.2;$ $P_{shk} = 0.3;$ $Q_{shk} = 0.1$	$V_j = 1.007 \angle 1.1085;$ $V_k = 1.006 \angle -1.212;$ $\theta_i = -3.6804;$	$V_{shi} = 1.0239 \angle -8.233;$ $m_i = 0.9654$	$V_{dcj} = 2.9986;$ $V_{dck} = 2.9988;$ $m_j = 0.9701; m_k = 0.9539;$ $V_{shj} = 1.0285 \angle 3.8647;$ $V_{shk} = 1.0113 \angle 0.4806;$
NI = 5						

Note: For the above case study, $i = 82, j = 93, k = 94$; values of voltage magnitudes and phase angles are in p.u. and degrees, respectively

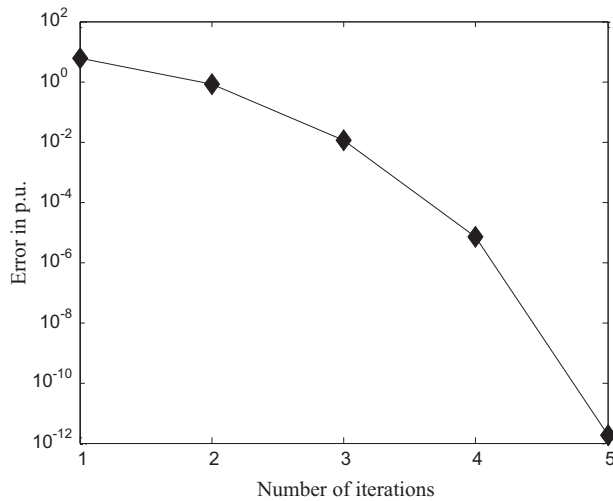


Fig. 9. Convergence characteristics for the case study of Table 2.

It is important to note that although the proposed model was not applied on larger-size networks for real-scale system validation, the convergence features of the model were tested on the standard IEEE 118-bus test system. Since the proposed model demonstrates quadratic convergence characteristics in the IEEE 118-bus test system, it is expected that these characteristics would be retained in larger-size networks too.

Table 4
Comparison between the different case studies.

Table no.	Case study no.	VSC-HVDC configuration	HVDC control mode		NI
			Primary converter	Secondary converters	
I	I	BTB	V_{dc}	PQ	5
II	II	PTP	V_{dc}	PQ	5
III	III	PTP	V_{dc}	PV	5
	IV	PTP	m	PQ	5

Conclusions

In this paper, the Newton Raphson Power Flow modeling of M-VSC-HVDC systems for both the BTB (connected at the common DC voltage) and the PTP (incorporating DC network) configurations have been presented. In the proposed model, the converter modulation indices appear as unknowns along with the converter DC side voltages and the phase angles of the converter AC side voltages. This is an advantage over most of the existing models, as practical considerations limit the maximum and the minimum values of 'm'. The proposed modeling strategy facilitates the application of multiple control modes for the M-VSC-HVDC. This model also offers the flexibility of choosing either the DC side voltage or the modulation index of the master converter as an unknown. This renders the model more versatile. It is observed that the convergence characteristic of the proposed algorithm is independent of the VSC-HVDC control modes adopted, the location of the DC network, or its topology (BTB or PTP). This demonstrates the robust-

Table 3
Studies of IEEE-118 bus system with different three-terminal PTP VSC-HVDC networks.

HVDC link		HVDC link specification		Power flow solution		
Primary Converter	Secondary Converters	Primary Converters	Secondary Converter	AC terminal buses	HVDC variables	
i	j, k				Primary Converters	Secondary Converter
		$V_{dci} = 3;$ $V_i = 1$	$P_{shj} = 0.4;$ $V_j = 1;$ $P_{shk} = 0.2;$ $V_k = 0.97$	$\theta_j = -14.0941;$ $\theta_k = -8.2963;$ $\theta_i = 5.2733$	$V_{shi} = 1.0481 \angle 1.9585;$ $m_i = 0.9882$	$V_{dcj} = 2.9989; V_{dck} = 2.999;$ $m_j = 0.9527; m_k = 0.9719;$ $V_{shj} = 1.0101 \angle -11.8297;$ $V_{shk} = 1.0305 \angle -7.1832$
NI = 5						
		$m_i = 0.99;$ $V_i = 0.99$	$P_{shj} = 0.6;$ $Q_{shj} = 0.2;$ $P_{shk} = 0.5;$ $Q_{shk} = 0.2$	$V_j = 1.010 \angle 1.9115;$ $V_k = 1.004 \angle -0.617;$ $\theta_i = -4.1752$	$V_{shi} = 1.035 \angle -10.37;$ $V_{dci} = 2.9569$	$V_{dcj} = 2.955; V_{dck} = 2.9551;$ $m_j = 0.988; m_k = 0.9821;$ $V_{shj} = 1.0322 \angle 5.1992;$ $V_{shk} = 1.0261 \angle 2.1512$
NI = 5						

Note: For the above case study, $i = 82, j = 93, k = 94$; values of voltage magnitudes and phase angles are in p.u. and degrees, respectively

ness of the model. Case studies carried out by applying different control modes to different topologies of multi-terminal DC networks in the IEEE-118 bus test system validate the proposed model.

References

- [1] Acha E, Agelidis VG, Anaya Lara O, Miller TJE. *Power electronic control in electrical systems*. Butterworth: Newnes; 2002.
- [2] Acha E, Fuente-Esquivel CR, Perez HA, Camacho CA. *FACTS modelling and simulation in power networks*. John Wiley; 2004.
- [3] Padiyar KR. *HVDC power transmission systems*. 2nd ed. New Age International Publishers; 2012.
- [4] Asplund Gunnar. Application of HVDC light to power system enhancement. In: Proc IEEE PES winter meeting; January 2000.
- [5] Blau J. Europe plans a north sea grid. *IEEE Spectr* 2010;12–3.
- [6] Haileselassie Temesgen M, Uhlen Kjetil. Power system security in a meshed north sea HVDC grid. *IEEE Proc Invited Paper* 2013;101(4):978–90.
- [7] Zhang XP, Rehtanz C, Pal B. *Flexible AC transmission systems: modelling and control*. Springer; 2006.
- [8] Lu W, Ooi BT. Premium quality power park based on multi-terminal HVDC. *IEEE Trans Power Del* 2005;20(2):978–83.
- [9] Xu L, Williams BW, Yao L. Multi-terminal DC transmission systems for connecting large offshore wind farms. *IEEE proc PES general meeting-conversion and delivery of electrical energy 21st century* 2008;1–7.
- [10] da Silva R, Teodorescu R, Rodriguez. Power delivery in MTDC transmission system for offshore wind power applications. *IEEE Proc PES ISGT Europe* 2010;1–8.
- [11] Moawwad A, El Moursi MS, Xiao W, Kirtley Jr JL. Novel configuration and transient management control strategy for VSC-HVDC. *IEEE Trans Power Syst* 2014;29(5):2478–88.
- [12] Angeles-Camacho C, Tortelli OL, Acha E, Fuente-Esquivel CR. Inclusion of a high voltage DC voltage source converter model in a Newton Raphson power flow algorithm. *Proc Inst Elect Eng Gen Transm Distrib* 2003;150(6):691–6.
- [13] Zhang XP. Multiterminal voltage-sourced converter-based HVDC models for power flow analysis. *IEEE Trans Power Syst* 2004;19(4):1877–84.
- [14] Martinez A, Esquivel C, Perez H, Acha E. Modeling of VSC-based HVDC systems for a Newton Raphson OPF algorithm. *IEEE Trans Power Syst* 2007;22(4):1794–9.
- [15] Martinez A, Esquivel C, Camacho C. Voltage source converter based high voltage DC system modelling for optimal power flow studies. *Electr Power Compon Syst* 2012;40(3):312–20.
- [16] Beerten J, Cole S, Belmans R. Generalized steady-state VSC MTDC model for sequential AC/DC power flow algorithms. *IEEE Trans Power Syst* 2012;27(2):821–9.
- [17] Acha E, Kazemtabrizi Behzad, Castro Luis M. A new VSC HVDC model for power flows using the Newton Raphson method. *IEEE Trans Power Syst* 2013;28(3):2602–12.
- [18] Wang W, Barnes Mike. Power flow algorithms for multi-terminal VSC-HVDC with droop control. *IEEE Trans Power Syst* 2014;29(4):1721–30.
- [19] Yazdani A, Iravani R. *Voltage-sourced converters in power systems: modeling, control and applications*. New Jersey, USA: Wiley-IEEE Press; 2010. p. 171.
- [20] Daelemans G. *VSC HVDC in meshed networks* [Master's thesis]. Belgium: Katholieke Universiteit Leuven; 2008. p. 11.
- [21] Kothari DP, Nagrath IJ. *Modern power system analysis*. 3rd ed. New Delhi: Tata McGraw Hill; 2003.
- [22] <http://www.ee.washington.edu/research/pstca>.

Green route synthesis of silicon/silicon oxide from bamboo

Vinay Kumar¹, Pranjala Tiwari¹, Lucky Krishnia¹, Reetu Kumari¹, Anshika Singh¹, Arnab Ghosh², Pawan K. Tyagi^{1*}

¹Department of Applied Physics, Delhi Technological University, Delhi 110042, India

²Institute of Physics, Sachivalaya Marg, Bhubaneswar 751005, India

*Corresponding author. Tel: (+91) 11-27852212; Fax: (+91) 11- 27871023; E-mail: pawan.phy@dce.edu

Received: 09 September 2015, Revised: 30 November 2015 and Accepted: 03 January 2016

ABSTRACT

Silica, generally known as silicon dioxide is insulating in nature whereas silicon is semiconducting. These two materials are widely used in sensing and electronic devices. In order to full-fill demand of silicon, sources other than sand, have to explore for silicon extraction. In this report, bamboo culms have been subjected to thermo chemical decomposition at high temperature (1250 °C) in an inert atmosphere. After pyrolysis, contents in residual of bamboo culms have been characterized by using scanning electron microscope (SEM), transmission electron microscope (TEM) and X-ray diffraction (XRD). Nanosized, pure crystalline Si has been formed. Si as well as charcoal is found to be crystalline in nature. No silicon carbide formation observed. Copyright © 2016 VBRI Press.

Keywords: Nano-sized Si; bamboo charcoal; pyrolysis process; EDX mapping.

Introduction

Silicon is an extremely versatile material, being semiconducting in nature and has myriad applications ranging from the electronic devices to glass fabrication processes [1]. With continued rapid development in the area of photovoltaics (PV), the overall demand for silicon in both monocrystalline and polycrystalline form has been increased [2]. Availability and well established scalability of silicon makes it one of the most widely used material in microelectronics and photovoltaics. In the recent years, applications of silicon in Li-ion batteries and photonics [3, 4, 5, 6] has emerged as a promising field. During the past decades, in Li-ion batteries silicon has been found to possess high theoretical capacity of 4200 mAh g⁻¹ when the Li₂₂Si₅ phase is formed [3] and emerged as an attractive anode material [3,4,5]. However, crack formation and failure of electrical contact those occurred during the cycling has limited its applications. Although use of silicon nanoparticles seemed to the performance of battery improves significantly [7]. Hence, much research interest is now being shifted in the area of Si nanoparticles. This happened because many applications of Si nanoparticles in various fields such as chemical and biomedical sensors [8, 9], solar cells [10, 11] and secondary batteries [12, 13] have been demonstrated. An extended range of applications of Si in the form of nanowire realized a multi-wavelength light source that can operate both in IR and visible ranges [14]. Furthermore, silica nanoparticles are also being used in photovoltaic systems to reduce the reflectance of protection glass by their coating [15]. Further, SiO₂ was used in photodetector as an interfacial layer. This happened

due to its passivation effect thereby suppressing surface leakage current and reduction in device capacitance resulting in quick photo-response of photo-detector [16]. SiO₂ composites either with Ag or other materials were reported to exhibit unique magnetic, catalytic, thermal, optical and electrical properties and many applications in the field of biomedical, electronic devices, adsorption and separation [17, 18] have been demonstrated. Despite from various applications silica is used in industrial applications for treatment of water and wastewater in form of nanocomposite containing amorphous silica nanoparticles and organic polymer due to low toxicity of silica nanoparticles [19, 20]. Since 2006, demand of mono or poly crystalline silicon as well as nanoparticle exceeded in other areas than that in microelectronics [21]. With aim to produce the cost effective photovoltaics or silicon-based devices, the vital issue is to produce the low-cost Solar Grade Silicon (SGS). Till date mostly, chemical route [21], so-called Siemens process [2, 22] and another route being metallurgical route [22] have been used to produce the SGS. Among all the published reports so far [22, 23, 24], extraction of pure polycrystalline or monocrystalline from bamboo have not been much explored [25], and the research is still in preliminary phase. However, extraction from the rice husks has been reported in recently published reports [26, 27]. Further, importance of bamboo can be understood as it is the fastest growing woody plant in the world, growing with the speed (up to 1 meter/per day) i.e. three times faster than the other rapidly fastest growing trees. This fast growth pattern makes the bamboo extract to be the richest known source of natural silica, containing over 70 % in the total inorganic constituents present in the

extract. In contrast to rice husks, once bamboo pyrolyzed or carbonized at high temperature ($> 600\text{ }^{\circ}\text{C}$) silica profusely formed in crystalline form. Furthermore, bamboo charcoal (BC) has attracted huge attention due to their myriad applications [28]. This BC has shown extraordinary properties such as large surface area, large pore volume, and high hydrophobicity, which was lacking in the activated carbon [29–32]. This endows BC with great potential applications [29]. In addition to the benefits of BC, extracted Si nanoparticle has profuse porosity that has high importance in the sensing applications [32]. Thus, Si nanostructures accompanied with porosity have demonstrated many exciting properties, and can serve as promising material for the development of new era of technology. Generally, porous silicon is made by the electrophoresis process and it has been reported that nanosized porous Si could be directly obtained by the carbonization or pyrolysis [33]. Furthermore, there are several techniques through which Si nanoparticles can be synthesized e.g. vapor–liquid–solid (VLS) mechanism [34, 35, 36], plasma-enhanced chemical vapor deposition (CVD) [37, 38], electrochemical methods using H_2O_2 plus HF solutions [39, 40], laser ablation [41, 42] and hot wire CVD [43]. But these processes are very lengthy, expensive and commercially unenviable. Hence all hurdles discussed above motivate us to develop a method that should be cost effective as well as should produce nanostructures in a controlled manner. The present study was performed with two objectives: first, to synthesize pure crystalline Si nanostructures, and second is to make the crystalline BC of having high porosity.

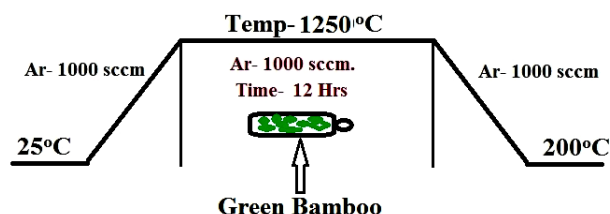


Fig. 1. Schematic diagram of the pyrolysis process for bamboo.

Experimental

Fresh bamboo was collected from a tree grown in Delhi region. The culms of bamboo have been cut in the pieces of 5 mm wide by using a knife. Outer coverings of culms were removed, and only inner part of the bamboo stem was used. These bamboo slices were subjected to pyrolysis process (Fig. 1). In the pyrolysis process, self-thermochemical decomposition of bamboo at high temperature was carried out in the presence of argon gas. In this process, simultaneous irreversible changes in both chemical composition, as well as physical phase, occurred. The pyrolysis was carried out at 1250 °C for 12 hrs in an argon atmosphere to remove water and certain organic groups from fresh bamboo slices as a result of which charcoal bio templates were produced. A heating rate of 5 °C/min was used to minimize the thermal stress that may occur during the pyrolysis. The produced charcoal biotemplates were

allowed to cool down to 200 °C naturally and then removed after shutting off the argon atmosphere. The produced charcoal was characterized by using SEM (Hitachi S-3700) HRTEM (JEOLTEM 2010) and X-ray Diffractometer (Bruker D8 Advance). Elemental analysis was performed to estimate the fractional quantity of Si/SiO₂ in the produced charcoal.

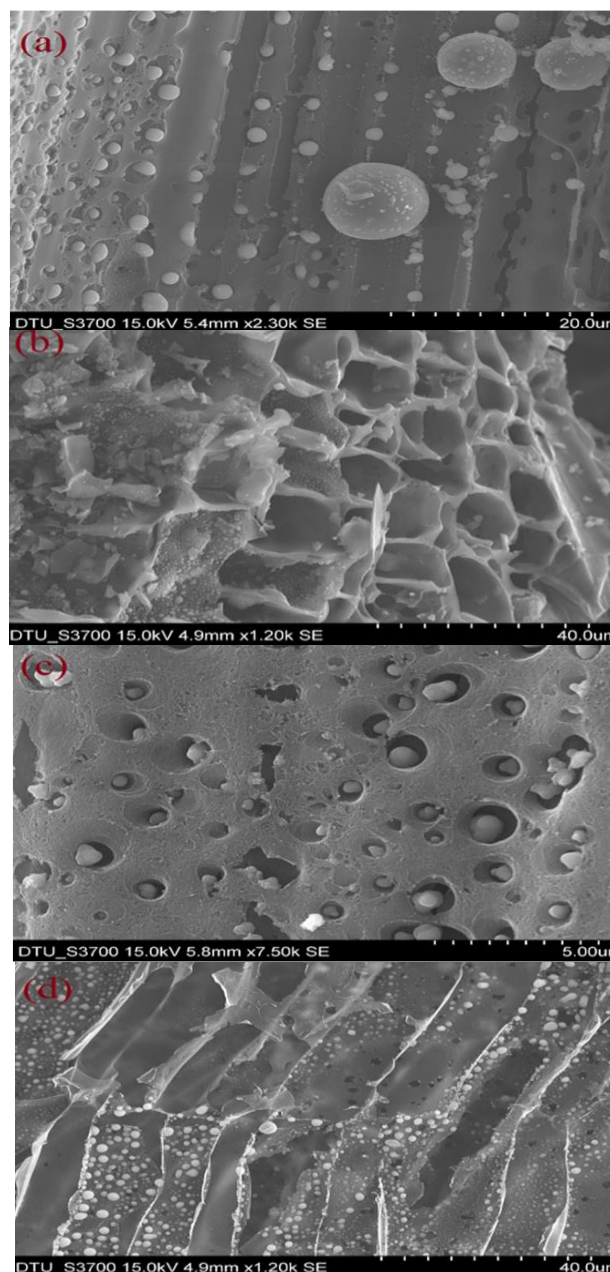


Fig. 2. SEM micrographs of bamboo charcoal (a), (b) and (d) shows lateral view of pyrolysed bamboo at different magnification scales. (c) Shows the magnified image of lateral view showing the pores and spherical silicon particles.

Results and discussion

The wall of the parenchyma, basic unit inside bamboo, and nanosized particles presented in the soot of BC has been analyzed by using Scanning Electron Microscope (SEM).

SEM images have been shown in **Fig. 2**. Scanning electron microscopy on the BC has been performed at various locations and at different magnification. As shown in **Fig. 2(b)** and **(d)** white spherical particles were observed and further characterized by using XRD and EDX and found to be of pure silicon. As evident in **Fig. 2(c)**, porous nature of BC was confirmed and Si nanoparticles were found to be embedded into the pores of BC. High density of nanoparticles was evident in **Fig. 2(d)**.

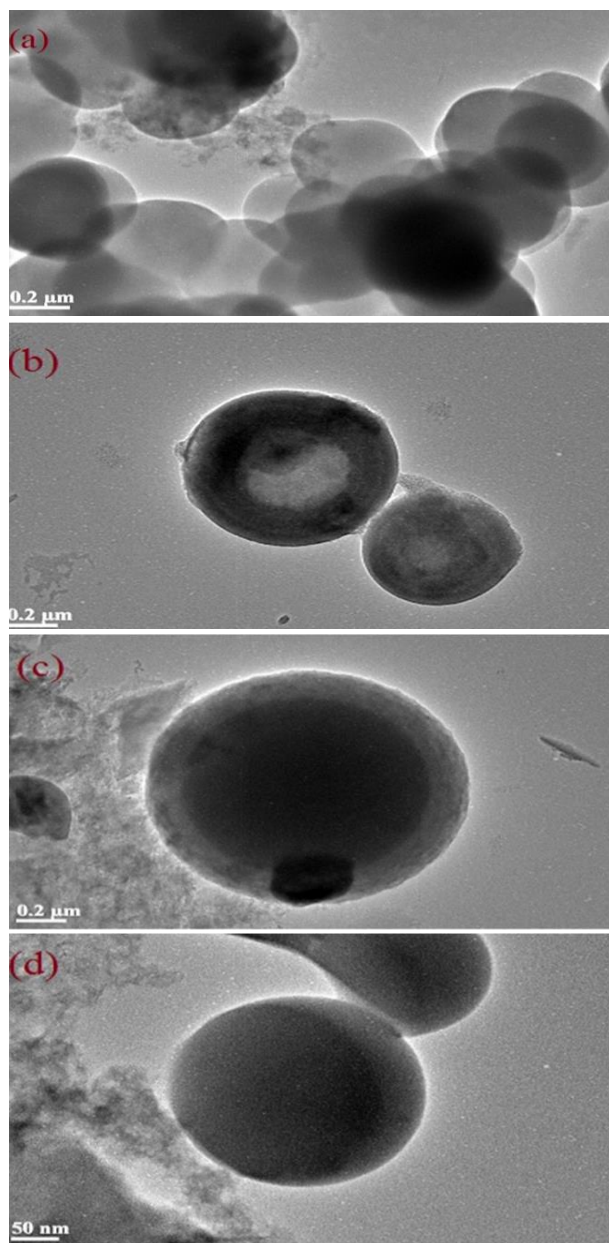


Fig. 3. Bright field TEM micrographs of bamboo charcoal (BC) (a) TEM image shows the presence of silicon spherical particles distributed randomly. (b) and (c) images confirm that particles formed are almost of the same size. (d) The size of silicon nanoparticle seen in figure and found to be approximately 200 nm.

Interestingly, periodic growth pattern of nanosized Si particle was observed as depicting in **Fig. 2(a)**. Periodicity of pattern was nearly uniform and depends on growth location in BC. Nanoparticle size was slightly lower than

pore size of BC. Particles of large size were not readily found as evident from **Fig. 2(a)**. The density of particles was found to be remarkably high in area where BC has convex curvature i.e. inner wall of parenchyma. As pore size of BC increases, cluster of nanoparticle was found to be embedded in pore, as shown in **Fig. 2(c)**. SEM images confirm that the pyrolysed BC has porous structure, and exhibit a wide pore distribution in the range from 100 nm to 1 μ m. Pore size was found to play a decisive role in controlling the size as well clustering of nanoparticles. The sample was further characterized by using transmission electron microscope (TEM).

As evident from bright field TEM images in **Fig. 3** random distribution of nanosized spherical particles has been observed. All the particles have almost uniform spherical shape. Core size nanoparticle with shell of carbon has been seen in **Fig. 3(c)**. Variation in contrast of both core and shell reflects that shell is made of material having low atomic mass that may be carbon. Approximate particle size determined and came out to be around 220 nm. As evident from **Fig. 3(b)**, silicon also possesses porous nature.

XRD measurement was performed on the residual soot of BC (**Fig. 4**). XRD results show the presence of mainly carbon and silicon along with other impurities like silica and phosphorous. Carbon is found to exist in two main phases, one which have characteristic peaks at $2\theta = 24.26^\circ$ & 31.733° positions. These peaks correspond to (110) and (111) planes of orthorhombic phase (PCPD file no.89-8493), respectively. Second phase, hexagonal structure (PCPD file no. 26-1083) was evident by the observation of peak at $2\theta = 43.9^\circ$ position which corresponds to (0010) plane of HCP carbon. Apart from carbon, silicon found to have their peaks at $2\theta = 22.9^\circ$, 49.9° , and 80.266° positions and assigned to (120), (412) and (640) planes of silicon of tetragonal structure (PCPD file no. 39-0973), respectively.

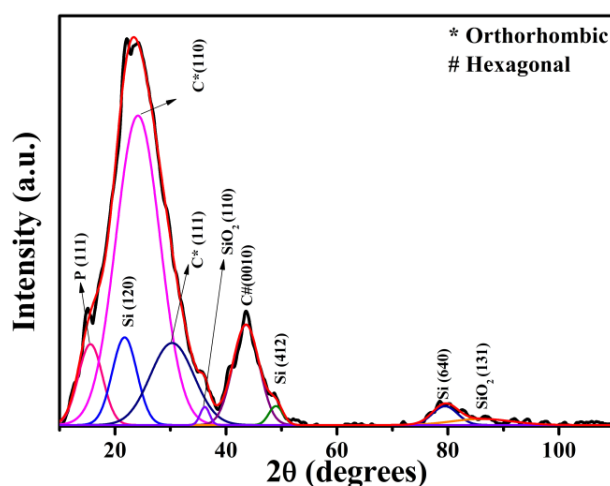


Fig. 4. XRD results for pyrolysed bamboo at 1250 $^\circ$ C.

These multiple peaks confirm that silicon present in BC soot is polycrystalline in nature. In previous published reports, silicon rarely exists alone in elemental state and forms compounds easily with various other elements present [44]. Here, we observed that pure silicon formed. However, silica is also present in very small quantity. Two

peaks observed at $2\theta = 36.54^\circ$, and 83.83° positions (PCPD file no. 89-8934) are assigned to be of silica. In earlier reports, along with main elements and their compounds, a large variety of different minerals have found in the BC depending on the geographical location where bamboo have grown and the processing route/conditions it went through [45]. In the reported pyrolyzed BC, we found the appreciable amounts of phosphorous. One single peak observed at $2\theta = 15.263^\circ$ position is assigned to (111) plane of phosphorous (PCPD file no. 75-0577).

In order to confirm the exclusive extraction of silicon only from the bamboo grown Delhi NCR region, EDX X-ray mapping on the pyrolyzed BC, residual pyrolyzed soot of the bamboo grown outside Delhi region, have been performed as shown in Fig. 5.

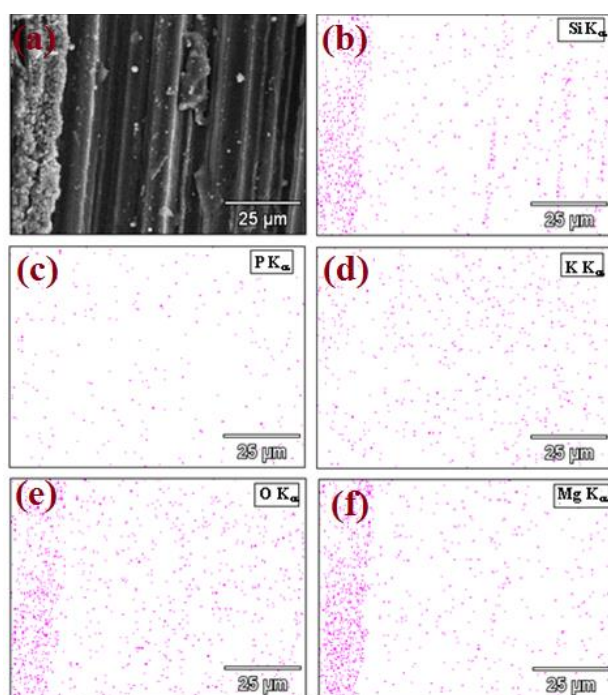


Fig. 5. EDX spectral mapping of elements present in bamboo charcoal in area shown in image (a).

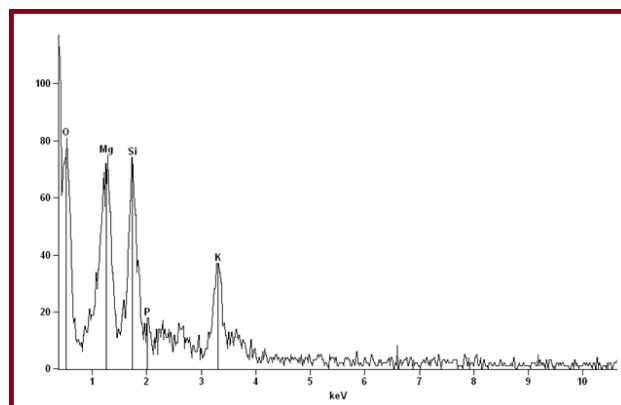


Fig. 6. Resulting EDX spectrum from mapped area revealing that Mg, Si, P, and K are the main elements present with oxygen.

Image in Fig. 5(a) shows an inspection area within where EDX mapping carried out by rastering the incident electron beam to produce the map of elements present. The tabulated (Table 1) results provide a semi-quantitative estimation of the elemental composition in the inspection area in units of both weight percent and atomic percent. The mapping reveals that Si, Mg, K and P are the main elements present within the inspection field. Si is being the third most abundant element. In Fig. 5, the maps of Si, P, K, O and Mg are shown individually and depicts that oxygen is present more in inspection area where Si and Mg are more abundant. P and K have been randomly distributed. This may be due the formation of anhydrous magnesium silicate.

Table 1. Tabulated results of EDX mapping area (Fig. 5a) revealing that Mg, Si, P, and K are the main elements present with oxygen, in pyrolysed bamboo charcoal (BC).

Element Line	Net Counts	Weight %	Weight % Error	Atom %	Atom % Error	Formula
O K α	1524	54.18	+/- 3.80	68.31	+/- 4.80	O
Mg K α	964	15.58	+/- 1.31	12.93	+/- 1.09	Mg
Si K α	882	14.71	+/- 1.37	10.56	+/- 0.98	Si
Si L α 1	0	---	---	---	---	---
P K α	79	1.37	+/- 0.61	0.89	+/- 0.40	P
P L α 1	0	---	---	---	---	---
K K α	526	14.16	+/- 1.88	7.30	+/- 0.97	K
K L α 1	0	---	---	---	---	---
Total		100.00		100.00		

Catalyst free synthesis of pure crystalline Si as well as Si nanostructures in BC was made by the pyrolysis of bamboo which was grown in Delhi NCR region. Growth mechanism of these structures can be understood as: first, during the pyrolysis at temperature below 100°C water vapors present in bamboo get released and subsequently large amount of CO_2 and CO gases released at temperature in the range 250°C - 400°C [46]. As temperature was raised above 700°C , aromatic rings, present in parenchyma, start rearranging and get converted into BC which has long-range graphitic order. However, scaffold of the bamboo remained unchanged but only carbon atoms rearranged their position. This resulted in the crystal structure change as evident from XRD pattern. During the pyrolysis, simultaneous aggregation as well as surface diffusion of atomic Si occurred on the wall/surface of BC and then Si atoms got trapped in the pore of BC. This resulted in the formation of Si nanoparticles. At high temperature migration of silicon particles is also possible. If this happened, then clustering of Si nanoparticles occurred as evident from Fig. 2(c). In present case, synthesis temperature is $\sim 1250^\circ\text{C}$ much lower than that of required for the formation of β -phase SiC [47.] and release of CO_2 & CO gases at this temperature prevents the formation of SiC. This resulted in the formation of pure silicon nanoparticles. Small fractions of Si nanoparticle get oxidized during the cooling which was evident from XRD pattern.

Conclusion

In present report, synthesis of pure polycrystalline silicon nanoparticles embedded in bamboo charcoal has been demonstrated. By adopting the green route for synthesis,

core-shell nanoparticles of almost uniform morphology have been synthesized along with formation of bamboo charcoal. These nanoparticles and bamboo charcoal were found to have porous structure. By estimating the fractional quantity; it was found that purity of silicon also depends on the geographical or soil condition of the region where bamboo grows. We envision that the present route for synthesizing Si/SiO₂ could pave the way for producing the low-cost solar grade silicon for photovoltaics.

Acknowledgements

We acknowledge the facilities of Advance Instrumentation Center, DTU and Mr. Sandeep Mishra for his assistance during the SEM, EDX and XRD measurements.

Reference

- Varlamov, S.; Dore, J.; Evans, R.; Ong, D.; Eggleston, B.; Kunz, O.; Schubert, U.; Young, T.; Huang, J.; Soderstrom, T.; Omaki, K.; Kim, K.; Teal, A.; Jung, M.; Yun, J.; Pakhruddin, Z. M.; Egan, R.; Green, M. A. *Solar Energy Materials & Solar Cells* **2013**, *119*, 246.
DOI: [10.1016/j.solmat.2013.08.001](https://doi.org/10.1016/j.solmat.2013.08.001)
- Ramos, A.; del Cañizo, C.; Valdehita, J.; Zamorano, J. C.; Rodríguez, A.; Luque, A. *Silicon for the Chemical and Solar Industry XI* **2012**, 25.
- Leblanc, D.; Hovington, P.; Kim, C.; Guerfi, A.; Belanger, D.; Zaghib, K. *Journal of Power Sources* **2015**, *299*, 529.
DOI: [10.1016/j.jpowsour.2015.09.040](https://doi.org/10.1016/j.jpowsour.2015.09.040)
- Feng, J.; Zhang, Z.; Ci, L.; Zhai, W.; Ai, Q.; Xiong, S. *Journal of Power Sources* **2015**, *287*, 177.
DOI: [10.1016/j.jpowsour.2015.04.051](https://doi.org/10.1016/j.jpowsour.2015.04.051)
- Veliscek, Z.; Perse, L.S.; Dominko, R.; Kelder, E.; Gaberscek, M. *Journal of Power Sources* **2015**, *273*, 380.
DOI: [10.1016/j.jpowsour.2014.09.111](https://doi.org/10.1016/j.jpowsour.2014.09.111)
- Faro, M.J. Lo.; D'Andrea, C.; Messina, E.; Fazio, B.; Musumeci, P.; Franzò, G.; Gucciardi, P.G.; Vasi, C.; Priolo, F.; Iacona, F.; Irrera, A. *Thin Solid Films* **2015**.
DOI: [10.1016/j.tsf.2015.11.028](https://doi.org/10.1016/j.tsf.2015.11.028)
- Chang, J.B.; Huang, X.K.; Zhou, G.H.; Cui, S.M.; Hallac, P.B.; Jiang, J.W.; Hurley, P.T.; Chen, J. H. *Adv. Mater.* **2014**, *26*, 758.
DOI: [10.1002/adma.201302757](https://doi.org/10.1002/adma.201302757)
- Jang, H.; Pell, L.E.; Korgel, B.A.; English, D.S.; *J. Photochem. Photobiol. A* **2003**, *158*, 111.
DOI: [10.1016/S1010-6030\(03\)00024-8](https://doi.org/10.1016/S1010-6030(03)00024-8)
- Wang, G.; Yau, S.-T.; Mantey, K.; Nayfeh, M.H. *Optics Commun.* **2008**, *281*, 1765.
DOI: [10.1016/j.optcom.2007.07.070](https://doi.org/10.1016/j.optcom.2007.07.070)
- Hao, X.J.; Cho, E.-C.; Scardera, G.; Shen, Y.S.; Bellet-Amalric, E.; Bellet, D.; Conibeer, G.; Green, M.A. *Solar Energ. Mater. Solar Cells* **2009**, *93*, 1524.
DOI: [10.1016/j.solmat.2009.04.002](https://doi.org/10.1016/j.solmat.2009.04.002)
- Shiratani, M.; Koga, K.; Ando, S.; Inoue, T.; Watanabe, Y.; Nunomura, S.; Kondo, M.; *Surf. Coat. Technol.* **2007**, *201*, 5468.
- Si, Q.; Hanai, K.; Imanishi, N.; Kubo, M.; Hirano, A.; Takeda, Y.; Yamamoto, O. *J. Power Sources* **2009**, *189*, 761.
DOI: [10.1016/j.jpowsour.2008.08.007](https://doi.org/10.1016/j.jpowsour.2008.08.007)
- Zheng, Y.; Yang, J.; Wang, J.; NuLi, Y. *Electrochim. Acta* **2007**, *52*, 5863.
DOI: [10.1016/j.electacta.2007.03.013](https://doi.org/10.1016/j.electacta.2007.03.013)
- Faro, M.J. Lo.; D'Andrea, C.; Messina, E.; Fazio, B.; Musumeci, P.; Franzò, G.; Gucciardi, P.G.; Vasi, C.; Priolo, F.; Iacona, F.; Irrera, A. *Thin Solid Films* **2015**.
DOI: [10.1016/j.tsf.2015.11.028](https://doi.org/10.1016/j.tsf.2015.11.028)
- Shin, J. H.; Kim, Y.D.; Choi, H. J.; Ryu, S. W.; Lee, H. *Solar Energy Materials & Solar Cells* **2014**, *126*, 1.
DOI: [10.1016/j.solmat.2014.03.002](https://doi.org/10.1016/j.solmat.2014.03.002)
- Kim, H.; Kumar, M.D.; Kim, J. *Sensors and Actuators A* **2015**, *233*, 290.
DOI: [10.1016/j.sna.2015.07.026](https://doi.org/10.1016/j.sna.2015.07.026)
- Xu, C.; Li, W.; Wei, Y.; Cui, X. *Materials & Design* **2015**, *83*, 745.
DOI: [10.1016/j.matdes.2015.06.036](https://doi.org/10.1016/j.matdes.2015.06.036)
- Shin, D.; Banerjee D. *International Journal of Heat and Mass Transfer* **2015**, *84*, 898.
DOI: [10.1016/j.ijheatmasstransfer.2015.01.100](https://doi.org/10.1016/j.ijheatmasstransfer.2015.01.100)
- Shariatmadar, F. S.; Nia, M. M. *Polymer Composites* **2012**, 1189.
DOI: [10.1002/pc.22248](https://doi.org/10.1002/pc.22248)
- Kandula, S.; Jeevanandam, P. *Eur. J. Inorg. Chem.* **2015**, 4260
DOI: [10.1002/ejic.201500444](https://doi.org/10.1002/ejic.201500444)
- Muller, A.; Ghosha, M.; Sonnenschein, R.; Woditsch, P. *Materials Science and Engineering B* **2006**, *134*, 257.
DOI: [10.1016/j.mseb.2006.06.054](https://doi.org/10.1016/j.mseb.2006.06.054)
- Braga, A.F.B.; Moreira, S.P.; Zampieri, P.R.; Bacchin, J.M.G.; Mei, P.R. *Solar Energy Materials & Solar Cells* **2008**, *92*, 418.
DOI: [10.1016/j.solmat.2007.10.003](https://doi.org/10.1016/j.solmat.2007.10.003)
- Bathery, B. R.; Cretella, M. C. *J. of Materials Science* **1982**, *17*, 3077
DOI: [10.1007/BF01203469](https://doi.org/10.1007/BF01203469)
- Balaji, S.; Du, J.; White, C.M.; Ydstie, B. E. *Powder Technology* **2010**, *199*, 23.
DOI: [10.1016/j.powtec.2009.04.022](https://doi.org/10.1016/j.powtec.2009.04.022)
- Hosseini, M. M.; Shao, Y.; Whalen, J. K. *Biosystems Engineering* **2011**, *110*, 351.
DOI: [10.1016/j.biosystemseng.2011.09.010](https://doi.org/10.1016/j.biosystemseng.2011.09.010)
- Concepcion, R.; Maria, D.; Alcal, A.; Jose, M. C. *J. Am. Ceram. Soc.* **2004**, *87*, 75.
DOI: [10.1111/j.1551-2916.2004.00075.x](https://doi.org/10.1111/j.1551-2916.2004.00075.x)
- Ahmed, Y.M.Z.; Ewais, E.M.; Zaki Z. I. *J. of University of Science and Technology Beijing* **2008**, *15*, 307.
DOI: [10.1016/S1005-8850\(08\)60058-4](https://doi.org/10.1016/S1005-8850(08)60058-4)
- Guo, X. Z.; Zhang, L. J.; Yan, L. Q.; Yang, H.; Zhu L. *Materials Letters* **2010**, *64*, 331.
DOI: [10.1016/j.matlet.2009.11.006](https://doi.org/10.1016/j.matlet.2009.11.006)
- Fan, Y.; Wang, B.; Yuan, S. H.; Wu, X. H.; Chen, J.; Wanga, L. *Bioresource Technology* **2010**, *101*, 7661.
DOI: [10.1016/j.biortech.2010.04.046](https://doi.org/10.1016/j.biortech.2010.04.046)
- Tan, Z.; Sun, L.; Xiang, J.; Zeng, H.; Liu, Z.; Hu, S.; Qiu, J. *Carbon* **2012**, *50*, 362.
DOI: [10.1016/j.carbon.2011.08.036](https://doi.org/10.1016/j.carbon.2011.08.036)
- Liao, P.; Ismael, Z. M.; Zhang, W. B.; Yuan, S. H.; Tong, M.; Wang, K.; Bao, J. *Chemical Engineering J.* **2012**, *339*, 195.
DOI: [10.1016/j.cej.2012.04.092](https://doi.org/10.1016/j.cej.2012.04.092)
- Dhanekar, S.; Jain, S.; *Biosensors and Bioelectronics* **2013**, *41*, 54.
DOI: [10.1016/j.bios.2012.09.045](https://doi.org/10.1016/j.bios.2012.09.045)
- Costa, V. T.; Lehto, J. V.P.; Palma, R. J. M.; Duart, J. M. M. *Microporous and Mesoporous Materials* **2008**, *111*, 636.
DOI: [10.1016/j.micromeso.2007.07.027](https://doi.org/10.1016/j.micromeso.2007.07.027)
- Wagner, R.S.; Ellis, W.C. *Appl. Phys. Lett.* **1964**, *4*, 89.
DOI: [10.1063/1.1753975](https://doi.org/10.1063/1.1753975)
- Kim, B.J.; Tersoff, J.; Kodambaka, S.; Reuter, M.C.; Stach, E.A.; Ross, F. M. *Science*. **2008**, *322*, 1070.
DOI: [10.1126/science.1163494](https://doi.org/10.1126/science.1163494)
- Schmidt, V.; Senz, S.; Gösele, U. *Nano Lett.* **2005**, *5*, 931.
DOI: [10.1021/nl050462g](https://doi.org/10.1021/nl050462g)
- Kim, K.; Park, J.-H.; Doo, S.-G.; Nam, J.-D.; Kim, T. *Thin Solid Films* **2009**, *517*, 4184.
DOI: [10.1016/j.tsf.2009.02.016](https://doi.org/10.1016/j.tsf.2009.02.016)
- Gracin, D.; Etlinger, B.; Juraic, K.; Gajovic, A.; Dubcek, P.; Bernstorff, S. *Vacuum* **2008**, *82*, 205.
DOI: [10.1016/j.vacuum.2007.07.039](https://doi.org/10.1016/j.vacuum.2007.07.039)
- O. Akcikir, J. Therrien, G. Belomoin, N. Barry, J.D. Muller, E. Gratton, M. Nayfeh, *Appl. Phys. Lett.* **2000**, *76*, 1857.
DOI: [10.1063/1.126191](https://doi.org/10.1063/1.126191)
- Wang, G.; Yau, S.-T.; Mantey, K.; Nayfeh, M.H. *Optics Commun.* **2008**, *281*, 1765.
DOI: [10.1016/j.optcom.2007.07.070](https://doi.org/10.1016/j.optcom.2007.07.070)
- Muramoto, J.; Inumaru, T.; Nakata, Y.; Okada, T.; Maeda, M. *Appl. Phys. A* **1999**, *69*, S239.
DOI: [10.1007/s003399900224](https://doi.org/10.1007/s003399900224)
- Wu, M.H.; Mu, R.; Ueda, A.; Henderson, D.O.; Vlahovic, B. *Mater. Sci. Eng. B* **2005**, *116*, 273.
DOI: [10.1016/j.mseb.2004.06.022](https://doi.org/10.1016/j.mseb.2004.06.022)
- Scriba, M.R.; Arendse, C.; Harting, M.; Britton, D.T. *Thin Solid Films* **2008**, *516*, 844.
DOI: [10.1016/j.tsf.2007.06.191](https://doi.org/10.1016/j.tsf.2007.06.191)
- Eranna, G. *Crystal Growth and Evaluation of Silicon for VLSI and ULSI*. CRC Press: Florida, **2014**, 6.
ISBN: [978-1-4822-3281-3](https://doi.org/10.1016/j.978-1-4822-3281-3)
- Zhu, J.; Jia, J.; Kwong, F. L.; Ng, D. H. L.; Tjong, S. C. *Biomass and Bioenergy*, **2012**, *36*, 12
DOI: [10.1016/j.biombioe.2011.08.023](https://doi.org/10.1016/j.biombioe.2011.08.023)

46. Zuo, S. L.; Gao, S. Y.; Yuan, X. G., Xu, B. S. *J. of Forestry Research* **2003**, *14*, 75.
DOI: [1007-662X\(2003\)01-0075-05](https://doi.org/10.1007-662X(2003)01-0075-05).
47. Dijen, F.K.; Metselaar, R. J. *Eur Ceram Soc* **1991**, *7*, 177.
DOI: [10.1016/0955-2219\(91\)90035-X](https://doi.org/10.1016/0955-2219(91)90035-X)


Advanced Materials Letters

Copyright © 2016 VBRI Press AB, Sweden
www.vbripress.com/aml

Publish your article in this journal

Advanced Materials Letters is an official international journal of International Association of Advanced Materials (IAAM, www.iaamonline.org) published monthly by VBRI Press AB from Sweden. The journal is intended to provide high-quality peer-review articles in the fascinating field of materials science and technology particularly in the area of structure, synthesis and processing, characterisation, advanced-state properties and applications of materials. All published articles are indexed in various databases and are available download for free. The manuscript management system is completely electronic and has fast and fair peer-review process. The journal includes review article, research article, notes, letter to editor and short communications.

A Monthly Journal



VBRI Press
a rapid publication platform

Interfacial interactions between Cu and Sn nanoparticles during soldering without flux

J. Mittal^{1,2*}, K. L. Lin²

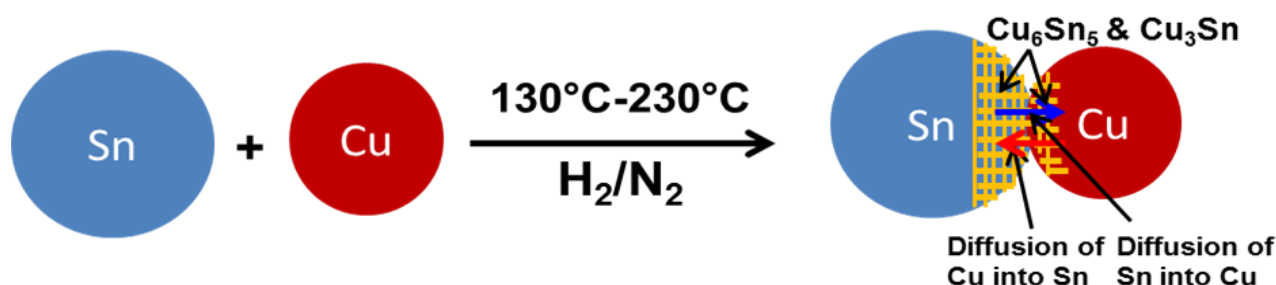
¹Amity Institute of Nanotechnology, Amity University, Noida Sector 125, Uttar Pradesh 201301, India

²Department of Material Science and Engineering, National Cheng Kung University, Tainan, Taiwan 70101, Republic of China

*Corresponding author. Tel: (+91) 1204586880 ; E-mail: jmittal@amity.edu



Table of contents



ABSTRACT

Interfacial interactions between Cu and Sn nanoparticles were studied without using chemical flux. Studies revealed the reaction between Cu and Sn and formation of intermetallic compounds when Cu and Sn nanoparticles heated between 120 °C and 230 °C under H₂/N₂. Most of the earlier soldering studies have been performed between Sn and Cu metals and films^{1,2}. However, no study has been undertaken between Cu and Sn nanoparticles. The present paper discusses the Cu-Sn interaction during heating of Cu and Sn nanoparticles. Commercial Cu and Sn nanoparticles of average size of 20 nm and 80 nm, respectively, were used in the present study. The particles were mixed randomly to enable contact between them. The heating of the nanoparticles were conducted in an infrared furnace under forming gas 5H₂/95N₂ at a rate of 25 °C/min to reach the peak temperatures of 120 °C, 150 °C, 170 °C, 190 °C, 210 °C, 230 °C, kept isothermally at the peak temperatures for 6 minutes and then cooled in furnace to room temperature. The interfacial regions were analyzed using high resolution transmission electron microscopy (HRTEM) with 200KeV beam energy. The HRTEM micrographs were further studied using Fast Fourier Transform (FFT) and inverse FFT (IFFT). Elemental analysis was carried out by energy dispersive X-ray spectroscopy (EDX) with 0.7 nm electron beam in the HRTEM. Crystal structures of the nanoparticles prior to and after heating were characterized using X-ray diffraction (XRD) and electron diffraction (ED). The heat flow during Cu-Sn interaction was measured by differential scanning calorimeter (DSC) at heating rate of 10 °C/min under argon atmosphere. Diffusion of Cu into was increased with the treatment temperature and the formation of Cu₆Sn₅ and Cu₃Sn intermetallic compounds are observed during reaction of Cu with Sn. The FFT diffraction pattern did show the existence of crystalline planes across the interface without observable amorphous diffusion zone. The electron diffraction patterns of the interface do not signify amorphous phenomenon. The prominent X-ray diffraction peaks imply that the crystallite sizes of the intermetallic compounds have grown which increases with temperature. This shows that the reactions at nano level are quite active in comparison with the bulk case. This may be linked to the higher energy at the outer layers of the nanoparticles and less activation energy of Cu diffusion in nanoparticles than bulk. The investigation of the interfacial reactions between Cu and Sn nanoparticles under H₂/N₂ shows that the interfacial reactions were driven by the massive diffusion of Cu into Sn nanoparticles which increase with treatment temperature. Cu₆Sn₅ was formed at low temperatures while Cu₆Sn₅ and Cu₃Sn were formed at high temperatures.

Keywords: Nanocrystalline metals; interfacial reactions; differential scanning calorimetry; transmission electron microscopy; energy dispersive X-ray spectroscopy.

Acknowledgements

The support of this study by the Ministry of Science and Technology (MOST) of the Republic of China (Taiwan) under Grant NSC101-2221-E006-117-MY3 is gratefully acknowledged. One of authors (J. Mittal) is grateful to MOST for his financial support under Grant NSC102-2811--E-006-048.

Reference

1. Tu, K. N.; *Mater. Chem. Phys.*, **1996**, *46*, 217.
2. Tu, K. N.; *Acta. Metall.*, **1973**, *21*, 347.

Prashant K. Sharma*

*Corresponding authot. Tel: (+91) 0326-2235918; Fax: (+91) 9471191339;
E-mail: prashantnac@gmail.com



Some smart functional nanomaterials for multifaceted applications

The elementary leaning in contemporary scientific endeavours is the attempt to smudge the limitations not only among the subareas of a specified field but also flanked by scientific fields themselves. For instance, every one accept the idea that physics and biology can work in tandem and advance our indulgent of these fields in ways that were hard to envisage even a few decades ago. With the manifestation of nanotechnology, nanoparticles are exploited owing to their impending applications in diverse phase of life. Nanoparticles are favored over micron size particles in a verity of applications not merely due to their particle size but also manifold superior properties. In this talk, synthesis of numerous multifaceted nanoparticles, their nucleation and growth mechanism are discussed in detail. The properties of these nanomaterials are also described in detail. The size dependent (i.e. quantum confinement) properties shall be also explained in detail. Futuristic advances towards the nanoparticles applications in solid state lightning, efficiency enhancement of solar cells, drug delivery, hyperthermia, MRI contrast enhancement, flat panel displays, lasing materials, and efficient gas sensors shall be described at length. For Instance, the multifunctional nanoparticles have materialized as one of the important futuristic material for variety of applications starting from data storage, security/sensors to biomedical applications. Similarly, the application of multifunctional magnetic nanoparticles in biological organisms has fashioned remarkable advances in research, diagnosis and therapy of various diseases. The multifunctional magnetic nanoparticles, capable of theragnosis, drug delivery and monitoring of therapeutic response, are expected to play a significant role in the emergence of the era of personalized medicine with much of research efforts devoted toward that goal. The present talk recapitulates the development of state-of-the-art multifunctional magnetic nanoparticles and the foremost

applications of these multifunctional magnetic nanoparticles in magnetic targeting, drug delivery, separation, and contrast agents in magnetic resonance imaging, hyperthermia and sensors.

Keywords: Multifunctional nanoparticles; LEDs; solar cells; sensors; theragnostics; nanomedicine.

Acknowledgements

PKS is thankful to Department of Science and Technology, Government of India for sanction of Fast Track Research Project for Young Scientists (Ref. No.: SR/FTP/PS-157/2011). Dr. Sharma (FRS/34/2012-2013/APH) is also thankful to Indian School of Mines, Dhanbad for grant of Major Research Project under Faculty Research Scheme. PKS is also thankful to Board of Research in Nuclear Sciences (BRNS), Department of Atomic Energy, and Government of India for major research project (Sanction No. 34/14/21/2014-BRNS/0295).

Non Mulberry silk as non-textile materials

Dipali Devi^{1*}, Bijit Talukdar¹, Saranga Dutta¹, Rashmi R Baruah¹,
Nandana Bhardwaj¹, Rangam Rajkhowa², Xungai Wang²

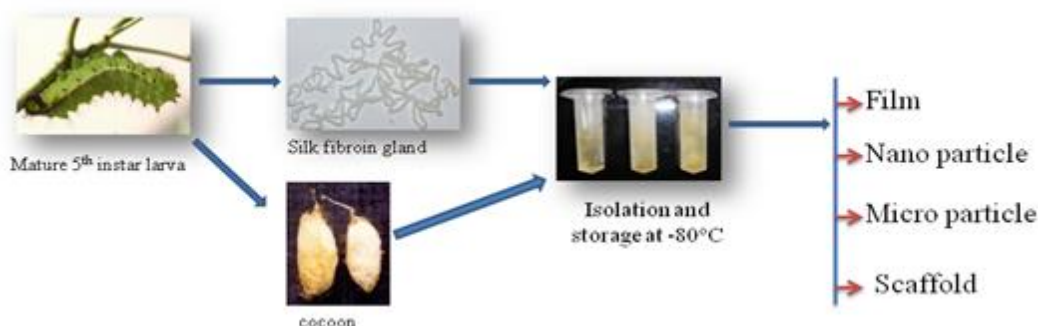
¹Institute of Advanced Study in Science and Technology, Paschim Boragaon, Guwahati, India

²Deakin University, Australia

*Corresponding author. Tel: (+91) 9678073712; E-mail: dipali.devi@gmail.com



Table of contents



Schematic representation of biomaterial fabrication

ABSTRACT

Silk from the mulberry silkworm *Bombyx mori* has been used as biomedical suture material for centuries which depart silk from traditional textile. The unique and remarkable mechanical properties of silk have promoted studies for the application in high performance materials. With improved analytical techniques, together with the advanced tools of biotechnology, a new generation of silk related materials is envisioned for medical and other non-textiles uses like cosmetics, hair replacement etc. from the silk of *Bombyx mori*. Our approach is for introducing non-mulberry silk viz. muga and Eri from of N.E. region of India for formulation of such non-textile materials owing to their high textile strength and availability. Film/nano /micro particles from gland as well as cocoon fiber silks have been fabricated using various methods. The materials were characterized using SEM, TEM, FTIR, TGA and particle size analyser. Cyto compatibility were tested using cell line. Herein, silk fibroin microparticles were fabricated via a top-down approach using a combination of wet-milling and spray drying techniques. Microparticles of mulberry silkworm (*Bombyx mori*) were also utilized for comparative studies. The fabricated microparticles were physico-chemically characterized for size, stability, morphology, chemical composition and thermal properties. The silk fibroin microparticles of all species were porous (>5µm in size) and showed nearly spherical morphology with rough surface as revealed from dynamic light scattering and microscopic studies. Non-mulberry silk microparticles maintained the typical silk-II structure with β -sheet secondary conformation with higher thermal stability. Additionally, non-mulberry silk fibroin microparticles supported enhanced cell adhesion, spreading and viability of mouse fibro-blasts than mulberry silk fibroin microparticles ($p < 0.001$) as evidenced from fluorescence microscopy and cytotoxicity studies. Furthermore, in vitro drug release from the microparticles showed a significantly sustained release over 3 weeks. Taken together, this study demonstrates promising attributes of non-mulberry silk fibroin microparticles as a potential drug delivery vehicle/micro carrier for diverse biomedical applications.

Keywords: Non-mulberry silk; fibroin; biomaterial; biomedical.

Acknowledgements

The authors duly acknowledge the Department of Biotechnology (DBT), Govt.of.India for financial support.

Reference

1. Bhardwaj, N.; Sow W. T.; Ng, K. W.; Mandal, B.B.; Cho, N. J.; *Integrative Biology*, **2015**, 7, 53.

2. Bhardwaj, N.; Devi, D.; Mandal, B. B.; *Macromolecular Bioscience*, **2015**, 15, 153.

3. Dutta,S.; Talukdar, B.; Bharali, R.; Rajkhowa, R.; Devi,D.; *Biopolymers*, **2013**, 99, 326.

4. Bhardwaja, N.; Rajkhowab, R.; Wangb, X.; Devi, D.; *International Journal of Biological Macromolecules*, **2015**, 31.

Filled carbon nanotubes: Possess exotic magnetic properties

Pawan K. Tyagi*

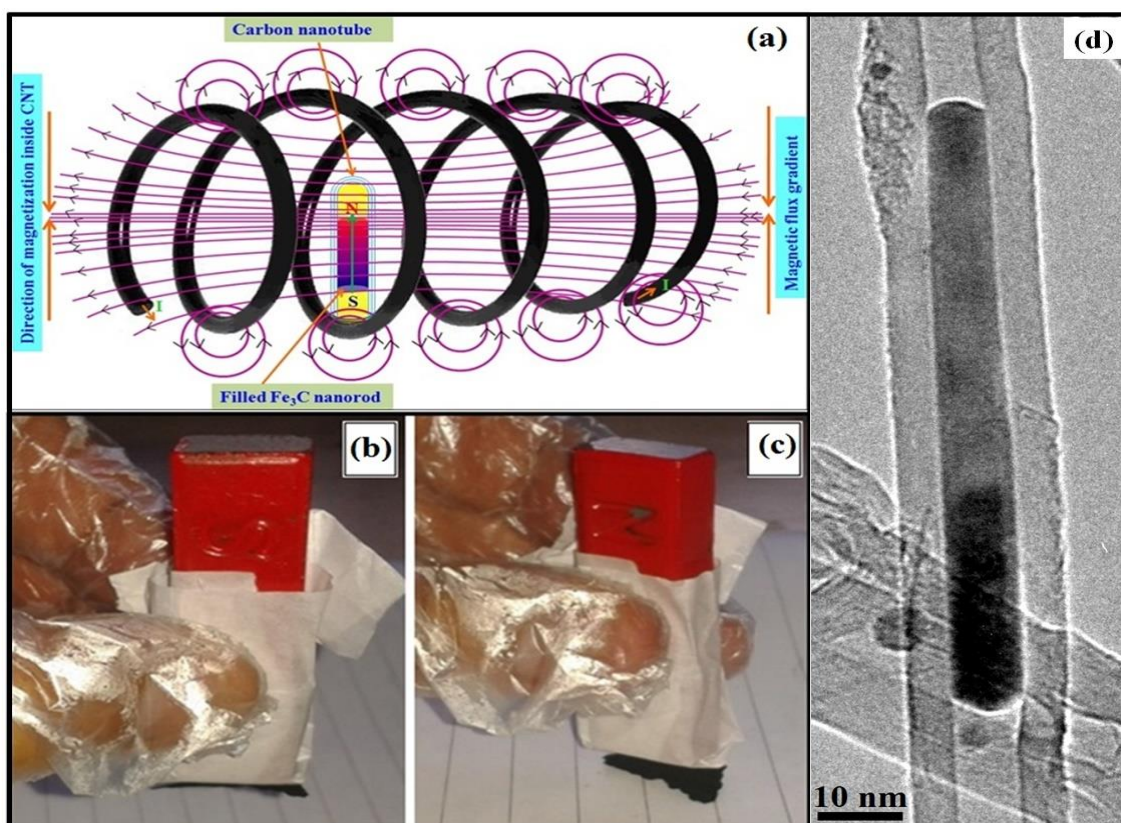
Department of Applied Physics, Delhi Technological University, Delhi, India

*Corresponding author. Tel: (+91) 11-27852212; Fax: (+91) 11- 27871023

E-mail: pawan.phy@dce.edu



Table of contents



Formation of magnetic poles in filled carbon nanotubes due to magnetic field gradient produced during growth

ABSTRACT

The filled carbon nanotubes exhibit superior electrical, mechanical and magnetic properties as compared to unfilled and used in various areas of nanotechnology such as: electro, photo and heterogeneous catalyst with high selectivity [1], magnetic data storage or magnetic resonance imaging [2] and nanotechnology in medicines [3, 4]. This has been attributed to the fact that in filled-CNT, superior physical, chemical or electronic properties of host nanotube and filled-nanomaterials have been observed. In order to further expand the applications of filled-carbon nanotube, synthesis in controlled manner which can alter the magnetic properties is needed. In this talk, I will discuss the parameters of optimized growth as well as growth mechanism of carbon nanotubes filled with Fe/Fe₃C, Ni and Co. Observations made during the characterization of filled-CNTs by using SEM, XRD, HRTEM, VSM and MFM will be discussed. This presentation will also aim to explain the confinement effect on the magnetic properties of nanorods filled inside the CNTs. Observed enhancement in the magnetic properties of nanorods is attributed to

tensile stress as well as compression present in radial direction and along the nanotube axis, respectively. Growth of such magnetized CNTs can be optimized by applying field gradient during the synthesis. This field gradient effectively dominates the direction of magnetization in filled CNTs. Here, besides detailed growth model of *in situ* filling, the mechanism of magnetization of the nanotubes will also be presented. The proposed magnetization mechanism helps in determination of easy axis of magnetization in magnetized CNTs.

Keywords: Filled-carbon nanotubes; thermal CVD; magnetic properties; growth mechanism; confinement.

Reference

1. Fu, Q.; Weinberg, G.; Su, D. S.; *Selective metals by selective washing, New Carbon Materials*, **2008**, 23, 17.
2. Ding, W.; Lou, C.; Qiu, J.; Zhao, Z.; Zhou, Q.; Liang, M.; Yang, S.; Ji, Z.; Xing, D.; *Nanomedicine: Nanotechnology, Biology and Medicine*, **2016**, 12, 235.
3. Bhirde, A. A.; Patel, V.; Gavard, J.; Zhang, G.; Sousa, A. A.; Masedunskas, A.; Leapman, R. D.; Weigert, R.; Gutkind, J. S.; Rusling, J. F.; *ACS Nano*, **2009**, 3, 307.
4. Liu, Z.; Cai, W.; He, L.; Nakayama, N.; Chen, K.; Sun, X.; Chen, X.; Dai, H.; *Nature Nanotechnology* **2007**, 2, 47.

Structure- property relationships in colloidal ITO nanoparticle thin films

Salil M. Joshi¹ and Rosario A. Gerhardt*

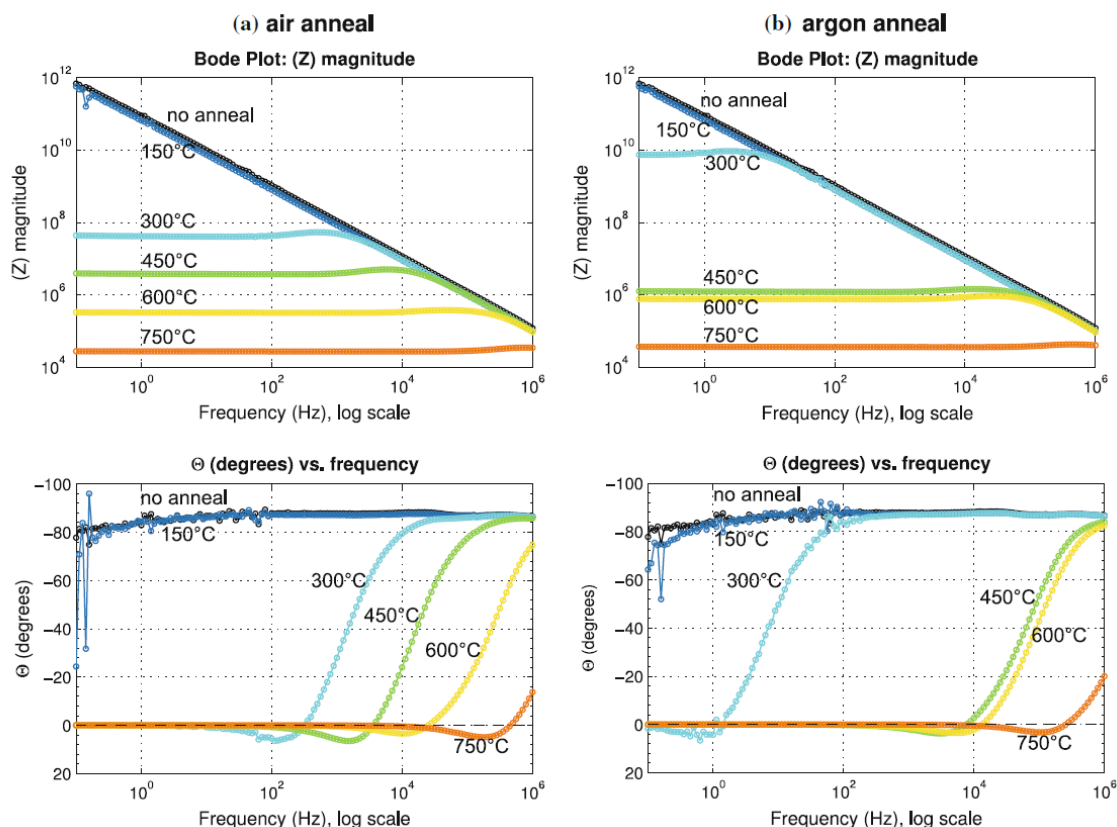
Georgia Institute of Technology, Atlanta, GA 30332-0245 USA

*Corresponding author. Tel: (+1) 4048946886; Fax: (+1) 4048949140;
E-mail: rosario.gerhardt@mse.gatech.edu



Table of contents

Eight order of magnitude changes in the impedance of a series of ITO thin films made from highly crystalline colloidal nanoparticles deposited onto quartz substrates.



Log impedance magnitude and phase angle as a function of frequency for colloidal ITO nanoparticle thin films measured after annealing at the temperatures and atmosphere indicated [3].

ABSTRACT

Indium tin oxide (ITO) is ubiquitous in all optoelectronic applications that require conducting electrodes that are transparent to visible light. In spite of much effort to identify an alternative material to replace ITO, its properties have been difficult to beat. Thus, in our research group we have focused on methods to fabricate ITO films using nanoparticles with the goal of developing ways to direct-write only the needed circuitry. This talk will describe the synthesis of ITO nanoparticles, their film formation via

spin coating as well as their structure and electrical and optical properties. Colloidal ITO single crystal nanoparticles of ~6-8 nm in diameter were synthesized following a non-aqueous method developed by Peng's group [1]. Films of ~200 nm thickness were obtained by spin coating the stable solutions onto fused quartz and /or glass substrates. The ITO films are highly transparent in the as-deposited condition, but are highly insulating electrically because of the passivating organics that are used to obtain the stable colloidal suspensions. Data for films annealed at temperatures from 150-750 °C will be used to demonstrate how changing the annealing atmosphere can result in very different electrical and optical properties that may be able to be utilized as patterned transparent coatings with different electrical properties.[2]. Impedance and dielectric spectroscopy is used to monitor the changes in the electrical properties. This technique is ideal for detecting the gradual changes observed as a function of frequency that result in orders of magnitude changes in the resistivity as the annealing temperature is increased from 150-750 °C. A microstructural model that incorporates changes in the organic coatings is proposed to account for the resistivity changes observed [3]. The best electrical resistivity obtained from these thin films so far is 0.1 Ω -cm, which is good enough for certain transparent conducting applications but needs to be improved for others. Films treated with alternating oxygen and argon plasma treatments to further improve the electrical properties, followed by air annealing at various temperatures from 150 °C to 750 °C will also be reported. The impedance results can be explained by a nested equivalent circuit that contains a parallel RL circuit inside a parallel RC circuit that changes in importance as the microstructure changes [4].

Keywords: ITO films; colloidal synthesis; impedance spectroscopy; optical properties.

Acknowledgements

The authors acknowledge the funding support from the Renewable Bioproducts Institute (formerly known as the Institute for Paper Science and Technology (IPST) for fellowship support for S.M. Joshi. R.A. Gerhardt acknowledges support from the National Science Foundation under grant DMR-1207323.

Reference

1. Narayanaswamy, A.; Xu, H.; Pradhan, N.; Kim, M.; Peng, X.; *J. Am. Chem. Soc.*, **2006**, 128, 10310.
2. Joshi, S. M.; Book, G. W.; Gerhardt, R. A.; *Thin Solid Films*, **2012**, 520, 2723.
3. Joshi, S. M.; Gerhardt, R. A.; *J Mater Sci.* **2013**, 48, 1465.
4. Joshi, S. M.; *PhD thesis*, Georgia Institute of Technology, **2013**.

Polymer nanocomposites and their applications

N. B. Singh*

Research and Technology Development Centre, Sharda University, Greater Noida 201306, India

*Corresponding author. E-mail: nbsingh43@gmail.com



ABSTRACT

Composites are one of the most widely used materials because of their adaptability to different situations and the relative ease of combination with other materials to serve specific purposes and exhibit desirable properties. The field of composites is undergoing a transformation from the use of traditional fillers (e.g. carbon fiber) to nanoscale fillers that add unique and often multifunctional properties to the neat polymer. Because nanoparticles have extremely high surface area to volume ratios and alter the mobility of polymer chains near their interfaces, even a small addition of nanoparticles has the potential to drastically transform the properties of the host polymer. A nanocomposite is a multiphase solid material where one of the phases has one, two or three dimensions of less than 100 nanometers (nm) or structures having nano-scale repeat distances between the different phases that make up the material. Polymer nanocomposites have received significant attention, both in the industry and academia during the past. The properties of nanocomposites depend on number of factors and promise new applications in many fields. In this paper we discuss the applications of Polymer nanocomposites as sensors and for purification of water.

High quality large area graphene for flexible electronics

Emre Ozan Polat, Ravinder Dahiya*

Electronics and Nanoscale Engineering, University of Glasgow, G12 8QQ, UK

*Corresponding author. Tel: (+44) 1413305653; E-mail: ravinder.dahiya@glasgow.ac.uk

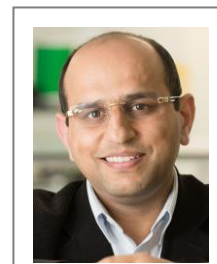
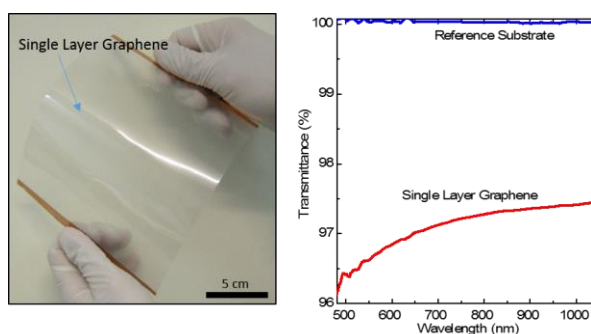


Table of contents



Single layer graphene on flexible PVC substrate and the corresponding transmittance spectrum

ABSTRACT

The surface morphology of copper foils and the transfer printing process greatly influence the performance and reliability of graphene based devices. Previous works have showed that the morphology of Cu surface is one of the key parameters to have better quality graphene films [1]. To obtain high quality graphene film with uniform properties over large area; defects, grain boundaries and other surface features should be carefully engineered. Here we demonstrate that the commercially available Cu foils can help open new pathways for large area flexible electronic systems such as electronic skin [2]. We studied the synthesis of graphene on commercially available smooth copper foils and provided a detailed comparison between graphene synthesized on ultra-smooth Cu foils and the one synthesized on the standard Cu foils in terms of structural, electrical and optical properties [3]. We observed a stark improvement in the electrical performance of the transistors realized on our graphene films and obtained more efficient transmittance modulation [4]. We propose that the copper used in the lithium-ion batteries could also be used to obtain high-quality graphene at much lower-cost, and the devices made from them have improved performance of electrical transport and optical properties.

Keywords: Graphene; flexible electronics.

Acknowledgements

This work was supported in part by the Engineering and Physical Sciences Research Council (EPSRC) through Grants EP/M002527/1 and EP/M002519/1, and in part by the European Commission under Grant PITN-GA-2012-317488-CONTEST.

Reference

1. Han, G. H.; Gunes, F.; Bae, J. J.; Kim, E. S.; S Chae, J. H.; Shin, J. *et al.*, *Nano Letters*, **2011**, *11*, 4144.
2. Dahiya, R. S.; Navaraj, W. T.; Khan, S.; Polat, E. O.; *Information Display*, **2015**, *31*, 6.
3. Polat, E. O.; Balci, O.; Kakenov, N.; Uzlu, H. B.; Kocabas, C.; Dahiya, R.; *Scientific Reports*, **2015**, *5*, 16744.
4. Polat, E. O.; Kocabas, C.; *Nano Letters*, **2013**, *13*, 5851.
- 5.

Disubstituted diphenyldithiophosphates of some 3d elements

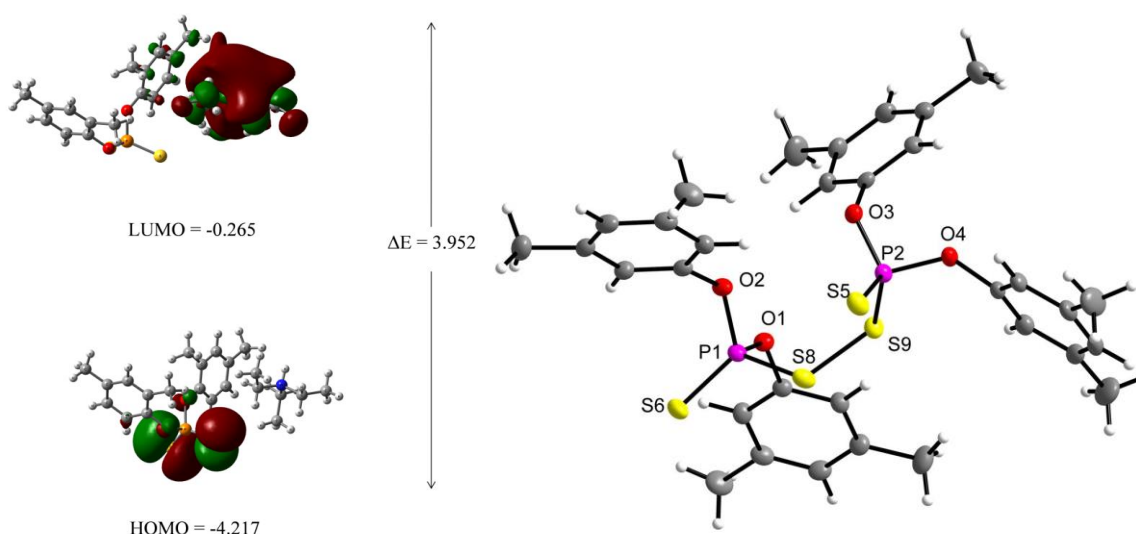
Sushil K. Pandey*, Sandeep Kumar and Mandeep Kour

Department of Chemistry, University of Jammu, Jammu (J&K) 180006, India

*Corresponding author. Tel: E-mail: kpsushil@rediffmail.com



Table of contents



ABSTRACT

Soft donor ligands such as *O,O'*-dialkyl-, alkylene- and ditolyldithiophosphoric acids are versatile ligands which show both monodentate and bidentate behavior and form chelates or salts with various metal ions. The chemistry of *O,O'*-dialkyl- and alkylendithiophosphato derivatives, which have been reviewed recently, indicates that a substantial amount of work has been done with main group and transition metals. We have recently reported for the first time new dithiophosphate ligands containing disubstituted phenyl ring instead of alkyl or alkylene moiety and disulfides of these ligands. The complexes of transition metals with newly isolated disubstituted diphenyldithiophosphates corresponding $[(\text{ArO})_2\text{PS}_2]_3\text{M}$ and $[(\text{ArO})_2\text{PS}_2]_2\text{ML}_2$ [Ar = 2,4-(CH₃)₂C₆H₃, 2,5-(CH₃)₂C₆H₃, 3,4-(CH₃)₂C₆H₃, 3,5-(CH₃)₂C₆H₃ and 4-Cl-3-(CH₃)C₆H₃; M = Cr, Fe, Co and Ni; L = C₅H₅N, 3,4-(CH₃)₂C₅H₃N and 4-(C₂H₅)C₅H₄N] were successfully isolated and characterized by elemental analyses, magnetic moment, IR, heteronuclear NMR (¹H, ¹³C and ³¹P) spectroscopy and single crystal X-ray analysis. Single crystal X-ray analysis of several complexes reveals the octahedral geometry around the metal centre. The dithio ligands are coordinated to the metal ion as a bidentate fashion *via* thiolate sulfur atoms. The theoretical studies of dimethyl diphenyldithiophosphate ligands and few complexes have been also carried to correlate the experimental and theoretical data. The biological activities of the ligands and complexes against specific bacteria and fungus have shown potential activity.

Keywords: Diphenyldithiophosphates; X-ray analysis; DFT.

High performance PVC for high altitude applications

A. K. Dixit^{1*}, Gaurav Kumar² and Arvind K. Saxena²

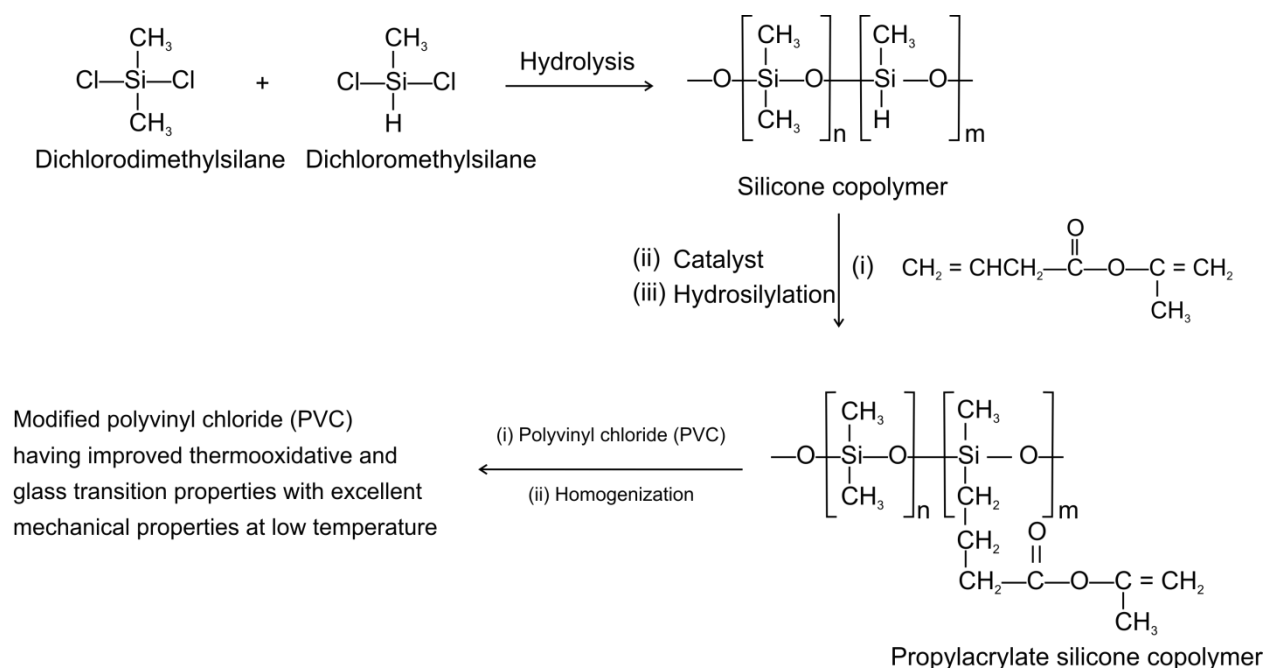
¹Department of Chemistry V.S.S.D. College, Kanpur 208002, U.P

²Defence Materials & Stores Research & Development Establishment,
G.T. Road, Kanpur 208013 (India)

*Corresponding author. Tel: (+91) 9415040226; E-mail: dixit_arvind2@yahoo.co.in



Table of contents



ABSTRACT

A co-polymer of silicone has been prepared by the hydrolysis of dichlorodimethylsilane (0.2M) and dichloromethylsilane (0.01M) and it has been reacted with allyl methacrylate in presence of Speier's catalysts to afford propyl methacryloxy pendant group bearing silicone. The hydrosilyl modified silicone has been used successfully as modifier to prepare high performance polyvinyl chloride (PVC) having low temperature performance up to -40 °C and stable in UV radiation (240 -400 nm). These polymers have shown enhanced thermo-oxidative stability as determined by Thermo gravimetric analysis (TGA). The glass transition studies were carried out using Differential scanning calorimetry (DSC). Mechanical properties of these polymers were also studied and found highly promising. The Scanning electron microscopy (SEM) and Atomic force microscopy (AFM) studies have also been carried out for these modified PVC, which showed the uniform distribution of silicone in PVC with chemical interaction of acrylate groups in the ratio of 85:15.

Keywords: Polyvinylchloride; organosilicones; allylmethacrylate; organic polymer.

Acknowledgements

Thanks are due to Director, DMSRDE for necessary encouragement and providing laboratory facilities to facilitate the work. We are also thankful to IPAC lab of Shriram Poly Tech, Gurgaon to carry-out physical, mechanical and analytical studies.

Reference

1. Pethrick, R. A.; Ballada, A.; Zaikov, G. E.; *Handbook of Polymer Research: Monomers, Oligomers, Polymers and Composites*, Nova Publishers, **2007**, 18.

2. Rochow, E.; *An Introduction Chemistry of the Silicones*, Read Books, **2008**, 79.
3. Rath, T.; Kumar, S.; Mahaling, R N.; Mukherjee, M.; Das, C. K.; Pandey, K. N.; Saxena, A. K.; *J. Appl. Polym. Sci.* **2007**, *104*, 3758.
4. Bose, S.; Mukherjee, M.; Rath, T.; Das, C. K.; Saxena, A. K.; *J. Reinf. Plast. Comp.* **2009**, *28*, 15.
5. Saxena, A. K.; Bisaria, C. S.; Saxena, A. K.; *J. Appl. Organo. Chem.* **2010**, *24*, 251.

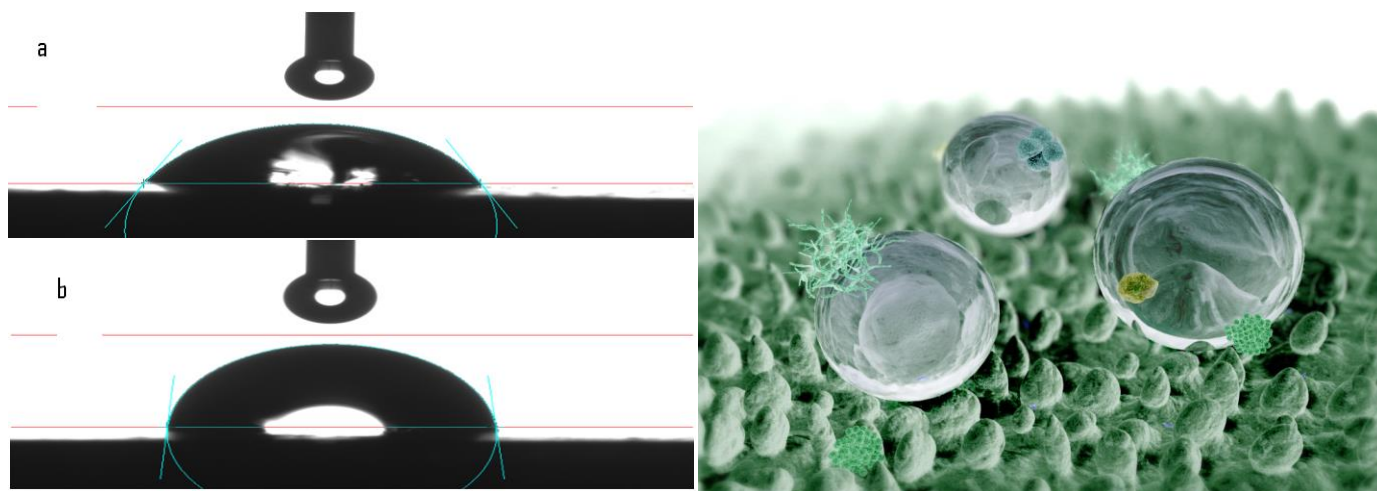
Self assembling nano films on metal surface as corrosion inhibitors

Susai Rajendran*

Professor of Chemistry, RVS School of Engineering and Technology, Dindigul 624005, India

*Corresponding author. Tel: (+91) 9443631628; E-mail: susairajendran@gmail.com

Table of contents



ABSTRACT

Nanoparticles have special properties such as optical, electrical, magnetic and thermal conductivity. So they have special applications in many fields. The synthesis and characterization of nano particles have attracted the attention of many researchers. Many chemical compounds, natural and synthetic have the ability to self-assemble on many surfaces. These self-assembled nano layers are hydrophobic in nature. These hydrophobic surfaces have high contact angle, poor adhesiveness, poor wettability and low solid surface free energy. Such hydrophobic surfaces are good candidates for development of anticorrosive surfaces, raincoats and water repellent glass window panes of cars. Self-assembling nano layers of many compounds such as glycine, many surfactants including sodium dodecylsulphate and natural products including aqueous extract of banana peels have been formed on metal surfaces like carbon steel and aluminium by simple immersion method. The corrosion inhibitive nature of the nanofilms has been evaluated by weight loss method. The mechanistic aspects of corrosion inhibition have been studied by electrochemical studies such as polarization study and AC impedance spectra. The protective film has been analyzed by fluorescence spectra and FTIR spectra. The surface morphology has been investigated by SEM and EDAX. The nanofilm has been studied by AFM. The hydrophobicity has been established by contact angle measurement. The self-cleaning effect of the nano films can be compared with the self-cleaning effect of lotus effect.

Keywords: Self-assembling nano film; corrosion inhibition; self-cleaning effect, lotus effect, hydrophobicity.

Ultrasonic and thermal characterization of the nanoparticle based advanced materials

Raja Ram Yadav*

Department of physics, University of Allahabad, 211002, India

*Corresponding author. E-mail: rryadav1@rediffmail.com

ABSTRACT

For any material characterization scheme, study of ultrasonic propagation behaviour in materials at different physical conditions is prerequisite. Now it has become possible to characterize the materials for advanced technology e.g. nanostructured materials, intermetallics, nanofluids, nanocomposites, liquid crystalline materials by ultrasonic methods. In this present investigation, theoretical study of thermoelectric nanowires has been done to develop ultrasonic mechanism to characterize diameter dependent properties. In experimental part, synthesis of CrO₂ nanoparticles based PVP nanofluids is prepared. Size of nanoparticles and their distributions using ultrasonic spectroscopy are determined. Results are comparable with the TEM measurements.

Luminescence Spectral Studies of Tm^{3+} ions doped Lead Tungsten Tellurite Glasses For Visible Red and NIR applications

M. Venkateswarlu, Sk. Mahamuda, K. Swapna, A. Srinivasa Rao, A. Mohan Babu, Suman Shakya, D. Haranath, G. Vijaya Prakash



PII: S0022-2313(15)30092-2
DOI: <http://dx.doi.org/10.1016/j.jlumin.2016.03.006>
Reference: LUMIN13884

To appear in: *Journal of Luminescence*

Received date: 12 June 2015
Revised date: 8 February 2016
Accepted date: 2 March 2016

Cite this article as: M. Venkateswarlu, Sk. Mahamuda, K. Swapna, A. Srinivasa Rao, A. Mohan Babu, Suman Shakya, D. Haranath and G. Vijaya Prakash Luminescence Spectral Studies of Tm^{3+} ions doped Lead Tungsten Tellurite Glasses For Visible Red and NIR applications, *Journal of Luminescence* <http://dx.doi.org/10.1016/j.jlumin.2016.03.006>

This is a PDF file of an unedited manuscript that has been accepted for publication. As a service to our customers we are providing this early version of the manuscript. The manuscript will undergo copyediting, typesetting, and review of the resulting galley proof before it is published in its final citable form. Please note that during the production process errors may be discovered which could affect the content, and all legal disclaimers that apply to the journal pertain.

Luminescence Spectral Studies of Tm³⁺ ions doped Lead Tungsten Tellurite Glasses**For Visible Red and NIR applications**

**M.Venkateswarlu¹, Sk. Mahamuda¹, K. Swapna¹, A. Srinivasa Rao^{*1,2}, A. Mohan Babu³,
Suman Shakya⁴, D.Haranath⁵ and G. Vijaya Prakash⁴**

¹Department of Physics, K L University, Green Fields, Vaddeswaram-522 502, Guntur (Dt.), A P, India

²Department of Applied Physics, Delhi Technological University, Bawana Road, New Delhi-110 042, India

³Department of Physics, Chadalahada Ramanamma Engineering College, Renigunta Road,
Tirupati-517 506, A.P, India

⁴Nanophotonics Laboratory, Department of Physics, Indian Institute of Technology-Delhi, Hauz Khas,
New Delhi-110 016, India.

⁵CSIR-National Physical Laboratory, Dr. K. S. Krishnan Marg, Pusa Road, New Delhi-110 012. India.

***Corresponding author, E-mail: drsallam@gmail.com, Tel: +91 85860 39007, Fax: +91 01127871023**

Abstract

Lead Tungsten Tellurite (LTT) glasses doped with different concentrations of Tm³⁺ ions of composition (60-x) TeO₂ + 25 WO₃ + 15 PbF₂ + x Tm₂O₃ (Here x=0.1, 0.5, 1.0, 1.5, 2.0, 2.5 mol %) were prepared by using melt quenching technique and characterized through optical absorption, photoluminescence and decay spectral studies to know the feasibility of using these glasses as luminescent devices in visible Red and NIR regions. Judd-Ofelt (J-O) theory has been applied to the optical absorption spectral profiles to calculate the J-O intensity parameters Ω_{λ} ($\lambda=2, 4$ and 6) and consecutively used to evaluate various radiative properties such as radiative transition probability (A_R), radiative lifetimes (τ_R) and branching ratios (β_R) for the prominent luminescent levels. The luminescence spectra for all the LTT glass samples have two intense peaks in bright red and near Infrared regions at 650 nm ($^1G_4 \rightarrow ^3F_4$) and 800 nm ($^3H_4 \rightarrow ^3H_6$) respectively for which effective band widths ($\Delta\lambda_p$), experimental branching ratios (β_{exp}) and stimulated emission cross-sections (σ_{se}) are evaluated. The decay profiles for all the glasses are recorded to measure the quantum efficiency by coupling the radiative with experimental lifetimes. From the measured emission cross-sections, quantum efficiency and CIE chromaticity co-ordinates, it was found that 0.5 mol% of Tm³⁺ ions doped LTT glass is most suitable for generating bright visible red and NIR lasers to operate at 650 and 800 nm respectively.

Keywords: Thulium, Glasses, JO parameters, Optical materials, Luminescence, Optical properties

1. Introduction

The upcoming research in the field photonics demands in search of new materials suitable for space applications with light weight, low volume (resulting in much reduced payload), immunity to electromagnetic interference, capability of operating in harsh environments and practically unlimited bandwidths [1]. Since last decade, the search for such photonic devices increases rapidly in the field of space systems. Among the photonic materials, glass being an excellent homogenised medium with high rare earth solvability, plays an important role because of its unique structural, thermos-mechanical and thermos-dynamical features. Apart from this, the rare earth doped glassy materials with their well-defined energy levels are useful to develop new laser systems, tuneable colour emissions suitable for white light generation [2-9]. Several key photonic devices are made of non-silica based oxide glasses belonging to the phosphate / borate / germanate / tellurite systems. Although these glass systems are not applied for mass production due to high cost of raw materials (compared to silicate), they possess excellent transmission bandwidth in the IR wavelength region (up to 5 μm) when compared with silica based glasses. Compared to other non-oxide glasses, non-silica based oxide glasses are non-hygroscopic with higher glass stability and corrosion resistive. These features patronages their usage in ambient air without any degradation to their transparency. Among all the oxide glasses, tellurite glasses exhibit lowest phonon energy around 780 cm^{-1} with large linear and nonlinear refractive indices [10]. Tellurium based materials became very interesting because of their wide band gap, large third order optical susceptibilities [11,12] and a distorted structure which consist of asymmetric covalent Te-O bonds [13]. These remarkable properties make these materials suitable for a variety of technical and industrial applications such as deflectors [14], tuneable filters [15], optical storage materials [16], laser devices [17], gas sensors [18], optical fibers, quantum electronic devices and sensor systems [19]. Being a conditional glass former, tellurium oxide individually cannot form a glass under normal quenching conditions without the accumulation of a network modifiers or intermediates such as heavy metal oxides, alkalis or halogens which can enhance the glass forming ability [20]. Hence the addition of tungsten oxide (WO_3) as a network/glass modifier or an intermediate oxide to the tellurite glasses gives several beneficial properties, such as doping with rare earth elements in a wide range, amending the composition by a 3rd, 4th and even 5th component, increasing the chemical stability and devitrification resistance. Moreover, In contrast to other tellurite glasses, tungsten-tellurite glasses possess higher values of phonon energy and glass transition temperature. Addition of the PbF_2 to $\text{TeO}_2\text{-WO}_3$ glass system increases the mechanical

strength and makes them stable in air as well as in moisture conditions. The presence of PbF_2 in glass decreases the transition temperature and increases the glass transparency up to MID-IR region. Due to the high polarizability of Pb^{2+} ions, the PbF_2 based glasses possess high refractive index, wide transmission range with a good number of applications in photonic devices. The fluorine ions present in PbF_2 can create non bridging oxygen atoms and F^- sites which are responsible for the local environment produced around the rare earth ions. The presence of PbF_2 in a glass also suppresses the OH^- content & phonon energies of the glasses which lead to increase the quantum efficiency of the glass [21-25]. Considering the scientific patronages offered by the lead fluoride, tungsten and tellurium oxides, for the present work we have prepared a germane glassy system namely Lead Tungsten Tellurite (LTT) glass.

In the field of colour tuneable emission, lot of efforts are being dedicated for the improvement of materials which can emit white light. Usually, white light is obtained by mixing Red-Green-Blue (RGB) (monochromatic light sources) colours. The most frequent method of getting RGB light emissions is to include a variety of rare earth ions with colourful emissions. For example, white light emission is observed in the triply doped Yb^{3+} , Tm^{3+} and Er^{3+} system with 980 nm excitation, in which blue emission is from Tm^{3+} ions due to the transitions $^1\text{D}_2 \rightarrow ^3\text{F}_4$, $^1\text{G}_4 \rightarrow ^3\text{H}_6$, green and red emissions are from Er^{3+} ions due to the transitions $^2\text{H}_{11/2}$ ($^4\text{S}_{3/2}$) \rightarrow $^4\text{I}_{15/2}$, $^4\text{F}_{9/2} \rightarrow ^4\text{I}_{15/2}$ respectively [26]. Even though green and red emissions can also ($^1\text{D}_2 \rightarrow ^3\text{H}_5$, $^1\text{G}_4 \rightarrow ^3\text{F}_4$) be produced from Tm^{3+} ion doped materials, but the main drawback is that these transitions are very weak due to low transition probabilities [26]. Subsequently, if the transition probabilities of these levels of Tm^{3+} ion ($^1\text{D}_2$ and $^1\text{G}_4$) could be sufficiently changed, the RGB light emissions from a single activator (Tm^{3+}) can be possible. Tm^{3+} ions doped materials are not only have the importance in the colour tunability but also have innumerable potential applications in the NIR and MID-IR regions, because of the $^3\text{F}_4 \rightarrow ^3\text{H}_6$ transition (1.8-2.2 μm). Laser beam in this wavelength range has several applications such as laser microsurgery (high quality laser is required for tissue cutting and welding and this is possible due to high absorption of water in this spectral region), environment monitoring, Light Detection and Ranging (LIDAR), Optical Parametric Oscillation (OPO) pump sources, coherent Doppler velocimetry [27-31]. The MID-IR laser emission shown by Tm^{3+} ion doped materials became popular because they possess a strong absorption spectrum that has been in good overlap with the luminescence band of commercially accessible AlGaAs laser diodes. Over and above, the energy level structure of Tm^{3+} ion encourages cross relaxation process ($^3\text{H}_4 + ^3\text{H}_6 \rightarrow ^3\text{F}_4 + ^3\text{F}_4$) resulting in improving

the quantum efficiency of materials [32]. Due to these spectacular characteristic features, the Tm^{3+} doped materials have gained so much of importance in science and technology [33]. In the present work, we prepared LTT glasses by varying Tm^{3+} ion concentration and studied their luminescent properties in order to identify better glass for the aforementioned photonic applications.

2. Experimental Methods

2.1 Glass synthesis

The Lead Tungsten Tellurite glasses were prepared by using melt quenching technique with a composition of $(60-x) \text{TeO}_2 + 25\text{WO}_3 + 15\text{PbF}_2 + x\text{Tm}_2\text{O}_3$, (where $x=0.1, 0.5, 1.0, 1.5, 2.0, 2.5$ mol %). All chemicals used in the present work are of higher purity (99.99%). These chemicals were thoroughly mixed and crushed in an agate mortar and melted in a silica crucible at 735°C for 30 min in an electrical furnace. The glass melts were removed from furnace and poured on a pre-heated brass plate and then pressed immediately with another brass plate. The obtained glasses are annealed at 350°C for 2 hrs to remove the thermal strains. Finally the prepared glasses were well polished with an emery paper before characterization.

2.2 Characterization

For the polished glass samples, density and refractive indices were measured using Archimedes principle (distilled water used as an immersion liquid) and Brewster's angle method (He-Ne laser - 632 nm) respectively. The absorption spectra for all the glasses were recorded using JASCO V-670 (UV-vis-NIR) spectrophotometer in the wavelength range of 450-1900 nm with a resolution 1 nm. The photoluminescence excitation and emission spectra were recorded at room temperature using Shimadzu RF-5301 PC Spectrofluorophotometer. Lifetime decay curves were recorded using an Edinburgh luminescence spectrometer (Model F 900) equipped with a microsecond Xe-flash lamp as the source of excitation (401 nm).

3. Results and discussion

3.1. Physical Properties

By using refractive index and density values various other physical properties of the LTT glasses were evaluated using the equations available in the literature [34] and are shown in Table 1. From Table 1, it can be seen that the values of refractive index and densities for all LTT glasses increases with increase in Tm^{3+} ions concentrations. The other physical properties such as average molecular weight, Tm^{3+} ion concentration, mean atomic volume,

dielectric constant, optical dielectric constant, Refraction losses, molar refraction and field strength values are also increasing with the concentration of Tm^{3+} ions. On the other hand polaron radius, inter ionic distance and molecular electronic polarizability values are decreasing with increase in Tm^{3+} ion concentration in LTT glasses.

3.2. Absorption spectral analysis - Energy band gap, Oscillator Strengths and J-O Parameters

3.2.1. Absorption spectral analysis

The absorption spectra for different concentrations of Tm^{3+} ions doped LTT glasses were recorded at room temperature in the wavelength range 450-1900 nm. Fig.1 shows the absorption spectrum of 0.5 mol% of Tm^{3+} ions doped LTT glass (LTTTm05). As the absorption spectra recorded for all the LTT glasses appear same with slight variation in intensity, we have shown only one absorption spectrum pertaining to LTTTm05 glass. The absorption spectra recorded for all the Tm^{3+} ions doped LTT glasses show 6 bands related to the transitions from the $^3\text{H}_6$ ground state to several higher energy states ($^1\text{G}_4$, $^3\text{F}_2$, $^3\text{F}_3$, $^3\text{H}_4$, $^3\text{H}_5$ and $^3\text{F}_4$). Identification of different bands observed in the present work has been done using the data given in carnall paper [35]. The bands are appeared at the wavelengths 474nm ($^3\text{H}_6 \rightarrow ^1\text{G}_4$), 660nm ($^3\text{H}_6 \rightarrow ^3\text{F}_2$), 689nm ($^3\text{H}_6 \rightarrow ^3\text{F}_3$), 793nm ($^3\text{H}_6 \rightarrow ^3\text{H}_4$), 1212nm ($^3\text{H}_6 \rightarrow ^3\text{H}_5$) and 1703nm ($^3\text{H}_6 \rightarrow ^3\text{F}_4$). All the absorption bands appeared in the Fig. 1 are very sharp and intense. The position of the absorption peaks are similar to the reported spectra of other glasses doped with thulium [36-38].

3.2.2 Energy band gap

By using absorption spectral data the energy band gaps for all the glasses were evaluated. The energy band gap is estimated by extrapolating the linear regions of the curves $(\alpha h\nu)^{1/2}$ vs. $h\nu$ as shown in Fig 2. From Fig 2, it is observed that there is no evidence for the sharp absorption edges which is the main feature of most of the oxide glasses. The energy band gap values of all the glasses are LTTTm01 (2.59 eV), LTTTm05 (2.50 eV), LTTTm10 (2.44 eV), LTTTm15 (2.41 eV), LTTTm20 (2.38 eV) and LTTTm25 (2.34 eV). The optical band gap values are decreasing with the increase in Tm^{3+} ions concentration in LTT glasses. The optical band gap of all the glasses is in the range of 2.34-2.59 eV which is very useful for the construction of optical devices.

3.2.3 Oscillator Strengths

The intensities of absorption bands known as experimental oscillator strengths (f_{exp}) were evaluated using the following equation [39] and are given in Table 2.

$$f_{exp} = \frac{2.303mc^2}{N\pi e^2} \int \varepsilon(\vartheta) d\vartheta \text{ ----- (1)}$$

Where e and m are charge and mass of an electron, N is the Avogadro's number; c is the velocity of light and $\varepsilon(\vartheta)$ is the molar absorptivity of a band at a wave number ϑ (cm^{-1}). The calculated oscillator strengths of absorption bands are evaluated using J-O theory with the conventional equations [40, 41].

$$f_{cal} = \left[\frac{8\pi^2 m c v}{3h(2J+1)} \right] \left[\frac{(n^2+1)^2}{9n} \right] \sum_{\lambda=2,4,6} \Omega_{\lambda} (\psi_J || U^{\lambda} || \psi'_J)^2 \text{ ----- (2)}$$

Where v is the wave number (cm^{-1}) of the transition from ground state (ψ_J) to excited state (ψ'_J), c is the velocity of light in vacuum, m is the rest mass of an electron, n is the refractive index of dielectric medium, J is the total angular momentum of the ground state, h is Planck's constant and $||U^{\lambda}||^2$ are doubly reduced matrix elements. The doubly reduced matrix elements were collected from the literature as they are independent of the environment of rare earth ions. The quality of the fit is calculated by root mean square deviation (δ_{rms}) between the calculated and experimental oscillator strengths. The values of f_{exp} and f_{cal} together with the r.m.s deviation are represented in Table 2. The deviation parameter δ_{rms} is calculated by using the following expression [42, 43].

$$\delta_{rms} = \left[\frac{\sum (f_{exp} - f_{cal})^2}{n} \right]^{1/2} \text{ ----- (3)}$$

Where n is the total number of transitions involved in the fitting procedure. From Table 2, it can be observed that, the variations in the magnitude of oscillator strengths are very small.

3.2.4 J-O Parameters Evaluation

The J-O intensity parameters Ω_2 , Ω_4 and Ω_6 are evaluated through least square fitting analysis by using equation (2) and are given in Table 3 along with the other reported values [44-47]. Few transitions of rare earths are found to be dependent on the doped rare earth ion concentration and composition of host glass. These absorption levels show remarkable intensity deviations and are called as hypersensitive levels. For the Tm^{3+} ion, the transition $^5\text{I}_8 \rightarrow ^5\text{G}_6$ is a hypersensitive transition and it satisfies the selection rules such as $|\Delta S|=0$, $|\Delta L| \leq 2$, $|\Delta J| \leq 2$. The spectral oscillator strengths of these transitions are strongly affected by the Judd-Ofelt intensity parameter Ω_2 . The J-O intensity parameters follow the trend $\Omega_2 > \Omega_6 > \Omega_4$ for all the glasses and Ω_2 value is found to be more than the parameters Ω_4 & Ω_6 . Hence

present glass systems have more covalent nature. The J-O intensity parameters magnitude is mainly correlated with the physical and chemical properties such as viscosity and covalent character of the chemical bonds. The large values of Ω_2 parameter are the indicators of the covalent character of the chemical bonds between the glass matrix and rare earth ions [48]. This is due to O^{2-} ions possess higher polarizability than F^- leading to the increment of the covalency of the bond between Tm^{3+} and ligand [49]. In the present series of glasses, LTTTm05 glass possesses maximum value of Ω_2 parameter. Therefore LTT glass with 0.5 mol% of Tm^{3+} ions possesses higher asymmetry and greater degree of covalency of thulium and oxygen bond than the other reported values [44-47]. The large values of Ω_4 and Ω_6 are related to the bulk properties such as viscosity and rigidity of the glass structure [49].

3.3. Emission spectral analysis

Fig 3 shows the excitation spectrum of LTTTm05 glass in the region 450-500 nm at an emission wavelength 650 nm. The excitation spectrum has one prominent peak at wavelength 472 nm corresponding to the transition $^3H_6 \rightarrow ^1G_4$. The luminescence spectra of the all LTT glasses were recorded at an excitation wavelength 472 nm in the visible and NIR regions. Fig.4 shows the luminescence spectrum recorded for LTTTm05 at 472 nm excitation wavelength. The inset in Fig. 4 shows the luminescence spectra of all the LTT glasses under 472 nm excitation. The luminescence spectra consists of two prominent emission bands at 650 nm (red region) and 800 nm (NIR region) corresponding to the transitions $^1G_4 \rightarrow ^3F_4$ and $^3H_4 \rightarrow ^3H_6$ respectively. Among the two emission bands, the intensity of the peak at 650 nm is higher than the peak at 800 nm. The peak corresponding to the transition $^1G_4 \rightarrow ^3F_4$ at 650 nm is very sharp and intense while the other one appears as broad. From Fig. 4, it is observed that the intensity of the two transitions at 650 nm, 800 nm increases with increasing concentration of Tm^{3+} ions up to 0.5 mol % and then decreases. Hence in the present series of glasses, the concentration quenching is observed at 0.5 mol % of Tm^{3+} ions concentration.

In order to verify the luminescence performance of present series of LTT glasses, various radiative parameters were calculated using J-O intensity parameters and are given in Table 4 and Table 5. The radiative parameters are evaluated using the expressions available in the literature [48]. From Table 4, it is observed that, the transition probability (A_R) and branching ratio (β_R) values of LTTTm05 glass are relatively large for the two transitions $^1G_4 \rightarrow ^3F_4$ (650 nm) & $^3H_4 \rightarrow ^3H_6$ (800 nm). From Table 5 it is also observed that the radiative and experimental branching ratios (β_R & β_{exp}) are in good agreement with each other. It is well known that if the branching ratio (β_R) of an emission level is greater than or equal to 50%, then that transition is known to be a potential transition for lasing action [50]. The lasing

potentiality of an emission transition can also be decided by the value of stimulated emission cross-section (σ_{se}). The peak wavelength, half width maxima ($\Delta\lambda_p$), stimulated emission cross-section (σ_{se}) values along with the optical gain parameters are given in Table 5 for all the Tm^{3+} ions doped LTT glasses. From this table it can be seen that, the LTTTm05 glass possesses maximum values of stimulated emission cross-section (σ_{se}) and optical gain parameters for the two transitions at 650 nm and 800 nm. From these results, we can suggest that the LTTTm05 glass is suitable to emit laser at 650 nm and 800 nm in visible Red and NIR regions respectively.

3.4 Luminescence decay analysis

The luminescence spectral decay curves of the 1G_4 fluorescent level of Tm^{3+} doped LTT glasses have been measured at room temperature and are shown in Fig 5. All the experimental spectral decay curves are single exponential in nature. The experimental lifetime (τ_{exp}) of the 1G_4 excited level has been found by taking the first e- fold times of the decay curves [51]. The experimental lifetimes (τ_{exp}) and the radiative lifetimes (τ_R) obtained for the present glasses are given in Table 6 for all Tm^{3+} doped LTT glasses. The experimental lifetimes are considerably smaller than the radiative lifetimes evaluated by using the J-O theory may be due to the energy transfer through cross-relaxation process [52].

For rare-earth ions, the quantum efficiency (η) is another important parameter; which is used to predict the efficiency/quality of the laser host material [5]. This can be evaluated by using following expression

$$\eta = \frac{\tau_{exp}}{\tau_R} \times 100$$

The quantum efficiency (η) depends on emission cross-section (σ_{se}), radiative transition probabilities (A_R), lifetimes (τ_R & τ_{exp}) of the excited states, concentration of rare-earth ions and ligand field produced by network modifiers. The quantum efficiency for all glasses are given in Table 6 along with the radiative and experimental lifetimes (τ_R & τ_{exp}) for $^1G_4 \rightarrow ^3F_4$ transition. From Table 6 it can be seen that, among the all glasses, the LTTTm05 glass possess maximum values of quantum efficiency. Hence it can be concluded that the LTTTm05 glass is quite able to emit bright red colour laser at 650 nm.

3.5 Evaluation of CIE colour co-ordinates:

The visible emission shown by the glasses doped with rare earth ions can be further confirmed by colour chromaticity diagram drawn from the emission spectral data. For different concentrations of Tm^{3+} ions doped LTT glasses, the colour chromaticity coordinates

were evaluated from the luminescence spectra using the CIE (Commission International de l'Eclairage France) system. Fig.6 represents the CIE plot with colour coordinates of the LTTTm05 glass. The chromaticity coordinates of the Tm^{3+} ions doped LTT glasses were premeditated using the expressions given in the literature [53] and are given in Table 6. All the evaluated colour co-ordinates of LTT glasses exactly fall in the red region. Hence among all these glasses, LTTTm05 glass colour co-ordinates are exactly falling in the bright red region. From the measured branching ratios, stimulated emitted cross-sections, quantum efficiency and colour chromaticity co-ordinates evaluated for Tm^{3+} ions doped LTT glasses, it is concluded that the LTTTm05 glass is the best optical material to generate bright red colour laser at 650 nm. The same glass is also suitable to emit NIR laser emission at 800 nm.

4. Conclusions

Different concentrations of Tm^{3+} ions doped LTT glasses have been synthesized by using melt quenching method and characterized with the help of the spectroscopic techniques such as optical absorption, excitation, emission and decay spectral measurements to optimise the concentration of the doped rare earth ion for better luminescence efficiency. The J-O intensity parameters (Ω_2 , Ω_4 and Ω_6) evaluated for LTT glasses are found to be high for LTTTm05 glass indicating that this glass is more asymmetric, and more covalent in nature than the other glasses. The emission spectra recorded for different concentrations of Tm^{3+} ions in LTT glasses show two emission bands at 650 and 800 nm corresponding transitions to $^1\text{G}_4 \rightarrow ^3\text{F}_4$ and $^3\text{H}_4 \rightarrow ^3\text{H}_6$ respectively. Among these two emission transitions observed, $^1\text{G}_4 \rightarrow ^3\text{F}_4$ is more intense and is falling in red region and the other one is broad and falling in the Near-Infrared region. Relatively higher values of stimulated emission cross-section and branching ratios values observed for all these LTT glasses suggest the possibility of using these materials as lasers in red ($^1\text{G}_4 \rightarrow ^3\text{F}_4$) and NIR ($^3\text{H}_4 \rightarrow ^3\text{H}_6$) regions. From the decay curves, experimental lifetimes were measured which are in turn used to evaluate the quantum efficiencies. The CIE chromaticity co-ordinates evaluated from the emission spectra recorded at 472 nm excitation for all LTT glasses confirms the suitability of these glassy materials for red emission. From the measured emission cross-sections, quantum efficiency and CIE chromaticity co-ordinates, it was found that 0.5 mol% of Tm^{3+} ions doped LTT glass (LTTTm05) is suitable for the improvement of bright visible red lasers to operate at 650 nm from these LTT glasses. The LTTTm05 glass is also equally capable to generate NIR lasers at 800 nm.

Acknowledgments

Two of the authors, Swapna Koneru (File No: SR/WOS-A/PS-35/2011) and Mahamuda Shaik (File No: SR/WOS-A/PS-53/2011) are very much thankful to Department of Science and Technology (DST), Government of India, New Delhi, for awarding them with a Women Scientist's scheme under DST-WOS (A) Program. One of the authors, Dr. Mohan Babu is expressing his sincere thanks to ADE-BRNS (Project No.2012/34/72) and DST-SERB (Project No. SR/FTP/PS-109/2012) for their financial support to carry out this work.

References

- [1] N. Karafolas, J. Armengol, and I. Mckenzie, IEEE Aerospace conference, 7-14 March (2009)1-15.
- [2] Sk. Mahamuda, K. Swapna, M. Venkateswarlu, A. Srinivasa Rao, Suman Shakya and G. Vijaya Prakash, J. Lumin.154 (2014) 410-424.
- [3] Sk. Mahamuda, K. Swapna, P. Packiyaraj, A. Srinivasa Rao and G. Vijaya Prakash, J. Lumin. 153(2014) 382-392.
- [4] K. Swapna, Sk. Mahamuda, A. Srinivasa Rao, M. Jayasimhadri, T. Sasikala and L. Rama Moorthy, J. Lumin.139 (2013) 119-124.
- [5] K. Swapna, Sk. Mahamuda, A. Srinivasa Rao, T. Sasikala and L. Rama Moorthy, J. Lumin. 146 (2014) 288-294.
- [6] K. Swapna, Sk. Mahamuda, A. Srinivasa Rao, P. Packiya Raj, T. Sasikala and L. Rama Moorthy, J. Lumin. 156 (2014) 80-86.
- [7] K. Swapna, Sk. Mahamuda, A. Srinivasa Rao, M. Jayasimhadri, Suman Shakya and G. Vijaya Prakash, J. Lumin.156 (2014) 180-187.
- [8] K. Swapna, Sk. Mahamuda, A. Srinivasa Rao, M. Jayasimhadri, Suman Shakya and G. Vijaya Prakash, J. Lumin. 163(2015) 55-63.
- [9] M. Venkateswarlu, Sk. Mahamuda, K. Swapna, M. V. V. K. S. Prasad, A. Srinivasa Rao, A. Mohan Babu, Suman Shakya and G. Vijaya Prakash, J. Lumin. 163(2015) 64-71.
- [10] L. Huang, S. Shen, and A. Jha, J. Non-Cryst. Solids. 349 (2004) 345-346.
- [11] S.N.B. Hodgson, L. Weng, J. Sol-Gel Sci. Technol. 18 (2000) 145-158.
- [12] S.N.B. Hodgson, L. Weng, J. Mater. Sci. Mater. Electron. 17 (2006) 723-733.
- [13] S. Park, S. An, H. Ko, C. Jin, C. Lee, Curr. Appl. Phys. 13 (2013) 576-580.
- [14] A.W. Warner, D.L. White, W.A. Bonner, J. Appl. Phys. 43 (1972) 4489-4495.
- [15] S.N. Antonov, Tech. Phys. 49 (2004) 1329-1334.
- [16] Z. Liu, T. Yamazaki, Y. Shen, T. Kikuta, N. Nakatani, T. Kawabata, Appl. Phys. Lett. 90 (2007)173119-1 -173119-3.
- [17] G.D. Khattak, M. A. Salim, J. Electron. Spectrosc. Relat. Phenom. 123(2002)47-55.
- [18] H. A. A. Sidek, S. Rosmawati, Z. A. Talib, M. K. Halimah, W. M. Daud, Am J Appl Sci. 6(2009)1489-94.
- [19] V. Ravi Kumar, N. Veeraiah, J Mater Sci Lett. 16 (1997)1816-1818.

- [20] Ali Erçin Ersundu, Miray Çelikkilek and Süheyla Aydın, Current Microscopy Contributions to Advances in Science and Technology (A. Méndez-Vilas, Ed.) 2012 FORMATEX, 1105-1114.
- [21] K J Rao, structural chemistry of glasses, Elsevier science Ltd., The Boulevard, Langford Lane, Kidington, Oxford OX51GB, UK.
- [22] D. F. Anderson, M. Kobayashi, Y. Yoshimura, C.L.Woody, FermiLab, Pub-89 (1989).
- [23] D. Ramachari, L. Rama Moorthy, C.K. Jayasankar, Mater. Res. Bull. 48 (2013) 3607-3613.
- [24] P.W. France, M. G. Drexage, J.M.Parken, M.W.Morre, S.F. Carter and J.W. Wright, Fluoride glass optical fibre, CRC Press, Boca Raton, 1990.
- [25] M. Venkateswarlu, Sk. Mahamuda, K. Swapna, M.V.V.K.S. Prasad, A. Srinivasa Rao, A. Mohan Babu, Suman Shakya, G. Vijaya Prakash, Opt. Mater. 39 (2015) 8-15.
- [26] G. Poirier, V. A. Jerez, C. B. de Araújo, Y. Messaddeq, S. J. L. Ribeiro and M. Poulain, J. Appl. Phys. 93 (2003) 1493-1497.
- [27] P. Myslinski, X. Pan, C. Barnard, J. chrostowski, B. T. Sullivan, and J. F. Bayon, Opt. Eng. 32 (1993) 2025-2030.
- [28] L. Esterowitz, Opt. Eng. 29 (1990) 676-680.
- [29] R. C. Stoneman and L. Esterowitz, Opt. Lett. 15 (1990) 486-488.
- [30] S. W. Henderson, P. J. M. Suni, C. P. Hale, S. M. Hannon, J. R. Magee, D. L. Bruns, and E. H. Yuen, IEEE Trans. Geosci. Remote Sens. 31 (1993) 4-15.
- [31] Kamel Damak, Ramzi Maâlej, El Sayed Yousef, Abdulla H. Quisti, Christian Rüssel J. Non-Cryst. Solids. 358 (2012) 2974-2980.
- [32] Xueqiang Liu, Ming Li, Xin Wang, Feifei Huang, Yaoyao Ma, Junjie Zhang, Lili Hu, Danping Chen, J. Lumin. 150(2014)40-45.
- [33] Frontiers in Guided Wave Optics and Optoelectronics, Book edited by: Bishnu Pal, ISBN 978-953-7619-82-4, pp. 674, February 2010, INTECH, Croatia, downloaded from SCIYO.COM.
- [34] A. S. Rao, Y. N. Ahammed, R. R. Reddy, T. V. R. Rao, ,Opt. Mater.10 (1998)245-252.
- [35] W. T. Carnall, P. R. Fields, K. Rajnak, J. Chem. Phys. 49 (1968) 4424-4442.
- [36] G. Ozen, A. Aydinli, S. Cenik, A. Sennaroglu, J. Lumin. 101(2003) 293-306.
- [37] E. W. J. L. Oomen, J. Lumin.50 (1992) 317-332.
- [38] J. R. Lincoln, W. S. Brocklesby, F. Cusso, J. E. Townsent, A. C. Tropper, A. Pearson, J. Lumin. 50 (1991)297-308.

- [39] A. Srinivasa Rao, B. Rupa Venkateswara Rao, M.V.V.K.S.Prasad, J.V. Shanmukha Kumar, M. Jayasimhadri, J.L. Rao, R.P.S. Chakradhar, *Physica B.* 404 (2009) 3717-3721.
- [40] B.R. Judd, *Phys. Rev.* 127 (1962) 750-761.
- [41] G.S. Ofelt, *J. Chem. Phys.* 37 (1962) 511-520.
- [42] P. A. Tanner, *Molec. Phys.* 57 (1986) 737-754.
- [43] A.Tanner, Anne De Piante, F.S.Richardson and M. F. Reid, *Mol. Phys.* 60(1987) 1037-1045.
- [44] R. Praveena, Kyoung Hyuk Jang, C.K. Jayasankar, Hyo JinSeo., *J. Alloy. Compd.* 496 (2010) 335-340.
- [45] K.S. Lim, P. Babu, C.K. Jayasankar, S.K. Lee, V.T. Pham, H.J. Seo, *J. Alloy. Compd.* 385 (2004) 12-18.
- [46] N. Spector, R. Reisfeld, L. Bochm, *Chem. Phys. Lett.* 49 (1977) 251-254.
- [47] K. Kadono, T. Yazawa, M. Shojiya, K. Kawamoto, *J. Non-Cryst. Solids.* 274 (2000) 75-80.
- [48] Sk. Mahamuda, K. Swapna, P. Packiyaraj, A. Srinivasa Rao, G. Vijaya Prakash, *Opt. Mater.* 36 (2013) 362-371.
- [49] M. Wang, L. Yi, Y. Chen, C. Yu, G. Wang, L. Hu, J. Zhong, *Mateu. Chem. Phys.* 114(2009) 295-299.
- [50] G. Ozen, B. Demirata, M.L. Ovecoglu, A. Genc, *Spectrochim. Acta A.* 57 (2001) 273-280.
- [51] V.M. Orera, P.J. Alonso, R. Cases, R. Alkala, *Phys. Chem. Glasses.* 29 (1988) 59-62.
- [52] F. Lahoz, I.R. Martin, J. Mendez-Ramos, P. Nunez, *J. Chem. Phys.* 120 (2004) 6180-6190.
- [53] N.Q. Wang, X. Zhao, C.M. Li, E. Y. B. Pun, H. Lin, *J. Lumin.* 130(2010) 1044-1047.

Figures

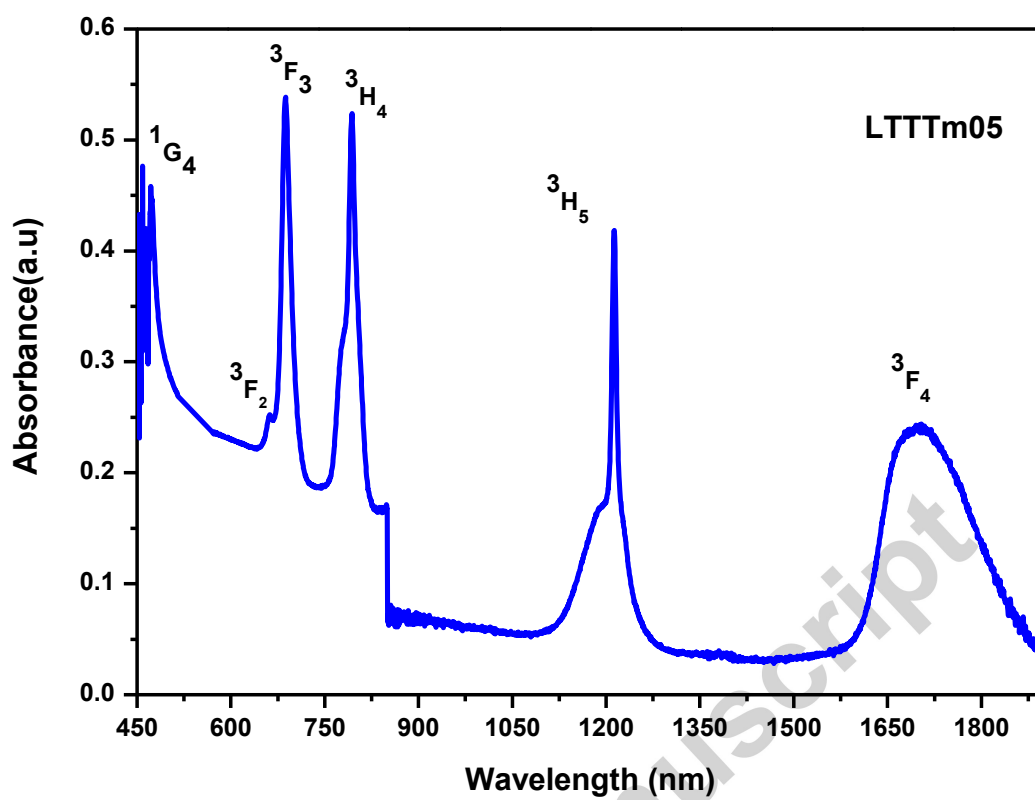


Fig 1: Optical absorption spectrum of the LTTTm05 glass

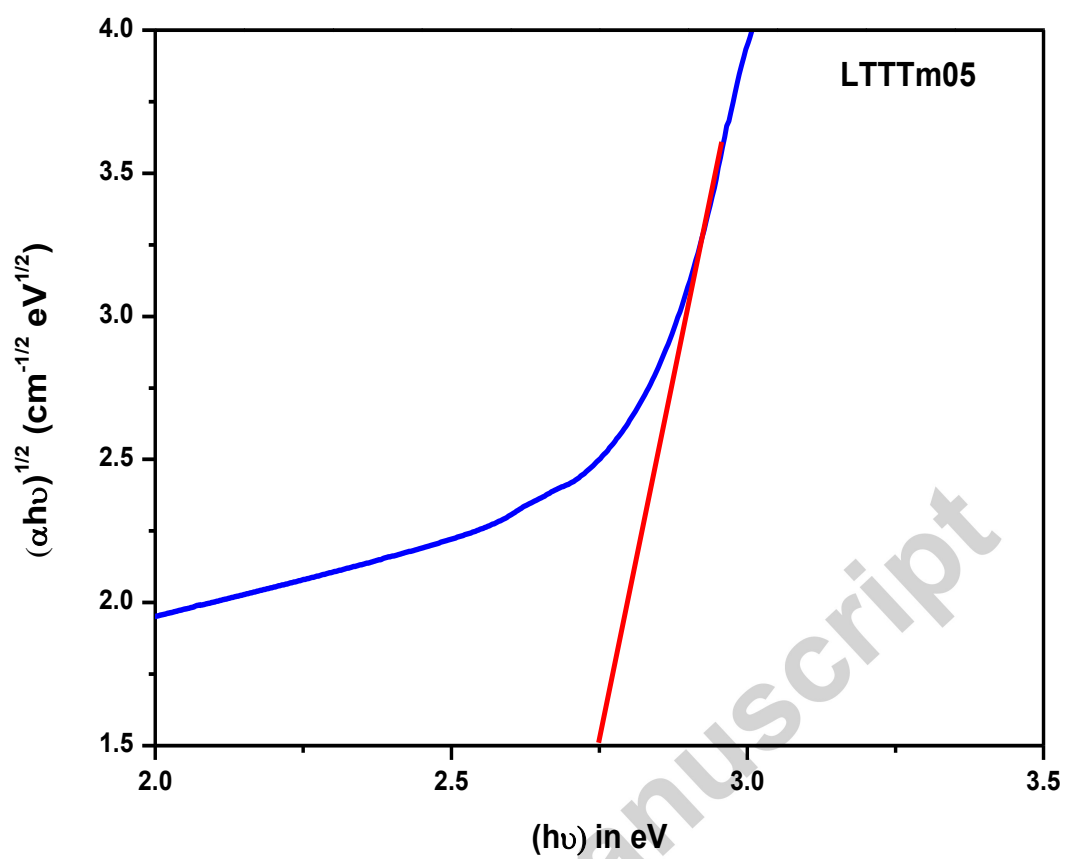


Fig 2: Energy band gap of the LTTTm05 glass

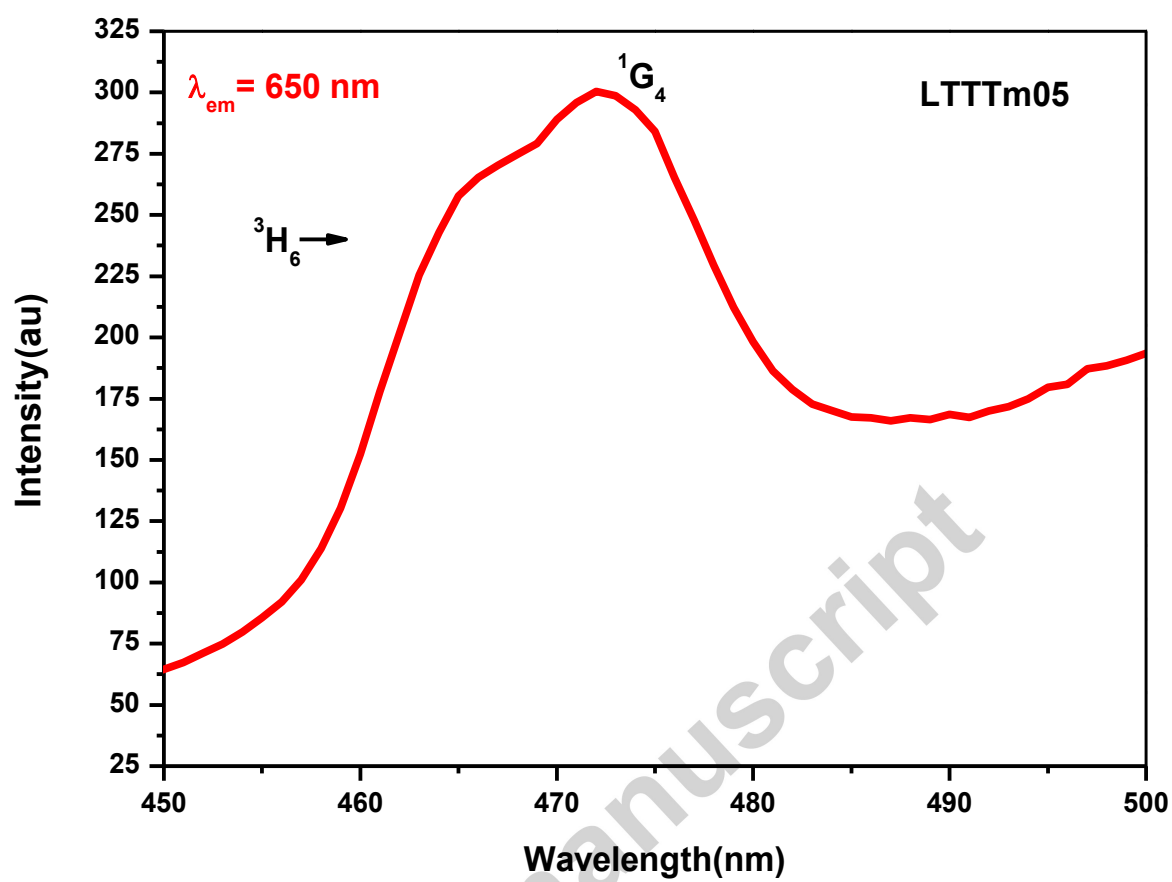


Fig 3: Excitation spectrum of the LTTTm05 glass

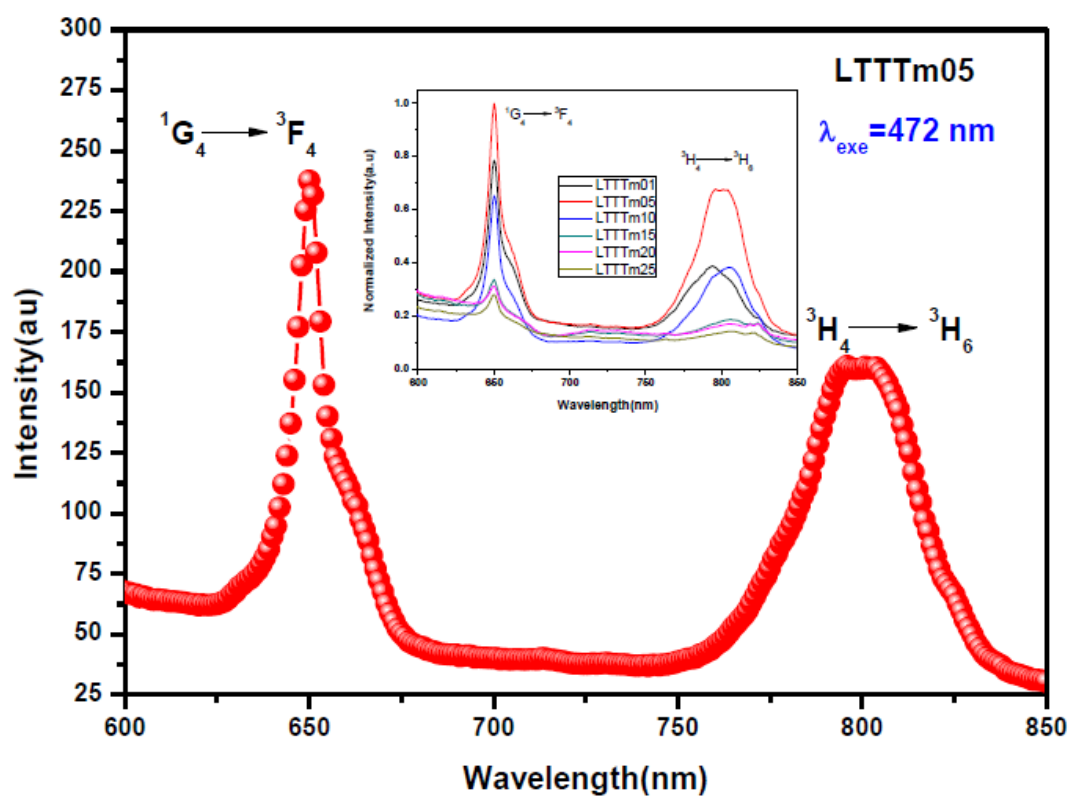


Fig 4: Emission spectrum of LTTTm05 glass . The inset figure shows the emission spectra of all the LTT glasses doped with different concentrations of Tm^{3+} ions.

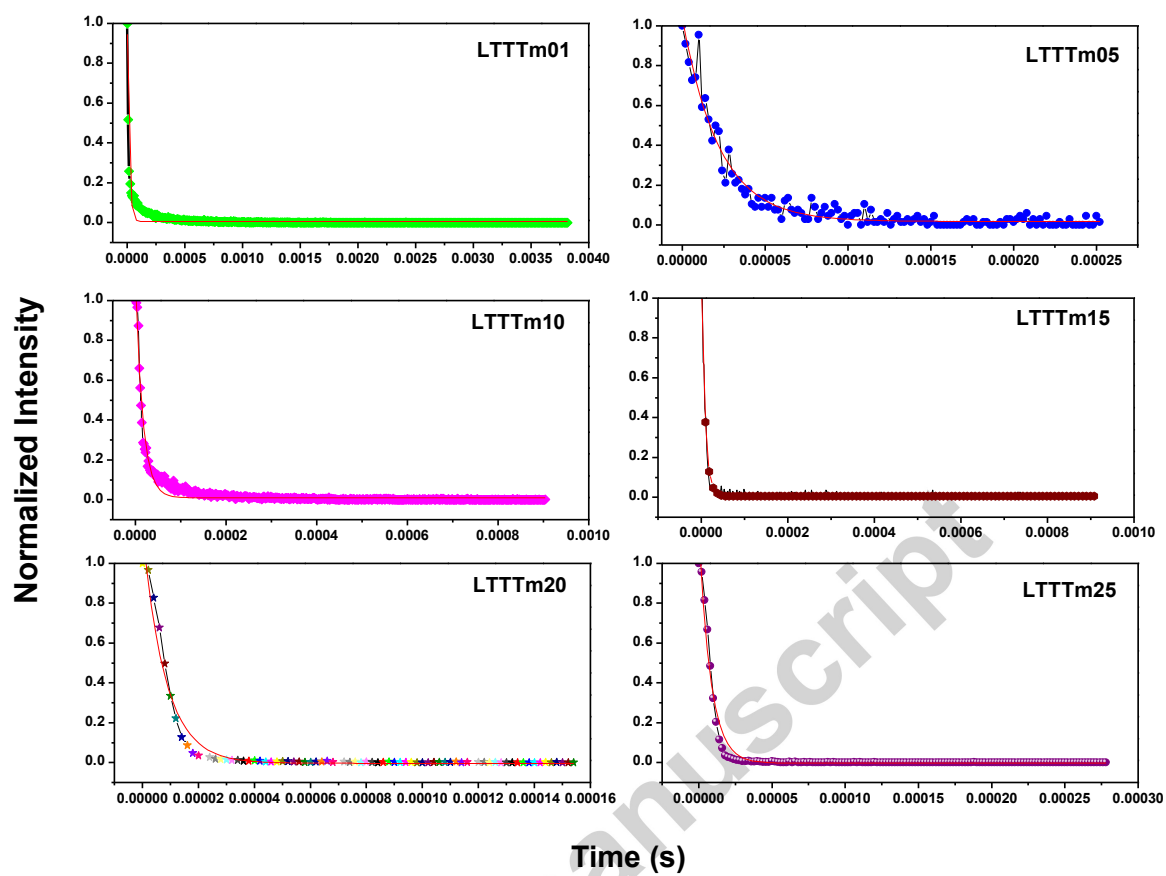


Fig 5: Decay curves for $^1G_4 \rightarrow ^3F_4$ luminescent transition of Tm^{3+} ions doped LTT glasses under 472 nm excitation

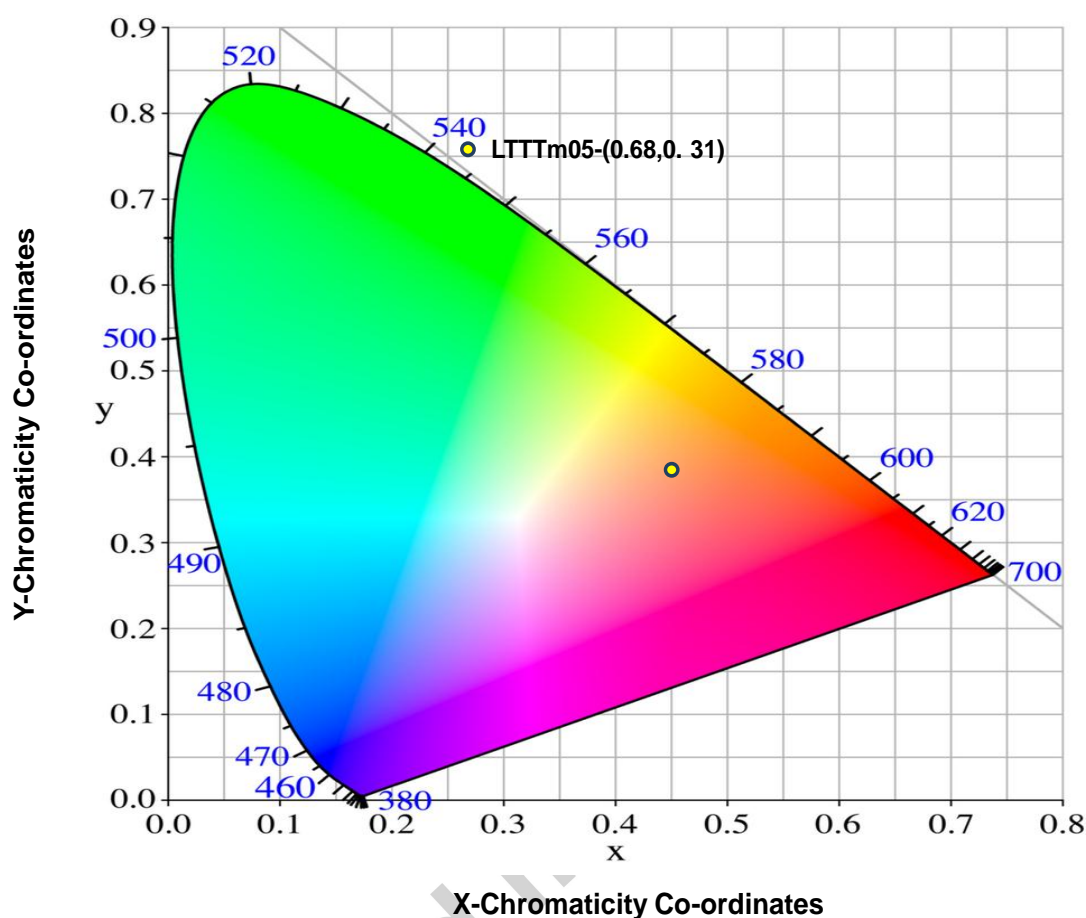


Fig 6: CIE 1931 colour chromaticity diagram for LTTm05 glass

Table 1:

Various physical properties of Tm^{3+} ions in LTT glasses

Physical Property	LTTm01	LTTm05	LTTm10	LTTm15	LTTm20	LTTm25
Refractive index(n_d)	2.481	2.510	2.543	2.548	2.554	2.572
Density(ρ)(g cm^{-3})	6.608	6.619	6.633	6.645	6.66	6.673

Average molecular weight, \bar{M} (g)	190.7	191.6	192.7	193.8	195.0	196.1
Tm ³⁺ ion concentration, N (10 ²² ions/cm ³)	0.208	1.04	2.072	3.095	4.112	5.121
Mean atomic volume(g/cm ³ /atom)	6.559	6.579	6.604	6.631	6.655	6.680
Dielectric constant(ϵ)	6.155	6.300	6.466	6.492	6.522	6.615
Optical dielectric constant ($\epsilon-1$)	5.155	5.300	5.466	5.492	5.522	5.615
Reflection losses (R %)	0.181	0.185	0.189	0.190	0.191	0.193
Molar refraction (R_m)(cm ⁻³)	18.24	18.48	18.76	18.87	18.97	19.15
Polaron radius (Å)	3.210	1.880	1.492	1.310	1.190	1.100
Inter ionic distance (Å)	7.960	4.660	3.703	3.240	2.950	2.74
Molecular electronic polarizability α (x10 ⁻²⁴ cm ³)	72.6	14.7	7.443	4.99	3.76	3.04
Field strength F (x10 ¹⁵ cm ⁻²)	2.91	8.51	13.445	17.6	21.30	24.60

Table 2:

Experimental ($f_{\text{exp}} \times 10^{-6}$), calculated ($f_{\text{cal}} \times 10^{-6}$) oscillator strengths and rms deviation of Tm^{3+} ions in LTT glasses

Transitions	LTTTm0		LTTTm05		LTTTm1		LTTTm15		LTTTm2		LTTTm2	
	1		0		0		0		0		5	
from $^3\text{H}_6 \rightarrow$	f_{exp}	f_{cal}	f_{exp}	f_{cal}	f_{exp}	f_{cal}	f_{exp}	f_{cal}	f_{exp}	f_{cal}	f_{exp}	f_{cal}
$^1\text{G}_4$	0.58	1.97	3.35	4.27	2.08	4.25	1.72	2.99	1.15	2.21	0.84	1.71
	2	8	7	7	4	0	0	3	0	9	0	0
$^3\text{F}_2$	0.37	1.36	2.23	4.01	0.89	2.96	0.82	2.89	0.50	2.00	0.31	1.46
	9	0	3	4	4	7	6	9	4	5	9	2
$^3\text{F}_3$	5.09	5.85	14.2	15.8	11.1	12.5	8.29	10.6	6.17	6.82	4.59	5.04
	0	1	28	75	1	0	0	72	0	5	0	1
$^3\text{H}_4$	6.58	6.96	16.2	17.0	14.5	15.1	11.3	12.5	9.27	9.52	7.00	7.16
	9	1	25	20	3	7	00	07	9	3	3	2
$^3\text{H}_5$	4.68	3.63	11.4	9.23	9.81	7.84	9.54	6.47	5.57	4.55	4.12	3.40
	0	7	16	5	0	7	0	9	0	5	7	7
$^3\text{F}_4$	5.99	6.03	13.1	13.2	12.9	12.9	9.20	9.35	6.94	7.00	5.33	5.38
	5	2	00	24	0	9	0	5	1	8	4	2
$\delta_{\text{rms}} (\times 10^{-6})$	± 0.887		± 1.422		± 1.593		± 1.931		± 0.906		± 0.685	

Table 3:Judd-Ofelt Parameters ($\Omega_\lambda \times 10^{-20} \text{cm}^2$) of Tm^{3+} ions in LTT glasses

Glass System	Ω_2	Ω_4	Ω_6	Trend	References
LTTTm01	5.21	1.36	1.41	$\Omega_2 > \Omega_6 > \Omega_4$	present work
LTTTm05	10.94	2.73	4.06	$\Omega_2 > \Omega_6 > \Omega_4$	present work
LTTTm10	10.90	2.61	2.92	$\Omega_2 > \Omega_6 > \Omega_4$	present work
LTTTm15	8.26	1.31	2.83	$\Omega_2 > \Omega_6 > \Omega_4$	present work
LTTTm20	6.99	0.41	1.96	$\Omega_2 > \Omega_6 > \Omega_4$	present work
LTTTm25	5.27	0.35	1.41	$\Omega_2 > \Omega_6 > \Omega_4$	present work
PKMAT	9.32	1.82	3.21	$\Omega_2 > \Omega_6 > \Omega_4$	[44]
Oxy-fluoroborate	8.37	3.20	4.34	$\Omega_2 > \Omega_6 > \Omega_4$	[45]
Tellurite	5.04	1.36	1.22	$\Omega_2 > \Omega_4 > \Omega_6$	[46]
GGLS	7.11	1.46	1.96	$\Omega_2 > \Omega_6 > \Omega_4$	[47]

Table 4:

Transition probabilities (A_R) (s^{-1}), luminescence branching ratios (β_R), total transition probability (A_T) (s^{-1}) and radiative lifetimes (τ_R) (μs) for the observed emission transitions of Tm^{3+} ions in LTT glasses

Transition	A_R	β_R	A_T	τ_R
LTTTm01				
$^1G_4 \rightarrow ^3F_4$	7085.07	0.424	16703.26	59.86
$^3H_4 \rightarrow ^3H_6$	24179.87	0.951	25404.76	39.36
LTTTm05				
$^1G_4 \rightarrow ^3F_4$	19456.54	0.472	41184.79	24.28
$^3H_4 \rightarrow ^3H_6$	58509.18	0.957	61097.41	16.36
LTTTm10				
$^1G_4 \rightarrow ^3F_4$	16309.50	0.428	38067.86	26.26
$^3H_4 \rightarrow ^3H_6$	52708.64	0.949	55508.97	18.01
LTTTm15				
$^1G_4 \rightarrow ^3F_4$	12752.83	0.412	30945.60	32.31
$^3H_4 \rightarrow ^3H_6$	40295.84	0.945	42614.89	23.46
LTTTm20				
$^1G_4 \rightarrow ^3F_4$	10873.87	0.382	28473.45	35.12
$^3H_4 \rightarrow ^3H_6$	39359.01	0.943	41729.04	23.96
LTTTm25				
$^1G_4 \rightarrow ^3F_4$	6225.45	0.346	17978.43	55.62
$^3H_4 \rightarrow ^3H_6$	24699.21	0.941	26232.78	38.41

Table 5:

Emission peak wavelength (λ_p)(nm), effective band widths ($\Delta\lambda_p$)(nm), radiative and experimental branching ratios (β_R & β_{exp}), stimulated emission cross-sections (σ_{se}) ($\times 10^{-18}$) (cm^2), gain band width ($\sigma_{se} \times \Delta\lambda_p$) ($\times 10^{-26}$) (cm^3) and optical gain ($\sigma_{se} \times \tau_R$) ($\times 10^{-22}$) ($cm^2 s$) parameters for the emission transitions of Tm^{3+} ions in LTT glasses.

Spectral parameters	LTTTm01	LTTTm05	LTTTm10	LTTTm15	LTTTm20	LTTTm25
$^1G_4 \rightarrow ^3F_4$ (Red)						
λ_p	650	650	650	650	650	650
$\Delta\lambda_p$	8.108	8.108	9.459	10.811	13.514	13.514
β_R	0.951	0.957	0.949	0.945	0.943	0.941
β_{exp}	0.507	0.589	0.559	0.489	0.462	0.446
σ_{se}	3.36	9.02	6.32	4.30	2.92	2.18
$\sigma_{se} \times \Delta\lambda_p$	2.73	7.32	5.97	4.65	3.95	2.95
$\sigma_{se} \times \tau_R$	2.01	2.19	1.66	1.39	1.03	1.21
$^3H_4 \rightarrow ^3H_6$ (Infrared)						
λ_p	806	800	806	793	806	806
$\Delta\lambda_p$	37.84	35.14	37.84	37.84	39.19	40.54
β_R	0.424	0.472	0.428	0.412	0.382	0.346
β_{exp}	0.412	0.482	0.440	0.437	0.410	0.393
σ_{se}	5.81	14.40	12.10	8.61	8.51	5.16
$\sigma_{se} \times \Delta\lambda_p$	22.0	50.50	45.60	32.60	33.80	20.90
$\sigma_{se} \times \tau_R$	2.29	2.36	2.17	2.02	2.04	1.98

Table 6:

Colour co-ordinates of Tm^{3+} ions in LTT glasses at $\lambda_{\text{exc}} = 472$ nm wavelength, τ_{R} (μs), τ_{exp} (μs) and Quantum Efficiency (η)

Name of the Sample	Colour Co-ordinates $\lambda_{\text{exc}} = 472$ nm	τ_{R} (μs)	τ_{exp} (μs)	Quantum Efficiency (η)%
LTTTm01	(0.670, 0.300)	59.86	15.84	26.46
LTTTm05	(0.680, 0.310)	24.28	22.076	90.92
LTTTm10	(0.670, 0.310)	26.26	16.29	62.03
LTTTm15	(0.670, 0.310)	32.37	8.38	25.88
LTTTm20	(0.685, 0.305)	35.12	8.22	23.40
LTTTm25	(0.690, 0.310)	55.62	7.96	14.31

Microstructural Indicators for Prognostication of Copper–Aluminum Wire Bond Reliability Under High-Temperature Storage and Temperature Humidity

Pradeep Lall, *Fellow, IEEE*, Shantanu Deshpande, Luu Nguyen, *Fellow, IEEE*, and Masood Murtuza

Abstract—Gold wire bonding has been widely used as the first-level interconnect in semiconductor packaging. The increase in the gold price has motivated the industry search for an alternative to the gold wire used in wire bonding and the transition to a copper wire bonding technology. Potential advantages of transition to a Cu–Al wire bond system include low cost of copper wire, lower thermal resistivity, lower electrical resistivity, higher deformation strength, damage during ultrasonic squeeze, and stability compared with gold wire. However, the transition to the copper wire brings along some tradeoffs, including poor corrosion resistance, narrow process window, higher hardness, and potential for cratering. Formation of excessive Cu–Al intermetallics may increase the electrical resistance and reduce the mechanical bonding strength. Current state of the art for studying the Cu–Al system focuses on the accumulation of statistically significant number of failures under accelerated testing. In this paper, a new approach has been developed to identify the occurrence of impending apparently random defect fall-outs and premature failures observed in the Cu–Al wire bond system. The use of intermetallic thickness, composition, and corrosion as a leading indicator of failure for the assessment of the remaining useful life for Cu–Al wire bond interconnects has been studied under exposure to high temperature. Damage in the wire bonds has been studied using an X-ray micro-Computed Tomography (CT). Microstructure evolution was studied under the isothermal aging conditions of 150 °C, 175 °C, and 200 °C until failure. Activation energy was calculated using the growth rate of intermetallic at different temperatures. An effect of temperature and humidity on a Cu–Al wire bond system was studied using the Parr bomb technique at different elevated temperature and humidity conditions (110 °C/100%RH, 120 °C/100%RH, and 130 °C/100%RH), and a failure mechanism was developed. The present methodology uses the evolution of the intermetallic compound thickness and composition in conjunction with the Levenberg–Marquardt algorithm to identify accrued damage in wire bond subjected to thermal aging. The proposed method

can be used for a quick assessment of Cu–Al parts to ensure manufactured part consistency through sampling.

Index Terms—Copper wire bond, corrosion, high-temperature storage life, intermetallics, Parr bomb test, prognostics.

I. INTRODUCTION

GOLD WIRE has been widely used in the electronic industry for the first-level interconnects because of its high electrical conductivity, low hardness, and resistance to oxidation. The recent steep rise in the gold prices has forced the electronic industry to look for the other low-cost alternatives. Copper and palladium-coated copper are leading candidates to replace the incumbent gold wire [1]. The transition to copper wire bond has been encouraged by not only the lower cost of copper wire but also desirable properties, such as higher thermal conductivity and electrical conductivity compared with gold. In addition, copper wire also has higher mechanical strength and a low reaction rate with aluminum, which bodes well for the long-term reliability of the copper–aluminum system [2], [3]. However, the introduction of copper into the wire bonding process has also created a new set of challenges. Copper is harder than gold, and thus requires more ultrasonic energy and mechanical force during the mechanical bonding process. Higher energy during the bonding process requires a narrow bonding window, increasing the potential for chip cratering beneath the bonding surface. Furthermore, copper and copper intermetallics tend to oxidize at high temperatures reducing the bond strength. A substantial amount of work has been done on developing and optimizing the thermosonic wire bonding process for copper, and significant improvements are noted in [4]–[8].

In spite of process advancements, reliability is still one of the major concerns for copper wire bonding. Past research has shown that the formation of excessive intermetallics at the Cu–Al interface is a major contributor to the failure of the wire bond accompanied by resistance increase and fracture or bond lifts [2], [9]. Past researchers have studied the intermetallic compound (IMC) growth under isothermal aging. IMC has been studied using various techniques, including the crystal structure, the effect of annealing time, and the effect of temperature on IMC growth [10]. Composition of IMC has been studied using Transmission electron Microscopy and X-ray powder diffraction and reported to be CuAl₂ and Cu₉Al₄; the

Manuscript received November 29, 2014; revised July 13, 2015 and September 8, 2015; accepted October 9, 2015. This work was supported by the Semiconductor Research Corporation under Research Grant 2284. Recommended for publication by Associate Editor Y.-S. Lai upon evaluation of reviewers' comments.

P. Lall and S. Deshpande are with the Department of Mechanical Engineering, Auburn University, Auburn, AL 36849 USA (e-mail: lall@auburn.edu).

L. Nguyen is with Texas Instruments, Santa Clara, CA 95051 USA (e-mail: luu.nguyen@ti.com).

M. Murtuza was with Texas Instruments, Santa Clara, CA 95051 USA. He is now with Octave Systems, Santa Clara, CA 95054 USA (e-mail: masood.murtuza@yahoo.com).

Color versions of one or more of the figures in this paper are available online at <http://ieeexplore.ieee.org>.

Digital Object Identifier 10.1109/TCPMT.2015.2495164

IMC growth behavior of a Cu–Al wire bond system when subjected to multiple thermal stresses has been reported in [11]–[14]. Cu–Al IMCs grow much faster in thermal aging compared with thermal shock, and the rate of growth is higher for higher aging temperatures. Three predominant phases of Cu–Al IMCs include CuAl_2 , Cu_9Al_4 , and CuAl . However, the timing of appearance of each phase is still not clear. It has also been found that the IMC growth is diffusion driven [15], [16]. Activation energy of Cu–Al IMCs reported in the literature has a wide range from 2.51 to 23.9 kcal/mol [13], [17]–[19]. Prior data indicate that the cracking in the vicinity of the Cu–Al intermetallics is a predominant location of failure. The initial cracks may form in the copper–aluminum bond because of ultrasonic squeeze during the bond process, and that the cracks may propagate with aging time [2]. The Cu–Al IMCs grow at a slower pace compared with the Au–Al system [17]. Oxidation of Cu–Al intermetallics during operation at high temperature and high humidity may cause oxidation of IMC, followed by crack initiation, and eventual failure. The process of corrosion is accelerated in the presence of ionic species, such as halide, hydroxyl ions, and elevated temperature. Prior data indicate that under 85%RH/85 °C conditions, the aluminum pad gets corroded faster and causes accelerated failure compared with the Au–Al wire bond system [2]. Different corrosion reactions have been proposed for Cu-rich and Al-rich phases of IMC. The copper-rich interface (Cu_9Al_4) undergoes preferential corrosion compared with the aluminum-rich phase. A reaction rate is greatly affected by the concentration of hydroxyl, halide ions in surrounding. Corrosion of IMC causes a sudden increase in resistance and reduction in ball shear strength [20]–[23]. Understanding this abnormal behavior is an important step in troubleshooting reliability issues related to Cu–Al wire bonding.

Electronic components operating in a harsh environment are often subjected to high temperature and/or humidity conditions. It is often not feasible to capture the continuous-time temperature operational history over the use life of the product. Current health management systems provide nearly zero visibility into the health of electronics and packaging for the prediction of impending failures [24]–[27]. The built-in-self-tests (BISTs) are generally used to give electronic assemblies the ability to test and diagnose themselves with the minimal interaction from external test equipment. The BIST has a built-in circuit capable of providing error detection and correction [28]–[31]. However, several studies conducted [30], [32], [33] have shown that the BIST can be prone to false alarms and can result in unnecessary costly replacement, requalification, delayed shipping, and loss of system availability. There is a need to develop scientific methodology to predict the damage in copper–aluminum electronic packages, without knowing their prior aging history. Prognostic health management (PHM) is a method for assuring the reliability of a system by monitoring the system in real time as it is used in the field. A PHM system if implemented for copper–aluminum wire bond interconnects could provide the information of the electronic system’s state and the possibility of impending failure. Leading information on near failure systems could allow enough time for repair or replacement

TABLE I
DIMENSIONS OF TEST VEHICLE

Parameter	Dimensions (mm)
Width of Package	4.5
Length of Package	5.5
Height of Package	0.7
Length of Pin	0.45
Width of Pin	0.3
Pitch	0.5

of the damaged modules. In addition, it is envisioned that the leading indicators for the copper–aluminum system could be used for defect detection.

Previously, leading indicator-based PHM methodologies for residual life computation of electronic solder joints subjected to single, multiple, and superimposed thermal environments comprising of isothermal aging and thermal cycling have been developed [34]–[36]. Examples of the second-level interconnect damage precursors include microstructural evolution, IMC growth, stress, and stress gradients. Previously, damage precursors have been developed for various lead-free alloy compositions on a variety of area-array architectures. The PHM methodology for the second-level interconnects was successfully developed for microstructure evolution of damage-based leading indicator for estimating prior accrued damage [34]–[38]. Researchers have also implemented the PHM technique for the assessment of damage and remaining useful life (RUL) in an electronic system, which are subjected to thermomechanical load and sequential multiple thermal environment [39]–[41]. In this paper, a PHM framework has been introduced using the Levenberg–Marquardt (LM) algorithm based on physics-based state vectors for the assessment of accrued damage and future degradation prediction, using IMC layer development when a Cu–Al system is subjected to thermal aging, as a leading indicator.

II. TEST VEHICLE

The test vehicle used for the study is a 32-pin chip-scale package. The package is 4.5 mm in length, 5.5 mm in width, and 0.7 mm in height. Each pin has a length of 0.45 mm and a width of 0.3 mm. The package interconnects have an I/O pitch of 0.5 mm. All the packages have 30- μm diameter copper wires and aluminum pads. The packages used for the study were not daisy chained. Package dimensions are listed in Table I.

Fig. 1 shows the optical microscopic images of the package bottom. Fig. 2 shows the package top view. Fig. 3 shows X-ray images of the package taken using the YXLON Cougar micro-CT system. Fig. 4 shows the 3-D micro-CT reconstruction showing copper–aluminum wire bonds. The chip and the electronic mold compound have been deselected for better visibility of the copper–aluminum interconnects. Fig. 5 shows the magnified view of a single wire bond.

III. TEST MATRIX

Test packages were subjected to 150 °C (25 samples), 175 °C (10 samples), and 200 °C (15 samples) isothermal aging environment. For aging at 150 °C and 175 °C,

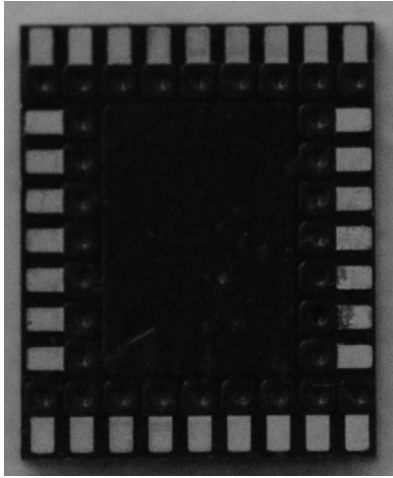


Fig. 1. Bottom view of an optical image.



Fig. 2. Top view of an optical image.

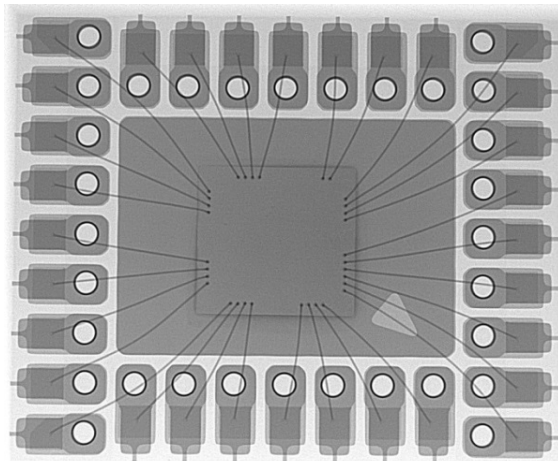


Fig. 3. Top view of an X-ray image.

the IMC growth was monitored at the interval of 168 h. For an aging temperature of 200 °C, the reading interval was 48 h. To study the effect of temperature-humidity bias, a set of packages was subjected to three different conditions: 1) 130 °C/100%RH; 2) 120 °C/100%RH; and 3) 110 °C/100%RH. A reading interval for these

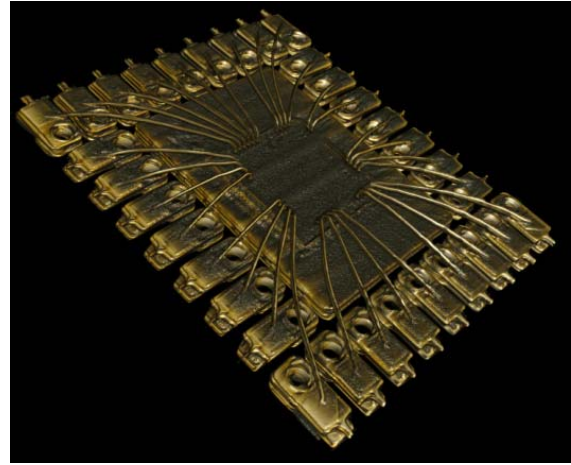


Fig. 4. 3-D micro-CT reconstruction of package.



Fig. 5. Close-up of copper wire bond.

tests was 24 h. Packages were potted into resin, polished, and then this polished surface was sputter coated with gold, at 25 μ A, for 45 s. Cross sectioning was performed to look at the center of the ball bond. This was selected, because this view covers the maximum wire bond in the cross section. The IMC growth was observed using scanning electron microscopy (an accuracy of 0.01 μ m). An IMC thickness at multiple locations was recorded in each image, and a mean value of readings was considered as a final IMC thickness. This ensured accuracy in measurement. Different modes of Energy-dispersive spectroscopy (EDS) scans (e.g., line scan and point scans) were performed for material characterization.

IV. EXPERIMENTAL RESULT AND ANALYSIS

A. High-Temperature Thermal Aging

Fig. 6 shows the development of an IMC layer when packages were subjected to the 150 °C isothermal aging. The IMC growth over the period of temperature can be observed. Similarly, images of IMC growth have been captured at the thermal aging conditions of 175 °C and 200 °C, and are shown in Figs. 7 and 8, and the area of interest in these images

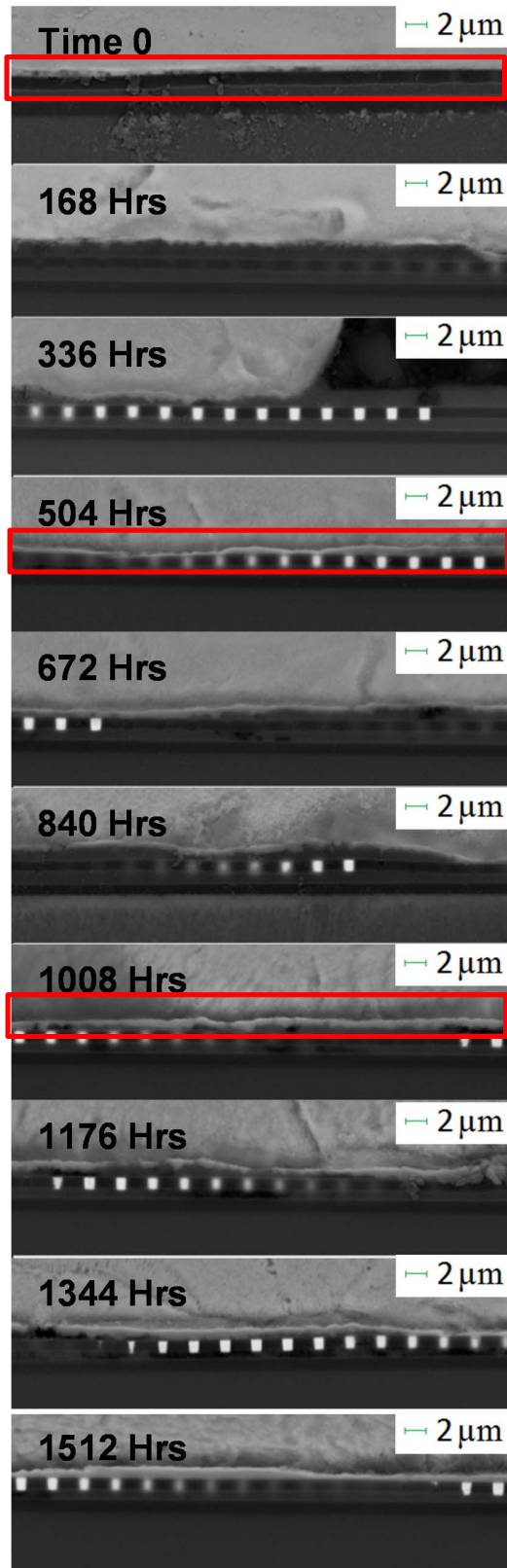


Fig. 6. IMC development at 150 °C.

is the area of Cu–Al interface. It is marked with red box. Intermetallic phase growth was observed in those regions. Bright square dots that appear in the image are tungsten (W) vias located below Al pad.

Even after aging for 3360 h, at 150 °C, IMC corrosion was not found. IMC growth is very slow. Initially, only the Cu-rich phase of IMC was visible. However, after aging for 840 h, an Al-rich phase was distinctly visible in the Cu–Al intermetallics. In case of thermal aging at 175 °C, the Al-rich phase was detected after aging after only 336 h of thermal aging, much sooner than the 840 h required at 150 °C. The initial cracking of wire bond was observed after 1008 h of aging at 175 °C. Initial cracks were observed at the edges of ball bond, in the copper-rich interface, and then, they propagated toward center, resulting into complete cracking in most of the wire bonds after 1176 h. Even after complete cracking, it was observed that the IMC growth continued resulting in the formation of a singular IMC phase below the crack. The aluminum from the Al-pad continued to diffuse into the IMC, but diffusion of copper from ball bond got restricted due to crack. IMC growth after crack formation resulted in the development of a continuous layer of an aluminum-rich phase below the crack. Similar trend was observed in the third thermal aging condition at 200 °C. IMC growth at 200 °C was the fastest of the three thermal conditions measured in this paper. Crack initiation and propagation were faster at a higher thermal aging temperature with the crack initiation observed after 432 h and near complete cracking in majority of the wire bonds after 528 h of 200 °C aging. Crack initiation and propagation are shown in Fig. 9.

Point scans and line scanning techniques were used to analyze IMC phases, as well as region of cracking, using Energy-dispersive X-ray spectroscopy (EDX). The average value of the IMC thickness was calculated, as shown in Fig. 10. The IMC thickness at each reading interval was measured using an rms average of the IMC thickness at 20-points. The EDX analysis on IMC phases to determine its composition is shown in Fig. 11. It was found that two phases found are Cu-rich and Al-rich phases. They primarily consist of Cu_9Al_4 (Spectrum-4; Fig. 11) and CuAl_2 (Spectrum-3; Fig. 11), respectively, which is in good agreement with [11]–[13]. The EDX spot scan also shows that the cracking takes place in the copper-rich interface, as shown in Fig. 12. The location of the crack has also been confirmed using the EDX elemental line scan in Fig. 13. In line scan image, as shown in Fig. 13, the area of crack and IMC is marked by black box, projected as circle in a scan result. An image analysis shows that Cu-rich zone has undergone oxidation and cracking. The source of this oxygen is hypothesized to be outgassing from the molding compound under thermal aging or broken polymer chain in molding compound. Fig. 14 shows the plot of log of normalized IMC versus log of aging duration. IMC was normalized by first subtracting and then dividing IMC thickness measurement by the IMC thickness of time 0. A plot shows that the IMC grows much faster at higher temperatures. These IMC growth data will be later used for the development of prognostics matrix.

B. Accelerated Test for Corrosion Susceptibility of Cu–Al

In this test, two sets of ten packages each were subjected to three different conditions of 110 °C/100%RH, 120 °C/100%RH, and 130 °C/100%RH. To achieve these test conditions, a Parr bomb test apparatus was used.

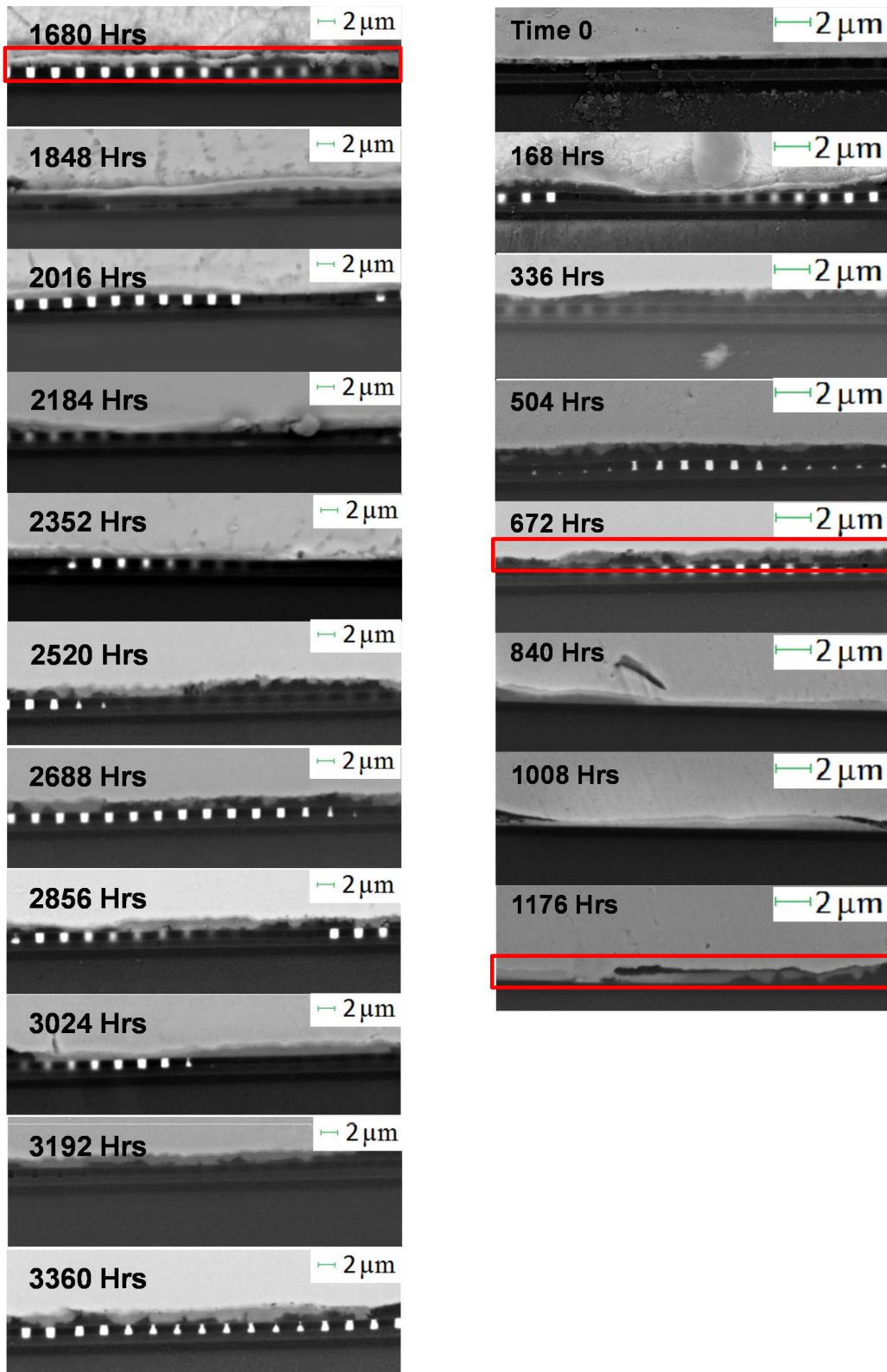


Fig. 7. IMC development at 175 °C.

The Parr bomb test apparatus, as shown in Fig. 15, is a closed pressure vessel in which 100%RH can be maintained at high ambient temperatures. The Polytetrafluoroethylene cup inside the Parr bomb was filled with water, and packages were placed

in a cup such that they will not be immersed into water but rather only in contact with the water vapors.

A microstructure analysis using a scanning electron microscope was performed on parts subjected to the highly

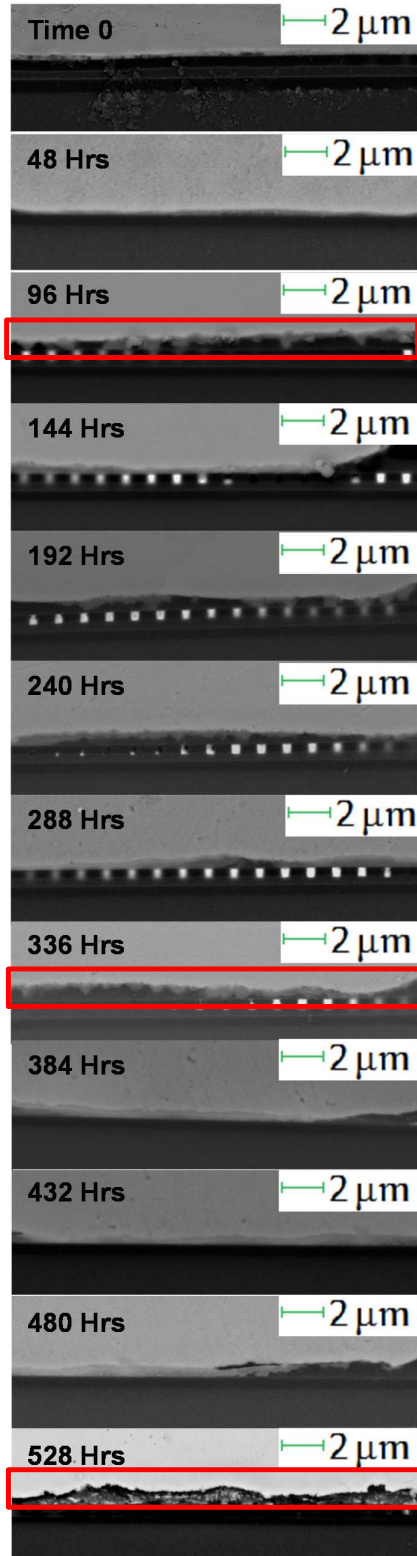


Fig. 8. IMC development at 200 °C.

accelerated stress test. Figs. 16–18 show the cross section images of the wire bond. In all the cases, no significant growth of IMC was found. Test temperatures are not high enough to accelerate IMC growth. Only other explanation for failure is the potential corrosion of either IMC or Al due to

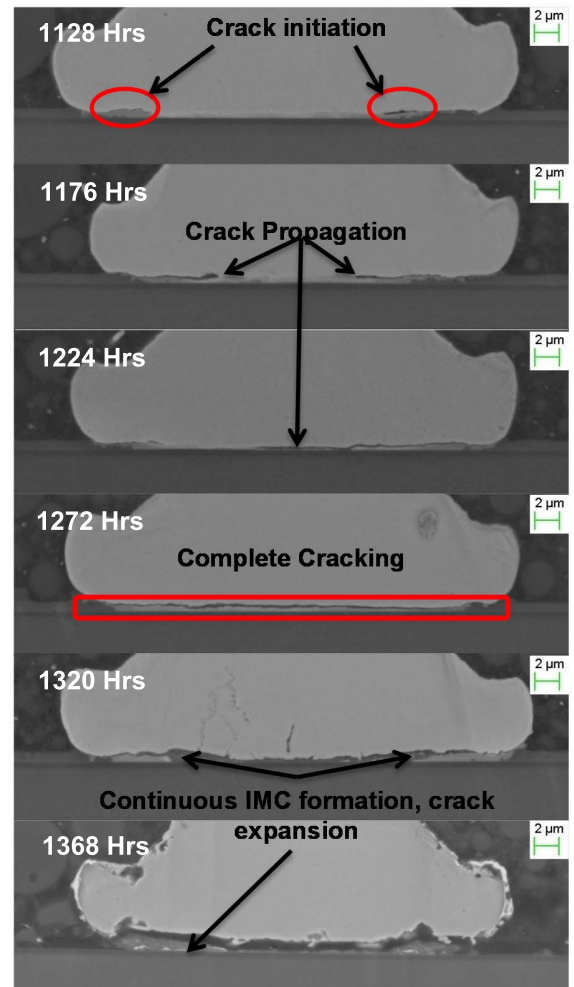


Fig. 9. Crack initiation and propagation.

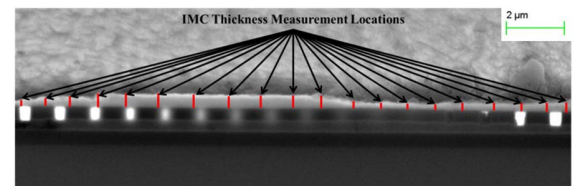
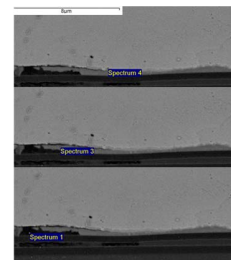


Fig. 10. Method for measurement of the IMC growth.



Element	S_1	S_3	S_4
C	10.25	-	-
O	53.80	-	-
Al	15.59	56.79	36.24
Si	15.89	10.17	-
Cl	0.40	-	-
Cu	4.07	33.05	63.76

Fig. 11. EDX spot analysis to determine IMC composition.

a high temperature and humidity condition. In Fig. 16, micro-crack initiation was found after aging duration of 96 h, at 110 °C/100%RH. Cracks are highlighted with red box.

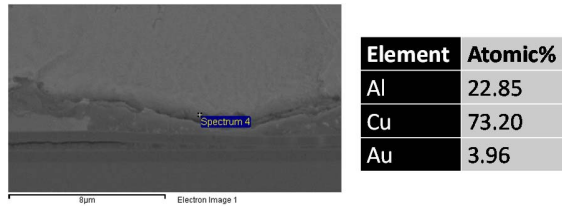


Fig. 12. EDX spot analysis of crack.

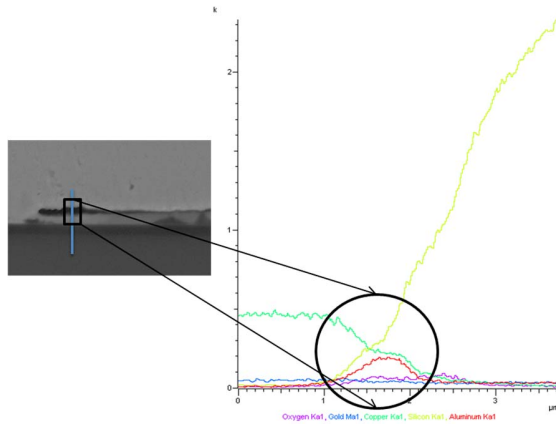


Fig. 13. EDX line scan through crack.

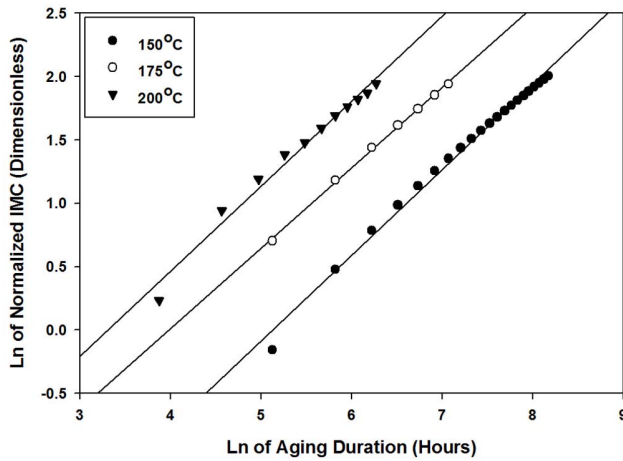


Fig. 14. IMC growth for thermal aging at 150 °C, 175 °C, and 200 °C.

Bigger cracks were found after 240 h of aging, but complete interfacial cracking was not observed. In case of higher temperatures, i.e., 120 °C, instead of crack, complete corrosion of IMC and Al pad was observed, as shown in Fig. 17. Completely corroded interface can be seen after 216 h of testing. For 130 °C/100%RH testing condition, a ball bond lift was observed after 168 h of aging. A thick layer of corroded interface is shown in Fig. 18(d). EDS line scans, point scans, and area scanning techniques were used.

Fig. 19 shows the point scan analysis at the Cu–Al wire bond interface. Three points, two at the end and one at the center, were selected from the same wire bond. Results (percent atomic weight) of all three point scans are tabulated in Table II. Analysis indicates that oxygen was present at the Cu–Al interface. The percentage atomic weight of oxygen was higher



Fig. 15. Parr bomb (courtesy of Parr Instruments Company).

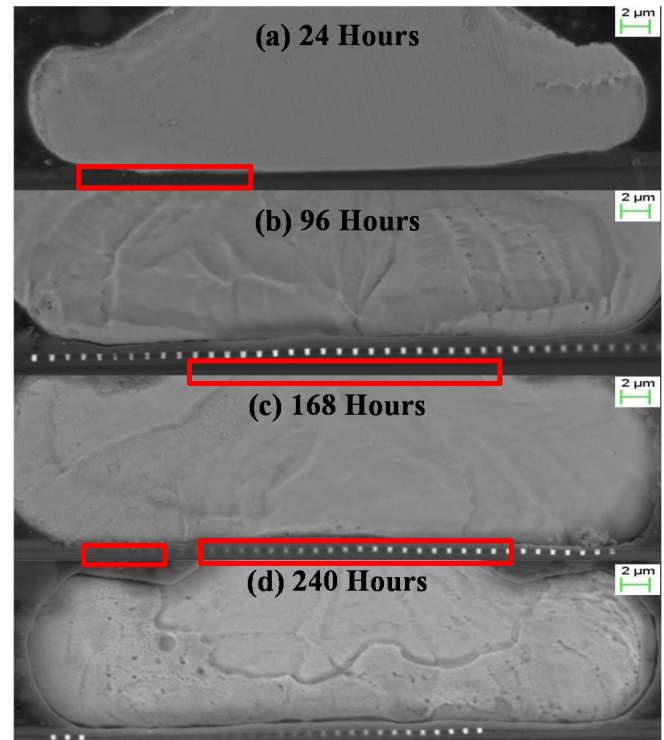


Fig. 16. Crack development and propagation at 110 °C/100%RH.

at edges, showing that the initial corrosion took place at edges, and then it propagated toward center. For all the three cases, oxidation was predominantly found in the Cu-rich phase.

Fig. 20 shows the EDS line scan from Cu ball bond through Al pad to the Si-chip. Analysis results indicate that the cracking of wire bond took place in Cu-rich zone, and the Al-rich zone was still intact. In order to ascertain that the cracking is due to corrosion, but a visual polishing artifact, area mapping was done. Fig. 21 shows area mapping performed to find oxygen content of selected area. The intensity of red dots

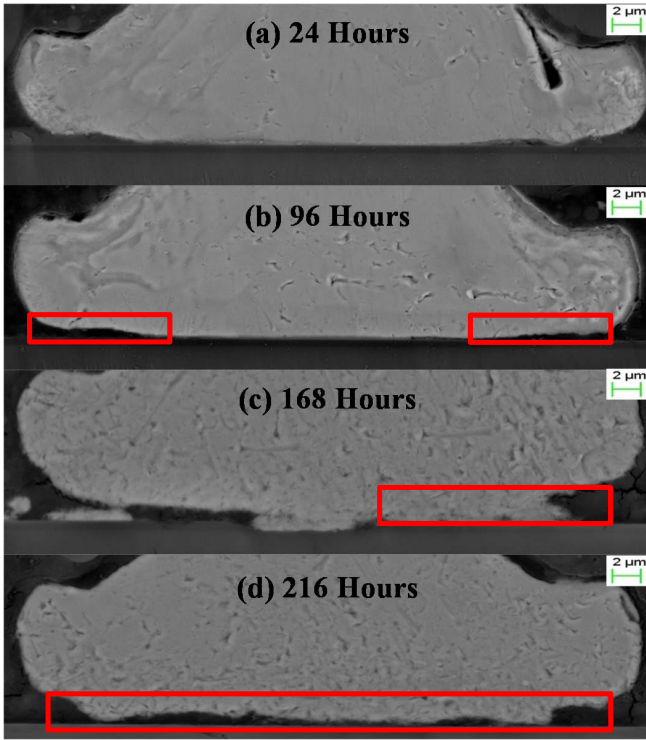


Fig. 17. Crack development and propagation at 120 °C/100%RH.

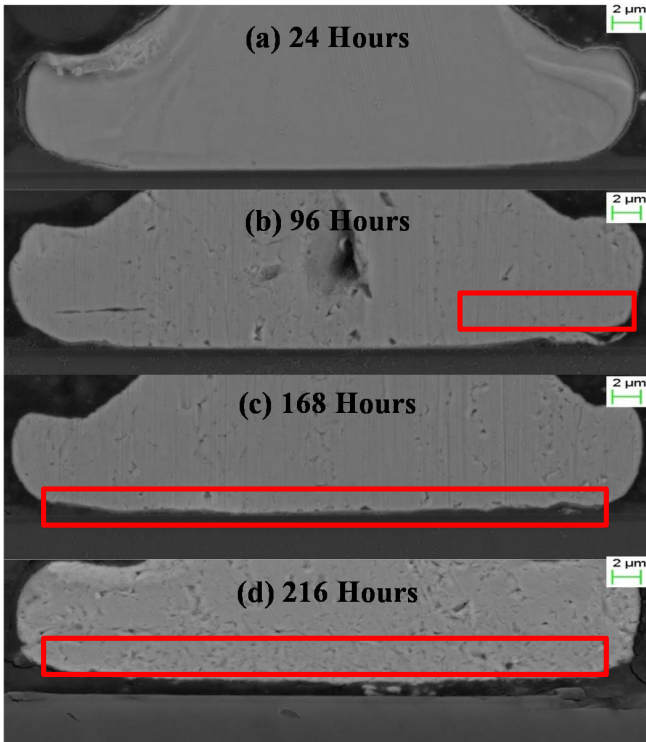


Fig. 18. Crack development and propagation at 130 °C/100%RH.

indicates the concentration of oxygen at the location of the red dot. Fig. 21 shows that the dark red spots were spotted in the region of cracking, and area near it. Density of the oxygen-rich region indicated by the red dots shows that the cracks shown are due to oxidation.

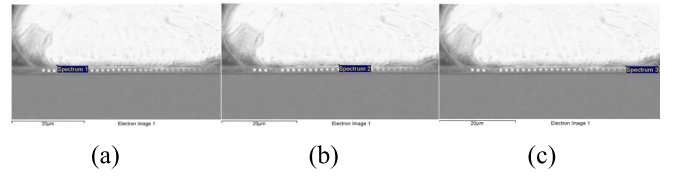


Fig. 19. EDS spot analysis. (a) Spectrum 1. (b) Spectrum 2. (c) Spectrum 3.

TABLE II
PERCENTAGE ATOMIC WEIGHT OF ELEMENTS

Elements	Spectrum 1	Spectrum 2	Spectrum 3
O	33.36	17.37	21.56
Al	3.08	2.74	2.63
Si	13.00	5.25	7.80
Cl	0.19	0.03	0.03
Cu	50.37	74.61	67.98

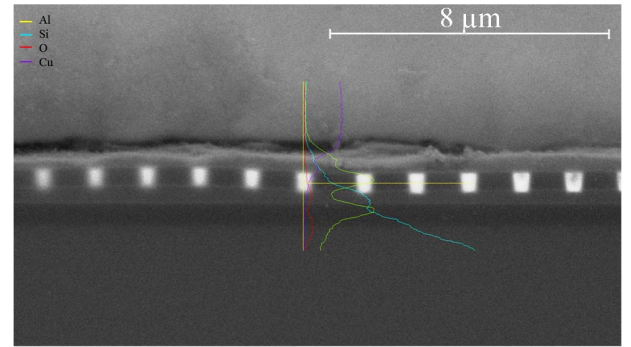


Fig. 20. EDS line scan of crack in wire bond.

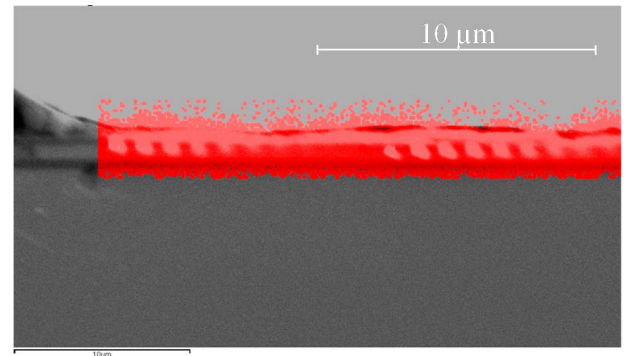


Fig. 21. Area mapping for oxygen in the region of cracking.

The corrosion mechanism has been analyzed using the Pourbaix diagram or the potential/pH diagram, which maps out the potential stable phases of the aqueous electrochemical system. Pourbaix diagrams are shown in Figs. 22 and 23. The vertical axis is labeled for the voltage potential with respect to a standard hydrogen electrode as calculated by the Nernst equation. The lines in the Pourbaix diagram show the equilibrium condition where the activities for each of the species are equal on either side of the line. On either side of the line, one of the ionic species is said to be predominant. The Pourbaix diagram has been used to identify the regions of immunity, corrosion, and passivity for both copper

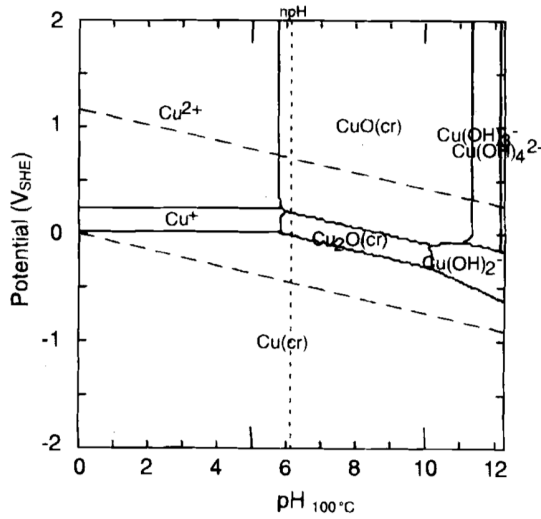


Fig. 22. Pourbaix diagram of copper at 100 °C [42].

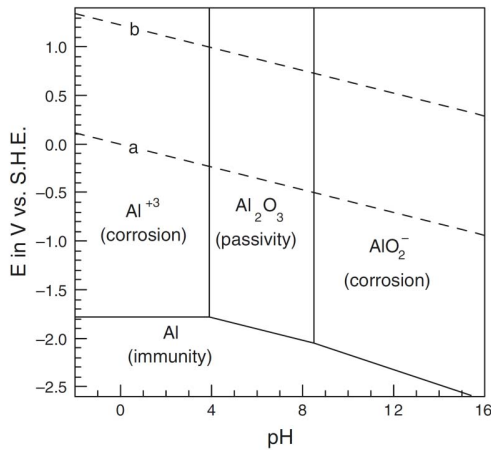
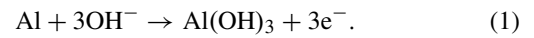


Fig. 23. Pourbaix diagram of aluminum [43].

and aluminum. The vertical lines indicate the species that are in acid–alkali equilibrium. The nonvertical lines separate the species at redox equilibrium. In particular, the horizontal lines separate redox equilibrium species not involving hydrogen or hydroxide ions. The diagonal lines separate redox equilibrium species involving hydrogen or hydroxide ions. The dashed lines enclose the practical region of stability of the aqueous solvent to oxidation or reduction, and thus the region of interest in aqueous systems. Outside the dashed region, water breaks down and not the metal.

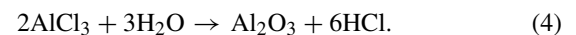
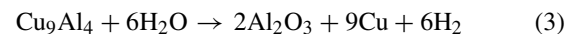
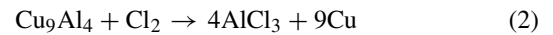
In general, the metal is not attacked and forms stable unreacted metal species in the region of immunity, metal forms a stable oxide or stable hydroxide in the region of passivity, and metal is susceptible to corrosion in the region labeled as corrosion. Low E (or pE) values represent a reducing environment. High E values represent an oxidizing environment. Electrochemical potential represents the driving force for oxidation or reduction. The electrochemical potential is generally cited as standard reduction potential and quantifies the tendency of the chemical species to be reduced. More positive values of reduction potential indicate higher ease with which that

the chemical species will be reduced. Corrosion of metal usually occurs at the anode. The standard electrochemical potential of pure Cu is +0.34 V. The electrochemical potential of aluminum is −1.67 V. Thus, in the copper–aluminum system, copper is easier to reduce, and aluminum is easier to oxidize. The exact value of electrochemical potential of IMC components, i.e., Cu_9Al_4 and CuAl_2 , is unknown, and it reported that it should be in between the potential values of pure Cu and Al [44]. Therefore, theoretically based on electrochemical potential values, being most active metal in the system, Al would act as sacrificial anode, and undergo the following reaction:



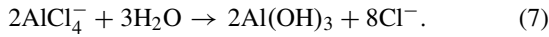
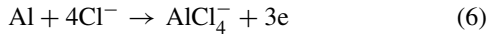
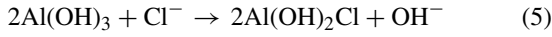
Figs. 22 and 23 show the Pourbaix diagram for Cu and Al, respectively, for 1e–6M concentration at 373 K. Corrosion proneness in Cu is much less than that in Al. In regions where Al^{+++} is stable, corrosion is possible. In the region where aluminum oxide is stable, resistance or passivity to corrosion is possible. If the pH is between 4 and 8.3, Al_2O_3 is stable, and thus protects the aluminum. Aluminum hydroxide forms a stable passivation layer around bare Al pad. The pH values of most of the commercial electronic molding compounds falls in this range of 4–8.3. Passivation layer stability window might get narrow at in the presence of ionic contaminations, such as halide ions. With the industry migration to green molding compound, which is halide ion free or having very less halide concentration, the possibility of narrowing of the stability window and the possibility corrosion of Al pad are lower.

During testing of samples in this paper, corrosion of a wire bond was found during highly accelerated stress test in the Parr bomb apparatus. Two main phases found in the IMC development study were Cu_9Al_4 and CuAl_2 . Cu_9Al_4 is on a copper ball side, while CuAl_2 was found on a Al pad side of IMC. A higher fraction of aluminum in Al-rich phase forms a strong passivation layer, which stops further reaction, even at low pH values [21], [45]. On the other hand, Cu_9Al_4 , which is a Cu-rich IMC layer, has lower Al fraction—which means it will have a weaker passivation layer than the CuAl_2 and Al pad. This layer can be easily attacked by moisture and even the small concentration of ionic contamination can trigger the corrosion reaction, making it corrosion prone. The detailed microstructure analysis of the aged samples revealed that the IMC formed during the bonding process was corroded. An IMC layer formed near a copper ball region (Cu-rich interface) found to be corrosion prone than the other IMC layers. Line scans and point scans showed that a higher oxygen content, i.e., corrosion followed by cracking was found in the Cu-rich interface (Figs. 20 and 21). There are different possibilities in which reaction may occur

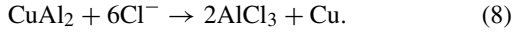


The main byproducts of reaction are Al_2O_3 and HCl. Al_2O_3 is brittle oxide and can cause cracks in an oxidized region. Hydrochloric acid further gets dissolved into moisture and

breaks into chlorine ions. These chlorine ions again attack Cu_9Al_4 and continue the corrosion process. The process continues and can eat away Cu-rich IMC phase, making it mechanically and electrically unstable, causing excessive stresses, and mostly results into crack formation and propagation. The observations noted in this experiment are in good agreement with [2], [4], [20], [21], and [23]. Prior studies were limited to maximum 120 h of aging. However, for 120 °C and 130 °C Parr bomb testing after 168+ h of aging, it was found that along with Cu-rich IMC, Al-rich IMC and Al pad were also oxidized. This might be due to extreme conditions, and prolonged exposure to such environment, which might have caused the degradation of molding compound, releasing some byproduct, which can make reaction more aggressive. Initially, Al will react with moisture to produce a passivation layer of $\text{Al}(\text{OH})_3$. This can be attacked by chlorine ions and broken down as follows:



One of the products of reaction is chlorine ion. Therefore, once the reaction initiates, it will keep on going and Al pad will undergo pitting corrosion. The typical corrosion reaction of CuAl_2 can be described by the following reaction [21]:



C. Calculation of Activation Energy for Cu–Al System

Consistent with the acquired data on the Cu–Al IMC system, the square dependence of the IMC thickness on the aging duration has been assumed to calculate the activation energy

$$X^2 = Kt + C \quad (9)$$

where X is the IMC thickness (μm), t is the aging time (s), K is the reaction rate of an IMC formation ($\mu\text{m}^2/\text{s}$), C is the constant related to the initial IMC thickness (μm^2), and the reaction rate is represented as a function of temperature

$$K = K_0 e^{\frac{-\Delta Q}{RT}} \quad (10)$$

where K_0 is the multiplication factor ($\mu\text{m}^2/\text{s}$), R is the gas constant (1.99 cal/mol K), T is the aging temperature (K), and ΔQ is the activation energy (Kcal/mol). Using (9), data on square of IMC thickness for the temperatures of 150 °C, 175 °C, and 200 °C have been fit versus aging time in seconds (Fig. 24). Three values of growth rate, i.e., k were obtained, and plotted against $1/T$, as shown in Fig. 25. Activation energy calculated from the plot is 12.893 Kcal/mol, i.e., 0.559 eV.

Tables III and IV show the comparison of energy of activation and IMC growth rate with data previously published in the literature. Activation energy obtained in current experiment is in good agreement with the activation energy reported in [10] and [17]. In [10] and [17], the growth rate of IMC because of the temperature bias is in the range of 10^{-6} – $10^{-8} \mu\text{m}^2/\text{s}$, which is also in good agreement with current study ($10^{-7} \mu\text{m}^2/\text{s}$).

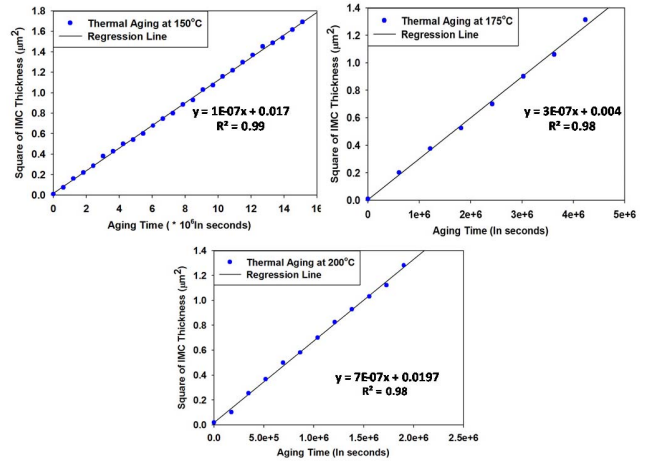


Fig. 24. Intermetallic growth rates at different temperatures.

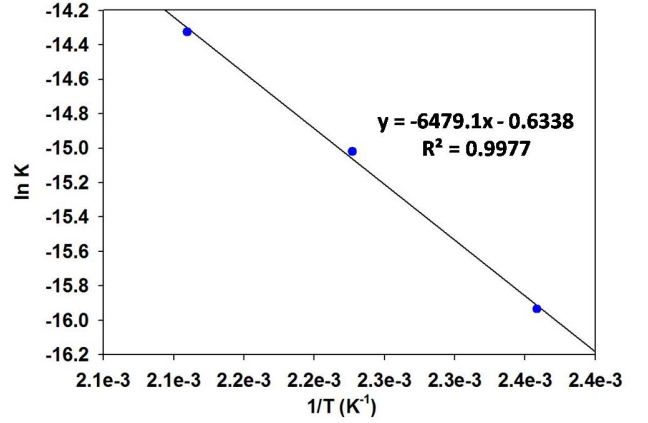


Fig. 25. $\ln(k)$ (IMC growth rate) versus $1/T$ (1/aging temperature).

TABLE III
COMPARISON OF ACTIVATION ENERGIES FOR Cu–Al

WB Type	Reference	Test Temperatures (°C)	ΔQ (Kcal/mol)
Copper	[17]	175, 200, 225	6.1
	[3]	150, 250, 300	26
	[10]	150, 200, 250	10.71
	Current Study	150, 175, 200	12.89

V. PROGNOSTICATION APPROACH FOR HIGH-TEMPERATURE STORAGE LIFE

In order to assess the accrued damage in the Cu–Al package, IMC growth is used as a leading indicator of failure for interrogation of state of system and RUL calculations. Measurements of IMC thickness growth have been fit into

$$\frac{y_1 - y_0}{y_0} = kt_1^n \quad (11)$$

Prior damage in each case has been prognosticated based on the IMC evolution. Prognostication involves withdrawal of three samples at three periodic intervals. The samples were then cross sectioned, potted, and polished to measure

TABLE IV
COMPARISON OF IMC GROWTH RATE FOR Cu–Al SYSTEM

WB Type	Reference Temperature	Temperature (°C)	Growth Rate (μm ² /s)
Copper	150°C	[3]	1.88*10 ⁻⁸
		[10]	2.15*10 ⁻⁸
		Current Study	1.21*10 ⁻⁷
	175°C	[17]	3.57*10 ⁻⁷
		Current Study	3.25*10 ⁻⁷
	200°C	[10]	2.56*10 ⁻⁸
		[17]	6.26*10 ⁻⁷
		Current Study	7.02*10 ⁻⁷

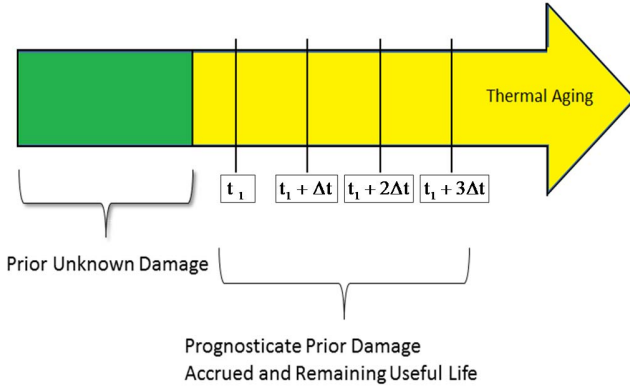


Fig. 26. Prognostication of thermally aged samples.

intermetallic thickness. Prior damage accrued was prognosticated. An IMC growth parameter was used to compute life consumed due to exposure to thermal aging

$$\frac{y_1 - y_0}{y_0} = kt_1^n \quad (12)$$

$$\frac{y_2 - y_0}{y_0} = k(t_1 + \Delta t)^n \quad (13)$$

$$\frac{y_3 - y_0}{y_0} = k(t_1 + 2\Delta t)^n \quad (14)$$

where y_1 is the IMC thickness at time t_1 , Δt is the time interval for the future IMC thicknesses, i.e., y_2 and y_3 , and k is the coefficient standing for square root of aging duration. The parameter y_0 is IMC thickness before initiation of thermal aging. The solution requires three equation and three unknowns. The LM algorithm was used to solve these three nonlinear equations (12)–(14) and optimization of three unknowns.

Fig. 26 shows an overview of the methodology used for the prognostication of a Cu–Al wire bond for prior accrued damage using an IMC layer as a leading indicator of failure. Consider a field deployed electronic package, which has been used for certain time, say t_1 , which is unknown. For prognostication, samples will be taken from field at the uniform interval of time Δt . The IMC layer of all the packages can be measured and then using (12)–(14) providing measurements of y_1 , y_2 , and y_3 . In case of isothermal aging, in which

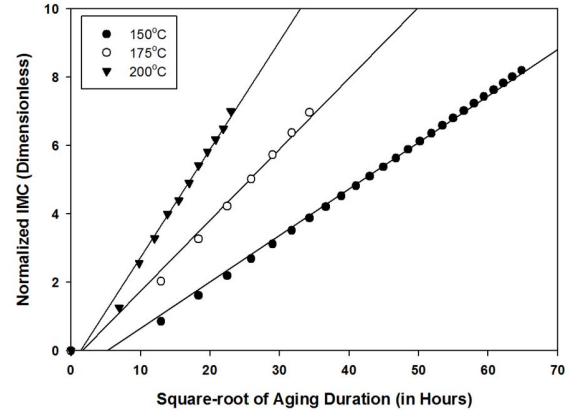


Fig. 27. Normalized IMC versus square root of aging time.

IMC development is primarily driven by diffusion, the value of n from (11) is theoretically known to be 0.5, so equation has been updated to

$$\frac{y_1 - y_0}{y_0} = kt_1^{0.5} \quad (15)$$

$$\frac{y_2 - y_0}{y_0} = k(t_1 + 168)^{0.5} \quad (16)$$

$$\frac{y_3 - y_0}{y_0} = k(t_1 + 336)^{0.5} \quad (17)$$

Equation (11) was used to plot a graph of normalized IMC against square root of aging time, for all three cases, as shown in Fig. 27. Linear plot implies that the value of n in (11) is 0.5. The LM algorithm was used to solve these three nonlinear equations and prediction of RUL.

A. Levenberg–Marquardt Algorithm

The relationship between the IMC growth parameter and the time is nonlinear. Inverse solution for interrogation of system state is challenging for damage evolution in such systems. The LM algorithm n iterative technique that computes the minimum of a nonlinear function in multidimensional variable space has been used for identifying the solution in the prognostication neighborhood. Let f be an assumed functional relation between a measurement vector referred to as prior damage and the damage parameter vector, p , referred to as predictor variables. The measurement vector is the current value of the leading indicator of failure, and the parameter vector includes the prior system state, accumulated damage, and the damage evolution parameters. An initial parameter estimate p_0 and a measured vector x are provided, and it is desired to find the parameter vector p that best satisfies the functional relation f , i.e., minimizes the squared distance or squared error, $\varepsilon^T \varepsilon$. The minimize parameter vector p , given by

$$F(p) = \frac{1}{2} \sum_{i=1}^m (g_i(p)^2) = \frac{1}{2} g(p)^T g(p) \quad (18)$$

$$F'(p) = J(p)^T g(p) \quad (19)$$

$$F''(p) = J(p)^T J(p) + \sum_{i=1}^m g_i(x) g_i''(x) \quad (20)$$

TABLE V
DAMAGE ACCRUAL RELATIONSHIP USING IMC AS LEADING INDICATORS

Aging Condition	150°C	175°C	200°C
Equation	$K_n = 0.023(t)^{0.482}$	$K_n = 0.427(t)^{0.498}$	$K_n = 0.045(t)^{0.513}$

where $F(p)$ represents the objective function for the squared error term $\varepsilon^T \varepsilon$, $J(p)$ is the Jacobian, and $F'(p)$ is the gradient, and $F''(p)$ is the Hessian. The variation of an F -value starting at p and with direction h is expressed as a Taylor expansion as follows:

$$F(p + ah) = F(p) + ah^T F'(p) + o\alpha^2 \quad (21)$$

where α is the step length from point p in the descent direction, h . Mathematically, h is the descent direction of $F(p)$ if $h^T F'(p) < 0$. If no such h exists, then $F'(p) = 0$, showing that in this case the function is stationary. Since the condition for the stationary value of the objective function is that the gradient is zero

$$F'(p + h) = L'(h) = 0. \quad (22)$$

The descent direction can be computed from

$$(J^T J + \mu I)h = -J^T g. \quad (23)$$

The term μ is called the damping parameter, $\mu > 0$ ensures that coefficient matrix is positive definite, and this ensures descent direction. When the value of μ is very small, then the step size for LM and Gauss–Newton is identical. An algorithm has been modified to take the equations of intermetallic growth under isothermal aging to calculate the unknowns.

The LM algorithm was developed based on (15)–(17) for the prediction of RUL, when packages were subjected to isothermal aging conditions. Table V represents the damage accrual relationships, where K_n is the IMC thickness at any time t . The equations were derived from experimental data. Exponent of time t in all three cases is in the vicinity of 0.5. It shows that the IMC growth in Cu–Al wire bond system is driven by Fickian diffusion. In the Fickian diffusion, kinetic exponent (exponent of time) is 0.5. It means that the rate of diffusion follows linear trend as a function of square root of aging duration. This exponent was then used as n in (11). Since it governs the IMC formation rate, a careful evaluation of exponent is required. This exponent was used in the prognostics model to capture prior accrued damage. For thermal aging at 150 °C, prognostication was done at 1176, 1344, and 1512 h of thermal aging. Results of the prognostication are shown in Table VI. The 3-D plots of algorithm output are shown in Fig. 28.

The z -axis shows error term. The LM algorithm iteratively tries to find such values of adding duration and normalized IMC so that the model will have a minimum error. Its aim is to find a single point, which will have minimum global error, i.e., point of convergence. This point represents solution, i.e., prior accrued damage. Solution points are marked in red circle, and their X - and Y -coordinate values show predicted prior accrued

TABLE VI
COMPARISON OF EXPERIMENTAL AND PROGNOSTICATED RESULTS, FOR ISOTHERMAL AGING AT 150 °C

	Experimental (Hours)	Prognosticated (Hours)	% Error
t_1	1176	1286	8.5%
t_2	1344	1298	3.5%
t_3	1512	1578	4.1%

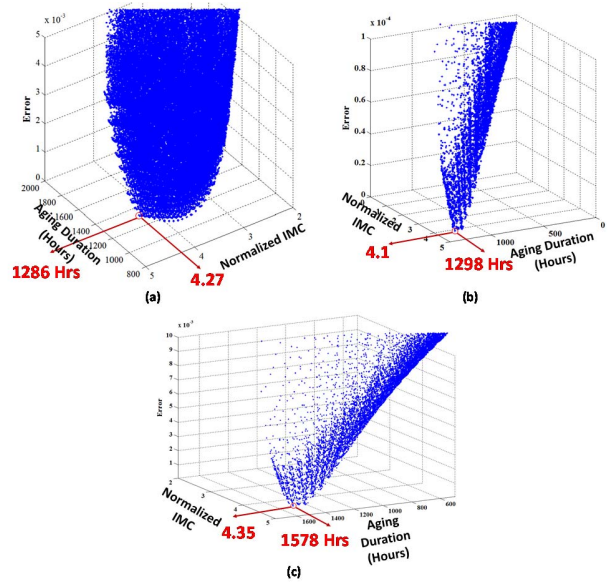


Fig. 28. 3-D plot of error versus aging duration in hours versus normalized IMC thickness, for isothermal aging at 150 °C, for time duration (a) 1176, (b) 1344, and (c) 1512 h.

TABLE VII
COMPARISON OF EXPERIMENTAL AND PROGNOSTICATED RESULTS, FOR ISOTHERMAL AGING AT 175 °C

	Experimental (Hours)	Prognosticated (Hours)	% Error
t_1	504	539	6.5%
t_2	672	656	2.5%
t_3	840	897	6.3%

damage and normalized IMC thickness. The percentage error in between experimental aging duration and prognosticated aging duration was calculated. The error bound was in the range of 3.5%–8.5%. The solution in Fig. 28 corresponds to the point at a minimum error. The minimum error point represents prognosticated aging duration.

Similar approach was used to prognosticate prior accrued damage when packages were subjected to thermal aging of 175 °C. Results are tabulated in Table VII, and the 3-D plot of output are shown in Fig. 29. The percentage error bound for this model was in between 2.5% and 6.5%. The approach was extended to packages subjected to thermal aging at 200 °C. Results are shown in Table VIII, and 3-D plots are shown

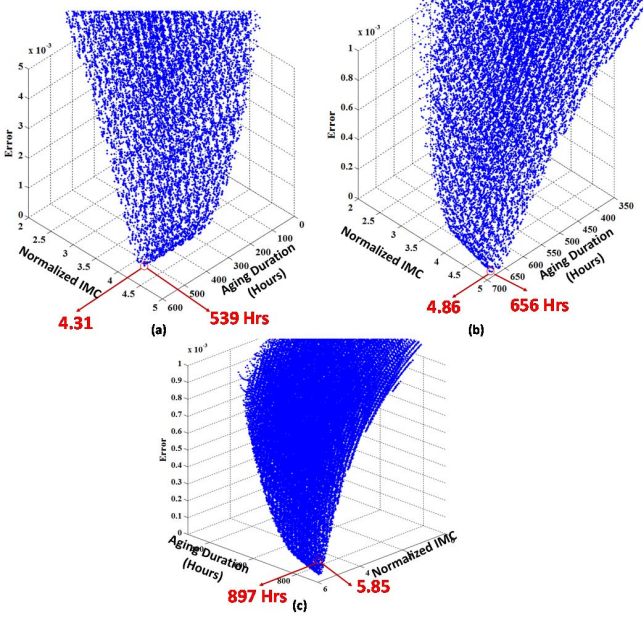


Fig. 29. 3-D plot of error versus aging duration in hours versus normalized IMC thickness, for isothermal aging at 175 °C, for time duration (a) 504, (b) 672, and (c) 840 h.

TABLE VIII
COMPARISON OF EXPERIMENTAL AND PROGNOSTICATED RESULTS,
FOR ISOTHERMAL AGING AT 200 °C

	Experimental (Hours)	Prognosticated (Hours)	% Error
t_1	288	265	8.7%
t_2	336	361	7.0%
t_3	384	395	2.8%

in Fig. 30. The percentage error in models prediction was in between 2.8% and 8.7%.

VI. PROGNOSTICS PERFORMANCE EVALUATION

In this paper, we will use different performance metrics [46], [47] to evaluate the performance of model developed based on the LM algorithm and IMC growth as a leading indicator of failure, when Cu–Al incorporated parts are subjected to sustained operation at elevated temperatures. The model will be evaluated based on average bias, precision, mean squared error (MSE), mean absolute percentage error (MAPE), α - λ performance, relative accuracy (RA), cumulative RA (CRA). These parameters were used to compare the performance of different prognostics metrics in [46] and [48].

A. Average Bias

This method averages prediction errors made at all subsequent time steps after ℓ th unit under test (UUT). This method is then extended to establish the overall bias over all UUT. In this form, variability in prediction and presence of outliers

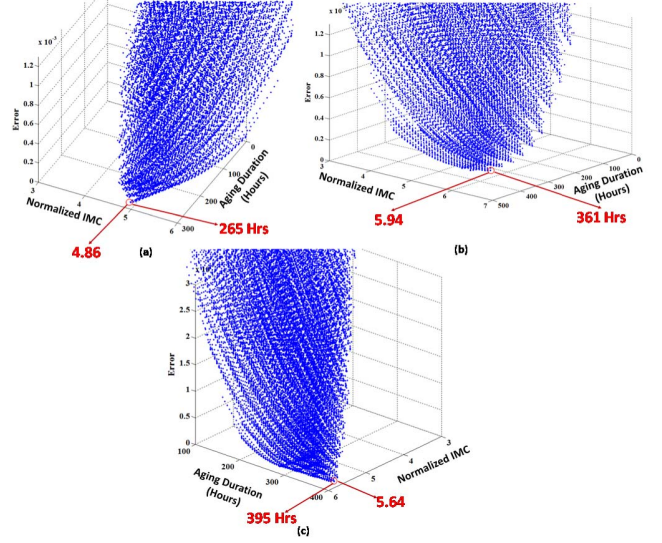


Fig. 30. 3-D plot of error versus aging duration in hours versus normalized IMC thickness, for isothermal aging at 200 °C, for time duration (a) 288, (b) 336, and (c) 384 h.

is neglected [46]. The average bias B_l can be calculated by

$$B_l = \frac{1}{\ell} * \sum_{i=P}^{EOP} \{\Delta^l(i)\} \quad (24)$$

where

$$\ell = EOP - P + 1 \quad (25)$$

where ℓ is the cardinality of the set of all time indices at which predictions are made, EOP is the end of prediction is earliest time index, i , after prediction crosses failure threshold, and P is the time index at which first prediction was made by the prognostic model [40]. $\Delta^l(i)$ is the error between predicted and true RUL at time index i for UUT l [47]. The LM algorithm predicts prior accrued damage, i.e., prior aging duration. If we know the total life expectancy of the part, subtraction of life expectancy from prior aging duration will yield predicted RUL.

B. Sample Standard Deviation

Precision in predictions is as important as accuracy. Sample standard deviation (SSD) calculates the variability in prediction by measured spread of error with respect to sample mean of the error. This metric is restricted to the assumption of normal distribution of errors [46]

$$SSD(i) = \sqrt{\frac{\sum_{l=1}^n [\Delta^l(i) - M]^2}{n - 1}} \quad (26)$$

where M is the sample mean of error.

C. Mean Squared Error

In simple average bias calculation, over prediction and under prediction cancel out each other, so it might not reflect actual accuracy and precision of model. To avoid this, average of

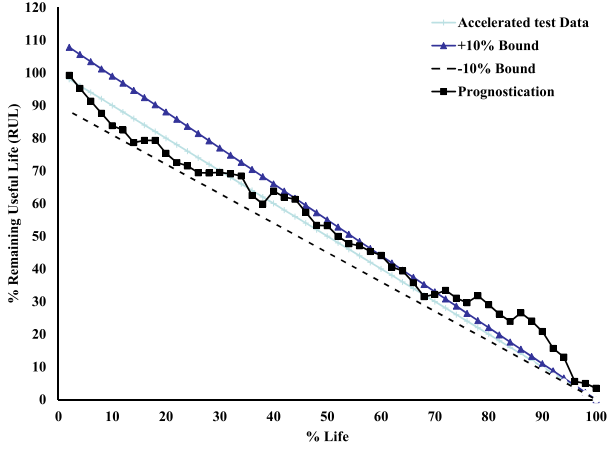


Fig. 31. α - λ curve for prognostication using IMC growth as a leading indicator of failure for thermal aging at 150 °C.

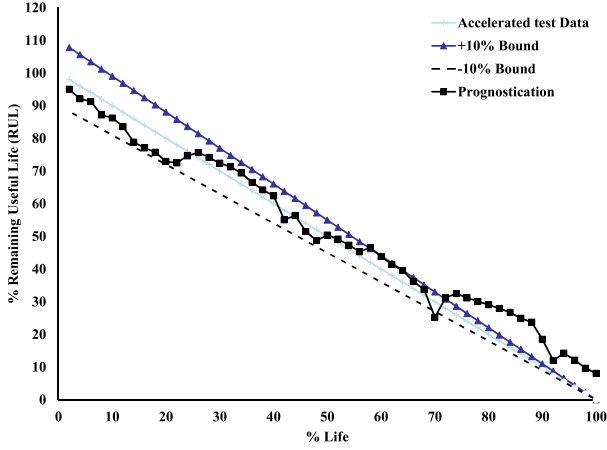


Fig. 32. α - λ curve for prognostication using IMC growth as a leading indicator of failure for thermal aging at 175 °C.

the square of prediction error for multiple UTTs is calculated, which is known as MSE. Derivative of MSE is root mean square error [46]

$$\text{MSE} = \frac{1}{\ell} \sum_{i=1}^{\ell} (\Delta^l(i))^2. \quad (27)$$

D. Mean Absolute Percentage Error

MAPE is unit free accuracy measure only for ratio-scaled data. MAPE weights errors with RUL and averages the absolute percentage error in the multiple predictions [46], [47]

$$\text{MAPE}(i) = \frac{1}{\ell} \sum_{i=1}^{\ell} \frac{100\Delta^l(i)}{r_*^l(i)} \quad (28)$$

where $r_*^l(i)$ in true RUL at time t_1 given that data are available up to ℓ th UTT.

E. α - λ Accuracy

It is essential to know whether the model predictions are within the specified limit of error bound at given time. Time instances are defined as a percentage of RUL after first prediction was made [46], [47]. α - λ accuracy curve is plotted for all three thermal aging conditions in Figs. 31–33, respectively.

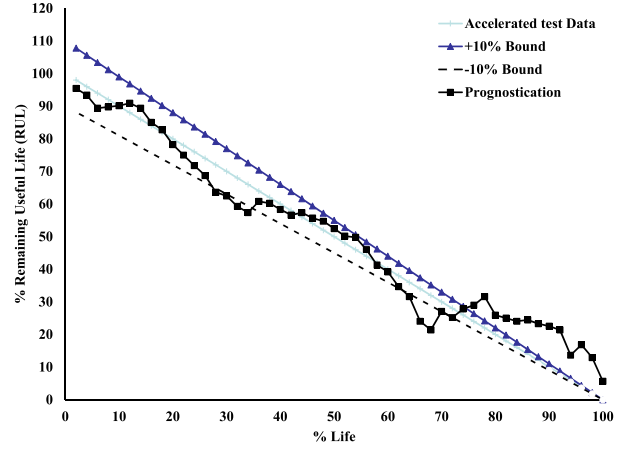


Fig. 33. α - λ curve for prognostication using IMC growth as a leading indicator of failure for thermal aging at 200 °C.

It is the plot of percentage RUL versus percentage life. In this case, a failure was defined as complete cracking of the wire bond interface.

Each prognosticated point in the plot represents algorithm prediction of prior accrued damage and RUL. It is plotted against actual accrued damage and RUL, which was obtained from accelerated test data. This provides the comparison between actual RUL and predicted RUL over complete life of the package. The plot shows whether predicted RUL stays in error bound of $\pm 10\%$ or not. Errors bounds are application specific. Critical applications have narrow error bounds, while for some other applications, it can go up to $\pm 20\%$. Prognostics prediction for 150 °C thermal aging is well within error bound for $\sim 73\%$ of total life, and then, it bounces beyond 10%. For 175 °C, prediction maintains error bound for $\sim 70\%$ of total life, and for 200 °C it dropped down to 64%. Predictions of developed model and acceptable for a major part of life of a Cu–Al incorporated device, when subjected to high-temperature sustained operations.

F. Relative Accuracy

RA for prediction is similar to α - λ curve, but here we measure accuracy level. The time instant is described as a fraction of actual RUL from the first prediction point

$$\text{RA}_\lambda = 1 - \frac{r_*(t_\lambda) - r^l(t_\lambda)}{r_*(t_\lambda)} \quad (29)$$

where $t_\lambda = P + \lambda(\text{EOL} - P)$ and $r^l(i)$ is the RUL estimation for the ℓ th UTT at time T_i as determined from measurements [46].

G. Cumulative Relative Accuracy

CRA aggregates the accuracy levels calculated at multiple time intervals. CRA is normalized weighted sum of relative prediction accuracies at specific instances [46]

$$\text{CRA} = \frac{1}{\ell} \sum_{i=1}^{\ell} w(r^l) \text{RA}_\lambda \quad (30)$$

TABLE IX
COMPARISON OF PROGNOSTICS METRICS
FOR THREE AGING CONDITIONS

Prognostic Parameter	LM Prognostication 150°C	LM Prognostication 175°C	LM Prognostication 200°C
Average Bias	-1.02356	-1.10249	-0.45483
SSD	209.621	63.5503	32.6862
MSE	49649.57	4374.163	1080.598
MAPE	0.78975	0.073164	0.03171
RA ($\lambda=0.5$)	0.9352	0.9916	0.09507
CRA	0.009164	0.0299	0.05812

where w is a weight factor as a function of RUL at all the time indices. In most cases, it is desirable to weight the RAs higher when closer to end of life.

Table IX shows the comparison of prognostics models based upon the parameters discussed in (24) and (26)–(30). Algorithm maintains higher RA at $\lambda = 0.5$ (i.e., after consuming 50% life) for all three temperature ranges. Higher RA is always desirable. SSD and MSE drop down as we increase the aging temperature. Testing at 150 °C goes on for 4200 h, while for 150 °C and 200 °C, it finished in about 1200 and 528 h, respectively. Since at high temperatures, test finishes in very short time, with less error bound SSD and MSD remain restricted. The overall developed model delivers satisfactory performance at all three aging conditions.

VII. CONCLUSION

Microstructure evolution of Cu–Al intermetallics when subjected to thermal aging has been studied in this paper. Two distinct phases were found, namely, Cu-rich interface (Cu_9Al_4) and Al-rich interface (CuAl_2). Complete cracking of wire bond was found after prolonged thermal aging at 175 °C and 200 °C. Crack initiates from edges of ball bond, and propagates toward center. Cu-rich IMCs were found to be corrosion at the Cu–Al interface. A method has been developed for prognostication of accrued prior damage and RUL after exposure to thermal aging. The presented approach uses the LM algorithm in conjunction with the development of damage-based leading indicator for estimating prior accrued damage. Specific damage proxies examined is the intermetallic thickness in a Cu–Al wire bond. The viability of this approach has been demonstrated with a 32-pin chip-scale package without any prior knowledge of aging duration, subjected to thermal aging at 150 °C, 175 °C, and 200 °C. The prognosticated values have been validated versus experimental data. Correlation between the prognosticated damage and the actual accrued damage demonstrates that the proposed approach can be used to assess prior damage accrued because of aging. Performance of prognostication model was evaluated for all three temperature conditions. The concept of CRA, RA, MAPE, SSD, and α - λ accuracy was used for evaluation purpose. It was found that the model developed based on the LM algorithm and IMC thickness growth as a leading indicator of failure for Cu–Al

wire-bonded devices when subjected to high-temperature storage life conditions delivers acceptable performance and predicts RUL and prior accrued damage with high confidence.

VIII. FUTURE WORK

More extensive analysis of a Cu–Al wire bond system subjected to high-temperature-humidity conditions can be undertaken. Various parameters such as ball shear strength and resistance change will be monitored to find appropriate leading indicator of failure for high-temperature-humidity condition. It can then be used to develop prognostics matrix to predict RUL.

REFERENCES

- [1] C. D. Breach, N. H. Shen, T. W. Mun, T. K. Lee, and R. Holliday, "Effects of moisture on reliability of gold and copper ball bonds," in *Proc. 12th Electron. Packag. Technol. Conf.*, Dec. 2010, pp. 44–51.
- [2] T. Boettcher *et al.*, "On the intermetallic corrosion of Cu–Al wire bonds," in *Proc. 12th Electron. Packag. Technol. Conf.*, Dec. 2010, pp. 585–590.
- [3] H.-J. Kim *et al.*, "Effects of Cu/Al intermetallic compound (IMC) on copper wire and aluminum pad bondability," *IEEE Trans. Compon. Packag. Technol.*, vol. 26, no. 2, pp. 367–374, Jun. 2003.
- [4] C. D. Breach, "What is the future of bonding wire? Will copper entirely replace gold?" *Gold Bull.*, vol. 43, no. 3, pp. 150–168, 2010.
- [5] I. Qin, A. Shah, C. Huynh, M. Meyer, M. Mayer, and Y. Zhou, "Role of process parameters on bondability and pad damage indicators in copper ball bonding," *Microelectron. Rel.*, vol. 51, no. 1, pp. 60–66, 2011.
- [6] A. Shah, M. Mayer, Y. N. Zhou, S. J. Hong, and J. T. Moon, "Low-stress thermosonic copper ball bonding," *IEEE Trans. Electron. Packag. Manuf.*, vol. 32, no. 3, pp. 176–184, Jul. 2009.
- [7] J. Chen, D. Degryse, P. Ratchev, and I. De Wolf, "Mechanical issues of Cu-to-Cu wire bonding," *IEEE Trans. Compon. Packag. Technol.*, vol. 27, no. 3, pp. 539–545, Sep. 2004.
- [8] S. Schmitz, M. Schneider-Ramelow, and S. Schröder, "Influence of bonding process parameters on chip cratering and phase formation of Cu ball bonds on AlSiCu during storage at 200 °C," *Microelectron. Rel.*, vol. 51, no. 1, pp. 107–112, 2011.
- [9] L. England, S. T. Eng, C. Liew, and H. H. Lim, "Cu wire bond parameter optimization on various bond pad metallization and barrier layer material schemes," *Microelectron. Rel.*, vol. 51, no. 1, pp. 81–87, 2011.
- [10] S. H. Na, T. Hwang, J. Park, J. Kim, H. Yoo, and C. Lee, "Characterization of intermetallic compound (IMC) growth in Cu wire ball bonding on Al pad metallization," in *Proc. IEEE 61st Electron. Compon. Technol. Conf.*, May/Jun. 2011, pp. 1740–1745.
- [11] K. Wiecek-Ciurawa, K. Gamrat, and Z. Sawłowicz, "Characteristics of CuAl_2 – $\text{Cu}_9\text{Al}_4/\text{Al}_2\text{O}_3$ nanocomposites synthesized by mechanical treatment," *J. Thermal Anal. Calorimetry*, vol. 80, no. 3, pp. 619–623, 2005.
- [12] A. Laik, K. Bhanumurthy, and G. B. Kale, "Diffusion in Cu(Al) solid solution," *Defect Diffusion Forum*, vol. 279, pp. 63–69, Aug. 2008.
- [13] W.-B. Lee, K.-S. Bang, and S.-B. Jung, "Effects of intermetallic compound on the electrical and mechanical properties of friction welded Cu/Al bimetallic joints during annealing," *J. Alloys Compounds*, vol. 390, nos. 1–2, pp. 212–219, 2005.
- [14] Y. H. Tian, C. J. Hang, C. Q. Wang, G. Q. Ouyang, D. S. Yang, and J. P. Zhao, "Reliability and failure analysis of fine copper wire bonds encapsulated with commercial epoxy molding compound," *Microelectron. Rel.*, vol. 51, no. 1, pp. 157–165, 2011.
- [15] J. Chen, Y.-S. Lai, Y.-W. Wang, and C. R. Kao, "Investigation of growth behavior of Al–Cu intermetallic compounds in Cu wire bonding," *Microelectron. Rel.*, vol. 51, no. 1, pp. 125–129, 2011.
- [16] C. J. Hang, C. Q. Wang, M. Mayer, Y. H. Tian, Y. Zhou, and H. H. Wang, "Growth behavior of Cu/Al intermetallic compounds and cracks in copper ball bonds during isothermal aging," *Microelectron. Rel.*, vol. 48, no. 3, pp. 416–424, 2008.
- [17] C. S. Goh, W. L. E. Chong, T. K. Lee, and C. Breach, "Corrosion study and intermetallics formation in gold and copper wire bonding in microelectronics packaging," *Crystals*, vol. 3, no. 3, pp. 391–404, 2013.
- [18] D. Simonovic and M. H. F. Sluiter, "Impurity diffusion activation energies in Al from first principles," *Phys. Rev. B*, vol. 79, pp. 054304-1–054304-12, Feb. 2009.

- [19] L. L. Levenson, "Grain boundary diffusion activation energy derived from surface roughness measurements of aluminum thin films," *Appl. Phys. Lett.*, vol. 55, no. 25, pp. 2617–2619, 1989.
- [20] H. Liu *et al.*, "Reliability of copper wire bonding in humidity environment," in *Proc. IEEE 13th Electron. Packag. Technol. Conf.*, Dec. 2011, pp. 53–58.
- [21] J. Osenbach, B. Q. Wang, S. Emerich, J. DeLucca, and D. Meng, "Corrosion of the Cu/Al interface in Cu-wire-bonded integrated circuits," in *Proc. IEEE 63rd Electron. Compon. Technol. Conf.*, May 2013, pp. 1574–1586.
- [22] P. Su *et al.*, "Effects of reliability testing methods on microstructure and strength at the Cu wire-Al pad interface," in *Proc. IEEE 63rd Electron. Compon. Technol. Conf.*, May 2013, pp. 179–185.
- [23] Y. Zeng, K. Bai, and H. Jin, "Thermodynamic study on the corrosion mechanism of copper wire bonding," *Microelectron. Rel.*, vol. 53, no. 7, pp. 985–1001, 2013. [Online]. Available: <http://dx.doi.org/10.1016/j.microrel.2013.03.006>.
- [24] K. A. Marko, J. V. James, T. M. Feldkamp, C. V. Puskorius, J. A. Feldkamp, and D. Roller, "Applications of neural networks to the construction of 'virtual' sensors and model-based diagnostics," in *Proc. 29th Int. Symp. Automotive Technol. Autom. (ISATA)*, Jun. 1996, pp. 133–138.
- [25] R. S. McCann and L. Spirkovska, "Human factors of integrated systems health management on next-generation spacecraft," in *Proc. 1st Int. Forum Integr. Syst. Health Eng. Manage. Aerosp.*, Napa, CA, USA, Nov. 2005, pp. 1–18.
- [26] J. R. Schauz, "Wavelet neural networks for EEG modeling and classification," Ph.D. dissertation, Georgia Inst. Technol., Atlanta, GA, USA, 1996.
- [27] J. Shiroishi, Y. Li, S. Liang, T. Kurfess, and S. Danyluk, "Bearing condition diagnostics via vibration and acoustic emission measurements," *Mech. Syst. Signal Process.*, vol. 11, no. 5, pp. 693–705, Sep. 1997.
- [28] R. Chandramouli and S. Pateras, "Testing systems on a chip," *IEEE Spectr.*, vol. 33, no. 11, pp. 42–47, Nov. 1996.
- [29] R. Drees and N. Young, "Role of BIT in support system maintenance and availability," *IEEE Aerosp. Electron. Syst. Mag.*, vol. 19, no. 8, pp. 3–7, Aug. 2004.
- [30] Y. Zorian, "A structured testability approach for multi-chip modules based on BIST and boundary-scan," *IEEE Trans. Compon., Packag., Manuf. Technol. B, Adv. Packag.*, vol. 17, no. 3, pp. 283–290, Aug. 1994.
- [31] R. X. Gao and A. Suryavanshi, "BIT for intelligent system design and condition monitoring," *IEEE Trans. Instrum. Meas.*, vol. 51, no. 5, pp. 1061–1067, Oct. 2002.
- [32] D. Rosenthal and B. C. Wadell, "Predicting and eliminating built-in test false alarms," *IEEE Trans. Rel.*, vol. 39, no. 4, pp. 500–505, Oct. 1990.
- [33] A. S. M. Hassan, V. K. Agarwal, B. Nadeau-Dostie, and J. Rajski, "BIST of PCB interconnects using boundary-scan architecture," *IEEE Trans. Comput.-Aided Design Integr. Circuits Syst.*, vol. 11, no. 10, pp. 1278–1288, Oct. 1992.
- [34] P. Lall *et al.*, "Interrogation of system state for damage assessment in lead-free electronics subjected to thermo-mechanical loads," in *Proc. 58th ECTC*, May 2008, pp. 918–929.
- [35] P. Lall, M. Hande, C. Bhat, V. More, R. Vaidya, and J. Suhling, "Algorithms for prognostication of prior damage and residual life in lead-free electronics subjected to thermo-mechanical loads," in *Proc. 11th ITherm*, May 2008, pp. 638–651.
- [36] P. Lall, M. Hande, C. Bhat, J. Suhling, and J. Lee, "Prognostics health monitoring (PHM) for prior-damage assessment in electronics equipment under thermo-mechanical loads," in *Proc. 57th ECTC*, May/Jun. 2007, pp. 1097–1111.
- [37] P. Lall, V. More, R. Vaidya, and K. Goebel, "Prognostication of latent damage and residual life in leadfree electronics subjected to multiple thermal-environments," in *Proc. 59th ECTC*, May 2009, pp. 1381–1392.
- [38] P. Lall, R. Vaidya, V. More, K. Goebel, and J. Suhling, "Assessment of residual damage in leadfree electronics subjected to multiple thermal environments of thermal aging and thermal cycling," in *Proc. 60th ECTC*, Jun. 2010, pp. 206–218.
- [39] P. Lall, M. Harsha, J. Suhling, and K. Goebel, "Sustained damage and remaining useful life assessment in leadfree electronics subjected to sequential multiple thermal environments," in *Proc. IEEE 62nd Electron. Compon. Technol. Conf.*, May/Jun. 2012, pp. 1695–1708.
- [40] P. Lall, M. Harsha, and K. Goebel, "Level of damage and remaining useful life assessment in leadfree electronics subjected to multiple thermo-mechanical environments," in *Proc. IEEE Int. Conf. Prognostics Health Manage.*, Jun. 2012, pp. 1–14.
- [41] P. Lall, M. Harsha, K. Goebel, and J. Jones, "Interrogation of thermo-mechanical damage in field-deployed electronics," in *Proc. IEEE 13th Int. Conf. Thermal, Mech., Multi-Phys. Simulation Experim. Microelectron. Microsyst.*, Apr. 2012, pp. 1/16–16/16.
- [42] B. Beverskog and I. Puigdomenech, "Revised Pourbaix diagrams for copper at 25 to 300 °C," *J. Electrochem. Soc.*, vol. 144, no. 10, pp. 3476–3483, 1997.
- [43] E. McCafferty, *Introduction to Corrosion Science*. New York, NY, USA: Springer-Verlag, 2010, p. 96.
- [44] A. V. Benedetti, P. T. A. Sumodjo, K. Nobe, P. L. Cabot, and W. G. Proud, "Electrochemical studies of copper, copper-aluminium and copper-aluminium-silver alloys: Impedance results in 0.5 M NaCl," *Electrochim. Acta*, vol. 40, no. 16, pp. 2657–2668, 1995.
- [45] N. Birbilis and R. G. Buchheit, "Investigation and discussion of characteristics for intermetallic phases common to aluminum alloys as a function of solution pH," *J. Electrochem. Soc.*, vol. 155, no. 3, pp. C117–C126, 2008.
- [46] A. Saxena, J. Celaya, B. Saha, S. Saha, and K. Goebel, "Evaluating algorithm performance metrics tailored for prognostics," in *Proc. IEEE Aerosp. Conf.*, Big Sky, MT, USA, Mar. 2009, pp. 1–13.
- [47] A. Saxena *et al.*, "Metrics for evaluating performance of prognostic techniques," in *Proc. Int. Conf. Prognostics Health Manage.*, Denver, CO, USA, Oct. 2008, pp. 1–17.
- [48] A. Saxena, J. Celaya, B. Saha, S. Saha, and K. Goebel, "On applying the prognostics performance metrics," in *Proc. Annu. Conf. PHM Soc.*, vol. 1. San Diego, CA, USA, 2009, pp. 1–16.



Pradeep Lall (M'93–SM'08–F'12) received the B.E. degree in mechanical engineering from the Delhi College of Engineering, Delhi, India, in 1988, the M.S. and Ph.D. degrees in mechanical engineering from the University of Maryland, College Park, MD, USA, in 1989 and 1993, respectively, and the M.B.A. degree from the Kellogg School of Management, Northwestern University, Evanston, IL, USA, in 2002.

He was with the Motorola's Wireless Technology Center. He is currently the John and Anne MacFarlane Endowed Professor with the Department of Mechanical Engineering, the Director of FHEMII Harsh Environment Node, and the Director of the NSF Center for Advanced Vehicle and Extreme Environment Electronics with Auburn University, Auburn, AL, USA. He has authored extensively in electronic packaging with an emphasis on modeling and predictive techniques. He has authored or co-authored two books, 14 book chapters, and over 430 journal and conference papers in electronic packaging with an emphasis on design, modeling, and predictive techniques. He holds three U.S. patents.

Dr. Lall is a fellow of the American Society of Mechanical Engineers (ASME) and the Alabama Academy of Science. He is a recipient of the IEEE Exceptional Technical Achievement Award, the ASME's Applied Mechanics Award, the SMTA's Member of Technical Distinction Award, Auburn University's Creative Research and Scholarship Award, the SEC Faculty Achievement Award, the Samuel Ginn College of Engineering Senior Faculty Research Award, Three-Motorola Outstanding Innovation Awards, Five-Motorola Engineering Awards, and 20 best paper awards at national and international conferences. He has served in several distinguished roles at national and international level, including serving as a member of the National Academies Committee on Electronic Vehicle Controls and the IEEE Reliability Society AdCom, the IEEE Reliability Society Representative on the IEEE-USA Government Relations Council for Research and Development Policy, the Chair of the Congress Steering Committee of the ASME Congress, a member of the Technical Committee of the European Simulation Conference EuroSIME, and an Associate Editor of the IEEE TRANSACTIONS ON COMPONENTS AND PACKAGING TECHNOLOGIES. He is a Six-Sigma Black-Belt in Statistics. He is the Founding Faculty Advisor of the SMTA Student Chapter at Auburn University, and a member of the Editorial Advisory Board of the *SMTA Journal*.



Shantanu Deshpande received the B.E. degree in mechanical engineering from Pune University, Pune, India, in 2011. He is currently pursuing the Ph.D. degree in mechanical engineering with the NSF Electronics Research Center, Auburn University, Auburn, AL, USA.

He is a Graduate Research Assistant under the guidance of Prof. P. Lall. His current research interests include developing failure mechanisms and prognostics models of Cu–Al wirebond system subjected to harsh environment.



Masood Murtuza received the B.Tech. degree in mechanical engineering from IIT Madras, Chennai, India, and the M.Sc. degree in naval architecture from University College, University of London, London, U.K.

He has been involved in memory, microprocessor, application specified integrated circuit, DSP, and analog device packaging for various applications in single chip and multichip configurations for commercial, industrial, automotive, space, and medical industries. He is currently a Packaging Engineer with over 25 years of experience in semiconductor IC packaging, research and development, and manufacturing. He has authored or co-authored over 15 papers in packaging, and holds 25 patents.



Luu Nguyen (F'01) received the Ph.D. degree in mechanical engineering from the Massachusetts Institute of Technology, Cambridge, MA, USA.

He has been with IBM Research, Yorktown Heights, NY, USA, and Philips Research, Durham, NC, USA. He is currently a TI Fellow with the Packaging Research and Development Group, Texas Instruments, Santa Clara, CA, USA, where he is involved in various aspects of wafer-level packaging, lead-free and halogen-free, thermal measurement and modeling, design for manufacturability, design

for reliability, high voltage, and sensors. He co-edited two books in packaging, and has authored over 200 publications. He holds over 70 patents and invention disclosures.

Dr. Nguyen is a fellow of the American Society of Mechanical Engineers, and a Fulbright Scholar. He has received many awards from the Components, Packaging and Manufacturing Technology Society, the International Microelectronics Assembly and Packaging Society, and the Scientific Research Committee.

Accepted Manuscript

Title: Mixing Enhancement by Degenerate Modes in Electrically Actuated Sessile Droplets

Author: Shubhi Bansal Prosenjit Sen

PII: S0925-4005(16)30403-8
DOI: <http://dx.doi.org/doi:10.1016/j.snb.2016.03.109>
Reference: SNB 19914



To appear in: *Sensors and Actuators B*

Received date: 31-7-2015
Revised date: 11-2-2016
Accepted date: 22-3-2016

Please cite this article as: Shubhi Bansal, Prosenjit Sen, Mixing Enhancement by Degenerate Modes in Electrically Actuated Sessile Droplets, *Sensors and Actuators B: Chemical* <http://dx.doi.org/10.1016/j.snb.2016.03.109>

This is a PDF file of an unedited manuscript that has been accepted for publication. As a service to our customers we are providing this early version of the manuscript. The manuscript will undergo copyediting, typesetting, and review of the resulting proof before it is published in its final form. Please note that during the production process errors may be discovered which could affect the content, and all legal disclaimers that apply to the journal pertain.

Mixing Enhancement by Degenerate Modes in Electrically Actuated Sessile Droplets

Shubhi Bansal and Prosenjit Sen

Centre for Nano Science and Engineering (CeNSE), Indian Institute of Science, Bangalore
Karnataka, India

Abstract

The dependence of oscillation dynamics of a sessile droplet on the actuation parameters (voltage and frequency) in AC electrowetting which leads to the manifestation of non-axisymmetric oscillation patterns were investigated through experiments and theoretical modeling. The symmetrical nature of the electrowetting force leads to a circular three phase contact line for low actuation voltages. At higher actuation voltages, despite of symmetrical actuation force the contact line showed a transition from axisymmetric to non-axisymmetric oscillations. We found a good match between the experimentally determined region in the actuation parameter space where non-axisymmetric modes are dominant and the theoretically modeled parametric instability region derived from the Mathieu equation. The results showed that these non-axisymmetric modes are degenerate sectoral modes defined by the spherical harmonic functions. In contrast to axisymmetric oscillations, for non-axisymmetric oscillations the variation of contact angle and base radius remained in-phase between successive resonant modes. Finally, mixing by these parametric oscillations was investigated and the best mixing time was approximately 2% of the diffusive mixing time.

Keywords: droplet dynamics; non-axisymmetric oscillations; degenerate modes; mixing; electrowetting.

A. Introduction

In depth understanding of the dynamics of sessile droplet oscillations is essential to build droplet based microfluidic devices. Several researchers have investigated droplet interfacial dynamics actuated using electrowetting^[1-4], surface acoustic waves^[5-7], ultrasonically levitated drops^[8] and vibrations^[9, 10]. Electrowetting, which is an electric field based actuation technique, has become a widely used tool for manipulating tiny amounts (nano-liter) of liquids in microfluidic devices^[11-13]. The dynamics of electrowetted sessile droplets is governed by a balance of capillary and inertial forces ($\omega_0^2 \propto \gamma/pr^3$) in the presence of viscous and contact line damping mechanisms^[14, 15]. Oscillating droplet interface at resonance frequencies exhibit periodic shape patterns called modes. At low actuation voltages in AC electrowetting the three phase contact line remains circular and the droplet modes show symmetry about the normal to the substrate. These axisymmetric modes have

been studied previously ^[16-18]. At higher actuation voltages, however, this symmetry breaks and non-axisymmetric modes with lobes are observed. The lobes appear in perpendicular directions in alternate cycles of spreading ^[16, 19]. Similar non-axisymmetric modes have also been observed at in liquid puddles actuated by inertial forces ^[20], in levitated droplets ^[21-22], in vibrating motions of drops ^[23] and in electrowetting-on-dielectric (EWOD) based actuation of droplets sandwiched between two substrates ^[24]. However, there has been no systematic study which illustrates the range of actuation parameters for which non-axisymmetric modes and the associated instability shows up for a EWOD system. We have identified that non-axisymmetric modes are the degenerate modes associated with spherical harmonic functions which are parametrically driven through variation of droplet radius during axisymmetric oscillations. We have also developed a model for this parametric oscillator for the EWOD actuation and found a good match with the experimental data.

Device applications utilizing particular droplet shapes can be developed by having control over the shape modes and various phenomena related to them like vortex flows. In the flows induced in the axisymmetric modes for droplets actuated with AC EWOD, the vortex position has been found to depend on the frequency of the actuating signal and thus it is related to the oscillation mode ^[25]. A correlation between droplet oscillation and induced hydrodynamic flows has been reported ^[26-27]. Rapid mixing of droplets using different electrowetting based methods has been studied in past ^[28-30]. Here, we study the mixing phenomenon in non-axisymmetric oscillations induced by AC EWOD. The non-axisymmetric shape modes and associated hydrodynamic flows have resulted in rapid mixing such that a 8 μ l water drop completely mixes with a 2 μ l food colour drop in 298 ± 8 milliseconds. It can improve the processing of biological samples by enhancing “on the spot mixing” in Lab on a Chip devices. These shape modes can also be used for making fluidic switches ^[31].

B. Methods

Device fabrication starts with cleaning of Borofloat wafers using piranha (H_2SO_4 & H_2O_2). The cleaned wafers were sputtered with 10nm chromium and 100nm gold. Actuation electrodes and contact pads were patterned and the metal layers were wet etched. Subsequently, a dielectric layer of SU-8 (5 μ m) was spin coated and patterned. The SU-8 layer was hard baked at 160°C for 10 minutes. Finally, 250nm Teflon was spin coated and hard baked at 200°C for 15 minutes.

As shown in Figure 1, the droplet was biased by inserting a thin wire of 100 μ m diameter from the top. A National Instruments multifunctional card (NI-DAQ 6363) was used to generate the sinusoidal actuation voltage and to trigger the high-speed camera for synchronized image acquisition. For droplet actuation, the generated signal was amplified by a high voltage amplifier (Trek 2205) having a gain of 50. The shape oscillation of the drop was recorded using a Photron Fastcam SA4 camera at a frame rate of 1000-3000 frames/s. The top view of the oscillating droplet was recorded by imaging through a mirror inclined at 45°. The images of the drop were extracted from the recorded videos using the software provided with the camera. A software was developed to analyze the extracted images to obtain the modal amplitudes.

C. Results and Interpretation

C.1. Non-Axisymmetric Oscillation: Degenerate modes

The contact angle of an 8 μ L deionized water droplet on the fabricated surface was measured to be $117^\circ \pm 3^\circ$ and the hysteresis was measured to be $10^\circ \pm 5^\circ$. The capacitance per unit area (c) was found to be 7.08×10^{-6} F/m² from fitting of measured contact angles for varying DC voltages to the Young-Lippmann equation (as shown in Figure 2).

$$\cos \theta = \cos \theta_0 + cV^2/2\gamma \quad 1$$

Here V is the applied potential, γ is the surface tension of the liquid-air interface, θ and θ_0 are the contact angles for the droplet with and without actuation voltage respectively.

The response of an 8 μ L droplet for a sinusoidal actuation signal ($V = V_0 \sin \omega t$, where $\omega/2\pi$ is the actuation voltage frequency) was investigated at frequencies varying from 20-100Hz (in 5Hz steps) and voltages varying from 20-160V_{rms}. At low voltages the triple phase contact line remains circular and the oscillation modes are axisymmetric. As the actuation voltage is increased the contact line loses its circular shape and the non-axisymmetric modes (see Figure 3) grow. Repeatability of these experiments depends strongly on the device to device variation of the surface quality. To get some statistical measure, the experiments were repeated on different surfaces at least three times at each voltage and frequency.

The shape oscillation of isolated droplets has been studied extensively ^[32-34] and drop shapes are expressed as a linear combination of spherical harmonic functions of degree k and order l :

$$r(t, \theta, \varphi) = R + \varepsilon \sum_{k=2}^{\infty} \sum_{l=-k}^k \alpha_{kl}(t) Y_{kl}(\theta, \varphi) \quad 2$$

Here R is the volume averaged droplet radius, α_{kl} is the time varying amplitude for a mode and ε is a small constant. Spherical harmonic functions are given as $Y_{kl}(\theta, \varphi) = NP_k^l(\cos \theta)e^{il\varphi}$, where P_k^l are associated Legendre polynomial, N is the normalization constant, θ is the polar angle and φ is the azimuthal angle. Each Y_{kl} represents drop shape for the natural capillary oscillation of mode k for spherical droplets with resonance frequency of $\Omega^2 = \gamma k(k-1)(k+2)/\rho R^3$. This implies the presence of $(2k+1)$ degenerate modes corresponding to the different values of l [35].

Following the assumptions in [32] we plot in Figure 4 the droplet shapes for individual Y_{kl} with the equator of the spherical droplets corresponding to the triple phase contact line (TPL). As can be seen from the comparison of Figure 3 and 4, we find a good qualitative similarity between the experimentally obtained non-axisymmetric modes and the computed degenerate modes (mode 2 with $Y_{2,2}$ and mode 3 with $Y_{3,3}$). In the limited number of modes investigated in this work, we observe a voltage dependent transition from droplet shapes corresponding to zonal harmonics ($Y_{k,0}$) for axisymmetric modes to shapes corresponding to sectoral harmonics ($Y_{k,k}$) for non-axisymmetric modes. Non-axisymmetric drop shape modes following tesseral harmonics (represented by $Y_{k,l}$ where $l \neq 0$ & $k \neq l$) are possible and have been observed in other works using different actuation techniques [36, 37]. It is well known that $\alpha_{kl}(t)$ for axisymmetric modes vary with a frequency of 2ω due to the V^2 term in the actuation force. However, it is interesting to note that for non-axisymmetric modes $\alpha_{kl}(t)$ varies with a frequency of ω and are sub-harmonic in comparison to the axisymmetric mode. This behavior is understandable as for the even $Y_{k,0}$ modes maximum contact area between the droplet and the solid surface happens once every cycle of $\alpha_{kl}(t)$. For sectoral harmonics $Y_{k,k}$ representing the non-axisymmetric modes the liquid-solid contact area is maximized twice for every cycle of $\alpha_{kl}(t)$.

The captured videos for each voltage and frequency were analyzed to extract the modal amplitudes as shown in Figure 5. The Cartesian coordinates of n points representing the drop's edge as viewed from top were extracted from the images. The corresponding Polar coordinates, radius r_n and angle φ_n , for the droplet profile were calculated with respect to the droplet center. The time varying mode amplitudes were obtained by expanding the shape function $r(\varphi)$ by using Fourier series.

$$r(\varphi, t) = r_0(t) + \sum_{l=2}^{\infty} \{A_l(t) \cos(l\varphi) + B_l(t) \sin(l\varphi)\} \quad 3$$

where r_0 is the amplitude for the axisymmetric mode. The choice of equation 3 in calculating the mode amplitudes is justified as the non-axisymmetric modes in our experiments follow sectoral harmonics for which the modal amplitude will be measurable at the equatorial points and will have an $e^{il\varphi}$ distribution. The amplitudes for the non-axisymmetric modes were calculated as the maximum of time varying $\alpha_{kl} = \sqrt{A_l^2 + B_l^2}$. For the axisymmetric (spherical) mode the mode amplitude was calculated as $\alpha_0 = \max(r_0) - \min(r_0)$. For our case we calculated the mode amplitudes for mode numbers 0, 2 and 3 only. The measured modal amplitudes were normalized with respect to the radius of the unactuated droplet for that experiment. In Figure 5 as expected a phase difference between the axisymmetric and non-axisymmetric modes was observed. Interestingly for the non-axisymmetric mode (mode $k = 2$) the amplitude of each lobe is different. We do not have an understanding of this difference in lobe amplitudes, but currently attribute this difference to the variation in the surface conditions.

Figure 6 plots the normalized amplitude data of axisymmetric mode ($k = 0$) and non-axisymmetric modes ($k = 2$ & $k = 3$) for actuation voltage frequencies varying from 30Hz to 55Hz. The amplitude of the axisymmetric mode ($k = 0$) is larger than the non-axisymmetric modes ($k = 2$ & $k = 3$) at lower voltages. As the actuation voltage is increased the non-axisymmetric modes grow and after a threshold voltage the mode amplitude for mode ($k = 2$) becomes larger than the axisymmetric mode. As seen in the plots, the growth of the non-axisymmetric mode ($k = 2$) was at the expense of the axisymmetric mode ($k = 0$) whose amplitude decreased after the threshold voltage. This indicates towards a coupling between the axisymmetric and the non-axisymmetric modes.

The threshold voltage is observed to first decrease and then increase with frequency and reaches a minimum at 50Hz. The amplitude of the modes (both axisymmetric and non-axisymmetric) is higher at lower frequencies (25Hz) and constantly decreases as the frequency of the actuation voltage is increased to 50Hz. This means that the optimum coupling was observed at 50Hz even though the mode amplitudes have been decreasing. To further investigate this we experimentally measured the axisymmetric modes by capturing videos from the side at an actuation voltage of 35V_{rms}. The mode amplitude was measured as the maximum change in the base contact radius of

the droplet for the frequency range of 10-60Hz. The first resonant frequency was found to be at 25Hz (see Figure 7), in good agreement with existing theory^[15] which predicts actuation voltage frequencies of 27Hz. The decrease in amplitudes for both axisymmetric and non-axisymmetric modes at higher frequencies away from the frequency of 25Hz is due to the reduced efficiency of energy transfer from the electrostatic actuation to the axisymmetric modes. Growth of sub-harmonic modes through coupling to the driven axisymmetric harmonic modes is characteristic of a parametric oscillator. The optimal parametric coupling at 50Hz which is twice the actuation voltage frequency for the first mode further strengthens our conjecture that the non-axisymmetric modes observed in our experiments are degenerate modes.

Another noteworthy aspect of non-axisymmetric modes is the behavior of the phase between the contact angle and contact radius. For axisymmetric modes it has been previously reported^[38] that the phase shows an alternating in-phase and out-phase behavior between successive resonance frequencies. We have studied this phenomenon for non-axisymmetric modes by imaging from side view. The contact angle and radius are found to increase and decrease together (i.e. in-phase) as seen in Figure 8 for all the non-axisymmetric modes explored in this study.

C.2. Modeling of the Non-Axisymmetric Oscillations

At low actuation frequencies where the droplet interface is able to follow the actuation signal, the $\sin^2 \omega t$ term in the Young-Lipmann equation expands as $0.5 (1 - \cos 2\omega t)$ to give a sinusoidal contact angle variation at twice the voltage frequency around an average contact angle of θ_a , which is different from the initial contact angle θ_0 . For axisymmetric drive the time varying contact angle in the limit of small changes is given by $\Delta\theta = -cV_0^2 \cos 2\omega t / 4\gamma \sin \theta_a$.

The non-axisymmetric modes in presence of viscous losses and static friction due to contact angle hysteresis can be modeled as^[3, 20]

$$\ddot{R} + \mu\dot{R} + \Omega_n^2 R + \lambda \operatorname{sgn}(\dot{R}) = 0 \quad 4$$

where μ is the coefficient of viscous dissipation, λ is the contribution due to hysteresis and $\operatorname{sgn}(\dot{R})$ gives the sign of the velocity. The parametric coupling in our case is from the periodic variation in the resonant frequency (Ω) of the non-axisymmetric oscillator due to the driven axisymmetric motion. The eigenfrequency for non-axisymmetric modes depends on the equatorial perimeter^[15]

$(\Omega^2 \propto \gamma/\rho R^3)$ which changes due to the periodic variation of the droplet radius (R). Under the assumption of small variations, the resonant frequency change with droplet radius is governed by

$$\Omega^2 = \Omega_0^2 \left\{ 1 - \frac{3\Delta R}{R_a} \right\} \quad 5$$

where subscript a signifies the average values around which the sinusoidal variation takes place. Detailed steps for the analysis are provided in the supplementary information. Under quasi-static approximation from volume conservation we can relate the radius change to the change in contact angle as $\Delta R = -R_a \Delta\theta \sin^3\theta_a / (2 - 3\cos\theta_a + \cos^3\theta_a)$. Substituting in equation 5 we get

$$\Omega^2 = \Omega_0^2 (1 + h \cos 2\omega t) \quad 6$$

where the amplitude for the parametric variation is given by

$$h = \frac{3cV_0^2}{4\gamma} \left\{ \frac{\sin^2\theta_a}{(2 - 3\cos\theta_a + \cos^3\theta_a)} \right\} \quad 7$$

For a parametric resonator with time dependent resonance frequency (Equation 6), the driving range for which non-axisymmetric modes show up are $\Omega\sqrt{1 - h/2} < \omega < \Omega\sqrt{1 + h/2}$. In Figure 9, the normalized mode amplitudes $3(\partial R/R)_{\text{total}}$ for which the non-axisymmetric modes arise and grow are plotted with respect to the actuation frequency. We see a good match between the theory and the experiments considering that we have neglected the nonlinear effects and various loss mechanisms in our analytical expressions. The region above these points (shown by the shaded region in the plot) is the region where non-axisymmetric modes are obtained. In Figure 10, we plot the voltages above which the non-axisymmetric modes become dominant. At lower frequencies (closer to the resonance frequency for axisymmetric modes) lower actuation voltages are enough to obtain the required $\partial R/R$ for obtaining non-axisymmetric modes. The variation from theory observed at low frequencies in Figure 10 is attributed to the failure of the approximate relation between $\partial R/R$ and actuation voltage near resonance.

Figure 11 shows the snapshots of the oscillating drops actuated by voltage 74 V_{rms} at 40Hz, 50Hz and 60Hz. At 40Hz and 60Hz, axisymmetric oscillations occurred while at 50Hz for same voltage non-axisymmetric oscillations are observed. It shows that a local minimum occurs at 50Hz where non-axisymmetric modes can be observed at lower voltages. Our mapping of the droplet dynamics

to a simple harmonic oscillator (Equation 4) is an approximation as it neglects non-linear effects which appear at large mode amplitudes. This approximation is however valid for this study as the model is used to compare the cross-over points which for most frequencies happen at low mode amplitudes (weakly non-linear regime).

C.3. Mixing using Non-Axisymmetric Oscillations

Mixing on a small scale is a challenge because of reversible nature of low Reynolds number flows. Micro-mixers have been reviewed and many active-passive mixing techniques have been proposed in the past [39, 40]. In active mixing technique, an external force is applied to enhance mixing. The capillary flows in droplets associated with evaporation [41] and electrowetting actuation [42, 43] leads to a way for increasing the hydrodynamic flows and mixing ability in the droplets. We report the mixing phenomenon in the case of non-axisymmetric oscillations.

For these experiments, EWOD devices with coplanar electrodes were fabricated, removing the need of inserting wire into the droplet. Use of indium tin oxide (ITO) electrodes and patterned SU8 as the dielectric allowed imaging from the bottom. Two droplets, one of DI water (8 μ l) and another diluted orange food colour droplet (2 μ l) were placed on the device separated by a small gap. The 8 μ l droplet was actuated with 115V_{rms} at different frequencies. The actuation leads to the merging followed by mixing of the droplets. The videos of mixing at different frequencies were recorded and analyzed.

For quantifying mixing, we recorded high speed videos of mixing at various frequencies (25-85Hz) and extracted images at definite time intervals as shown in Figure 12. We calculated the mean and standard deviation (ϕ) of hue distribution for the images captured at each frequency (see Figure 13). Progress of mixing is characterized through mixing index which for the k^{th} frame is defined as [46]

$$M.I.(k) = \frac{\phi_f - \phi_k}{\phi_f - \phi_i} \quad 8$$

where subscript f denotes the final frame and subscript i denotes the initial frame. The mixing index for various frequencies is shown in Figure 14. We have selected the frame in which the droplets merge as the initial frame (time = 0ms) for the calculation in all the mixing videos. The image with maximum standard deviation is observed after some time of the droplet merger image.

Hence, we see an initial increase in mixing index for all videos with mixing index reaching values larger than 1. The 3D nature of the modes limits our accuracy in the calculation of mixing index from the captured images.

We have used the mixing index limit of 0.02 ± 0.01 for calculation of the mixing time. For evaluating this limit, from all the videos we have selected at least 10 frames of completely mixed droplets as identified visually and by the standard deviation values. We use the average of the maximum mixing index values (~ 0.02) of the completely mixed droplets as the limit. The number of cycles required for mixing of droplets with $115V_{\text{rms}}$ actuation at different frequencies are plotted in Figure 15. For parametric mode 2, the mixing time was found to increase with frequency (25-50Hz). This is attributed to the fact that the mode amplitudes are highest at 25Hz and decrease with increase in frequency. For higher parametric modes at 70Hz and 85Hz, the mixing time reduced again. The minimum time taken for mixing of the same droplets by non-axisymmetric oscillations and pure diffusion was found to be around $298 \pm 8\text{ms}$ and 14518ms respectively.

The mixing mechanism was quantified for a particular parametric mode $k = 2$. The Peclet number (Pe) for droplet oscillations is given by the ratio of convective to diffusive transport ^[44] as $Pe = UL/D = fR\Delta R/D$, where U is the characteristic velocity given by $f\Delta R$ (with ΔR = average mode amplitude and f as the frequency), L is the characteristic length equal to droplet radius and D is the diffusivity. Diffusivity of food color was approximated by calculating the mixing time for pure diffusion between two droplets in absence of external actuation as $D = R^2/t = 1.42 \times 10^{-7} \text{ m}^2/\text{s}$. In these oscillations, the food color distribution gets stretched and folded when the droplet oscillates azimuthally in the consecutive expanding and receding lobe patterns [as shown in figure 16]. By Ranz approach for mixing evolution in pure extension, the mixing time is given by the $t = \ln Pe/2\delta$, where δ is the strain rate, which represents the instantaneous extensional component of the local flow experienced along the direction of the striation^[45] and is given here by $f\Delta R/R$. Since the mixing time expression depends on logarithm of Pe , so its dependence on Pe is found to be weaker than δ and this behavior has been previously observed for the chaotic flows in Ranz stretch model ^[45]. In Figure 16, we see that the mixing time indeed follows the expression given by the previous equation.

D. Conclusion

Droplets undergoing non-axisymmetric oscillations in AC-EWOD were investigated. Based on modal amplitude calculations, the actuation parameter values required for obtaining non-axisymmetric mode ($k = 2$) were determined experimentally. These values defined a region in the actuation parameter space. The resemblance of this region to the region of instability of a classical parametric oscillator and the subharmonic behavior of the non-axisymmetric oscillations lead us to model the EWOD system as a parametric oscillator. This theoretical model for electrowetting based parametrically oscillating droplet derived using Mathieu equation showed a good match with the experimental results.

Non-axisymmetric shapes observed in our case were degenerate modes. The axisymmetric modes follow zonal harmonics whereas non-axisymmetric modes follow sectoral harmonics. The contact angle and base radius were in-phase for consecutive non-axisymmetric modes while they show alternate in-phase and out-of-phase behavior for successive axisymmetric modes ^[38]. Finally, “on the spot mixing” through non-axisymmetric oscillations was performed and analyzed using Ranz stretch and fold mixing model. The mixing time in non-axisymmetric oscillations was 2-10% of the mixing time required for pure diffusion depending on the frequency at which the non-axisymmetric modes are actuated. In comparison axisymmetric resonant modes have been reported to require 7.4% of the time taken by a non-oscillated droplet ^[46]. The present work would be helpful for design of AC-EWOD based devices like switches, lenses where non-axisymmetric oscillations can be useful and for lab-on-a-chip applications where sample processing can be improvised using enhanced mixing.

E. Acknowledgements

We would like to thank Dr. Rudra Pratap, Dr. Ambarish Ghosh and Dr. Akshay Naik for their helpful discussions. The fabrication of the devices was done at the National Nanofabrication Facility supported by the Department of Science and Technology and the Ministry of Communication and Information Technology. We would like to thank CSIR for financial support in the form of JRF. This work was supported by DST-SERB grant.

F. References

- [1] C. Quilliet and B. Berge, "Electrowetting: a recent outbreak," *Current opinion in Colloid and Interface Science*, 6(2001), 34-39.
- [2] J.M. Oh, S.H. Ko, and K.H. Kang, "Analysis of electrowetting-driven spreading of a drop in air," *Physics of Fluids*, 22(2010), 032002.
- [3] P. Sen and C.-J. Kim, "Capillary spreading dynamics of electrowetted sessile droplets in air," *Langmuir*, 25(2009), 4302-4305.
- [4] L. Chen and E. Bonaccorso, "Electrowetting - From statics to dynamics," *Advances in Colloid and Interface Science*, 210(2014), 2-12.
- [5] B.A. Korshak, V.G. Mozhaev, and A.V. Zyryanova, "Observation and interpretation of SAW-induced regular and chaotic dynamics of droplet shape," *IEEE Ultrasonics Symposium*, 2(2005), 1019-1022.
- [6] E. Trinh and T.G. Wang, "Large-amplitude free and driven drop-shape oscillations: experimental observations," *J. Fluid Mechanics*, 122(1982), 316-338.
- [7] P. Brunet, M. Baudoin, O. Bou Matar, and F. Zoueshtiagh, "Droplet displacements and oscillations induced by ultrasonic surface acoustic waves: A quantitative study," *Physical review E*, 81(2010), 1539-3755.
- [8] E.H. Trinh, R.G. Holt, and D.B. Thiessen, "The dynamics of ultrasonically levitated drops in an electric field," *Physics of Fluids*, 8(1996), 43.
- [9] X. Noblin, A. Buguin and F. Brochard-Wyart, "Vibrations of sessile drops," *Eur. Phys. J. Special Topics*, 166(2009), 7-10.
- [10] X. Noblin, A. Buguin, and F. Brochard-Wyart, "Vibrated sessile drops: Transition between pinned and mobile contact line oscillations," *Eur. Phys. J. E*, 14(2004), 395-404.
- [11] W.C. Nelson and C.-J. Kim, "Droplet Actuation by Electrowetting-on-Dielectric(EWOD): A Review," *Journal of Adhesion Science and Technology*, 26(2012), 1747-1771.
- [12] F. Mugele and J.-C. Baret, "Electrowetting: from basics to applications-topical review," *Journal of physics: condensed matter*, 17(2005), R705-R774.
- [13] Y.-P. Zhao and Y. Wang, "Fundamentals and Applications of Electrowetting: A Critical Review," *Rev. Adhesion Adhesives*, 1(2013).

- [14] W.C. Nelson, P. Sen, and C.-J. Kim, "Dynamic Contact Angles and Hysteresis under Electrowetting-on-Dielectric," *Langmuir*, 27(2011), 10319–10326.
- [15] S. Sharp, J. Farmer and J. Kelly, "Contact Angle Dependence of the Resonant Frequency of Sessile Water Droplets," *Langmuir*, 27(2011), 9367–9371.
- [16] F.J. Hong, D.D. Jiang and P. Cheng, "Frequency-dependent resonance and asymmetric droplet oscillation under ac electrowetting on coplanar electrodes," *J. Micromech. Microeng.*, 22(2012), 085024.
- [17] X.L. Li, G.W. He and X. Zhang, "Numerical simulation of drop oscillation in AC electrowetting", *Science China-Phys Mech Astron*, 56(2013), 383–394.
- [18] J.M. Oh, S.H. Ko and K.H. Kang, "Shape Oscillation of a Drop in ac Electrowetting," *Langmuir*, 24(2008), 8379-8386.
- [19] S. Bansal and P. Sen, "Non-Axisymmetric Oscillations of Droplets in Electrowetting-on-Dielectric," *Proceedings of the IEEE International Conference on Emerging Electronics*, (2014).
- [20] X. Noblin, A. Buguin, and F. Brochard-Wyart, "Triplon Modes of Puddles," *Phys. Rev. Lett.*, 94(2005), 166102.
- [21] W. Bouwhuis, K.G. Winkels, I.R. Peters, P. Brunet, D. van der Meer and J.H. Snoeijer, "Oscillating and star-shaped drops levitated by an airflow," *Physical Review E*, 88(2013), 023017.
- [22] T.A. Caswell, "Dynamics of the Vapor Layer below a Leidenfrost Drop," *Phys. Rev. E*, 90(2014), 013014.
- [23] P. Casal and H. Gouin, "Vibrations of liquid drops in film boiling phenomena," *Int. J. Engineering Science*, 32(1994), 1553-1560.
- [24] D. Mampallil, H.B. Eral, A. Staicu, F. Mugele and D. van den Ende, "Electrowetting driven oscillating drops sandwiched between two substrates," *Phys. Rev. E*, 88(2013), 053015.
- [25] R. Malk, Y. Fouillet and L. Davoust, "Rotating flow within a droplet actuated with AC EWOD," *Sensors and Actuators B*, 154(2011), 191-198.
- [26] S.H. Ko, H. Lee and K.H. Kang, "Hydrodynamic flows in electrowetting," *Langmuir*, 24(2008), 1094–1101.
- [27] V. Palero, J. Lobera, P. Brunet, N. Andres and M.P. Arroyo, "3D characterization of the inner flow in an oscillating drop," *Exp.in Fluids*, 54(2013), 1-12.

- [28] J. Fowler, H. Moon and C.-J. Kim, “Enhancement of mixing by droplet-based microfluidics” *Proceedings of the IEEE 15th International Conference on Micro Electro Mechanical Systems*, (2002), 97–100.
- [29] P. Paik, V.K. Pamula and R.B. Fair "Rapid Droplet Mixers for Digital Microfluidic Systems," *Lab on a Chip*, 3(2003), 253-259.
- [30] F. Mugele, A. Staicu, R. Bakker and D. van den Ende, “Capillary Stokes drift: a new driving mechanism for mixing in AC-electrowetting,” *Lab on a Chip*, 11(2011), 2011–2016.
- [31] P. Sen and C.-J. Kim, “A Fast Liquid-Metal Droplet Microswitch Using EWOD-Driven Contact-Line Sliding,” *Journal of Microelectromechanical Systems*, 18(2009).
- [32] J.B. Bostwick and P.H. Steen, “Dynamics of sessile drops. Part 1. Inviscid theory,” *J. Fluid Mech.*, 760(2014), 5-38.
- [33] C.-T. Chang, J.B. Bostwick, P.H. Steen and S. Daniel, “Substrate constraint modifies the Rayleigh spectrum of vibrating sessile drops,” *Physical Review E*, 88(2013), 023015(17).
- [34] J.B. Bostwick and P.H. Steen, “Capillary oscillations of a constrained liquid drop,” *Physics of Fluids*, 21(2009), 032108.
- [35] L. Landau and M. Lifshitz, "Fluid Mechanics," *Butterworth-Heinemann*, 2nd. ed., 1987.
- [36] C.-T. Chang, J.B. Bostwick, P.H. Steen and S. Daniel, “Dynamics of sessile drops. Part 2. Experiment”, *J. Fluid Mech.*, 768(2015), 442-467.
- [37] S. Mettu and M.K. Chaudhury, “Vibration Spectroscopy of a Sessile Drop and Its Contact Line,” *Langmuir*, 28(2012), 14100-14106.
- [38] S. Dash, N. Kumari, and S.V. Garimella, “Frequency-dependent Transient Response of an Oscillating Electrically Actuated Droplet,” *Journal of Micromechanics and Microengineering*, 22(2012).
- [39] V. Hessel, H. Löwe and F. Schönfeld, “Micromixers—a review on passive and active mixing principles,” *Chemical Engineering Science*, 60(2005), 2479-2501.
- [40] C.-Y. Lee, C.-L. Chang, Y.-N. Wang and L.-M. Fu, “Microfluidic Mixing: A Review,” *Int. J. Mol. Sci.*, 12(2011), 3263-3287.
- [41] R.D. Deegan, O. Bakajin, T.F. Dupont, G. Huber, S.R. Nagel and T.A. Witten, “Capillary flow as the cause of ring stains from dried liquid drops,” *Nature*, 389(1997), 827-829.
- [42] F. Mugele, J.C. Baret and D. Steinhauser, “Microfluidic mixing through electrowetting-induced droplet oscillations,” *Appl. Phys. Lett.*, 88, 204106, 2006.

- [43] R. Miraghaie, J. D. Sterling, and A. Nadim, “Shape oscillation and internal mixing in sessile liquid drops using electrowetting-on-dielectric(EWOD),” *Technical Proceedings of the 2006 NSTI Nanotechnology Conference and Trade Show*, 2(2006), 610-613.
- [44] J.M. Ottino and S. Wiggins, “Introduction: mixing in microfluidics” *Phil. Trans. R. Soc. Lond. A*, 362(2004), 923-935.
- [45] P. Sundararajan and A.D. Stroock, “Transport Phenomena in Chaotic Laminar Flows,” *Annu. Rev. Chem. Biomol. Eng.*, 3(2012), 473-96.
- [46] C.-P. Lee, H.-C. Chen, and M.-F. Lai “Electrowetting on dielectric driven droplet resonance and mixing enhancement in parallel-plate configuration,” *Biomicrofluidics*, 6(2012), 012814.

Biography



microfluidics.

Shubhi Bansal received her B.Tech degree in Engineering Physics from Delhi Technological University (formerly Delhi College of Engineering) in 2013. She is a Ph.D. student in Centre for Nano Science and Engineering (CeNSE) at Indian Institute of Science, Bangalore since 2013. Her research interests are electrowetting, interfacial dynamics and



Innovative Micro Technology in Santa Brabara, USA from 2010-2012.

Prosenjit Sen received his Ph.D. degree in Mechanical Engineering from University of California, Los Angeles in 2007. He received his B.Tech. degree in Manufacturing Science and Engineering from Indian Institute of Technology, Kharagpur, India in 2000. He was a postdoctoral scholar with Micromanufacturing Laboratory in University of California, Los Angeles from 2008-2010. He subsequently worked at

Since 2013 he has been an Assistant Professor in Centre for Nano Science and Engineering at Indian Institute of Science, Bangalore. His research interest includes microfluidic systems, droplet dynamics, liquid-metal based RF MEMS and reliability of electrowetting-on-dielectric (EWOD) devices. Dr. Sen is recipient of Institute Silver Medal at Indian Institute of Technology, Kharagpur.

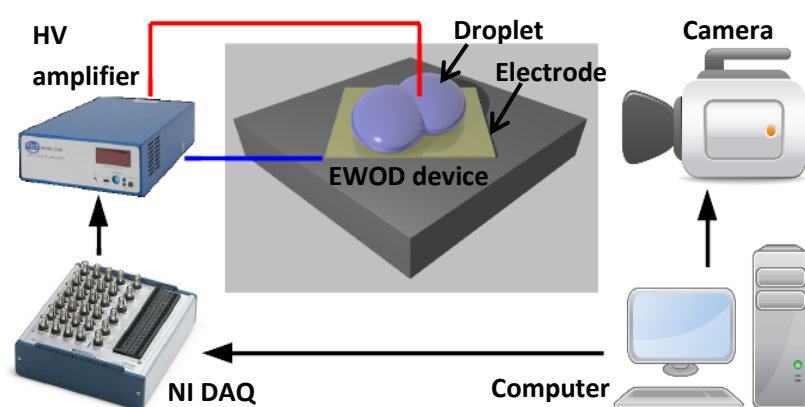


Figure 1: Schematic diagram of the experimental setup.

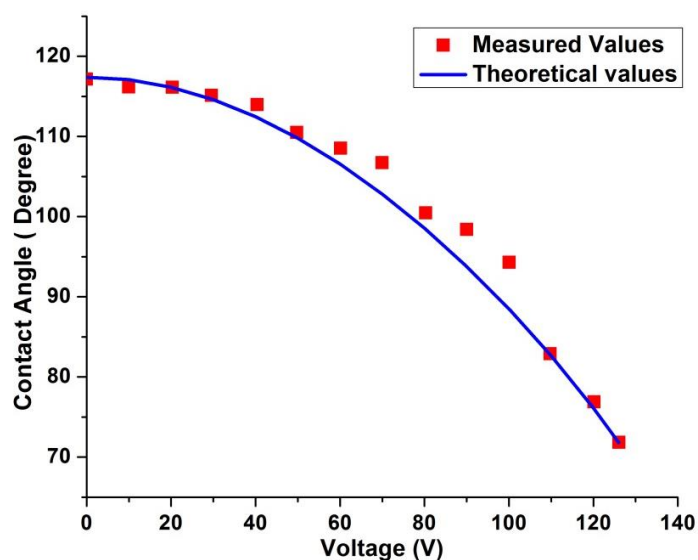


Figure 2: Contact angle variation in response to the applied DC voltages in EWOD.

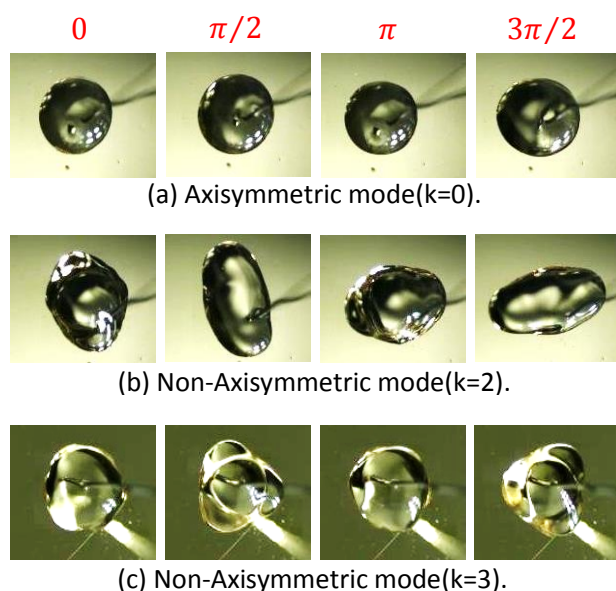


Figure 3: Oscillation patterns (top view) of a $8\mu\text{l}$ droplet at different voltages and frequencies (a) mode $k = 0$ at 35Hz , 74V_{rms} ; (b) mode $k = 2$ at 35Hz , 117V_{rms} ; (c) mode $k = 3$ at 100Hz , 117V_{rms} . [supplementary videos available]

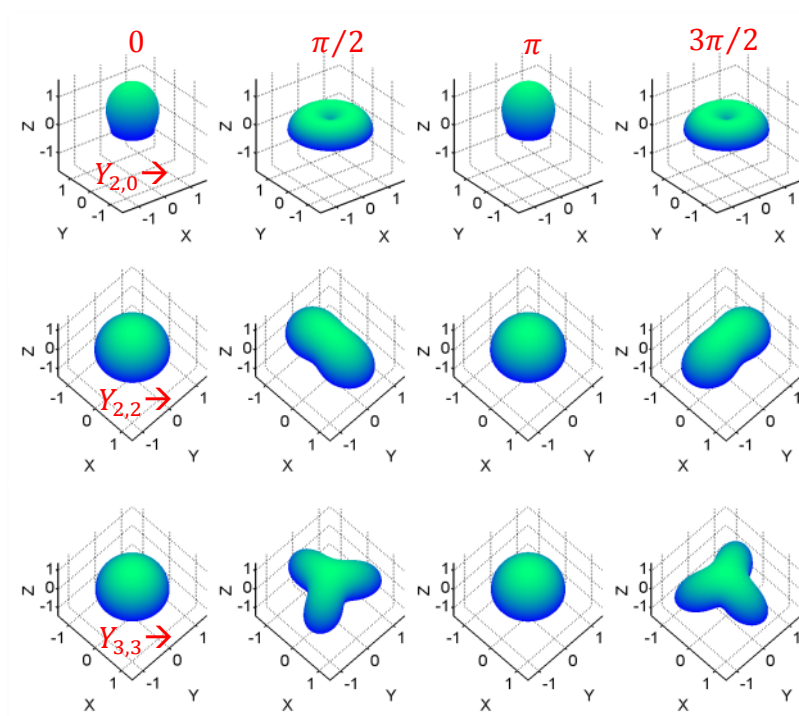


Figure 4: Degenerate modes shapes of droplet oscillations plotted using MATLAB by solving spherical harmonic functions ($Y_{k,l}$) for different (k,l) values. Axisymmetric modes follow zonal harmonics and non-axisymmetric modes follow sectoral harmonics.

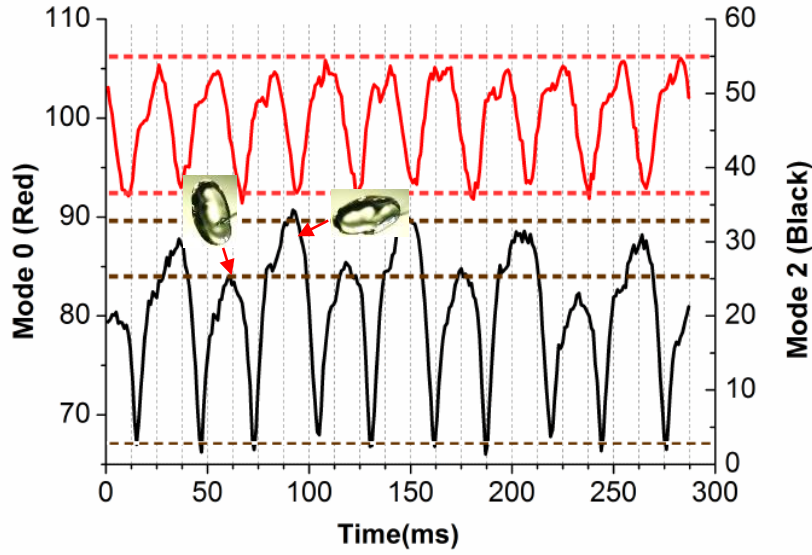


Figure 5: Temporal evolution of the modal amplitudes and associated phase difference between axisymmetric (red) and non-axisymmetric (black) oscillations for actuation at 35Hz and $102V_{rms}$. The amplitudes of the two lobes for non-axisymmetric mode 2 is different.

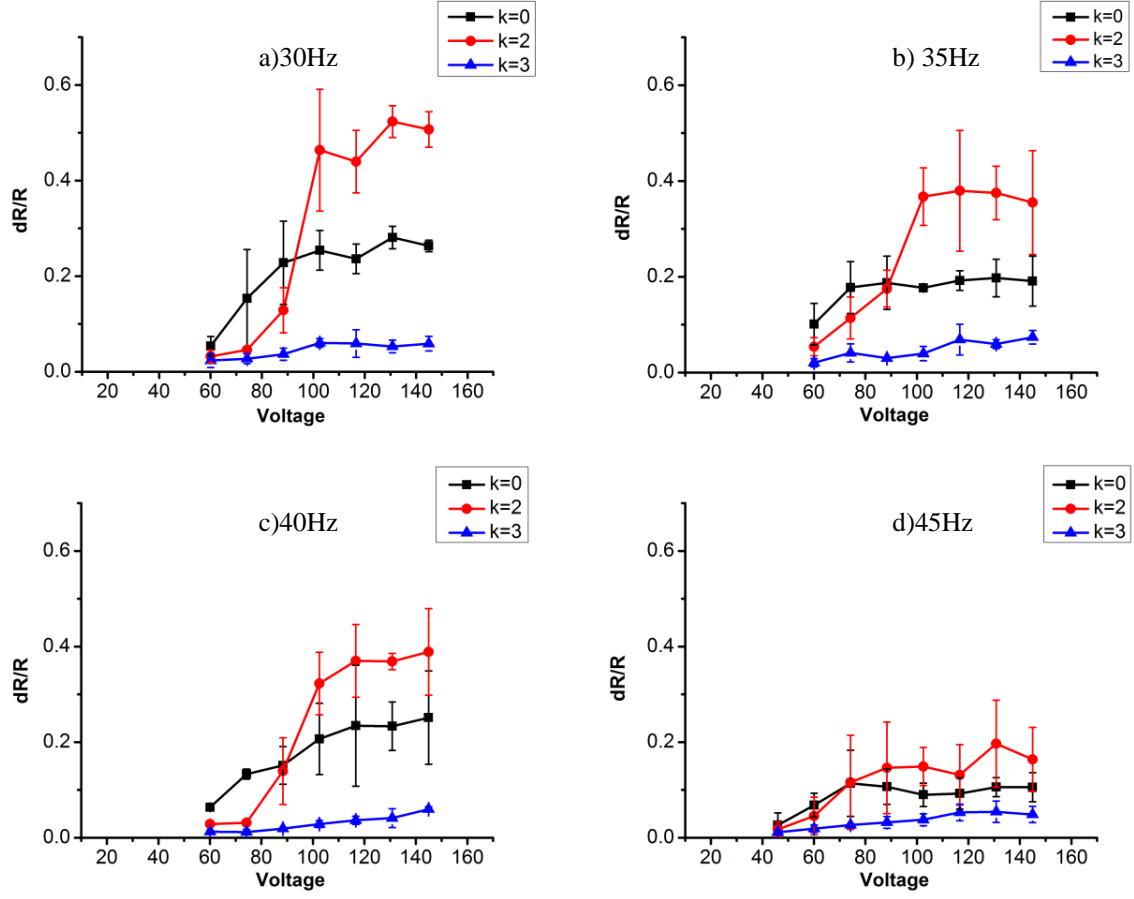


Figure 6: Nondimensionalized modal amplitude variation with voltage (V_{rms}) for modes $k=0$ (black), $k=2$ (red) and $k=3$ (blue) for different frequencies (a)30Hz (b)35Hz (c)40Hz (d)45Hz. Error bars show standard deviation of amplitudes calculated from atleast three experiments.

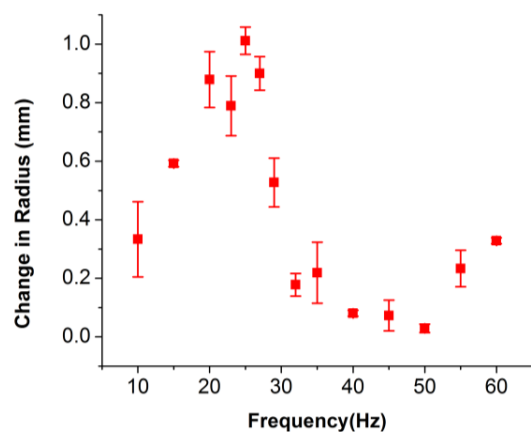


Figure 7: Change in base radius of an drop at different frequencies for $35V_{\text{rms}}$. Axisymmetric oscillations at $35V_{\text{rms}}$ voltage are found to have a resonance peak at 25Hz (having an average contact angle $\theta_a \sim 113^\circ$).

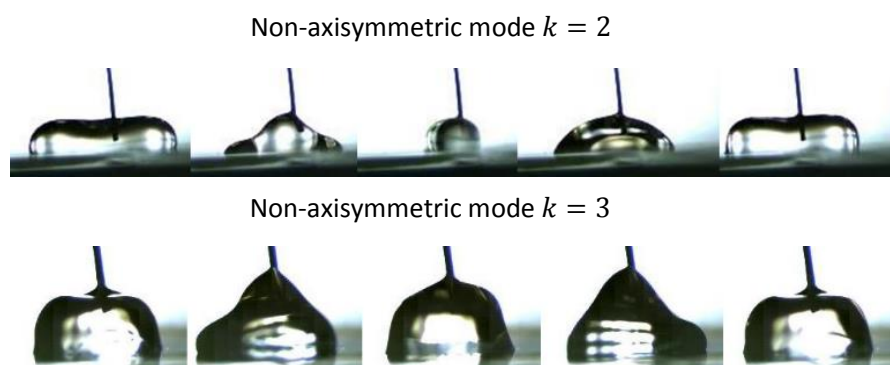


Figure 8: Sideview of droplet oscillation patterns for non-axisymmetric modes: (Top) $k = 2$ mode at 35Hz, 117V_{rms}; and (Bottom) $k = 3$ mode at 100Hz, 117V_{rms}. [supplementary videos available]

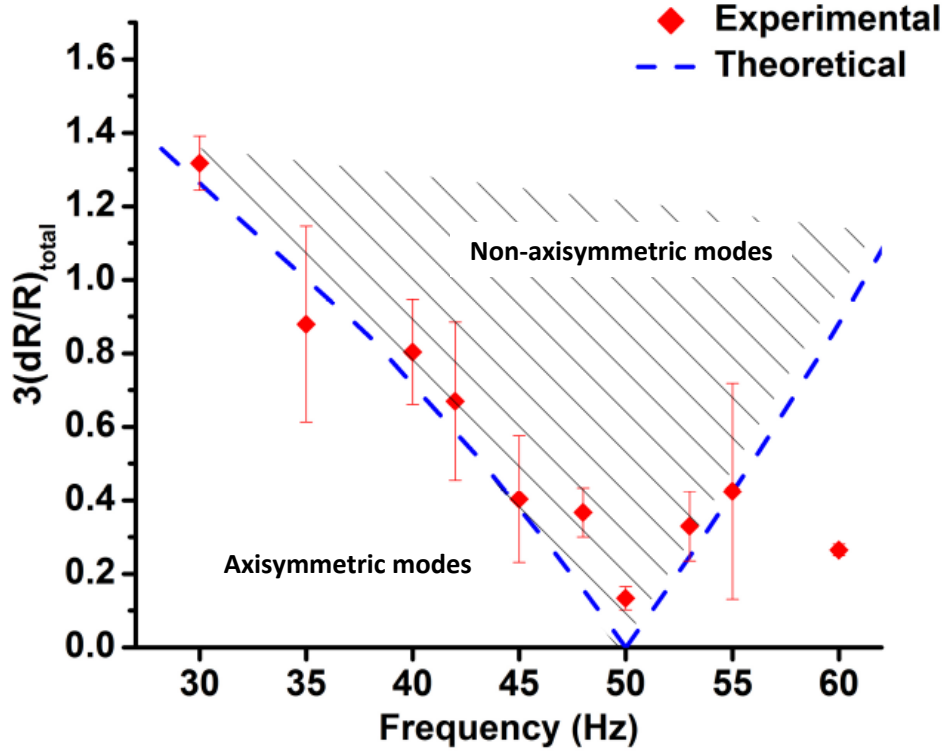


Figure 9: Region of instability where non-axisymmetric mode amplitudes are dominant in the parameter space of nondimensionalized modal amplitude $(3dR/R)_{\text{total}}$ with frequency. The experimental data represents the mode cross-over points (i.e. data points where amplitude of mode $k = 2$ becomes larger than amplitude of mode $k = 0$).

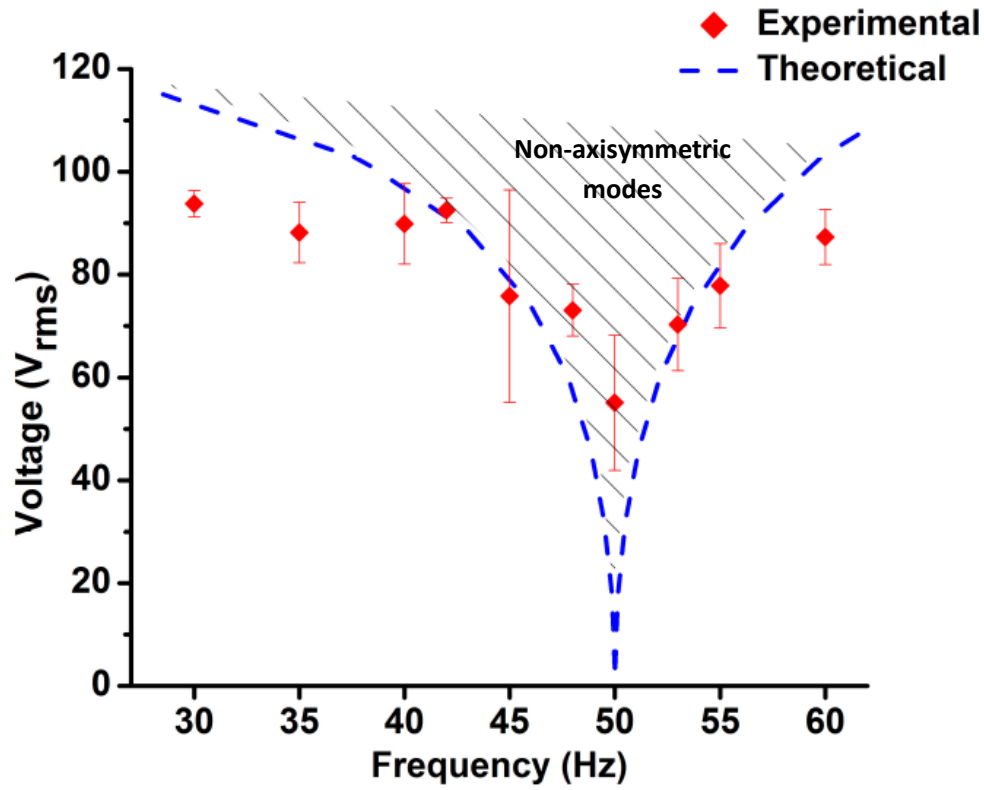


Figure 10: Comparison of theoretical and experimental actuation parameter values (voltage and frequency) defining a region for obtaining non-axisymmetric mode $k = 2$. For droplet oscillation at frequencies near axisymmetric resonance frequency of 25Hz (got at average contact angle $\theta_a \sim 113^\circ$ and voltage $35V_{rms}$), voltages lower than theoretical voltages are sufficient to obtain non-axisymmetric modes.

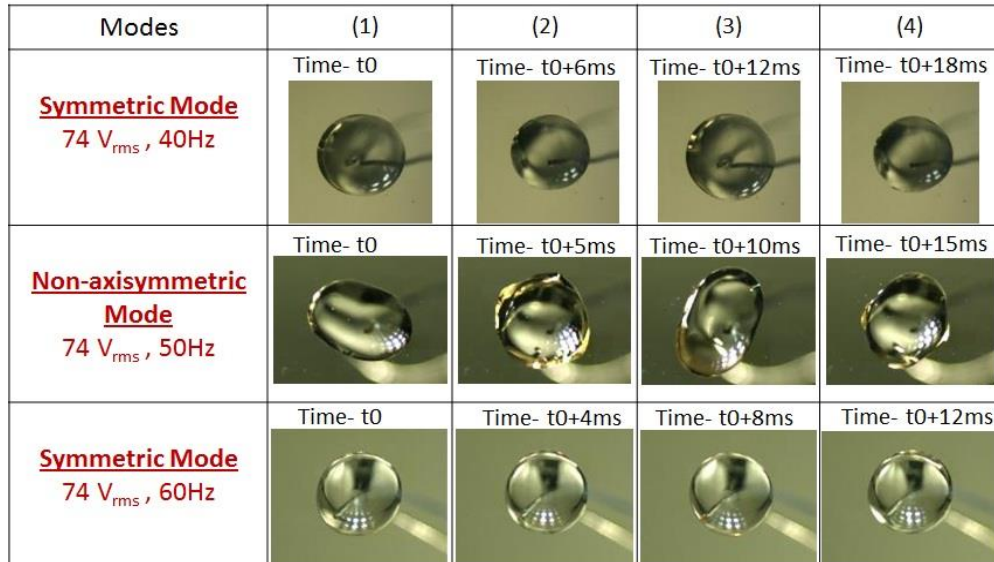


Figure 11: Comparison of axisymmetric oscillations and non-axisymmetric oscillations observed for frequencies 40Hz/60Hz and 50Hz respectively, for the same actuation voltage 74V_{rms}. This figure depicts the existence of a local minimum at 50Hz where non-axisymmetric modes can be observed at lower voltages.

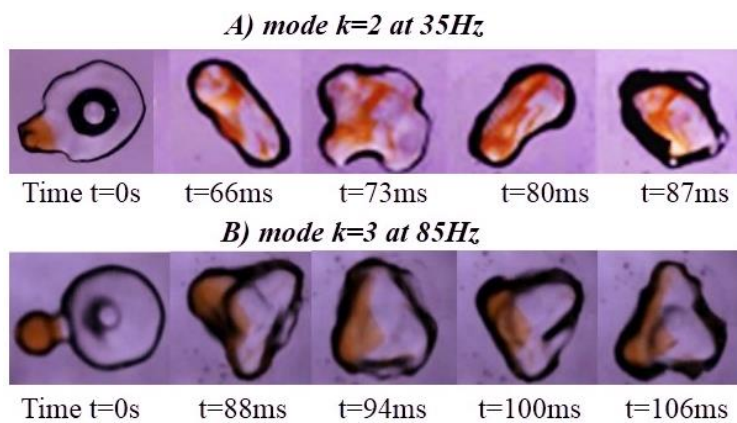


Figure 12: Mixing of droplets of DI water (8μl) and diluted orange food colour droplet (2μl) using non-asymmetric oscillations with 115V_{rms} and frequencies (A) 35Hz (mode $k = 2$) and (B) 85Hz (mode $k = 3$). [supplementary videos available]

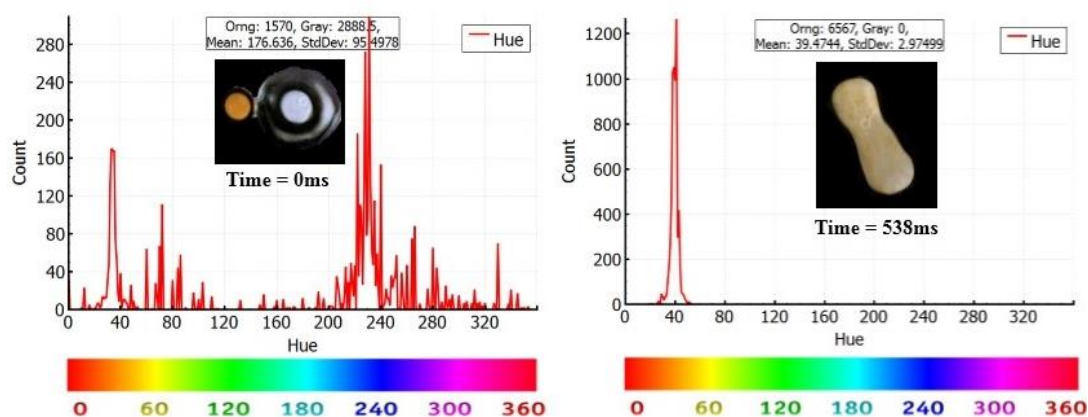


Figure 13: Hue distribution of unmixed droplets (left) and well-mixed droplets (right) actuated with voltage $115V_{rms}$ and frequency 30Hz (mode $k = 2$). Orange hue peak increases and background hue peak decreases while going from unmixed to well-mixed state. Standard deviation is shown as a measure for progression of the mixing process.

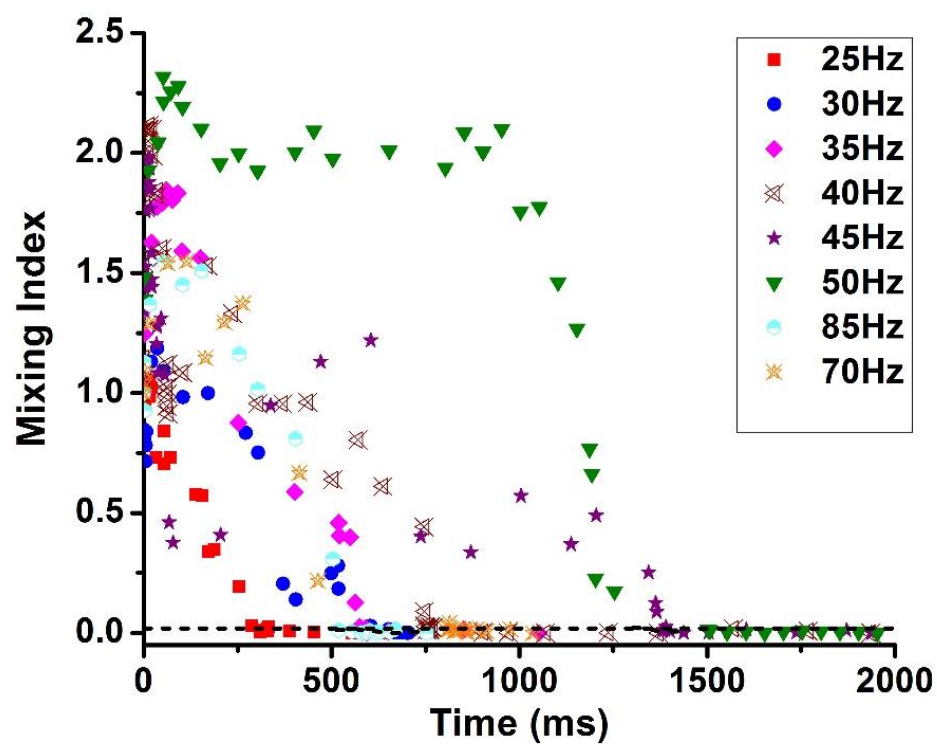


Figure 14: Progression of mixing demonstrated with temporal evolution of mixing index for different frequencies. Based on analysis of post-mixing images when the mixing index is less than the mixing index limit (0.02), we assume that the mixing is complete.

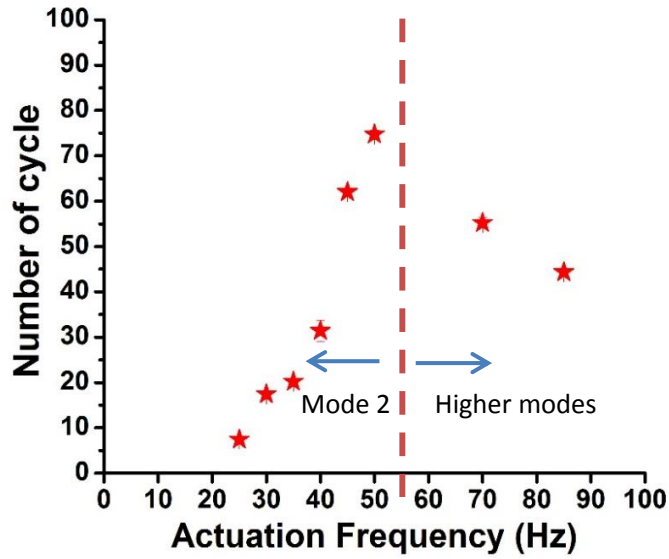


Figure 15: Number of cycles required for mixing of droplets at different actuation frequencies for $115V_{\text{rms}}$ using non-axisymmetric modes. Below 55Hz, only $k = 2$ mode oscillations exist and the number of cycles required for mixing increase with the frequency. Beyond 55Hz, other higher oscillation modes exist.

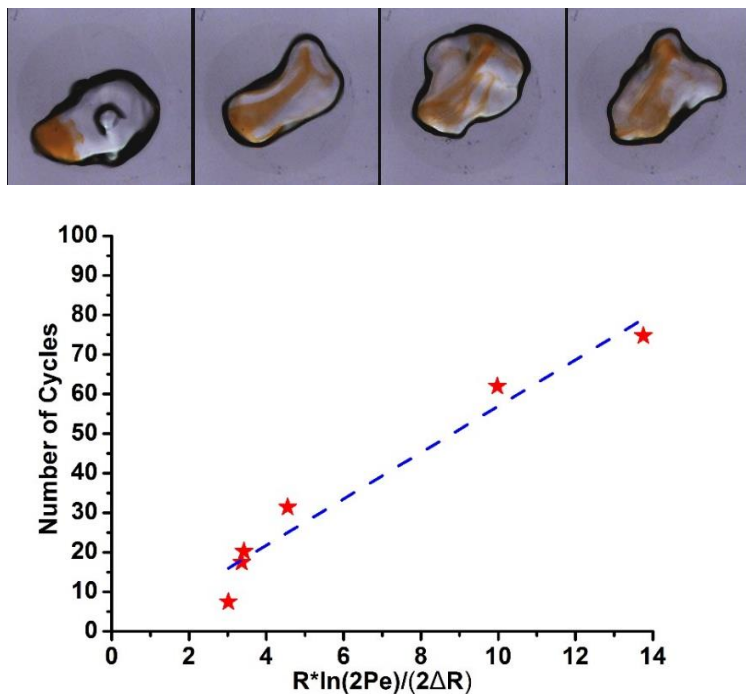


Figure 16: (Top) Progression of mixing of droplets using non-axisymmetric modes. (Bottom) Relationship between number of cycles required for mixing of droplets and the theoretical expression obtained from Ranz stretch model for pure extension.

HOSTED BY



Contents lists available at ScienceDirect

Engineering Science and Technology, an International Journal

journal homepage: <http://www.elsevier.com/locate/jestch>

Full Length Article

Optimal AGC with redox flow batteries in multi-area restructured power systems

Yogendra Arya ^{a,*}, Narendra Kumar ^b^a Department of Electrical and Electronics Engineering, Maharaja Surajmal Institute of Technology, C-4, Janakpuri 110058, New Delhi, India^b Department of Electrical Engineering, Delhi Technological University, Bawana Road, Shahbad Daultpur 110042, Delhi, India

ARTICLE INFO

Article history:

Received 30 July 2015

Received in revised form

18 December 2015

Accepted 18 December 2015

Available online

Keywords:

Automatic generation control

Restructured power systems

Sensitivity analysis

Redox flow batteries

Multi-source power plant

Optimal AGC regulator

ABSTRACT

This paper attempts to investigate the effect of Redox flow batteries (RFB) in Automatic Generation Control (AGC) of multi-area restructured power systems. Initially, a two-area restructured thermal power system is investigated. For the analysis, optimal AGC regulators (OARs) are designed employing performance index minimization criterion. The advantages of the OARs are shown by comparing the results with Genetic Algorithm (GA) based integral controllers for the same restructured system. MATLAB simulation results further demonstrate significant improvements in the dynamic performance of the system with RFB. System stability enhancement with OARs/RFB is outlined by conducting the system modes study. The study is additionally extended to a more realistic two-area multi-source thermal–hydro–gas restructured system with/without RFB. To add nonlinearities, appropriate generation rate constraints (GRCs) are considered for the thermal, hydro and gas plants. Results verify that OARs are able to satisfy the AGC requirement under varied power transactions taking place in an open power market. The robustness of OARs is demonstrated by sensitivity analysis, which is carried out with wide variation in initial loading, system parameters and magnitude/position of the uncontracted power demands. Finally, the study is extended to a two-area multi-source thermal–hydro power system with/without considering RFB.

Copyright © 2015, The Authors. Production and hosting by Elsevier B.V. on behalf of Karabuk University. This is an open access article under the CC BY-NC-ND license (<http://creativecommons.org/licenses/by-nc-nd/4.0/>).

1. Introduction

The prime objective of Automatic Generation Control (AGC) is to adjust the active power generation in response to variable power demand and hence to maintain scheduled system frequency and scheduled tie-line power flows with neighboring control areas at desired tolerance values [1]. In a conventional scenario, generation, transmission, distribution and control of electrical energy are owned by a single monopolistic entity termed as Vertically Integrated Utility (VIU), which sells power at regulated tariff. However, since some decades, with the emergence of restructured scenario, VIU configuration no longer exists and several independent players namely Distribution Companies (DISCOs), Generation Companies (GENCOs), Transmission Companies (TRANSCOs) and Independent System Operator (ISO) have been introduced in a competitive trade market [2–4]. In open power market scenario, consumers/DISCOs are supposed to get an opportunity to make a choice among different GENCOs to buy power at reduced competitive prices. In the deregulated power environment, GENCOs may or may not participate in the AGC task and DISCOs have the liberty to have contracts

with any available GENCOs of its own area (termed as poolco transaction) or other areas (termed as bilateral transaction) [5]. These transactions have to be passed by the ISO or any other responsible authority [6–11]. Literature survey indicates that several researchers, to tackle AGC issue in restructured system, have presented various conventional and intelligent methodologies such as Particle Swarm Optimization (PSO) based fuzzy control [3], Quasi-oppositional Harmony Search (QOHS) algorithm [4], Bacteria Foraging (BF) [5], fuzzy control [4,6], Genetic Algorithm (GA) [7,8], classical [9] and optimal control strategies [3,10–12]. Optimal control strategy is also implemented in traditional AGC system [13]. To represent bilateral power contracts, Donde et al. [2] have proposed the concept of DISCO participation matrix (DPM) and area participation factor (apf). DPM provides the information about the contract of a DISCO with a GENCO. The rows and columns of the DPM represent a number of GENCOs and DISCOs respectively while apf denotes the area control error (ACE) participation factor. The contract participation factors (cpfs) refer to the entries of a DPM and denote a fraction of total power contracted by a DISCO with a GENCO. Hence, the sum of the total entries of a column corresponding to a DISCO is equal to 1. Most of the AGC researches quoted above own only a single source of energy in all control areas, but in a realistic system, a mix of thermal, hydro, gas etc., power plants simultaneously work in each control area [10,11,14–17]. AGC of a multi-area

* Corresponding author. Tel.: +919891484801.

E-mail address: mr.y.arya@gmail.com (Y. Arya).

multi-source thermal-hydro/gas [10], thermal-hydro [11] and thermal-hydro-gas [15] deregulated power systems is prevalent in the state-of-the-art literature. Additionally, multi-area multi-source AGC of traditional thermal-hydro [14], thermal-hydro-gas [16] and thermal-hydro-wind/diesel [17] power systems is also discussed.

The Battery Energy Storage Systems (BESS) recently have emerged as one of the most promising storage technology to solve wide spectrum of operational problems faced by modern restructured power systems. The available literature extensively explores the effect of BESS on power system dynamic performance [18–23]. Literature reviews reported in References 18 and 19 present a critical investigation of all aspects of AGC starting from conventional to recent methodologies and importance of BESS. Beside conventionally assigned applications of load leveling and peak shaving, BESS applications include area regulation, area protection, spinning reserve, improving the power quality of the distribution system, etc. [20]. BESS is found to be very effective to damp frequency and tie-line power oscillations following sudden small load disturbances in traditional single-area wind-diesel [20], single-area reheat [21], two-area thermal-hydro [22] and deregulated two-area reheat thermal [23] power systems. There are various types of BESS used in power systems such as lithium ion, flooded, lead acid, valve regulated, sodium sulfur, metal air and redox flow type batteries. Among all the types, redox flow batteries (RFB) show potential for the applications, which necessitate high power, hasty response equivalent to SMES and extended duration storage [24–29]. Importance of RFB in power system applications is showcased in References 18 and 19. RFB are well suited for generation control and absorption of power fluctuation. Effective use of RFB includes interconnected two-area reheat thermal restructured [5,24], reheat thermal-hydro restructured [24] and conventional [26–29] power systems.

Literature survey reflects that only a few number of articles have been witnessed about the application of RFB in AGC of restructured power systems [5,24]. The above articles portray the benefits of RFB in two-area reheat thermal or reheat thermal-hydro systems. However, no literature is available on the use of RFB for AGC of two-area restructured system with thermal-hydro-gas multi-sources in each area as well as for single-source two-area restructured system with reheat thermal in first and non-reheat thermal sources in second area. In addition, no attempt is made until now to design OARs for the said systems. Hence, AGC study with OARs and RFB is further required.

In light of the above, following studies are carried out:

- The optimal AGC regulators (OARs) are designed to optimize the feedback gains of a two-area restructured thermal system under the presence and absence of RFB and their dynamic performance is compared with Genetic Algorithm (GA) based controllers for the same AGC system.
- The state space model of a two-area restructured multi-source thermal-hydro-gas system is developed and OARs are designed with and without considering RFB. OARs are proved to be superior over GA.
- The performance of OARs and RFB is studied during various power contracts taking place in a deregulated environment with/without RFB and GRC.
- Sensitivity analysis of the optimum feedback gains of OARs obtained at nominal condition is carried out; also their robustness is examined to wide variations in the loading pattern and time constants of hydrogovernor, speed governor and valve positioner from the nominal values and also changes in size and location of uncontracted power demand of DISCOs.
- Finally, OARs are designed for a multi-area multi-source thermal-hydro power system and their advantage is verified over GA tuned PI and hybrid Firefly Algorithm-Pattern Search (hFA-PS) algorithm tuned PI and PID controllers.

2. System models

Three AGC systems have been considered under the present study. First system is a two-area restructured thermal system with two reheat units in first and two non-reheat units in the second area. Two numbers of DISCOs and two numbers of GENCOs are considered in each control area of the system. The transfer function model of the system with integral controller is shown in Reference 8. Second system is a two-area restructured multi-source system with three units viz., thermal, hydro and gas in each area [15]. Three numbers of DISCOs and three numbers of GENCOs are considered in each control area of the second system. The thermal and hydro GENCOs in multi-source system are provided with reheat turbine and mechanical governor respectively. The transfer function model of the system with RFB installed in area-1 is shown in Fig. 10. Third system is a two-area multi-source thermal-hydro system as shown in Fig. 34. The nominal parameters of the AGC systems are depicted in Appendix B. A bias setting of $B_i = \beta_i$ is considered in areas of all systems. MATLAB software version 7.5.0 (R2007b) is employed for SIMULINK models and workspace program codings to achieve various dynamic responses of the systems under study.

3. State space modeling of the systems under study

The state space model of a two-area restructured thermal system is already given in Reference 8. However, state space model of the two-area restructured multi-source thermal-hydro-gas system under investigation is tried to be developed using the various system states shown in Fig. 10. The system state space model of Fig. 10 is characterized by the following standard state space equations:

$$\dot{X} = AX + BU + \Gamma P_d, X(0) = 0 \quad (1)$$

$$Y = CX \quad (2)$$

where X , U , P_d , Y are the state, control, load disturbance and output vectors respectively; and A , B , C and Γ are system, input distribution, output and disturbance distribution matrices of compatible dimensions and are given in Appendix A. In the optimal control theory the term ΓP_d in Eqn. (1) will vanish. Eqn. (2) will not alter while Eqn. (1) will change to Eqn. (3) as:

$$\dot{X} = AX + BU, X(0) = -X_{ss} \quad (3)$$

where new state vector X is equal to the old state vector minus its steady state value X_{ss} . The vectors X , U and P_d are given as:

$$\text{State vector: } X = [\Delta F_1 \Delta P_{tie}^{actual} \Delta F_2 \Delta P_{T1} \Delta P_{R1} \Delta X_{t1} \Delta P_{Th1} \Delta X_{h1} \Delta P_{RH1} \Delta P_{G1} \Delta P_{FC1} \Delta P_{VP1} \Delta X_{g1} \Delta P_{T2} \Delta P_{R2} \Delta X_{t2} \Delta P_{Th2} \Delta X_{h2} \Delta P_{RH2} \Delta P_{G2} \Delta P_{FC2} \Delta P_{VP2} \Delta X_{g2} \int ACE_1 dt \int ACE_2 dt]^T, \quad (4)$$

$$\text{Control vector: } U = [\Delta P_{C1} \Delta P_{C2}]^T \text{ and} \quad (5)$$

$$\text{Disturbance vector: } P_d = [\Delta P_{L1} \Delta P_{L2} \Delta P_{L3} \Delta P_{L4} \Delta P_{L5} \Delta P_{L6} \Delta P_{UC1} \Delta P_{UC2}]^T. \quad (6)$$

The state space model of a two-area multi-source thermal-hydro power system shown in Fig. 34 is not given due to brevity in the present study. However, the vectors X , U and P_d are stated as:

$$\text{State vector: } X = [\Delta F_1 \Delta F_2 \Delta P_{tie} \Delta P_{Gt1} \Delta P_{Gh1} \Delta X_{hy1} \Delta P_{Gt2} \Delta P_{Gh2} \Delta X_{hy2} \Delta X_{t1} \Delta P_{RH1} \Delta X_{t2} \Delta P_{RH2} \int ACE_1 dt \int ACE_2 dt]^T, \quad (7)$$

$$\text{Control vector: } U = [\Delta P_{C1} \Delta P_{C2}]^T \text{ and} \quad (8)$$

$$\text{Disturbance vector: } P_D = [\Delta P_{D1} \Delta P_{D2}]^T. \quad (9)$$

Here, ΔP_{Li} denotes the load demand of i th DISCO and ΔP_{UCi} is the uncontracted demand of i th area. The states are selected as the deviation in frequency in area-1 and 2 (ΔF_1 ; ΔF_2), the deviation in load demand in area-1 and 2 (ΔP_{D1} ; ΔP_{D2}), the deviation in speed changer position in area-1 and 2 (ΔP_{C1} ; ΔP_{C2}), the deviation in the intermediate power or power outputs of GENCOs in area-1 (ΔP_{T1} ; ΔP_{Th1} ; ΔP_{Gg1}) and 2 (ΔP_{T2} ; ΔP_{Th2} ; ΔP_{Gg2}), the deviation in thermal turbine output in area-1 and 2 (ΔP_{Rt1} ; ΔP_{Rt2}), the deviation in thermal governor output in area-1 and 2 (ΔX_{t1} ; ΔX_{t2}), the deviation in intermediate outputs of hydro governor in area-1 (ΔP_{RH1} ; ΔX_{h1}) and 2 (ΔP_{RH2} ; ΔX_{h2}), the deviations in hydro governor output in area-1 and 2 (ΔX_{hy1} ; ΔX_{hy2}), the deviation in intermediate output of gas turbine governor in area-1 and 2 (ΔX_{g1} ; ΔX_{g2}), the deviation in intermediate output of fuel system and combustor in area-1 and 2 (ΔP_{FC1} ; ΔP_{FC2}), the deviations in output of valve positioner in area-1 and 2 (ΔP_{VP1} ; ΔP_{VP2}), the deviation in actual tie-line power (ΔP_{tie_actual} ; ΔP_{tie2}) and the integral of area control error in area-1 and 2 ($\int ACE_1 dt$; $\int ACE_2 dt$).

4. Design of optimal AGC regulators

Full state feedback optimal AGC regulators are designed using performance index minimization criterion as reported in the literature [3,10–13]. According to optimal control theory, the optimal control signal used to minimize a quadratic cost performance index:

$$J = \int_0^{\infty} \frac{1}{2} [X^T Q X + U^T R U] dt \quad (10)$$

is given by

$$U^* = -K^* X \quad (11)$$

where optimum feedback gain matrix $K^* = R^{-1} B^T P$ and the matrix P presents the solution of algebraic matrix Riccati equation:

$$PA + A^T P - PBR^{-1} B^T P + Q = 0. \quad (12)$$

Q is a positive semi-definite symmetric state cost weighting matrix and R is a positive definite symmetric control cost weighting matrix. The Q and R matrices for two-area multi-source restructured system are given in Appendix A.

5. Redox flow batteries (RFB)

Developed since the 1970s, the RFB are rechargeable electro-chemical energy storage devices suitable for large-scale utility applications [30]. RFB are used to convert and store electrical energy into chemical form and generate electricity when needed in a controlled manner by a reduction–oxidation (redox) reaction [31]. The RFB reactor, which consists of electrolyte of sulfuric acid (H_2SO_4) solution with vanadium pentoxide (V_2O_5), has two compartments segregated by a proton exchange membrane where each

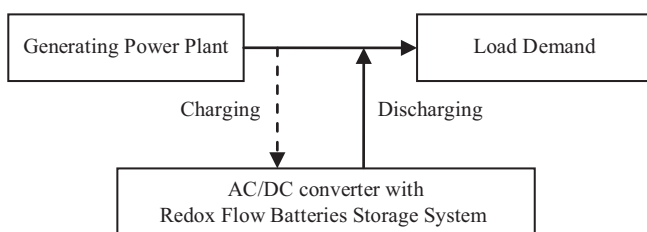


Fig. 1. General block diagram of RFB in AGC.

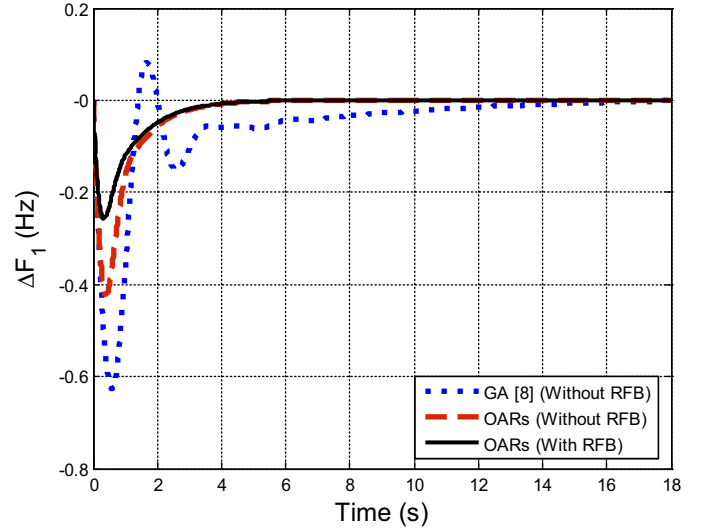


Fig. 2. Deviation in frequency of area-1.

compartment is linked to a reservoir tank and a pump so that very large volumes of the electrolytes can be circulated through the cell. The general block diagram of RFB system is shown in Fig. 1, whereas descriptive figure is shown in References 5,27,30,31. During normal load requirements the battery charges and instantly delivers the energy back to the system during the peak/sudden load demands. AC/DC or DC/AC conversions are performed by a dual converter (Fig. 1). RFB details including their various characteristics, mathematical modeling and critical reviews are available in References 30–32. RFB provide an alternative solution to the problem of mismatch of power generation and demand. Thus, they can be recommended for AGC of interconnected electrical power systems. RFB model in actual is a high order model and has nonlinearity. However, in this work, the transfer function is represented by first order lag as [5,24,27]:

$$G_{RFB}(s) = \frac{K_{RFB}}{1 + sT_{RFB}} \quad (13)$$

where, K_{RFB} is gain and T_{RFB} is the time constant of RFB. Due to the economical reasons, placement of RFB is not suggested in all the

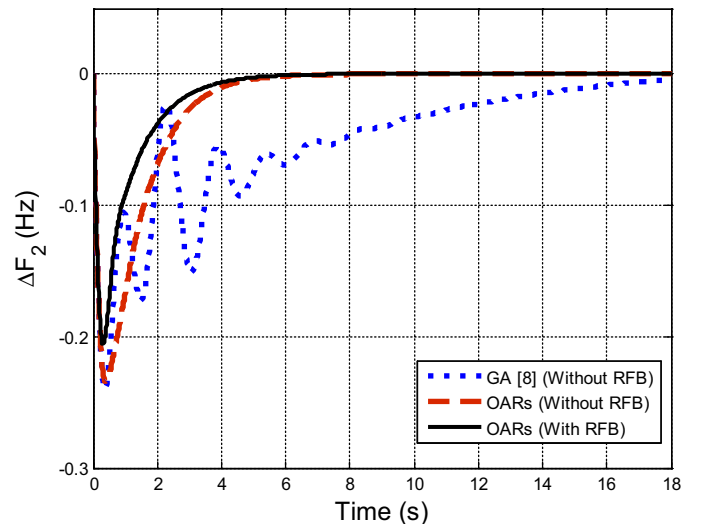


Fig. 3. Deviation in frequency of area-2.

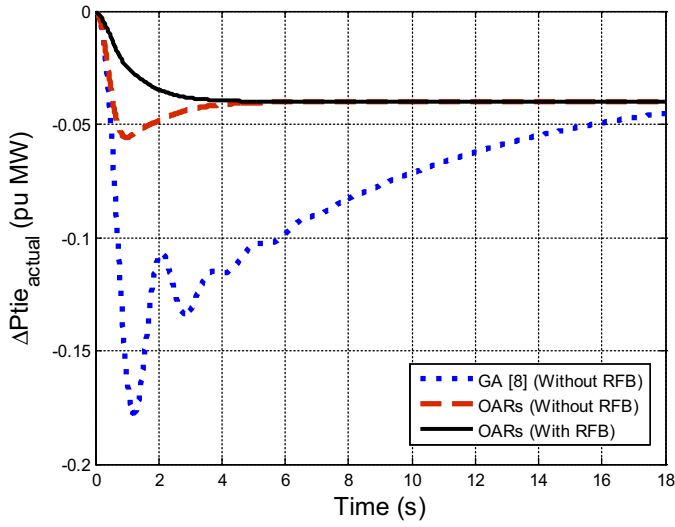


Fig. 4. Deviation in tie-line power flow (actual).

areas. Hence, in the present study, RFB are assumed to be available as an active power source to only area-1 of the two-area restructured/traditional system and ΔF_1 error signal is directly used for the RFB in AGC [5,24,27].

6. Simulation results and analysis

6.1. Two-area thermal restructured system

The two-area thermal restructured test system with two reheat units in first and two non-reheat units in the second-area is taken from Reference 8. Moreover, case 3 of Reference 8 is considered; thus all four DISCOs individually demand a load power (ΔP_{Li}) of 10% in the bilateral contract. Additionally DISCO₁ demands 10% excess uncontracted power, i.e., $\Delta P_{UC1} = 0.1$ pu MW and $\Delta P_{UC2} = 0$ pu MW. So total load demand in area-1 will be $\Delta P_{D1} = \Delta P_{L1} + \Delta P_{L2} + \Delta P_{UC1} = 0.3$ pu MW, whereas $\Delta P_{D2} = \Delta P_{L3} + \Delta P_{L4} + \Delta P_{UC2} = 0.2$ pu MW. The DPM under study is given as follows:

$$DPM = \begin{bmatrix} 0.10 & 0.24 & 0.33 & 0.18 \\ 0.20 & 0.16 & 0.17 & 0.22 \\ 0.27 & 0.40 & 0.50 & 0.00 \\ 0.43 & 0.20 & 0.00 & 0.60 \end{bmatrix} \quad (14)$$

It is assumed that all four GENCOs participate equally in AGC, i.e., $apf_{11} = apf_{12} = apf_{21} = apf_{22} = 0.5$. As per state vector given in Reference 8, the set of optimized feedback gains of OARs for the system with and without RFB is displayed in Table 1, while the set of GA tuned ACE integrator gains is $K_{I1} = 0.071$ and $K_{I2} = 0.022$ [8]. Based on system data given in Appendix B, the dynamic responses with/without RFB are shown in Figs. 2–9. Critical investigations of all the responses without RFB confess that OARs are far superior to GA tuned integral controllers in terms of shorter settling time, damped out oscillations and peak overshoots/undershoots. Additionally with RFB, the responses that have been observed further improved in terms of ripples and settling time. In steady state the deviations in frequency of both areas settle to zero while contracted generations of different GENCOs can be defined using Eqn. (15).

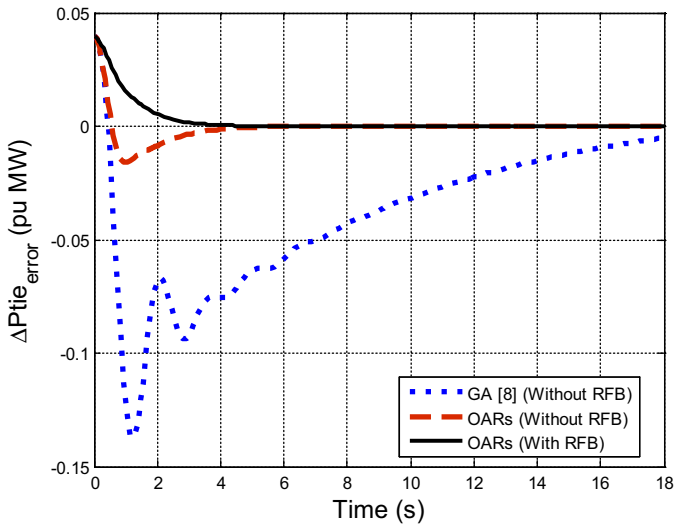


Fig. 5. Deviation in tie-line power flow (error).

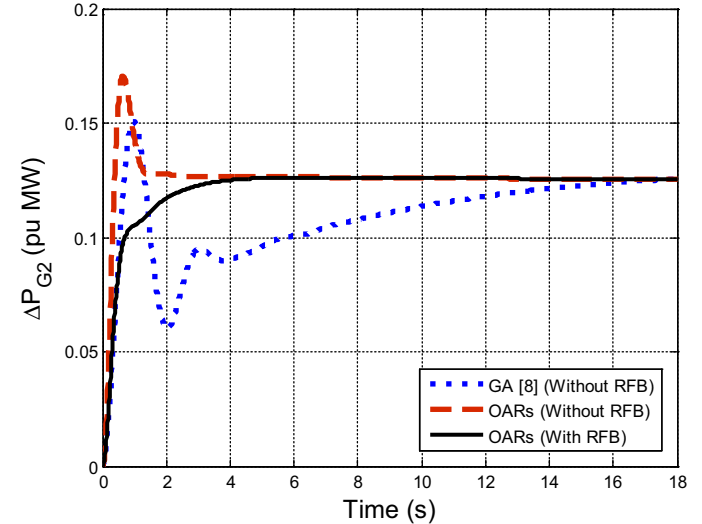


Fig. 7. Deviation in power output of GENCO-2.

Table 1

Optimal feedback gain matrices [K*] for thermal restructured system.

Without RFB	[4.2721	7.4843	7.4843	-1.3648	-1.3648	0.5049	0.5049	-0.4510
	-0.3371	-0.3371	-0.0568	-0.0568	1.6796	7.8906	0.4884;	-1.0348
	-0.8225	-0.8225	0.0555	0.0555	-0.0568	-0.0568	4.0931	3.8496
	3.8496	0.7464	0.7464	-3.9354	-0.4884	7.8906]		
With RFB	[1.6535	4.7187	4.7187	-1.1323	-1.1323	0.2849	0.2849	-0.5895
	-0.3707	-0.3707	-0.0582	-0.0582	4.5830	7.8759	0.6859;	-0.5772
	-0.7335	-0.7335	0.0755	0.0755	-0.0582	-0.0582	4.0926	3.8458
	3.8458	0.7458	0.7458	-4.1836	-0.6859	7.8759]		

$$\Delta P_{Gi} = \text{cpf}_{i1}\Delta P_{L1} + \text{cpf}_{i2}\Delta P_{L2} + \text{cpf}_{i3}\Delta P_{L3} + \text{cpf}_{i4}\Delta P_{L4}. \quad (15)$$

Hence, in steady state $\Delta P_{G1} = 0.085$ pu MW, $\Delta P_{G2} = 0.075$ pu MW, $\Delta P_{G3} = 0.117$ pu MW, $\Delta P_{G4} = 0.123$ pu MW. However, as per industrial practice uncontracted demand of 10% made by DISCO₁ must be supplied by the GENCO₁ and GENCO₂ based on respective ACE participation factors (apfs). Therefore, under contract violation

condition, $\Delta P_{G1} = \Delta P_{G1} + \text{apf}_{11}\Delta P_{UC1} = 0.085 + 0.05 = 0.135$ pu MW and $\Delta P_{G2} = 0.075 + 0.05 = 0.125$ pu MW. The simulation results of generations of GENCOs in steady state correspond to calculated values as shown with/without RFB in Figs. 6–9. From Figs. 6–7, it is also observed that OARs generate more power at step load demand as well as they settle to desired value very fast in comparison to GA controllers. On the other hand, Figs. 8–9 indicate that OARs generate less power to achieve the desired generation in comparison to GA controllers as power demand in area-2 is less than in area-1. Scheduled tie-line power, i.e., $\Delta P_{tie}^{\text{scheduled}} = (\text{Demand of DISCOs in area-2 from GENCOs in area-1}) - (\text{Demand of DISCOs in area-1 from GENCOs in area-2})$, can be given as:

$$\Delta P_{tie}^{\text{scheduled}} = (\text{cpf}_{13} + \text{cpf}_{23})\Delta P_{L3} + (\text{cpf}_{14} + \text{cpf}_{24})\Delta P_{L4} - (\text{cpf}_{31} + \text{cpf}_{41})\Delta P_{L1} - (\text{cpf}_{32} + \text{cpf}_{42})\Delta P_{L2}. \quad (16)$$

$\Delta P_{tie}^{\text{scheduled}}$ can also be defined as the total power exported from area-1 to area-2 minus total power imported to area-1 from area-2. The Fig. 4 shows the $\Delta P_{tie}^{\text{actual}} = -0.04$ pu MW, which is the $\Delta P_{tie}^{\text{scheduled}}$ in the steady state. It is clear from Fig. 5 that $\Delta P_{tie}^{\text{error}}$ settles to zero but with OARs and RFB it vanishes faster. Hence, OARs show amazingly superior dynamic performance over GA and all the responses further have been improved because of RFB unit.

The system modes with GA tuned controller and OARs with/without RFB are shown in Table 2. It is observed that none of the system modes lie in the right half of 's' plane, hence the system is stable with GA [8] and OARs with/without RFB. Without RFB, five out of fifteen system modes due to OARs are the same while the remaining ten are highly negative as compared to that of GA tuned controller. Additionally, only four complex system modes are with OARs in comparison to six system modes with GA. Therefore, the system with OARs shows significantly higher stability margins with excellent damping. With RFB, five system modes due to OARs are the same here too while most of the remaining modes lie more negative in the left half of 's' plane, which results in rapid and smooth decay of dynamic responses.

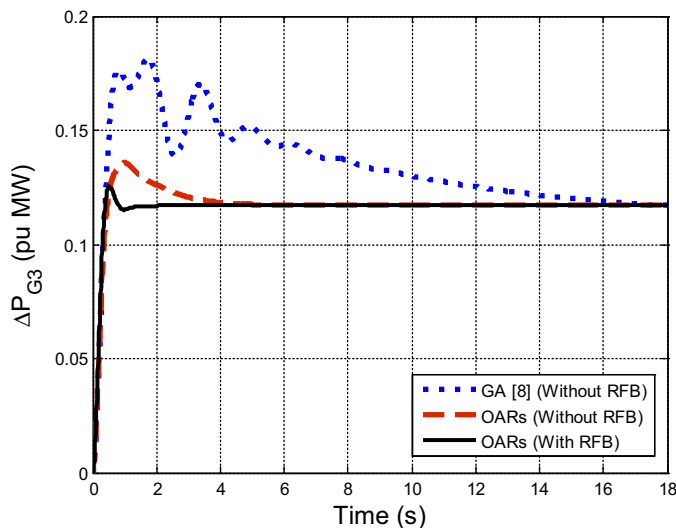


Fig. 8. Deviation in power output of GENCO-3.

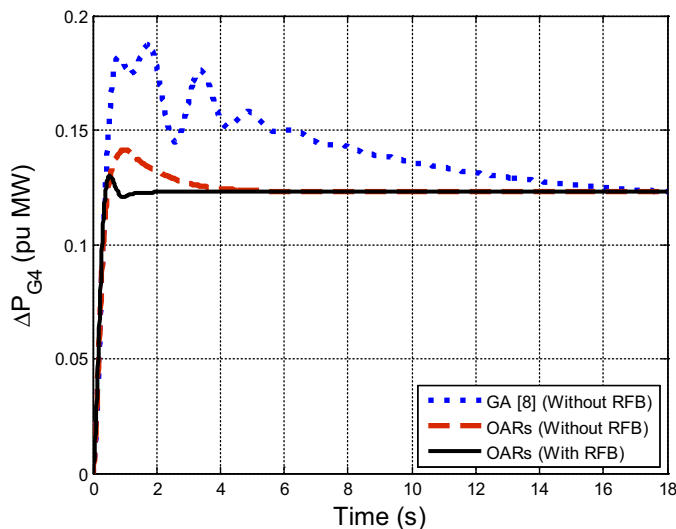


Fig. 9. Deviation in power output of GENCO-4.

Table 2

Pattern of closed-loop system modes for thermal restructured system.

OARs (With RFB)	OARs (Without RFB)	GA [8] (Without RFB)
-14.3917	-14.3910	-13.8996
-13.7128	-13.4527	-13.2704
-4.2410 ± 6.5892i	-4.2392 ± 6.5786i	-0.5799 ± 4.2171i
-3.9318 ± 4.6780i	-3.3390 ± 4.7736i	-0.9756 ± 2.8834i
-2.2249	-2.3555	-1.4083
-1.0005	-0.9647	-0.0141
-0.8943	-0.9874	-0.0816 + 0.0257i
-0.2006	-0.2001	-0.0816 - 0.0257i
-0.1000	-0.1000	-0.1000
-12.5000	-12.5000	-12.5000
-12.5000	-12.5000	-12.5000
-3.3333	-3.3333	-3.3333
-3.3333	-3.3333	-3.3333

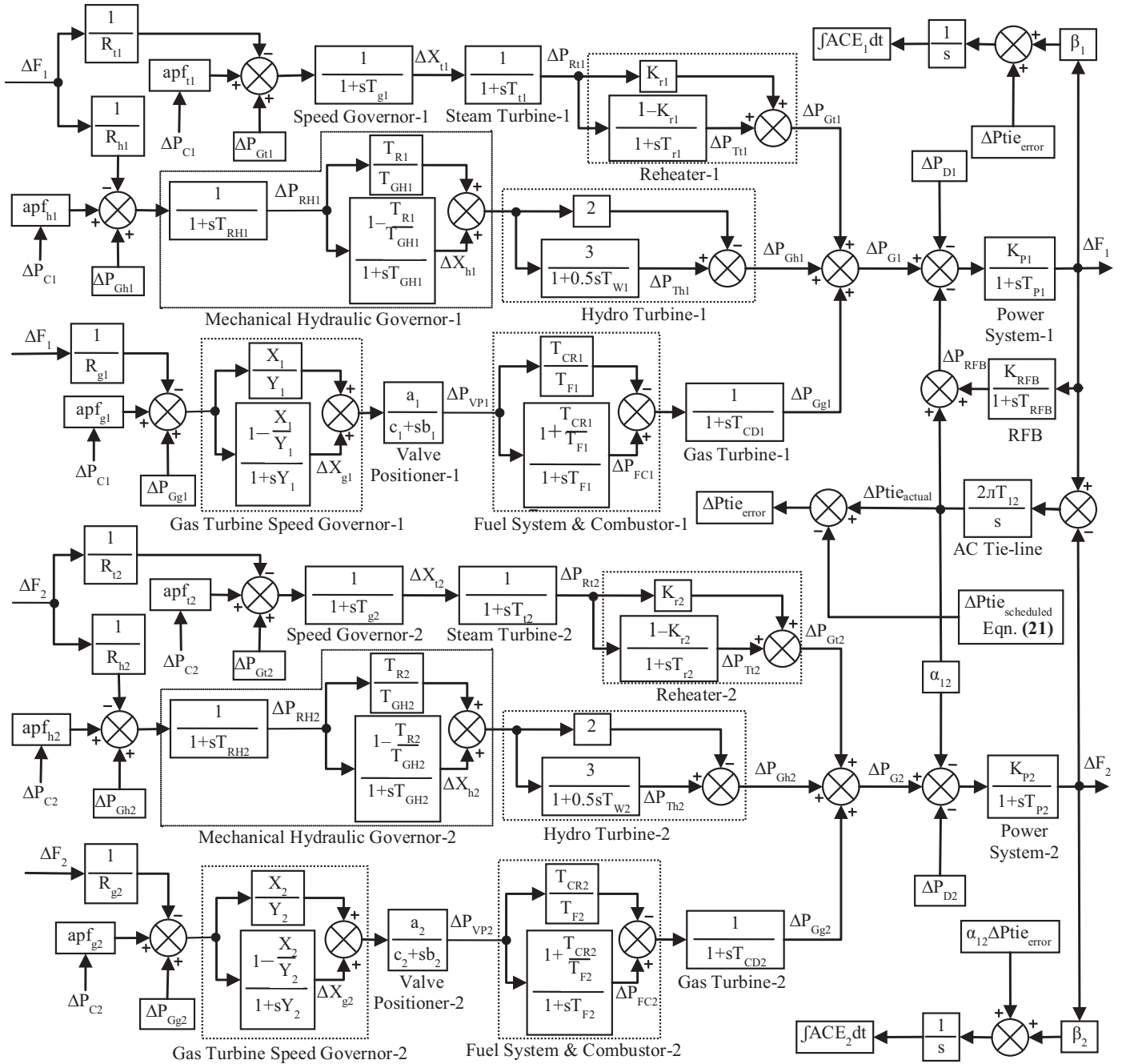


Fig. 10. Transfer function model of two-area multi-source restructured thermal-hydro-gas power system.

6.2. Two-area multi-source thermal-hydro-gas restructured system

To express the ability of the OARs to cope with multi-source system, the study is further extended to a two-area multi-source restructured thermal-hydro-gas system [15] as shown in Fig. 10. The effectiveness of OARs is tested in four cases related to three different transactions available in an open market scenario.

6.2.1. Case 1: poolco based transactions

In this case, DISCOs negotiate power purchase contracts with GENCOs situated only in their own area [5,24]. Poolco based transactions are also termed as unilateral transactions [8]. It is assumed

that the load change occurs in both areas. Hence, the load is demanded by all six DISCOs. Let $\Delta P_{L1} = \Delta P_{L2} = \Delta P_{L3} = 0.03$ pu MW and $\Delta P_{L4} = \Delta P_{L5} = \Delta P_{L6} = 0.001$ pu MW and thus $\Delta P_{D1} = 0.09$ pu MW and $\Delta P_{D2} = 0.003$ pu MW. The selected DPM is given as follow:

$$DPM = \begin{bmatrix} 0.50 & 0.50 & 0.50 & 0.00 & 0.00 & 0.00 \\ 0.25 & 0.25 & 0.25 & 0.00 & 0.00 & 0.00 \\ 0.25 & 0.25 & 0.25 & 0.00 & 0.00 & 0.00 \\ 0.00 & 0.00 & 0.00 & 0.40 & 0.20 & 0.20 \\ 0.00 & 0.00 & 0.00 & 0.20 & 0.30 & 0.40 \\ 0.00 & 0.00 & 0.00 & 0.40 & 0.50 & 0.40 \end{bmatrix} \quad (17)$$

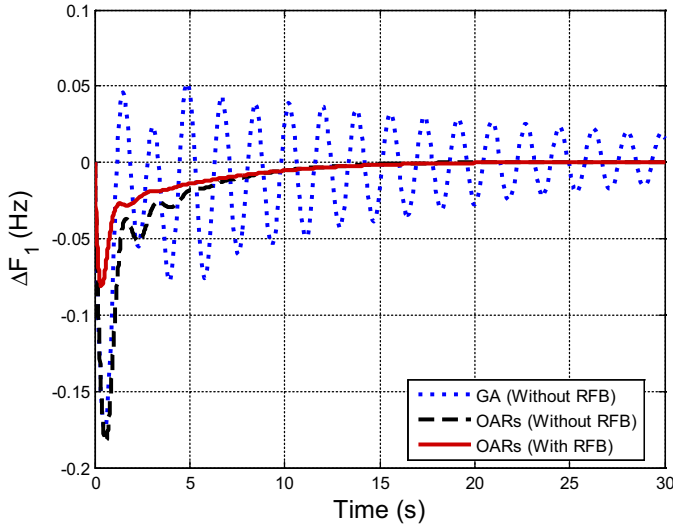


Fig. 11. Deviation in frequency of area-1 for case 1.

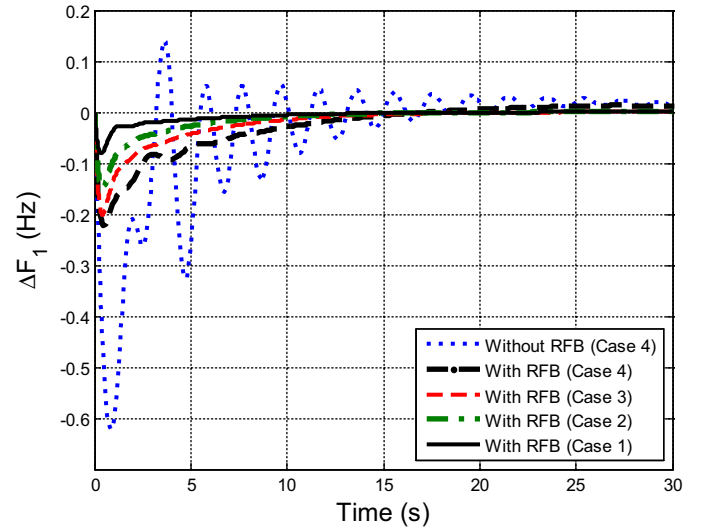


Fig. 13. Deviation in frequency of area-1.

Note that DISCOs of area-1 and 2 do not demand power from GENCOs of area-2 and 1 respectively; hence the corresponding cpfs of DPM are zero. For all cases, ACE participation factors are selected as: $apf_{i1} = apf_{i2} = 0.5$ and $apf_{h1} = apf_{h2} = apf_{g1} = apf_{g2} = 0.25$. Eqns. (15–16) stated that for steady state, contracted generations of different GENCOs and $\Delta P_{tie_scheduled}$ respectively will be modified for multi-source power system as:

$$\Delta P_{Gti} = cpf_{i1}\Delta P_{L1} + cpf_{i2}\Delta P_{L2} + cpf_{i3}\Delta P_{L3} + cpf_{i4}\Delta P_{L4} + cpf_{i5}\Delta P_{L5} + cpf_{i6}\Delta P_{L6}, \quad i = 1, 4, \quad (18)$$

$$\Delta P_{Ghi} = cpf_{i1}\Delta P_{L1} + cpf_{i2}\Delta P_{L2} + cpf_{i3}\Delta P_{L3} + cpf_{i4}\Delta P_{L4} + cpf_{i5}\Delta P_{L5} + cpf_{i6}\Delta P_{L6}, \quad i = 2, 5, \quad (19)$$

$$\Delta P_{Ggi} = cpf_{i1}\Delta P_{L1} + cpf_{i2}\Delta P_{L2} + cpf_{i3}\Delta P_{L3} + cpf_{i4}\Delta P_{L4} + cpf_{i5}\Delta P_{L5} + cpf_{i6}\Delta P_{L6}, \quad i = 3, 6, \quad (20)$$

$$\begin{aligned} \Delta P_{tie_scheduled} = & (cpf_{i4} + cpf_{24} + cpf_{34})\Delta P_{L4} + (cpf_{i5} + cpf_{25} + cpf_{35})\Delta P_{L5} \\ & + (cpf_{i6} + cpf_{26} + cpf_{36})\Delta P_{L6} \\ & - (cpf_{41} + cpf_{51} + cpf_{61})\Delta P_{L1} \\ & - (cpf_{42} + cpf_{52} + cpf_{62})\Delta P_{L2} \\ & - (cpf_{43} + cpf_{53} + cpf_{63})\Delta P_{L6}. \end{aligned} \quad (21)$$

Considering Eqns. (18–21), in steady state, GENCOs must generate load powers given by $\Delta P_{Gt1} = 0.045$ pu MW, $\Delta P_{Gh1} = 0.0225$ pu MW, $\Delta P_{Gg1} = 0.0225$ pu MW, $\Delta P_{Gt2} = 0.0008$ pu MW, $\Delta P_{Gh2} = 0.0009$ pu MW, $\Delta P_{Gg2} = 0.0013$ pu MW and $\Delta P_{tie_scheduled} = 0$ pu MW.

The optimal feedback gains of OARs obtained for the system with/without RFB are shown in Table 3. Dynamic responses for states ΔF_1 and ΔF_2 with OARs and GA controllers are shown in Figs. 11–12. The ACE integral controller gains ($K_{I1} = 0.0490$; $K_{I2} = 0.0003$) are optimized with the same performance index and GA parameters as used in Reference 8. From Figs. 11–12, it is observed that without RFB unit, undershoots of the responses with GA and OARs are more or

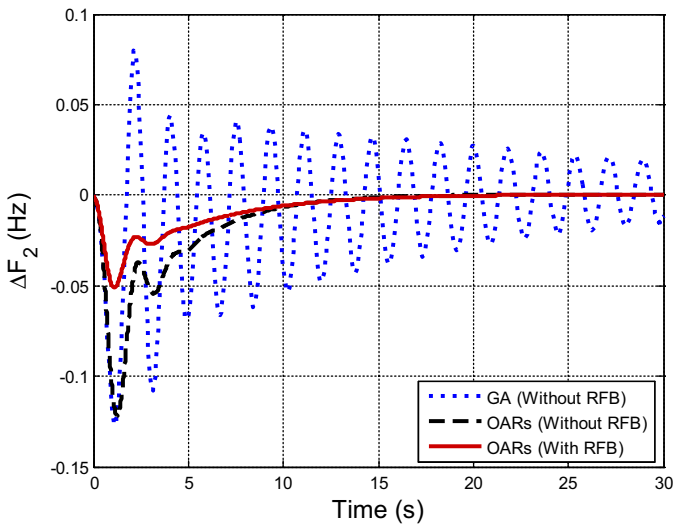


Fig. 12. Deviation in frequency of area-2 for case 1.

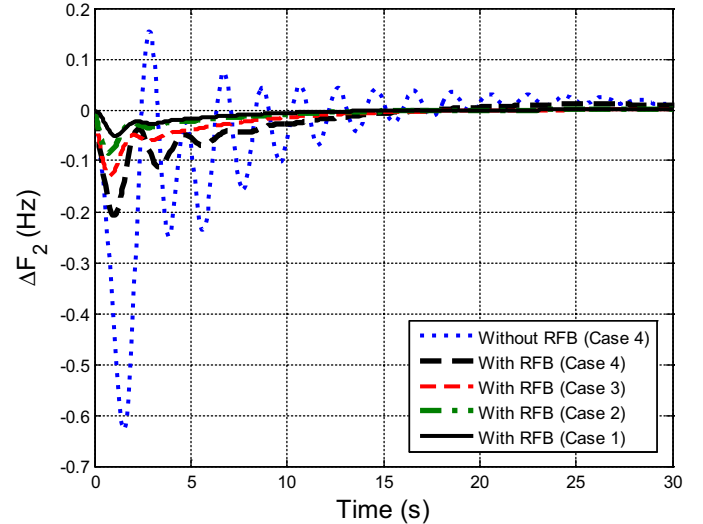


Fig. 14. Deviation in frequency of area-2.

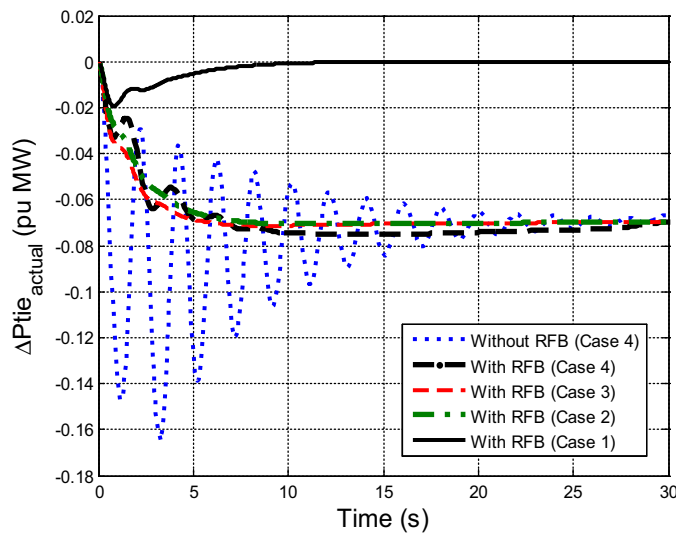
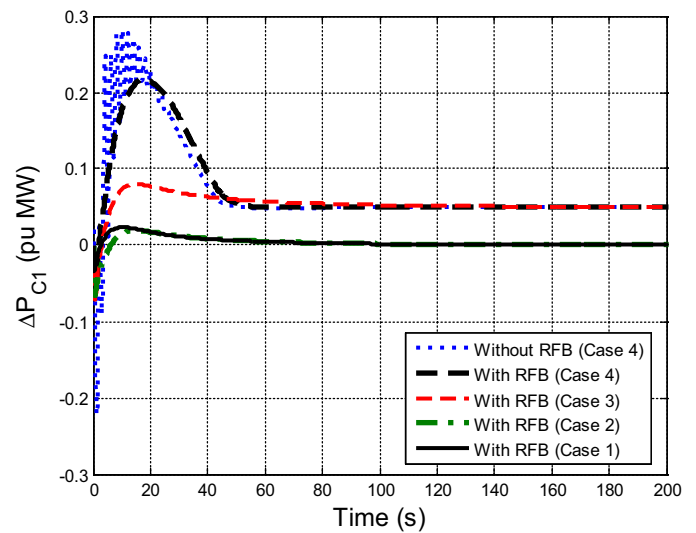
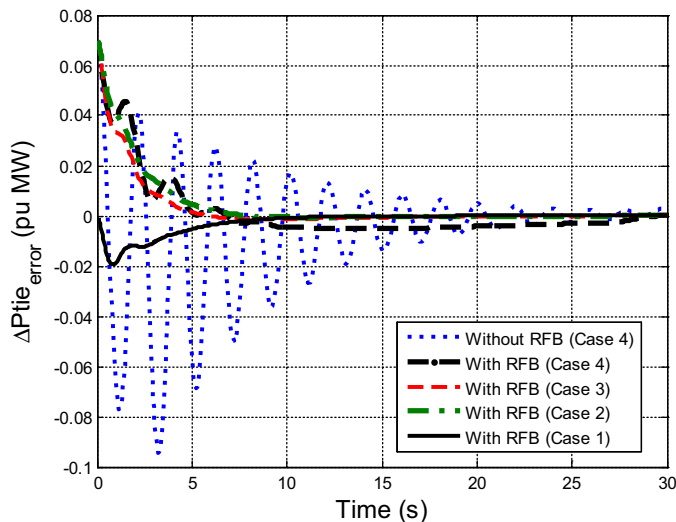
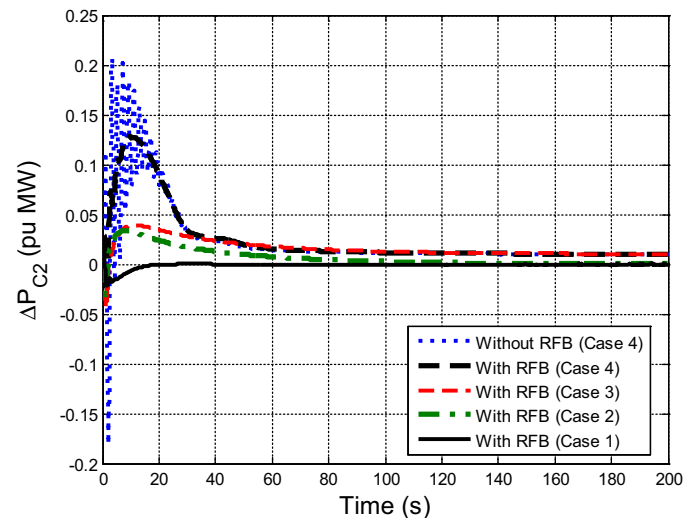
Table 3

Optimal feedback gain matrices [K*] for multi-source thermal-hydro-gas restructured system.

Without RFB	[0.5870	-1.4907	-0.0085	3.9763	0.8564	0.4236	1.9502	-0.9540
	-9.7173	1.0235	1.0907	0.2905	0.9012	-0.1497	-0.0606	-0.0151
	-0.1008	0.3873	3.2983	-0.0933	-0.0735	-0.0122	0.0763	1.0000
	-0.0000;	-0.0085	1.4907	0.5870	-0.1497	-0.0606	-0.0151	-0.1008
	0.3873	3.2983	-0.0933	-0.0735	-0.0122	0.0763	3.9763	0.8564
	0.4236	1.9502	-0.9540	-9.7173	1.0235	1.0907	0.2905	0.9012
	-0.0000	1.0000]						
With RFB	[0.0375	0.4657	-0.1544	2.0647	0.3228	0.3071	0.4844	0.1670
	2.7356	0.2209	0.3336	0.1428	0.5953	-0.1905	-0.0680	-0.0122
	-0.1147	0.3666	3.1417	-0.1185	-0.0423	-0.0038	0.0467	0.9892
	0.1466;	0.0954	1.2851	0.5214	-0.2310	0.0081	-0.0007	-0.0259
	-0.2539	-2.4028	0.0329	-0.0305	-0.0097	-0.2148	3.8158	0.7994
	0.4113	1.8004	-0.8224	-8.2545	0.9351	1.0163	0.2766	0.8839
	-0.1466	0.9892]						

less same; however, overshoots vanish, and oscillations and settling time are reduced noticeably with OARs in comparison to GA. Results are further improved with the use of RFB. The various dynamic responses are also shown in Figs. 13–24. For case 1, system responses for ΔF_1 and ΔF_2 settle to zero while all simu-

lated generations attain desired values in steady state. Steady state scheduled tie-line power flows are zero because no power is demanded by area-1 and 2 from area-2 and 1, respectively. All dynamic responses are smooth, non-oscillatory and fast due to the presence of RFB.

**Fig. 15.** Deviation in tie-line power flow (actual).**Fig. 17.** Deviation in speed changer position of area-1.**Fig. 16.** Deviation in tie-line power flow (error).**Fig. 18.** Deviation in speed changer position of area-2.

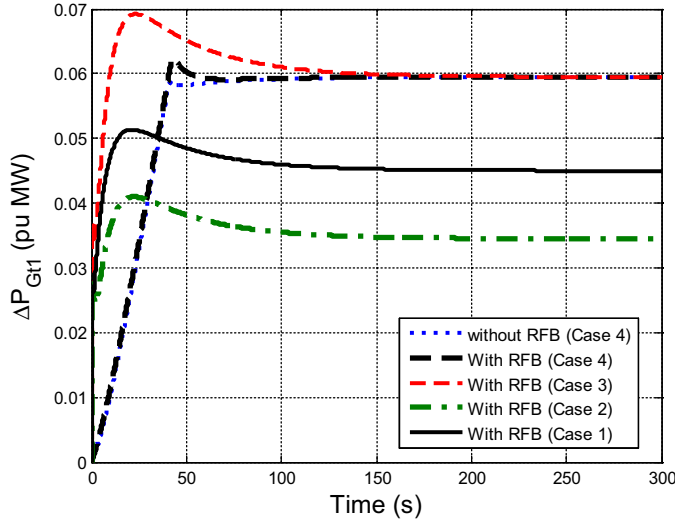


Fig. 19. Deviation in power output of GENCO-1.

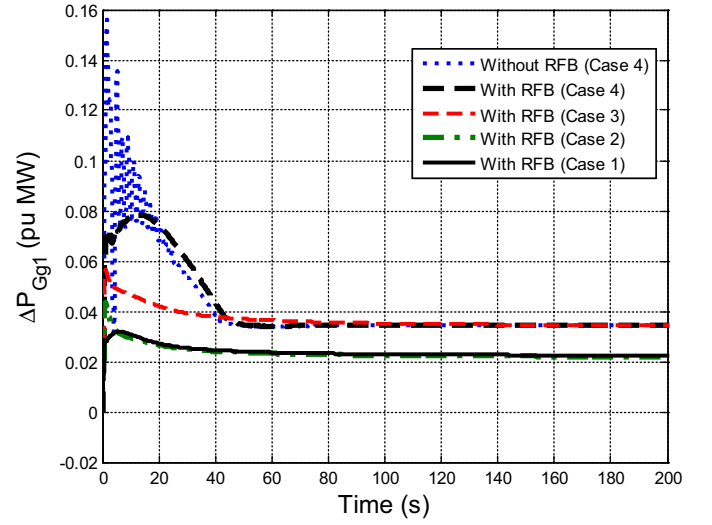


Fig. 21. Deviation in power output of GENCO-3.

6.2.2. Case 2: poolco and bilateral transactions

In this case, all DISCOs have the freedom to have contracts with GENCOs of its own and other control areas. In this case, power demand of DISCOs from GENCOs is assumed $\Delta P_{L1} = \Delta P_{L2} = \Delta P_{L3} = 0.05$ pu MW and $\Delta P_{L4} = \Delta P_{L5} = \Delta P_{L6} = 0.01$ pu MW. Consider that all the six DISCOs have contracts with the available six GENCOs for power as per the following DPM.

$$\text{DPM} = \begin{bmatrix} 0.20 & 0.20 & 0.25 & 0.10 & 0.05 & 0.05 \\ 0.20 & 0.10 & 0.15 & 0.00 & 0.00 & 0.10 \\ 0.05 & 0.20 & 0.15 & 0.10 & 0.05 & 0.05 \\ 0.10 & 0.20 & 0.05 & 0.20 & 0.30 & 0.35 \\ 0.20 & 0.20 & 0.15 & 0.30 & 0.25 & 0.25 \\ 0.25 & 0.10 & 0.25 & 0.30 & 0.35 & 0.20 \end{bmatrix} \quad (22)$$

Regarding the above DPM, GENCOs must generate contracted power of $\Delta P_{Gt1} = 0.0345$ pu MW, $\Delta P_{Gh1} = 0.0235$ pu MW, $\Delta P_{Gg1} = 0.022$ pu MW, $\Delta P_{Gt2} = 0.026$ pu MW, $\Delta P_{Gh2} = 0.0355$ pu MW, $\Delta P_{Gg2} = 0.0385$ pu MW and $\Delta P_{\text{tie,scheduled}} = -0.07$ pu MW. The values of scheduled/actual/error tie-line power flows and different genera-

tions are verified using simulated responses shown in Figs. 15–16 and 19–24 respectively. It is noticed that in deregulated environment the contract type not only affects the load demand of an area but also the scheduled tie-line power flow. Further, when uncontracted demands are absent, apf value does not affect the steady state behavior but only the transient behavior of the system will be affected.

6.2.3. Case 3: contract violation

In some situations, DISCOs in an area may violate a contract by demanding excess power than that specified in the contract. This excess power demand, which is not contracted to any of the GENCOs, must be supplied only by the GENCOs operating in the same area as that of DISCOs [2–12,24]. Consider case 2 once again with a modification that DISCO₁ and DISCO₄ demand respectively 0.05 pu MW and 0.01 pu MW of excess power, i.e., $\Delta P_{UC1} = 0.05$ pu MW and $\Delta P_{UC2} = 0.01$ pu MW. Hence, $\Delta P_{D1} = 0.15 + 0.05 = 0.2$ pu MW and $\Delta P_{D2} = 0.04$ pu MW. Figs. 13–24 also include the stabilized dynamic responses in the event of contract violation with RFB. With OARs, AGC requirement is satisfied as frequency deviations and tie-line power flow error settle to zero in the steady state. All generation in steady state will be affected as excess power is demanded in both areas. ACE

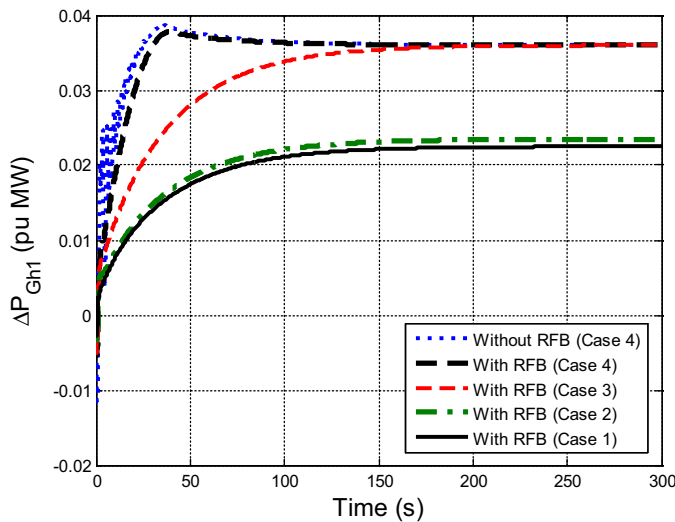


Fig. 20. Deviation in power output of GENCO-2.

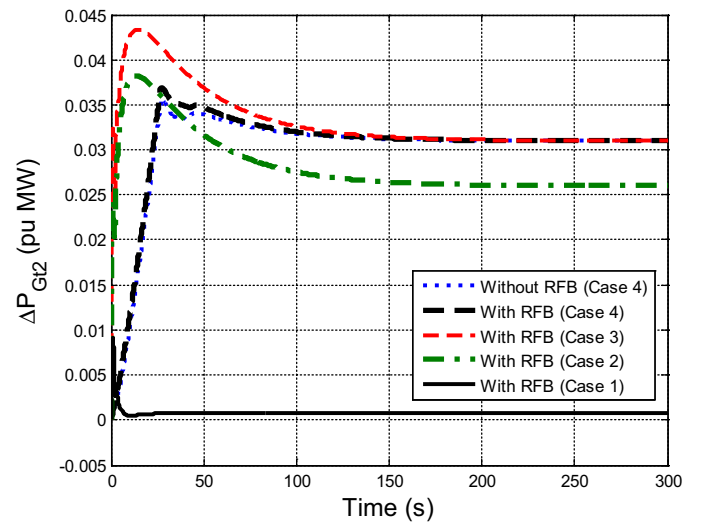


Fig. 22. Deviation in power output of GENCO-4.

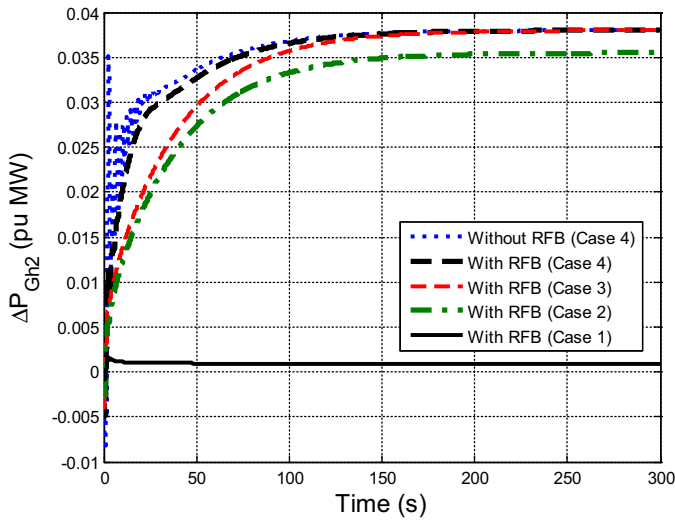


Fig. 23. Deviation in power output of GENCO-5.

participation factors of area-1 and 2 will decide the distribution of the uncontracted load demand among respective area GENCOs in the steady state. Therefore, $\Delta P_{Gt1} = 0.0345 + 0.5 \cdot 0.05 = 0.0595$ pu MW and $\Delta P_{Gh1} = 0.0235 + 0.25 \cdot 0.05 = 0.036$ pu MW. Similarly, $\Delta P_{Gt2} = 0.0345$ pu MW, $\Delta P_{Gh2} = 0.031$ pu MW, $\Delta P_{Gt2} = 0.038$ pu MW, $\Delta P_{Gh2} = 0.041$ pu MW and steady state tie-line power flows are the same as in case 2. The uncontracted demand in both areas is reflected in outputs of all six GENCOs as shown in Figs. 19–24. It also specifies the fruitful potential of OARs. The absence of uncontracted power demand for cases 1–2 is also shown by settlement of speed changer position (ΔP_{Ci}) to zero in steady state for area-1 and 2 respectively in Figs. 17–18. Additionally, they show the uncontracted demand of 0.05 pu MW and 0.01 pu MW in area-1 and 2 respectively for case 3. From Figs. 20 and 23, it is observed that the dynamic responses of power generations due to hydro sources are characterized by an initial fast negative dip followed by slower exponential increase in power generation. This is due to non-minimum phase characteristic of hydro turbines. Hence, hydro plants in comparison to thermal and gas require more time to meet desired power demand of DISCOs. On comparing Figs. 2–9 and Figs. 11–24, it is observed that the dynamic responses of multi-source system due to OARs are more oscillatory in comparison to that of thermal system.

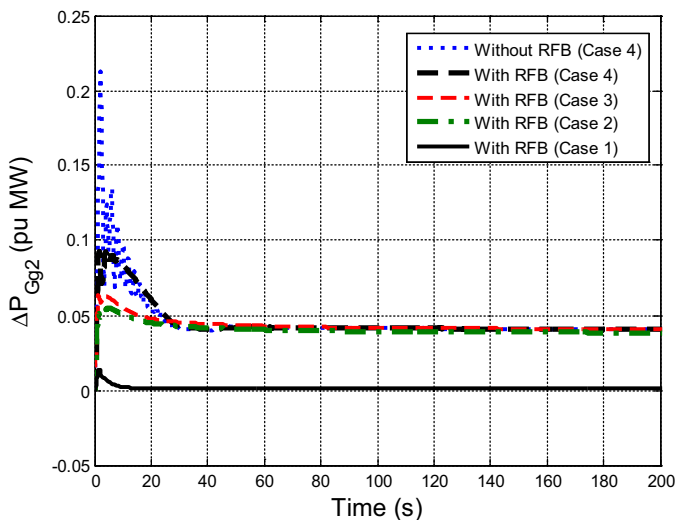


Fig. 24. Deviation in power output of GENCO-6.

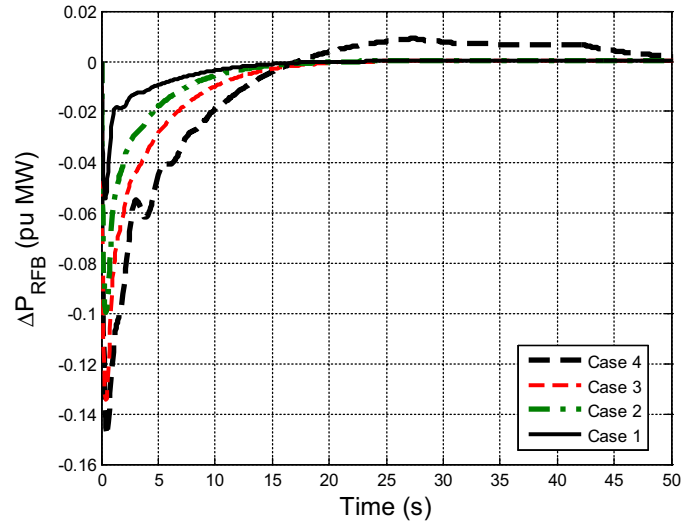


Fig. 25. Deviation in power output of RFB.

6.2.4. Case 4: effect of generation rate constraints

In practical power systems having steam, hydro and gas power plants, a maximum limit exists on the rate of the change in the generating power. Under the absence of GRC, undesirably, generators are expected to chase large momentary disturbances. Therefore, GRC must be incorporated for a pragmatic study of the system. In most of the research articles, the effect of GRC in restructured systems is not considered [2–8,12]. For testing the effectiveness of the OARs, the GRCs for hydro unit for raise and for lower generations are considered as ± 0.045 pu/s and -0.06 pu/s respectively; while ± 0.0005 pu/s GRC is considered for reheat thermal turbine and ± 0.025 pu/s GRC is considered for gas turbine of the studied system. Here, case 3 is again simulated with GRC and with/without RFB. Simulation results for case 4 are also shown in Figs. 13–24. It is observed that for case 4 with RFB, ameliorated system dynamic performance is observed as compared to system performance without RFB. The settling time and peak over/under shoot of the area frequencies and tie-line power flow deviations have been noticed decreased significantly with the use of RFB unit. Thus, RFB efficiently suppress the oscillation and stabilize the system hastily. However, in case 4, due to GRC dynamic performance of the system deteriorates and the responses present larger overshoots and longer setting times

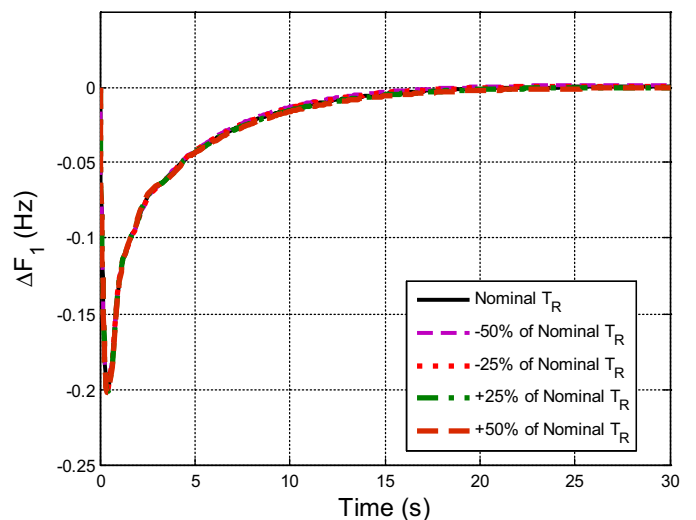


Fig. 26. Deviation in frequency of area-1.

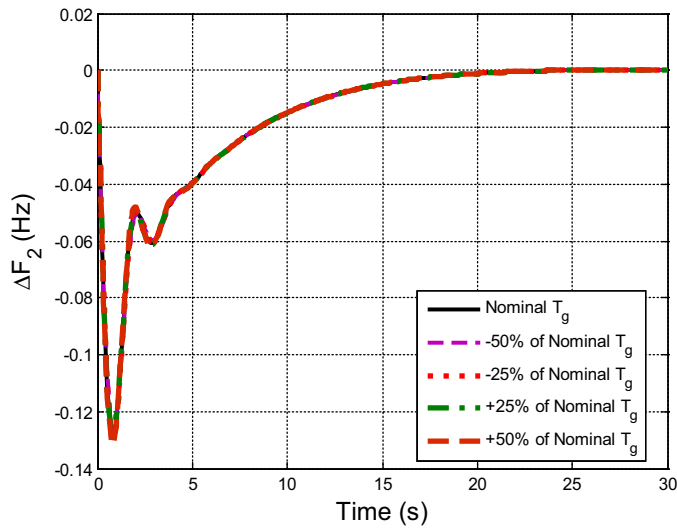


Fig. 27. Deviation in frequency of area-2.

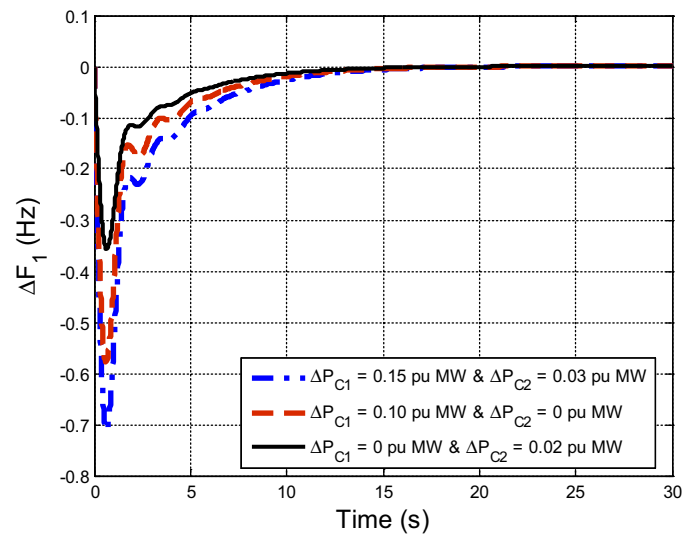


Fig. 30. Deviation in frequency of area-1.

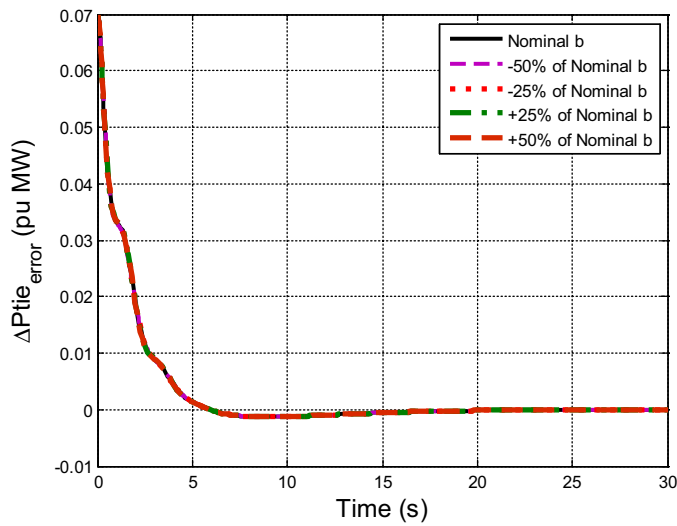


Fig. 28. Deviation in tie-line power flow (error).

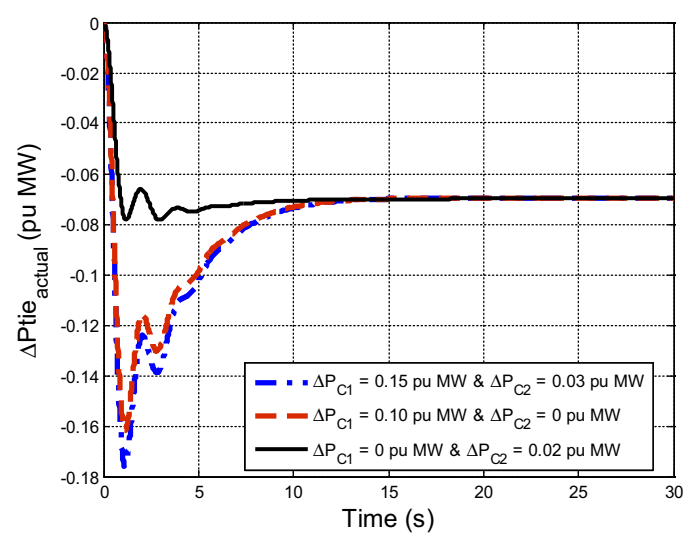


Fig. 31. Deviation in tie-line power flow (actual).

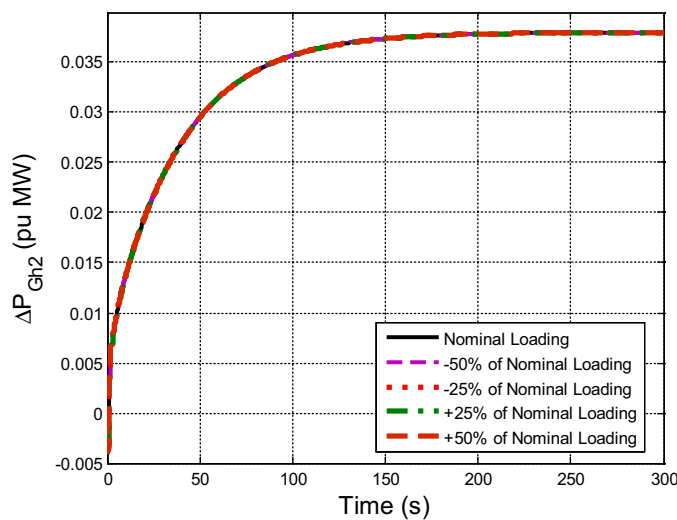


Fig. 29. Deviation in power output of GENCO-5.

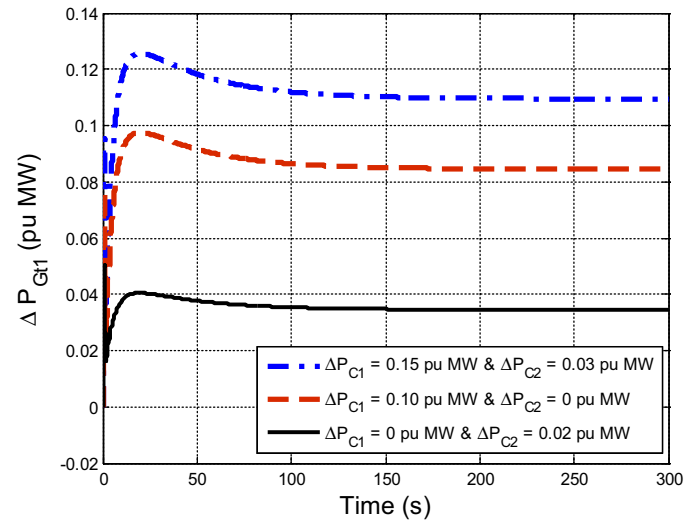


Fig. 32. Deviation in power output of GENCO-1.

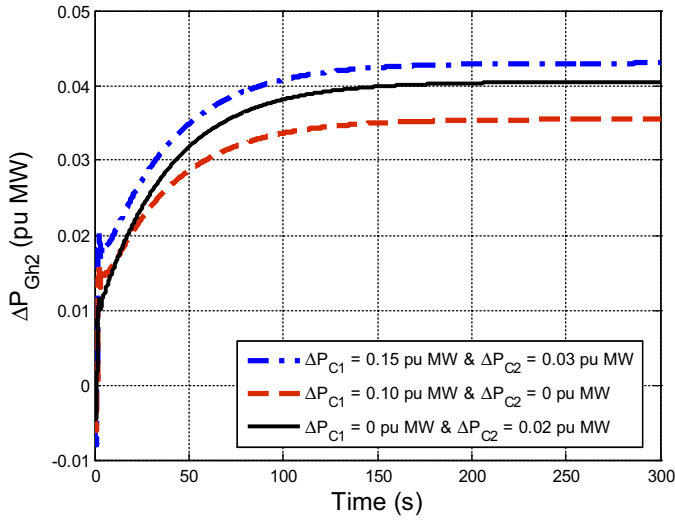


Fig. 33. Deviation in power output of GENCO-5.

in comparison to case 3. However, system responses show stabilized outcomes and satisfy AGC problem requirement. Fig. 25 presents the power outputs of RFB in different scenarios. RFB assist power generation to balance transient load requirements.

6.2.4.1. Sensitivity analysis. Sensitivity analysis is undertaken to study the robustness of the optimum feedback gains of OARs obtained at nominal condition for wide changes in system parameters [4,10,11,14,16,17,24]. On the basis of the relations given in Appendix B, the variation in system loading condition affects the power system damping constant (D_i), power system gain (K_{pi}), power system time constant (T_{pi}) and area frequency response characteristic (β_i). These

power system parameters, to be used in the multi-source restructured power system model, are calculated for different loading conditions. Selecting one at a time, system loading and time constants of hydrogovernor (T_R), speed governor (T_g) and valve positioner (b) are changed from their nominal values in the range of $\pm 50\%$ in steps of 25%. For case 3, system dynamic responses with RFB for ΔF_1 , ΔF_2 , ΔP_{tie_error} and ΔP_{Gh2} are shown in Figs. 26–29 for changed operating conditions of T_R , T_g , b and system loading respectively. Critical examination of the responses clearly unveils that all these responses show imperceptible variations. So it can be concluded that optimized feedback gains obtained at the nominal loading of 50% and nominal parameters need not be reset for wide changes in the system loading or system parameters.

In practical multi-area restructured power systems, uncontracted power demand can occur in any one area or in all the areas simultaneously. If the controller is not designed to tackle such cases, the system will certainly turn unstable. Here, simulations of the multi-source restructured system for case 2 are realized for three situations such as: (a) $\Delta P_{UC1} = 0.10$ pu MW, (b) $\Delta P_{UC2} = 0.02$ pu MW and (c) simultaneous $\Delta P_{UC1} = 0.15$ pu MW and $\Delta P_{UC2} = 0.03$ pu MW. Moreover in this scenario, OARs success is tested for the system without RFB because of more prospects of system instability. Evaluation of Figs. 30–33 clearly reveals the efficacy of OARs for higher intensity and changed location of contract violation. To save space, only four dynamic responses are shown for rationale of this statement. Similar stabilized outcomes due to sensitivity analysis are observed for restructured thermal system; however, these responses are not displayed in the paper, aiming to save space.

6.3. Two-area multi-source thermal–hydro power system

In order to demonstrate potential and effectiveness of OARs, the study is finally extended to a two-area multi-source thermal–hydro power system as shown in Fig. 34 [14]. Each area consists of

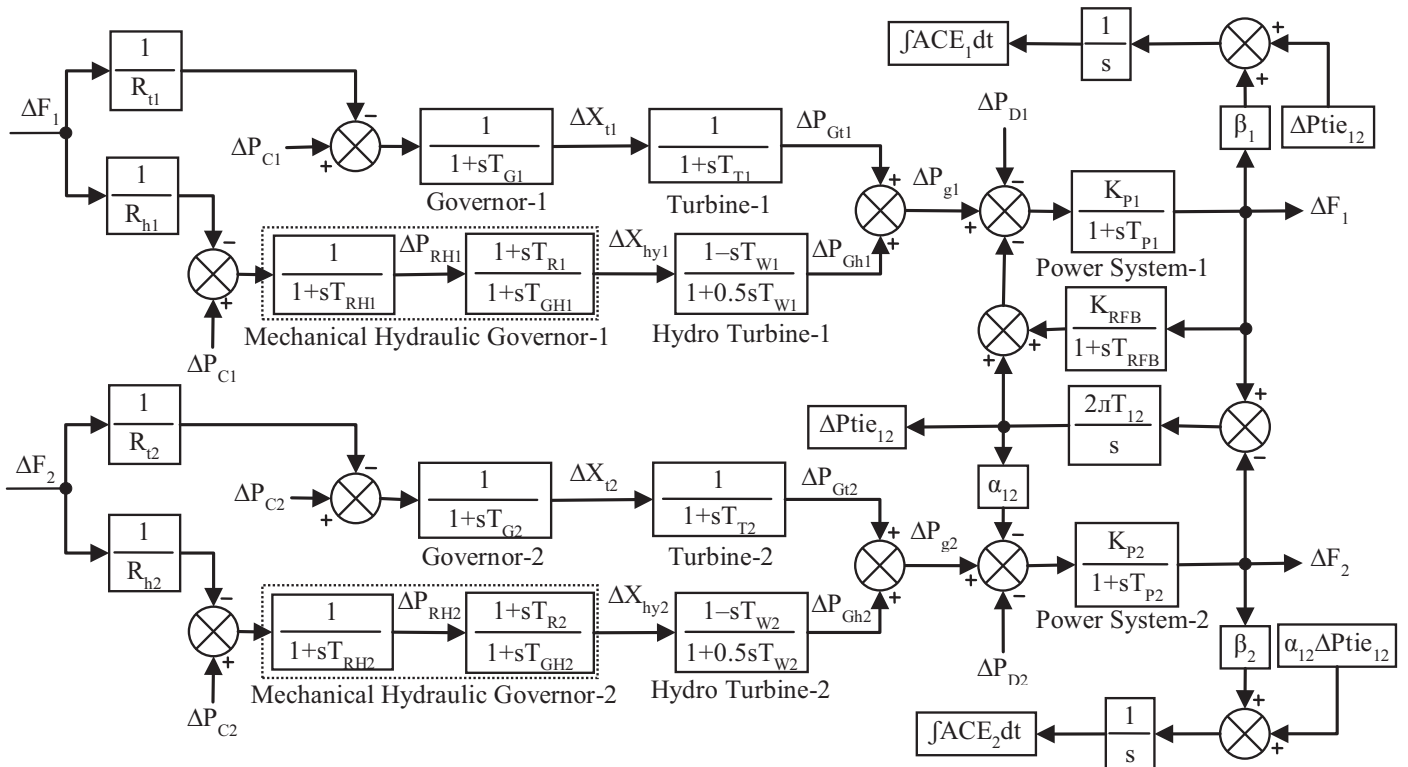


Fig. 34. Transfer function model of two-area multi-source thermal–hydro power system [14].

Table 4

Optimal feedback gain matrices [K*] for multi-source thermal-hydro system.

Without RFB	7.8861	-1.1222	8.6580	5.6534	6.4573	3.8845	-0.5374	-0.5757
	-0.1641	1.0594	-2.1341	-0.0786	0.1005	14.1421	0.0000;	-1.1222
	7.8861	-8.6580	-0.5374	-0.5757	-0.1641	5.6534	6.4573	3.8845
	-0.0786	0.1005	1.0594	-2.1341	0.0000	14.1421]		
With RFB	4.2058	-1.1833	10.8830	3.8095	4.4598	3.2268	-0.5457	-0.5840
	-0.1644	0.7752	-1.7040	-0.0786	0.1007	14.1420	0.0516;	-0.7663
	7.8876	-8.7863	-0.4510	-0.4966	-0.2036	5.6533	6.4572	3.8846
	-0.0752	0.1411	1.0594	-2.1342	-0.0516	14.1420]		

two generating units, one non-reheat thermal and other mechanical governor based hydro power plant with area capacity of 2000 MW and initial loading of 50%. The nominal data are given in Appendix B. The OARs are designed with the optimized full state feedback gains with/without RFB as shown in Table 4. The system dynamic responses of OARs for 1.5% step load perturbation (SLP) in area-1 applied at $t = 0$ s are shown in Figs. 35–37. For comparison, the simulation results for the same system due to GA based PI [14] and hybrid Firefly Algorithm–Pattern Search (hFA-PS) algorithm [14] based PI/PID controllers are also shown in these figures. It is clear from Figs. 35–37 that OARs outperform GA and hFA-PS based PI controllers for ΔF_1 , ΔF_2 and ΔP_{tie12} responses. Further, PI structured OARs also show a superb performance in comparison to hFA-PS based PID controller, specially in terms of reduced settling time and oscillations. The system performance further improves with consideration of RFB installed in area-1.

7. Conclusions

The effect of RFB on AGC of two-area restructured power systems is investigated. Full state vector feedback optimal AGC regulators (OARs) are designed by employing performance index minimization criterion. At first, a two-area restructured four unit thermal power system is investigated and the superiority of OARs is shown by comparing the responses with Genetic Algorithm (GA) tuned controllers for the same system. Advantage of OARs over GA is evident from the simulation results in terms of significantly smooth and fast responses with minimal settling time. Since RFB can share the instantaneous need of extra active power, improved system performance using OARs is observed with RFB. Next, system mode analysis shows an appreciable improvement in stability margins with

OARs in comparison to GA. In addition, system stability is further improved with RFB. To demonstrate the ability of OARs to cope with multi-source system, the study is also extended to a more realistic two-area six unit multi-source thermal-hydro-gas restructured system with/without RFB. It is observed that the frequency and

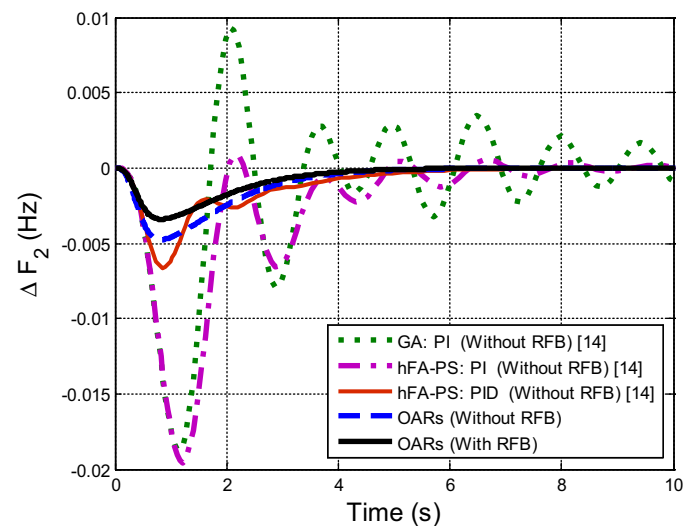


Fig. 36. Deviation in frequency of area-2 for 1.5% SLP in area-1.

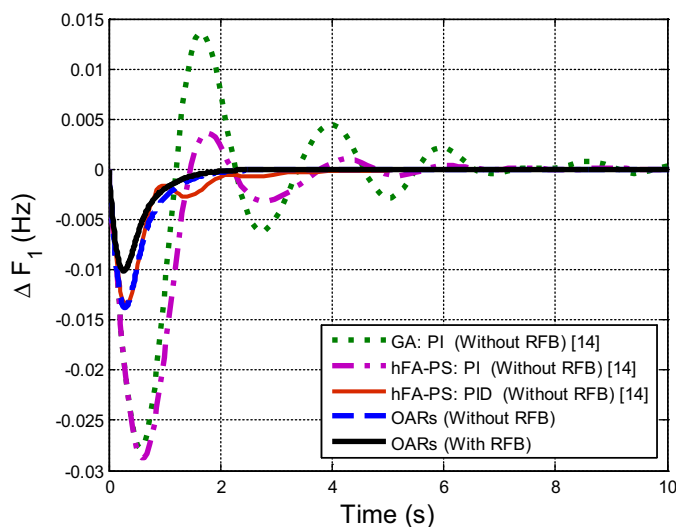


Fig. 35. Deviation in frequency of area-1 for 1.5% SLP in area-1.

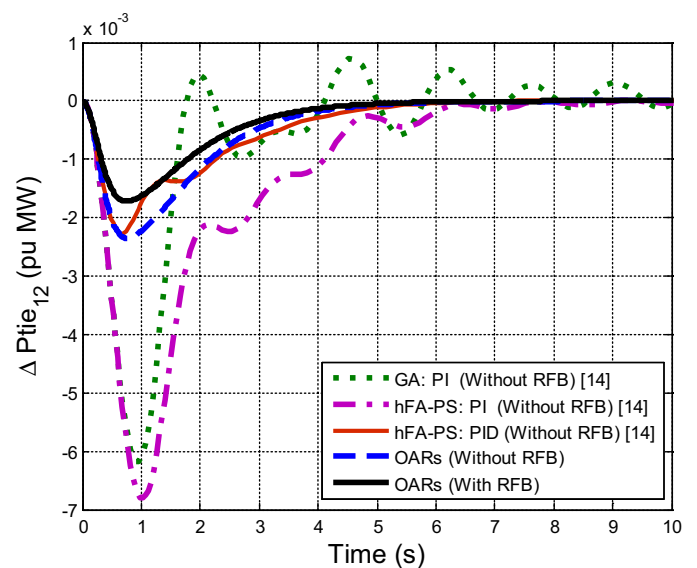


Fig. 37. Tie-line power deviation for 1.5% SLP in area-1.

tie-line power responses of the system with/without RFB settle to zero in the steady state during different transactions taking place in an open market and satisfy AGC requirement. Simulated generations and tie-line power flows due to OARs are found matching with the corresponding desired values with/without RFB/GRC. Sensitivity analysis reveals that the OARs with the optimized feedback gains obtained at the nominal loading of 50% are robust enough and need not be reset if the system is subjected to wide changes in system loading or parameters such as T_R , T_g and b from their nominal values. Furthermore, robustness of OARs is confirmed at bigger size and changed positions of uncontracted power demand of DISCOs. It is also observed that the optimized feedback gain values and system modes show no change for different possible power contracts and structures of DPM. Finally, the approach is extended to a two-area multi-source thermal-hydro power system. From the simulation results, it is revealed that OARs outperform GA optimized PI and recently proposed hFA-PS algorithm optimized PI and PID controllers.

Appendix A: State space model matrices

For two-area multi-source thermal-hydro-gas restructured power system model with RFB, the system matrix A is of the order of 25×25 and its nonzero (a_{ij}) elements are given as:

$$\begin{aligned} a_{1,1} &= -\frac{(K_{RFB}K_{P1} + 1)}{T_{P1}}, \quad a_{1,2} = -\frac{K_{P1}}{T_{P1}}, \quad a_{1,4} = \frac{K_{P1}}{T_{P1}}, \quad a_{1,5} = \frac{K_{R1}K_{P1}}{T_{P1}}, \\ a_{1,7} &= \frac{K_{P1}}{T_{P1}}, \quad a_{1,8} = -\frac{2K_{P1}}{T_{P1}}, \quad a_{1,9} = -\frac{2T_{R1}K_{P1}}{T_{GH1}T_{P1}}, \quad a_{1,10} = \frac{K_{P1}}{T_{P1}}, \\ a_{2,1} &= 2\pi T_{12}, \quad a_{2,3} = -2\pi T_{12}, \quad a_{3,2} = -\frac{\alpha_{12}K_{P2}}{T_{P2}}, \quad a_{3,3} = -\frac{1}{T_{P2}}, \\ a_{3,14} &= \frac{K_{P2}}{T_{P2}}, \quad a_{3,15} = \frac{K_{F2}K_{P2}}{T_{P2}}, \quad a_{3,17} = \frac{K_{P2}}{T_{P2}}, \quad a_{3,18} = -\frac{2K_{P2}}{T_{P2}}, \\ a_{3,19} &= -\frac{2T_{R2}K_{P2}}{T_{GH2}T_{P2}}, \quad a_{3,20} = \frac{K_{P2}}{T_{P2}}, \quad a_{4,4} = -\frac{1}{T_{R1}}, \quad a_{4,5} = \frac{1-K_{R1}}{T_{R1}}, \\ a_{5,5} &= -\frac{1}{T_{t1}}, \quad a_{5,6} = \frac{1}{T_{t1}}, \quad a_{6,1} = -\frac{1}{R_{t1}T_{g1}}, \quad a_{6,6} = -\frac{1}{T_{g1}}, \\ a_{7,7} &= -\frac{2}{T_{W1}}, \quad a_{7,8} = \frac{6}{T_{W1}}, \quad a_{7,9} = \frac{6T_{R1}}{T_{GH1}T_{W1}}, \quad a_{8,8} = -\frac{1}{T_{GH1}}, \\ a_{8,9} &= \frac{T_{GH1}-T_{R1}}{T_{GH1}^2}, \quad a_{9,1} = -\frac{1}{R_{h1}T_{RH1}}, \quad a_{9,9} = -\frac{1}{T_{RH1}}, \quad a_{10,10} = -\frac{1}{T_{CD1}}, \\ a_{10,11} &= \frac{1}{T_{CD1}}, \quad a_{10,12} = -\frac{T_{CR1}}{T_{F1}T_{CD1}}, \quad a_{11,11} = -\frac{1}{T_{F1}}, \quad a_{11,12} = \frac{T_{F1}+T_{CR1}}{T_{F1}^2}, \\ a_{12,1} &= -\frac{a_1X_1}{R_{g1}b_1Y_1}, \quad a_{12,12} = -\frac{c_1}{b_1}, \quad a_{12,13} = \frac{a_1}{b_1}, \quad a_{13,1} = \frac{X_1-Y_1}{R_{g1}Y_1^2}, \\ a_{13,13} &= -\frac{1}{Y_1}, \quad a_{14,14} = -\frac{1}{T_{r2}}, \quad a_{14,15} = \frac{1-K_{r2}}{T_{r2}}, \quad a_{15,15} = -\frac{1}{T_{r2}}, \\ a_{15,16} &= \frac{1}{T_{t2}}, \quad a_{16,3} = -\frac{1}{R_{t2}T_{g2}}, \quad a_{16,16} = -\frac{1}{T_{g2}}, \quad a_{17,17} = -\frac{2}{T_{W2}}, \\ a_{17,18} &= \frac{6}{T_{W2}}, \quad a_{17,19} = \frac{6T_{R2}}{T_{GH2}T_{W2}}, \quad a_{18,18} = -\frac{1}{T_{GH2}}, \quad a_{18,19} = \frac{T_{GH2}-T_{R2}}{T_{GH2}^2}, \\ a_{19,3} &= -\frac{1}{R_{h2}T_{RH2}}, \quad a_{19,19} = -\frac{1}{T_{RH2}}, \quad a_{20,20} = -\frac{1}{T_{CD2}}, \quad a_{20,21} = \frac{1}{T_{CD2}}, \\ a_{20,22} &= -\frac{T_{CR2}}{T_{F2}T_{CD2}}, \quad a_{21,21} = -\frac{1}{T_{F2}}, \quad a_{21,22} = \frac{T_{F2}+T_{CR2}}{T_{F2}^2}, \\ a_{22,3} &= -\frac{a_2X_2}{R_{g2}b_2Y_2}, \quad a_{22,22} = -\frac{c_2}{b_2}, \quad a_{22,23} = \frac{a_2}{b_2}, \quad a_{23,3} = \frac{X_2-Y_2}{R_{g2}Y_2^2}, \\ a_{23,23} &= -\frac{1}{Y_2}, \quad a_{24,1} = \beta_1, \quad a_{24,2} = 1, \quad a_{25,2} = \alpha_{12}, \quad a_{25,3} = \beta_2. \end{aligned}$$

The control matrix B is of the order of 25×2 and its nonzero elements (b_{ij}) are given as:

$$\begin{aligned} b_{6,1} &= \frac{apf_{t1}}{T_{g1}}, \quad b_{9,1} = \frac{apf_{h1}}{T_{RH1}}, \quad b_{12,1} = \frac{a_1X_1apf_{g1}}{b_1Y_1}, \quad b_{13,1} = \frac{apf_{g1}(Y_1-X_1)}{Y_1^2}, \\ b_{16,2} &= \frac{apf_{t2}}{T_{g2}}, \quad b_{19,2} = \frac{apf_{h2}}{T_{RH2}}, \quad b_{22,2} = \frac{a_2X_2apf_{g2}}{b_2Y_2}, \\ b_{23,2} &= \frac{apf_{g2}(Y_2-X_2)}{Y_2^2}. \end{aligned}$$

The disturbance matrix Γ is of the order of 25×8 and its nonzero elements (d_{ij}) are given as:

$$\begin{aligned} d_{1,1} &= -\frac{K_{P1}}{T_{P1}}, \quad d_{1,2} = -\frac{K_{P1}}{T_{P1}}, \quad d_{1,3} = -\frac{K_{P1}}{T_{P1}}, \quad d_{1,7} = -\frac{K_{P1}}{T_{P1}}, \quad d_{3,4} = -\frac{K_{P2}}{T_{P2}}, \\ d_{3,5} &= -\frac{K_{P2}}{T_{P2}}, \quad d_{3,6} = -\frac{K_{P2}}{T_{P2}}, \quad d_{3,8} = -\frac{K_{P2}}{T_{P2}}, \quad d_{6,1} = \frac{cpf_{t1}}{T_{g1}}, \\ d_{6,2} &= \frac{cpf_{t2}}{T_{g1}}, \quad d_{6,3} = \frac{cpf_{t3}}{T_{g1}}, \quad d_{6,4} = \frac{cpf_{t4}}{T_{g1}}, \quad d_{6,5} = \frac{cpf_{t5}}{T_{g1}}, \\ d_{6,6} &= \frac{cpf_{t6}}{T_{g1}}, \quad d_{9,1} = \frac{cpf_{h1}}{T_{RH1}}, \quad d_{9,2} = \frac{cpf_{h2}}{T_{RH1}}, \quad d_{9,3} = \frac{cpf_{h3}}{T_{RH1}}, \\ d_{9,4} &= \frac{cpf_{h4}}{T_{RH1}}, \quad d_{9,5} = \frac{cpf_{h5}}{T_{RH1}}, \quad d_{9,6} = \frac{cpf_{h6}}{T_{RH1}}, \quad d_{12,1} = \frac{a_1X_1cpf_{g1}}{b_1Y_1}, \\ d_{12,2} &= \frac{a_1X_1cpf_{g2}}{b_1Y_1}, \quad d_{12,3} = \frac{a_1X_1cpf_{g3}}{b_1Y_1}, \quad d_{12,4} = \frac{a_1X_1cpf_{g4}}{b_1Y_1}, \\ d_{12,5} &= \frac{a_1X_1cpf_{g5}}{b_1Y_1}, \quad d_{12,6} = \frac{a_1X_1cpf_{g6}}{b_1Y_1}, \quad d_{13,1} = \frac{cpf_{g1}(Y_1-X_1)}{Y_1^2}, \\ d_{13,2} &= \frac{cpf_{g2}(Y_1-X_1)}{Y_1^2}, \quad d_{13,3} = \frac{cpf_{g3}(Y_1-X_1)}{Y_1^2}, \quad d_{13,4} = \frac{cpf_{g4}(Y_1-X_1)}{Y_1^2}, \\ d_{13,5} &= \frac{cpf_{g5}(Y_1-X_1)}{Y_1^2}, \quad d_{13,6} = \frac{cpf_{g6}(Y_1-X_1)}{Y_1^2}, \quad d_{16,1} = \frac{cpf_{t1}}{T_{g2}}, \\ d_{16,2} &= \frac{cpf_{t2}}{T_{g2}}, \quad d_{16,3} = \frac{cpf_{t3}}{T_{g2}}, \quad d_{16,4} = \frac{cpf_{t4}}{T_{g2}}, \quad d_{16,5} = \frac{cpf_{t5}}{T_{g2}}, \\ d_{16,6} &= \frac{cpf_{t6}}{T_{g2}}, \quad d_{19,1} = \frac{cpf_{h1}}{T_{RH2}}, \quad d_{19,2} = \frac{cpf_{h2}}{T_{RH2}}, \quad d_{19,3} = \frac{cpf_{h3}}{T_{RH2}}, \\ d_{19,4} &= \frac{cpf_{h4}}{T_{RH2}}, \quad d_{19,5} = \frac{cpf_{h5}}{T_{RH2}}, \quad d_{19,6} = \frac{cpf_{h6}}{T_{RH2}}, \quad d_{22,1} = \frac{a_2X_2cpf_{g1}}{b_2Y_2}, \\ d_{22,2} &= \frac{a_2X_2cpf_{g2}}{b_2Y_2}, \quad d_{22,3} = \frac{a_2X_2cpf_{g3}}{b_2Y_2}, \quad d_{22,4} = \frac{a_2X_2cpf_{g4}}{b_2Y_2}, \\ d_{22,5} &= \frac{a_2X_2cpf_{g5}}{b_2Y_2}, \quad d_{22,6} = \frac{a_2X_2cpf_{g6}}{b_2Y_2}, \quad d_{23,1} = \frac{cpf_{g1}(Y_2-X_2)}{Y_2^2}, \\ d_{23,2} &= \frac{cpf_{g2}(Y_2-X_2)}{Y_2^2}, \quad d_{23,3} = \frac{cpf_{g3}(Y_2-X_2)}{Y_2^2}, \\ d_{23,4} &= \frac{cpf_{g4}(Y_2-X_2)}{Y_2^2}, \quad d_{23,5} = \frac{cpf_{g5}(Y_2-X_2)}{Y_2^2}, \\ d_{23,6} &= \frac{cpf_{g6}(Y_2-X_2)}{Y_2^2}, \quad d_{24,1} = cpf_{41} + cpf_{51} + cpf_{61}, \\ d_{24,2} &= cpf_{42} + cpf_{52} + cpf_{62}, \quad d_{24,3} = cpf_{43} + cpf_{53} + cpf_{63}, \\ d_{24,4} &= -(cpf_{14} + cpf_{24} + cpf_{34}), \quad d_{24,5} = -(cpf_{15} + cpf_{25} + cpf_{35}), \\ d_{24,6} &= -(cpf_{16} + cpf_{26} + cpf_{36}), \quad d_{25,1} = \alpha_{12}(cpf_{41} + cpf_{51} + cpf_{61}), \\ d_{25,2} &= \alpha_{12}(cpf_{42} + cpf_{52} + cpf_{62}), \\ d_{25,3} &= \alpha_{12}(cpf_{43} + cpf_{53} + cpf_{63}), \\ d_{25,4} &= -\alpha_{12}(cpf_{14} + cpf_{24} + cpf_{34}), \\ d_{25,5} &= -\alpha_{12}(cpf_{15} + cpf_{25} + cpf_{35}), \\ d_{25,6} &= -\alpha_{12}(cpf_{16} + cpf_{26} + cpf_{36}). \end{aligned}$$

The output matrix C, the state cost weighting matrix Q and the control cost weighting matrix R for the multi-source restructured

power system model are taken identity matrices of 25×25 , 25×25 and 2×2 dimensions respectively.

Appendix B: System data

Thermal and multi-source thermal–hydro–gas restructured power systems [5,13,16]:

$P_{r1} = P_{r2} = 2000$ MW, $P_{tie_max} = 200$ MW, Base power = 2000 MVA, initial loading (ΔP_{Di}^0) = 50%, $f^0 = 60$ Hz, $\alpha_{12} = -1$,
 $D_i = 8.33 \times 10^{-3}$ pu MW/Hz, $H_i = 5$ MW s/MVA, $T_{gi} = 0.08$ s,
 $T_{ti} = 0.3$ s, $K_{ri} = 0.5$, $T_{ri} = 10$ s, $R_{hi} = R_{gi} = 2.4$ Hz/puMW,
 $K_{pi} = 120$ Hz/puMW, $T_{pi} = 20$ s, $B_i = \beta_i = 0.425$ pu MW/Hz,
 $T_{12} = 0.0866$ pu MW/rad, $\sigma = 0.04$, $\delta_{12} = 30^\circ$, $T_{RHi} = 48.7$ s,
 $T_{GHi} = 0.513$ s, $T_{Ri} = 5$ s, $T_{Wi} = 1$ s, $a_i = 1$, $b_i = 0.05$ s, $c_i = 1$, $X_i = 0.6$ s,
 $Y_i = 1$ s, $T_{CRi} = 0.01$ s, $T_{Fi} = 0.23$ s, $T_{CDi} = 0.2$ s, $K_{RFB} = 0.67$, $T_{RFB} = 0$ s,
 $T_{pi} = 2H/f^0 D_i$ s, $K_{pi} = 1/D_i$ pu MW/Hz,
 $D_i = \Delta P_{Di}^0 / f^0 P_{ri}$ pu MW/Hz, $\beta_i = D_i + 1/R_i$ pu MW/Hz.

Multi-source thermal–hydro power system [14]:

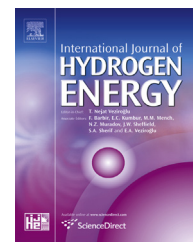
$P_{r1} = P_{r2} = 2000$ MW, $P_{tie_max} = 200$ MW, Base power = 2000 MVA, initial loading (ΔP_{Di}^0) = 50%, $f^0 = 60$ Hz, $\alpha_{12} = -1$, $T_{gi} = 0.08$ s,
 $T_{ti} = 0.3$ s, $R_{ti} = 2.0$ Hz/pu MW, $R_{hi} = 2.4$ Hz/pu MW,
 $K_{pi} = 100$ Hz/pu MW, $T_{pi} = 20$ s, $\beta_i = 0.425$ pu MW/Hz,
 $T_{12} = 0.0707$ pu MW/rad, $T_{RHi} = 48.7$ s, $T_{GHi} = 0.513$ s, $T_{Ri} = 5$ s,
 $T_{Wi} = 1$ s, $K_{RFB} = 0.67$, $T_{RFB} = 0$ s.

References

- [1] S.C. Tripathy, V. Bhardwaj, Automatic generation control of a small hydro-turbine driven generator, *Energy Convers. Manage.* 37 (11) (1996) 1635–1645.
- [2] V. Donde, M.A. Pai, I.A. Hiskens, Simulation and optimization in an AGC system after deregulation, *IEEE Trans. Power Syst.* 16 (3) (2001) 481–489.
- [3] S. Sinha, R. Patel, R. Prasad, Application of AI supported optimal controller for automatic generation control of a restructured power system with parallel AC-DC tie lines, *Eur. Trans. Electr. Power* 22 (5) (2012) 645–661.
- [4] C.K. Shiva, V. Mukherjee, A novel quasi-oppositional harmony search algorithm for AGC optimization of three-area multi-unit power system after deregulation, *Eng. Sci. Tech. Int. J.* (2015) doi:10.1016/j.jestech.2015.07.013.
- [5] I.A. Chidambaram, B. Paramasivam, Optimized load-frequency simulation in restructured power system with redox flow batteries and interline power flow controller, *Int. J. Electr. Power Energy Syst.* 50 (2013) 9–24.
- [6] Y.P. Verma, A. Kumar, Load frequency control in deregulated power system with wind integrated system using fuzzy controller, *Front. Energy* 7 (2) (2013) 245–254.
- [7] A. Demiroren, H.L. Zeynelgil, GA application to optimization of AGC in three-area power system after deregulation, *Int. J. Electr. Power Energy Syst.* 29 (3) (2007) 230–240.
- [8] M. Deepak, R.J. Abraham, Load following in a deregulated power system with Thyristor Controlled Series Compensator, *Int. J. Electr. Power Energy Syst.* 65 (2015) 136–145.
- [9] R.J. Abraham, D. Das, A. Patra, AGC system after deregulation considering TCPS in series with the tie-line, *Int. J. Emerging Electr. Power Syst.* 16 (3) (2015) 281–295.
- [10] Y. Arya, N. Kumar, Ibraheem, AGC of a two-area multi-source power system interconnected via AC/DC parallel links under restructured power environment, *Optim. Control Appl. Meth.* (2015) doi:10.1002/oca.2181.
- [11] Y. Arya, N. Kumar, AGC of a multi-area multi-source hydrothermal power system interconnected via AC/DC parallel links under deregulated environment, *Int. J. Electr. Power Energy Syst.* 75 (2016) 127–138.
- [12] Ibraheem, P. Kumar, N. Hasan, Y. Singh, Optimal automatic generation control of interconnected power system with asynchronous tie-lines under deregulated environment, *Elect. Power Compon. Syst.* 40 (10) (2012) 1208–1228.
- [13] M.L. Kothari, J. Nanda, Application of optimal control strategy to automatic generation control of a hydrothermal system, *IEEE Proc. Control Theory Appl.* 135 (4D) (1988) 268–274.
- [14] R.K. Sahu, S. Panda, S. Padhan, A hybrid firefly algorithm and pattern search technique for automatic generation control of multi area power systems, *Int. J. Electr. Power Energy Syst.* 64 (2015) 9–23.
- [15] K.P.S. Parmar, S. Majhi, D.P. Kothari, LFC of an interconnected power system with multi-source power generation in deregulated power environment, *Int. J. Electr. Power Energy Syst.* 57 (2014) 277–286.
- [16] P.C. Pradhan, R.K. Sahu, S. Panda, Firefly algorithm optimized fuzzy PID controller for AGC of multi-area multi-source power systems with UPFC and SMES, *Eng. Sci. Tech. Int. J.* (2015) doi:10.1016/j.jestech.2015.08.007.
- [17] R.K. Sahu, T.S. Gorripotu, S. Panda, Automatic generation control of multi-area power systems with diverse energy sources using teaching learning based optimization algorithm, *Eng. Sci. Tech. Int. J.* (2015) doi:10.1016/j.jestech.2015.07.011.
- [18] Ibraheem, P. Kumar, D.P. Kothari, Recent philosophies of automatic generation control strategies in power systems, *IEEE Trans. Power Syst.* 20 (1) (2005) 346–357.
- [19] S.K. Pandey, S.R. Mohanty, N. Kishor, A literature survey on load-frequency control for conventional and distribution generation power systems, *Renew. Sustain. Energy Rev.* 25 (2013) 318–334.
- [20] M.M.T. Ansari, S. Velusami, DMLHFLC (Dual mode linguistic hedge fuzzy logic controller) for an isolated wind-diesel hybrid power system with BES (battery energy storage) unit, *Energy* 35 (9) (2010) 3827–3837.
- [21] S.K. Aditya, D. Das, Application of battery energy storage system to load frequency control of an isolated power system, *Int. J. Energy Res.* 23 (3) (1999) 247–258.
- [22] S.K. Aditya, D. Das, Load frequency control of an interconnected hydro-thermal power system with new area control error considering battery energy storage facility, *Int. J. Energy Res.* 24 (6) (2000) 525–538.
- [23] K. Chatterjee, Effect of battery energy storage system on load frequency control under deregulation, *Int. J. Emerging Electr. Power Syst.* 12 (3.2) (2011) 1–25.
- [24] T.S. Gorripotu, R.K. Sahu, S. Panda, AGC of a multi-area power system under deregulated environment using redox flow batteries and interline power flow controller, *Eng. Sci. Tech. Int. J.* 18 (4) (2015) 555–578.
- [25] E. Kazuhiro, S. Tetsuo, S. Toshio, D. Hiroshige, Evaluation study about redox flow battery response and its modeling, *IEEE Trans. Power Energy* 122 (4) (2002) 554–560.
- [26] T. Sasaki, T. Kadoya, K. Enomoto, Study on load frequency control using redox flow batteries, *IEEE Trans. Power Syst.* 19 (1) (2004) 660–667.
- [27] I.A. Chidambaram, B. Paramasivam, Control performance standards based load-frequency controller considering redox flow batteries coordinate with interline power flow controller, *J. Power Sources* 219 (2012) 292–304.
- [28] B. Paramasivam, I.A. Chidambaram, ABC algorithm based load-frequency controller for an interconnected power system considering nonlinearities and coordinated with UPFC and RFB, *Int. J. Eng. Innovat. Tech.* 1 (3) (2012) 1–11.
- [29] R. Francis, I.A. Chidambaram, Optimized PI+ load-frequency controller using BWNN approach for an interconnected reheat power system with RFB and hydrogen electrolyser units, *Int. J. Electr. Power Energy Syst.* 67 (2015) 381–392.
- [30] M.R. Mohamed, P.K. Leung, M.H. Sulaiman, Performance characterization of a vanadium redox flow battery at different operating parameters under a standardized test-bed system, *Appl. Energy* 137 (2015) 402–412.
- [31] C.P. de Leon, A. Frías-Ferrer, J. Gonzalez-García, D.A. Szanto, F.C. Walsh, Redox flow cells for energy conversion, *J. Power Sources* 160 (1) (2006) 716–732.
- [32] G. Kear, A.A. Shah, F.C. Walsh, Development of the all-vanadium redox flow battery for energy storage: a review of technological, financial and policy aspects, *Int. J. Energy Res.* 36 (11) (2012) 1105–1120.

Available online at www.sciencedirect.com

ScienceDirect

journal homepage: www.elsevier.com/locate/he

Oxygen anion diffusion in double perovskite $\text{GdBaCo}_2\text{O}_{5+\delta}$ and $\text{LnBa}_{0.5}\text{Sr}_{0.5}\text{Co}_{2-x}\text{Fe}_x\text{O}_{5+\delta}$ ($\text{Ln} = \text{Gd}, \text{Pr}, \text{Nd}$) electrodes

Uzma Anjum^a, Saumye Vashishtha^b, Manish Agarwal^c, Pankaj Tiwari^a,
Nishant Sinha^d, Ankit Agrawal^e, S. Basu^a, M. Ali Haider^{a,*}

^a Department of Chemical Engineering, Indian Institute of Technology Delhi, New Delhi 110016, India

^b Department of Applied Chemistry and Polymer Technology, Delhi Technological University (DTU), New Delhi 110042, India

^c Computer Services Centre, Indian Institute of Technology Delhi, New Delhi 110016, India

^d Dassault Systemes, Galleria Commercial Tower, 23 Old Airport Road, Bangalore 560008, India

^e Department of Chemical Engineering, Indian Institute of Technology Kharagpur, West Bengal 721302, India

ARTICLE INFO

Article history:

Received 15 September 2015

Received in revised form

23 January 2016

Accepted 18 February 2016

Available online xxx

Keywords:

Molecular dynamics

Solid oxide fuel cell

Diffusion coefficient

Oxygen reduction

Electrochemical performance

Peak power density

ABSTRACT

Simulations utilizing molecular dynamics (MD) were applied to study the anisotropic diffusion in the a – b plane of double perovskite structure, $\text{GdBaCo}_2\text{O}_{5.5}$ ($\text{GBCO}_{5.5}$). Diffusion coefficient of $\text{GBCO}_{5.5}$ was calculated to be $5 \times 10^{-8} \text{ cm}^2 \text{ s}^{-1}$ at 873 K. The calculated diffusion coefficient was observed to increase on increasing temperature with an activation energy of 50.8 kJ/mol. Similar MD simulations were employed to study the effect of the level of Fe doping at the B-site of the co-doped $\text{GdBa}_{0.5}\text{Sr}_{0.5}\text{Co}_{2-x}\text{Fe}_x\text{O}_{5+\delta}$. In the co-doped structure, increasing diffusion was observed on increasing the Fe doping to $x = 1$ ($D = 7.5 \times 10^{-8} \text{ cm}^2 \text{ s}^{-1}$ at 923 K). This was contrary to the Pr or Nd based co-doped materials, $\text{LnBa}_{1-y}\text{Sr}_y\text{Co}_{2-x}\text{Fe}_x\text{O}_{5+\delta}$ ($\text{Ln} = \text{Pr}, \text{Nd}$), where maximum diffusion was calculated for Fe doping level at $x = 0.5$ ($D = 5.16 \times 10^{-8} \text{ cm}^2 \text{ s}^{-1}$ for $\text{Ln} = \text{Pr}$ and $D = 1.18 \times 10^{-7} \text{ cm}^2 \text{ s}^{-1}$ for $\text{Ln} = \text{Nd}$ at 873 K). The trend in diffusivity correlates well with the trends in the measured peak power density of a solid oxide fuel cell fabricated with these electrode materials.

Copyright © 2016, Hydrogen Energy Publications, LLC. Published by Elsevier Ltd. All rights reserved.

Introduction

Solid Oxide Fuel cell (SOFC) technology has a promising case for efficient conversion of chemical energy into electrical energy, with a prospect to achieve sustainability, in terms of fuel flexibility [1]. In general, SOFCs are operated at high temperatures (>973 K) where the applied materials are required to be stable

and non-reactive with a desirable thermal expansion coefficient (TEC) match between the components [2,3]. These conditions offer a limited choice in materials development. Thus, it is imperative to reduce the operating temperature to an intermediate (773–973 K) or even to a lower (<773 K) regime [4], which constitute the state of the art research. While operating a SOFC at an intermediate temperature [5], significant increase in the

* Corresponding author. Tel.: +91 11 2659 1016; fax: +91 11 2658 2037.

E-mail address: haider@iitd.ac.in (M.A. Haider).

<http://dx.doi.org/10.1016/j.ijhydene.2016.02.090>

0360-3199/ Copyright © 2016, Hydrogen Energy Publications, LLC. Published by Elsevier Ltd. All rights reserved.

activation losses at the oxygen electrode is observed, which is ascribed to the sluggish oxygen reduction reaction (ORR) [6]. The ORR kinetics and transport of oxygen anions can be significantly improved by a thoughtful design of novel electrode materials [7], which are suitable for intermediate temperature operations [8–10]. In this attempt, an interest is shown in synthesizing compounds with a layered perovskite structure such as double perovskite ($AA'BO_{5+\delta}$, where $A = \text{La, Pr, Nd, Sm, Gd}$; $A' = \text{Ba, B = Co}$, and $0 < \delta < 1$) materials to be employed as cathode in a SOFC [11,12]. As compared to the simple perovskite structure ($\text{La}_{1-x}\text{Sr}_x\text{Co}_{1-y}\text{Fe}_y\text{O}_{3-\delta}$ and $\text{La}_{1-x}\text{Sr}_x\text{MnO}_{3-\delta}$) [13] anisotropy of oxygen diffusion in layered perovskite structure facilitates enhanced oxygen transport and surface exchange, resulting in better electrochemical performance [11,14]. For example, the double perovskite material, $\text{GdBaCo}_2\text{O}_{5+\delta}$ (GBCO, Fig. 1) shows relatively fast oxygen diffusion ($D = 10^{-9} \text{ cm}^2 \text{ s}^{-1}$ at 973 K) and low activation energy of 58 kJ/mol [15] as compared to the commonly utilized mixed ion-electron conducting [16] $\text{La}_{1-x}\text{Sr}_x\text{Co}_{1-y}\text{Fe}_y\text{O}_{3-\delta}$ ($D = 10^{-10} \text{ cm}^2 \text{ s}^{-1}$ at 973 K and $E_a = 104 \text{ kJ/mol}$) electrode [17]. The layered structure of GBCO shows the stacking order, [Gd–O] [Co–O] [Ba–O] [18,19] along the c-axis in which the majority of oxygen vacancies are observed to be confined in the Gd plane as shown in Fig. 1. The presence of cation ordering in the structure was ascribed to improve oxygen transport relative to the disordered structure [20]. In addition, GBCO shows no reactivity at the sintering temperatures ($>1173 \text{ K}$) and TEC ($\sim 16 \times 10^{-6} \text{ K}^{-1}$) match with commonly utilized $\text{Ce}_{0.9}\text{Gd}_{0.1}\text{O}_{1.95}$ (TEC = $8.6 \times 10^{-6} \text{ K}^{-1}$) electrolyte [21]. The area specific resistance (ASR, $0.25 \Omega \text{ cm}^2$ at 898 K) of the electrode was measured to be significantly low when tested in a symmetric cell arrangement [15]. Due to these aforementioned properties, GBCO has been proposed as a candidate material for cathode in an IT-SOFC.

In a breakthrough attempt in designing cathode materials for enhanced oxygen anion transport, Liu and co-workers have recently reported a double perovskite structure material of composition $\text{PrBa}_{0.5}\text{Sr}_{0.5}\text{Co}_{2-x}\text{Fe}_x\text{O}_{5+\delta}$ (PBSCFO) as the highly efficient and robust cathode. Test cells having cathode made up of PBSCFO were measured to achieve a peak power density of about 2200 mW cm^{-2} at 873 K [22]. Enhanced electrocatalytic activity was attributed to the formation of unique pore channels in PBSCFO structure providing low energy pathways for faster oxygen anion transport. In our previous work we have calculated the diffusion coefficient of the $\text{PrBa}_{0.5}\text{Sr}_{0.5}\text{Co}_{1.5}\text{Fe}_{0.5}\text{O}_{5.5}$ (PBSCFO_{5.5}) by molecular dynamics simulations and indeed observed it to be significantly higher ($D = 1.18 \times 10^{-7} \text{ cm}^2 \text{ s}^{-1}$ at 873 K) than that of $\text{PrBaCo}_2\text{O}_{5.5}$ (PBCO_{5.5}) ($D = 3 \times 10^{-8} \text{ cm}^2 \text{ s}^{-1}$) [23]. High diffusivity of oxygen anions in PBSCFO_{5.5} could be a combined synergistic effect of co-doping Sr and Fe at A' and B-site respectively, which can be partially attributed to the improved electrochemical performance. Effect of Sr doping at the A-site of co-doped perovskite materials have been studied in the past, where Sr doping is attributed to the improvement in electronic conductivity and oxygen anion diffusion [24–26]. For example in case of $\text{La}_{1-x}\text{Sr}_x\text{Mn}_{0.8}\text{Co}_{0.2}\text{O}_{3-\delta}$ the diffusivity of the material was observed to increase ($D = 10^{-12} \text{ cm}^2 \text{ s}^{-1}$ at 1423 K for $x = 0.2$) on increasing the Sr doping levels to 50% ($D = 10^{-11} \text{ cm}^2 \text{ s}^{-1}$ at 1173 K for $x = 0.5$) [27,28]. However, the role of Fe doping in the co-doped materials remains unclear. Fe is suggested to improve the TEC match, sintering property and stability of the electrode [22]. Our previous results suggest an increase in the diffusivity of PBSCFO_{5.5} ($D = 1.18 \times 10^{-7} \text{ cm}^2 \text{ s}^{-1}$) as compared to the $\text{PrBa}_{0.5}\text{Sr}_{0.5}\text{Co}_2\text{O}_{5.5}$ (PBSCO_{5.5}) ($D = 8.33 \times 10^{-8} \text{ cm}^2 \text{ s}^{-1}$) calculated at 873 K. However, from the past studies a decreasing trend in oxygen diffusivity was observed with

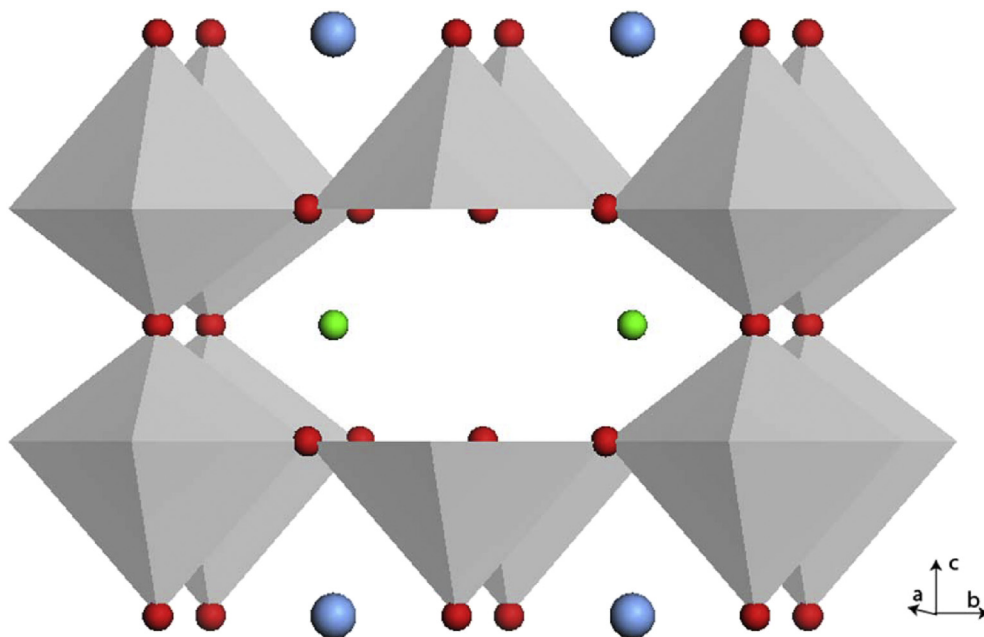


Fig. 1 – Polyhedral representation of tetragonal $\text{GBCO}_{5.5}$ with space group $P4/mmm$. Cobalt ions are present in pyramid (CoO_5) and octahedra (CoO_6), gadolinium atoms are shown in green, oxygen atoms in red and barium atoms are represented by blue colour respectively. Vacancies are present in a–b plane [15]. (For interpretation of the references to colour in this figure legend, the reader is referred to the web version of this article.)

increasing Fe-substitution. The diffusion co-efficient of $\text{La}_{0.6}\text{Sr}_{0.4}\text{Co}_{1-x}\text{Fe}_x\text{O}_{3-\delta}$ was measured to decrease from $2.15 \times 10^{-8} \text{ cm}^2 \text{ s}^{-1}$ ($x = 0$) [29] to $5 \times 10^{-9} \text{ cm}^2 \text{ s}^{-1}$ ($x = 0.8$) at $\sim 973 \text{ K}$ on increasing the Fe doping [17].

In the co-doped double perovskite structured materials an interesting trend in electrochemical performance was observed, wherein an optimum amount of Fe doping in the layered structure led to a better performance of the fuel cell. For example, in $\text{GdBa}_{0.5}\text{Sr}_{0.5}\text{Co}_{2-x}\text{Fe}_x\text{O}_{5+\delta}$ (GBSCFO), iron doping up to 50% ($x = 1$) leading to the formation of the structure $\text{GdBa}_{0.5}\text{Sr}_{0.5}\text{CoFeO}_{5+\delta}$ (GBSCFO50), has been reported to provide maximum electrochemical performance measured in terms of peak power density value of 1310 mW cm^{-2} as compared to the un-doped $\text{GdBa}_{0.5}\text{Sr}_{0.5}\text{Co}_2\text{O}_{5+\delta}$ (GBSCO) and 25% Fe doped, $\text{GdBa}_{0.5}\text{Sr}_{0.5}\text{Co}_{1.5}\text{Fe}_{0.5}\text{O}_{5+\delta}$ (GBSCFO25). In contrast, in case of PBSCFO, maximum electrochemical performance of a SOFC was measured for electrodes fabricated with 25% iron doped structure $\text{PrBa}_{0.5}\text{Sr}_{0.5}\text{Co}_{1.5}\text{Fe}_{0.5}\text{O}_{5+\delta}$ (PBSCFO25) as compared to the un-doped $\text{PrBa}_{0.5}\text{Sr}_{0.5}\text{Co}_2\text{O}_{5+\delta}$ (PBSCO) and 50% iron doped $\text{PrBa}_{0.5}\text{Sr}_{0.5}\text{CoFeO}_{5+\delta}$ (PBSCFO50) [22]. Similar trends have been reported for a co-doped cathode containing Nd ions at A-site. These experiments highlight an important role of achieving an optimum level of Fe substitution, which should be studied in detail to obtain the desired electro-catalytic activity.

The electrochemical performance of an electrode or a SOFC, depends on several factors such as fabrication techniques, composition, impurities and properties of other components of the cell. However, the trend in measured electrochemical performance of the double perovskite structured electrode on increasing Fe doping can be partially explained by the trend in calculated diffusivity of the respective structure, assuming that the diffusion is either co-limiting or dominating as the operating mechanism [30]. Most of the aforementioned experimental observations could possibly be explained by conducting a systematic study ascertaining the effect of the levels of Fe doping on the transport of oxygen anions. In this work, molecular dynamic simulations are utilized to calculate the diffusion coefficient of $\text{GdBaCo}_2\text{O}_{5.5}$ (GBCO_{5.5}). The results are compared to the previous experimental and theoretical studies [15,31]. Once the efficacy of the method is established, the effect of Fe doping on co-doped $\text{LnBr}_{1-y}\text{Sr}_y\text{Co}_{2-x}\text{Fe}_x\text{O}_{5.5}$ ($\text{Ln} = \text{Gd, Nd, Pr}$) material is discussed by calculating oxygen anion diffusivities in the respective structures. The results thus obtained provide an insight into establishing a role of Fe on oxygen anion transport in the co-doped double perovskite structured materials.

Methodology

In order to study the oxygen transport properties of the double perovskite materials, MD simulations were performed using Forcite module of Material Studio 8.0 (Biovia, San Diego, USA). Interactions between ions were described by means of long range coulombic interactions calculated using Ewald summation [32] and a short range Buckingham pair potential [33]. The formal charges value of +2, +3, +3, +3, +2 and -2 were used for Ba, Ln (Pr, Gd, Nd), Co, Fe, Sr and O respectively

[34–36]. The Buckingham potential values can be described by the following equation:

$$Q_{ij}(r) = A_{ij} \exp\left(\frac{-r}{\rho_{ij}}\right) - \frac{C_{ij}}{r^6} \quad (1)$$

where r is the distance between the specified atom pair, and A_{ij} , ρ_{ij} and C_{ij} are the potential parameters for ion pairs whose values were taken from previous studies and are listed in Table 1.

Simulations for oxygen diffusion were carried out for supercell box comprising of 304 atoms (i.e. $4 \times 4 \times 2$ unit cell) under periodic boundary conditions. The choice of super cell is based on a similar molecular dynamics study [31]. The oxygen stoichiometry value was fixed at 5.5 per formula unit for the entire temperature range, which amounted to 16 vacancies per structure. In all simulations oxygen content was fixed at $\delta = 0.5$ for the entire temperature range which is taken similar to the previous MD simulations studies, having an associated advantage of charge neutrality of the corresponding perovskite crystal [1,31]. The structural parameters such as space group, fractional co-ordinates and lattice parameters were taken from existing literature data and are included in Table 2.

Prior to the simulations, structures were geometrically optimized through an iterative process to achieve the minimum energy arrangement of atoms in the perovskite crystal, until the potential energy and forces converged to a pre specified criteria of 42 J/mol and 21 J/mol/Å respectively. Subsequently, perovskites were first subjected through an equilibration process at all temperatures using isobaric-isothermal (NPT) ensemble [37] for a duration of 10 ps. A time step of 1 fs was specified using Nosé-Hoover thermostat [37,38], with a Q-ratio of 0.01 and Berendsen barostat [39], having a decay constant of 0.1 ps for achieving desired control of temperature and pressure. Next run at constant volume (NVT) ensemble was conducted for 10,000 time steps (10 ps) to calculate equilibrium lattice parameters. With the specified set of potential values, all the perovskites were able to retain their structural symmetry. The resulting lattice parameters were found to be in good agreement with experimentally determined values. Diffusion data of oxygen ions was collected from mean square displacement (MSD) curves obtained from the simulation run of 100 ps using a NVT ensemble with the Nosé-Hoover Thermostat. A similar study by Seymour et al. have reported the duration of 100 ps to be sufficient and reliable in calculating oxygen anion diffusivity in such materials [1]. However, in order to ascertain the effect

Table 1 – Interatomic paired Buckingham potentials value used for MD simulations.

Ion pair	A (eV)	ρ (Å)	C (eV Å ⁶)	Reference
Gd ⁺³ –O ^{2–}	1885.75	0.3399	20.34	[31]
Co ⁺³ –O ^{2–}	1226	0.3087	0	[31]
Fe ⁺³ –O ^{2–}	1156.36	0.3299	0	[34]
Ba ⁺² –O ^{2–}	905.7	0.3976	0	[31]
Sr ⁺² –O ^{2–}	1950.86	0.3252	0	[54]
O ^{2–} –O ^{2–}	9547.96	0.2192	32	[31]
Nd ⁺³ –O ^{2–}	1995.19	0.3430	22.589	[55]
Pr ⁺³ –O ^{2–}	2049.95	0.3438	23.88	[1]

Table 2 – Space group, lattice parameter, and fractional co-ordinate of the corresponding double perovskite structured electrode materials.

Material composition	a (Å)	b (Å)	c (Å)	Space group	Reference
GdBaCo ₂ O _{5+δ}	3.92	3.92	7.51	P4/mmm	[56]
GdBa _{0.5} Sr _{0.5} Co ₂ O _{5+δ}	3.8624	3.8624	7.5578	P4/mmm	[48]
GdBa _{0.5} Sr _{0.5} Co _{1.5} Fe _{0.5} O _{5+δ}	3.8694	3.8694	7.5936	P4/mmm	[48]
GdBa _{0.5} Sr _{0.5} CoFeO _{5+δ}	3.8710	3.8710	7.6368	P4/mmm	[48]
PrBa _{0.5} Sr _{0.5} Co ₂ O _{5+δ}	3.869	3.869	7.732	P4/mmm	[22]
PrBa _{0.5} Sr _{0.5} Co _{1.5} Fe _{0.5} O _{5+δ}	3.871	3.871	7.757	P4/mmm	[22]
PrBa _{0.5} Sr _{0.5} CoFeO _{5+δ}	3.875	3.875	7.767	P4/mmm	[22]
NdBa _{0.5} Sr _{0.5} Co ₂ O _{5+δ}	3.846	3.846	7.699	P4/mmm	[22]
NdBa _{0.5} Sr _{0.5} Co _{1.5} Fe _{0.5} O _{5+δ}	3.849	3.849	7.709	P4/mmm	[22]
NdBa _{0.5} Sr _{0.5} CoFeO _{5+δ}	3.864	3.864	7.718	P4/mmm	[22]

of simulation time, a longer duration simulation of 5000 ps at 1173 K was performed to calculate the diffusivity in GBCO_{5.5}. The MSD curve for 5000 ps simulation is shown in Fig. S1(a). The oxygen anion diffusivity was calculated in time interval of 500 ps and is reported in Table S1. The standard error of the mean for the 5000 ps long range simulation was calculated to be <10%. The average oxygen anion diffusivity value was estimated to be $2.47 \pm 0.216 \times 10^{-7} \text{ cm}^2 \text{ s}^{-1}$ at 1173 K, which is similar to the one calculated for 100 ps ($D = 2.82 \times 10^{-7} \text{ cm}^2 \text{ s}^{-1}$ at 1173 K). In general, the standard deviation error for the reported calculations was observed to be more pronounced at low temperatures (10–20% at 873 K) as compared to high temperature calculations (<10% at $T > 1173 \text{ K}$). In order to be consistent with the short-duration (100 ps) simulation the long duration (5000 ps) simulation was truncated at 40 ps. The corresponding MSD plots are shown in Fig. S1(b), where negligible difference was observed between the two simulations. Thus the diffusion coefficient from the truncated plot of long duration simulation was calculated to be $D = 2.72 \times 10^{-7} \text{ cm}^2 \text{ s}^{-1}$ at 1173 K which compares well with the short duration value. Therefore the simulations for a period of 100 ps can be considered reliable enough to calculate the diffusivity and predicting the trends in diffusion coefficient on altering the composition of a double perovskite electrode. Visual molecular dynamics (VMD1.9.2) was used to visualize oxygen density profile. With respect to the anionic position $r_i(t)$, compared to its initial position $r_i(0)$, MSD is given by the following equation:

$$\langle r_i^2(t) \rangle = \frac{1}{N} \sum_{i=1}^N [r_i(t) - r_i(0)]^2 \quad (2)$$

The oxygen diffusivity was estimated from the slope of the MSD curve fitted in the linear region taken upto 40 ps and given by the following equation:

$$\langle r_i^2(t) \rangle = 6Dt + B \quad (3)$$

where D is the diffusion co-efficient, and B is the parameter corresponding to the thermal vibrations in a crystal.

Results and discussion

Oxygen transport properties for the double perovskite materials were calculated using time dependent MSD data over a

temperature range of 873–1273 K. Previous studies have indicated a high temperature phase transition in GBCO perovskite from an orthorhombic ($Pmmm$) to a tetragonal symmetry ($P4/mmm$) at temperatures around 800 K which is accompanied by a rearrangement of oxygen anion vacancies in the perovskite lattice [11]. The tetragonal GBCO has been reported to show improved stability in terms of electrochemical and structural properties without the presence of undesirable phases, over the working range of SOFC's at temperatures above 800 K [11,40]. Therefore, a tetragonal symmetry for GBCO is employed in all simulations. Fig. 2(a) shows the MSD curve for GBCO_{5.5} as obtained from the MD simulations at 873 K along the a – b and c directions. Consistent with the previously reported theoretical and experimental observations on these layered anisotropic oxides [9], oxygen diffusion at 873 K was calculated to be higher in the a – b plane ($D = 5 \times 10^{-8} \text{ cm}^2 \text{ s}^{-1}$) by an order of magnitude as compared to the diffusion along the c -axis ($D = 3.33 \times 10^{-9} \text{ cm}^2 \text{ s}^{-1}$) as shown in Fig. 2(a). Therefore, in the following discussion the diffusion in the a – b plane is considered to be preferential and the diffusion along the c -axis is considered to be negligible. During the MD simulation, all instances of diffusion were observed primarily in the a – b plane. Thus, any other pathway or mechanism of oxygen anion diffusion is not considered. The diffusion was observed to be thermally activated which increased with increasing temperatures.

In all the materials studied the linear regression (R-squared) fits of diffusivities calculated at different temperatures follow an Arrhenius law with a R^2 value > 0.9 , which can be considered reasonably good to assume a thermally activated diffusion. Fig. 2(b) shows this preferential diffusion at different temperatures in the operating range of a SOFC (873 K–1273 K). Experimentally, diffusion coefficient has been measured for GBCO by $^{18}\text{O}/^{16}\text{O}$ by isotope exchange depth profile (IEDP) method. The diffusion coefficient was estimated to be $4.8 \times 10^{-10} \text{ cm}^2 \text{ s}^{-1}$ at 848 K [15]. In another experimental study, erroneously high diffusivity of the order of $1.36 \times 10^{-5} \text{ cm}^2 \text{ s}^{-1}$ is reported at 873 K for GBCO [41]. The discrepancy, in the measurement of the diffusion coefficient by experimental methods could lie in the incorrect determination of oxygen content with respect to the measured oxygen partial pressures. Furthermore, unreliability in the simultaneous measurements of chemical diffusivity and surface exchange is reported in conductivity relaxation experiments [42]. In contrast, MD simulations may provide a more accurate calculation of the

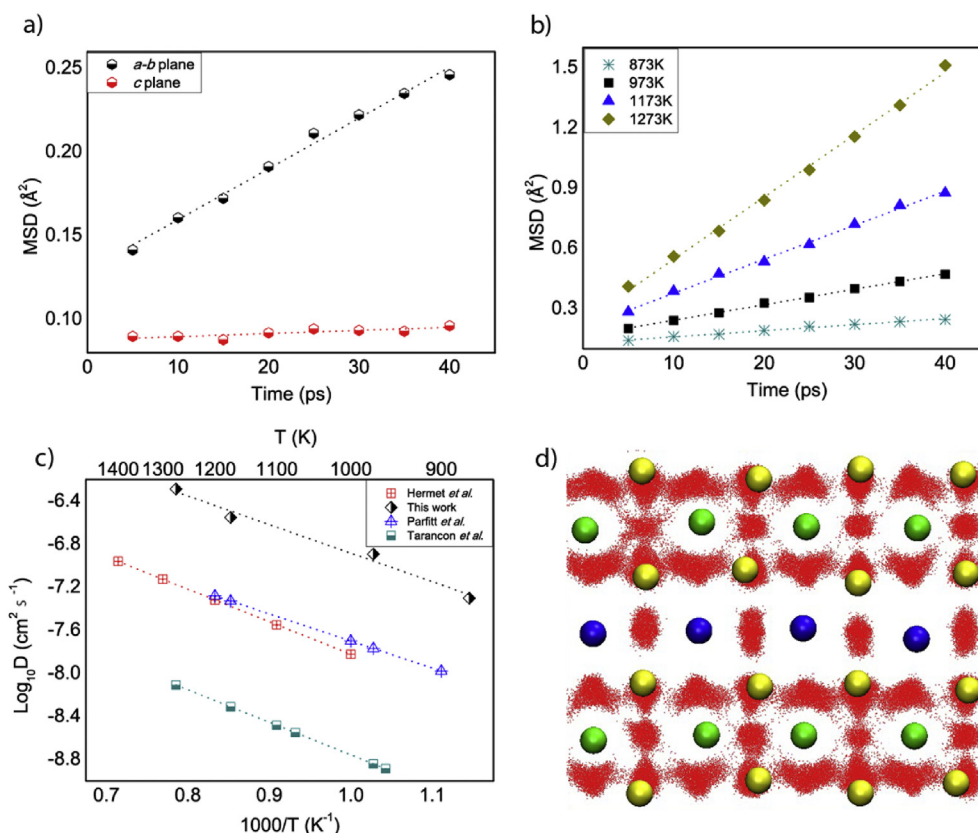


Fig. 2 – a) MSD curve for diffusion in a – b plane versus the c -axis calculated at 873 K, b) MSD plots for diffusion in a – b plane for the temperature range of 873–1273 K c) corresponding Arrhenius plot of GBCO_{5.5} and its comparison to the experimental and theoretical study [15,31] and d) oxygen density plot representing diffusion at 1173 K, wherein cobalt, barium and gadolinium atoms are shown in yellow, blue and green respectively. (For interpretation of the references to colour in this figure legend, the reader is referred to the web version of this article.)

diffusion coefficient on a variety of structures, including simple perovskites ($\text{La}_{1-x}\text{Sr}_x\text{Co}_{1-y}\text{Fe}_y\text{O}_{3-\delta}$, $\text{La}_{1-x}\text{Sr}_x\text{MnO}_{3-\delta}$, and $\text{Ba}_{1-x}\text{Sr}_x\text{Co}_{1-y}\text{Fe}_y\text{O}_{3-\delta}$) [34,36,43] and layered perovskites (PBCO, GBCO) [1,13]. However, the computational method is limited only to the simulation of fixed oxygen content ($\delta = 0.5$) in the double perovskite structure. Considering these limitations in both experimental and theoretical methods of calculating the diffusion coefficient, we may consider the theoretically calculated value of diffusivity of GBCO at 873 K to be accurate enough and comparable to the experimental value. Previous theoretical study utilizing MD simulation, have reported diffusivity values for GBCO at temperatures above 1000 K [31] which cannot be compared accurately. The calculated value for the diffusion coefficient thus obtained can be taken as a basis to apply the same simulation method in understanding the changes in diffusivity on applying various doping in the structure of the GBCO double perovskite.

MD simulations further confirm the presence of ordering in Gd and Ba ions into consecutive layers within the lattice. These observations are in agreement with the experimentally reported crystallographic data [20]. The ordering has been observed to exert a key influence on the arrangement of oxygen vacancies and hence on the overall oxygen migration process, allowing for a preferential diffusion to take place

along the a – b plane [44,45]. In simulations, oxygen transport process was observed to follow the Arrhenius law, with an activation energy value of 50.2 kJ/mol, Fig. 2(c). This value was found to be in reasonable agreement with the experimentally reported value of 63.7 kJ/mol by Tarancon et al. [15].

MD simulation technique is well suited for providing insight into oxygen diffusion mechanism [36,46]. Fig. 2(d) shows oxygen density plots for a portion of the whole system at 1173 K after integration over a simulation time of 5000 ps. This view shows diffusion process primarily taking place through the oxygen atoms in the Co–O plane through vacancy sites in Gd–O plane, consistent with the results of previous experimental and theoretical studies [11,31]. The anisotropic diffusion is clearly observed from the fact that oxygen atoms in Ba–O plane remain confined, and primarily oscillating about their equilibrium positions, taking no part in the diffusion process. The oxygen trajectories across Co–O and Gd–O planes were found to be connected to a certain extent. Oxygen atoms from cobalt plane were actively observed to make jumps to neighbouring Gd–O plane, undergoing back and forth motion and even crossing the Gd plane in the overall migration process. These observations suggest active involvement of Gd-plane vacancies as real pathways in oxygen diffusion (Table 3).

Table 3 – Calculated diffusion coefficient of GBCO from MSD curve and its comparison to the experimentally measured value.

Material composition	Diffusion coefficient ($\text{cm}^2 \text{s}^{-1}$)	Temperature (K)	Activation energy (kJ/mol)	Reference
GBCO _{5.5}	5.00×10^{-8}	873	50.8	This work
GBCO	6.63×10^{-10}	873	63.7	IEDP experiment [15]

Variation of Fe doping level in co-doped cubic perovskite has been suggested to play an important role in determining the electro catalytic activity. A sharp decrease in the value of oxygen permeability and a corresponding increase in ASR values were observed by Chen et al. for $\text{Ba}_{0.5}\text{Sr}_{0.5}\text{Co}_{1-x}\text{Fe}_x\text{O}_{3-\delta}$ (BSCFO) on increasing iron content [47]. The polarization resistance was measured to be $0.085 \Omega \text{cm}^2$ corresponding to 20% Fe doped BSCFO structure, which was observed to increase to $0.613 \Omega \text{cm}^2$ on 100% Co replacement by Fe [47]. In contrast, for the co-doped GBSCFO structures, lowest ASR value of $0.067 \Omega \text{cm}^2$ was reported for 50% Fe doped GBSCFO50 as compared to the un-doped GBSCO and 25% Fe doped GBSCFO25 [48]. MD simulations were therefore performed to understand the effect of Fe doping level on the diffusivity of the GBSCFO structure, which may in turn explain the trends in the measured polarization resistances. Fig. 3(a–c), show the calculated oxygen displacement profile in the co-doped perovskites with levels of Fe concentrations ranging from $x = 0$, $x = 0.5$ to $x = 1$. The corresponding activation energies were calculated

from the Arrhenius plots, shown in Fig. 3(d). In case of $\text{GdBa}_{0.5}\text{Sr}_{0.5}\text{Co}_{2-x}\text{Fe}_x\text{O}_{5.5}$ (GBSCFO), oxygen diffusivity linearly increases on increasing the doping levels of iron at the B-site, with the maximum value of oxygen diffusion coefficient calculated to be $7.5 \times 10^{-8} \text{cm}^2 \text{s}^{-1}$ at 923 K for 50% Fe doping. For comparison, the diffusion coefficient of GBSCO and GBSCFO25 is reported in Table 4. The enhancement in diffusivity with Fe doping can be partially attributed to increasing cell volumes of the co-doped perovskite (at $x = 0.0$, $V = 112.74 \text{Å}^3$; $x = 0.5$, $V = 113.69 \text{Å}^3$; $x = 1.0$, $V = 114.43 \text{Å}^3$), in order to accommodate the larger Fe ions below the solubility limit, which allows for a greater mobility of oxygen ions within the lattice space. However, the effect can-not be directly correlated, as the calculated expansion in the cell volume is lesser than 2%, while the diffusivity was calculated to increase by 87%. Interestingly, the electro-chemical performance, measured in terms of peak power densities were observed to follow a similar trend, which increases from 1600mW cm^{-2} to 2000mW cm^{-2} [48] on changing the iron content from $x = 0.0$ to 1.0 at 923 K as

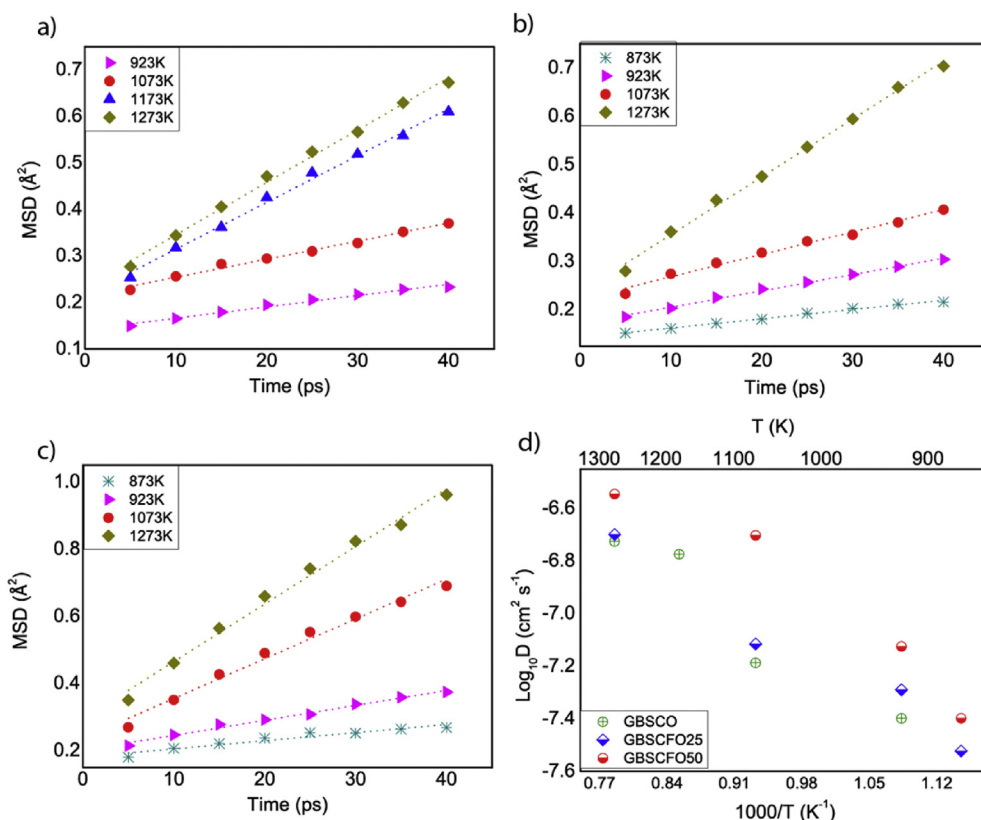
**Fig. 3 – MSD plots of a) GBCO, b) GBSCFO25 (adapted from Ref. [23]), c) GBSCFO50 and d) corresponding Arrhenius plot for a temperature range of 873–1273 K.**

Table 4 – Diffusion coefficient calculated from MD simulations of $\text{LnBa}_{0.5}\text{Sr}_{0.5}\text{Co}_{2-x}\text{Fe}_x\text{O}_{5+\delta}$ ($\text{Ln} = \text{Gd, Pr, Nd}$) materials at the reported temperatures. For correlation purpose, peak power density of a SOFC fabricated with the respective electrode material measured at the same temperature is shown.

Material composition	Diffusion coefficient ($\text{cm}^2 \text{s}^{-1}$)	Temperature (K)	Peak power density (mW cm^{-2})	Activation energy (kJ/mol)
$\text{GdBa}_{0.5}\text{Sr}_{0.5}\text{Co}_2\text{O}_{5+\delta}$	4×10^{-8}	923	1600 [48]	47.2
$\text{GdBa}_{0.5}\text{Sr}_{0.5}\text{Co}_{1.5}\text{Fe}_{0.5}\text{O}_{5+\delta}$	5.13×10^{-8}	923	~1700 [48]	40.6
$\text{GdBa}_{0.5}\text{Sr}_{0.5}\text{CoFeO}_{5+\delta}$	7.5×10^{-8}	923	2000 [48]	44.9
$\text{NdBa}_{0.5}\text{Sr}_{0.5}\text{Co}_2\text{O}_{5+\delta}$	4×10^{-8}	873	1700 [22]	28.7
$\text{NdBa}_{0.5}\text{Sr}_{0.5}\text{Co}_{1.5}\text{Fe}_{0.5}\text{O}_{5+\delta}$	5.16×10^{-8}	873	2100 [22]	46.5
$\text{NdBa}_{0.5}\text{Sr}_{0.5}\text{CoFeO}_{5+\delta}$	3.8×10^{-8}	873	1500 [22]	28.6
$\text{PrBa}_{0.5}\text{Sr}_{0.5}\text{Co}_2\text{O}_{5+\delta}$	8.33×10^{-8}	873	1900 [22]	29.1
$\text{PrBa}_{0.5}\text{Sr}_{0.5}\text{Co}_{1.5}\text{Fe}_{0.5}\text{O}_{5+\delta}$	1.18×10^{-7} [23]	873	2200 [22]	31.5
$\text{PrBa}_{0.5}\text{Sr}_{0.5}\text{CoFeO}_{5+\delta}$	5.50×10^{-8}	873	1600 [22]	41.6

shown in Table 4. Thus iron doping in case of GBSCFO helps in facilitating faster diffusion and consequently enhances the electrochemical performance. Further substitution effect at $x > 1.0$ has not been studied because of the formation of secondary GdFeO_3 phase [48]. Nevertheless, these results highlight the importance of facile oxygen anion transport within the bulk of the double perovskite structure, which may be linked to the measured electrochemical performance.

Substitution with a different lanthanide cation at the A-site has been reported to significantly improve the electrochemical performance of the co-doped double perovskite material. For example introduction of Nd^{+3} at A-site in place

of Sm^{+3} led to a considerable increase in the ASR value ($0.071 \Omega \text{cm}^2$ at 973 K) [10] of $\text{Nd}_{0.5}\text{Sr}_{0.5}\text{Cu}_{0.2}\text{Fe}_{0.8}\text{O}_{3-\delta}$ cathode as compared to the ASR ($0.085 \Omega \text{cm}^2$ at 973 K) of $\text{Sm}_{0.5}\text{Sr}_{0.5}\text{Cu}_{0.2}\text{Fe}_{0.8}\text{O}_{3-\delta}$ [26]. MD simulations were performed on altering the A-site lanthanide cation to study the effect of Fe content on their diffusion property. Fig. 4(a–c) show the oxygen anion diffusivity with increasing Fe content for $\text{NdBa}_{0.5}\text{Sr}_{0.5}\text{Co}_{2-x}\text{Fe}_x\text{O}_{5.5}$ (NBSCFO). An increase in the value of oxygen diffusion coefficient was observed in NBSCFO with increasing Fe content to 25%. Maximum diffusion coefficient on increasing Fe content in NBSCFO was calculated to be $5.16 \times 10^{-8} \text{cm}^2 \text{s}^{-1}$ for NBSCFO25 at 873 K, as shown in Table 4. Enhanced diffusion in NBSCFO25 corresponds to the

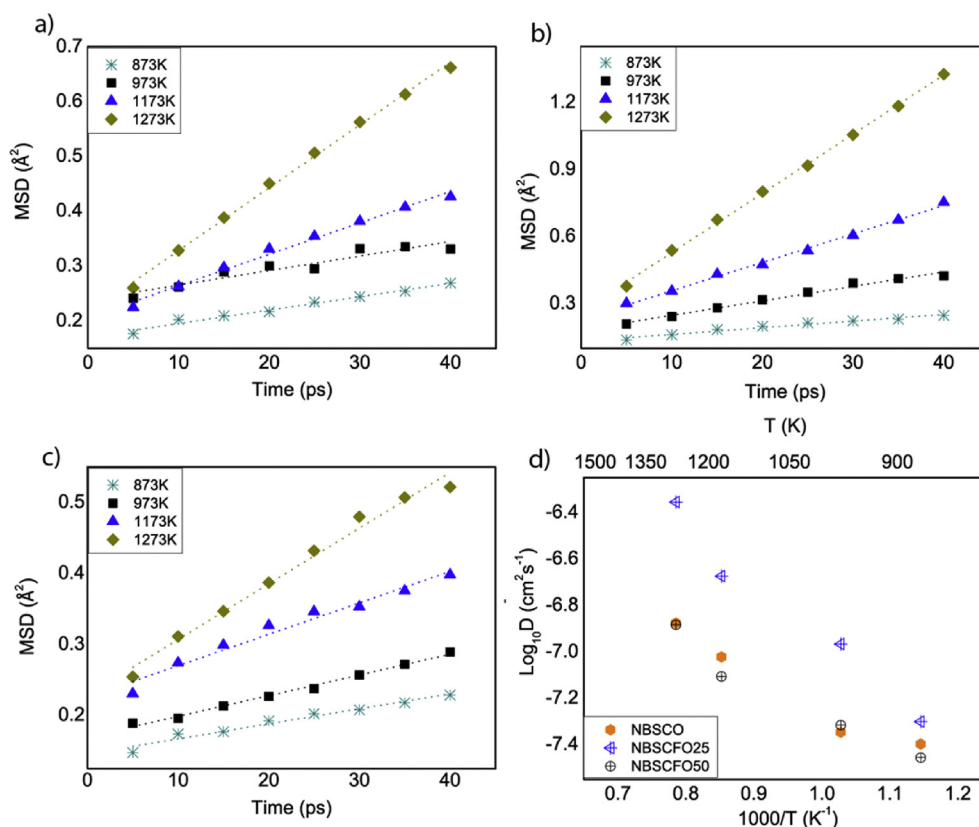


Fig. 4 – MSD plots of a), NBSCO, b) NBSCFO25 (adapted from Ref. [23]), c) NBSCFO50 and d) corresponding Arrhenius plot for a temperature range of 873–1373 K.

improvement in measured peak power densities of the NBSCFO25 electrode as compared to the NBSCO and NBSCFO50, Table 4. A similar trend in the electrochemical performance was observed for PBSCFO electrode with increasing Fe content. Fig. 5(a–c) shows the MSD plots for PBSCO, PBSCFO25 and PBSCFO50 electrode. The calculated diffusion coefficient as shown in Table 4 was observed to be maximum ($D = 1.18 \times 10^{-7} \text{ cm}^2 \text{ s}^{-1}$ at 873 K) for the 25% Fe doped PBSCFO25 structure.

The cation size difference between A and A' layers play an important role in anisotropic diffusion [49,50]. The ionic radius of the cation decreases in the order of $\text{Ba}^{+2} > \text{Gd}^{+3} > \text{Nd}^{+3} > \text{Pr}^{+3}$. Consequently, the size difference between the A site (Gd^{+3} , Nd^{+3} , Pr^{+3}) and A' site (Ba^{+2}) cation increases in the order of $\text{Gd}^{+3} < \text{Nd}^{+3} < \text{Pr}^{+3}$, leading to higher anisotropy [44,50–52] in PBSCFO as compared to GBSCFO structure. Therefore the calculated diffusivity in $\text{LnBa}_{0.5}\text{Sr}_{0.5}\text{Co}_{2-x}\text{Fe}_x\text{O}_{5+\delta}$ ($\text{Ln} = \text{Gd}, \text{Nd}$ or Pr) structures reduces in the order $\text{Gd}^{+3} < \text{Nd}^{+3} < \text{Pr}^{+3}$ [53]. Interestingly, in Pr and Nd-containing co-doped perovskites, optimal levels of Fe concentration was obtained to give maximum diffusion at $x = 0.5$. Any further increase in levels of Fe ions led to a decrease in the calculated oxygen diffusion coefficient, for the entire temperature range of simulations. It can therefore be hypothesize that on increasing the Fe doping levels to higher than 25% a stronger Fe–O bond relative to Co–O bond may restrict the oxygen diffusion. Contrary to GBSCFO, the enhancement in diffusivity of NBSCFO and PBSCFO structure does not correlate

with the increase in cell volume. The trends in diffusivity, however; could be correlated to the increased anisotropy in the structure. For example the ratio of diffusion coefficient in the a – b and c direction was calculated for PBSCF for $x = 0, 0.5$ and 1 and a maximum ratio was observed for $x = 0.5$ as shown in Table S2. Interestingly, the electrochemical performance of these cathode material were observed to follow a parallel trend with oxygen diffusivity, where the maximum peak power density values of 2100 mW cm^{-2} and 2200 mW cm^{-2} were calculated for NBSCFO25 and PBSCFO25 respectively and on any further increase in Fe substitution levels a drop in the power was observed, Table 4. Therefore, the variations in diffusivities were observed to be in direct correlation with corresponding peak power densities [22] measured for a SOFC fabricated from these double perovskite materials.

Conclusion

Molecular dynamics simulations were utilized to calculate diffusivity in double perovskite GBCO and $\text{LnBr}_{0.5}\text{Sr}_{0.5}\text{Co}_{2-x}\text{Fe}_x\text{O}_{5.5}$ structures in the range of temperatures where a SOFC is operated. Preferential diffusion was observed in the a – b plane as compared to the c plane. The diffusion was thermally activated with activation energies ranging from 50.8 to 30.6 kJ/mol in GBCO and in doped $\text{LnBr}_{0.5}\text{Sr}_{0.5}\text{Co}_{2-x}\text{Fe}_x\text{O}_{5.5}$. In the Fe doped structures the amount of Fe doping shows a direct correlation with the calculated diffusivity and

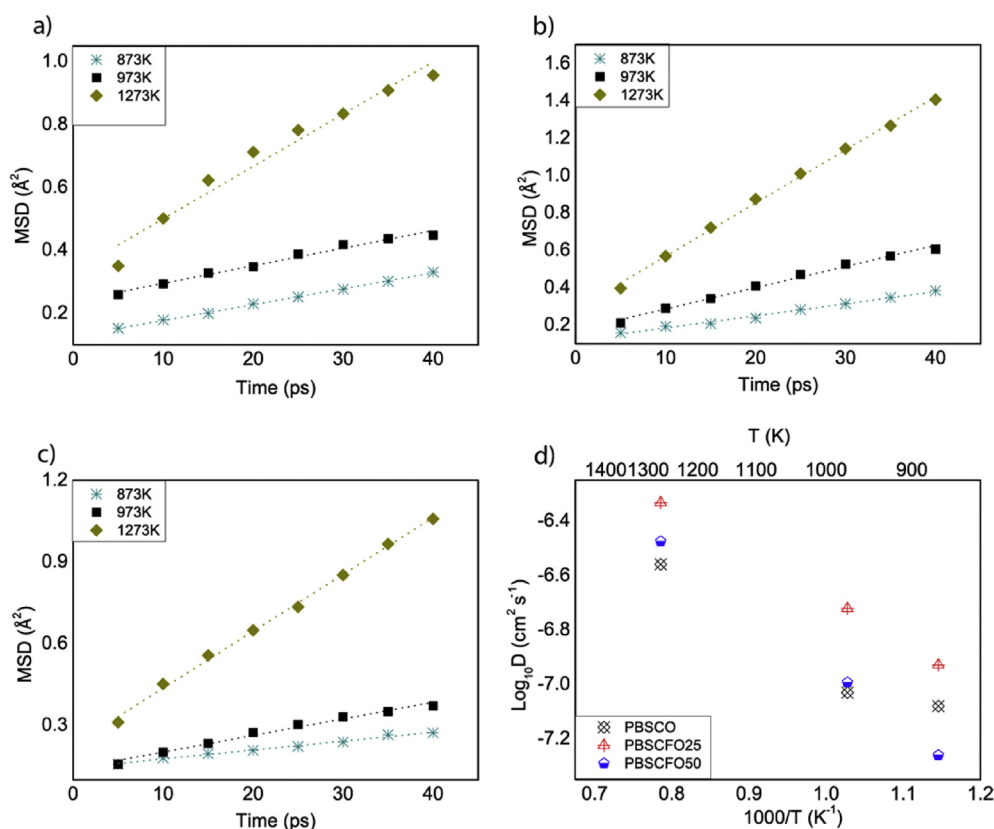


Fig. 5 – MSD plots of a), PBSCO, b) PBSCFO25 (adapted from Ref. [23]), c) PBSCFO50 and d) corresponding Arrhenius plot for a temperature range of 873–1273 K.

electrochemical performance of the respective structure. For example in case of GBSCF, 50% Fe doped structure showed maximum diffusion as compared to the undoped and 25% doped GBSCF. Interestingly, peak power density of the SOFC fabricated with GBSCFO50 was observed to be the maximum as compared to GBSCO and GBSCFO25. The oxygen diffusion properties of a co-doped layered perovskite were calculated to increase in the order of changing A-site cation $\text{Pr}^{+3} > \text{Nd}^{+3} > \text{Gd}^{+3}$ [52]. In general, maximum diffusivity was calculated for least distorted structure. However, on replacing the A-site cation by Pr or Nd, the trends in diffusivity with increasing Fe content were observed to be different, wherein, maximum diffusivity was calculated for 25% Fe doped structures, which corresponds to the maximum peak power density measured for a SOFC made of the respective electrode material. The results thus highlight an operating regime where diffusion is either co-limiting or limiting the electrochemical performance of the SOFC. An optimum amount of Fe loading leads to higher diffusivity and consequently better electrochemical performance of the electrode.

Acknowledgement

The authors would like to acknowledge the financial support provided by the Department of Science and Technology (Grant No: SB/S3/CE/037/2014), and Council of Scientific and Industrial Research (Grant No: 01/2798/14 (EMR-II)), Government of India. Authors would like to acknowledge IIT Delhi HPC facility for providing computational resources to carry out MD simulations. Uzma Anjum and Saumye Vashishtha have contributed equally to this work.

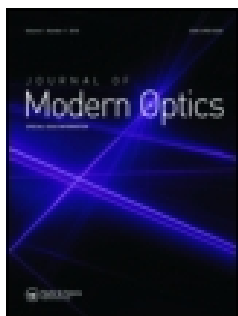
Appendix A. Supplementary data

Supplementary data related to this article can be found at <http://dx.doi.org/10.1016/j.ijhydene.2016.02.090>.

REFERENCES

- [1] Seymour I, Tarancón A, Chronos A. Anisotropic oxygen diffusion in $\text{PrBaCo}_2\text{O}_{5.5}$ double perovskites. *Solid State Ionics* 2012;216:41–3.
- [2] Ullmann H, Trofimenko N, Tietz F, Stover D. Correlation between thermal expansion and oxide ion transport in mixed conducting perovskite-type oxides for SOFC cathodes. *Solid State Ionics* 2000;138:79–90.
- [3] Steele BC, Heinzel A. Materials for fuel-cell technologies. *Nature* 2001;414(November):345–52.
- [4] Gu H, Chen H, Gao L, Zheng Y, Zhu X, Guo L. Oxygen reduction mechanism of $\text{NdBaCo}_2\text{O}_{5+\delta}$ cathode for intermediate-temperature solid oxide fuel cells under cathodic polarization. *Int J Hydrogen Energy* 2009;34:2416–20.
- [5] Patra H, Rout SK, Pratihari SK, Bhattacharya S. Thermal, electrical and electrochemical characteristics of $\text{Ba}_{1-x}\text{Sr}_x\text{Co}_{0.8}\text{Fe}_{0.2}\text{O}_{3-\delta}$ cathode material for intermediate temperature solid oxide fuel cells. *Int J Hydrogen Energy* 2011;36:11904–13.
- [6] Adler SB. Factors governing oxygen reduction in solid oxide fuel cell cathodes. *Chem Rev* 2004;104:4791–840.
- [7] Haider MA, Capizzi AJ, Murayama M, McIntosh S. Reverse micelle synthesis of perovskite oxide nanoparticles. *Solid State Ionics* 2011;196:65–72.
- [8] Meng F, Xia T, Wang J, Shi Z, Lian J, Zhao H, et al. Evaluation of layered perovskites $\text{YBa}_{1-x}\text{Sr}_x\text{Co}_2\text{O}_{5-\delta}$ as cathodes for intermediate-temperature solid oxide fuel cells. *Int J Hydrogen Energy* 2014;39:4531–43.
- [9] Pang S, Jiang X, Li X, Su Z, Xu H, Xu Q, et al. Characterization of cation-ordered perovskite oxide $\text{LaBaCo}_2\text{O}_{5+\delta}$ as cathode of intermediate-temperature solid oxide fuel cells. *Int J Hydrogen Energy* 2012;37:6836–43.
- [10] Ling Y, Zhao L, Lin B, Dong Y, Zhang X, Meng G, et al. Investigation of cobalt-free cathode material $\text{Sm}_{0.5}\text{Sr}_{0.5}\text{Fe}_{0.8}\text{Cu}_{0.2}\text{O}_{3-\delta}$ for intermediate temperature solid oxide fuel cell. *Int J Hydrogen Energy* 2010;35:6905–10.
- [11] Tarancón A, Burriel M, Santiso J, Skinner SJ, Kilner JA. Advances in layered oxide cathodes for intermediate temperature solid oxide fuel cells. *J Mater Chem* 2010;20:3799–813.
- [12] Kim JH, Irvine JTS. Characterization of layered Perovskite oxides $\text{NdBaSrCo}_2\text{O}_{5+\delta}$ ($\delta = 0$ and 0.5) as cathode material for IT-SOFC. *Int J Hydrogen Energy* 2012;37:5920–9.
- [13] Chen D, Shao Z. Surface exchange and bulk diffusion properties of $\text{Ba}_{0.5}\text{Sr}_{0.5}\text{Co}_{0.8}\text{Fe}_{0.2}\text{O}_{3-\delta}$ mixed conductor. *Int J Hydrogen Energy* 2011;36:6948–56.
- [14] Li H, Sun LP, Li Q, Xia T, Zhao H, Huo LH, et al. Electrochemical performance of double perovskite $\text{Pr}_2\text{NiMnO}_6$ as a potential IT-SOFC cathode. *Int J Hydrogen Energy* 2015;40:12761–9.
- [15] Tarancón A, Skinner SJ, Chater RJ, Hernández-Ramírez F, Kilner JA. Layered perovskites as promising cathodes for intermediate temperature solid oxide fuel cells. *J Mater Chem* 2007;17:3175.
- [16] Haider MA, McIntosh S. The influence of grain size on $\text{La}_{0.6}\text{Sr}_{0.4}\text{Co}_{0.2}\text{Fe}_{0.8}\text{O}_{3-\delta}$ thin film electrode impedance. *J Electrochem Soc* 2011;158:B1128.
- [17] Armstrong EN, Duncan KL, Wachsman ED. Effect of A and B-site cations on surface exchange coefficient for ABO_3 perovskite materials. *Phys Chem Chem Phys* 2013;15:2298–308.
- [18] Zapata J, Burriel M, García P, Kilner JA, Santiso J. Anisotropic ^{18}O tracer diffusion in epitaxial films of $\text{GdBaCo}_2\text{O}_{5+\delta}$ cathode material with different orientations. *J Mater Chem A* 2013;1:7408.
- [19] Maignan A, Martin C, Pelloquin D, Nguyen N, Raveau B. Structural and magnetic studies of ordered oxygen-deficient perovskites $\text{LnBaCo}_2\text{O}_{5+\delta}$, closely related to the “112” structure. *J Solid State Chem* 1999;142:247–60.
- [20] Taskin AA, Lavrov AN, Ando Y. Fast oxygen diffusion in A-site ordered perovskites. *Prog Solid State Chem* 2007;35:481–90.
- [21] Lee SJ, Kim DS, Kim DK. High-performance $\text{GdBaCo}_2\text{O}_{5+\delta}$ – $\text{Ce}_{0.9}\text{Gd}_{0.1}\text{O}_{1.95}$ composite cathode for solid oxide fuel cells. *Curr Appl Phys* 2011;11:S238–41.
- [22] Choi S, Yoo S, Kim J, Park S, Jun A, Sengodan S, et al. Highly efficient and robust cathode materials for low-temperature solid oxide fuel cells: $\text{PrBa}_{0.5}\text{Sr}_{0.5}\text{Co}_{2-x}\text{Fe}_x\text{O}_{5+\delta}$. *Sci Rep* 2013;3:2426.
- [23] Anjum U, Vashishtha S, Sinha N, Haider MA. Role of oxygen anion diffusion in improved electrochemical performance of layered perovskite $\text{LnBa}_{1-y}\text{Sr}_y\text{Co}_{2-x}\text{Fe}_x\text{O}_{5+\delta}$ ($\text{Ln} = \text{Pr, Nd, Gd}$) electrodes. *Solid State Ionics* 2015;280:24–9.
- [24] Park S, Choi S, Kim J, Shin J, Kim G. Strontium doping effect on high-performance $\text{PrBa}_{1-x}\text{Sr}_x\text{Co}_2\text{O}_{5+\delta}$ as a

- cathode material for IT-SOFCs. *Electrochem Lett* 2012;1:29–32.
- [25] Ding X, Kong X, Jiang J, Cui C. Evaluation of Sr substituted Nd_2CuO_4 as a potential cathode material for intermediate-temperature solid oxide fuel cells. *Int J Hydrogen Energy* 2009;34:6869–75.
- [26] Yin J-W, Yin Y-M, Lu J, Zhang C, Minh NQ, Ma Z-F. Structure and properties of novel cobalt-free oxides $\text{Nd}_x\text{Sr}_{1-x}\text{Fe}_{0.8}\text{Cu}_{0.2}\text{O}_{3-\delta}$ ($0.3 \leq x \leq 0.7$) as Cathodes of intermediate temperature solid oxide fuel cells. *J Phys Chem C* 2014;118:13357–68.
- [27] De Souza RA, Kilner JA. Oxygen transport in $\text{La}_{1-x}\text{Sr}_x\text{Mn}_{1-y}\text{Co}_y\text{O}_{3-\delta}$ perovskites part I. Oxygen tracer diffusion. *Solid State Ionics* 1998;106:175–87.
- [28] De Souza RA, Kilner JA. Oxygen transport in $\text{La}_{1-x}\text{Sr}_x\text{Mn}_{1-y}\text{Co}_y\text{O}_{3-\delta}$ perovskites part II. oxygen surface exchange. *Solid State Ionics* 1999;126:153–61.
- [29] Berenov AV, Atkinson A, Kilner JA, Bucher E, Sitte W. Oxygen tracer diffusion and surface exchange kinetics in $\text{La}_{0.6}\text{Sr}_{0.4}\text{CoO}_{3-\delta}$. *Solid State Ionics* 2010;181:819–26.
- [30] Tomkiewicz AC, Meloni M, McIntosh S. On the link between bulk structure and surface activity of double perovskite based SOFC cathodes. *Solid State Ionics* 2014;260:55–9.
- [31] Hermet J, Geneste G, Dezanneau G. Molecular dynamics simulations of oxygen diffusion in $\text{GdBaCo}_2\text{O}_{5.5}$. *Appl Phys Lett* 2010;97:174102.
- [32] Ewald PP. Die Berechnung optischer und elektrostatischer Gitterpotentiale. *Ann Phys* 1921;369:253–87.
- [33] Buckingham RA. The classical equation of state of gaseous helium, neon and argon. *Proc R Soc A Math Phys Eng Sci* 1938;168:264–83.
- [34] Fisher CAJ, Iwamoto Y, Asanuma M, Anyashiki T, Yabuta K. Atomistic simulations of oxide ion diffusion in heavily doped lanthanum cobaltite. *J Eur Ceram Soc* 2005;25:3243–8.
- [35] Islam MS, Cherry M, Catlow CRA. Oxygen diffusion in LaMnO_3 and LaCoO_3 perovskite-type oxides: a molecular dynamics study. *J Solid State Chem* 1996;124:230–7.
- [36] Fisher C, Yoshiya M, Iwamoto Y, Ishii J, Asanuma M, Yabuta K. Oxide ion diffusion in perovskite-structured $\text{Ba}_{1-x}\text{Sr}_x\text{Co}_{1-y}\text{Fe}_y\text{O}_{2.5}$: a molecular dynamics study. *Solid State Ionics* 2007;177:3425–31.
- [37] Hoover W. Canonical dynamics: equilibrium phase-space distributions. *Phys Rev A Mar.* 1985;31:1695–7.
- [38] Martyna GJ, Klein ML, Tuckerman M. Nose-Hoover chains - the canonical ensemble via continuous dynamics. *J Chem Phys* 1992;97:2635–43.
- [39] Berendsen HJC, Postma JPM, van Gunsteren WF, Dinola A, Haak JR. Molecular dynamics with coupling to an external bath. *J Chem Phys* 1984;81:3684.
- [40] Chang A, Skinner SJ, Kilner JA. Electrical properties of $\text{GdBaCo}_2\text{O}_{5+x}$ for ITSOFC applications. *Solid State Ionics* 2006;177:2009–11.
- [41] Taskin AA, Lavrov AN, Ando Y. Achieving fast oxygen diffusion in perovskites by cation ordering. *Appl Phys Lett* 2005;86:091910.
- [42] Cox-Galhotra RA, McIntosh S. Unreliability of simultaneously determining k_{chem} and D_{chem} via conductivity relaxation for surface-modified $\text{La}_{0.6}\text{Sr}_{0.4}\text{Co}_{0.2}\text{Fe}_{0.8}\text{O}_{3-\delta}$. *Solid State Ionics* 2010;181:1429–36.
- [43] Haider MA, McIntosh S, Steven M. Evidence for two activation mechanisms in LSM SOFC cathodes. *J Electrochem Soc* 2009;156:B1369.
- [44] Uberuaga BP, Pilania G. Effect of cation ordering on oxygen vacancy diffusion pathways in double perovskites. *Chem Mater* 2015;27:5020–6.
- [45] Pen J, Chater RJ, Fearn S, Berenov AV, Skinner SJ, Kilner JA. Anisotropic oxygen ion diffusion in layered $\text{PrBaCo}_2\text{O}_{5+\delta}$. *Chem Mater* 2012;24:613–21.
- [46] Rupasov D, Chroneos A, Parfitt D, Kilner JA, Grimes RW, Antipov EV, et al. Oxygen diffusion in $\text{Sr}_{0.75}\text{Y}_{0.25}\text{CoO}_{2.625}$: a molecular dynamics study. *Phys Rev B* 2009;79. 172102(1)–172102(4).
- [47] Chen Z, Ran R, Zhou W, Shao Z, Liu S. Assessment of $\text{Ba}_{0.5}\text{Sr}_{0.5}\text{Co}_{1-y}\text{Fe}_y\text{O}_{3-\delta}$ ($y=0.0-1.0$) for prospective application as cathode for IT-SOFCs or oxygen permeating membrane. *Electrochim Acta* 2007;52:7343–51.
- [48] Kim J, Jun A, Shin J, Kim G. Effect of Fe doping on layered $\text{GdBa}_{0.5}\text{Sr}_{0.5}\text{Co}_2\text{O}_{5+\delta}$ perovskite cathodes for intermediate temperature solid oxide fuel cells. *J Am Ceram Soc* 2014;97:651–6.
- [49] Mogensen M, Lybye D, Bonanos N, Hendriksen P, Poulsen F. Factors controlling the oxide ion conductivity of fluorite and perovskite structured oxides. *Solid State Ionics* 2004;174:279–86.
- [50] Klyndyuk AI, Chizhova EA. Synthesis and properties of $\text{LnBaFeCoO}_{5+\delta}$ ($\text{Ln} = \text{Nd, Sm, Gd}$). *Inorg Mater* 2013;49:319–24.
- [51] Azad AK, Kim JH, Irvine JTS. Structure – property relationship in layered perovskite cathode $\text{LnBa}_{0.5}\text{Sr}_{0.5}\text{Co}_2\text{O}_{5+\delta}$ ($\text{Ln} = \text{Pr, Nd}$) for solid oxide fuel cells. *J Power Sources* 2011;196:7333–7.
- [52] Zhang K, Ge L, Ran R, Shao Z, Liu S. Synthesis, characterization and evaluation of cation-ordered $\text{LnBaCo}_2\text{O}_{5+\delta}$ as materials of oxygen permeation membranes and cathodes of SOFCs. *Acta Crystallogr* 2008;56:4876–89.
- [53] Murias BR, Rivas J, Rodriguez MAS. Synthesis, characterization and transport properties of $\text{Pr}_{0.5}\text{Ln}_{0.5}\text{BaCo}_2\text{O}_{5+\delta}$ ($\text{Ln} = \text{Pr, Nd, Sm, Eu, Gd, Tb and Dy}$). *J Alloys Compd* 2012;516:113–8.
- [54] Kilo M. Modeling of cation diffusion in oxygen ion conductors using molecular dynamics. *Solid State Ionics* 2004;175:823–7.
- [55] Howard MA, Clemens O, Knight KS, Anderson PA, Hafiz S, Panchmatia PM, et al. Synthesis, conductivity and structural aspects of $\text{Nd}_3\text{Zr}_2\text{Li}_{7-3x}\text{Al}_x\text{O}_{12}$. *J Mater Chem A* 2013;1:14013.
- [56] Allietta M. Diffraction studies on strongly correlated perovskite oxides. University of Milan; 2011.



Photonic crystal-based RGB primary colour optical filter

Brahm Raj Singh, Swati Rawal & R. K. Sinha

To cite this article: Brahm Raj Singh, Swati Rawal & R. K. Sinha (2016): Photonic crystal-based RGB primary colour optical filter, Journal of Modern Optics, DOI: [10.1080/09500340.2016.1149240](https://doi.org/10.1080/09500340.2016.1149240)

To link to this article: <http://dx.doi.org/10.1080/09500340.2016.1149240>



Published online: 26 Feb 2016.



Submit your article to this journal [↗](#)



Article views: 6



View related articles [↗](#)



View Crossmark data [↗](#)

Photonic crystal-based RGB primary colour optical filter

Brahm Raj Singh^a, Swati Rawal^a and R. K. Sinha^b

^aDepartment of Physics and Material Science Engineering, Jaypee Institute of Information Technology, Noida, India; ^bDepartment of Applied Physics, TIFAC-Centre of Relevance and Excellence in Fiber Optics and Optical Communication, Delhi Technological University (Formerly Delhi College of Engineering), Delhi, India

ABSTRACT

We have presented an RGB optical filter, based on photonic crystal (PhC) waveguides, with the hexagonal arrangement of GaP rods in air. It filters out the three primary colours of the visible range, red (R, $\lambda = 648$ nm), green (G, $\lambda = 540$ nm) and blue (B, $\lambda = 470$ nm). The plane wave expansion method is applied for estimating the dispersion curves and finite element method is utilized in examining the propagation characteristics of the designed PhC-based optical filter. Transmittance, extinction ratio and *tolerance analysis* have further been calculated to confirm the performance of the proposed optical filter to work in the visible range of optical spectrum and filter out the three primary colours (red, green, blue) along different output ports.

ARTICLE HISTORY

Received 7 September 2015
Accepted 25 January 2016

KEYWORDS

Photonic crystal; extinction ratio; photonic band gap

1. Introduction

Photonic crystals (PhCs) or dielectric materials, having dielectric constant, varying periodically in space. These materials control light propagation and open up new routes for ultra compact, high wavelength selective optical devices [1,2]. They provide a flexibility to the propagation of electromagnetic wave within certain frequency bands, called photonic band gap (PBG). The light waves could not propagate through the PhCs for frequency range lying within the photonic band gap. On introducing a defect in an otherwise perfect PhC, localized modes or a group of modes produced allow light to propagate through such structures [3–6]. Optical filters are devices that selectively transmit light of different frequencies (colours) blocking the remaining frequencies within a certain spectral range. There are filters which allow only longer wavelengths to pass through (long-pass filters), or they allow only shorter wavelengths to pass through (short-pass filters), while certain optical filters allow only a band of wavelengths to pass through (band-pass filters), blocking both short and long wavelengths [7]. Specifically, more attention has been paid to optical filters which operate in the optical communication frequency range and visible light optical filter is still lagging behind in this field. There is an intense demand of devices having viewability in environments

like sunlight where telecom wavelength-based devices do very poorly [8].

In this paper, a PhC structure-based optical filter, to work in the visible range of the electromagnetic spectrum, is being designed with the hexagonal arrangement of gallium phosphide (GaP) rods in air. The optical filter is designed and explained with the help of plane wave expansion (PWE) method and finite element method (FEM) method [9,10]. PWE method calculates the photonic band gap and the existence of guided modes in different waveguides, while the FEM method demonstrates that the three primary colours (red, green and blue visible spectrum) filter out along different ports efficiently. The designed optical filter can be used as a colour separator, as it separates out the three basic colours of the seven colours of the rainbow. The primary colours red, green and blue are the sets of colours that can be combined to make a useful range of vibrant colours [11–14]. The basic idea behind the working of the proposed RGB optical filter is to filter out the three primary colours: red, green and blue from the input visible range spectrum of 400–700 nm, along three different output ports, respectively. Transmittance and extinction ratio (ER) have been calculated to check the crosstalk among the ports.

2. Structure design

PhC-based RGB optical filter having a hexagonal arrangement of GaP rods in air has been designed [Figure 1(a)]. Selection of the radii of rods in different arms of the structure is based on the fact that input waveguide allows the entire visible range to pass through, output waveguide 1 allows only red colour to pass through while green and blue suffer band gap, output waveguide 2 allows blue colour to pass through while red and green suffer band gap and output waveguide 3 allows green colour to pass through while red and blue suffer band gap. Figure 1(b) gives the range of PBG obtained by varying the radii of GaP rods, lattice constant used here is $0.209 \mu\text{m}$. It is observed that for $r = 0.035 \mu\text{m}$, PBG exists for TM modes of normalized frequency range $(0.2875 \leq a/\lambda \leq 0.5284)$ corresponding to the visible spectrum (400–700 nm). The input waveguide is then created by removing a few rods from the direction of propagation. The designed waveguide thus supports the entire visible spectrum and allows the three primary colours (red, green and blue) to pass through it. Figure 1(c) shows the existence of guided

modes for red, green and blue colours within the input waveguide obtained by removing a few rods in the PhC structure along the direction of propagation. The three output ports have then been designed by varying the radii of GaP rods as r_1 , r_2 and r_3 in the respective ports to filter out the three primary colours red, green and blue of the visible spectrum. Output waveguide 1 has GaP rods of radius $r_1 = 0.028 \mu\text{m}$ to filter out red colour, output waveguide 2 has GaP rods of radius $r_2 = 0.056 \mu\text{m}$ to filter out green colour, output waveguide 3 has GaP rods of radius $r_3 = 0.045 \mu\text{m}$ to filter out blue colour. The three radii are selected from Figure 1(b) such that in output waveguide 1, there is no band gap for red colour ($a/\lambda = 0.322$ and $\lambda = 648 \text{ nm}$), while the band gap exists for green ($a/\lambda = 0.387$ and $\lambda = 540 \text{ nm}$) and blue colours ($a/\lambda = 0.44$ and $\lambda = 470 \text{ nm}$); similarly, in output waveguide 2, there is no band gap for green, whereas red and blue colours experience band gap and in output waveguide 3, there is no band gap for blue while red and green colours experience band gap.

Figure 2(a) shows the existence of guided modes for red colour ($a/\lambda = 0.322$, $\lambda = 648 \text{ nm}$), by introducing

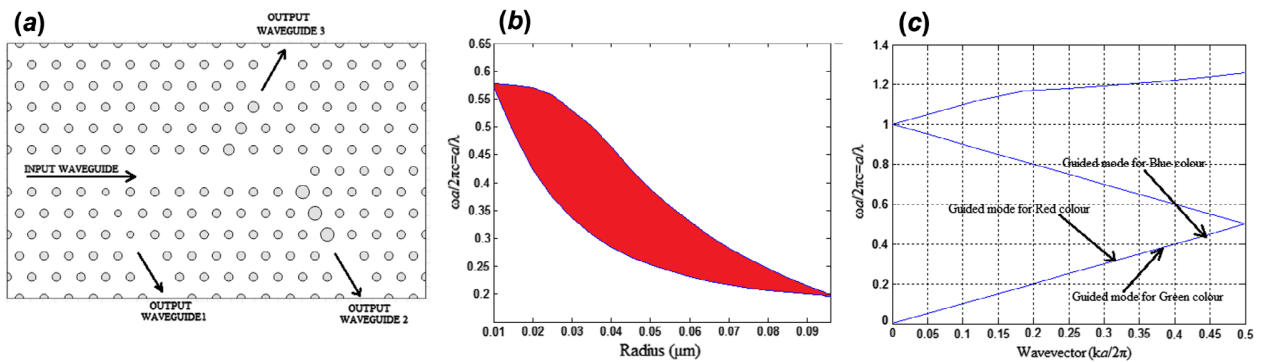


Figure 1. (a) Schematic diagram of the proposed optical filter having GaP rods in air. (b) Dispersion diagram for photonic crystal GaP rods in air with $a = 0.209 \mu\text{m}$ and $r = 0.035 \mu\text{m}$. (c) Band structure for hexagonal lattice GaP rods in air with lattice constant $a = 0.209 \mu\text{m}$, $r = 0.035 \mu\text{m}$, $r_1 = 0.028 \mu\text{m}$, $r_2 = 0.056 \mu\text{m}$, $r_3 = 0.045 \mu\text{m}$. (The colour version of this figure is included in the online version of the journal.)

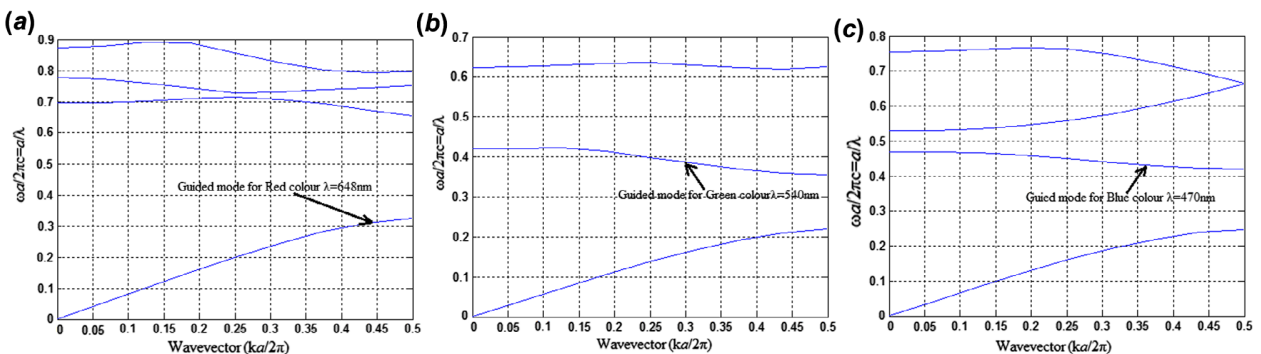


Figure 2. Existence of guided modes in (a) output port for red colour (648 nm), (b) output port 2 for green colour (540 nm) and (c) output port 3 for blue colour (470 nm). (The colour version of this figure is included in the online version of the journal.)

GaP rods of radius $r_1 = 0.028 \mu\text{m}$. However, no guided modes are present for wavelengths corresponding to green ($a/\lambda = 0.387$, $\lambda = 540 \text{ nm}$) and blue ($a/\lambda = 0.44$, $\lambda = 470 \text{ nm}$) as they experience band gap in output waveguide 1. Thus, the incident red light propagates through this waveguide, while green and blue are radiated out. Figure 2(b) shows the presence of guided modes for green colour ($a/\lambda = 0.387$ and $\lambda = 540 \text{ nm}$), which has been obtained by introducing GaP rods of radius $r_2 = 0.056 \mu\text{m}$ in output waveguide 2 where red and blue colours show band gap (absence of guided modes) and hence are radiated out or not allowed to propagate through the output waveguide 2. Figure 2(c) shows guided modes for blue colour, which has been obtained by introducing GaP rods of radius $r_3 = 0.045 \mu\text{m}$ in output waveguide 3 which corresponds to wavelength $\lambda_3 = 470 \text{ nm}$ and absence of guided modes for red and green colours.

3. Transmittance

Transmittance (TR) of the designed optical filter is defined as the ratio of output power to the total input power and mathematically it can be written as

$$\text{TR} = P_{\text{out}}/P_{\text{in}}$$

where P_{out} is the power at either of the output ports 1, 2 and 3, respectively, for three different colours of the visible spectrum and P_{in} is the power at the input port.

Figure 3(a) shows the field pattern for TM polarization, corresponding to the three primary colours red, green and blue. FEM simulations are carried out to observe this pattern. It shows that red colour is obtained from output waveguide 1, green colour from output waveguide 2 and blue colour from output waveguide 3.

The spectral response of the proposed optical filter is plotted in Figure 4 for the TM polarization of the entire visible range (400–700 nm) along three output waveguides. Figure 4(a) shows the plot of normalized transmission with visible range spectrum at output port 1 and it shows that the maxima is obtained corresponding to red colour ($\lambda = 648 \text{ nm}$), Figure 4(b) shows the plot of normalized transmission with visible range spectrum at output port 2 and it is observed that maxima is obtained corresponding to green colour ($\lambda = 540 \text{ nm}$), while Figure 4(c) gives the variation of normalized transmission with visible range spectrum at output port 3 and maxima is observed for blue colour ($\lambda = 470 \text{ nm}$). Hence, the proposed RGB optical filter successfully splits out the three primary colours (red, green and blue) from the three output waveguides, respectively.

4. Extinction ratio

ER can be defined as:

$$\text{ER} = 10 \log_{10} (P_1/P_0) \quad (2)$$

where P_1 is the power obtained from the desired output port and P_0 is the power obtained from the remaining two output ports. The ER is used to describe the efficiency with which the transmitted optical power is modulated over the designed waveguide. The wavelength variation considered here is 400–700 nm. Figure 5(a) shows the ER obtained for output port 1 (red colour) which is nearly equal to 19 dB. Figure 5(b) shows the ER obtained from output port 2 (green colour) which is nearly 17 dB. Figure 5(c) gives the ER obtained from output port 3 (blue colour) which is 13 dB.

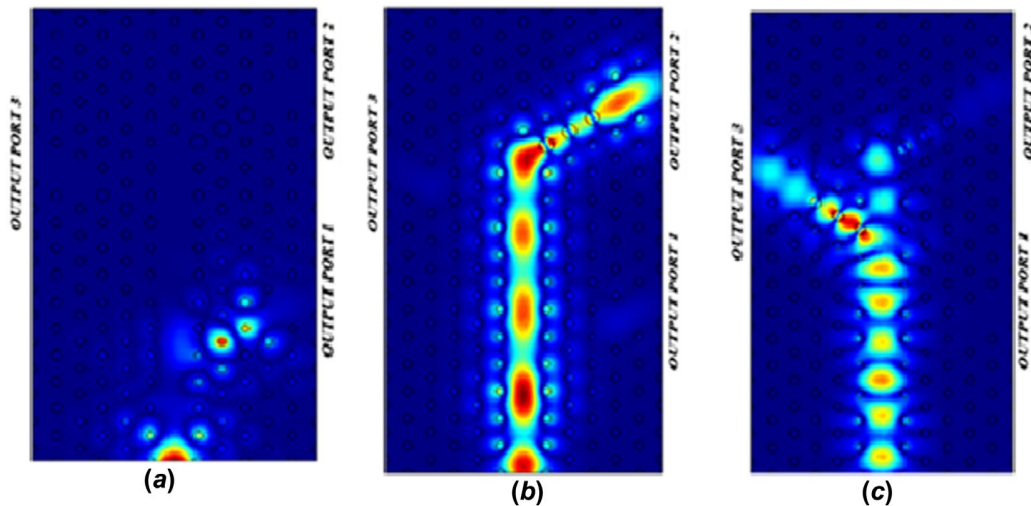


Figure 3. Electric field distribution of the three primary colour optical filters. (a) $\lambda_1 = 648 \text{ nm}$ (Red); (b) $\lambda_2 = 540 \text{ nm}$ (Green) (c) $\lambda_3 = 470 \text{ nm}$ (Blue). (The colour version of this figure is included in the online version of the journal.)

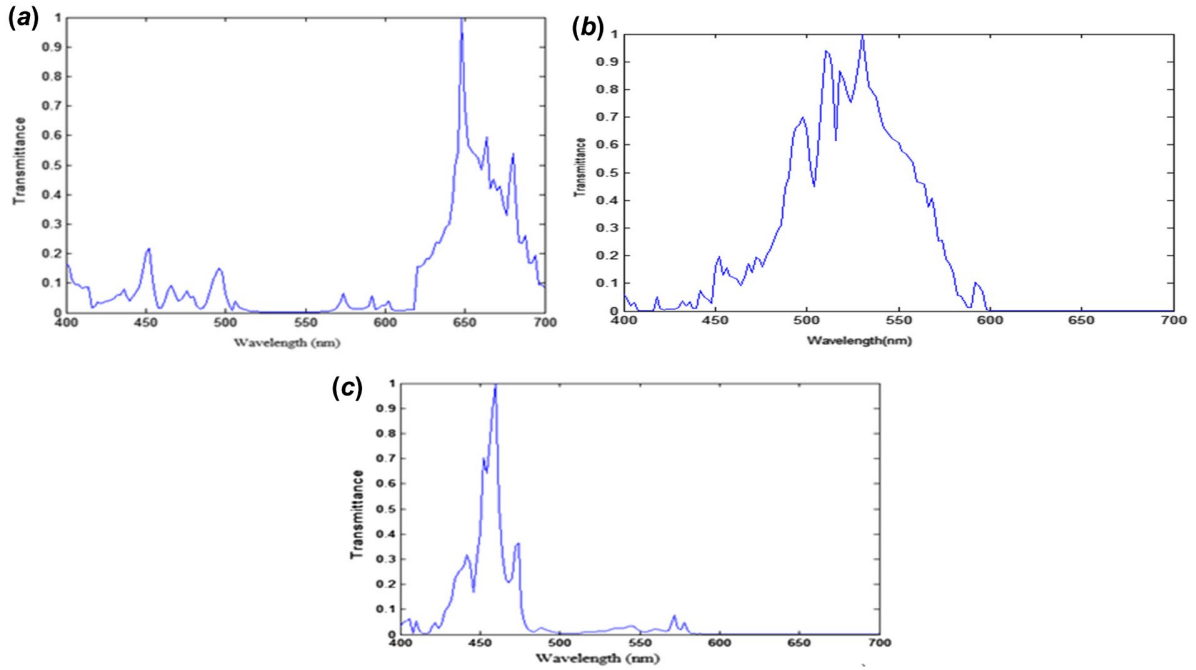


Figure 4. Normalized transmission curve for (a) red light, (b) green light and (c) blue light. (The colour version of this figure is included in the online version of the journal.)

5. Tolerance analysis

In this section, we have presented the effect of change in GaP rod's radius on the transmission characteristics of optimized RGB filter in PhC. We have calculated the transmission changes for -3 to $+3\%$ variation in radius of GaP rods for red, green and blue output. It is observed from the tolerance curve (Figure 6(a)), at -3% change in radius (r_1) of GaP rods corresponding to output port 1, i.e. wavelength corresponding to red colour, transmission is nearly 72%, whereas at $+3\%$ variation in radius (r_1), it has been changed to 63%. It is deduced from the tolerance curve (Figure 6(b)), at -3% change in radius (r_2) of GaP rods corresponding to output port 2, i.e. wavelength corresponding to green colour, transmission is nearly 67%, whereas at $+3\%$ variation in radius (r_2), it has been increased to 78%. It is observed from the tolerance curve (Figure 6(c)), at -3% change in radius (r_3) of GaP rods corresponding to output port 3, i.e. wavelength corresponding to blue colour, transmission is nearly 61%, whereas at $+3\%$ variation in radius (r_3), it has reached to 71%. Tolerance analysis of above factors leads us to conclude that the proposed optical RGB filter-based PhC has a reasonable fabrication tolerance.

6. Conclusion and discussions

In the paper, we have designed the three primary colour optical filter based on PhCs for GaP rods in air. The idea behind the selection of this topic is that the

optical filters can be used in various applications based on laser communication and in electronics industry. In optical communication, wavelength division multiplexing systems and optical filters are essential components to multiplex (add) and demultiplex (drop) wavelengths. However, in the reported literature, the operating range of optical communication is mainly infrared region, i.e. at wavelengths 1.55 and 1.31 μm [15–17]. Now, there is a high demand of devices having viewability in environments like sunlight where optical communication wavelength-based devices perform very poorly. A majority of the natural and artificial light sources emits a broad range of wavelengths that cover the entire visible light spectrum, with some extending into the ultraviolet and infrared regions as well. For simple lighting and technical applications, the wide wavelength spectrum is acceptable and quite useful. We have carried out the tolerance analysis of the device for $\pm 3\%$ change in radius (r_1 , r_2 , r_3) of the GaP rods for three output ports in designed structure. It is found that the working wavelength region of the guided mode remains unaffected for the proposed optical RGB filter with an increase or decrease in defect radii by 3%, though there is a decrease/increase in transmission accordingly. Dingwen Liu et al. [18] has reported a three-colour combiner having dimensions nearly equal to 10.98 $\mu\text{m} \times 4.0 \mu\text{m}$ in a square lattice arrangement of GaP rods in air substrate using the concept of waveguide coupling in between two waveguides. In the present paper, we have designed optical filter with lower

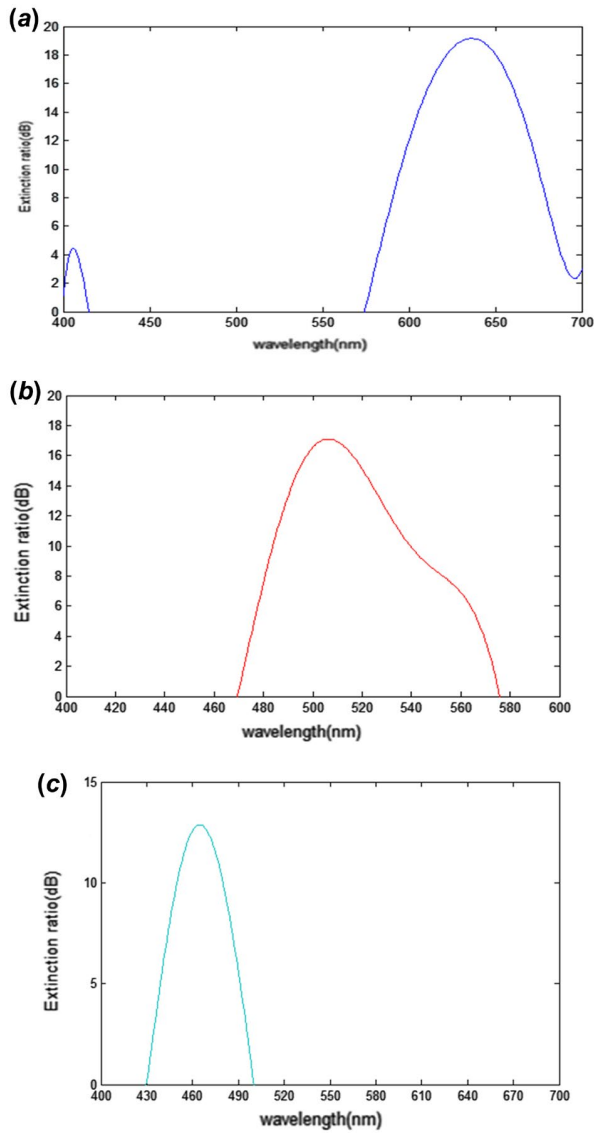


Figure 5. ER curve for (a) red colour, (b) green colour and (c) blue colour. (The colour version of this figure is included in the online version of the journal.)

dimensions, i.e. $3.55 \mu\text{m} \times 2.16 \mu\text{m}$ in hexagonal lattice arrangement of PhC, to filter out the three primary colours of visible spectrum. The hexagonal lattice has high packing efficiency of 90.69% as compared to square lattice (78.54%), due to which hexagonal arrangement crystal is more stable. Practically, further demultiplexing function for the three primary colours is carried out using the phenomenon of photonic band gap guidance in horizontal direction and total internal reflection in vertical direction. This causes the appearance of true guided modes supported by the three output waveguide ports. ER has also been taken into consideration while doing the analysis which is found to be nearly 19, 17 and 13 dB for red, green and blue colours, respectively. High

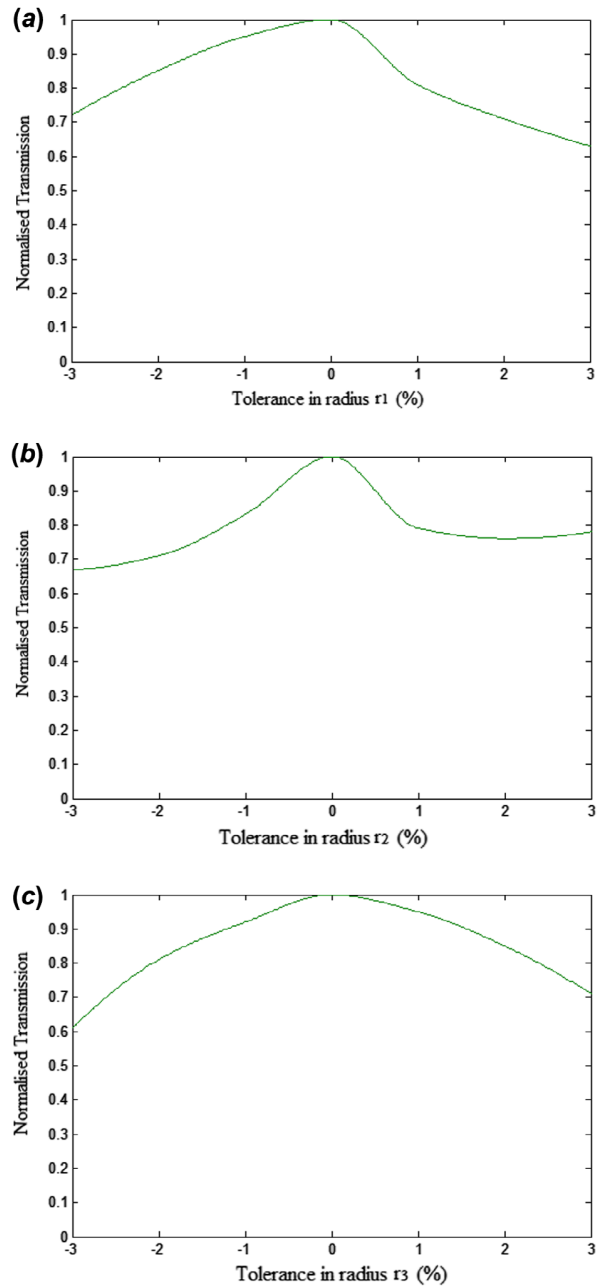


Figure 6. Tolerance analysis curve for variation in radius of the rods (a) red colour (output port 1) (b) green colour (output port 2) (c) blue colour (output port 3). (The colour version of this figure is included in the online version of the journal.)

transmittance is being achieved in the visible range for red, green and blue colour light in the desired wavelength range. The proposed design is efficient and high data rate can be achieved with these types of PhC structures.

Acknowledgements

The authors Swati Rawal and Brahm raj Singh acknowledge IIIT Noida, for providing research support for the

present research work. The authors gratefully acknowledge the initiatives and support towards establishment of “TIFAC Centre of Relevance and Excellence in Fiber Optics and Optical Communication at Delhi Technological University (Formerly Delhi College of Engineering), Delhi” through “Mission REACH” program of Technology Vision-2020, Government of India.

Disclosure statement

No potential conflict of interest was reported by the authors.

References

- [1] Yablonovitch, E. *Phys. Rev. Lett.* **1987**, 58, 2059–2062.
- [2] John, S. *Phys. Rev. Lett.* **1987**, 58, 2486–2489.
- [3] Wang, L.H.; Yang, S.H. *Nano Photoelectric Material Structures – Photonic Crystals*; IEEE 2nd International Symposium on Next-Generation Electronics (ISNE): Kaohsiung, **2013**.
- [4] Meade, R.D.; Brommer, K.D.; Rappe, A.M.; Joannopoulos, J.D. *Appl. Phys. Lett.* **1992**, 61, 495–497.
- [5] Joannopoulos, J.D.; Jhonson, S.G.; Winn, J.N.; Meade, R.D. *Photonic Crystals-molding the flow of light*, 2nd ed.; Princeton University Press: Princeton, NJ, **2008**.
- [6] Qiu, M.; Jaskorzynska, B. *Appl. Phys. Lett.* **2003**, 83, 1074–1076.
- [7] Madsen, C.K.; Zhao, J.H. *Optical Filter Design and Analysis*; Wiley: New York, **1999**.
- [8] Liu, Y.Z.; Liu, R.J.; Feng, S.; Ren, C.; Yang, H.F.; Zhang, D.Z.; Li, Z.Y. *Appl. Phys. Lett.* **2008**, 93, 2411071–2411073.
- [9] Johnson, S.G.; Fan, S.; Villeneuve, P.R.; Joannopoulos, J.D.; Kolodziejski, L.A. *Phys. Rev. B* **1999**, 60, 5751–5758.
- [10] Costa, R.; Melloni, A. *IEEE Photonics Technol. Lett.* **2003**, 15, 407–403.
- [11] Grimley, C.; Love, M. *Color Space, and Style: All the Details Interior Designers Need to Know but Can Never Find*; Rockport Publishers, **2007**; p 137.
- [12] Kim, S.; Park, I.; Lim, H. *Opt. Express* **2004**, 12, 5518–5525.
- [13] Qiang, Z.; Zhou, W. *Opt. Express* **2007**, 15, 1823–1831.
- [14] Takano, H.; Song, B.S.; Asano, T.; Noda, S. *Opt. Express* **2006**, 14, 3491–3496.
- [15] Little, B.E.; Chu, S.T.; Haus, H.A.; Foresi, J.; Laine, J.P. *J. Lightwave Technol.* **1997**, 15, 998–1005.
- [16] Fan, S.; Villeneuve, P.R.; Joannopoulos, J.D.; Haus, H.A. *Opt. Express* **1998**, 3, 4–11.
- [17] Min, B.K.; Kim, J.E.; Park, H.Y. *Opt. Commun.* **2004**, 237, 59–63.
- [18] Liu, D.; Sun, Y.; Ouyang, Z. *Appl. Opt.* **2014**, 53, 4791–4794.

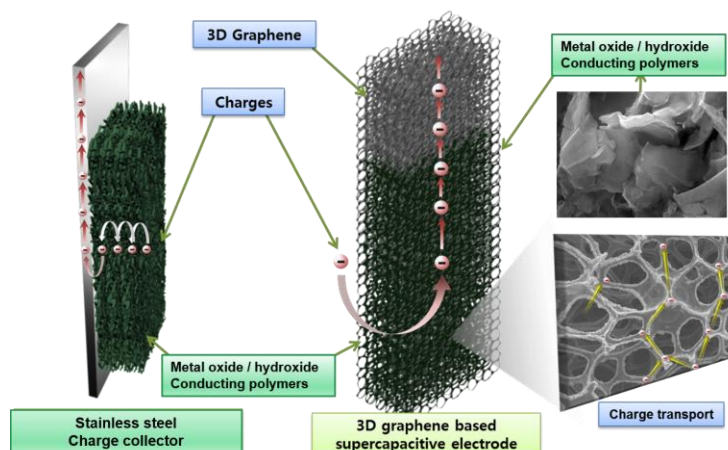
Porous carbon structure for supercapacitors

Min Sik Nam, Umakant M. Patil, Seong Chan Jun*

Nano-Electro Mechanical Device Laboratory, School of Mechanical Engineering, Yonsei University, Seoul 120-749, South Korea

*Corresponding author. Tel: (+82) 2-312-2159; Fax: (+82) 2-2123-5817; E-mail: scj@yonsei.ac.kr

Table of contents



Nanostructured pseudocapacitive materials decorated 3D graphene.

ABSTRACT

Porous structure electrode show improved efficiency for energy storage application and electro device because it has very large surface area than other electrode materials. Especially, porous structure collectors such as three-dimensional graphene nickel foam have extraordinarily high conductivity and unique mechanical properties, so these are promising materials for supercapacitor applications. In this study, we apply the methodologies and performance evaluation for several 3D graphene based metal oxides/hydroxides and conducting polymer electrodes with improved electrochemical properties for next-generation supercapacitors.

Keywords: Three dimensional graphene; porous structure; conductivity; supercapacitor.

Acknowledgements

The research was supported by the Korea Research Fellowship Program funded by the Ministry of Science, ICT and Future Planning through the National Research Foundation of Korea (2015-11-1063). This work was partially supported by the Priority Research Centers Program (2009-0093823), Basic Science Research Program (2013R1A1A2A10013147), and the Korean Government (MSIP) (No. 2015R1A5A1037668) through the National Research Foundation of Korea (NRF) funded by the Ministry of Education, Science and Technology (MEST), and the Korea Railroad Research Institute (2015-11-0165).

Reference

1. Wang, G.; Zhang L.; Zhang, J.; *Chem. Soc. Rev.*, **2012**, *41*, 797.
2. Burke, A. F.; *Proc. IEEE*, **2007**, *95*, 806.
3. Obreja, V. V.; *Phys. E.*, **2008**, *40*, 2596.

Synthesis of nitrogen-heterocycles using sustainable metal catalysts

Gopalaiah Kovuru*

Department of Chemistry, University of Delhi, Delhi 110007, India

*Corresponding author. E-mail: gopal@chemistry.du.ac.in

ABSTRACT

The development of sustainable, more efficient and selective organic synthesis is one of the essential research goals in chemistry. In this respect, catalysis is a key technology, since approximately 80 % of chemical and pharmaceutical products are made on an industrial scale by catalysts. In particular, organometallic catalysts have become an established synthetic tool for both fine and bulk chemicals. However, most of the catalysts employed today rely on rare and expensive transition metals with potentially high toxicity and life cycle-wide environmental impacts. Furthermore, these metals cannot be metabolized by biological systems, and resulting catalyst waste may cause environmental problems in the long-term. As a result, researchers are increasingly looking into alternatives including (a) biocatalysis, (b) organocatalysis, and (c) sustainable metal catalysis. The term “sustainable metal catalysis” refers to the use of metals that are nontoxic, abundant, and biologically relevant, for example, magnesium, calcium, manganese, iron, cobalt, nickel, copper, zinc, and molybdenum. Especially iron offers significant advantages compared with precious metals, since it is the second most abundant metal in the earth crust. Several iron salts and iron complexes are commercially available on a large scale or easy to synthesize. We have recently investigated iron-catalyzed oxidative coupling reactions, and we could report the first example of iron-catalyzed oxidative coupling of benzylamines with 2-amino/hydroxy/mercapto-anilines using iron(II) bromide as catalyst to synthesize 1, 3-benzazoles. On the basis of these studies we could further investigate new approaches for the synthesis of bis(indolyl)methanes and quinoxalines using iron catalysts for the first time. These synthetic tools could be applied for the preparation of various biologically potent heterocyclic molecules. We will discuss about our recent studies on the iron-catalyzed oxidative coupling reactions for the synthesis of nitrogen-heterocycles.

Reference

1. Gopalaiah, K.; *Chem. Rev.* **2013**, *113*, 3248.
2. Gopalaiah, K.; Chandrudu, S. N.; *RSC Adv.* **2015**, *5*, 5015.
3. Gopalaiah, K. *et al. Synthesis* **2015**, 1766.

First principles study of fluorine adsorption on zigzag graphene nanoribbons

Neeraj K. Jaiswal^{1*}, Neha Tyagi², Pankaj Srivastava³

¹Discipline of Physics, PDPM-Indian Institute of Information Technology, Design & Manufacturing, Jabalpur 482005, India

²Department of Applied Physics, Delhi Technological University, New Delhi 110042, India

³ABV-Indian Institute of Information Technology & Management, Gwalior 474015, India

*Corresponding author. Tel: (+91) 0761- 2794352; E-mail: neerajkjaiswal@gmail.com



Table of contents

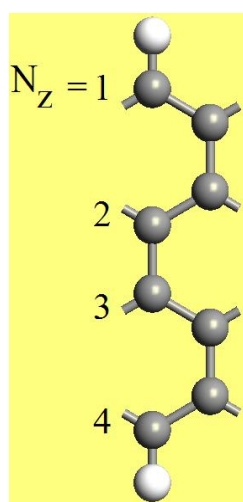


Fig. 1. The schematic figure of pristine ($N_z=4$) ZGNR and the convention used to define the ribbon width.

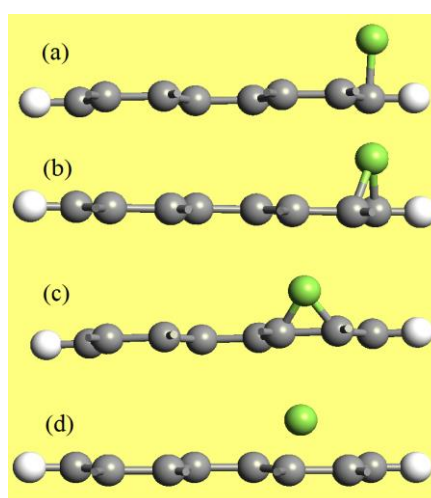


Fig. 2. The side view of fluorine adsorbed ZGNR ($N_z=4$). Grey, white and green spheres represent C, H and F atoms respectively.

ABSTRACT

Density functional theory (DFT) based first principles investigations have been performed to study the structural and electronic properties of fluorine (F) adsorbed H-terminated zigzag graphene nanoribbons (ZGNR). The adsorption of F has been considered at the edge as well as at the centre of the ribbon. We investigate various adsorption sites to reveal the structural stability of F adsorbed ZGNR. The bridge (above C-C bond), top (above the C atom) and the hole (above the centre of hexagon) sites were considered and named as B, T and H respectively for the present study. The convention of defining the ribbon width and various sites used for adsorption are depicted in **Fig. 1** and **Fig. 2**. It is revealed that the F atom forms a chemical bond with the nearest available C atom except for the H site which exhibit a physical adsorption. Adsorption at the edge of ribbon is more energetically stable than the centre adsorption except for H site. Further, ribbons undergo a structural deformation upon the adsorption of F atoms. Particularly, the C atom bonded with guest F atom is elevated from the planar geometry for edge as well as for centre adsorption. The magnitude of elevation varies as a function of adsorption site. Interestingly, the adsorption at T site is found more energetically favourable than that of B or H site. The energy difference of T configuration from B and H site is 0.61 eV and 1.65 eV respectively. After optimization, F atom finds minimum energy configuration slightly off the T site and the angle between F and nearest C atoms (i.e. $\angle F-C-C$) is found to be 107.81° instead of ideal 90° (for T position). The terminating H atom and adsorbed F atom both are displaced in opposite directions so that the angle between them ($\angle F-C-H$) comes out to be 104.36° . The F-C bond length varies from 1.43 \AA to 1.47 \AA which is in excellent agreement with the previous studies on confined graphene/graphene nanodots [1, 2]. The adsorption of F on ZGNR also affects the electronic properties of considered structures in a significant manner. Additional electronic states are originated in the vicinity of Fermi level which indicates towards the possibility of induced magnetism. Further, the changes in electronic properties confirm that H-terminated ZGNR can be used for applications in F sensing.

Keywords: Nanoribbon; fluorine; adsorption; band structure.

Acknowledgements

NKJ is thankful to DST SERB for providing financial assistantship through research grant SB/FTP/PS-101/2014. Authors also acknowledge ABV-Indian Institute of Information Technology & Management, Gwalior for computational facilities and PDPM-Indian Institute of Information Technology, Design & Manufacturing Jabalpur for infrastructural facilities.

Reference

1. Zheng, H.; Duley, W.; *Phys. Rev. B*, **2008**, 78, 045421-1-5.
2. Karki, D. B.; Adhikari, N. P.; *Int. J. Mod. Phys. B* **2014**, 28, 1450141-1-15.

Applications of nanotechnology for rural development

Narendra Jain

DRDO Fellow & Former Director, Defence Lab, Jodhpur

*Corresponding author. E-mail: nkjainjd@yahoo.com

ABSTRACT

With more than 60 % of country's population still residing in rural areas India is considered basically to be a rural country. This means that rural economy is the deciding factor for country's economy. In the words of **Mahatma Gandhi**- Father of the Nation "**India lives in villages**". It is ironic that in spite of more than six decades of our independence and consistent efforts of successive governments, both at center and state, most of rural population still lack the same quality of life as is enjoyed by people living in urban and sub urban areas. The underlying reason behind it is the dependence of rural population on agriculture and in turn dependency of agriculture on Mother Nature. Moreover, rural population lacks in adequate health care, safe drinking water, sanitation and employment at local level.

Despite significant efforts by Govt. in implementing various schemes like MNREGA, food security bill etc. together with the work by some NGO's the persisting poverty and backwardness in the rural areas still continue to be major challenge and a matter of serious concern. Some economists correlate the poor rural economic growth to the inadequacy of the public expenditure. But it may not be the only reason as less emphasis has been laid on using advanced technologies to boost up rural economy. We believe that the use of newly emerging technologies such as **nanotechnology** can address many of the problems and may prove highly beneficial for enhancing productivity in agriculture sector, generating new employment opportunities, better healthcare etc. in rural areas.

Nanotechnology is the act of manipulating materials in the size range of few of atoms or molecules thereby generating novel chemical, physical and biological properties. The areas where Nanotechnologies can impact rural development include:

1. **Water:** Safe drinking water
2. **Energy:** Harnessing solar energy (photovoltaic, thermal)
3. **Agriculture:** Increasing production by minimizing use of insecticides, pesticides and even under harsh environmental conditions
4. **Waste Biomass Management:** Converting waste biomass into useful products.

My talk will focus, with examples, on nanomaterials and technologies developed, underdevelopment or should be developed for application in the above four areas together with special mention about some functional materials derived from biomass waste from water remediation and soil management applications.

Nano materials used in water purification include metal oxide nanoparticles, carbon based nano materials (carbon nanotubes and graphene), dendrimers and nanoporous materials. These materials are used in the form of adsorbents, membranes or catalysts to effect water disinfection, removal of impurities and/or desalination to make water, received from ponds, rivers etc., fit for consumption by human and live stocks.

Similarly, nanomaterials and nanodevices can profitably be used for harnessing and conversions of abundantly available solar energy into heat or electrical energy which should be useful in rural areas for illumination of homes, irrigation, running cottage industries etc. In the field of agriculture nano sized fertilizers, pesticides, etc. should be able to minimize their wastage and enhancing the efficacy while nano catalysts should be able to convert the waste biomass into many useful products produced at cottage industries level, run on solar energy resources, in villages. Such ventures are conducive for generating family level self-employment for the rural population and reduce their dependency on agriculture alone. Finally, implementation of such simple nanotechnologies in selected area, training of rural people, etc appear very promising to realize the dreams of Father of the Nation – "**Self-Reliant India**" through rural development.

Multiferroic bismuth ferrite thin films: Nanostructure and doping effect

Sushil Kumar Singh*

Solid State Physics Laboratory, DRDO, Lucknow Road, Timarpur, Delhi 110054, India

*Corresponding author. Tel: (+91) 1123903433; Fax: (+91) 13137568; E-mail: sk.singh@sspl.drdo.in

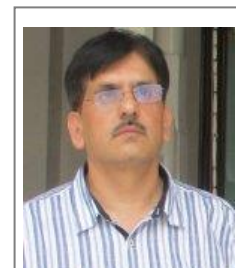
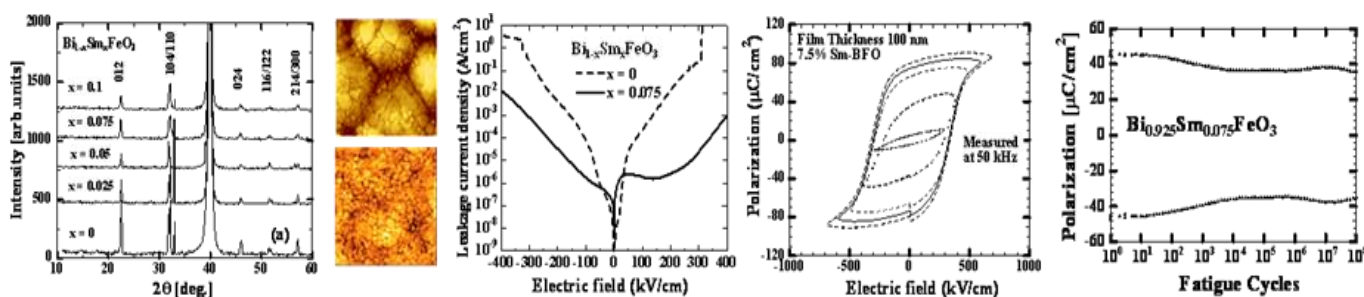


Table of contents



Nanostructure and ions doping effect in Multiferroic BiFeO₃ thin films.

ABSTRACT

BiFeO₃ (BFO) is one of the most widely studied multiferroics for potential device applications because of only multiferroic shows the ferroelectric and magnetic coupling above the room temperature. We thoroughly investigated Mn, Cr, and Ni-substitution at the Fe -site and La, Nd, Sm- substitution at the Bi site of BFO for reducing the leakage current above the coercive field (E_c). BFO shows enhance ferroelectric polarization around $100 \mu\text{C}/\text{cm}^2$ and piezoelectric coefficient $60 \text{ pm}/\text{V}$. The chemical substitution at Bi-site with smaller ionic radii such as Sm^{3+} than Bi^{3+} of the perovskite structure is expected to cause more significant structure distortion and improved ferroelectric, piezoelectric and magnetic properties. The electrical properties are enhanced due to the structural modification with Sm-substitution. The saturated P - E hysteresis loops were measured first time successfully in a 100 nm-thick films with 5V coercive voltages¹. The Sm-substitution in BFO improved the fatigue endurance, no significant degradation in polarization has been observed after 10^8 fatigue cycles. The results are important since it increases the potential of the material for semiconductors devices such as ferroelectric random access memory (FeRAM), spintronics and MEMS based device fabrications. These substitutions are expected to suppress the impurity phases, improve the surface morphology and reduce the leakage current in the films. We observed that Sm-substituted BFO films, reduction in grains size and improved the leakage characteristics. The leakage current in BFO thin film flows through not only grain boundary but also the grain itself. It shows that the grain size in BFO films plan a crucial role and leakage current of BFO strongly depends on its microstructure of the films. The multiferroic properties of BFO films highly depend on doping and nanostructure of the films.

Keywords: BFeO₃; multiferroic thin films; nano-structure; doping effect.

Acknowledgements

The project is funded by SSPL, DRDO (TASK-24).

Reference

1. Singh, S. K.; *Solid Thin Films*, **2013**, 527, 126,

Electronic circuit and functional devices with green materials: State-of-the art and challenges

K. Sreenivas

Department of Physics and Astrophysics, University of Delhi, Delhi, 110007, India

*Corresponding author. E-mail: kondepudysreenivas@gmail.com



ABSTRACT

Designing electronic circuitry with graphite-on-paper alongwith an assembly of surface mounted passive and active devices/sensors promises a cost-efficient and an “environmental friendly” technology. The possibility for using paper is very intriguing when compared with the well-established use of semiconductor silicon in the form single crystal wafers/membranes/ribbons), and the use of other flexible glass/plastic sheets. Simple pencil drawn electrically conducting wires/electrodes and use of graphite-ink based technologies for (2D/3D) printable electronics is gradually emerging. Fabrication of conformable/configurable and deformable sensors, flexible/foldable circuits and displays, on unusual and unfamiliar substrates including paper, transparent paper, nano-paper are being envisaged. Normal paper used in daily life provides an interesting platform. It is electrically insulating, heat resistant, light weight and can be easily shaped, and conveniently disposed. Its surface is amenable for easy exfoliation of conducting graphite particles through mechanical abrasion, cleavage of bulk graphene, or graphitic deposition by normal evaporation/sputter deposition techniques. Interesting developments have been reported and potential use of conducting graphite tracks/resistors, UV sensors, piezo-resistive, bio-sensors, thin film batteries and super capacitors have been demonstrated, but there is still room for improvement. To attain the desired specifications, standards, and acceptability by the electronics industry presents numerous challenges. Issues related to patterning, resolution, contacting and design methodology demand special attention. To compete with the device performance already achieved on other substrates, although the development of carbon and paper based electronics appears like a pipe dream this emerging area offers new possibilities and opportunities. Some recent results in the authors laboratory combining three strategic materials of interest on paper substrates will be presented, and the focus will be on (i) Growth of ZnO on paper which exhibits multifunctional properties and is bio-compatible (ii) use of graphitic electrodes, and (iii) the response of ultraviolet (UV) sensors on paper will be discussed.

Preparation and applications of lipid carriers

Pao Chi Chen*

Department of Chemical and Materials Engineering, Lunghwa University of Science and Technology, Taiwan

*Corresponding author. Tel: (+886) 2-82093211-5205, (+886) 2-82000506; E-mail: chenpc@mail2000.com.tw

ABSTRACT

Lipid carriers, such as SLN (solid lipid nanoparticle) and NLC (nano structured lipid carriers), are useful innovation materials for cosmetic and pharmaceuticals in 21 century. In order to better understand the applications of both materials, it needs to be studied for the preparation, characterization, and application of both. First, this talk focuses on the preparation, by hot homogenization process, and physical characterization of SLN and NLC aqueous dispersions concerning their particle size, zeta potential, crystallinity index, and rheological properties for different operating conditions, i.e., pre-emulsion time, pressure, cycle time, and storing temperature. The structure of lipid carriers was investigated by using TEM and NMR. It was found that the major composition of lipid carriers is oil, wax, surfactant and excipient. The characteristics of NLC and SLN are influenced by liquid lipid, solid lipid, surfactant and other additives. Therefore, how to obtain the optimum composition of SLN and NLC becomes significant in the final applications. In addition, the NLC has multiple advantages and could be concluded into SOPI (stabilization, occlusion, protection, and integrity) in literature. Due to this, numerous studies on the applications of NLC and SLN have been conducted. In order to obtain desired formulation, an effective experimental design is required to search for the optimal formula of SLN and NLC. Important outcome data, such as emulsion rate, encapsulation efficiency and percutaneous absorption, are explored in here. Finally, commercial applications of SLN and NLC are also discussed.

Keywords: Lipid carriers; particle size; zeta potential; crystallinity index; rheological properties.

Acknowledgements

We thank the financial support from AC Scientific Co. and Lunghwa University of Science and Technology.

Interaction of hydrogen atoms and molecules with zinc oxide single crystal surfaces

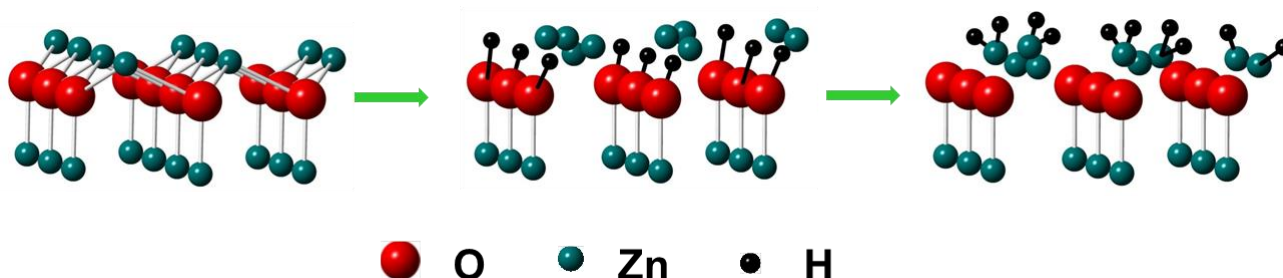
Md. Abdul Motin, Porbir Chandra Roy, Chang Min Kim*

Department of Chemistry, Kyungpook National University, Daegu, 702-701, Korea

**Corresponding author. Tel: (+82) 539505330; Fax: (+82) 539506330; E-mail: cmk@knu.ac.kr



Table of contents



Adsorption of atomic hydrogen on $\text{ZnO}(000\bar{1})$

ABSTRACT

Zinc oxide (ZnO) has attracted a significant amount of attention because of its potential applications as catalysts, gas sensors, wide band gap semiconductors and other microelectronic devices. Intense research effort has been focused to understand the unique properties of ZnO related to hydrogen in the bulk. It is generally proposed that intrinsic hydrogen in the bulk is responsible for the *n*-type conductivity of ZnO. Interstitial hydrogen is believed to be incorporated during crystal growth and/or by the dissociative adsorption of H_2 molecules in the atmosphere. Even though there are some controversial reports about the role of hydrogen in the bulk, ZnO shows higher conductivity under hydrogen ambient. So, it is crucial to understand the interaction of hydrogen with ZnO surfaces for the fabrication of ZnO-based devices. We have been studying the initial adsorption of atomic hydrogen on ZnO single crystal surfaces and subsequent diffusion into the bulk by using TPD and XPS. In this talk, we will present the adsorption of atomic hydrogen on three different ZnO single crystal surfaces; $\text{ZnO}(0001)$, $\text{ZnO}(000\bar{1})$, and $\text{ZnO}(10\bar{1}0)$. We will report the identification of surface and bulk hydrogen atoms and the activation energy for the bulk diffusion of the surface hydrogen atoms. Anisotropic migration of H in the bulk of ZnO will be discussed. We have also examined the interaction of molecular hydrogen (H_2) with a ZnO (0001) surface *in situ* over a wide pressure (10^{-3} – 250 mTorr) and temperature (300 – 600 K) range using ambient-pressure XPS (AP-XPS). We have identified the formation of surface O-H bonds on $\text{ZnO}(0001)$ under hydrogen environment as a function of temperature and pressure. The surface has been successfully monitored while maintaining equilibrium between dissociative adsorption and associative desorption of hydrogen.

Keywords: ZnO; hydrogen; surface adsorption; bulk diffusion; ambient pressure.

Physicochemical aspects of dye-surfactant interactions

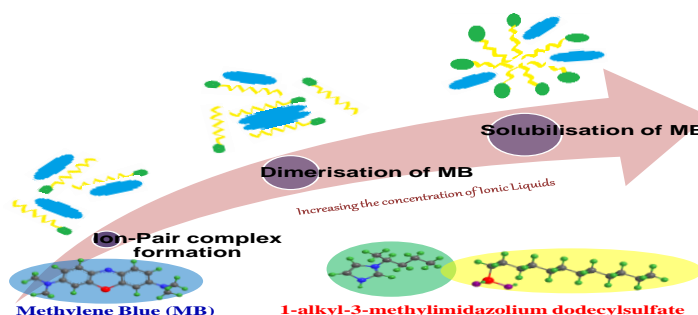
Rakesh Kumar Mahajan*, Renu Sharma, Reshu Sanan

Department of Chemistry, Guru Nanak Dev University, Amritsar, 143005, India

*Corresponding author. Tel: (+91) 9872856579; Fax: (+91) 1832258820; E-mail: rakesh_chem@yahoo.com



Table of contents



ABSTRACT

In view of the diverse applications of dye-surfactant mixed systems in several areas of science, dye-surfactant mixtures have been an area of recent research. The association of surfactant and dyes are a subject of numerous investigations since surfactants are used as auxiliaries in most textile finishing processes. Dye-surfactant complexes find applications in extraction of dyes by enhanced micellar ultra-filtration, surfactant mediated cloud point extraction and also used to customize the uptake of dye into various substrates like cellulose. So, we aim to characterize the dye-surfactant mixtures comprised of new class of surfactants *i.e.* ionic liquids and functionalized monomeric and dimeric (gemini) pyridinium cationic surfactants and cationic/anionic dyes with regard to their micellar, interfacial and binding behavior. Ionic liquids are a new class of surfactants with improved physicochemical characteristics and much better surface properties than conventional cationic surfactants. Interactions among biamphiphilic ionic liquids (BAILs)/alkyloxypyridinium/gemini pyridinium surfactants and methylene blue/alizarin red S/eosin yellow dyes have been explored and micellar, interfacial, binding and electrochemical parameters are obtained. A combination of various techniques *viz.* conductivity, surface tension, dynamic light scattering, fluorescence, UV-visible absorption, $^1\text{H-NMR}$ and electrochemical techniques such as cyclic voltammetry, linear sweep voltammetry, differential pulse voltammetry and potentiometry have been used to provide a comprehensive appraisal of the dye-surfactant mixed systems.

Keywords: Biamphiphilic ionic liquids; voltammetry; binding studies.

Acknowledgements

The corresponding author thanks CSIR, DST, UGC, UGC-DAE and BRNS funding agencies for financial support.

Reference

1. Kaur, R.; Sanan, R.; Mahajan, R. K.; *J. Colloid Interface Sci.* **2016**. DOI: [10.1016/j.jcis.2016.02.006](https://doi.org/10.1016/j.jcis.2016.02.006)
2. Sharma, R.; Kamal, A.; Mahajan, R. K.; *Soft Matter*, **2016**, 12, 1736.
3. Sharma, R.; Kamal, A.; T. S. Kang, R.K. Mahajan, *Phys. Chem. Chem. Phys.* **2015**, 17, 23582.
4. Sanan, R.; Kang, T. S.; Mahajan, R. K.; *Phys. Chem. Chem. Phys.* **2014**, 16, 5667.

New synthetic approaches to heterohelices

Ryo Irie^{1*}, Masaki Furusawa¹, Yusuke Shigeta¹, Daiki Ueda¹, Sachie Arae¹, Hitoshi Fujimoto¹, Michinori Sumimoto², Kazunobu Igawa³, Katsuhiko Tomooka³

¹Department of Chemistry, Graduate School of Science and Technology, Kumamoto University, 2-39-1 Kurokami, Chuo-ku, Kumamoto 860-8555, Japan

²Materials Chemistry, Graduate School of Science and Engineering, Yamaguchi University, 2-16-1 Tokiwadai, Ube 755-8611, Japan

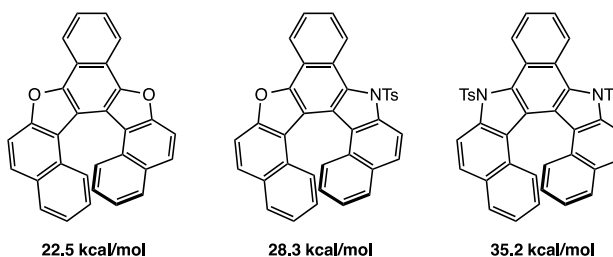
³Institute for Materials Chemistry and Engineering, Kyushu University, 6-1 Kasuga-koen, Kasuga 816-8580, Japan



*Corresponding author. Tel: (+81) 963423379; Fax: (+81) 963423379; E-mail: irie@sci.kumamoto-u.ac.jp

Table of contents

New dioxa-, aza-oxa-, and diaza-hetero [7] helicenes were synthesized by Pd-catalyzed cyclodehydrogenation of aromatic diyne systems and their stereochemical stabilities were evaluated by DFT calculations. Another synthetic approach based on base-catalyzed cycloisomerization will be also reported.



Racemization barriers ΔG^\ddagger of the heterohelicenes (B3LYP/6-311G(d,p) level).

ABSTRACT

Extended π -conjugated heterocycles, in which heteroaromatic and aromatic rings are condensed alternately, have aroused enormous interest and have been exploited as components of photoelectronic devices [1]. In this context, it should be intriguing to investigate practical synthesis of heterohelicenes, angularly fused heteroaromatic compounds with helical chirality, for producing novel functional materials of chiroptical properties. Herein, we will report new synthetic approaches to unique heterohelicenes containing a dibenzofuran and a carbazole structure based on the palladium-catalyzed dehydrogenation [2,3] of aromatic diynes and base-catalyzed cycloisomerization [4,5] of *o*-alkynyl heterobiaryls. The stereochemical behavior of the heterohelicenes thus obtained will be also presented on the basis of kinetic analysis as well as DFT calculations.

Keywords: Heterohelicene; catalytic domino reaction; cyclodehydrogenation; cycloisomerization

Acknowledgements

This work was partially supported by a Grant-in-Aid for Scientific Research on Innovative Areas "Advanced Molecular Transformations by Organocatalysts" (No. 26105749) from MEXT, and the Cooperative Research Program of the "Network Joint Research Center for Materials and Devices (IMCE, Kyushu University)".

Reference

1. Y. Shen, C.-F. Chen, *Chemical Reviews*, 112(3), 1463-1535, **2012**.
2. R. Irie, A. Tanoue, S. Urakawa, T. Imahori, K. Igawa, T. Matsumoto, K. Tomooka, S. Kikuta, T. Uchida, T. Katsuki, *Chemistry Letters*, 40(12), 1343-1345, **2011**.
3. M. Furusawa, T. Imahori, K. Igawa, K. Tomooka, R. Irie, *Chemistry Letters*, 42(10), 1134-1137, **2013**.
4. M. Furusawa, K. Arita, T. Imahori, K. Igawa, K. Tomooka, R. Irie, *Tetrahedron Letters*, 54(52), 7107-7110, **2013**.
5. R. Irie, M. Furusawa, K. Arita, K. Igawa, K. Tomooka, *Journal of Synthetic Organic Chemistry, Japan*, 72(10), 1131-1142, **2014**.

Quantum dot and carbon assisted cost-effective photovoltaic power generation

Sayan Bhattacharyya*

Department of Chemical Sciences, Indian Institute of Science Education and Research (IISER) Kolkata, Mohanpur 741246, India

*Corresponding author. E-mail: sayanb@iiserkol.ac.in

ABSTRACT

A promising approach towards low-cost third-generation photovoltaic devices involves semiconductor quantum dots (QDs) as solar harvesters owing to their band gap tunability, high absorption coefficient, solution processability and multiple exciton generation. Although QD solar cells (QDSCs) are expected to cross the Shockley-Queisser power conversion limit of ~32 %, the device performance have only reached moderate power conversion efficiencies (PCE) of 6–9 % due to interfacial charge recombination at the TiO₂/QD-electrolyte interface which drives back the photo-generated electrons into the oxidized polysulfide electrolyte. This lecture will discuss few validated strategies with colloidal QDs to improve the PCEs. The first strategy is heteroatom doping in QDs to increase the lifetime of excited charge carriers and mitigate the deleterious charge recombination at the interface. Maximal substitutional doping of Mn²⁺ ions inside CdS QD lattice could boost the PCE by 66.4% as compared to undoped CdS solar cells [1]. Secondly dual sensitization through linker-assisted self-assembly of CdTe/CdS core/shell QDs on porous TiO₂ and deposition of another CdS *quasi-shell* could achieve PCE as high as 6.32(9) % (6.41 % for the champion cell), the highest for any aqueous processed QDSC [2]. Third, combinations of graphene oxide ribbons and Cu_xS nanostructures with tuned Cu:S stoichiometry in the counter electrode could boost the PCE further to 6.81(8) % [3]. Lastly, a bio-waste derived highly catalytic porous carbon counter electrode will be discussed as a greener non-metal alternative to conventionally used metal-based counter electrodes [4].

Reference

1. G. Halder and S. Bhattacharyya, *J. Phys. Chem. C* **2015**, *119*, 13404.
2. A. Sahasrabudhe and S. Bhattacharyya, *Chem. Mater.* **2015**, *27*, 4848.
3. D. Ghosh, G. Halder, A. Sahasrabudhe and S. Bhattacharyya, **2016** (Unpublished).
4. A. Sahasrabudhe, S. Kapri and S. Bhattacharyya, **2016** (Unpublished).

See discussions, stats, and author profiles for this publication at: <https://www.researchgate.net/publication/297904169>

Prediction of Surface Roughness in CNC Turning of Aluminum 6061 Using Taguchi Method and ANOVA for the Effect of Tool Geometry

ARTICLE · JANUARY 2016

READS

19

3 AUTHORS, INCLUDING:



Ranganath M Singari

Delhi Technological University, Formerly D...

56 PUBLICATIONS 105 CITATIONS

SEE PROFILE



Vipin vp

Delhi Technological University

33 PUBLICATIONS 69 CITATIONS

SEE PROFILE

Prediction of Surface Roughness in CNC Turning of Aluminum 6061 Using Taguchi Method and ANOVA for the Effect of Tool Geometry

Ranganath M Singari¹, Vipin², Sanchay Gupta³

^{1,2,3}(Department of Mechanical, Production and Industrial Engineering, Delhi Technological University, Delhi, India)

¹ ranganathdce@gmail.com

Abstract : Surface Roughness is one of the major attributes that define and evaluate the quality characteristics of the product after it is machined. Consequently, it is an important criterion of determining the quality of the product post machining processes and analysis of the response becomes important. The paper delves the parameters that affect the surface roughness in CNC Turning of Aluminum 6061. The process factors taken are rake angle, nose radius, cutting speed, feed rate and depth of cut and the analysis of influence of these parameters is carried out using Taguchi Method. An L27 orthogonal array has been employed to carry out the analysis and the influence of the factors are studied using Analysis of Variance (ANOVA) method. Feed Rate is found to be the most influential and significant factor followed by rake angle of the tool.

Keywords: Surface Roughness, CNC Turning, Taguchi Method, Orthogonal Array, ANOVA, rake angle

I. INTRODUCTION

Surface roughness is an important characteristic used to determine and evaluate the quality of a turned product. However, the study and optimization of surface roughness is not as easy as determining any other variation. The study of Surface Roughness is harder to achieve as it depends on various variables. These variables are both controllable and uncontrollable. The controllable variables being tool rake angle, feed rate, spindle speed, depth of cut etc. while factors such as wearing of tool, material friction, tool degradation are much harder to control. Surface roughness of a machined product could affect several of the product's features such as surface friction, wearing, light reflection, heat transmission, ability of distributing and holding a lubricant, coating and resisting fatigue [1]. Thus, achieving an optimal roughness response has become vital for industries to improve their quality and merit. Identifying the most influential and important parameter allows proper selection of tool material that prolongs the life of tool and minimizes the surface roughness. Consequently, A recent advent of Design of Experiments has given vent to various methods such as Taguchi Method, Response Surface Methodology, etc., that have not only allowed scholars and industrialists to efficiently organize the process of optimizing roughness but has also given way to several techniques to reduce the number of trials that have to be carried out to obtain optimal response. The Taguchi Method is a statistical tool that allows creation of a design by choosing the most optimal path in an operation environment. Since noise factors are also present in the process that cannot be controlled, this method identifies the values of controllable factors that minimizes the effect of noise factors and provide an optimal response. Thus design of experiments by Taguchi method was adopted for analyzing the surface

roughness and Analysis of Variance (ANOVA) was used for finding the most significant factor that affects the surface response.

Prajwalkumar M. Patil et al. [7] observed and analyzed the effect of cutting parameters on the surface roughness and hardness. Taguchi method was analyzed by the authors in the optimization of cutting parameters. L9 orthogonal array was employed to carry out the analysis. The analysis of means (ANOM) and Analysis of variance (ANOVA) were carried out to determine the optimal parameters level and obtain level of importance of each parameter. From the ANOVA the feed had maximum significance in case of Ra and Rz. Ranganath M S et al. [15] developed a prediction model of surface roughness for turning EN-8 steel with uncoated carbide inserts using Response Surface Methodology (RSM). A multiple regression model was developed in the form of correlating dependent parameter surface roughness with cutting speed, feed rate and depth of cut, in a turning process. The Box Behnken Design was used to plan the experiment. The Analysis of variance (ANOVA) was done to test for significance of regression model. The control parameter of cutting speed was found out to have the strongest effect on the surface roughness among the selected parameters; and varied inversely with response. Also surface Roughness was inversely proportional to depth of cut. Murat Sarikaya et al. [5] used Taguchi design and RSM Technique under MQL for analyzing CNC turning parameters. The results were analyzed using 3D surface graphs, signal to noise ratios and main effect graphs of means. Also Mathematical model output showed that the developed RSM model was statistically significant and suitable for all the cutting conditions because of higher R² value. Ranganath M S et al. [12] presented a paper on analysis of the effect of the cutting speed, feed rate and depth of cut on surface roughness.

The author employed an L27 orthogonal array to carry out the analysis. The ANOVA values proved that speed is the most significant factor, the next significant factor was depth of cut followed by feed. The response tables for S/N ratios and the means showed that feed is the dominant factor followed by depth of cut and speed. It was concluded that increase in cutting speed decreases the surface up to a certain level but as speed increases beyond a certain level the surface roughness increases. The optimal combination of process parameters for the work with regard to minimum surface roughness were speed at 1900 rpm, depth of cut 0.25 mm and feed of 0.12 mm/rev. İlhan Asiltürk et al. [4] used the Taguchi method and L9 orthogonal array were used to reduce number of the experiments. Analysis of Variance (ANOVA) was applied to investigate effects of cutting speed, feed rate and depth of cut on surface roughness. Results indicated that the feed rate had the most significant effect on Ra and Rz. The effects of two factor interactions of the feed rate-cutting speed and depth of cut-cutting speed appeared to be important. Chinnasamy Natarajan et al. [2] predicted and analyzed surface roughness factors of a non-ferrous material using Artificial Neural Network (ANN). A model was developed to predict the surface roughness of material (Brass C26000) through Artificial Neural Networks technique by utilizing feed-forward back propagation training algorithm using Matlab (2009a) software for the data obtained. As the spindle speed increases, for lower feed rates, the surface roughness decreases, for higher feed rates, the surface roughness changes considerably. The depth of cut influences the surface roughness considerably for a given feed rate. The increase in feed rate causes the surface roughness to increase and then decrease. For lower depth of cut, surface roughness decreases and then increases.

This paper presents the experimental approach for studying the effects of machining parameters on the surface roughness of the machined work-piece. The experimentation produced strong interactions between the various control factors. The analysis of variance (ANOVA) technique and the study of F-test statistics revealed strong interactions between the tool geometry and the various turning parameters undertaken. For different levels of the factors, different output values of surface roughness were obtained. The most influential and significant interactions were obtained between the tool geometry and cutting parameters. A systematic and organized study of the response values and the control factors in the experiment were tabulated for the design table with maximum utility of the resources.

II. TAGUCHI METHOD

Taguchi Method is an important tool for robust design based on Orthogonal Array which gives much reduced variance for the experiments with the optimum setting of the control parameters. Taguchi method provides a way of developing a robust design that reduces the number of experimentations by creating a design table of the levels for the control factors. The inherent principle of orthogonality in the technique provides a simple, effective and systematic qualitative optimal design to a lower relative cost. Taguchi designs estimate the effects of factors on the response mean and variation. An orthogonal array means the design is balanced so that the factor levels are

weighted equally. Because of this, each factor can be assessed independently of all the other factors, so the effect of one factor does not affect the estimation of a different factor. This reduces the time and cost associated with the experiment when fractionated designs are used. In this paper Taguchi approach is used to study and analyze the effect of control parameters viz. rake angle, nose radius, cutting speed, feed rate and depth of cut on the roughness of Aluminum 6061 using cemented carbide tool inserts in CNC turning to achieve optimal setting. To find the most influential and significant factor Analysis of variance (ANOVA) is used by fitting a general linear model.

The steps involved in Taguchi technique are:

1. Determination of main function to be optimised, side effects and failure mode.
2. Determination of noise factor, testing condition and quality characteristics.
3. Determination of the control factor and their levels.
4. Choosing the orthogonal array and matrix experiment and conducting the matrix experiment.
5. Carrying out the analysis of the data and predicting the optimum level and performance.
6. Performing the verification experiment and planning the future action.

III. EXPERIMENTAL SETUP

CNC Lathe

The entire turning was carried out on CNC Lathe LMW LL20TL3 which consists of the machining unit with a three jaw self-centering independent chuck and a computer numerically controlled tool slide containing 8 tool posts. The tool post assembly can move in x and z directions where x axis represents the movement in vertical direction which provides the depth of cut. The movement in z direction represents vertical displacement of the tool post assembly and is responsible for the feed of the tool to the work piece and also gives the location of the tool slide. The offset or the zero with respect to the work-piece, in both the x and z directions, is defined and the commands for the turning program are provided in the form of a program which is fed into the system. The machine is also provided with a automatic lubrication motor for its slides.

Cutting Tool material

Cemented Carbide Insert type Tools were used as the cutting tool in the turning operation. The Carbide cutting tool provided with the CNC lathe Trainer was a 30 mm square tool with 60 mm length having the same tool angles as for a normal turning tool. The tool used was cemented carbide insert type. The geometry of tool is: Rake angle 60(+ve), 50 (+ve) clearance angle, 600 (+ve) major cutting edge angle, 600 (+ve) included angle and 00 cutting edge inclination angle [8]. All the three elements-tungsten, molybdenum and cobalt help in achieving high hot hardness; the first two do so by forming complex carbides and the cobalt forms an alloy by going into solid solution in the ferrite matrix and thus raising the recrystallization temperature [8]. Vanadium in high speed steels increases the wear resistance of tool at all operating

temperatures. Vanadium also helps to inhibit grain growth at the high temperatures required in heat treatment [8].

Work piece Material

Industry grade Aluminium 6061 was used as the work-piece material for the turning operation. Standardized material was selected to ensure consistency of the alloy, and is a common wrought alloy used in industries. Aluminum 6061 marks as one of the most extensively used aluminium in the series 6000. This structural alloy is one of the most versatile of the heat-treatable alloys, is popular for medium to high strength requirements and has good toughness characteristics. Several applications of this structural alloy range from transportation components to machinery and equipment applications to recreation products and consumer durables. It is also widely used in turning processes for producing various automotive components.

It has excellent atmospheric corrosion resistance to atmospheric conditions and sea water. This alloy also offers good finishing characteristics and responds well to anodizing. Alloy 6061 can be easily welded and joined by various commercial methods. Alloy 6061 has adequate machinability characteristics in the heat-treated condition in screw machine applications. The control inputs were fed in the form of part program including dimensions of the work piece, cutting parameters viz., depth of cut in mm, feed rate and the Speed which was available from 50-3500 rpm and feed in mm/min. The elemental composition of the aluminium 6061 alloy is given in table 1.

Table 1: Elemental Composition of work-piece

Composition	% weight
Magnesium (Mg)	0.8 to 1.2
Silicon (Si)	0.4 to 0.8
Iron (Fe)	0 to 0.7
Copper (Cu)	0.15 to 0.4
Chromium (Cr)	0.04 to 0.35
Zinc (Zn)	0 to 0.25
Manganese (Mn)	0 to 0.15
Titanium (Ti)	0 to 0.15
Residuals	0 to 0.15

IV. EXPERIMENTATION AND ANALYSIS

Table 2 gives the various control factors taken and the subsequent levels defined for the parameters during the experiment. The first column specifies the codes assigned to each factors during the analysis, the second column names the corresponding factor for the code while the last three columns instantiate the three levels specified for each control factor.

Table 2: Cutting parameters and levels

Code	Cutting Parameter	Level 1	Level 2	Level 3
A	Rake Angle	16	18	20
B	Nose Radius	0.4	0.8	1.2
C	Cutting Speed (rpm)	175	225	275
D	Feed Rate (mm/rev)	0.05	0.10	0.15
E	Depth of Cut (mm)	0.1	0.2	0.3

The surface roughness of the machined surface has been measured Taylor Hobson Tally surf instrument, Surtronic 3, is a portable, self-contained instrument for the measurement of surface texture and is suitable for use in both the workshop and laboratory. The evaluation of parameters and other functions of the instrument are microprocessor based. The measurement values of surface texture of the work-piece are displayed on the LCD screen or the output can be further produced by connected the tally surf to the computer.

Surface Roughness being a dependent variable has been analyzed by designing an L27 orthogonal array. Table 3 shows a standard L27 (3^5) orthogonal array of Taguchi design with experimental results and various levels of control factors.

The objective of the present work is to minimise the surface roughness of the machined work-piece, thus 'Smaller is better' type classification of Taguchi technique for analysing surface roughness is exploited. The main effects plot for means is given in fig.1. They depict the variation of individual response with the five control parameters viz., rake angle, nose radius, cutting speed, feed rate and depth of cut. The value of each process parameter and the response value are represented by the x and y-axis respectively. The central horizontal line indicates the mean value of the surface response. The subsequent plot gives information on the individual dependency of response on each control parameter and is used to determine the optimal design for experiments to minimise surface roughness.

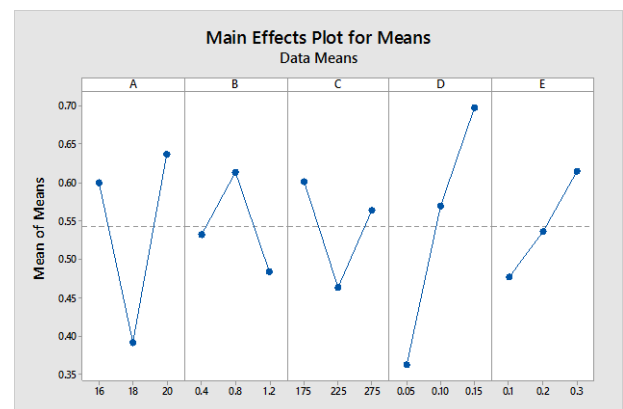


Figure 1: Main Effect Plot for Means

Table 3: Design Table and Response readings

Expt No.	Control Factors					Ra (μm)	S/N Ratio
	A	B	C	D	E	Mean	
1	1	1	1	1	1	0.42	7.5350
2	1	1	1	1	2	0.47	6.5580
3	1	1	1	1	3	0.51	5.8486
4	1	2	2	2	1	0.57	4.8825
5	1	2	2	2	2	0.62	4.1522
6	1	2	2	2	3	0.66	3.6091
7	1	3	3	3	1	0.65	3.7417
8	1	3	3	3	2	0.71	2.9748
9	1	3	3	3	3	0.79	2.0475
10	2	1	2	3	1	0.42	7.5350
11	2	1	2	3	2	0.45	6.9357
12	2	1	2	3	3	0.5	6.0206
13	2	2	3	1	1	0.26	11.700
14	2	2	3	1	2	0.31	10.172
15	2	2	3	1	3	0.34	9.3704
16	2	3	1	2	1	0.36	8.8739
17	2	3	1	2	2	0.41	7.7443
18	2	3	1	2	3	0.48	6.3752
19	3	1	3	2	1	0.6	4.4370
20	3	1	3	2	2	0.68	3.3498
21	3	1	3	2	3	0.74	2.6154
22	3	2	1	3	1	0.75	2.4988
23	3	2	1	3	2	0.87	1.2096
24	3	2	1	3	3	1.14	-1.138
25	3	3	2	1	1	0.27	11.372
26	3	3	2	1	2	0.31	10.172
27	3	3	2	1	3	0.37	8.6360

As is evident from the graph, since the ordinates represent the measured response values and abscissa denotes the various levels for the variables, surface roughness is minimum for rake angle (A) at level 2 (18), nose radius (B) at level 3 (1.2), cutting speed (C) at level 2 (225 rpm), feed rate (D) at level 1 (0.1 mm/rev) and depth of cut (E) at level 1 (0.1 mm). Table 4 is the response table for means and gives the ranking of various parameters as achieved by Taguchi analysis.

Main effects plot for S/N ratio of surface roughness for the data means is as depicted in fig. 2. The S/N ratio plot provides the

information on degree of performance of the control parameters in the presence of the Noise factors. The aim of using this plot is to develop a product insensitive to the variance factor. Since the effect of noise should be minimum on the design parameters, the control factor with the maximum signal to noise ratio finds the optimal value. Thus, the ideal conditions for minimum Surface Roughness as depicted by the plot is level 2 (18) of rake angle (A), level 3 (1.2) of nose radius (B), level 2 (225 rpm) of cutting speed (C), level 1 (0.05 mm/rev) of feed rate, level 1 (0.1 mm) of depth of cut.

Table 4: Response table for Means

Level	A	B	C	D	E
1	0.600000	0.5322	0.6011	0.3622	0.4778
2	0.392200	0.6133	0.4633	0.5689	0.5367
3	0.636700	0.4833	0.5644	0.6978	0.6144
Delta	0.244400	0.1300	0.1378	0.3356	0.1367
Rank	2	5	3	1	4

Table 5 is the response table for S/N ratio and gives the ranking of various parameters as achieved by Taguchi analysis on the basis of SN ratio.

Table 5: Response table for S/N ratio

Level	A	B	C	D	E
1	4.594	5.648	5.056	9.041	6.953
2	8.303	5.162	7.035	5.115	5.919
3	4.795	6.882	5.601	3.536	4.821
Delta	3.709	1.720	1.979	5.505	2.133
Rank	2	5	4	1	3

Regression Equation:

$\text{Roughness} = 0.037 + 0.0092 \text{ rake angle} - 0.0611 \text{ nose radius} - 0.000367 \text{ cutting speed} + 3.356 \text{ feed rate} + 0.683 \text{ depth of cut}$

The purpose of the analysis of variance (ANOVA) is to investigate which design parameter significantly affects the surface roughness^[18]. A better feel for the relative effect of the different factors can be obtained by the decomposition of the variance, which is commonly known as analysis of variance (ANOVA)^[7]. ANOVA and the F-test are applied to analyze the experimental data. ANOVA table shows that the percentage contribution of feed Rate is Maximum followed by rake angle. The most significant control parameter is feed rate and the second most significant factor is rake angle. The significance of other three factors is similar and much lower.

Table 6: Analysis of Variance

Source	DF	Adj	SS	Adj	MS
A	2	0.31281	0.156404	59.66	0.000
B	2	0.07761	0.038804	14.80	0.000
C	2	0.09165	0.045826	17.48	0.000
D	2	0.51576	0.257881	98.36	0.000
E	2	0.08459	0.042293	16.13	0.000
Error	16	0.04195	0.002622		
Total	26	1.12436			

Table 7: Model Summary

S	R-sq	R-sq (adj)	R-sq (pred)
0.0512031	96.27%	93.94%	89.38%

The interaction plots for mean are depicted in fig. 3. Fig.4 gives the interaction plot for S/N for the controlling factors.

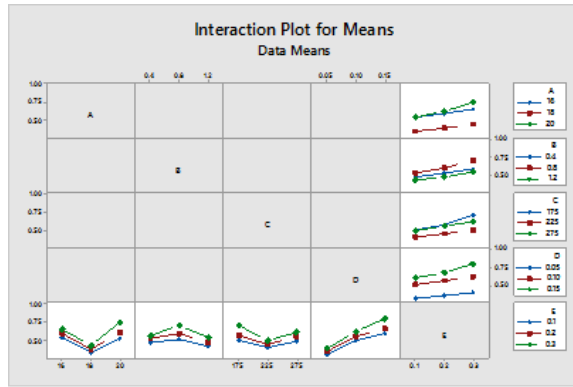


Figure3:Interaction plot for means

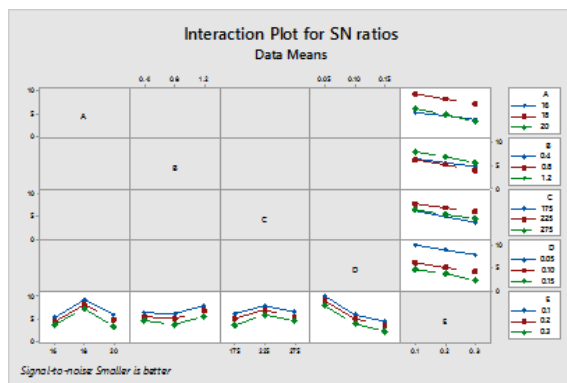


Figure 4: Interaction plot for SN ratio



Figure 5: Residuals plot for mean

The diagnostic checking has been performed through residual analysis for the developed model. The Residual plots for surface roughness are shown in Fig.5. These fall on a straight line implying that errors are distributed normally. From figure

5 it can be further concluded that all the values are within the control range, indicating that there is no obvious pattern and unusual structure and also the residual analysis does not indicate any model inadequacy. The four plots shown in the fig. 5 are residual versus fits plot, residual as a plot of frequency (histogram), Residuals versus order graph and the normal probability plot.

V. CONCLUSIONS

The following are the conclusions drawn based on the experimental investigation conducted at three levels of the five turning parameters by employing Taguchi technique to determine the optimal level of the factors.

- ✦ From the data collection and the subsequent analysis, it is found that increase in feed rate increases surface roughness and the finish becomes poor. Hence lower the feed rate, higher is the surface finish.
- ✦ The surface roughness first decreases with the rake angle and the minimum surface roughness is achieved at the second level (18) of the rake angle. Roughness then increases from second level to the third level and hence the optimal surface finish is achieved at the second level of the rake angle.
- ✦ The optimal combination of control variables for minimum Surface Roughness is level 2 (18) of rake angle (A), level 3 (1.2) of nose radius (B), level 2 (225 rpm) of cutting speed (C), level 1 (0.05 mm/rev) of feed rate, level 1 (0.1 mm) of depth of cut.
- ✦ ANOVA table and F-test of the variables show that the feed rate is the most dominant factor with the highest percentage contribution followed by the rake angle. The other three factors namely nose radius, cutting speed and the depth of cut have similar and much lower contribution.
- ✦ Taguchi gives systematic simple approach and an efficient robust design method for the optimum operating conditions.

REFERENCES

- [1] A. Agrawal, S Goel, W. B Rashidc, M. Price Prediction of surface roughness during hard turning of AISI 4340 steel (69 HRC). ELSEVIER Applied Soft Computing 30 (2015) 279–286.
- [2] C. Natarajan, S. Muthu, P. Karuppuswamy (2011) Prediction and analysis of surface roughness characteristics of a non-ferrous material using ANN in CNC turning. International journal for Advanced Manufacturing Technology (2011) 57:1043-1051.
- [3] Devesh Pratap Singh, R. N. Mall, "Optimization of Surface Roughness of Aluminum by ANOVA based Taguchi Method using Minitab15 Software", International Journal For Technological Research In Engineering Volume 2, Issue 11, 2015, 2782-2787.
- [4] I. Asilturk, Harun Akkus Determining the effect of cutting parameters on surface roughness in hard turning using the Taguchi method. ELSEVIER Measurement 44 (2011) 1697-1704.

- [5] M. Sarikaya, A. Gullu Taguchi design and response surface methodology based analysis of machining parameters in CNC turning under MQL ELSEVIER Measurement 65 (2014) 604-616.
- [6] Montgomery, D.C., 1997. "Design and Analysis of Experiments", 4th ed. Wiley, New York.
- [7] P.M. Patil, R.V. Kadi, S.T. Dundur, A.S. Pol Effect of cutting Parameters on Surface Quality of AISI 316 Austenitic Stainless Steel in CNC Turning International Research Journal Of Engineering and Technology, Volume: 02 Issue: 04/ july-2015.
- [8] Ranganath M. S., Vipin, R.S.Mishra, "Optimization of Process Parameters in Turning Operation of Aluminium (6061) with Cemented Carbide Inserts Using Taguchi Method and ANOVA". International Journal of Advance Research and Innovation, Volume1, Issue 1(2013) 13-21.
- [9] Ranganath. M. S., Vipin Optimization of Process Parameters in Turning Operation Using Taguchi Method and Anova: A Review International Journal of Advance Research and Innovation volume 1 (2013) 31-45.
- [10] Ranganath M. S., Vipin, Nand Kumar, R Srivastava, "Surface Finish Monitoring in CNC Turning Using RSM and Taguchi Techniques". International Journal of Emerging Technology and Advanced Engineering Website Volume 4, Issue 9, 2014, 171-179.
- [11] Ranganath. M. S., Vipin, S. MAurya, S. Yadav Parametric Analysis of Surface roughness Studies in Turning Using Artificial Neural Network, International Journal of Advance Research and Innovation volume 2, Issue 3 (2014) 676-683.
- [12] Ranganath. M. S., Vipin, R.S. Mishra, Prateek, Nikhil Optimization of Surface Roughness in CNC Turning of Aluminum 6061 Using Taguchi Techniques, International Journal of Modern Engineering research (IJMER), volume 5, Issue 5, May 2015,42-50
- [13] Ranganath. M. S., Vipin Effect of Rake Angle on Surface Roughness in CNC Turning International Journal of Advance Research and Innovation, Volume 2, Issue 2 (2014) 522-530
- [14] Ranganath. M. S., Vipin, R.S. Mishra Effect of Cutting Parameters on MRR and Surface Roughness in Turning of Aluminium (6061) International Journal of Advance Research and Innovation Volume 2, Issue 1 (2014) 32-39.
- [15] Ranganath M. S., Vipin, Harshit, "Surface Roughness Prediction Model for CNC Turning of EN-8 Steel Using Response Surface Methodology". International Journal of Emerging Technology and Advanced Engineering Volume 5, Issue 6, 2015, 135-143
- [16] Ranganath. M. S., Vipin, N Kumar, R Kumar Experimental Analysis of Surface Roughness in CNC Turning of Aluminium Using Response Surface Methodology. International Journal of Advance Research and Innovation Volume 3, Issue 1 (2015) 45-49.
- [17] U. Caydas, S. Ekici Support vector machines models for surface roughness prediction in CNC turning of AISI 304 Austenitic stainless steel Journal of Intelligent Manufacturing (2012) 23: 639-650.
- [18] Upinder Kumar Yadav, Deepak Narang, Pankaj Sharma Attri, "Experimental Investigation and Optimization Of Machining Parameters For Surface Roughness In CNC Turning By Taguchi Method". International Journal of Engineering Research and Applications (IJERA) Vol. 2, Issue4, July-August 2012, pp.2060-2065.

Author's Accepted Manuscript

Pure orange color emitting Sm^{3+} doped BaNb_2O_6 phosphor for solid state lighting applications

Amit K. Vishwakarma, M. Jayasimhadri



PII: S0022-2313(15)30515-9
DOI: <http://dx.doi.org/10.1016/j.jlumin.2016.03.025>
Reference: LUMIN13903

To appear in: *Journal of Luminescence*

Received date: 17 September 2015

Revised date: 11 February 2016

Accepted date: 19 March 2016

Cite this article as: Amit K. Vishwakarma and M. Jayasimhadri, Pure orange color emitting Sm^{3+} doped BaNb_2O_6 phosphor for solid state lighting applications, *Journal of Luminescence*, <http://dx.doi.org/10.1016/j.jlumin.2016.03.025>

This is a PDF file of an unedited manuscript that has been accepted for publication. As a service to our customers we are providing this early version of the manuscript. The manuscript will undergo copyediting, typesetting, and review of the resulting galley proof before it is published in its final citable form. Please note that during the production process errors may be discovered which could affect the content, and all legal disclaimers that apply to the journal pertain.

Pure orange color emitting Sm^{3+} doped BaNb_2O_6 phosphor for solid state lighting applications

Amit K. Vishwakarma¹, M. Jayasimhadri^{1,*}

¹*Luminescent Materials Research Lab, Department of Applied Physics, Delhi Technological University, Delhi 110 042, India*

Abstract:

Single phase pure orange light emitting $\text{BaNb}_2\text{O}_6: x\text{Sm}^{3+}$ ($0.5 \leq x \leq 3.0$ mol %) phosphors with orthorhombic structure have been synthesized via high temperature solid state reaction method. Crystal structure, morphology, luminescent and decay properties were studied extensively for the synthesized phosphor. The luminescence spectrum of Sm^{3+} doped BaNb_2O_6 phosphor exhibit three intense peaks centered at 565, 599 and 645 nm corresponding to the $^4\text{G}_{5/2} \rightarrow ^6\text{H}_{5/2}$, $^4\text{G}_{5/2} \rightarrow ^6\text{H}_{7/2}$ and $^4\text{G}_{5/2} \rightarrow ^6\text{H}_{9/2}$ transitions, respectively. The optimum concentration for Sm^{3+} doped BaNb_2O_6 is observed as 1.5 mol% and the probable energy transfer mechanisms between Sm^{3+} ions caused for concentration quenching have been explained in detail. The calculated Commission Internationale de L'Eclairage (CIE) chromaticity coordinates have been found to be (0.557, 0.440) lies in pure orange region, which is in the close proximity to the Nichia corporation developed amber LED. The luminescence decay lifetime for $^4\text{G}_{5/2}$ excited level was found to be in the microseconds (μs) range. The Sm^{3+} doped BaNb_2O_6 phosphor could be a potential candidate for use in the display and solid state lighting applications.

Keywords: Phosphor, Luminescence, Niobates, Orange emission

*Corresponding author: Tel.: +91-9013553360

E-mail: jayaphysics@yahoo.com (M. Jayasimhadri)

1. Introduction:

In recent years, white light emitting diodes (w-LEDs) have attracted immense attention in the field of solid state lighting (SSL) over their counterpart such as incandescent and fluorescent lighting due to many advantages including superior efficiencies, longer operating lifetimes, reliability and environmental friendliness. There are several ways to fabricate the w-LEDs. The most popular and well-established method is the combination of the blue GaN LED chip with yellow emitting phosphor $\text{Y}_3\text{Al}_5\text{O}_{12}:\text{Ce}^{3+}$ (YAG: Ce^{3+}). However, w-LEDs fabricated by this approach suffer from poor color rendering index (R_a), which is due to the absence of red component, halo effect and low thermal quenching temperature [1, 2]. To overcome these shortcomings in fabricating w-LEDs a combination of n-UV LED chip with RGB phosphors have been studied to enhance white light emission with better R_a value [3]. The shortcoming of this approach is that the efficiency of the red phosphor $\text{Y}_2\text{O}_2\text{S}:\text{Eu}^{3+}$ is only about 1/8 of blue phosphor ($\text{BaMgAl}_{10}\text{O}_{17}:\text{Eu}^{2+}$) or green phosphor ($\text{ZnS}:\text{Cu}^+, \text{Al}^{3+}$). To solve this difficulty, researchers have synthesized red phosphors based on Eu^{2+} doped CaAlSiN_3 or $\text{M}_2\text{Si}_5\text{N}_8$ ($\text{M}=\text{Ca}, \text{Sr}, \text{Ba}$), which offers high quantum efficiency and stability. However, the high processing temperature and high nitrogen pressure limit their practical applications [4-6]. Another approach to generate white light is combination of the n-UV excitation source with cyan plus orange light emitting single phase phosphor. Thus, the development of orange emitting phosphors by using n-UV excitation source is essential and needs to be investigated in the fields of solid state lighting and display technologies [7-9]. Among all lanthanides, samarium (Sm^{3+}) ion with $4f^5$ electronic configuration exhibit a strong orange red emission in the visible region.

Alkaline-earth/transition/heavy metal niobates with general formula $\text{M}^{2+}\text{Nb}_2\text{O}_6$ (where $\text{M} = \text{Mg}, \text{Ca}, \text{Sr}, \text{Ba}, \text{Mn}, \text{Fe}, \text{Co}, \text{Ni}, \text{Cu}, \text{Zn}, \text{Cd}, \text{and Pb}$) are widely known and have been

intensively studied on ferroelectric, piezoelectric, pyroelectric, electro-optic and dielectric properties. Most of these compounds exist in isomorphic orthorhombic phase and belongs to sub component of the complex perovskite family, $A(M_{1/3}Nb_{2/3})O_3$ [10-12]. Among several niobate families, europium ion doped barium niobate phosphor has been reported by our group to reveal the utility, importance and colorimetric properties [13]. However, further investigations on producing orange emission is still of great interest in the process of achieving white light by using new combination of cyan plus orange-red, which has been rarely performed. To the best of our knowledge, however, luminescence properties of Sm^{3+} doped $BaNb_2O_6$ phosphor have not been reported so far.

In the present study, Sm^{3+} doped $BaNb_2O_6$ phosphor has been synthesized by solid state reaction method to investigate the structural, morphological, luminescent and chromaticity properties of as prepared phosphor have been investigated in detail to examine the potentiality of the barium niobate phosphor for the applications in display devices, LEDs and solid state lighting. The energy transfer processes in Sm^{3+} doped $BaNb_2O_6$ have also been discussed in detail.

2. Sample Preparation:

A series of $BaNb_2O_6: xSm^{3+}$ ($0.5 \leq x \leq 3.0$ mol %) phosphors with different doping concentrations were synthesized via high-temperature solid-state reaction method. The stoichiometric amounts of $BaCO_3$ (Fisher Scientific, 99.9%), Nb_2O_5 (CDH chemicals, 99.9%) and Sm_2O_3 (Sigma-Aldrich, 99.99%) precursors were used as the starting materials. These chemicals were mixed with acetone and ground thoroughly for an hour in agate mortar and the mixed powders were transferred into alumina crucible and placed inside the programmable

muffle furnace. In order to obtain the pure compound, two step heating process was adopted. In first step mixture was heated at 625 °C for an hour to remove the CO₂ and then sintered at 1200 °C for 5 h to obtain the single phase compound. Finally, the sintered samples were cooled naturally to the room temperature and ground into fine powder for further characterizations.

The powder samples were characterized by X-ray diffractometer Model: Mini flex-II (Rigaku Corp.) using nickel-filtered Cu K_α radiation ($\lambda = 1.54056 \text{ \AA}$) in the range of $20^\circ \leq 2\theta \leq 60^\circ$ and the accelerating voltage was kept at 30.0 kV and tube current at 15 mA. The morphological observations were studied with SEM (Hitachi, Model- S-3700N). A Shimadzu Spectrofluorophotometer (Model: RF-5301PC) fitted with Xenon flash lamp (in the range 200-900 nm) was used to record the photoluminescence excitation and emission properties. The lifetime measurement was carryout using time resolved luminescence spectrometer (Model: F900 Edinburgh), equipped by time correlated single photon counter system with micro second xenon flash lamp. All these measurements were carried out at room temperature.

3. Result and Discussions:

3.1 Structural and morphological properties

Fig. 1 (a) represents the X-ray powder diffraction pattern of BaNb₂O₆: xSm³⁺ (x= 0.0, 0.5, 1.0, 1.5 and 2.0 mol%) phosphors along with the standard BaNb₂O₆ pattern PDF4+ (ICDD) No. 04-012-8861. The diffraction patterns for BaNb₂O₆: xSm³⁺ phosphor indicate the orthorhombic structure (space group: C222₁) as all the observed peaks are well-matched with the standard diffraction patterns (PDF4+ ICDD NO: 04-012-8861) of the BaNb₂O₆ published by Sirotinkin *et al.* and no second phase is observed [14]. The calculated lattice parameters are (a=12.1992 Å, b=10.2775 Å and c=7.8582 Å), (a=12.1702 Å, b=10.2574 Å and c=7.8470 Å),

($a=12.1680$ Å, $b=10.2533$ Å and $c=7.8456$ Å), ($a=12.1609$ Å, $b=10.2493$ Å and $c=7.8413$ Å), ($a=12.1533$ Å, $b=10.2413$ Å and $c=7.8372$ Å), corresponding to 0.0, 0.5, 1.0, 1.5, 2.0 mol % of Sm^{3+} doped phosphor, respectively and unit cell volume (V) decreases from 985.23 to 975.76 Å³ with increasing concentration. The ionic radii of Sm^{3+} and Ba^{2+} are 1.08 Å and 1.42 Å, respectively. The diffraction peaks are slightly shifting towards larger 2θ angles with increasing Sm^{3+} concentration compared to those of standard BaNb_2O_6 pattern as depicted in Fig. 1(b). This is due to the decrease in interatomic spacing which results from the substitution of higher content of Sm^{3+} ions in Ba^{2+} ions [15]. It indicates that the doped Sm^{3+} ions are successfully incorporated in the host cation at Ba^{2+} sites. The shifting of peak causes due to an expansion of unit cell and result the tensile stress in the host crystal lattice. The peak shift in the XRD pattern may also arise due to the presence of strain in the crystal lattice [16]. The crystallite size and strain were estimated from the most reliable Williamson- Hall (W-H) [17, 18] plot using equation $[\beta \cos \theta = \left(\frac{K\lambda}{D}\right) + 4\varepsilon \sin \theta]$ where β is full width half maximum, λ is wavelength of x-ray (1.5406), θ is diffraction angle, K is shape factor, D is crystallite size and ε is strain. The crystallite size and strain were determined from the plot between $\beta \cos \theta / \lambda$ versus $\sin \theta / \lambda$ as shown in Fig. 2. The reciprocal of intercept on the $\beta \cos \theta / \lambda$ axis gave the average crystallite size. The strain (%) obtained from the slope = $(4 \times \text{strain})$ of this graph. The calculated crystallite size and strain (%) were found to be 62.9, 59.0, 58.9, 52.5, 51.4 nm and 0.028, 0.062, 0.065, 0.066, 0.081 for $\text{BaNb}_2\text{O}_6: x\text{Sm}^{3+}$ ($x=0.0, 0.5, 1.0, 1.5$ and 2.0 mol%) phosphors, respectively.

Fig. 3 (a & b) shows the SEM micrographs at different magnifications for the $\text{BaNb}_2\text{O}_6: x\text{Sm}^{3+}$ ($x=1.5$ mol%) phosphors prepared through solid state reaction method. The agglomerated, uneven and dense solid particles were observed in the range of 3-5 μm size [7]. It

is obvious that, micrometer crystalline powder would be very much suitable to produce an efficient luminescence for solid state lighting applications.

3.2. Luminescent studies :

Fig. 4 depicts the photoluminescence excitation and emission spectra of $\text{BaNb}_2\text{O}_6: \text{xSm}^{3+}$ ($\text{x} = 1.5 \text{ mol\%}$) phosphors sintered at 1200°C . The PLE spectrum exhibits ten excitation bands corresponding to the intra-configurational 4f-4f transitions of Sm^{3+} ions originating from the ground state $^6\text{H}_{5/2}$ to excited state level $^4\text{P}_{1/2}$, $^4\text{H}_{9/2}$, $^4\text{D}_{3/2}$, $^4\text{D}_{1/2}$, $^4\text{G}_{11/2}$, $^4\text{F}_{7/2}$, $^4\text{M}_{19/2}$, $^4\text{G}_{9/2}$, $^4\text{I}_{13/2}$ and $^4\text{M}_{15/2}$ at 325, 345, 363, 378, 388, 405, 419, 440, 463 and 479 nm, respectively [19,20]. In order to know the optimized excitation wavelength, the four intense excitation wavelengths, (405, 418, 463 and 479 nm) have been chosen to measure photoluminescence spectrum. The three emission bands were observed in orange- reddish (550-700 nm) spectral region for all excitation wavelengths, which are attributed to de-excitation of $^4\text{G}_{5/2}$ level of Sm^{3+} ions to its lower multiplets of $^6\text{H}_j$ ($J = 5/2, 7/2$ and $9/2$). Among these excitation bands, the emission intensity measured at 405 nm excitation was more intense than other wavelengths and considered as optimum excitation wavelength.

The emission spectra of $\text{BaNb}_2\text{O}_6: \text{xSm}^{3+}$ ($\text{x} = 0.5, 1.0, 1.5, 2.0, 2.5$ and 3.0 mol\%) phosphors measured at $\lambda_{\text{ex}} = 405$ ($^6\text{H}_{5/2} \rightarrow ^4\text{F}_{7/2}$) excitation wavelength is shown in Fig. 4. Three emission peaks were observed at 565, 599 and 645 nm corresponding to $^4\text{G}_{5/2} \rightarrow ^6\text{H}_{5/2}$, $^4\text{G}_{5/2} \rightarrow ^6\text{H}_{7/2}$, and $^4\text{G}_{5/2} \rightarrow ^6\text{H}_{9/2}$ respectively. The emission peak centered at 565 nm ($^4\text{G}_{5/2} \rightarrow ^6\text{H}_{5/2}$) is originated due to purely magnetic dipole moment, second peak at 645 nm ($^4\text{G}_{5/2} \rightarrow ^6\text{H}_{9/2}$) is due to purely electric dipole moment and the other at 599 nm ($^4\text{G}_{5/2} \rightarrow ^6\text{H}_{7/2}$) is due to both magnetic and electric dipole moments [9, 15, 20]. Generally, the intensity ratio of electric dipole to magnetic dipole transitions is useful to understand the symmetry of local environment around the

trivalent $4f^5$ ions. In the present phosphor, the magnetic dipole transition is more intense than electric dipole transition suggested that there is no deviation from inversion center and more symmetric in nature [9, 21, 22]. It is observed from Fig. 5 that there is no change in the position of emission band for all doping concentrations. However, the emission intensity changes with doping concentration of Sm^{3+} ions. Initially, the emission intensity increases, then reaches to a maximum at $x=1.5$ mol% (critical concentration), beyond that the emission intensity begins to decrease with increase in concentration due to concentration quenching effect [23]. Thus the optimum concentration of Sm^{3+} ions in BaNb_2O_6 host is 1.5 mol% and also the graph between Sm^{3+} ions doped concentration and emission intensity of $^4\text{G}_{5/2} \rightarrow ^6\text{H}_{7/2}$ peak represented the same inset of Fig. 5. The concentration quenching may be induced by cross relaxation processes due to proximity in Sm^{3+} ions. When the Sm^{3+} ions doping increases, there is more possibility of enhancing the energy transfer within Sm^{3+} ions beyond the optimal doping concentration through non radiative process.

The critical energy transfer distance (R_c) in $\text{BaNb}_2\text{O}_6:\text{Sm}^{3+}$ can be calculated by substituting the values of critical concentration (X_c) and structural parameters such as unit cell volume (V) and the number of Z ions in the unit cell (N), in the equation as suggested by Blasse [24, 25]:

$$R_c \approx 2 \left[\frac{3V}{4\pi X_c N} \right]^{\frac{1}{3}}$$

For the $\text{BaNb}_2\text{O}_6:\text{Sm}^{3+}$ system, $N=8$, $V=977.35 \text{ \AA}^3$, $N=8$ and $X_c = 0.015$. The calculated critical distance between Sm^{3+} ions is 24.60 \AA .

Usually, the non-radiative energy transfer occurs due to exchange interaction, radiation re-absorption or multipolar interaction between rare earth ions. Exchange interaction may occur when the critical distance between the activator ions is less than 5 \AA , which is much less than the calculated distance for Sm^{3+} doped BaNb_2O_6 phosphor. Hence, the multipolar interaction may

be responsible for energy transfer mechanism in the present system. According to the Dexter [26-28] theory, if the doping concentration is large enough, the relationship between the luminescent emission intensity (I) and the activator ion concentration (x) can be expressed as:

$$I = \frac{x}{K(1 + \beta x^{Q/3})}$$

where x is the activator ion concentration; K and β are constants under the same excitation condition for the host. $Q = 6, 8$ or 10 for dipole-dipole (d-d), dipole-quadrupole (d-q) or quadrupole - quadrupole (q-q) interactions, respectively. In order to obtain the Q value, plot of $\log(I/x)$ as a function of $\log(x)$ is fitted linearly as shown in Fig. 6. The slope is equal to $-Q/3$ from the graph. The calculated Q value is 5.20, which is approximately equal to 6 indicates that the electric dipole-dipole (d-d) interaction is responsible for the luminescence quenching of $^4G_{5/2}$ level in Sm^{3+} doped $BaNb_2O_6$ host.

The partial energy level diagram of Sm^{3+} ions in $BaNb_2O_6$ is shown in Fig. 7. When the population is excited to $^4F_{7/2}$ level for Sm^{3+} ions by 405 nm wavelength, the initial population relaxes non radiatively to the $^4G_{5/2}$ level. There are several energy levels between $^4F_{7/2}$ and $^4G_{5/2}$ levels with little energy differences, which leads non-radiative relaxation to the population of the $^4G_{5/2}$ state [29]. This energy level is separated from the next lower-lying $^6F_{11/2}$ level by $\sim 7407 \text{ cm}^{-1}$. Thus, it could be confirmed that radiative transitions and relaxation by non-radiative energy transfer are the two main processes, which could finally depopulate the $^4G_{5/2}$ state. The luminescence spectra exhibit three intense emission bands at 565, 599 and 645 nm. The possible cross relaxation channels (CRC) responsible for non-radiative emission beyond the optimum doping concentration shown in Fig. 7. The possible cross relaxation channels in present $BaNb_2O_6:Sm^{3+}$ phosphors are as follows: CRC1: ($^4G_{5/2} + ^6H_{5/2}$) \rightarrow ($^6F_{5/2} + ^6F_{11/2}$), CRC2: ($^4G_{5/2} + ^6H_{5/2}$) \rightarrow ($^6F_{7/2} + ^6F_{9/2}$), CRC3: ($^4G_{5/2} + ^6H_{5/2}$) \rightarrow ($^6F_{9/2} + ^6F_{7/2}$) and CRC4: ($^4G_{5/2} + ^6H_{5/2}$) \rightarrow

(${}^6F_{11/2}$ + ${}^6F_{5/2}$). Energy transfer through cross relaxation channels may take place between Sm^{3+} ions from ${}^4G_{5/2}$ populated state to nearby Sm^{3+} ions in the ground state [30]. The energy difference between the ${}^4G_{5/2}$ state to intermediate levels of Sm^{3+} ions ${}^6F_{5/2}$, ${}^6F_{7/2}$, ${}^6F_{9/2}$, and ${}^6F_{11/2}$ are 10824, 9947, 8798 and 7407 cm^{-1} respectively, which are closely matching with the energy difference between ${}^6H_{5/2}$ ground state to various excited levels ${}^6F_{11/2}$ (10471 cm^{-1}), ${}^6F_{9/2}$ (9090 cm^{-1}), ${}^6F_{7/2}$ (7931 cm^{-1}) and ${}^6F_{5/2}$ (7054 cm^{-1}).

The chromaticity diagrams and CIE coordinates are very important to disclose the exact emission color and color purity of the sample [31]. The calculated CIE chromaticity coordinate were found to be (0.557, 0.440) for the optimized $\text{BaNb}_2\text{O}_6:\text{xSm}^{3+}$ (x=1.5 mol%) phosphor based on emission spectrum under 405 nm excitation, which is located exactly on the NTSC color gamut as shown in Fig. 8. The obtained CIE chromaticity coordinates are very much close to the Nichia corporation developed amber LED NSPAR 70BS (0.575, 0.425). It is observed from Fig. 8 that the (x, y) chromaticity coordinates located in pure orange region and the calculated color purity was found to be 99.5%, which confirms the pure emission of orange light from $\text{BaNb}_2\text{O}_6:\text{xSm}^{3+}$ phosphors. The calculated color correlated temperature (CCT) value was found to be 1970 K, which is unusual in other Sm^{3+} doped hosts and this emission could be useful for solid state lighting and displays applications.

3.3. Luminescence Decay analysis:

The lifetime values for the ${}^4G_{5/2}$ excited level of Sm^{3+} ions in the prepared $\text{BaNb}_2\text{O}_6:\text{xSm}^{3+}$ (x= 0.5, 1.5 and 2.5 mol%) phosphor have been determined by using decay curve profile measured for ${}^4G_{5/2} \rightarrow {}^6H_{7/2}$ transition (599 nm) under 405 nm excitation

wavelength are depicted in Fig. 9. The decay curves of the as prepared phosphor are well fitted with a double exponential function as [32]:

$$I = A_1 e^{-t/\tau_1} + A_2 e^{-t/\tau_2}$$

where I is the luminescence intensity; t is time; τ_1 and τ_2 are the decay time for the exponential component and A_1 and A_2 are the fitting parameter constants, respectively. Thus, the average lifetime in case of double exponential fitting can be determined by using equation:

$$\tau_{avg} = \frac{A_1 \tau_1^2 + A_2 \tau_2^2}{A_1 \tau_1 + A_2 \tau_2}$$

The decay curves exhibit double-exponential nature, may be due to energy transfer process between the Sm^{3+} ions. The average lifetimes for the $^4\text{G}_{5/2}$ excited level are found to be 369.74, 196.82 and 142.85 μs corresponding to 0.5, 1.5 and 2.5 mol % Sm^{3+} concentration. These results indicate that the average lifetime decreased with increasing concentration of Sm^{3+} ions, which confirm the possibility of energy transfer between Sm^{3+} ions.

4. Conclusions:

In the present work, Sm^{3+} doped BaNb_2O_6 phosphors have been successfully synthesized by conventional solid state reaction method. The XRD patterns of these phosphor confirmed their single phase with an orthorhombic structure and irregular dense morphology was observed in the SEM image. The intense orange emission at 599 nm ($^4\text{G}_{5/2} \rightarrow ^6\text{H}_{7/2}$ transition) was observed from the emission spectra under $\lambda_{\text{ex}}=405$ nm, and the optimized doping concentration is observed at 1.5 mol%. The CIE chromaticity coordinates were found to be (0.557, 0.440), which is in close proximity to the Nichia corporation developed amber LED. The calculated color purity was found to be 99.5 % that confirms the emitting color of the synthesized phosphor falling in pure orange region and also the CCT value was 1970 K. The decay curves were well

fitted to the double exponential function, and average lifetimes for the $^4G_{5/2}$ excited level of Sm^{3+} in the present host is in the range of micro-seconds. The above mentioned results suggest that the Sm^{3+} doped $BaNb_2O_6$ phosphor is a potential candidate for use in the fabrication of orange, white LEDs and displays applications.

Acknowledgements:

The author (M. Jayasimhadri) is grateful to DST-SERB, Govt. of India for the sanction of a research project (No. SB/FTP/PS-082/2014, dt. 02/03/2015).

References:

- [1] X. Bai, G. Caputo, Z. Hao, V.T. Freitas, J. Zhang, R.L. Longo, O. L. Malta, A. S. Ferreira, N. Pinna, Nat. Commun. 5 (2014) 5702-5710.
- [2] E. Mantioli, S. Brinkley, K. M. Kelchner, Y. L. Hu, S. Nakamura, S. DenBaars, J. Speck, C. Weibuch, Light Sci. Appl. 1 (2012) e22-29.
- [3] R. Zhou, L. Wang, M. Xu, D. Jia, J. Alloys Compd. 647 (2015) 136-140.
- [4] H. Zhu, C. C. Lin, W. Luo, S. Shu, Z. Liu, Y. Liu, J. Kong, E. Ma, Y. Cao, R. S. Liu, X. Chen, Nat. Commun. 5 (2014) 4312-4322 .
- [5] J. Chen, Y. Liu, L. Mei, H. Liu, M. Fang, Z. Huang, Sci. Rep. 5 (2015) 9673-9682.
- [6] Z. Wang, P. Li, X. Zhang, Q. Li, T. Li, Z. Yang, Q. Guo, Physica B 414 (2013) 56-59.
- [7] H. Deng, Z. Zhao, J. Wang, Z. Hei, M. Li, H. Mi Noh, J. H. Jeong, R. Yu, J. Solid State Chem. 228 (2015) 110-116.
- [8] G. S. R. Raju, J. S. Yu, J. Y. Park, H. C. Jung, B. K. Moon, J. Am. Ceram. Soc. 95 (2012) 238-242.
- [9] B. V. Ratnam, M. Jayasimhadri, K. Jang, Spectrochim. Acta - Part A Mol. Biomol. Spectrosc. 132 (2014) 563-567.

- [10] F. Huang, Q. Zhou, C. Ma, L. Li, X. Huang, F. Li, Q. Cui, D. Xu, W. Wang, T. Cui, G. Zou, *RSC Adv.* 3 (2013) 13210-13213.
- [11] S. Lei, D. Guo, C. Wang, D. Cheng, X. Gao, S. Zeng, Y. Xiao, B. Cheng, *Cryst. Engg. Comm.* 16 (2014) 7949-7955.
- [12] R. C. Pullar, J. D. Breeze, N. M. Alford, *J. Am. Ceram. Soc.* 88 (9) (2005) 2466-2471.
- [13] A. K. Vishwakarma, K. Jha, M. Jayasimhadri, A. S. Rao, K. Jang, B. Sivaiah, D. Haranath, *J. Alloys Compd.* 622 (2015) 97-101.
- [14] V. P. Sirotkin, S. P. Sirotkin, *Russ. J. Inorg. Chem.* 35 (1990) 1246-1248.
- [15] B. Ding, C. Han, L. Zheng, J. Zhang, R. Wang, Z. Tang, *Sci. Rep.* 5 (2015) 9443-9453.
- [16] K. K. Rasu, D. Balaji, S. M. Babu, *J. Lumin.* 170 (2016) 547-555.
- [17] B. D. Cullity, *Elements of X-Ray Diffraction*, Addison-Wesley, Massachusetts, 1956, pp. 312.
- [18] S. Bathula, B. Gahtori, M. Jayasimhadri, S. K. Tripathy, K. Tyagi, A. K. Srivastava, A. Dhar, *Appl. Phys. Lett.* 105 (2014) 061902-061904.
- [19] W.T. Carnall, P.R. Fields, K. Rajnak, *J Chem. Phys.* 49 (1968) 4424-4442.
- [20] R. Yu, H. M. Noh, B. K. Moon, B. C. Choi, J. H. Jeong, H. S. Lee, K. Jang, S. S. Yi, *J Lumin.* 145 (2014) 717-722.
- [21] N. Kaneko, M. Hagiwara, S. Fujihara, *ECS J. Solid State Sci. Technol.* 3 (2014) R109–R114.
- [22] Z. Xia, D. Chen, *J. Am. Ceram. Soc.* 93 (2010) 1397-1401.
- [23] J. Zheng, J. Feng, Q. Cheng, Z. Guo, L. Cai, C. Chen, *Funct. Mater. Lett.* 8 (2015) 1550042-1550047.
- [24] G. Blasse, *Philips Res. Rep.* 24 (2) (1969) 131-144.

- [25] Q. Xu, J. Sun, D. Cui, Q. Di, J. Zeng, J. Lumin. 158 (2015) 301-305.
- [26] D. L. Dexter, J. Chem. Phys. 21 (1953) 836-850.
- [27] D. L. Dexter, J. H. Schulman, J. Chem. Phys. 22 (1954), 1063-1070.
- [28] J. Xu, Z. Ju, X. Gao, Y. An, X. Tang, W. Liu, Inorg. Chem. 52 (2013) 13875-13881.
- [29] D. Ramachari, L. Rama Moorthy, C. K. Jayasankar, Mater. Res. Bull. 48 (2013) 3607–3613.
- [30] D. Umamaheswari, B.C. Jamalaiah, T. Sasikala, I.G. Kim, L.R. Moorthy, J. Non. Cryst. Solids. 358 (2012) 782–787.
- [31] R. Yu, H. M. Noh, B. K. Moon, B. C. Choi, J. H. Jeong, H. S. Lee, K. Jang, S. S. Yi, J. Lumin. 152 (2014) 133–137.
- [32] S. K. Gupta, P. S. Ghosh, N. Pathak, A. Arya, V. Natarajan, RSC Adv. 4 (2014) 29202-29215.

Figure Captions:

Fig. 1: X-ray diffraction patterns of $\text{BaNb}_2\text{O}_6: x\text{Sm}^{3+}$ ($x=0.0, 0.5, 1.0, 1.5$ and 2.0 mol%) powder calcined at 1200°C for 5 h.

Fig. 2: W-H plot of $\text{BaNb}_2\text{O}_6: x\text{Sm}^{3+}$ ($x=0.0, 0.5, 1.0, 1.5$ and 2.0 mol%).

Fig. 3: Scanning electron micrograph of $\text{BaNb}_2\text{O}_6: x\text{Sm}^{3+}$ ($x = 1.5$ mol %) sintered at 1200°C

Fig. 4: Photoluminescence excitation spectrum at $\lambda_{\text{em}}=599$ nm and emission spectra of Sm^{3+} doped BaNb_2O_6 phosphor at various prominent excitation wavelengths.

Fig. 5: Photoluminescence spectra of $\text{BaNb}_2\text{O}_6: x\text{Sm}^{3+}$ ($x= 0.5, 1.0, 1.5, 2.0, 2.5, 3.0$ mol%) at $\lambda_{\text{ex}}=405$ nm. (Inset shows the dependence of emission intensity on the Sm^{3+} doping concentration.)

Fig. 6: The relationship between $\log(I/x)$ versus $\log x$ in Sm^{3+} doped BaNb_2O_6 phosphors.

Fig. 7: Partial energy level diagram and cross relaxation channels of Sm^{3+} ions.

Fig. 8: Chromaticity coordinates for optimized Sm^{3+} doped BaNb_2O_6 phosphor in CIE 1931 chromaticity diagram.

Fig. 9: Decay curves of $\text{BaNb}_2\text{O}_6: x\text{Sm}^{3+}$ ($x= 0.5, 1.5$ and 2.5 mol%) concentrations ($\lambda_{\text{ex}}=405$ nm and $\lambda_{\text{em}}=599$ nm).

Fig. 1:

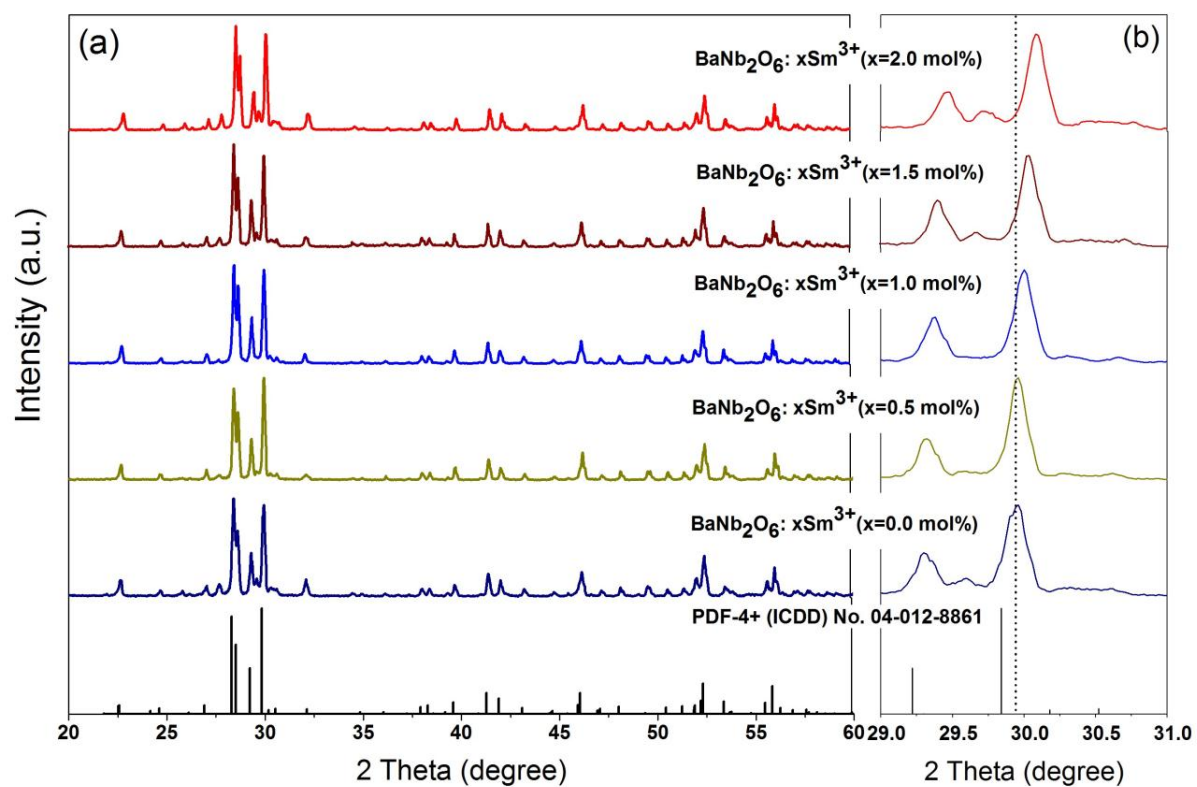


Fig. 2:

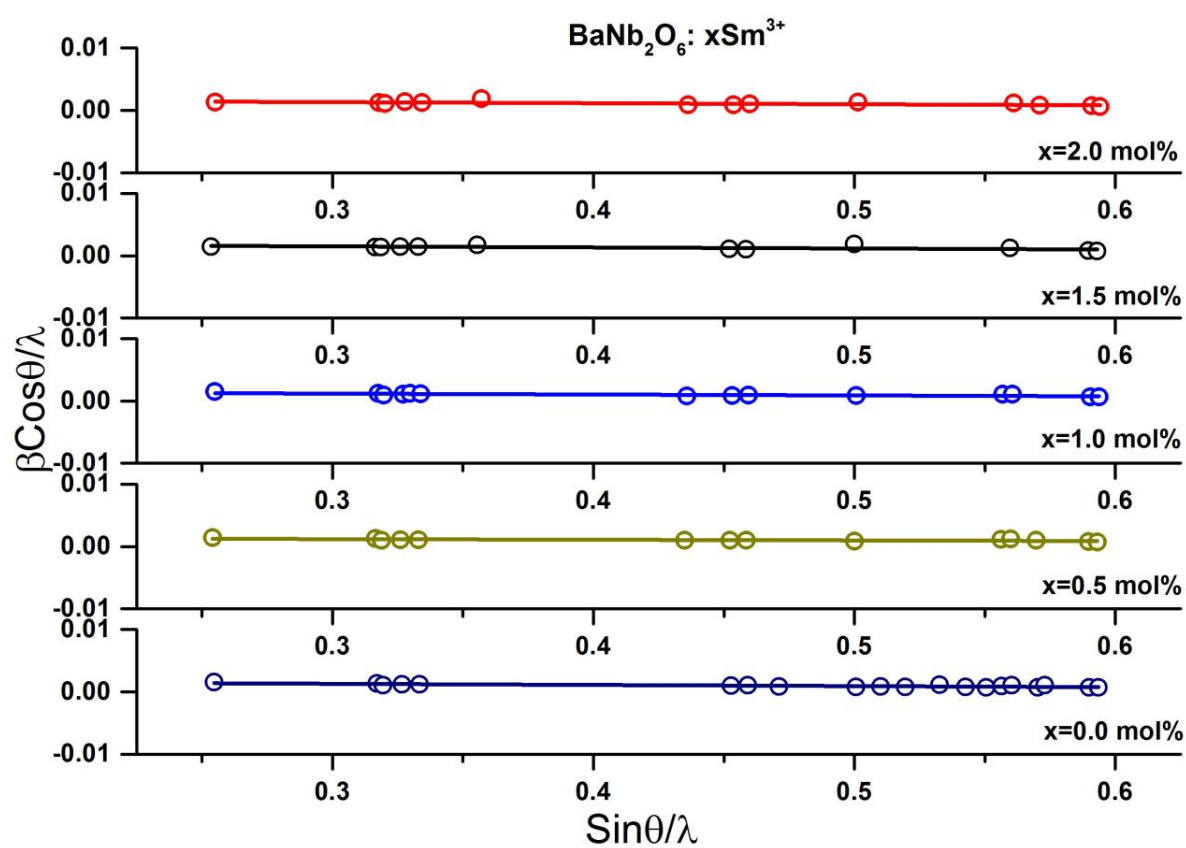


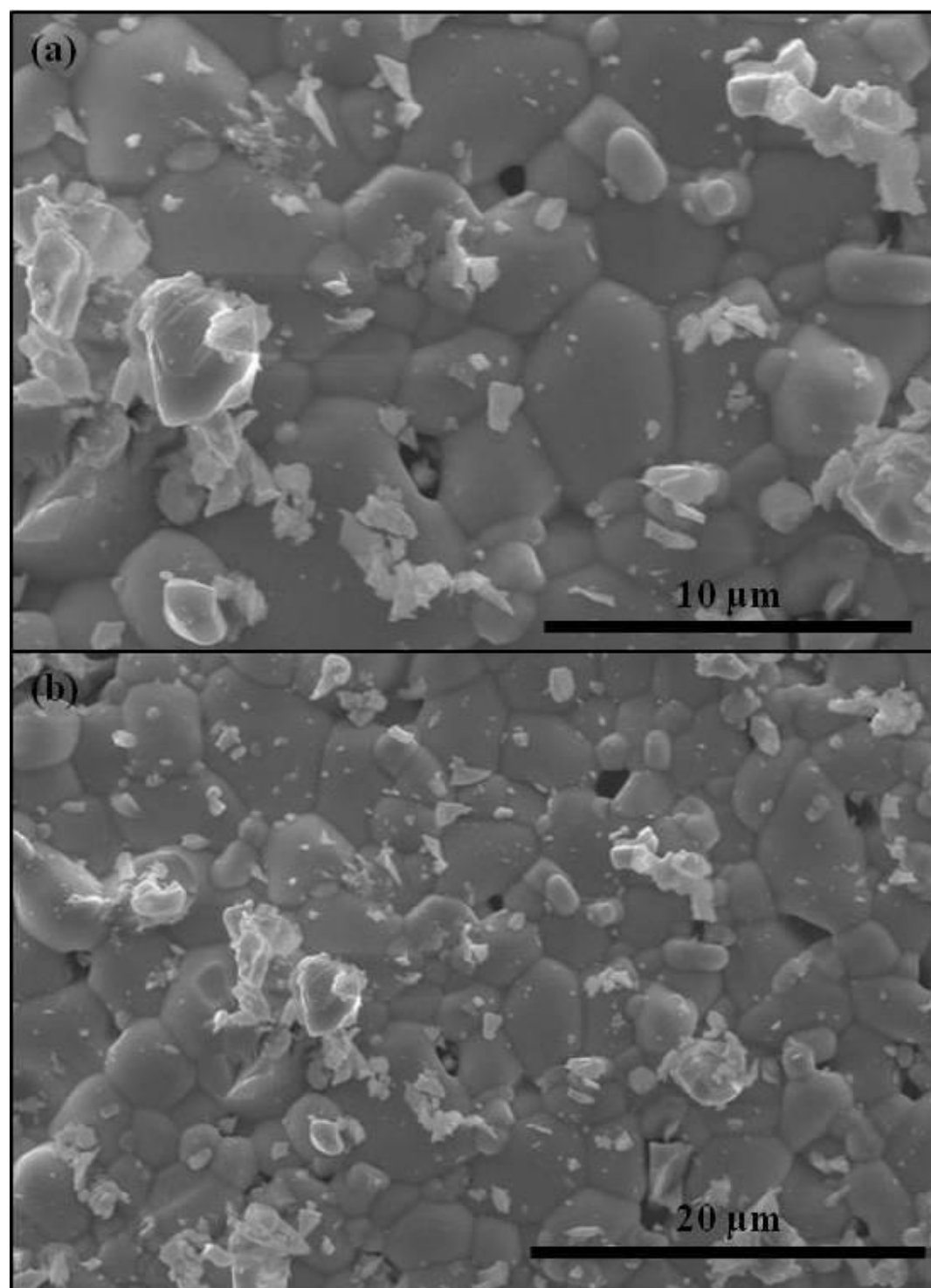
Fig. 3:

Fig. 4:

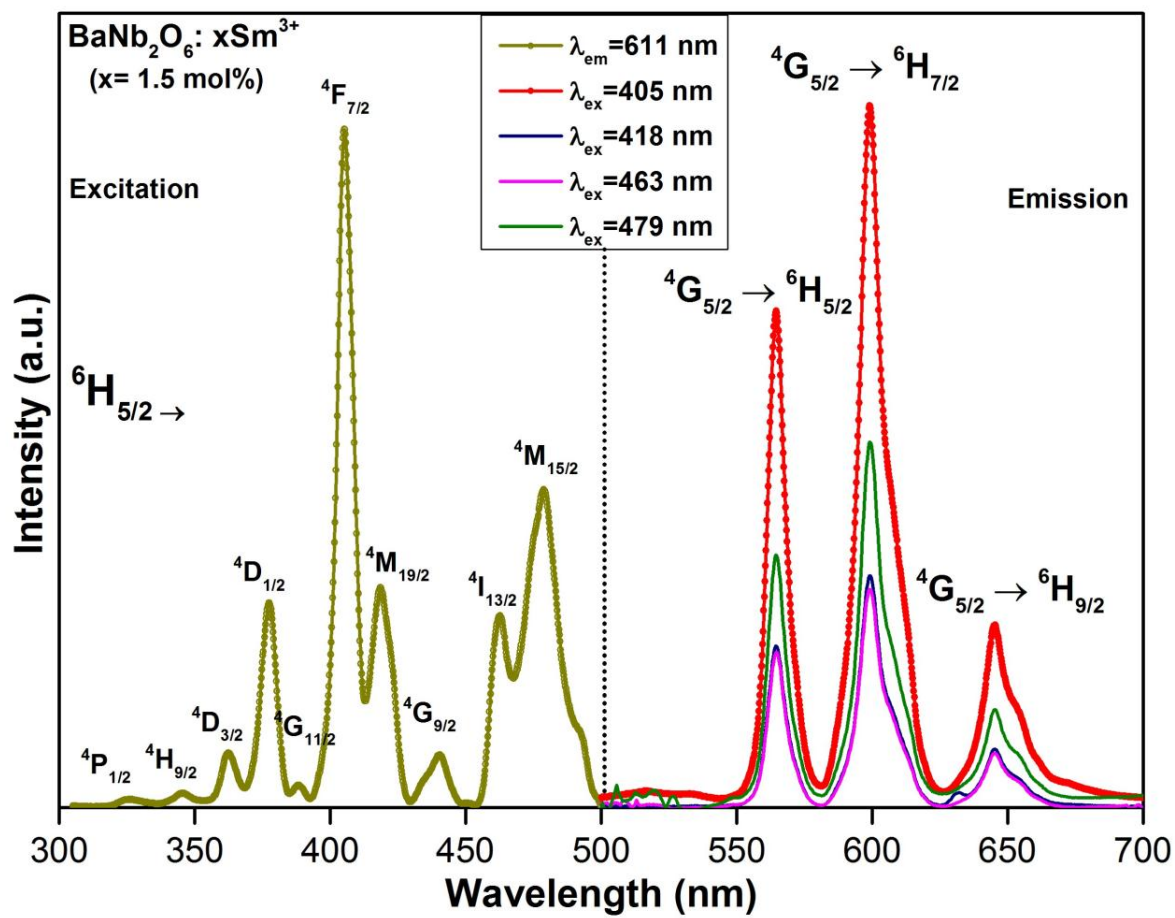


Fig. 5:

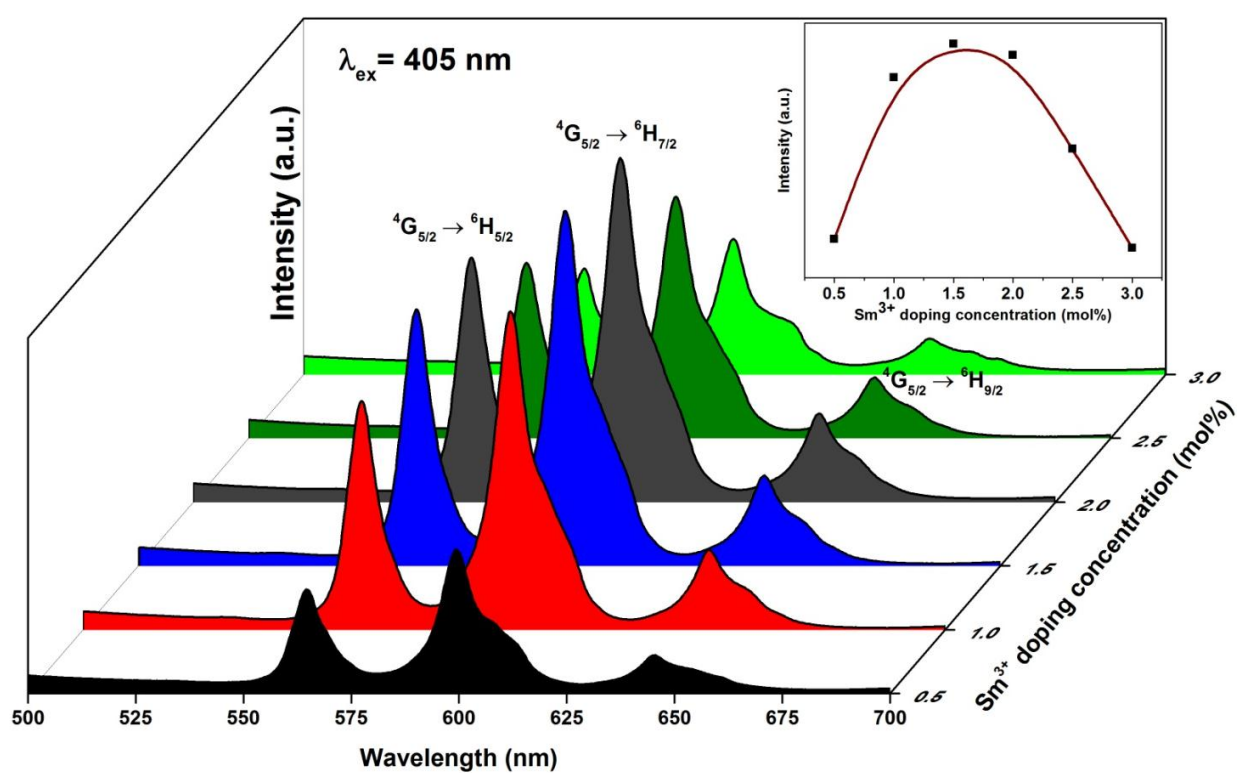


Fig. 6:

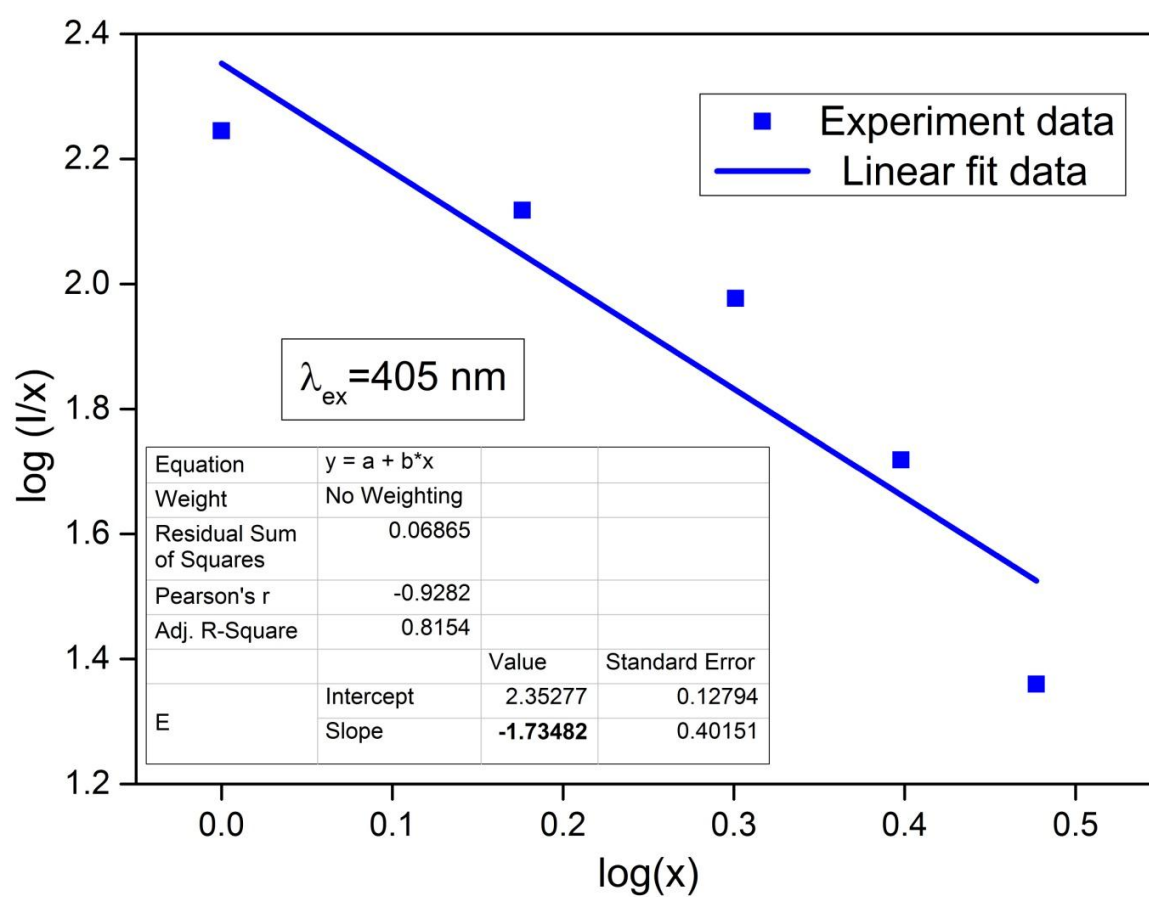


Fig. 7:

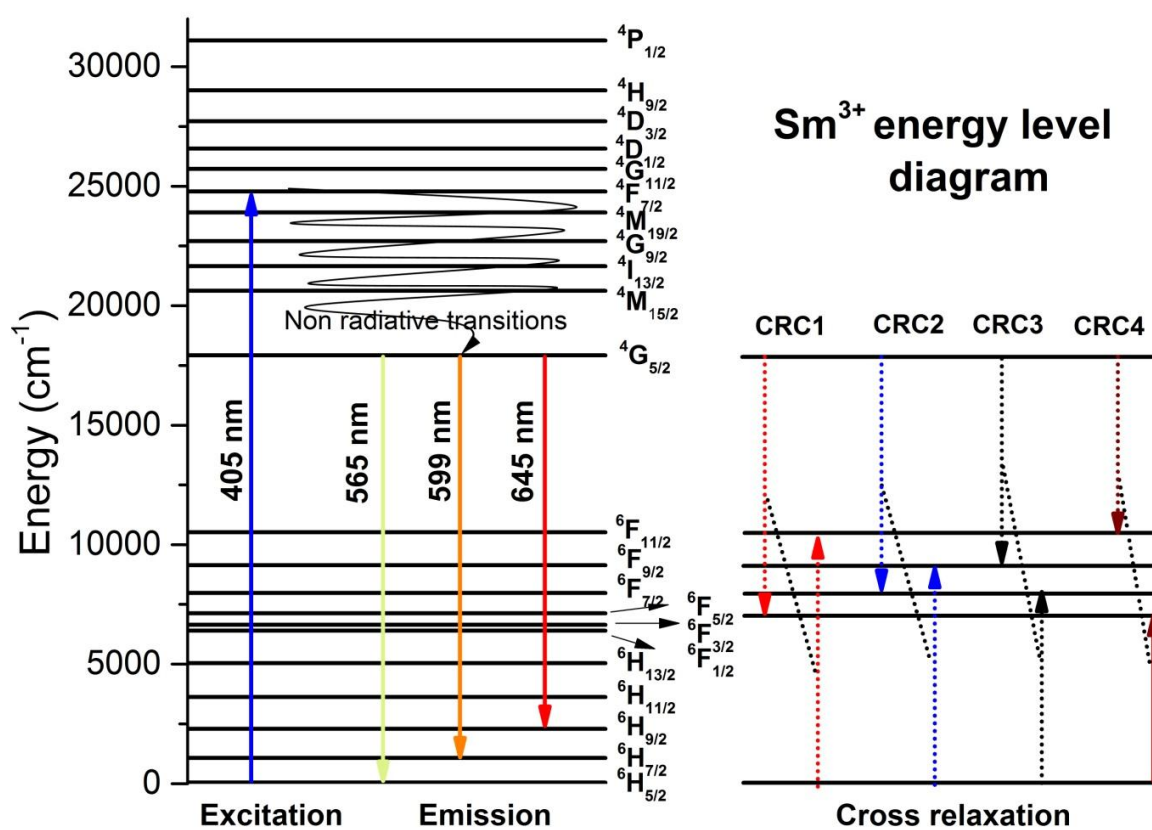


Fig. 8:

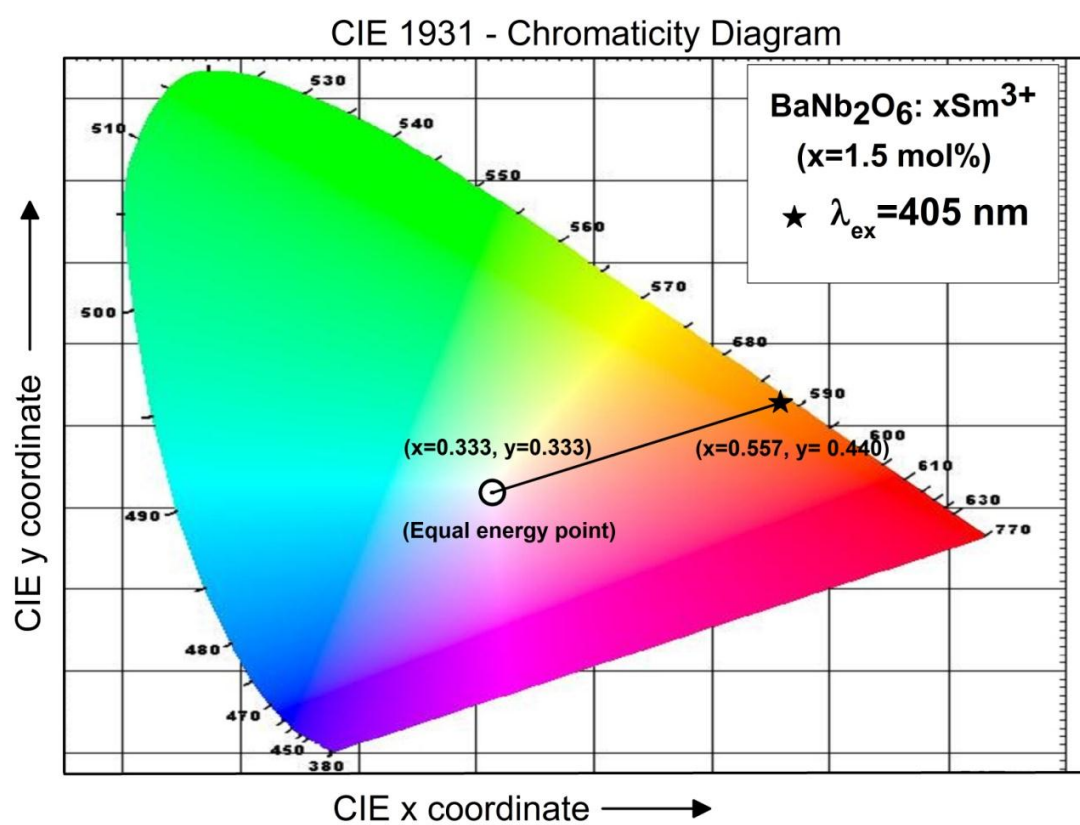
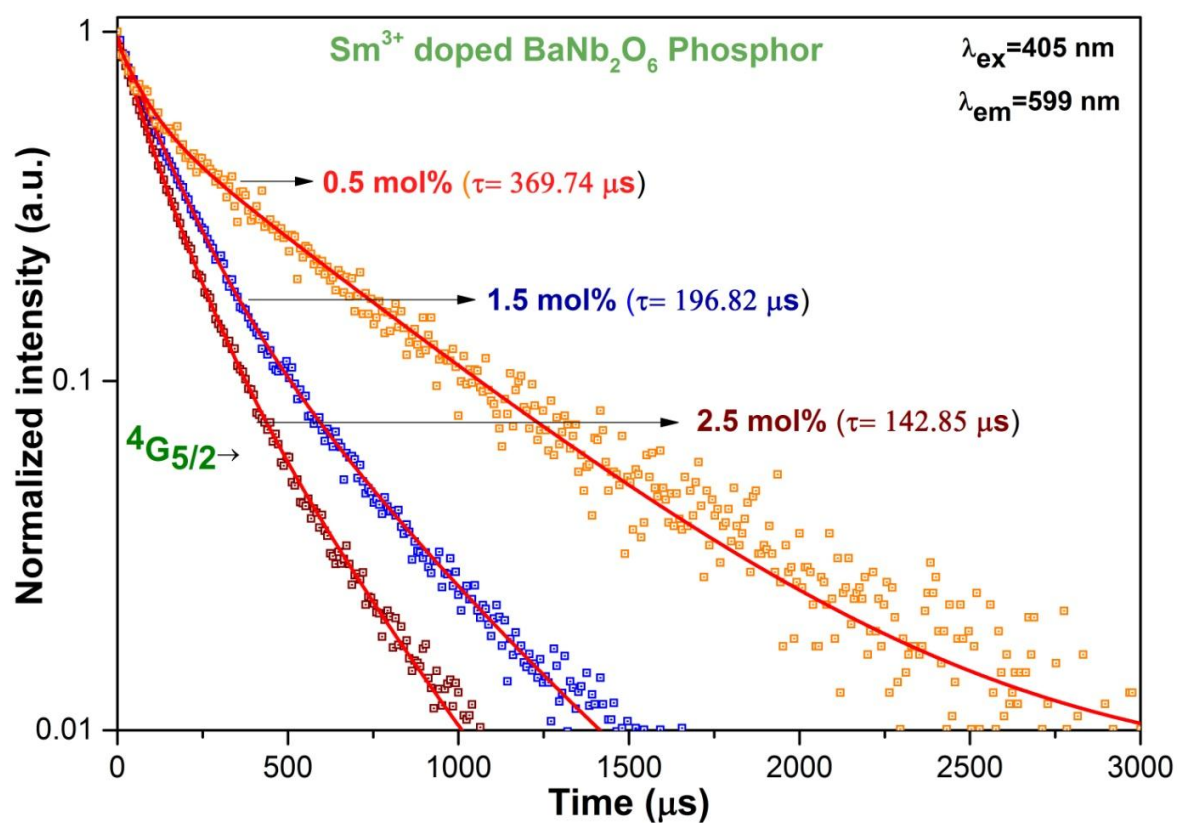
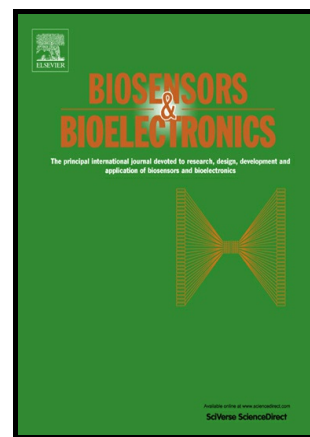


Fig. 9:



Recent Advances in Mycotoxins Detection

Ruchika Chauhan, Jay Singh, Tushar Sachdev, T. Basu, B.D. Malhotra



www.elsevier.com/locate/bios

PII: S0956-5663(16)30196-8
DOI: <http://dx.doi.org/10.1016/j.bios.2016.03.004>
Reference: BIOS8515

To appear in: *Biosensors and Bioelectronics*

Received date: 17 December 2015
Revised date: 25 February 2016
Accepted date: 3 March 2016

Cite this article as: Ruchika Chauhan, Jay Singh, Tushar Sachdev, T. Basu and B.D. Malhotra, Recent Advances in Mycotoxins Detection, *Biosensors and Bioelectronics*, <http://dx.doi.org/10.1016/j.bios.2016.03.004>

This is a PDF file of an unedited manuscript that has been accepted for publication. As a service to our customers we are providing this early version of the manuscript. The manuscript will undergo copyediting, typesetting, and review of the resulting galley proof before it is published in its final citable form. Please note that during the production process errors may be discovered which could affect the content, and all legal disclaimers that apply to the journal pertain.

Recent Advances in Mycotoxins Detection

Ruchika Chauhan,^{1a} Jay Singh,^{2b} Tushar Sachdev,^{3a} T. Basu^{4a*} and B.D. Malhotra,^{5c}

^aAmity Institute of Nanotechnology, Amity University Uttar Pradesh, NOIDA India

*^bDepartment of Applied Chemistry & Polymer Technology, Delhi Technological University,
Delhi-110042, India*

^cDepartment of Biotechnology, Delhi Technological University, Delhi, India

Email addresses: ¹ruchikachauhan@hotmail.com, ²jaimnnit@gmail.com,

³tsachdev0430@gmail.com, ⁴basu002@yahoo.com, ⁵bansi.malhotra@gmail.com

Abstract

Mycotoxins contamination in both food and feed is inevitable. Mycotoxin toxicity in foodstuff can occur at very low concentrations necessitating early availability of sensitive and reliable methods for their detection. The present research thrust is towards the development of a user friendly biosensor for mycotoxin detection at both academic and industrial levels in replace of conventional expensive chromatographic and ELISA techniques. This review critically analyze the recent research trend towards the construction of immunosensor, aptasensor, enzymatic sensors and others for mycotoxin detection with a reference to label and label free methods, synthesis of new material including nano dimension, and transuding techniques. Technological aspects in the development of biosensors for mycotoxin detection, current challenges and future prospects are also included to provide a overview and suggestions for future research directions.

Keywords: Immunosensor; Mycotoxins; Aptamers, Molecularly Imprinted Polymers Mimotopes, Enzymatic inhibition.

*Corresponding Author; Email address: basu002@yahoo.com

Contents

1. Introduction
 - 1.1 Origin of concept
 - 1.2 Conventional techniques used for detection of mycotoxins
2. Recent trends for detection of mycotoxins
 - 2.1 Immunosensor for mycotoxins
 - 2.1.1. Labeled immunosensors
 - 2.1.2. Label-free immunosensors
 - 2.2 Aptasensors for the mycotoxin detection
 - 2.2.1. Factors affecting aptamer affinity
 - 2.2.1.1. Presence of divalent cation
 - 2.2.1.2. Effect of pH
 - 2.2.2. Labeled aptasensor
 - 2.2.2.1. Signal On
 - 2.2.2.2. Advanced approach for signal amplification
 - 2.2.2.3. Signal Off
 - 2.2.3. Label-free aptasensor
 - 2.3. Molecularly Imprinted Polymers
 - 2.4. Enzymatic inhibition
 - 2.5. Mimotopes
3. Conclusions
4. Future trends

1. Introduction

1.1 Origin of concept

The word mycotoxin originated from the Greek word mukos meaning “fungus” and latin word toxicum referring “poison” is secondary metabolite produced by fungus, that colonizes on crops either during harvesting or during storage (**Robbins et.al. 2000**). The consumption of contaminated food causes severe toxic effects on humans and animals health (**CAST 2003, Zheng et.al 2006, Rodrigues et.al. 2011**) and they are more dangerous than food additives or pesticide residues (**Van Egmond et.al. 2007**). They are teratogenic, mutagenic, nephrotoxic, immunosuppressive and carcinogenic. They are highly resistive in nature and hence remain in the food chain. International Agency for Research on Cancer (IARC) has categorized aflatoxin B1 (AFB1) as Group 1 (potent human carcinogen) and may be responsible for human liver cancer in many developing countries (**Henry et.al. 1999**) while ochratoxin A (OTA) and fumonisin are classified as Group 2B carcinogens (possibly carcinogenic in humans) (**IARC 2002**). Therefore, European commission has set maximum permitted levels for certain mycotoxins in a majority of foods (**Table S1**). Low molecular weight mycotoxins posses variety of chemical structures (**Fig. S1**) which is the main constraint to develop one standard technique for analysis (**Tamerler et.al. 2006**).

There has been a major international research effort, aimed at the identification and quantification of mycotoxins and evaluation of their biological effects in humans and animals (**Zain et.al. 2011**). The main group of moulds and mycotoxins of world-wide concern are *Aspergillus* spp. (producing aflatoxins B1, B2, G1, G2, OTA and patulin), *Fusarium* spp. (producing T-2 toxin, deoxynivalenol (DON), zearalenone and fumonisin B1) and *Penicillium* spp. (producing OTA).

1.2. Conventional techniques used for the detection of mycotoxins

Conventional analytical methods for mycotoxin detection include thin-layer chromatography (TLC), high-performance liquid chromatography (HPLC) coupled with ultraviolet (UV), diode array (DAD), fluorescence (FD) or mass spectrometry (MS) detectors, gas chromatography (GC) coupled with electron capture (ECD), flame ionization (FID) or MS detectors (Lippolis et.al. 2008, Visconti et.al 2005) and enzyme-linked immunoassay (ELISA) (Wang 2011, Zheng et.al. 2005). Though these methods are well known for their accurate and precise detection of mycotoxin in food or feed samples, they require skilled operators, extensive sample pretreatment, equipment and may lack accuracy at low analyte concentration (Cigić & Prosen 2009, Goryacheva et.al. 2007). Therefore, a rapid, sensitive and specific assay technique is required for the routine analysis of foods, and beverages. The main objective is to review the research work carried out in process of development of an efficient user friendly and reliable biosensing tool which can quantify the amount of mycotoxins in our daily diet.

2. Recent trends towards the detection of mycotoxins

The recent advanced techniques such as biosensors have focused on some general features such as simplicity, easy-to-use, relatively fast and easy portability. The receptors developed for mycotoxin detection are biomolecules (antibodies, DNA and enzymes) and synthetic chemicals (aptamers, MIP, mimotopes etc). Being small and neutral molecules, mycotoxins can be better detected through labels like enzymes, nanoparticles, redox molecules and fluorophores etc. Therefore, the developed sensors are categorized in two groups like labeled (Fig 1a) and label-free sensors (Fig.1b) which can be further divided into competitive and non-competitive on the basis of detection strategy. In the present review, emphasis has been given on

the material construction of the transducer matrix along with the detection principle. Based on the type of receptor, biosensors for mycotoxin detection are described as below:

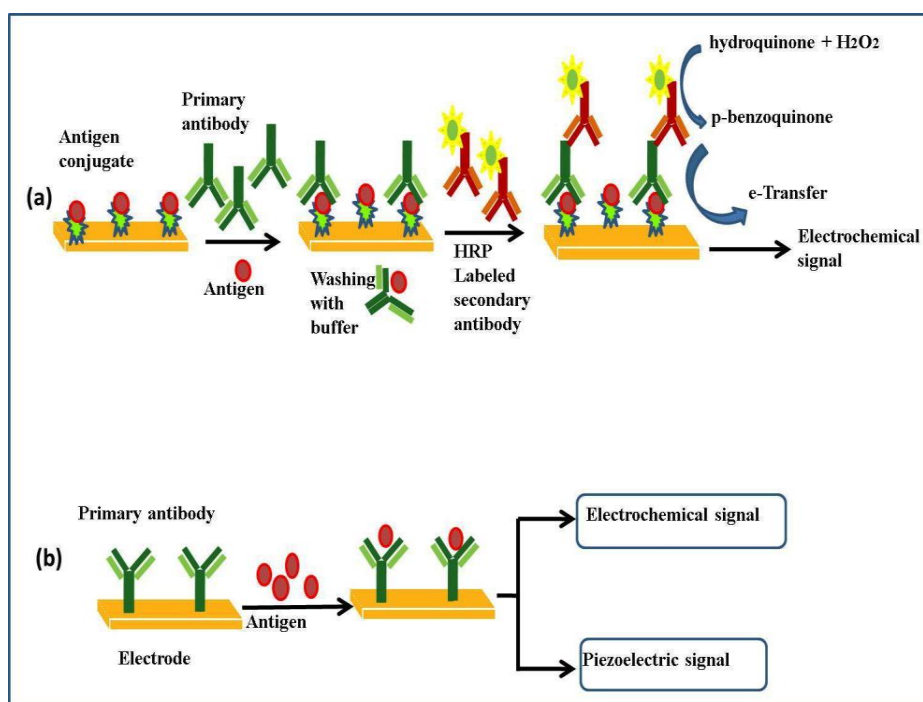


Fig.1a: Labeled detection of antigen. **(b):** Label free detection of antigen.

2.1. Immunosensors for mycotoxin

2.1.1. Labeled Immunosensor

The detection of small analytes (low molecular weight molecule) is mostly conducted using a competitive immunoassay format. In this assay, the sample analyte competes with coated labeled analyte or analyte-protein conjugate for a limited number of antibody binding sites. As the analyte concentration in sample increases, more labeled analytes are displaced (**Prieto-Simón et.al. 2012, Pemberton et.al. 2006, Piermarini et.al 2007**). In the competitive assays, two types of protocols are followed. In the first mode, the surface of electrode is coated with the saturated concentration of labeled analyte-protein conjugate and competition takes place between

free analyte and immobilized labeled analyte-protein conjugate for the fixed amount of antibody named as “indirect” method. The most common analyte-protein is found to be BSA-mycotoxin conjugate. Sometimes, a linker molecule such as polyethylene glycol (PEG) is employed as a spacer in between OTA and ovalbumin (OVA) conjugate (OTA-PEG-OVA) to reduce the steric effect (Yuan et.al. 2009).

Recent research work demonstrates that the nanomaterial or quantum dots (QDs) modified immobilizing matrix, coated antigen or secondary antibody can enhance the response signal (Bonel et.al. 2010, Liu et.al. 2009). A signal amplification of surface plasmon resonance (SPR) by a factor of more than 10 has been achieved using AuNPs labeled secondary antibody in a sandwich mode as compared to AuNPs tagged with primary anti-OTA and results in the 60 pg/mL as limit of detection of OTA (Urusov et.al. 2011). Gan et al. have employed magnetic Fe₃O₄-graphene oxides (Fe-GO) as the absorbent and antibody-labeled with cadmium telluride QDs (CdTe QDs) as the signal tag for aflatoxin M₁(AFM₁) detection and achieved the LOD of 0.3 pg/mL ($S/N = 3$) (Gan et.al. 2013). With the introduction of upconversion nanoparticles (UCNPs), Wu et.al. (Wu et.al. 2011) have introduced an immunoassay for simultaneous fluorescence detection of AFB₁ and OTA in food samples.

In the direct mode, free sample analyte competes with the absorbed labeled analyte-protein conjugate for the fixed amount of immobilized antibody. The transducer monitors the label concentration and hence measure the target analyte concentration, present in the solution. Alarcon et al. (Alarcon et.al. 2006) have observed that direct method is more sensitive than indirect method for OTA estimation.

The sensitivity of quartz crystal microbalance (QCM) transducer can be enhanced for sensitive analysis of low molecular weight mycotoxin using sandwich format through labeled secondary antibody. Jin et.al. have enhanced the sensitivity using the oxidative label HRP, that oxidized 4- chloro-1-naphthol into insoluble product (benzo-4-chlorohexadienone) and AuNP tagged secondary antibody as mass inducer over the crystal (**Jin et.al. 2009a, 2009b**) and achieved a linear range of 0.01-10.0 ngmL⁻¹ for the determination of AFB1 in buffer or sample solutions.

The use of magnetic bead (MBs) micro/nanoparticles in the separation process offers great advantages such as easy handling, reusability, homogeneous dispersion and a great surface area(**Aguilar-Arteaga et.al. 2010, Vidal 2012**). The magnetic particles have helped in separations with efficiency close to 100 % with complete removal from interfering substances (**Prieto-Simon et.al. 2008**). Identical approach is followed by Parrota et al. for the estimation of OTA from untreated red wine samples with the LOD of 0.008 ppb level without magnetic separation (**Parrota et.al. 2012**). Multiplexed, competitive immunoassay-based detection of different mycotoxins and the feasibility of running sandwich and competitive immunoassays formats on a single waveguide surface (**Sapsford et.al. 2006**) have been reported.

Labeled non-competitive immunoassay often follows the sandwich format and the enzymes/fluorescent material/nanoparticles tagged secondary antibody generates signal on capturing the antigen. Masoomi et al. (**Masoomi et.al. 2013**) have designed a sandwiched type electrochemical immunosensor for AFB1 estimation. The oxidation of catechol to o-quinone attached to secondary antibody via gold-coated iron nanoparticles is trapped for signal generation and iron nanoparticles offers regeneration of immunosensor using an external magnetic field. Though, the above immuno-platform has achieved a wide linear range of 0.6–110 ngmL⁻¹ with a

LOD of 0.2 ng mL^{-1} , the construction of sensor architecture is complex in nature. A zearanol immunosensor comprising of multiple labels such as sodium montmorillonites clay NPs (Na-Mont), thionine (TH), HRP attached to the secondary anti-zearanol antibody (Na-TH-HRP-Ab2) and Na-Mont NPs modified nanoporous gold (NPG) as an electrode material has been fabricated to detect Zearalenone up to 3 pg/ml (Feng et.al 2013).

2.1.2. Label-free immunosensor

The innovation of label free immunosensors can also be classified as non-competitive and competitive. The main advantage of these label free immunosensors is simplicity and single-stage reagent less operation. However, such immunosensors are often inadequate to meet the demand of sensitive detection. As concern of simplicity and speed of immunosensors, the non-competitive protocol is favored over the competitive one. The major drawback of noncompetitive label free immunosensor is false positive response due to nonspecific binding.

In a label free non-competitive immunosensor, the interaction of immobilized antibodies and analyte is read out by the transducer. The transducer and mode of detection play the important role for obtaining the enhanced sensitivity of the label free immunosensor. The sensing ability of an electrochemical immunosensor can be enhanced by incorporating either a metal (PtCo NP) or metal oxide nanoparticles (such as CeO_2 , Fe_3O_4 , TiO_2 , ZnO etc.) or conducting polymer etc into a given matrix (Sharma et.al. 2010, Srivastava et.al. 2013, Solanki et.al. 2009, Feng 2013).

Compared to the amperometric immunosensors, electrochemical impedance spectroscopy (EIS) based immunosensors have been found to be more sensitive and reliable. EIS studies investigate the electrical properties of the interface of sensing device and trace the reactions

occurring on its surface (**Radi et.al. 2009, Zamfir et.al. 2011**). The EIS technique coupled with online flow detection tool have been found to lower the detection limit of AFB1 and AFB2 up to a level of 1 pg/mL in drinking yogurt and flavored milk (**Kanungo et.al 2014**) as compared to lateral flow system (**Andreou and Nikolelis 1998**). EIS immunosensing platform based on 11-mercaptoundecanoic acid (11-MUA) self-assembled on silver wire has detected AFB1 in groundnut extract with the LOD of 0.01 pgmL^{-1} and AFB1 detection ($6.25\text{-}100 \text{ pgmL}^{-1}$) in milk (**Bacher et al. 2012**).

Using the fluorescence resonance energy transfer (FRET) mechanism Li et al. have demonstrated a label-free non-competitive immunoassay while antibodies with tryptophan (Trp) residues excited at 280 nm acts as a donor on interaction with antigen (AFB1). The fragment of antibody (Fab) promotes the detection of AFB1 about 10 times higher than the complete aAFB1 antibody (**Li et.al. 2013**). The label-free optical immunosensors based on the concept of reflection of light are found to be a promising approach (**Nabok et.al. 2007, Nabok et.al. 2005**). The gold bounded protein G (GBP-ProG) offers higher SPR signal intensity (**Park et.al. 2014**) in comparison to the ProG or thiol-modified surface (**Tamerler et.al. 2006**). Adyani et.al. have reported superiority of competitive mode ($0.5\text{-}10 \text{ ng mL}^{-1}$) over non-competitive [$5\text{-}10 \text{ ngmL}^{-1}$] using optical waveguide light mode spectroscopy (OWLS) technique for detection of AFB1 and OTA (**Adanyi et.al. 2007**). The application of nano material at an appropriate platform can overcome the challenge of label-free estimation of AFB1 (**Ah et.al 2012**). An optical approach with gold nanorods (GNRs) has been employed for the label-free competitive detection of AFB1 with the LOD of 0.16 ngmL^{-1} (**Xu et.al. 2013**). The disadvantages of these (optical) techniques include costly equipment, challenges of regenerating the sensor chip and non specific adsorption.

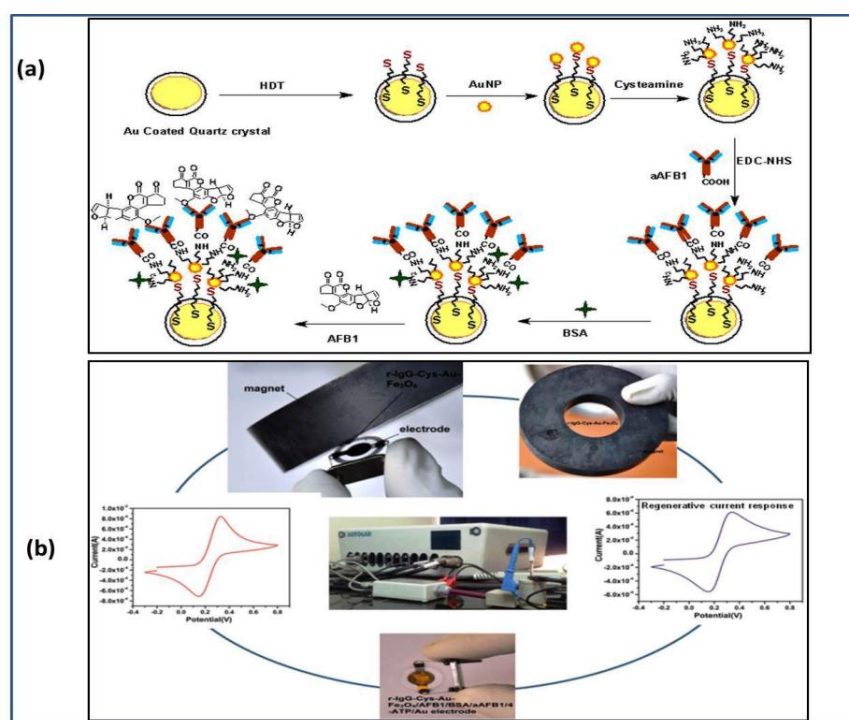


Fig.2 (a): AFB1 detection using label free noncompetitive technique. **(b):** Schematic diagram represents the regeneration of sandwich type immunoelectrode for the detection of AFB1.

Label-free approach with QCM transducer is currently not popular due to small size of mycotoxins (Cheng 2012, Tsai & Hsieh 2007, Vidal et.al 2009). QCM or Cantilever based technique is exploited for detection of AFB1 and OTA (Ricciardi et.al. 2013). Chauhan et.al. (Chauhan et.al. 2015a, Chauhan et.al. 2016) have developed label free electrochemical quartz crystal microbalance (EQCM) immunosensor based on AuNP coated self assembled monolayer with a LOD of 8 pgmL^{-1} for AFB1 detection (Fig. 2a). While gold coated Fe_3O_4 nanostructure

tagged secondary polyclonal antibodies have been exploited in a competitive sandwiched format

<i>SN</i>	<i>Matrix</i>	<i>Electrode</i>	<i>Type of Ab</i>	<i>Mode of detection</i>	<i>Label</i>	<i>Technique</i>	<i>Toxin</i>	<i>Response range</i>	<i>LOD</i>	<i>Sensitivity</i>	<i>Relative Standard Deviation (RSD)in %</i>	<i>Coefficient of variation (CV)in %</i>	<i>Reference</i>
-----------	---------------	------------------	-------------------	--------------------------	--------------	------------------	--------------	-----------------------	------------	--------------------	--	--	------------------

to develop a reusable immunosensor using strong external magnet (**Fig.2b**) (**Chauhan et al.2015b**). A brief summary of developed immunosensors for mycotoxin analysis are presented in Table 1.

Table 1: The characteristics of the reported labeled and label free immunosensors.

1	Graphite/ silver	SPCE	mAb	Competitive	OTA- ALP	DPV	OT A	0.05- 2.5ng/ml 0.1-7.5 ng/ml	60 ng/ml 0.4 ng/ml 100 ng/ml	-	8-16	7	Alarco n et.al. 2006
2	Graphite based ink	SPCE	pAb	Competitive	Au- labeled ALP- Sec Ab	DPV	OT A	0.9-9 ng/mL 0.3-8.5 ng/mL	0.86 ng/mL 0.20 ng/mL	-	8, 10	6	Bonel et.al. 2010
3	Nitrocellulose Membrane	-	pAb	Competitive	Au coloids -pAb	Lateral Flow immun oassay	OT A	1-10 µg/kg	1.5 µg/kg	-	14-18	>20	Laura et.al. 2011
4	1,6- Hexanedithiol	Au	mAb	Competitive	ALP	Electro chemic al (DPV)	OT A	10 pg/mL – 100ng/mL	8.2 pg/mL	-	-	-	Liu et.al. 2009
5	Magnetic beads with Protein G	SPCE	mAb	Competitive	HRP	SWV	OT A	0.01-20 ppb	0.008 ppb	-	5.56	-	Parrot ta et.al. 2012
6	-	SPE	mAb	Competitive	OTA	-	OT A	0.3 ng/L- µg/L	-	-	20, 36	-	Prieto- Simon et.al. 2012
7	Poly(methyl methacrylate) (PMMA) beads		mAb	Competitive	HRP	-	OT A	-	0.7 ng/mL	-	-	-	Simon et.al. 2008
8	16-MHDA	Au	pAb	Competitive	Au NPs	QCM	OT A	10-128 ng/mL	8 ng/mL	-	-	8.96	Vidal et.al. 2009
9	Magnetic Beads	SPCE	mAb	Competitive	HRP	DPV	OT A	0.1 pg/mL- 1µg/mL	10 pg/L	-	9	-	Vidal et.al. 2012
10	11-MUOH	Au	mAb	Competitive	Au NPs	SPR	OT A	-	1.5 ng/mL Au- 0.042 ng/mL	-	-	-	Yuan et.al. 2009
11	-	SPCE	mAb	Competitive	Au NPs	Impedi metric	AF M 1	15 - 1000 ng/mL	15 ng/ mL	-	20	-	Vig, et.al.

													2009
12	MPA-BSA		mAb	Competitive	HRP	QCM	AFB 1	0.01–10.0 ng mL ⁻¹	0.01 ng mL ⁻¹ .	-	4-7	-	Jin et.al. 2009
13			mAb		Fe ₂ O ₃ nanoparticles	GMR	AFB 1	50pg/mL-50ng/mL	50 pg/mL	-	-	-	Mak et.al. 2010
							AFB 1						
							ZE R	330pg/mL and 33ng/mL					
							HT-2						
14		SPCE	mAb	Competitive	ALP	Electrochemical	AFB 1	0.1–10 ngmL ⁻¹ ,	90 pgmL ⁻¹ .	-	18-22	-	Mmida et.al. 2006
15	GCE/PTH/Au NP AFB1-BSA-polythionine (PTH)/gold nanoparticles	GCE	pAb	Competitive	HRP	Electrochemical	AFB 1	0.6 - 2.4 ng/mL	0.07 ng/mL	-	2-5	-	Owino et.al. 2008
16			pAb	Competitive	ALP	Intermittent pulse amperometry (IPA)	AFB 1	0.05 and 2 ng/mL	-	-	7-10	-	Piermarini et.al. 2007

								xyni vale nol	enol: 20.20– 69.23					
								OT A	OTA: 35.68– 363.18					
								T-2, ZO N	T-2 toxin : 0.11–1.81 Zearaleno ne : 0.08– 7.47 ng/mL					
18	magnetic nanoparticles (MNPs)	-	mAb	Competitive	NaY0.7 8 F4 :Yb0.2 , Tm0.02 and NaY0.2 8 F4 :Yb0.7 ,Er0.02 UCNPs	Flourescent	AFB 1	0.01 to 10 ng mL ⁻¹	0.01ng mL ⁻¹	-	5.19	-	Wu et.al. 2011	
							OT A				2.14			
19	Au/ 3- Mercaptopropi onic acid (MPA)		mAb	Competitive	Au NPs	Piezoelectric	AFB 1	0.1– 100ngmL ⁻¹	0.01 ng mL ⁻¹	-	4-7	-	Jin et.al. 2009	
20	MWCNT- GCE	GCE	mAb	Competitive	HRP	flow injection (FI) system	ZO N	-	-	-	-	-	Pei et.al. 2013	
21	heterobifunctionalsilane	-	mAb	Competitive	Fluorescein isothiocyanate label	fiber-optic immunosensor	FB1	10- 1000 ng /mL	10 ng /mL	-	3.9	-	Urraca et.al. 2005	
22	-	-	mAb	Competitive	HRP	Flow- Through Immunosensors	ZO N	0.019 to 0.422 ng mL ⁻¹	0.007 ng mL ⁻¹	-	-	-	Wang et.al. 2010	

or

23	Fe ₃ O ₄ -graphene oxides	SPCE	mAb	Non-competitive	CdTe-CNT QDs Conjugate	ECL	AFM 1	1.0 to 1.0 × 10 ⁵ pg/mL	0.3 pg/mL	-	3.5	-	Gan et.al. 2013
24	AET- Au NPs	Au interdigitated electrodes (150nm thick)	mAb	Non-competitive	HRP	conductometric	AFB 1	0.5 to 10 ng/mL	0.1 ng/mL at 3δ.		7	7.1	Liu et.al. 2006
25	GCE/chitosan/Au nanoparticle (AuNP)/anti-Aflatoxin B ₁ (a AFB ₁),	GCE	pAb	Non-competitive	catechol-Au-Fe ₃ O ₄ NPs	Electrochemical	AFB 1	0.6–110 ng mL ⁻¹	0.2 ngmL ⁻¹	-	-	6.2, 5.7	Masoomi et.al. 2013
26	nanoporous gold films (NPG)	GCE	mAb	Non-competitive(NC)	Na-Mont-Ti-HRP-Ab ₂	Electrochemical	ZON	0.01–12 ng mL ⁻¹	3 pg mL ⁻¹	-	2.46-5.17	4.2-5.2	Feng et.al. 2013
27	Chitosan-iron oxide	ITO	pAb	NC	-	DPV	OT A		0.5 ngdL ⁻¹	36μA ng ⁻¹ dL ⁻¹	-	-	Kaushik et.al. 2009
28	Nano SiO ₂ – CH	ITO	pAb	NC	-	DPV	OT A	0.5-6 ngdL ⁻¹	0.3 ngdL ⁻¹	-	-	-	Kaushik et.al. 2009
29	Chitosan-PANI	ITO	pAb	NC		EIS	OT A	Upto 10 ngmL ⁻¹	1.0 ngmL ⁻¹	-	-	-	Raju Khan et.al. 2009
30	CS/TiO ₂ (Chitosan)	-	pAb	NC	-	EIS	OT A	1-10 ngmL ⁻¹		7.5 nM	-	-	Khan et.al. 2008
31	4-carboxyphenyl	Au	-	NC	-	EIS	OT	1- 20	0.5	-	3.7-5.5	-	Radi et.al.

	SAM						A	ngmL ⁻¹	ngmL ⁻¹				2009
32	BSA/AO-IgG/AUT/Au (SAM of AUT)	Au	pAb	NC	-	EIS	OT A	0.5-6 ng/dL	0.08 ngdL ⁻¹	36.86 ohm ng ⁻¹ dL ⁻¹	-	-	Solanki et.al. 2010
33	16MHDA	Au	pAb	NC	-	QCM	OT A	50-1000 ngmL ⁻¹	16.1 ngmL ⁻¹		-	64	Tsai et.al. 2007
34	Au/TA/Glu/BSA/MNP-Ab	Au	mAb	NC	-	EIS, CV	OT A	0.01-5 ngmL ⁻¹	0.01 ngmL ⁻¹	-	4.7	-	Zamfir et.al. 2011
35	BSA/aAFB1-C-AuNP/MBA/Au Gold	Au	mAb	NC	-	Volta metric	AF M 1	10 – 100 ngdL ⁻¹	17.90 ngdL ⁻¹	0.45 μAng ⁻¹ dL	-	-	Aditya et.al. 2010
36	anti- AFB ₁ /MWCNTs/ITO	ITO	mAb	Non-competitive	-	Volta metric	AFB 1	0.25–1.375 ngmL ⁻¹	0.08 ngmL ⁻¹	(95.2 μAng ⁻¹ mL ⁻²)	-	-	Singh et.al. 2013
37	SAM of 11-MUA	Silver Wire	mAb	Non-competitive	-	Impedimetric	AF M 1	(6.25–100pgmL ⁻¹)	1 pgmL ⁻¹	6.25 pgmL ⁻¹	-	-	Bacher et.al. 2012
38	BSA/AbAFB1/n-Sm2O3/ITO	ITO	mAb	Non-competitive	-	Volta metric	AFB 1	10–700 pg mL ⁻¹	57.82 pg mL ⁻¹ cm ⁻²	48.39 μAp ⁻¹ mL cm ⁻²	0.39	-	Singh et.al. 2013
39	-	-	Fragment Ab	Non-competitive	-	FRET based Immunoassay	AFB 1	-	0.85 and 0.09 ng mL ⁻¹	-	-	-	Li et.al. 2013
40	Nano-sized gold hollow balls (NGB) with dendritic	Au		NC	-	QCM	AFB 1		0.05 ng mL ⁻¹		2.3, 5.8	3.8-5.1	Liao et.al. 2007

surface													
41	Silica gel-ionic liquid-antibody	GCE	pAb	NC	-	EIS	AFB 1	0.1–10 ng mL ⁻¹	0.01 ng mL ⁻¹	1.7	-	Zaijun et.al. 2010	
42	APTES , Silane, Protein G	-	mAb	NC	-	Microcantilever	Aflatoxins OTA 1 : 6	Aflatoxins ; 3 ngmL ⁻¹ ng mL ⁻¹	-	-	-	Ricciardi et.al. 2013	
43	RGO/ITO	ITO	mAb	NC	-	Electrochemical	AFB 1	-	0.12 ng mL ⁻¹	68 μ Ang ⁻¹ mL ⁻² cm	-	Srivastava et.al. 2013	
44	DSP (3,3'-Dithiodipropionic-acid-di-N-hydroxysuccinimide ester)	Au	mAb	NC	-	QCM	AFB 1	0.5 - 10 ppb	-	-	-	Spinella et.al. 2013	
45	Fe ₃ O ₄ /SiO ₂ composite nanoparticles	Au	mAb	NC	-	QCM	AFB 1	0.3– 7.0 ng mL ⁻¹	0.3 ng mL ⁻¹	-	8.0	6.3 Wang et.al. 2009	
46	Au/DDT SAM	Polycrystalline gold electrode	mAb	NC	-	TIRE and QCM	AFB 1	100 μ g mL ⁻¹ to 0.15 ng mL ⁻¹	-	-	-	Nabok et.al. 2007	
47	CS–PtCo–Ab/Graphene-Thionine/GCE	GCE	mAb	NC	-	Electrochemical	ZON	0.05 to 5.0 ng mL ⁻¹	13 pg mL ⁻¹	-	4.5	Feng et.al. 2013	
48	1-dodecanethiol (DDT)	Au	pAb	NC	-	Electrochemical	alter toxin I (ATX-I)	-	4 x 10 ⁻⁸ moldm ⁻³ (14 ppb)	-	7	-	Moressi et.al. 2007

49	-	-	mAb	Com/ NC	-	OWLS	AFB 1	5-10ngmL ⁻¹	-	-	-	-	Adányi et.al. 2007
							OT A	0.5-10ngmL ⁻¹					
50	Au NPs	-	-	Competitive	-	SPR	OT A	0.1 ngmL ⁻¹ -0.1 μgmL ⁻¹	60 pgmL ⁻¹	-	-	-	Urusov et.al. 2011
51			mAb	Competitive	-	EIS	AF M 1	1-100pgmL ⁻¹	1pgmL ⁻¹	-	-	-	Kanungo et.al. 2014
52	Au NPs	Si-FET channel	mAb mAb mAb	Competitive	-	Si-FET	AFB 1	2.5 – 20 ngmL ⁻¹	-	-	-	~11	ChilSeong et.al. 2012
							ZE N	0.5 – 50 ngmL ⁻¹	-				
							OT A	0.5 - 100 ngmL ⁻¹					
53	GNRs	-	mAb	Competitive	-	Optical	AFB 1	0.5 to 20 ng mL ⁻¹	0.16ng mL ⁻¹ ,	-	-	-	Xu et.al. 2013

2.2. Aptasensor for the mycotoxin detection

The key part of the aptasensor is the aptamer, a synthetic oligonucleotide ligand (either single stranded DNA (ssDNA) or RNA containing 10–50 variable bases and are known to exhibit high specificity and strong binding affinity (Cho et.al. 2009, Willner and Zayats 2007). Aptamers can fold into well-defined three-dimensional structures and bind to their ligands by complementary shape interactions (Hermann and Patel 2000). In comparison to the antibody,

an aptamer has several advantages such as ease of synthesis and modification with a variety of chemical groups, stability, cost-effectiveness etc (**Schmidt et.al. 2004, Yang et.al 2013**). The aptamers can maintain their structures over repeated cycles of denaturation and show high binding affinities and specificities towards the broad range of target (macro to micro molecules, like toxins, drugs, peptides, proteins and whole cells etc.). The aptamers are thus, considered to be a better alternative to antibodies in many biological applications. In 2008 Cruz-aguado and Penner have briefly studied the aptamer sequence (see supplementary file **Table S2**) for OTA (Cruz-aguado & Penner 2008) using *in-vitro* process SELEX.

2.2.1. Factors affecting aptamer affinity

2.2.1.1. Presence of divalent cation

The binding of OTA to the DNA aptamers depends on the presence of divalent cations. It is observed that negatively charged DNA forms a coordination complex with OTA (**Yang et.al. 2013, Yang et.al. 2011, Bonel et.al. 2011**) via carboxyl and 8-hydroxyl groups in presence of calcium or magnesium ions. It is shown that the aptamer has rather high affinity to OTA in the presence of 20 mM Ca^{2+} (dissociation constant $K_d=49$ nM) (**Cheng et.al. 2012**). Circular dichroism and spectroscopic experiments reveal that, on addition of OTA, aptamer changes from random coil structure to compact rigid antiparallel G-quadruplex structure (**Yang et.al. 2011**).

2.2.1.2. Effect of pH

The pH is known to affect the binding affinity. Aptamer shows high affinity at pH 7.0. In acidic pH, the 8-hydroxyl group in OTA is protonated which in turn inhibits the complex formation resulting in decreased binding to the aptamer. Aptasensors can be divided in two categories labeled and label-free as described below:

2.2.2. Labeled Aptasensors

The signaling in aptasensors occurs due to changes in the conformation of aptamer as the target (mycotoxin) molecules are introduced into the reaction chamber. The detection can be achieved through transducer either in “signal on” or “signal off” form, depending on the format of the assay (**Fig.3**). Commonly used labels are fluorescence material (fluorescein, luminols, QDs etc), enzyme HRP, GO, ALP, electroactive compounds (ferrocene, ferro- cyanide, methylene blue (MB), Pt and Cds QDs, and other metal nanoparticles (NPs)). In the “signal on” format, target detection is based on the signal enhanced after the interaction with target. While the signal off refers to diminish in signal due to the formation of target-aptamer complex.

2.2.2.1. Signal On

“Signal On” format is represented by the scheme (**Fig. 3a**). The fluorescent labeled aptamer, and quencher moiety (QDNA) has been used to detect OTA with a linear dynamic range of 1-100 ngmL⁻¹ (**Cheng et.al. 2012**). Carbon nanomaterials like graphene, single-walled carbon nanotubes (SWCNT) etc. (**Sheng et.al 2011, Guo et.al. 2011, Cruz-Aguado and Penner 2008b**) are mostly utilized as quencher. For example, the fluorescence of carboxyfluorescein (FAM) is quenched readily via energy transfer from dye to carbon nanomaterials through " $\pi-\pi$ " stacking interaction while FAM modified aptamer interacts with a carbon nanomaterial (**Zheng et.al. 2003, Zhu 2010**). Sheng et al. have reported that poly (vinyl pyrrolidone coated graphene-oxide) has significantly improved detection limit and sensitivity than uncoated graphene or SWCNT due to the control of the non-specific adsorption (**Guo et.al. 2011**).

In the series of fluorescence nanoparticles, up-conversion nanoparticles have brought a new avenue of simultaneous multi analyte detection. On the basis of doping with rare earth elements on UCNPs, varieties of multicolor finely tuned multiplexed-FRET donor-acceptor

pair can be developed with a combination UCNPs, doped with various rare earth elements like Er, Tm and Ho and graphene oxide having a wide range of absorption wavelengths (approximately 300–700 nm). Wu et al. have reported (Wu et.al. 2010) “signal on” aptasensor for multiplexed FRET-based turn-on assay for the simultaneous detection of OTA and fumonisin B1 (FB1). In another approach, it is demonstrated that N-(aminobutyl)-N-(ethylisoluminol) (ABEI), a luminol derivative, with AuNPs- modified electrode has been found to detect OTA ($0.2\text{--}5.0\text{ ngmL}^{-1}$) with a detection limit of 0.06 ngmL^{-1} which is tenfold higher than the bare gold electrode (Wang et.al. 2010).

The nucleic acids, having ability to perform both as receptor and catalysis, are known as functional nucleic acids (FNAs) (Li 2009) or DNAzyme and hence, can be used for signal enhancement. Hemin as a ligand can specifically bind with several G-quadruplexes with high affinity and acts as a HRP-mimicking DNAzyme that may display a highly enhanced catalytic activity compared with hemin itself (Cheng et.al. 2009, Li, et.al. 2009b). Yang et.al. have designed a nucleic acid hairpin structure of hemin–G-quadruplex which opens up on addition of OTA. The activity of this DNAzyme is monitored spectrophotometrically via H_2O_2 mediated-oxidation with tetramethylbenzidine (TMB) as a colorimetric substrate (Yang et.al. 2013). Single, double, and triple HRP-DNAzymes coupled to the AFB1 aptamer have been tested and found signal amplification depends on number of the DNAzymes that produce chemiluminescence (CL) while binding to AFB1-ovalbumin (OVA) used as a coating antigen (Shim et.al. 2014)

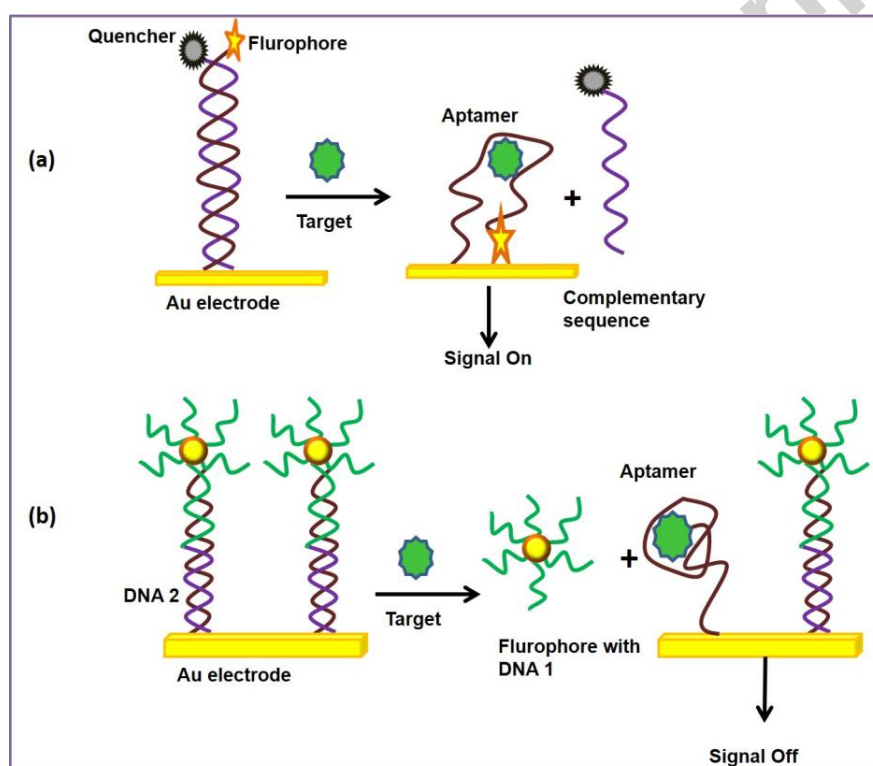


Fig.3 (a): Aptasensor ‘signal on’ phenomenon. **(b):** schematic representation of ‘signal off’ phenomenon based aptasensor

2.2.2.2. Advanced approach for signal amplification

The 1:1 binding ratio of the aptamer and target limits the signal enhancement and the sensitivity of the assay (**Tong et.al. 2011**). Signal amplification is an efficient way to improve the sensitivity of an aptasensor. Some signal amplification approaches such as polymerase chain reaction (PCR) (**Schmittgen and Livak 2008**), rolling circle amplification (RCA) (**Li et.al. 2010**), loop-mediated isothermal amplification (LAMP) (**Wang et.al. 2010, Fang et.al 2011**) and nicking endonuclease signal amplification (**Hun et.al. 2010**) have been reported. Chen et.al. have designed a sandwich nanostructured self-assembly of OTA binding aptamer and the DNAzymes on a gold electrode surface to quench the ECL emission of the dissolved O_2 . On addition of OTA, the RecJf exonuclease leads to the target recycling disassembly of the nanostructures and “signal on” for significant ECL for OTA detection with the LOD of 75 fg mL^{-1} (**Chen et.al. 2014**). The exploitation of the target recycling in the field of aptasensor is limited (**Tong et.al. 2012**). Therefore, for enhancing the labeling ratio with aptamer, Tong et.al. have applied RCA, an isothermal DNA replication technique, for nucleic acid amplification by phi29 DNA polymerase (see supplementary file **Fig.S2**) to detect OTA down to 0.2 pg mL^{-1} the level

with a dynamic range spanning more than 4 orders of magnitude. The nicking endonuclease enzyme has attracted researchers' attention for circular amplification and design the sensitive analysis of targets (**Hun et.al. 2013**). The strategy based on combined cleavage of nicking endonuclease with target-induced strand release can be used to develop a bioassay for the detection of OTA.

2.2.2.3. Signal Off

In the signal off format, a significant reduction in signal due to formation of the target aptamer complex is monitored (**Fig. 3b**). The influence of non-specific adsorption of DNA to the final sensing results could be avoided by the “signal-off” detection model. Therefore, this “signal-off” sensor could potentially reduce the false positive results compared with the reported “turn-on” sensor. For example, the electrochemical signal of Au NP assisted methylene blue (MB), acting as a electrochemical redox probe, decreases significantly on adding OTA to the solution (**Kuang et.al. 2010**).

The use of magnetic bead functionalised aptamer fulfills two objectives: (i) non covalent immobilization by external magnetic field and (ii) sensing tool for OTA (**Rhouati et.al. 2013**). It may be noted that all above mentioned sensors require multiple steps which are not beneficial for the real applications. Wu et.al. (**Wu et.al. 2012**) have designed a one-step electrochemical aptasensor using the thiol- and methylene blue- (MB-) dual-labeled aptamer modified gold electrode for determination of OTA with a wide linear range from 0.1 pgmL^{-1} - 1000 pgmL^{-1} (see supplementary file **Fig.S3**) with the LOD of 0.095 pgmL^{-1} .

2.2.3. Label-free aptasensor

In a label free aptasensor, the transducer measures direct interaction of aptamer and analyte through the change in transducer signal (**Schoning & Poghossian 2002, Li et.al. 2011**).

The electrochemical aptasensors based on modified surface of electrode with polymer, metal nanoparticles and metal oxide (eg. TiO_2 -chitosan, chitosan/polyaniline, and acacia gum) yields enhanced sensitivity for OTA detection (**Khan & Dhayal 2009, Khan et al. 2011**). Click chemistry helps immobilization and uniform distribution of aptamer over the electrode that may help in improving sensitivity and LOD (**Hayat et al. 2013, Ran et al. 2011**). To develop label free sensor and overcome the background current, conformational change of aptamer upon target mycotoxin binding is monitored for the mycotoxin analysis. Hayat et al. have fabricated polyethylene glycol–aptamer conjugate to form two piece macromolecules. The macromolecules results in the formation of long tunnels on screen printed carbon electrode (SPCE) surface, while aptamer acts as gate of the tunnels for the detection of OTA (**Hayat et al. 2013**). The similar strategy has been followed to construct label free “signal on” aptasensor for OTA assay based on formation of G-quadruplex and release of two single strands, to bind with the Tb^{3+} ions resulting in enhanced fluorescence intensity (**Fig. 4**). The LOD have been noticed to be as 20pg/mL (**Zhang et al. 2013**).

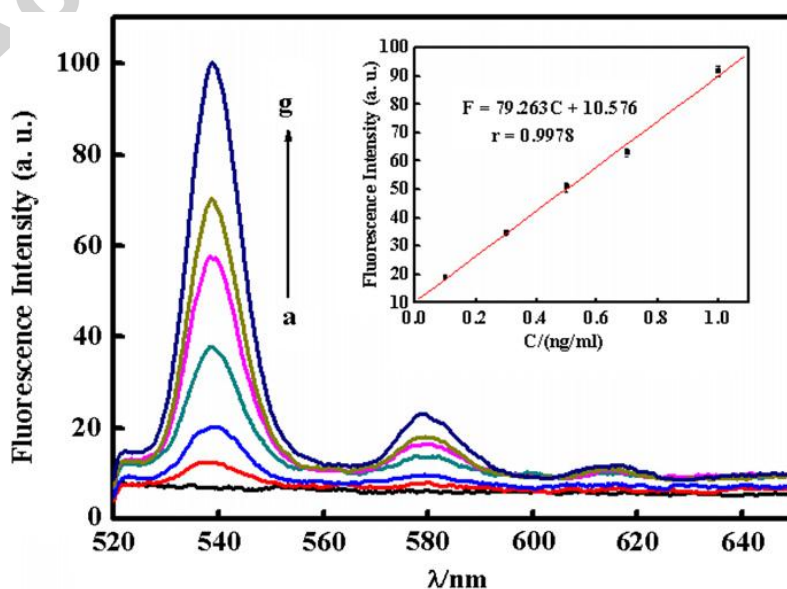


Fig. 4. Fluorescence spectra of the aptasensor with different concentrations of OTA (from a to g): 0.00, 0.05, 0.1, 0.3, 0.5, 0.7, and 1 ng/mL respectively. Inset: A calibration curve demonstrating peak fluorescence intensity versus OTA concentration (**Zhang et.al. 2013**).

For label free detection of small molecules, surface plasmon resonance spectroscopy is one of the highly sensitive technique. Hardly, any efforts have been made to utilize SPR spectroscopy in aptasensor for mycotoxins detection as that the change of SPR signal resulting from the adsorption on lower molecular weight aptamer is lower than that of antibody (**Wang et.al. 2009**). label-free aptasensor for OTA detection based on thickness shear mode acoustic method (TSM) (**Lamberti et.al. 2011**) and surface-enhanced Raman spectroscopy (SERS) (**Kim et.al. 2010, Galarreta et.al. 2011**) have also been reported.

In 2010 Neoventures Biotechnology Inc. (Canada) has patented specific aptamers to AFB1 and zearalenone. Firstly, Guo et.al. (**Guo 2014**) have fabricated a real-time quantitative polymerase chain reaction (RT-qPCR) based aptasensor for AFB1 detection. The RT-qPCR greatly improves detection sensitivity, and specificity of aptamer, functionalized at end 3'-with biotin groups. The sensing is accomplished in a single PCR tube with the detection limit of 25 fg/mL⁻¹ for AFB1. The reported aptasensor for detection of mycotoxins are summarized in **Table 2**.

Table 2: Summary of labeled and label-free Aptasensor for the detection of Mycotoxins

S.N.	Matrix	Electrodes	Type of receptor	Mode	Label	Technique	Mycotoxin	Response Range	LOD	Sensitivity	Relative standard deviation (RSD) %	Coefficient of variation (CV) in %	References
------	--------	------------	------------------	------	-------	-----------	-----------	----------------	-----	-------------	-------------------------------------	------------------------------------	------------

n %													
1	Magnetic Beads	-	Aptamer	Competitive	ALP	DPV	OTA	-	0.11 ng/mL	-	-	-	Barthelmebs et.al. 2011
2	Paramagnetic microparticle beads	SPCE	Aptamer	Competitive	HRP	DPV	OTA	0.78-8.74 ng/mL	0.07 ng/mL	-	-	-	Bonel et.al. 2011
3	SH-Apta	Au	Aptamer	Competitive	Fluorescein aptamer	Microfluidic channel SERS	OTA	0.05 to 4 μM.		-		-	Galarreta et.al. 2013
4	Magnetic beads based DNA (ssDNA) aptamers		DNA (ssDNA) aptamers	Non competitive	-	Fluorometer	ZON	3.14×10 ⁻⁹ to 3.14×10 ⁻⁵ M	7.85×10 ⁻¹⁰ M.	-	-	-	Chen et.al. 2013
5	6-mercaptop-1-hexanol/captured probe(MCH)/(CP)/AuE	Au	aptamer	Competitive	-	Electrochemiluminescent	OTA	0.2 pg mL ⁻¹ to 1 ng mL ⁻¹	75 fg mL ⁻¹		9.1, 6.0	-	Chen et.al. 2014
6	Carboxy fluorescein	SWCNT	Aptamer	Competitive	-	Fluorescence	OTA	25 nM to 200 nM	24.1 nM		-	-	Guo et.al. 2011
7		magnetic bead (MB).	sing DNA		ABEI labeled carboxylic silica nanoparticles	chemiluminescence,	OTA	1.0x10 ⁻¹² to 5.0x10 ⁻⁸ g mL ⁻¹	3.0 x 10 ⁻¹³ g mL ⁻¹				Hun et.al. 2013
8	-	-		Competitive	Au NP - DNA	Electrochemical	OTA	0.1 to 20 ng/mL.	30 pg/mL,		-	10	Kuang et.al. 2010

9	-	-				Fluorescent	OTA	1 ng/mL-100 mg/mL	1 ng/mL	-	-	Lv et.al.2014
10	Magnetic beads	SPCE		Competitive	Biotin labeled OTA, ALP	Automated flow electrochemical aptasensor	OTA	1 µL to 3µL	0.05 µg/L	4-5	5	Rhouati et.al. 2013
11	Graphene oxide			Competitive	FAM (carboxyfluorescein)		OTA	2µM to 35µM.	21.8 nM	-	-	Sheng et.al. 2011
12	Graphene				UCNPs	FRET	OTA, FB1	0.05 to 100 ng·mL ⁻¹ for OTA and 0.1 to 500 ng·mL ⁻¹ for FB1	OTA 0.02 ng·mL ⁻¹ and FB1 0.1 ng·mL ⁻¹ .	4.74, 5.86	-	Wu et.al. 2012
13	Phi 29 DNA	Magnetic bead	Aptamer	-	QDs	Electrochemical	OTA	0.5 pg/mL-10 ng/mL	0.2 pg/mL	-	-	Tong et.al. 2012
14	Au NPs	Au	Aptamer	-	DNA 1- Au NPs DNA 2- ABEI	Electrochemiluminescence	OTA	0.02-3 ng/mL	0.007 ng/mL	-	3.8	Wang et.al.2010
15	BSA or OVA	-	-	Competitive	Luminol or HRP	Chemiluminescence	AFB1	0.1 – 10 ng/mL	0.11 ng/mL	-	-	Shim et.al. 2013
16	OTA chemisorbed on Au	-	Aptamer	-	-	EIS	OTA	0.1-100 nM	0.12-0.4nM	-	0.2-3.5	Castillo et.al. 2012
17		-	Aptamer	NC D	-	Fluorescence	OTA	-	5nM to 1	-	-	Cruz-Aguado

			mer			nce		pmol				et.al 2008	
18		-	Apta mer	-	-	Spectro- fluoromet er	OTA	1-100 ng/mL	0.8 ng/mL	-	4.7	-	Chan et.al 2012
19	16- mercapt o- hexaned ecanoic acid	-	Apta mer	D C	-	Thicknes s Shear Mode Acoustic Method (TSM)	OTA	25-740 nM	30 nM	-	-	-	Lamber ti et.al 2011
20	Magneti c beads based DNA (ssDNA) aptamer s		DNA (ssDN A) apta mers	Non compet itive		Fluorome ter	Zeara lenon e (ZEN)	3.14×10 ⁻⁹ to 3.14×10 ⁻⁵ M	7.85×10 ⁻¹⁰ M	-	-	-	Chen et.al 2013
21	solution		Carb oxyfl uores cein- OTA Apta mer	SWCN T		Fluorose nce	OTA	25 nM to 200 nM	24.1 nM	-	-	-	Guo et.al 2011
22		magn etic bead (MB).	DNA		ABEI carbo xylic silica nano partic les	chemilum inescence (CL) probe,	OTA	1.0 x 10 ⁻¹² to 5.0x10 ⁻⁸ g mL ⁻¹	3.0 x 10 ⁻¹³ g mL ⁻¹	-	3.4	-	Hun et.al 2013
23	streptavi din– biotin– DNA probe conjugat es	chro mato graph ic strip assay				scanning reader.	OTA		0.18 ng/mL	-	-	6.7	Wang et.al 2011
24									1.9 ng mL ₋₁	-	4.7	-	Wang et.al 2010
25			apta mer			Electroch emical	OTA	0.1pg/mL – 1000pg/mL	0.095pg/ mL	-	4.9	-	Wu et.al 2012
26	Tb3p, structur e- switchin			signal -on		Fluoresce nt	OTA		20 pg/mL OTA with high specificit	-	1.67	-	Zhang et.al 2013

	g aptamer and magnetic beads(M Bs),a												y
27	label-free for rapid and high-throughput detection of Ochratoxin A		DNAzyme – aptamer conjugate			colorimetric	OTA	upto30nM	4nM	-	-	-	Yang et.al 2013
28	Ferrocene labeled DNA probe	Au	Aptamer	-	-	DPV	OTA	5pg/mL-10 ng/mL	1 pg/mL	-	-	-	Tong et.al 2011
29	Au NPs and DNA probe	Gold	ssHS DNA	Non-competitive	-	Impedimetric	AFM 1	1–14 ng/mL	-	-	-	6.2	Dinckaya et.al 2011
30	Biotin-Streptavidin	-	AFB1 Aptamer	Non-competitive	-	Electrochemical	AFB 1	5.0×10^{-5} to 5.0 ng mL ⁻¹	25 fg/ mL	-	2	-	Guo et.al 2014
31	(Fe ₃ O ₄ / PANI) film	Micro-IDE of Pt	21-mer aptamer	Non-competitive	-	Electrochemical based Aptasensor	AFM 1	6–60 ng·L ⁻¹ , 1.98 ng·L ⁻¹ .	-	5	-	-	Nguyen et.al 2013
32	11-mercaptoundecanol, Dextran 500,	Gold	-	-	-	DNA-based piezoelectric	AFB 1		1.5 ng/ g	-		10	Tombelli et.al 2009

2.3. Molecularly Imprinted Polymer (MIP)

Molecularly imprinted polymers (MIPs) are synthetic materials which can provide high affinity to specific target molecules. The self-assembly of functional monomers around the template molecule (target), followed by polymerization in the presence of excess cross-linkers to form a solid material. After removal of the template, cavities are created that are complementary in both shape and functionality to the original template. However, there are hardly any successful attempts have been reported for the development of MIP based mycotoxin analysis (**Piletsky et.al.2001**). Yu et al. have doped polypyrrole (PPy) with chloride (PPy-Cl) via electropolymerization of pyrrole on the gold surface of a miniaturized surface plasmon resonance (SPR) device for detecting OTA (**Yu and Lai, 2004, Yu and Lai, 2005**). A MIP electrochemical sensor has been recently constructed for the selective detection of T-2 by introducing iron ions (Fe^{3+}) to increase the chelation of the metal ions and templates (**Gao et al 2014**).

2.4. Enzymatic inhibition

An enzymatic inhibition analysis based on a variety of enzymes (cholinesterase, urease, glucose oxidase etc.) is commonly applied. Acetylcholinesterase (AChE) is the most frequently used enzyme due to its sensitivity towards mycotoxins (**Puiu et.al. 2012**). Based on the inhibitory effect of AFB1 to AChE activity, biosensors for AFB1 detection is constructed using AChE (**Moscone et.al. 2011, Ben Rejeb et.al. 2009**). The enzymatic inhibition of AChE with AFB1 is a reversible binding and can real-time monitor mycotoxins through SPR etc. (**Puiu et.al. 2012**). Mycotoxins are reversible inhibitors that are non-covalently bound to the enzyme (**Stepurska et.al. 2015**). Out of a group of toxins, aflatoxin shows the maximum sensitivity of 0.015 μM (**Soldatkin et.al. 2013**).

2.5. Mimotope

Mycotoxins are toxic in nature, the necessity of pure toxin in synthesis of mycotoxin conjugates with protein molecules that may cause a toxicity risk to the manufacturers, users, and the environment. From a safety standpoint, it is advantageous to use a nontoxic chemical as an immunochemical reagent in place of toxic compound to enhance laboratory and environmental safety. And another disadvantage of using the conjugate is the release of analyte moiety from the conjugate that may give false signal to transducer. The mycotoxin conjugates can be replaced by mimotopes. Mimotopes are the peptides sequence of amino acids which show good affinity towards toxins, mimotopes selected from random phage displayed peptide libraries. Researchers have synthesized the mimotopes for various mycotoxins viz. OTA, ZEN, DON (**Bazin et.al. 2013, Lai et.al. 2009, He et.al. 2013**) and applied for the fast and accurate detection of mycotoxins.

3. Conclusions

Development of an appropriate biosensor for mycotoxin analysis in place of conventional chromatographic and ELISA technique is one of the thrust area in the field of biosensing research. The attempt of innovation is dedicated towards the choice of receptor (protein, nucleotides, MIP etc), strategy of transduction (electrochemical, optical, and EQCM), miniaturization (lab-on-chip, microfluidic etc), development of novel material (NPs, UCNPs), designing of signal generation (labeled and label free techniques) etc which lead to lowering of detection limit (up to the level of pg/mL), broad linear range and enhanced shelf life of the developed sensor etc.. In few cases, the researchers have applied the developed sensing system successfully on the contaminated food sample. No doubt, the research findings have shown the pathway of new science, novel technology, innovative material and state of art sensing technique etc but they are far away from the application in real life.

4. Future Trends

With the intervention of nano science and technology a new horizon has opened up in the field of device architecture. Researchers have paid their attention to exploit the advancement of technology for the construction of mycotoxin sensing tool. Unfortunately, till now the innovation is restricted in the laboratory scale, it has not reached to end user who badly needs a smart quick sensing reliable tool. Mycotoxin contamination is inhomogeneous in nature and demand extensive sampling to comply the legislation set by European Commission and other International agency. Carrying the exhaustive analysis using conventional tool such as chromatography with fluorescence (FLD) or mass (MS) detectors and ELISA technique requires time, cost, skilled man power and sophisticated instruments. Furthermore, these methods sometime may not reach to a very low limit of detection. In this context, biosensor is very promising for mycotoxin assay provided few challenges pertaining to technology and thought can be addressed judiciously such as (i) development of a synthetic receptor like aptamer, MIP etc in replace of costly unstable monoclonal antibody (ii) adaptation of label free easy scheme for detection and (iii) integration of modern technologies e.g, microfluidic and sensing design etc and (iv) finally a determined step for the conversion of innovation to application. Possibly future research can be directed to multi analyte detection on a lab-on chip platform with affordable cost.

Acknowledgements

We thank Dr. Ashok Kumar Chauhan (Founder President, Amity University Uttar Pradesh) for providing the facilities. We also thanks to Dr. (Mrs) Balwinder Shukla, Vice-chancellor Amity University Uttar Pradesh and Prof. L.M. Bhardwaj, Director, AINT. Author J.S. acknowledges the Department of Science & Technology, Govt of India for awarding the DST-INSPIRE Fellowship [IFA-13 CH-105] 2013.

References:

- Adanyi, N., Levkovets, I.A., Rodriguez-Gil, S., Ronald, A., Varadi, M., Szendro, I., 2007. *Biosens Bioelectron* 22, 797-802.
- Aguilar-Arteaga, K., Rodriguez, J.A., Barrado, E., 2010. *Anal Chim Acta* 674, 157-165.
- Ah, C.S., Park, C.W., Yang, J.-H., Lee, J.S., Kim, W.-J., Chung, K.H., Choi, Y.H., Baek, I.B., Kim, J., Sung, G.Y., 2012. *Biosens Bioelectron* 33, 233-240.
- Alarcon, S.H., Palleschi, G., Compagnone, D., Pascale, M., Visconti, A., Barna-Vetro, I., 2006. *Talanta* 69, 1031-1037.
- Andreou, V.G., Nikolelis, D.P., 1998. *Anal Chem* 70, 2366-2371.
- Bacher, G., Pal, S., Kanungo, L., Bhand, S., 2012. *Sens Actuat B* 168, 223-230.
- Barthelmebs, L., Jonca, J., Hayat, A., Prieto-Simon, B., Marty, J.-L., 2011. *Food Control* 22, 737-743.
- Basic food safety for health workers (1999) WHO.
- Bazin, I., Andreotti, N., Hassine, A.I., De Waard, M., Sabatier, J.M., Gonzalez, C., 2013. *Biosens Bioelectron* 40, 240-246.
- Ben Rejeb, I., Arduini, F., Arvinte, A., Amine, A., Gargouri, M., Micheli, L., Bala, C., Moscone, D., Palleschi, G., 2009. *Biosens Bioelectron* 24, 1962-1968.
- Bonel, L., Vidal, J.C., Duato, P., Castillo, J.R., 2010. *Anal Meth* 2, 335.
- Bonel, L., Vidal, J.C., Duato, P., Castillo, J.R., 2011. *Biosens Bioelectron* 26, 3254-3259.
- Chauhan, R., Solanki, P.R., Singh, J., Mukherjee, I., Basu, T., Malhotra, B.D., 2015a. *Food Control* 52, 60-70.
- Chauhan, R., Singh, J., Solanki, P.R., Basu, T., O'Kennedy, R., Malhotra, B.D., 2015b. *Biochem Eng J* 103, 103-113.
- Chauhan, R., Singh, J., Solanki, P. R., Manaka, T., Iwamoto, M., Basu, T., Malhotra, B.D., 2016. *Sens Actuat B* 222, 804-814.
- Chen, J., Fang, Z., Liu, J., Zeng, L., 2012. *Food Control* 25, 555-560.
- Chen, X., Huang, Y., Duan, N., Wu, S., Ma, X., Xia, Y., Zhu, C., Jiang, Y., Wang, Z., 2013. *Anal Bioanal Chem* 405, 6573-6581.
- Chen, Y., Yang, M., Xiang, Y., Yuan, R., Chai, Y., 2014. *Nanoscale* 6, 1099-1104.

- Cheng, C.I., Chang, Y.-P., Chu, Y.-H., 2012. *Chem Soc Rev* 41, 1947-1971.
- Cheng, X., Liu, X., Bing, T., Cao, Z., Shangguan, D., 2009. *Biochemistry* 48, 7817-7823.
- Cho, E.J., Lee, J.W., Ellington, A.D., 2009. *Annu Rev Anal Chem* 2, 241-264.
- Cigić, I.K., Prosen, H., 2009. *Int J Mol Sci* 10, 62-115.
- Council for Agricultural Science and Technology (CAST). *Mycotoxins: Risks in Plant, Animal and Human Systems. Task Force Report, No. 139*, CAST, Ames, Iowa, 2003.
- Cruz-Aguado, J.A., Penner, G., 2008a. *Anal Chem* 80, 8853-8855.
- Cruz-Aguado, J.A., Penner, G., 2008b. *J Agric Food Chem* 56, 10456-10461.
- Fang, X., Chen, H., Yu, S., Jiang, X., Kong, J., 2011. *Anal Chem* 83, 690-695.
- Feng, R., Zhang, Y., Li, H., Wu, D., Xin, X., Zhang, S., Yu, H., Wei, Q., Du, B., 2013. *Anal Chim Acta* 758, 72-79.
- Feng, R., Zhang, Y., Yu, H., Wu, D., Ma, H., Zhu, B., Xu, C., Li, H., Du, B., Wei, Q., 2013. *Biosens Bioelectron* 42, 367-372.
- Galarreta, B.C., Norton, P.R., Laguné-Labarthet, F.O., 2011. *Langmuir* 27, 1494-1498.
- Galarreta, B.C., Tabatabaei, M., Guieu, V., Peyrin, E., Lagugne-Labarthet, F., 2013. *Anal Bioanal Chem* 405, 1613-1621.
- Gan, N., Zhou, J., Xiong, P., Hu, F., Cao, Y., Li, T., Jiang, Q., 2013. *Toxins* 5, 865-883.
- Gao, X., Cao, W., Chen, M., Xiong, H., Zhang, X., Wang, S., 2014. *Electroanalysis* 26, 2739-2746.
- Goryacheva, I.Y., De Saeger, S., Nesterenko, I.S., Eremin, S.A., Van Peteghem, C., 2007. *Talanta* 72, 1230-1234.
- Guo, L., Jackman, J.A., Yang, H.-H., Chen, P., Cho, N.-J., Kim, D.-H., 2015. *Nano Today* 10, 213-239.
- Guo, X., Wen, F., Zheng, N., Luo, Q., Wang, H., Wang, H., Li, S., Wang, J., 2014. *Biosens Bioelectron* 56, 340-344.
- Guo, Z., Ren, J., Wang, J., Wang, E., 2011. *Talanta* 85, 2517-2521.
- Hayat, A., Andreescu, S., Marty, J.L., 2013. *Biosens Bioelectron* 45, 168-173.
- Hayat, A., Sassolas, A., Marty, J.L., Radi, A.E., 2013. *Talanta* 103, 14-19.
- He, Z.Y., He, Q.H., Xu, Y., Li, Y.P., Liu, X., Chen, B., Lei, D., Sun, C.H., 2013. *Anal Chem* 85, 10304-10311.
- Henry, S.H., Bosch, F.X., Troxell, T.C. and Bolger, P.M. 1999. *Science* 286, 2453-2454.

- Hermann, T., Patel, D.J., 2000. *Science* (New York, N.Y.) 287, 820-825.
- Hu, W., Chen, H., Zhang, H., He, G., Li, X., Zhang, X., Liu, Y., Li, C.M., 2014. *J Colloid Interface Sci* 431, 71-76.
- Hun, X., Chen, H., Wang, W., 2010. *Biosens Bioelectron* 26, 248-254.
- Hun, X., Liu, F., Mei, Z., Ma, L., Wang, Z., Luo, X., 2013. *Biosens Bioelectron* 39, 145-151.
- I. Lamberti, L. Mosiello, T. Hianik, 2011. *Chem Sensors* 1: 11.
- International Agency for Research on Cancer, IARC Lyon, 2002. 82, 171-274.
- Jin, X., Jin, X., Chen, L., Jiang, J., Shen, G., Yu, R., 2009b. *Biosens Bioelectron* 24, 2580-2585.
- Jin, X., Jin, X., Liu, X., Chen, L., Jiang, J., Shen, G., Yu, R., 2009a. *Anal Chim Acta* 645, 92-97.
- Kanungo, L., Bacher, G., Bhand, S., 2014. *Appl Biochem Biotech* 174, 1157-1165.
- Khan, R., Dey, N.C., Hazarika, A.K., Saini, K.K., Dhayal, M., 2011. *Anal Biochem* 410, 185-190.
- Kim, N.H., Lee, S.J., Moskovits, M., 2010. *Nano Letters* 10, 4181-4185.
- Kuang, H., Chen, W., Xu, D., Xu, L., Zhu, Y., Liu, L., Chu, H., Peng, C., Xu, C., Zhu, S., 2010. *Biosens Bioelectron* 26, 710-716.
- Lai, W., Fung, D.Y.C., Yang, X., Renrong, L., Xiong, Y., 2009. *Food Control* 20, 791-795.
- Lee, J., Jo, M., Kim, T.H., Ahn, J.-Y., Lee, D.-k., Kim, S., Hong, S., 2011. *Lab on a Chip* 11, 52-56.
- Li, J., Deng, T., Chu, X., Yang, R., Jiang, J., Shen, G., Yu, R., 2010. *Anal Chem* 82, 2811-2816.
- Li, T., Byun, J.-Y., Kim, B.B., Shin, Y.-B., Kim, M.-G., 2013. *Biosens Bioelectron* 42, 403-408.
- Li, T., Shi, L., Wang, E., Dong, S., 2009b. *Chem Europ J* 15, 1036-1042.
- Li, Y., Lu, Y., 2009. *Functional Nucleic Acids for Analytical Applications*. Springer.
- Lippolis, V., Pascale, M., Maragos, C.M., Visconti, A., 2008. *Talanta* 74, 1476-1483.
- Liu, J., Liu, J., Yang, L., Chen, X., Zhang, M., Meng, F., Luo, T., Li, M., 2009. *Sensors* 9, 7343-7364.
- Masoomi, L., Sadeghi, O., Banitaba, M.H., Shahrjerdi, A., Davarani, S.S.H., 2013. *Sens Actuat B* 177, 1122-1127.
- McKeague, M., Bradley, C.R., De Girolamo, A., Visconti, A., Miller, J.D., Derosa, M.C., 2010. *Int J Mol Sci* 11, 4864-4881.
- Moscone, D., Arduini, F., Amine, A., 2011. *T Microbial Toxins*, pp. 217-235.

- Nabok, A.V., Tsargorodskaya, A., Hassan, A.K., Starodub, N.F., 2005. *Appl Surf Sci* 246, 381-386.
- Nabok, A.V., Tsargorodskaya, A., Holloway, A., Starodub, N.F., Gojster, O., 2007. *Biosens Bioelectron* 22, 885-890.
- Palchetti, I., Mascini, M., 2012. *Anal Bioanal Chem* 402, 3103-3114.
- Park, J.H., Kim, Y.-P., Kim, I.-H., Ko, S., 2014. *Food Control* 36, 183-190.
- Pemberton, R.M., Pittson, R., Biddle, N., Drago, G.A., Hart, J.P., 2006. *Anal Lett* 39, 1573-1586.
- Perrotta, P.R., Arévalo, F.J., Vettorazzi, N.R., Zón, M.A., Fernández, H., 2012. *Sens Actuat B* 162, 327-333.
- Piermarini, S., Micheli, L., Ammida, N.H., Palleschi, G., Moscone, D., 2007. *Biosens Bioelectron* 22, 1434-1440.
- Prieto-Simon, B., Campas, M., Marty, J.L., Noguer, T., 2008. *Biosens Bioelectron* 23, 995-1002.
- Prieto-Simón, B., Karube, I., Saiki, H., 2012. *Food Chemistry* 135, 1323-1329.
- Puiu, M., Istrate, O., Rotariu, L., Bala, C., 2012. *Anal Biochem* 421, 587-594.
- Radi, A.E., Munoz-Berbel, X., Lates, V., Marty, J.L., 2009. *Biosens Bioelectron* 24, 1888-1892.
- Ran, Q., Peng, R., Liang, C., Ye, S., Xian, Y., Zhang, W., Jin, L., 2011. *Talanta* 83, 1381-1385.
- Rhouati, A., Hayat, A., Hernandez, D.B., Meraihi, Z., Munoz, R., Marty, J.-L., 2013. *Sens Actuat B* 176, 1160-1166.
- Ricciardi, C., Castagna, R., Ferrante, I., Frascella, F., Marasso, S.L., Ricci, A., Canavese, G., Lore, A., Prella, A., Gullino, M.L., Spadaro, D., 2013. *Biosens Bioelectron* 40, 233-239.
- Richard, J.L., 2007. *Int J Food Microbiol* 119, 3-10.
- Robbins, C.A., Swenson, L.J., Nealley, M.L., Kelman, B.J., Gots, R.E., 2000. *Appl Occup Environ Hyg* 15, 773-784.
- Rodrigues, I., Handl, J., Binder, E.M., 2011. *Food Addit Contam B* 4, 168-179.
- Sapsford, K.E., Ngundi, M.M., Moore, M.H., Lassman, M.E., Shriver-Lake, L.C., Taitt, C.R., Ligler, F.S., 2006. *Sens Actuat B* 113, 599-607.
- Schmidt, K.S., Borkowski, S., Kurreck, J., Stephens, A.W., Bald, R., Hecht, M., Friebe, M., Dinkelborg, L., Erdmann, V.A., 2004. *Nucl Acids Res* 32, 5757-5765.
- Schmittgen, T.D., Livak, K.J., 2008. *Nature protocols* 3, 1101-1108.
- Schoning, M.J., Poghosian, A., 2002. *Analyst* 127, 1137-1151.

- Sharma, A., Matharu, Z., Sumana, G., Solanki, P.R., Kim, C.G., Malhotra, B.D., 2010. *Thin Solid Films* 519, 1213-1218.
- Sheng, L., Ren, J., Miao, Y., Wang, J., Wang, E., 2011. *Biosens Bioelectron* 26, 3494-3499.
- Shim, W.-B., Mun, H., Joung, H.-A., Ofori, J.A., Chung, D.-H., Kim, M.-G., 2014. *Food Control* 36, 30-35.
- Solanki, P.R., Kaushik, A., Ansari, A.A., Malhotra, B., 2009. *Appl Phys Lett* 94, 143901.
- Soldatkin, O.O., Burdak, O.S., Sergeyeveva, T.A., Arkhypova, V.M., Dzyadevych, S.V., Soldatkin, A.P., 2013. *Sens Actuat B* 188, 999-1003.
- Srivastava, S., Kumar, V., Ali, M.A., Solanki, P.R., Srivastava, A., Sumana, G., Saxena, P.S., Joshi, A.G., Malhotra, B.D., 2013. *Nanoscale* 5, 3043-3051.
- Stepurska, K.V., Soldatkin, C.O., Kucherenko, I.S., Arkhypova, V.M., Dzyadevych, S.V., Soldatkin, A.P., 2015. *Anal Chim Acta* 854, 161-168.
- Tamerler, C., Oren, E.E., Duman, M., Venkatasubramanian, E., Sarikaya, M., 2006. *Langmuir* 22, 7712-7718.
- Tong, P., Zhang, L., Xu, J.J., Chen, H.Y., 2011. *Biosens Bioelectron* 29, 97-101.
- Tong, P., Zhao, W.W., Zhang, L., Xu, J.J., Chen, H.Y., 2012. *Biosens Bioelectron* 33, 146-151.
- Tothill, I., 2011. *World Mycot J* 4, 361-374.
- Tsai, W.C., Hsieh, C.K., 2007. *Anal Lett* 40, 1979-1991.
- Tuerk, C., Gold, L., 1990. *Science* 249, 505-510.
- Turner, N.W., Subrahmanyam, S., Piletsky, S.A., 2009. *Anal Chim Acta* 632, 168-180.
- Urusov, A.E., Kostenko, S.N., Sveshnikov, P.G., Zherdev, A.V., Dzantiev, B.B., 2011. *Sens Actuat B* 156, 343-349.
- Vidal, J., Bonel, L., Ezquerro, A., Duato, P., Castillo, J., 2012. *Anal Bioanal Chem* 403, 1585-1593.
- Vidal, J.C., Duato, P., Bonel, L., Castillo, J.R., 2009. *Anal Bioanal Chem* 394, 575-582.
- Vidal, J.C., Duato, P., Bonel, L., Castillo, J.R., 2012. *Anal Lett* 45, 51-62.
- Visconti, A., Lattanzio, V.M., Pascale, M., Haidukowski, M., 2005. *J chromat A* 1075, 151-158.
- Wang, H., Li, J., Wang, Y., Jin, J., Yang, R., Wang, K., Tan, W., 2010. *Anal Chem* 82, 7684-7690.
- Wang, J., Munir, A., Zhou, H.S., 2009. *Talanta* 79, 72-76.

- Wang, X., Zhang, H., Liu, H., He, C., Zhang, A., Ma, J., Ma, Y., Wu, W., Zheng, H.A.O., 2011. *J Food Saf* 31, 408-416.
- Wang, Y., Bao, L., Liu, Z., Pang, D.-W., 2011. *Anal Chem* 83, 8130-8137.
- Wang, Z., Duan, N., Hun, X., Wu, S., 2010. *Anal Bioanal Chem* 398, 2125-2132.
- Willner, I., Zayats, M., 2007. *Angew Chem Int Ed* 46, 6408-6418.
- Wu, J., Chu, H., Mei, Z., Deng, Y., Xue, F., Zheng, L., Chen, W., 2012. *Anal Chim Acta* 753, 27-31.
- Wu, S., Duan, N., Ma, X., Xia, Y., Wang, H., Wang, Z., Zhang, Q., 2012. *Anal Chem* 84, 6263-6270.
- Wu, S., Duan, N., Zhu, C., Ma, X., Wang, M., Wang, Z., 2011. *Biosens Bioelectron* 30, 35-42.
- Xu, X., Liu, X., Li, Y., Ying, Y., 2013. *Biosens Bioelectron* 47, 361-367.
- Yang, C., Lates, V., Prieto-Simon, B., Marty, J.L., Yang, X., 2013. *Talanta* 116, 520-526.
- Yang, M., Javadi, A., Li, H., Gong, S., 2010. *Biosens Bioelectron* 26, 560-565.
- Yang, X.-H., Kong, W.-J., Yang, M.-H., Zhao, M., Ouyang, Z., 2013. *Chin J Anal Chem* 41, 297-306.
- Yu, J.C.C., Lai, E.P.C., 2004. *Synt Metals* 143, 253-258.
- Yu, J.C.C., Lai, E.P.C., 2005. *React Funct Polm* 63, 171-176.
- Yuan, J., Deng, D., Lauren, D.R., Aguilar, M.-I., Wu, Y., 2009. *Anal Chim Acta* 656, 63-71.
- Zain, M.E., 2011. *J Saudi Chem Soc* 15, 129-144.
- Zamfir, L.-G., Geana, I., Bourigua, S., Rotariu, L., Bala, C., Errachid, A., Jaffrezic-Renault, N., 2011. *Sens Actuat B* 159, 178-184.
- Zhang, J., Liu, B., Liu, H., Zhang, X., Tan, W., 2013. *Nanomedicine* 8, 983-993.
- Zhang, J., Zhang, X., Yang, G., Chen, J., Wang, S., 2013. *Biosens Bioelectron* 41, 704-709.
- Zhao, Q., Wu, M., Chris Le, X., Li, X.-F., 2012. *TrAC Trends Anal Chem* 41, 46-57.
- Zhao, Y., Luo, Y., Li, T., Song, Q., 2014. *RSC Advances* 4, 57709-57714.
- Zheng, M., Jagota, A., Strano, M.S., Santos, A.P., Barone, P., Chou, S.G., Diner, B.A., Dresselhaus, M.S., McLean, R.S., Onoa, G.B., Samsonidze, G.G., Semke, E.D., Usrey, M., Walls, D.J., 2003. *Science* 302, 1545-1548.
- Zheng, M., Richard, J., Binder, J., 2006. *Mycopathologia* 161, 261-273.
- Zheng, Z., Humphrey, C.W., King, R.S., Richard, J.L., 2005. *Mycopathologia* 159, 255-263.
- Zhu, Z., Yang, R., You, M., Zhang, X., Wu, Y., Tan, W., 2010. *Anal Bioanal Chem* 396, 73-83.

Highlights

- Immunosensor based on food mycotoxins detection
- Review focuses on the current research relating to development of immunoassays
- Immunoassay methods with emphasis on recent advances, challenges and trends.
- Present technological aspects in the development of immunosensors

Synthesis CNTs Particle Based Abrasive Media for Abrasive Flow Machining Process

This content has been downloaded from IOPscience. Please scroll down to see the full text.

2016 IOP Conf. Ser.: Mater. Sci. Eng. 115 012034

(<http://iopscience.iop.org/1757-899X/115/1/012034>)

View [the table of contents for this issue](#), or go to the [journal homepage](#) for more

Download details:

IP Address: 14.139.251.107

This content was downloaded on 15/03/2016 at 06:03

Please note that [terms and conditions apply](#).

Synthesis CNTs Particle Based Abrasive Media for Abrasive Flow Machining Process

Sonu Kumar^a, Q.Murtaza^{b*}, R.S Walia^a, S. Dhull^a, P. K. Tyagi^c

^aPrecision Engineering Laboratory, Mechanical & Production Engg., Delhi Technological University (formerly Delhi College of Engineering), Delhi, India

^bMechanical Engineering Department, Aligarh Muslim University, Aligarh, India

^cApplied Physic Department, Delhi Technological University (formerly Delhi College of Engineering), Delhi, India

*E-mail: qasimmurtaza@gmail.com, Phone: +91-9654364948

Abstract. Abrasive flow machining (AFM) is a modern fine finishing process used for intricate and internal finishing of components or parts. It is based on flowing of viscoelastic abrasive media over the surface to be fine finished. The abrasive media is the important parameter in the AFM process because of its ability to accurately abrade the predefined area along its flow path. In this study, an attempt is made to develop a new abrasive, alumina with Carbon nanotubes (CNTs) in viscoelastic medium. CNTs in house produced through chemical vapour deposition technique and characterized through TEM. Performance evaluation of the new abrasive media is carried out by increasing content of CNTs with fixed extrusion pressure, viscosity of media and media flow rate as process parameters and surface finish improvement and material removal as process responses in AFM setup. Significantly improvement has been observed in material removal and maximum improvement of 100 % has been observed in the surface finish on the inner cylindrical surface of the cast iron work piece.

Keywords: AFM, CNTs, TEM

1. Introduction

Abrasive flow machining (AFM) is used to fine machining by flowing of viscoelastic abrasive media over predetermined surface areas. AFM process has capability of fine finishing of intricate shapes and holes which are not accessible easily [1]. In addition AFM process has many attractive advantages, such as self-sharpening, self-adaptability, controllability and finishing tool requires neither compensation nor dressing. AFM can be classified based on motion or flow of abrasive media as: One way AFM, Two-way AFM and Orbital AFM process [2-7]. In AFM process parameters, extrusion pressure has a major role in material removal and reduction of surface roughness [5-15]. On the other hand, abrasive media acts as deformable grinding tool. It is the key of Abrasive Flow machining. In general, abrasive media flow volume is increased than material removal increases. Theoretically it can be understood that as media flow



volume is increased, more number of abrasive particles comes in contact with work piece and more abrasion takes place. Rhoades [10] has reported that media flow rate is less influential parameter in respect to material removal. Slower slug flow rates are best for uniform material removal and high slug flow rates produce large edge radii. The media flow rate is insignificant with regard to material removal. On the other hand, it has been claimed by Jain and Jain [7] Singh [11] the media flow rate influences both of the material removal and surface roughness. Williams and Raju [5] and Williams et. al. [12] have reported that viscosity of the media is one of the significant parameters of the AFM process. Keeping all other parameters constant, an increase in viscosity improves both material removal and reduction of surface roughness. According to one thumb rule [14] finer abrasives should be used when the initial roughness of the work surface is less. The reason for a decrease in material removal is that with an increase in mesh size (or decrease in grain size in mm) the depth of penetration as well as width of penetration, decreases. There are various abrasive particles like Al_2O_3 , SiC, CBN, diamond powder and so on are available which are being used for abrasive finishing process [6-14]. Al_2O_3 and SiC are most suitable abrasives for many applications but Cubic boron nitride (CBN) and diamond are specifically used for special applications. Abrasive particles to base material ratio can be varying from 2 to 12. The abrasives have limited life. The additives are used to enhance the base carrier to get the desired flowability and rheological characteristic of the media. In the present study, a new type of abrasive media is developed to insure faster finishing and reduction of surface roughness. The new type of abrasive flow media is based on synthesis of iron filled CNTs with Al_2O_3 and its performance evaluation of cast iron workpiece in AFM as CNTs is known very strong mechanical properties. CNTs has been synthesised through chemical vapour deposition technique as it is fast and economical viable process [15-18].

2. Materials and Methods

The newly developed abrasive media, as shown in fig. 1, which having Al_2O_3 (180 mesh size), polymer and hydrocarbon gel (Polymer to gel ratio:1:1) is mixed properly in predetermined proportion to get the viscous elastic media which can machine effectively. Hydrocarbon gels are commonly used lubricants in the media. All additives including CNT particles (0, 5grams and 10 grams) in different percentages are carefully blended in predetermined quantities to obtain consistent formulation with 810 Pas media viscosity. CNTs with filled Fe was synthesized by Chemical Vapour Deposition. In this process, heating the solution of Ferrocene(5gm) and Toluene(25ml) in the oven, maintaining the oven temperature around $800^{\circ}C$ and argon gas(100 sccm) is passed to get inert atmosphere (setup fig. 2). The performance evaluation of the newly developed abrasive media was conducted in Precision Manufacturing Laboratory developed vertical double acting AFM machine setup (table 1), of Delhi Technological University. Cast Iron work piece (fig. 3) were prepared with initial surface roughness and weight were taken. The surface roughness was measured in five different locations using Taylor Hobson. The internal cylindrical surface was finished by AFM process. Each workpiece was machined for a predetermined number of cycles (8 cycles) and extrusion pressure.



Fig. 1:- Abrasive laden Media (carrier+Al₂O₃+CNT) Fig.2. Thermal CVD Setup Fe-filled CNTs.

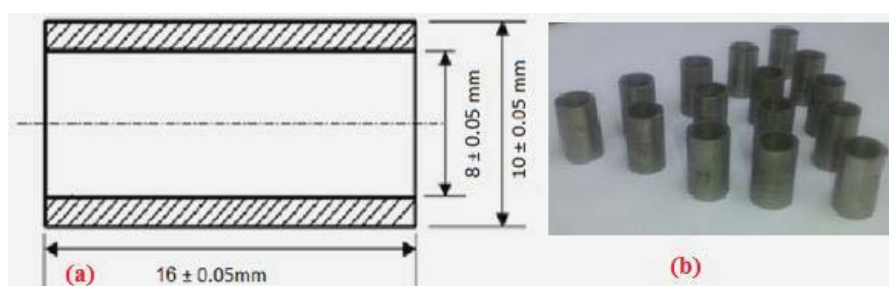


Fig. 3:- Cast Iron work pieces used in trials and its dimensional details.

Table1:- Process parameter of AFM setup.

S. No.	Process Parameter	Range	Unit
1	Extrusion Pressure	5-35	MPa
2	No. of Cycle	1-9	Number
3	Temperature	32± 2	°C
4	Media Flow volume	290	cm ³
5	Capacity	25 + 25	Ton
6	Stroke length	96	mm
7	Hydraulic cylinder Bore diameter-2 No.	130	mm
8	Hydraulic cylinder Stroke	90	mm
9	Working Pressure	210	kg/cm ²
10	Maximum Pressure in the Cylinder	35	MPa
11	Stroke Length of Piston	300	mm

3. Results and discussion

3.1. Characterization of CNTs filled with Iron

Fig. 4 shows the TEM micrographs of Fe filled CNTs at different locations and it shows that the growth of CNTs is uniform and there is very less amount of other carbon impurities such as amorphous carbon, soot or carbon particles.

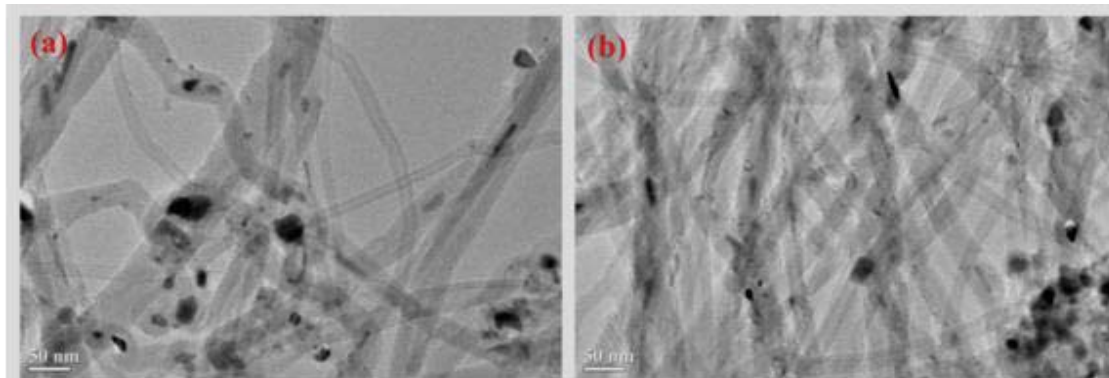


Fig. 4:- TEM images of CNTs at different locations.

3.2. Characterization of developed abrasive Media

The three abrasive media has developed. The first abrasive media has aluminium oxide, polymer and hydrocarbon gel is mixed properly in predetermined proportion to get the viscous elastic media with no content of CNTs particles. The second and third abrasive media added with 5 and 10 grams CNTs with iron filled respectively. Fig. 5 is the SEM micrograph of the media (Al_2O_3 and Carrier only) before addition of CNTs where, (a) is the SEM micrograph at scale bar of 100 μm in which abrasives edges are not clearly visible, (b) is the SEM micrograph at a scale bar of 5 μm in which abrasive edges are visible. This SEM micrograph (Fig. 5 (a)) of the media (Al_2O_3 +carrier+ Fe-filled CNTs) shows the sharp edges of alumina particle are clearly visible which is responsible for machining the work surface.

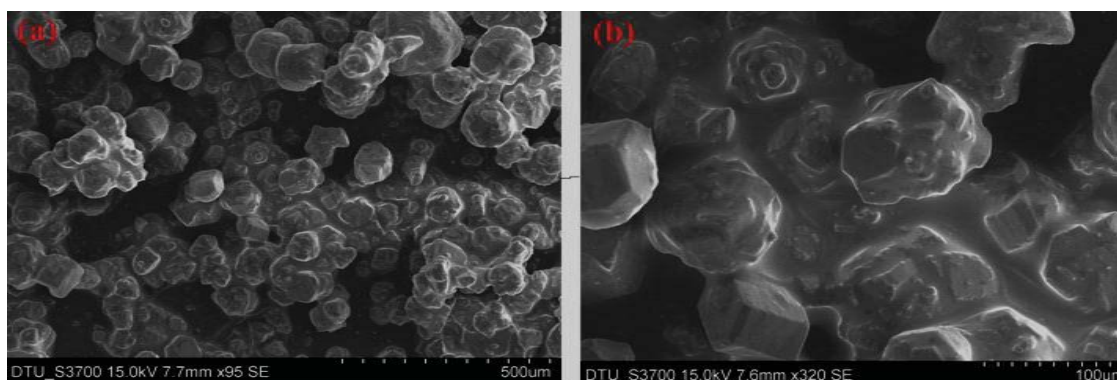


Fig. 5:- SEM image of media (Al_2O_3 +carrier+ Fe-filled CNT).

3.3. Effect of CNTs on material removal

Fig. 6 shows that as the amount of CNT particles increased, the material removal of cast iron workpiece increased when other AFM machining parameters are constant. As we know that CNT particles are harder as compare to the aluminium oxide and CNT has very sharp cutting edges. So when the extrusion pressure is applied, it easily cuts the peak of the surface material and causes more material removal.

3.4. Effect of CNT on surface finish

It can be seen from the fig. 7, that as the amount of CNT increases the % increase in surface finish (R_a) slightly increases but after level 2 (10 grams CNTs), % improvement in R_a sharply increased (100%).

This is due to more number of abrasive particles taking part in machining process and also continues to remove fresh materials from the work surface which lead to increase in MR and surface finish.

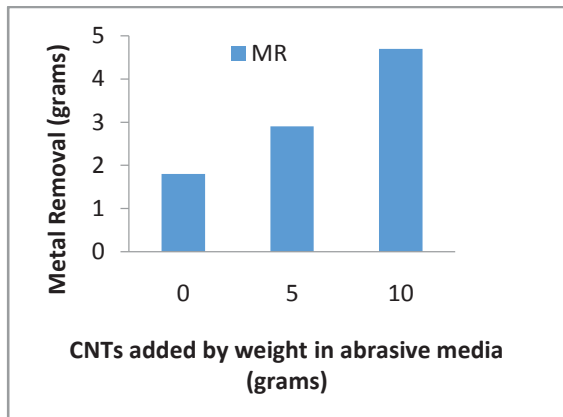


Fig. 6:-Effect of CNT particles on MR.

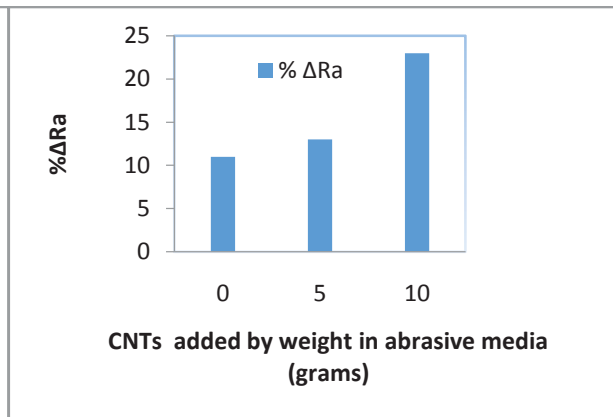


Fig. 7:- Effect of CNT on Ra.

4. Conclusion

The present study was carried out to develop CNTs based abrasive media for AFM successfully. It has been found and showed that the use of CNTs with abrasive media led to an improvement in the response parameter of percentage improvement in surface finish and material removal. At selected parameters a maximum improvement of 100% has been observed in the Surface finish on the inner cylindrical surface of the cast iron work piece.

References

- [1] L.J. Rhoades, Abrasive Flow Machining, *Technical Paper of the Society of Manufacturing Engineers (SME)*, MR(1989) 89-145.
- [1] R.E. William and K.P. Rajurkar L.J, Rhoades, Performance Characteristics of abrasive flow machining, *SME Technical paper No. FC*(1989) 89-806.
- [3] Tzeng, Yan, Hsu and Lin, Self-modulating abrasive medium and its application to abrasive flow machining for finishing micro channel surfaces, *Int. J. of Advanced Manufacturing Technology* 32(2007) 1163-1169.
- [4] S. Rajesha, G. Venkatesh, A.K. Sharma and K. Pradeep, Performance study of a natural polymer based media for abrasive flow machining, *Indian Journal of Engineering & materials Sciences* (2010) 407-413.
- [5] R.E. William R.E and K.P. Rajurkar, Stochastic modeling and analysis of abrasive flow machining, *Trans. ASME, J Engg. For Ind*, 114 (1992), 74-81.
- [6] R.K. Jain and V.K. Jain, Abrasive fine finishing process-a review, *Int. J. of Manufacturing science and Production* 2(1) (1999) 55-68.
- [7] R.K. Jain, V.J.C. Jain and P.M. Dixit, Modelling of material removal and surface roughness in abrasive flow machining process, *Int. J. of Machine Tool and Manufacture* 39(1999)1903-1923.

- [8] U.S. Shan and A.K. Dubey, Micro machining by flow of abrasives, *Proceedings 17th MMTDR Conference, Warangal, India* (1997) 269-275.
- [9] G.F. Benedict, Nontraditional Manufacturing Processes, *Marcel Dekker, New York* (1987).
- [10] L.J. Rhoades and T.A. Kohut, Reversible Unidirectional AFM, (1991) *US patent number 5,070,652*.
- [11] S. Singh, Studies in metal finishing with magnetically assisted abrasive flow machining, *Ph.D. Thesis* (2002) IIT Roorkee, India.
- [12] Williams R.E., and Rajurkar K.P, Monitoring of abrasive flow machining using acoustic emission, *Proc. First S.M. Wu Symposium on Manufacturing Sciences*1 (1994) 35-41.
- [13] K. Przyklenk, Abrasive flow machining- A process for surface finishing and deburring of work pieces with a complicated shape by means of abrasive laden media, *Advances in Non-Traditional machining, PED, ASME* 22 (1986) 101-110.
- [14] A. Agrawal, V.K. Jain and K. Muralidhar, Experimental determination of viscosity of abrasive flow machining media, *Int. J. of Manufacturing Technology and Management* 7(2005) 142-156.
- [15] S. Devanshu, K. Amulya, Q. Murtaza (CNT reinforced aluminium matrix composite-A Review, *Materials Today: Proceedings*2 (2015) 2886–2895.
- [16] R. Kumar, Q. Murtaza, R.S. Waila (2014), Three start helical abrasive flow machining for ductile material, *Procedia Materials Science*6 (2014) 1884–1890.
- [17] S. R. Ruoff, D. Qian, W.K. Liu, Mechanical properties of carbon nanotubes: theoretical predictions and experimental measurements, *C. R. Physique* 4 (2003) 993–1008.
- [18] V. N. Popov, (2014), Carbon nanotubes: properties and application, *Materials Science and Engineering* 43 (2014) 61–102.



ELSEVIER

Contents lists available at ScienceDirect

Transportation Research Part D

journal homepage: www.elsevier.com/locate/trdTailpipe emission from petrol driven passenger cars [☆]Abhinav Pandey ^{a,1}, Govind Pandey ^{b,2}, Rajeev Kumar Mishra ^{c,*}^a Engineering Manager (Civil) – EDRC, Larsen & Toubro Construction, Delhi 110 065, India^b Civil Engineering Department, Madan Mohan Malaviya University of Technology, Gorakhpur 273 010, India^c Environmental Engineering Department, Delhi Technological University, Delhi 110 042, India

ARTICLE INFO

Article history:

Keywords:

Compliance period

Inspection/maintenance programme

MUL

Tailpipe emission

Vehicle-related parameters

ABSTRACT

Realizing the dominance of petrol-driven passenger cars of MUL over the fleet of cars in India, a case study of different models of petrol-driven passenger cars of Maruti reporting at an authorized service station of M/s R.K.B.K. Automobiles, Gorakhpur was taken up and the tailpipe emissions along with individual vehicle-related parameters were monitored for idle and fast idle test conditions. The outcome of the study relating to the effect of various vehicle-related parameters on CO and HC emissions of petrol-driven passenger cars of Maruti has led to the useful inferences, which can be used not only for predicting the emission of vehicles with respect to vehicle age and mileage, but also for automobile manufacturing sector to help them produce such environmentally benign petrol-driven passenger cars having long-lasting compliance of pollution control systems with respect to vehicle age and mileage of the petrol-driven passenger cars in the country.

© 2016 Elsevier Ltd. All rights reserved.

Introduction

Most of the Indian Cities are experiencing rapid urbanization and the majority of the country's population is expected to be living in cities within a span of next two decades. The rapid urbanization in India has also resulted in a tremendous increase the number of motor vehicles imposing a serious effect on human life and its environment in recent years – what is being referred to as Urban Air Pollution (UAP) in the context of ever-expanding urban areas.

According to Census reports, the urban population has increased from 10% in 1901 to 28% in 2001. And ever-increasing, the urban growth rate is running at 31.8% i.e., almost three times higher than rural areas in 2011 (Census, 2011). The World Health Organization (WHO) has estimated that in developing countries, increasing UAP has resulted in more than 2 million deaths per annum along with various cases of respiratory illnesses (WHO, 2005, 2014). It is reported that over 70–80% of air pollution in mega cities in developing nations is attributed to vehicular emissions caused by a large number of older vehicles coupled with poor vehicle maintenance, inadequate road infrastructure and low fuel quality (Auto Fuel Policy, 2002; Badami, 2005; Singh et al., 2007; Wang et al., 2010). Among the criteria pollutants, CO is the major pollutant coming from the transport sector, contributing 90% of total emission. Hydrocarbons are next to CO. It is indeed interesting to observe that the contribution of transport sector to the particulate pollution is as less as 3–5%, most of the SPM (Suspended Particulate Matter) are generated due to re-suspension of dust out of which PM₁₀ is the most prominent air pollutant.

[☆] Capsule: The study finds that vehicle age & mileage parameters are directly proportional to tailpipe emission from petrol driven passenger cars.

* Corresponding author. Tel.: +91 8800486298; fax: +91 11 27871023.

E-mail addresses: navabhighkp@gmail.com (A. Pandey), pandey_govind@rediffmail.com (G. Pandey), rajeevctrans@gmail.com (R.K. Mishra).

¹ Tel.: +91 11 49135310/400.

² Tel.: +91 511 2272272.

Table 1
Vehicle model and model codes.

S. No.	Vehicle code	Vehicle model	Idle RPM (Designated)	Fast idle RPM
1.	MB	M-800	710	2200–2800
2.	MRF	M-ALTO (Lx/Vx)	710	2200–2800
3.	MT	M-OMNI	710	2200–2800
4.	MH	M-ZEN (Lxi/Vxi)	810	2200–2800
5.	MRD	M-WAGON R	820	2200–2800
6.	ME	M-ESTEEM	850	2200–2800

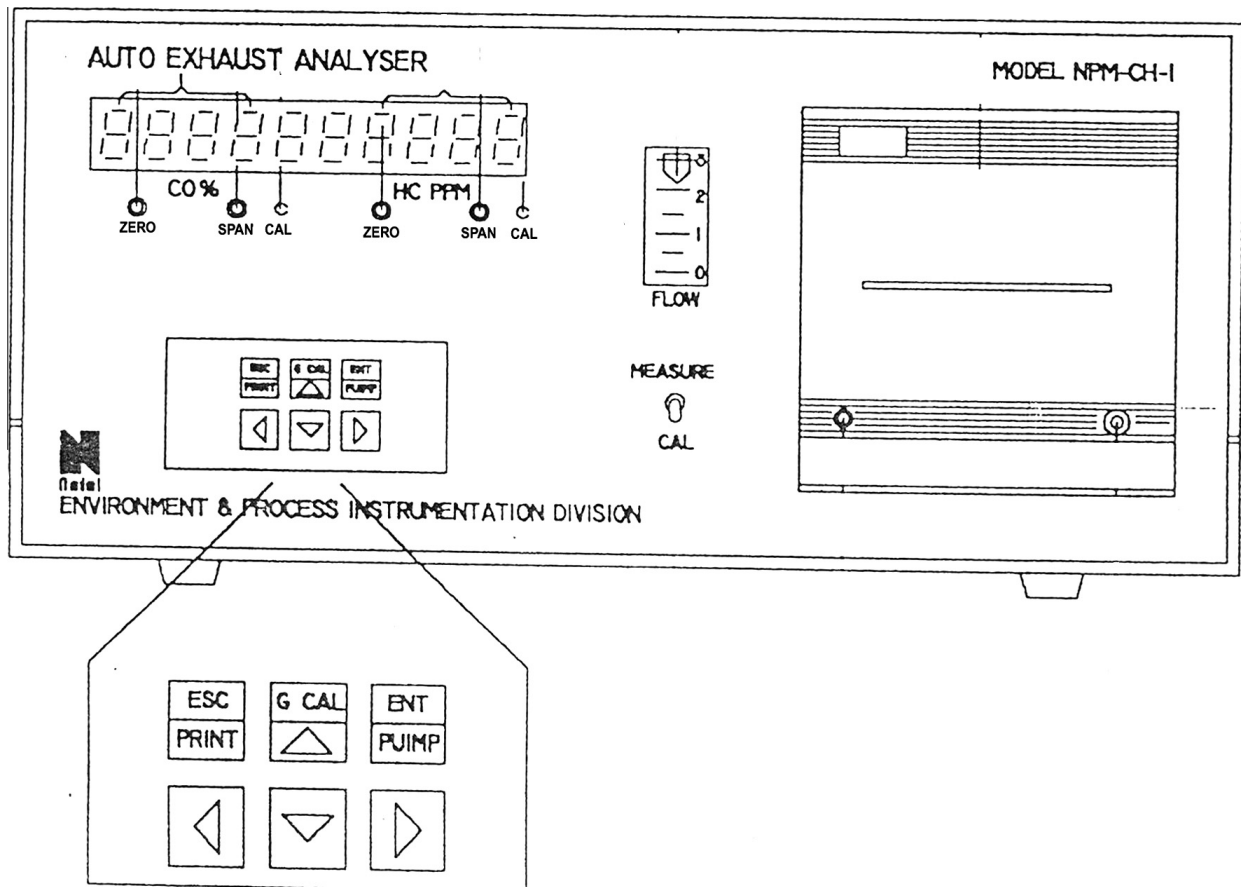


Fig. 1. Front views of the auto exhaust analyzer.

In an effort to improve air quality resulting from the transport sector, various pollution control strategies have been adopted or proposed worldwide for urban passenger transport. These measures generally include travel demand control, cleaner fuel standards, upgraded engine technology and stricter mandates on motor vehicle emissions (Bogdanovic et al., 1997). An important part of motor vehicle emission control relies on implementing a proper inspection and maintenance (I/M programme), since it is the best way to identify vehicles that need remedial maintenance or adjustment (Walsh, 1994). Engine maintenance has been shown to be the most significant parameter affecting the level of emissions (Pattas et al., 1994). In a typical I/M program, motorists are required to get their vehicles periodically inspected for exhaust emissions. A vehicle with malfunctioning emission controls or excessive exhaust pollution may or may not be repaired. In the case of repair, the vehicle should be retested to determine the post-repair emission rate. In case the vehicle is not repaired the motorist should pay an emission fee (Harrington et al., 1996, 2000). In major cities of India, there exists a mandatory system for inspection and maintenance in conformance to which every commercial vehicle has to go for a mandatory fitness test. The renewal period for fitness certification in general, is 2 years for new commercial vehicle and every 1 year for old vehicles. For private vehicles, no mandatory periodic fitness check is required in India but there exist a system of re-registration of private vehicles after 15 years of initial registration. But all in-use vehicles are required to obtain emission check certificate called Pollution Under Control (PUC). Frequency of this PUC certification varies from 2 to 4 times a year which is issued based on conformity to idle emission test for gasoline vehicles and free acceleration smoke test for diesel vehicles and is required to be carried out using authenticated Auto-exhaust gas analyzers only (CPCB, 2010).

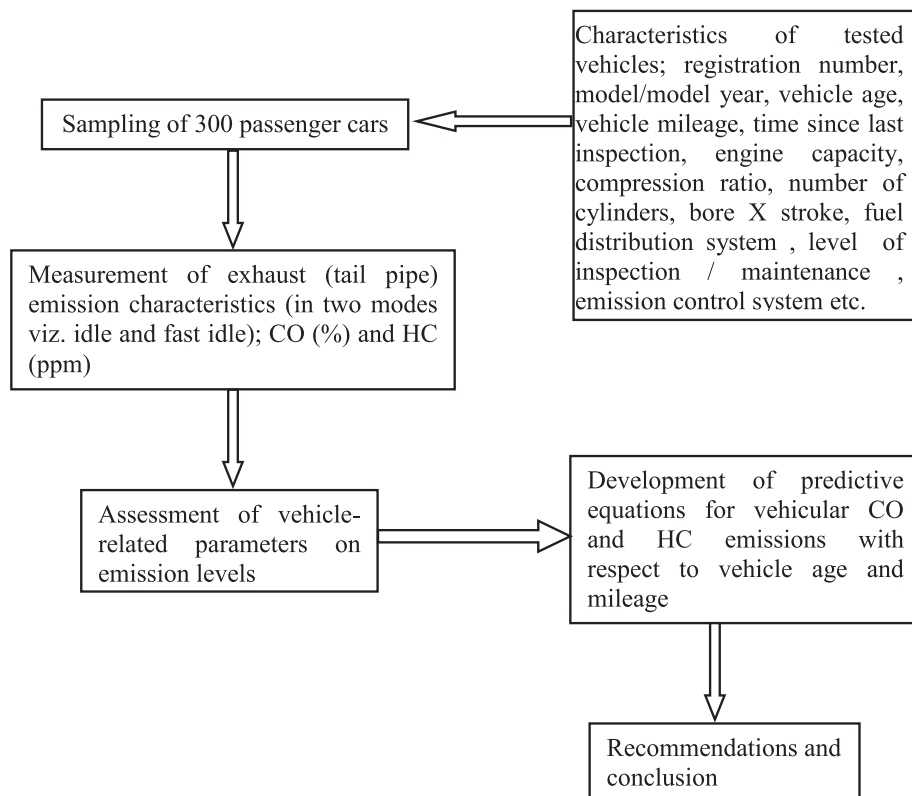


Fig. 2. Methodology of the study.

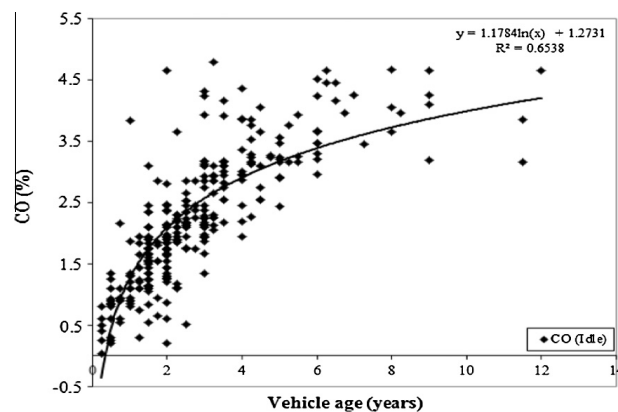


Fig. 3. Vehicle age vs. CO emission (Idle).

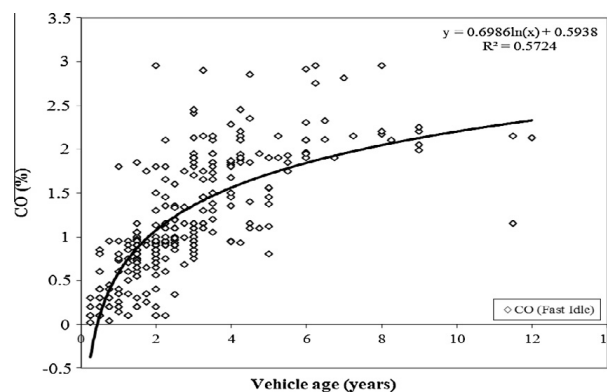


Fig. 4. Vehicle age vs. CO emission (Fast Idle).

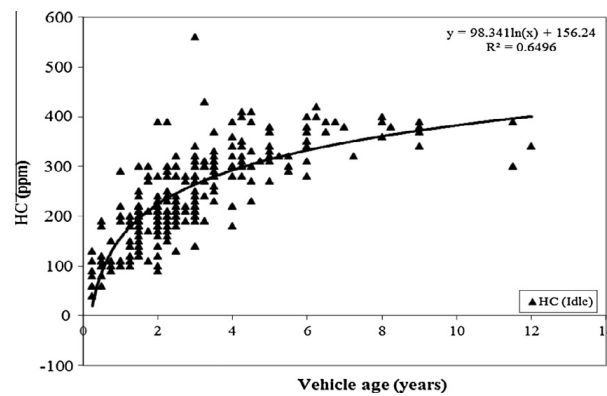


Fig. 5. Vehicle age vs. HC emission (Idle).

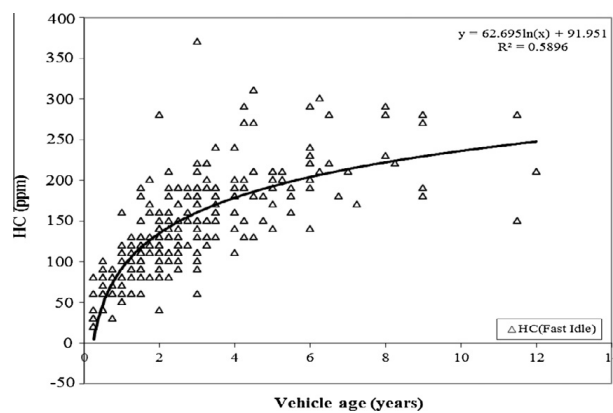


Fig. 6. Vehicle age vs. HC emission (Fast Idle).

Table 2

Equations relating CO emissions with vehicle age (model-wise).

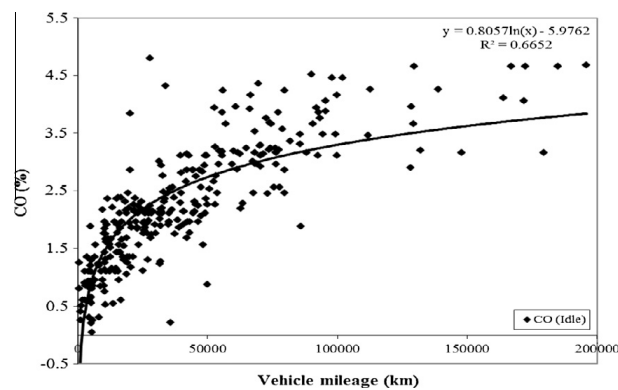
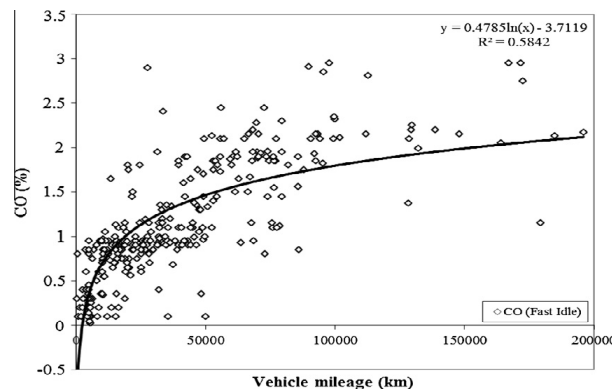
S. No.	Model	Test mode	Equation(s)	R ² value(s)
1.	M-800	Idle	$y = 1.2484 \ln(x) + 1.2617$	0.5479
		F. Idle	$y = 0.8227 \ln(x) + 0.5269$	0.5225
2.	M-ALTO	Idle	$y = 0.9306 \ln(x) + 1.3034$	0.6203
		F. Idle	$y = 0.513 \ln(x) + 0.6452$	0.491
3.	M-ESTEEM	Idle	$y = 1.1252 \ln(x) + 1.4413$	0.8385
		F. Idle	$y = 0.8104 \ln(x) + 0.6335$	0.803
4.	M-OMNI	Idle	$y = 1.3171 \ln(x) + 1.2903$	0.7385
		F. Idle	$y = 0.7508 \ln(x) + 0.7123$	0.7139
5.	M-WGN R	Idle	$y = 0.9341 \ln(x) + 1.1349$	0.5654
		F. Idle	$y = 0.5478 \ln(x) + 0.4948$	0.4257
6.	M-ZEN	Idle	$y = 1.1235 \ln(x) + 1.4042$	0.6974
		F. Idle	$y = 0.5876 \ln(x) + 0.6581$	0.5884

Gallagher and Livo (1991), while working on emission and age distribution of vehicles in the Colorado I/M programme, reported that the vehicle age and maintenance have an impressive effect on CO emissions whereas Watkins (1991) in his work on air pollution from road vehicles assessed that the total amount of air pollutants, especially CO and HC, has not been decreased significantly because of continued increase of motorization whereas another reason is believed to be an increase in the annual mileage which occurs practically all over the globe and reflects the human life level. Faiz (1993) and Faiz et al. (1996) reported that the share of road traffic for CO is more than 90% and that of HC close to 100%, while studying the automotive emissions in developing countries, he implicated such emissions for global warming, acidification and urban air quality. Knepper et al. (1993) performed a study of repeated FTP (Federal Test Procedure) tests on the same vehicles and reported that CO and HC emissions from malfunctioning vehicles can change by over a factor of seven on independent FTP tests

Table 3

Equations relating HC emissions with vehicle age (model-wise).

S. No.	Model	Test mode	Equation(s)	R ² value(s)
1.	M-800	Idle	$y = 107.7 \ln(x) + 150.89$	0.6107
		F. Idle	$y = 76.215 \ln(x) + 86.414$	0.5374
2.	M-ALTO	Idle	$y = 70.206 \ln(x) + 163.76$	0.4553
		F. Idle	$y = 49.073 \ln(x) + 96.771$	0.4792
3.	M-ESTEEM	Idle	$y = 124.64 \ln(x) + 144.3$	0.7877
		F. Idle	$y = 69.881 \ln(x) + 80.709$	0.8412
4.	M-OMNI	Idle	$y = 108.6 \ln(x) + 162.45$	0.7687
		F. Idle	$y = 57.151 \ln(x) + 95.294$	0.7067
5.	M-WGN R	Idle	$y = 78.211 \ln(x) + 153.42$	0.5463
		F. Idle	$y = 47.622 \ln(x) + 91.98$	0.5198
6.	M-ZEN	Idle	$y = 91.949 \ln(x) + 159.73$	0.6807
		F. Idle	$y = 59.588 \ln(x) + 90.512$	0.5942

**Fig. 7.** Vehicle mileage vs. CO emission (Idle).**Fig. 8.** Vehicle mileage vs. CO emission (Fast Idle).

although the uncertainty is much less for properly functioning vehicles. [Anilovich and Hakkert \(1996\)](#) studied the tailpipe emissions relating to vehicle age and periodic inspection in Israel and found that the vehicle age distribution and the time from last inspection are important considerations, when evaluating the effect of vehicle-related parameters on exhaust emissions. The analysis conducted by them indicated that maintenance of vehicle engine and the test performance must be improved with respect to vehicle emission control and represented a foundation for elaboration of the I/M programme which would use the differentiated approach for various age groups of vehicles.

[Goodwin and Ross \(1996\)](#) studied the effect of engine load on vehicle emission and found that the relationship between emissions and load depended on the fuel delivery and emission control technology. Further, under high speed and acceleration requirements, vehicles of present times are designed to have excess fuel injected into the engine's cylinder and this enrichment of the air/fuel mixture, in turn, leads to elevated CO and HC emissions. [Beaton et al. \(1995\)](#) have found that the high-emitter problem spans all model-years. Because vehicle emissions and fuel efficiency standards are distinct entities,

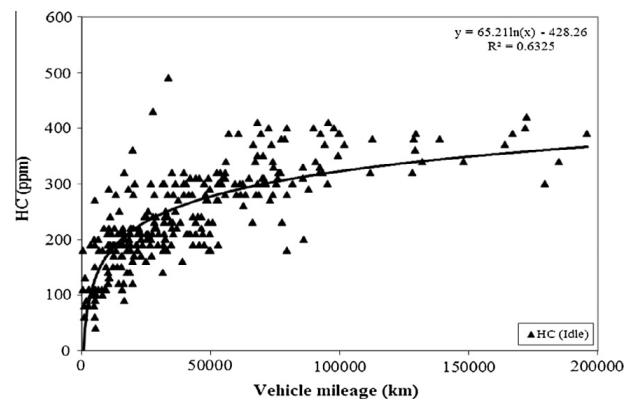


Fig. 9. Vehicle mileage vs. HC emission (Idle).

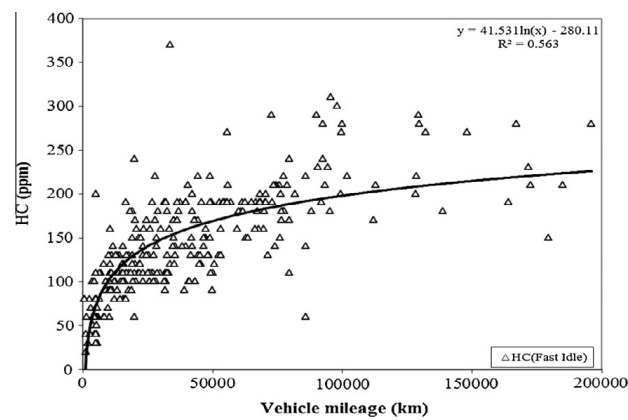


Fig. 10. Vehicle mileage vs. HC emission (Fast Idle).

Table 4
Equations relating CO emissions with vehicle mileage (model-wise).

S. No.	Model	Test mode	Equation(s)	R ² value(s)
1.	M-800	Idle	$y = 0.7313 \ln(x) - 5.1711$	0.5234
		F. Idle	$y = 0.4062 \ln(x) - 2.9641$	0.4244
2.	M-ALTO	Idle	$y = 0.8151 \ln(x) - 6.0792$	0.6734
		F. Idle	$y = 0.5752 \ln(x) - 4.6624$	0.64
3.	M-ESTEEM	Idle	$y = 1.3327 \ln(x) - 11.452$	0.7334
		F. Idle	$y = 0.8094 \ln(x) - 7.1282$	0.4734
4.	M-OMNI	Idle	$y = 0.8499 \ln(x) - 6.4773$	0.7949
		F. Idle	$y = 0.4819 \ln(x) - 3.7962$	0.7138
5.	M-WGN R	Idle	$y = 0.9932 \ln(x) - 7.9069$	0.8265
		F. Idle	$y = 0.5631 \ln(x) - 4.5784$	0.7321
6.	M-ZEN	Idle	$y = 0.7985 \ln(x) - 5.8958$	0.8302
		F. Idle	$y = 0.4979 \ln(x) - 3.9051$	0.7815

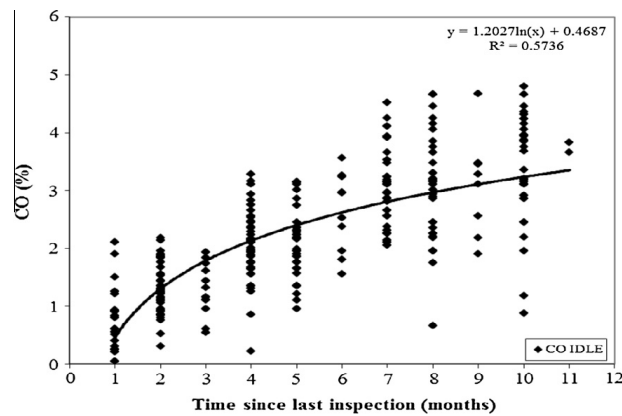
the relationship between fuel economy and emissions is unclear. Indeed, more fuel-efficient vehicles have lower emissions only in the absence of emission controls, thus equating engine and tail-pipe emissions. Bishop et al. (1996) argued that average emissions increase as vehicles age because of poor maintenance practices and tampering. A minority of vehicles on the road disproportionately contribute to aggregate emissions. Most studies suggest that, on average, 10% of vehicles produce 50–60% of all vehicular emissions, although claims range from 20% being responsible for 50% of emissions, to 5% generating 80% of emissions. These differences stem mainly from how high-emitters are defined or classified and from the methodology used to measure vehicular emissions and activity (Wolf et al., 1998).

The distributions of emissions from large numbers of vehicles are highly skewed. The majority of vehicles have relatively low emissions, while a relatively small number of malfunctioning vehicles have extremely high emissions (Stephens, 1994;

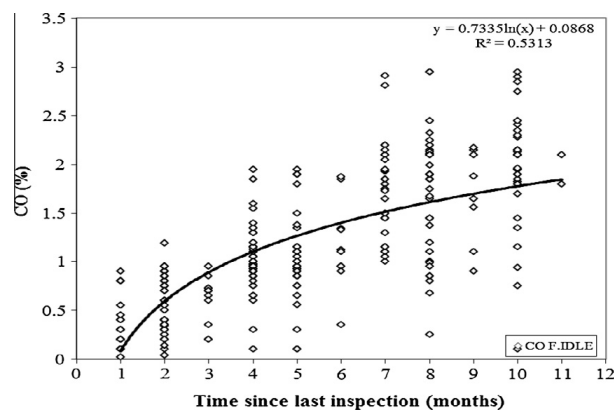
Table 5

Equations relating HC emissions with vehicle mileage (model-wise).

S. No.	Model	Test mode	Equation(s)	R ² value(s)
1.	M-800	Idle	$y = 54.867 \ln(x) - 318.42$	0.4993
		F. Idle	$y = 33.176 \ln(x) - 188.5$	0.4203
2.	M-ALTO	Idle	$y = 67.079 \ln(x) - 445.3$	0.6024
		F. Idle	$y = 46.32 \ln(x) - 392.03$	0.5303
3.	M-ESTEEM	Idle	$y = 99.399 \ln(x) - 769.86$	0.5969
		F. Idle	$y = 67.554 \ln(x) - 540.32$	0.5799
4.	M-OMNI	Idle	$y = 72.074 \ln(x) - 499.55$	0.7814
		F. Idle	$y = 42.664 \ln(x) - 300.03$	0.802
5.	M-WGN R	Idle	$y = 24.489 \ln(x) - 106.88$	0.4397
		F. Idle	$y = 52.495 \ln(x) - 394.14$	0.6699
6.	M-ZEN	Idle	$y = 69.445 \ln(x) - 474.15$	0.7354
		F. Idle	$y = 45.072 \ln(x) - 320.24$	0.7243

**Fig. 11.** TSLI vs. CO emission (Idle).

Bishop et al., 1996; Schwartz, 2000). To overcome this difficulty, analysts have typically used the forms of the log-normal (Stephens, 1994) and gamma (Zhang et al., 1994) distributions to model vehicle emission data. Washburn et al. (2001) found that vehicle type, manufacturer, country of origin, engine characteristics, and type of fuel are also critical factors. They used three-stage least squares regression to estimate simultaneous equations for CO, CO₂, and HC while the data used ranged from standard I/M testing to remote sensing and roadside pullover. I/M tests vary, from complete IM240 to idle and 2-speed (idle + cruising) tests. Beydoun and Guldman (2006) performed the logit models of test failure and detailed regression analyses of I/M data for three pollutants (CO, HC and NO_x) from Massachusetts, Maryland and Illinois in respect of vehicle characteristics and emissions for each make (BMW, Hyundai, Mitsubishi, Chrysler and GM) and type of vehicle. They reported that the older vehicles were more likely to fail the overall emission test together with the poorly-maintained vehicles than new as

**Fig. 12.** TSLI vs. CO emission (Fast Idle).

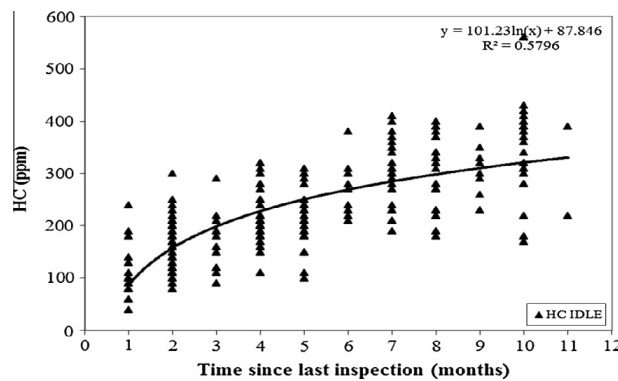


Fig. 13. TSLI vs. HC emission (Idle).

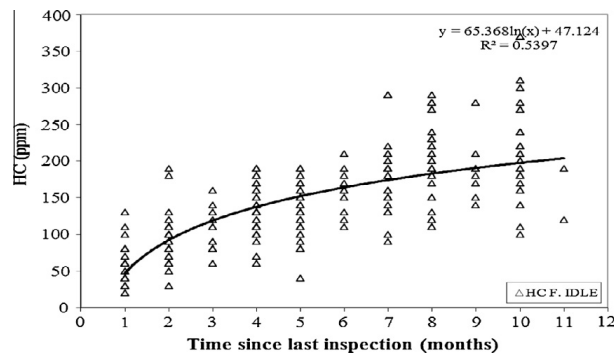


Fig. 14. TSLI vs. HC emission (Fast Idle).

well as well-maintained ones respectively and the policy implications of the relationship between fuel efficiency and emissions were profound. Kazopoulos et al. (2005) performed the measurements of exhaust emissions for a sample of 100 vehicles to characterize the emission levels and to develop emission standards for CO and HC under a basic I/M programme and set, by measuring the actual distribution of emissions in the sample of Labanese vehicles, the emission standards such that a maximum of 20% of the vehicles would fail.

In the present work, the petrol-driven passenger cars reporting for inspection/maintenance at the authorized workshop of Maruti Udyog Limited (MUL) owned & operated by M/s R.K.B.K. Automobiles (Pvt.) Limited, Mohaddipur, Gorakhpur, India have been scrutinized in a period of time and the data pertaining to vehicle-related factors and CO and HC emissions have been collected and analyzed with a view to ascertain the effect of various vehicle-related parameters (such as vehicle age, vehicle mileage, time since last inspection, engine capacity, compression ratio, number of cylinders, bore X stroke, fuel distribution system, level of inspection/maintenance, and emission control system) on the emission level of petrol-driven passenger cars of Maruti. The data have been analyzed to find out correlations, if any, of vehicle-related factors with CO and HC emissions and to suggest suitable steps and remedies for the pollution control of petrol-driven passenger cars.

Materials and methods

Both idle and fast idle tests were performed in the present study attending to total number of about 300 vehicles, distributed across model years. The data collection included vehicle registration number, vehicle model & model year, vehicle age, vehicle mileage, time since last inspection, engine capacity, compression ratio, number of cylinders, bore X stroke, fuel distribution system, level of inspection/maintenance, emission control system, etc. Testing of vehicles was conducted in summer (May–June, characterized by relatively warm temperatures around 38 °C, in the forenoon and afternoon hours (10 a.m. to 3 p.m.) and under hot start conditions for 2/3 min or until concentrations stabilized.

Table 1 shows the different models of the petrol-driven passenger cars of Maruti which underwent the study. The vehicle model codes, vehicle model or brand names along with the idle RPM (Revolutions Per Minute) designated by the manufacturer and the fast idle by United State Environmental Protection Act (USEPA) are given in this table. The fast idle test conditions are consistent with those prescribed by the USEPA (58 FR 58402, Nov. 1, 1993), and Central Pollution Control Board (CPCB, 1999).

Table 6

Equations relating CO emissions with vehicle TSLI (model-wise).

S. No.	Model	Test mode	Equation(s)	R ² value(s)
1.	M-800	Idle	$y = 1.3286 \ln(x) + 0.159$	0.4851
		F. Idle	$y = 0.7543 \ln(x) + 0.03$	0.4109
2.	M-ALTO	Idle	$y = 1.212 \ln(x) + 0.3065$	0.5387
		F. Idle	$y = 0.8745 \ln(x) + 0.1892$	0.5352
3.	M-ESTEEM	Idle	$y = 1.3166 \ln(x) + 0.3203$	0.6439
		F. Idle	$y = 0.817 \ln(x) + 0.003$	0.4338
4.	M-OMNI	Idle	$y = 1.4878 \ln(x) + 0.3145$	0.8298
		F. Idle	$y = 0.837 \ln(x) + 0.0626$	0.7337
5.	M-WGN R	Idle	$y = 0.8171 \ln(x) + 0.0369$	0.6034
		F. Idle	$y = 0.817 \ln(x) + 0.0368$	0.603
6.	M-ZEN	Idle	$y = 1.0646 \ln(x) + 0.7571$	0.6962
		F. Idle	$y = 0.6807 \ln(x) + 0.2234$	0.689

Table 7

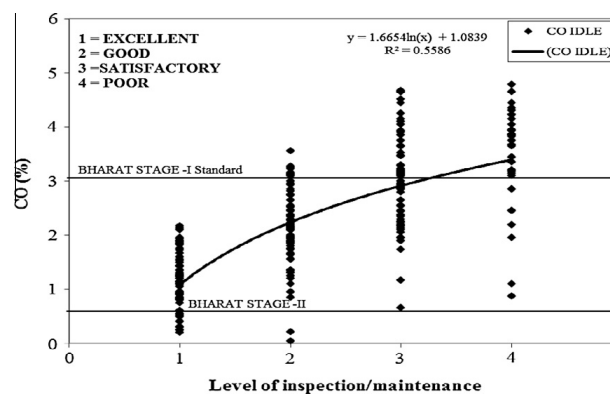
Equations relating HC emissions with vehicle TSLI (model-wise).

S. No.	Model	Test mode	Equation(s)	R ² value(s)
1.	M-800	Idle	$y = 102.31 \ln(x) + 77.834$	0.4654
		F. Idle	$y = 62.988 \ln(x) + 48.862$	0.4255
2.	M-ALTO	Idle	$y = 108.8 \ln(x) + 64.612$	0.5733
		F. Idle	$y = 69.255 \ln(x) + 33.188$	0.4289
3.	M-ESTEEM	Idle	$y = 101.37 \ln(x) + 103.61$	0.5586
		F. Idle	$y = 66.227 \ln(x) + 0.003$	0.5014
4.	M-OMNI	Idle	$y = 124.42 \ln(x) + 78.62$	0.7932
		F. Idle	$y = 75.522 \ln(x) + 39.846$	0.856
5.	M-WGN R	Idle	$y = 117.83 \ln(x) + 69.322$	0.6613
		F. Idle	$y = 77.462 \ln(x) + 34.054$	0.5708
6.	M-ZEN	Idle	$y = 97.262 \ln(x) + 98.871$	0.6805
		F. Idle	$y = 63.104 \ln(x) + 51.695$	0.6698

Table 8

Criteria for classification of I/M level.

S. No.	Number of visits during a year	I/M level
1.	1–3	Poor
2.	4–6	Satisfactory
3.	7–9	Good
4.	10–12	Excellent

**Fig. 15.** Level of I/M vs. CO emission (Idle).

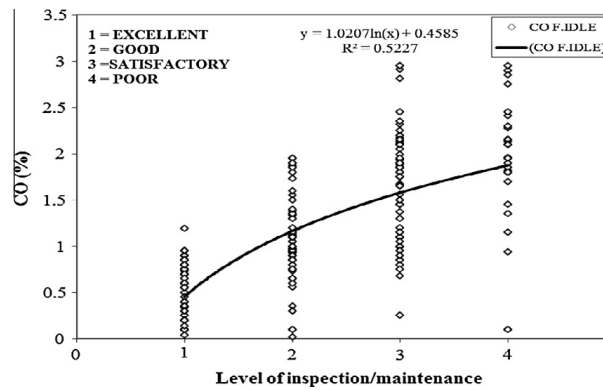


Fig. 16. Level of I/M vs. CO emission (Fast Idle).

A CH-1, 2-Gas Analyzer (NETEL India Ltd.) was used to measure instantaneous as well as fast idle mass concentrations of CO (%) and HC (ppm). The analyzer uses NDIR (Non-dispersive Infrared) method to measure CO and HC levels (Fig. 1). The entire methodology of study is depicted in Fig. 2.

Data analysis, results and discussion

Effect of vehicle age on CO and HC emissions

The effect of vehicle age on CO emission for entire data range is shown in Figs. 3 and 4 and the effect of vehicle age on HC emission is shown in Figs. 5 and 6 which reveal that the emission characteristics for both the parameters are best described by a logarithmic curve even though the scatter in data is conspicuous. A glance at the trendlines relating to the two test conditions reveals that fast idle test condition yields lower values of CO and HC emissions than those for the idle test condition. It, therefore, reflects that, if the fast idle test condition is also permitted in the country, the standardization procedure must look into the lowering of the values suitably than those prescribed for idle test conditions.

It is again observed that the dependence of emission levels on vehicle age is logarithmic in nature. The equations obtained for the best-fit logarithmic trend lines in each case are given in Tables 2 and 3.

A glance at emission equations having vehicle age as variable reveals that, the ageing of cars has a direct influence on the emission characteristics and it may render them to exceed the prescribed emission norms after certain age, which may further necessitate a thorough inspection and suitable maintenance, tuning of the cars as well.

Effect of vehicle mileage on CO and HC emissions

Figs. 7 and 8 show the effect of vehicle mileage on CO emission in both idle as well as fast idle test modes for entire data range and the same on HC emission has been shown in Figs. 9 and 10. It is revealed that a logarithmic curve best describes the emission characteristics for both the parameters, even if the scatter in data is vivid.

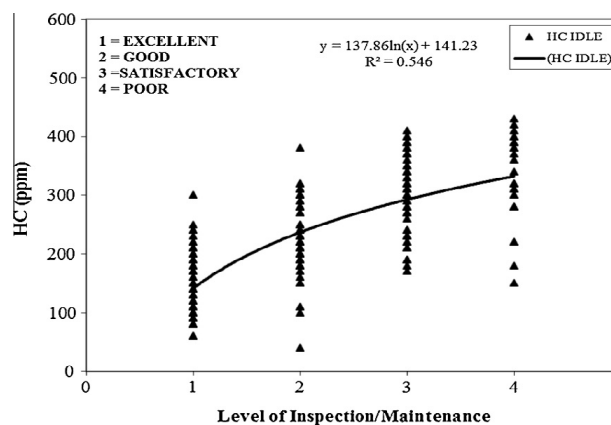


Fig. 17. Level of I/M vs. HC emission (Idle).

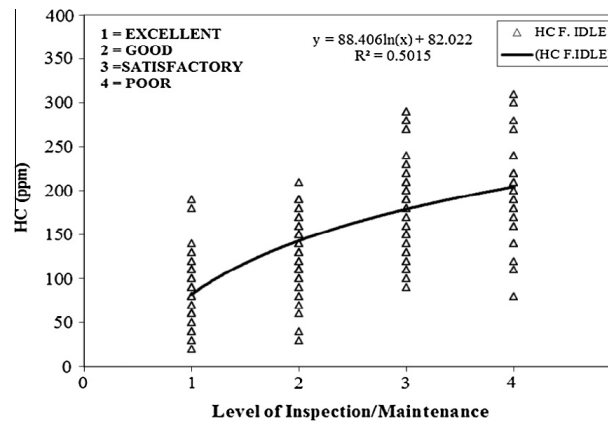


Fig. 18. Level of I/M vs. HC emission (Fast Idle).

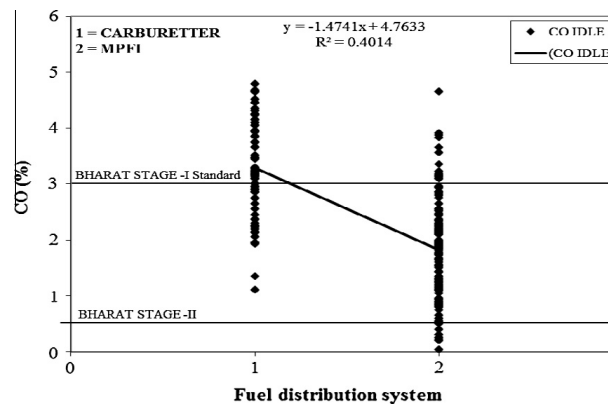


Fig. 19. FDS vs. CO emission (Idle).

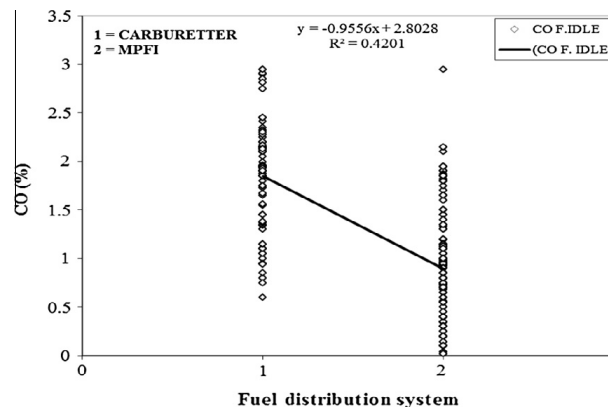


Fig. 20. FDS vs. CO emission (Fast Idle).

As elucidated by the emission equations having vehicle mileage as variable, it is found that the accumulated kilometers has a direct effect on the emission characteristics and owing to this accumulation the vehicles, after a certain mileage, becomes non-compliant to the relevant emission norms.

It is revealed from the analysis that the nature of dependence of CO and HC emissions on vehicle mileage is again logarithmic and the equations obtained for the best-fit logarithmic trend lines in each case are given in [Tables 4 and 5](#).

As elucidated by the emission equations having vehicle mileage as variable, it is found that the accumulated kilometers has a direct effect on the emission characteristics and owing to this accumulation the vehicles, after a certain mileage, becomes non-compliant to the relevant emission norms.

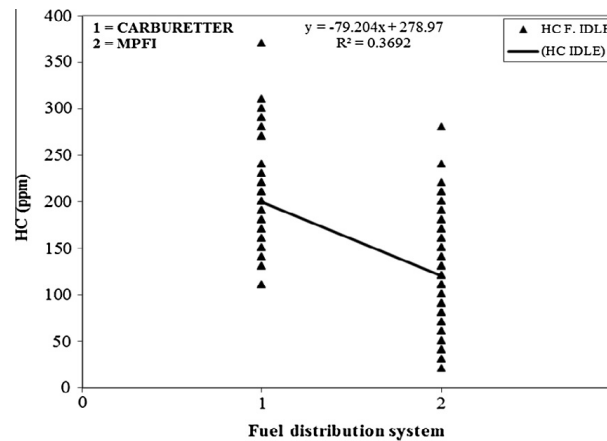


Fig. 21. FDS vs. HC emission (Idle).

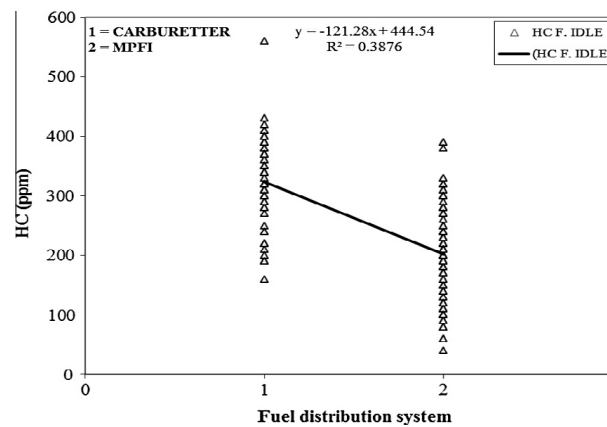


Fig. 22. FDS vs. HC emission (Fast Idle).

Effect of time since last inspection (TSLI) on CO and HC emissions

In the present work, the effect of time elapsed since last inspection on the tailpipe CO and HC emissions was also evaluated. The elapsed time was recorded in units of month with respect to idle and fast idle CO and HC mass concentration. The graphical representation of the results are shown in Figs. 11 and 12, which depict the effect of time elapsed since last inspection on CO emission for idle as well as fast idle test modes for entire data range, whereas Figs. 13 and 14 show the effect of TLSI on HC emissions for idle and fast idle test modes respectively.

It is evident from the analysis that the correlation between CO–HC emissions and vehicle TLSI is again of logarithmic in nature and the equations obtained thereby for the best-fit logarithmic trendlines in each case are given in Tables 6 and 7.

The emission equations having vehicle TLSI as variable show that the time elapsed since last inspection has a direct influence on the CO and HC emission characteristics and the CO and HC emissions are shown to increase with increase in time that has passed since the previous inspection/maintenance. This increase, as evidenced by the analysis, is of logarithmic nature and it is also shown that CO and HC emissions may even exceed the existing emission norms for in-use vehicles after a certain time since previous inspection.

Effect of level of inspection/maintenance on CO and HC emissions

The level of inspection/maintenance (I/M level) was categorized as excellent, good, satisfactory or poor on the basis of criteria adopted in this study. For this purpose, the frequency of inspection/maintenance got carried out in the workshop was chosen as the indicator. The criteria for classifying I/M level is given in Table 8.

Figs. 15 and 16 depict the status of CO emission with respect to I/M level for idle and fast idle test modes whereas Figs. 17 and 18 show the variation of HC emission with reference to I/M level for idle and fast idle test modes.

It is revealed that for CO emissions, all the vehicles having excellent and most of the vehicles having good I/M level emit within BHARAT Stage-I norms. However, vehicles having good I/M level show a mixed trend while most of the vehicles having poor I/M level do not comply to BHARAT Stage-I norms and only a few emit within BHARAT Stage-I norms. It has also been found that a few cars having excellent or good I/M level even comply to BHARAT Stage-II norms, whereas, none of the vehicles having satisfactory or poor I/M level comply to BHARAT Stage-II norms.

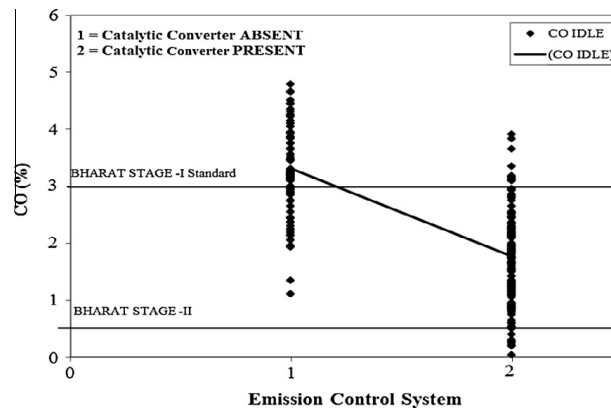


Fig. 23. ECS vs. CO emission (Idle).

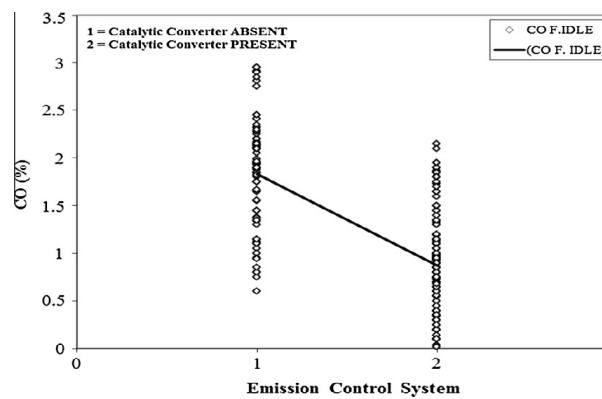


Fig. 24. ECS vs. CO emission (Fast Idle).

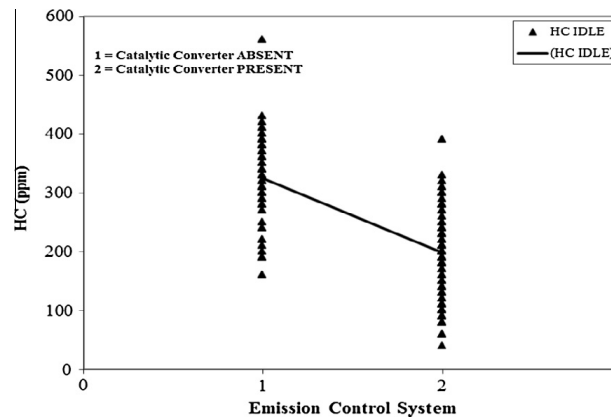


Fig. 25. ECS vs. HC emission (Idle).

In case of HC emission with reference to I/M level as depicted in Figs. 17 and 18 for idle and fast idle test conditions, it is found that emission from all the vehicles lies within the limits of BHARAT Stage-II norms. Even though the I/M level is found to have a positive effect towards the reduction in CO and HC emissions, it is revealed that CO emission is the most crucial factor being influenced by I/M level of the cars and should be taken care of suitably during the maintenance schedule through the proper tuning of engine.

Effect of fuel distribution system on CO and HC emissions

The effect of fuel distribution system (FDS) on CO and HC emissions for idle and fast idle test conditions as depicted in Figs. 19–22 respectively reveals that the multi-point fuel injection (MPFI) systems are more compliant than the carburettor systems.

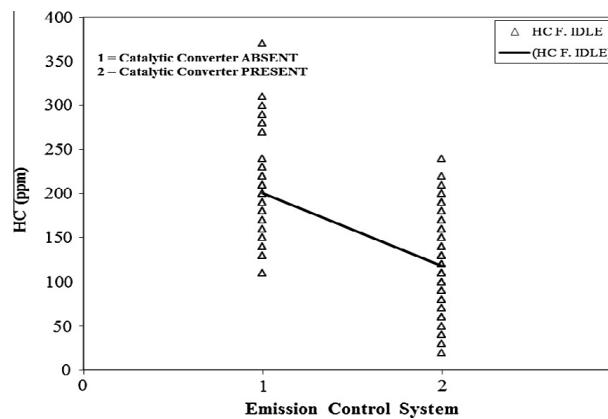


Fig. 26. ECS vs. HC emission (Fast Idle).

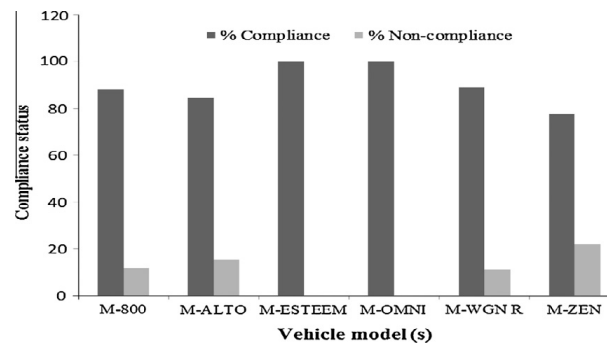


Fig. 27. Model-wise vehicle compliance to BHARAT Stage-I norms.

It is also revealed that all the vehicles having MPFI or carburettor systems are compliant to BHARAT Stage-II norms in terms of HC emissions but, in case of CO emissions, none of the cars having carburettor system is BHARAT Stage-II compliant and the majority being non-compliant to BHARAT Stage-I norms also, whereas, some of the vehicles having MPFI system are compliant to BHARAT Stage-II norms with a majority complying to BHARAT Stage-I norms as well. So, the criticality of CO as against HC is obvious in this case too.

Effect of emission control system (ECS) on CO and HC emissions

The effect of emission control system (i.e., catalytic converter) on CO and HC emissions under idle as well as fast idle test conditions for entire data range is shown in Figs. 23–26. It is revealed that none of the cars devoid of catalytic converter comply to BHARAT Stage-II norms and the majority is non-compliant to BHARAT Stage-I norms also, whereas, in the range of cars provided with catalytic converters, some cars comply to BHARAT Stage-II norms and the majority complies to BHARAT Stage-I norms barring only a few, which might have some inherent problems in catalytic converters *per se*.

The compliance of standards for different vehicle models

The compliance status in terms of the percentage (% age) of the total number of vehicles that underwent this study for different models of petrol-driven passenger cars of Maruti having BHARAT Stage-I and BHARAT Stage-II certification of norms is shown in Figs. 27 and 28 respectively. On the basis of these figures, the level of compliance of different models of petrol-driven passenger cars of Maruti in descending order is shown in Table 9.

The emission equations and compliance period of standards for different models were also reviewed with reference to vehicle age and mileage. It was found that all the vehicles covered during the study remained compliant in terms of HC emissions, whereas, CO emission was found to be a crucial factor in assessing the compliance of standards for different models of petrol-driven passenger cars of Maruti in terms of vehicle age and vehicle mileage.

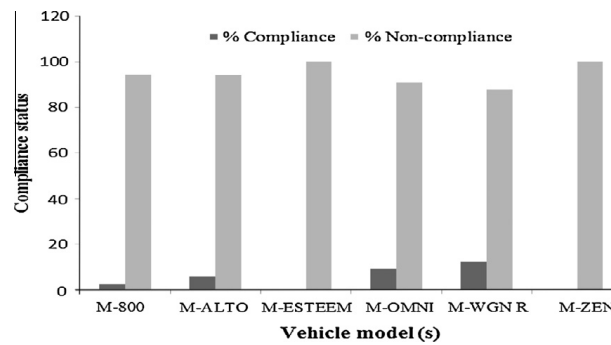


Fig. 28. Model-wise vehicle compliance to BHARAT Stage-II norms.

Table 9

Relative standing of different models in respect of compliance level.

S. No	Compliance level					
	BHARAT Stage-I	% Compliance	% Non-compliance	BHARAT Stage-II	% Compliance	% Non-compliance
1.	M-WGN R	88.88	11.12	M-WGN R	12.12	87.88
2.	M-ALTO	84.62	15.38	M-ZEN	0.00	100.00
3.	M-ZEN	77.78	22.22	M-ALTO	5.88	94.12
4.	M-800	88.24	11.76	M-800	2.56	97.44
5.	M-ESTEEM	100.00	0.00	M-OMNI	9.09	91.91
6.	M-OMNI	100.00	0.00	M-ESTEEM	0.0	100.0

Table 10

Emission equation(s) and compliance period of standards for CO (Idle) for different vehicle models with reference to vehicle age and mileage.

S. No.	Particulars	Emission equation(s)		Compliance period of standard			
		Vehicle age	Vehicle mileage	In terms of age (yrs)		In terms of mileage (km)	
				B.S.-II Compliant	B.S.-I Compliant	B.S.-II Compliant	B.S.-I Compliant
1.	Entire data range	$y = 1.1784 \ln(x) + 1.2731$	$y = 0.8057 \ln(x) - 5.9762$	0.5188	4.3295	3096.350	68931.689
2.	M-800	$y = 1.2484 \ln(x) + 1.2617$	$y = 0.7313 \ln(x) - 5.1711$	0.5432	4.0072	2332.780	71210.094
3.	M-ALTO	$y = 0.9306 \ln(x) + 1.3034$	$y = 0.815 \ln(x) - 6.0792$	0.4217	6.1911	3205.547	68880.107
4.	M-ESTEEM	$y = 1.1252 \ln(x) + 1.4413$	$y = 1.3327 \ln(x) - 11.452$	0.4332	3.9958	7849.930	51223.606
5.	M-OMNI	$y = 1.3171 \ln(x) + 1.2903$	$y = 0.8499 \ln(x) - 6.4773$	0.5488	3.6667	3675.902	69638.760
6.	M-WGN R	$y = 0.9341 \ln(x) + 1.1349$	$y = 0.9932 \ln(x) - 7.9069$	0.5067	7.3645	4743.157	58781.044
7.	M-ZEN	$y = 1.1235 \ln(x) + 1.4042$	$y = 0.7985 \ln(x) - 5.8958$	0.4471	4.1387	3010.219	68915.658

Conclusion

This study covered the tailpipe emission data collection from 300 petrol-driven passenger cars of Maruti Udyog Limited make plying on Gorakhpur area's city roads and found that vehicle-related parameters do have effect on the tailpipe exhaust and when compared to in-use concurrent Indian emission norms, exhibited different failure rates. A systematic review of the pertinent emission equations of entire data range and different models of petrol-driven passenger cars of Maruti along with compliance of standards with reference to vehicle age and vehicle mileage is presented in Table 10 which can be used for predicting CO and HC emissions of the vehicles with reference to vehicle age and vehicle mileage with an understanding that there is scope of refining the equations with a large data set for better accuracy.

It can not only be used as the proposed line for the suitable tuning and adjustment of pollution control systems for different models petrol-driven passenger cars of Maruti complying to BHARAT Stage-I or BHARAT Stage-II standards, as the case may be, in terms of the vehicle age or vehicle mileage, whichever is reached earlier, but also for the automobile manufacturing and maintenance sector to help them produce such environmentally benignant petrol-driven passenger cars having long-lasting compliance of pollution control systems with respect to vehicle age and mileage of the petrol-driven passenger cars in the country.

Acknowledgements

The authors would like to express their thanks to the staff of M/s RKBK Ltd. for their support extended during the setup of tailpipe exhaust monitoring station and data collection.

References

- Anilovich, I., Hakkert, A.S., 1996. Survey of vehicle emissions in Israel related to vehicle age and periodic inspection. *Sci. Total Environ.* 189 (190), 197–203.
- Auto Fuel Policy, 2002. Report of the Expert Committee on Auto Fuel Policy – Executive Summary, Ministry of Petroleum and Natural Gases, The Government of India.
- Badami, M.G., 2005. Transport and urban air pollution in India. *Environ. Manage.* 36, 195–204.
- Beaton, S.P., Bishop, G.A., Zhang, Y., Ashbaugh, L.L., Lawson, D.R., Stedman, D.H., 1995. On-road vehicle emissions: regulations, costs, and benefits. *Science* 268, 991–993.
- Beydoun, M., Guldman, J., 2006. Vehicle characteristics and emissions: logit and regression analyses of I/M data from Massachusetts, Maryland and Illinois. *Transp. Res. Part D* 11, 59–76.
- Bishop, G.A., Stedman, D.H., Ashbaugh, L., 1996. Motor vehicle emissions variability. *J. Air Waste Manage. Assoc.* 46, 67–75.
- Bogdanovic, R., Petrovic, J., Bazik, D., 1997. The concept of sustainable transport: implications for potential of residential streets. In: Sucharov, L., Bidini, G. (Eds.), *Urban Transport and the Environment for the 21st Century III*. Computational Mechanics, Boston, pp. 255–264.
- Census of India, 2011. The Government of India, New Delhi, India.
- Central Pollution Control Board, 1999. Parivesh: Newsletter. 6(1) June, CPCB, Ministry of Environment and Forests, Delhi.
- Central Pollution Control Board, 2010. Status of the Vehicular Pollution Control Programme in India. CPCB, Ministry of Environment and Forests, Delhi.
- Faiz, A., 1993. Automotive emissions in developing countries: relative implications for global warming, acidification and urban air quality. *Transp. Res.* (27 A, N3), 167–186.
- Faiz, A., Weaver, C.S., Walsh, M.P., 1996. Air Pollution from Motor Vehicles: Standards and Technologies for Controlling Emissions. World Bank.
- Gallagher, J., Livo, R., 1991. Emissions and Age Distribution of Vehicles in the Colorado I/M Program – Winter 1989–1990. SAE, Warrendale.
- Goodwin, R., Ross, M., 1996. Off-Cycle Emissions from Modern Passenger Cars with Properly Functioning Emission Controls. SAE Technical Paper Series, 960064. SAE, Warrendale.
- Harrington, W., McConnell, V.D., Albertini, A., 1996. Economic Incentive Policies Under Uncertainty: The Case of Vehicle Emission Fees. Discussion Paper. Resources for the Future, Washington, DC, pp. 96–32.
- Harrington, W., McConnell, V., Ando, A., 2000. Are vehicle emission inspection programs living up to expectations? *Transp. Res. Rec. Part D* 5 (3), 153–172.
- Kazopoulos, M., Fadel, M.E., Kaysi, I., 2005. Emission standards development for an inspection/maintenance program. *J. Environ. Eng.* 131 (9), 1330–1339.
- Knepper, J.C., Koehl, W.J., Benson, J.D., Burns, V.R., Gorse Jr., R.A., Hochhauser, A.M., Leppard, W.R., Rapp, L.A., Reuter, R.M., 1993. Fuel Effects in Auto/Oil High Emitting Vehicles. SAE Technical Paper Series, 930137. SAE, Warrendale.
- Pattas, K.N., Kyriakis, N.A., Samaras, K., 1994. Actual emissions of vehicles of the N1 category. *Sci. Total Environ.* 146 (7), 191–199.
- Schwartz, J., 2000. Smog Check II Evaluation Part II: Overview of Vehicle Emissions. Final Report. California Inspection and Maintenance Review Committee, Sacramento, CA.
- Singh, A.K., Gupta, H.K., Gupta, K., Singh, P., Gupta, V.B., Sharma, R.C., 2007. A comparative study of air pollution in Indian cities. *Bull. Environ. Contam. Toxicol.* 78, 411–416.
- Stephens, R.D., 1994. Remote sensing data and a potential model of vehicle exhaust emissions. *J. Air Waste Manage. Assoc.* 44, 1284–1292.
- Walsh, M.P., 1994. Transport and the environment: challenges and opportunities around the world. *Sci. Total Environ.* 146 (147), 1–9.
- Wang, H., Fu, L., Zhou, Y., Du, X., Ge, W., 2010. Trends in vehicular emissions in China's mega cities from 1995 to 2005. *Environ. Pollut.* 158, 394–400.
- Washburn, S., Seet, J., Mannering, F., 2001. Statistical modeling of vehicle emissions from inspection/maintenance testing data: an exploratory analysis. *Transp. Res. Part D* 6, 21–36.
- Watkins, L.H., 1991. Air Pollution from Road Vehicles. TRRL, London, pp. 151.
- WHO (World Health Organization), 2005. Air Quality Guidelines for Particulate Matter, Ozone, Nitrogen Dioxide and Sulphur Dioxide, Global update 2005. Geneva, 22 pages.
- WHO (World Health Organization), 2014. <<http://www.who.int/mediacentre/news/releases/2014/air-pollution/en/>> (accessed in September 2014).
- Wolf, J., Guensler, R., Washington, S., Bachman, W., 1998. High-emitting vehicle characterization using regression tree analysis. *Transp. Res. Rec.* 1641, 58–65.
- Zhang, Y., Bishop, G.A., Stedman, D.H., 1994. Automobile emissions are statistically y-distributed. *Environ. Sci. Technol.* 28, 1370–1374.

Thermodynamic Analysis of Single-effect LiBr-H₂O Absorption Refrigeration System

Rajesh Kumar*¹ and Ravindra Kannojiya²

^{1,2}Department of Mechanical Engineering, Delhi Technological University
 (Government of NCT of Delhi), Bawana Road, Delhi-110042, India
 E-mail: *dr.rajeshmits@gmail.com

Abstract—Thermodynamic analysis of single-effect LiBr-H₂O refrigeration system has been performed to investigate the effect of temperature variation in the major components of the cycle. The effect of governing parameters such as generator temperature, absorber temperature, condenser temperature and evaporator temperature on COP, ECOP and circulation ratio has been observed and accordingly suitable application for the system has been found in the real world scenario.

Keywords: Energy, single-effect, absorption, circulation ratio.

1. INTRODUCTION

The real world application of absorption refrigeration through single-effect lithium bromide-water absorption refrigeration technique has been an area of interest for researchers since last sixty years. Analysis of this system shows that performance of the system is limited to only low-temperature applications. For efficient utilization of the low-temperature heat sources, absorption refrigeration cycle has been analyzed to determine the change in performance of the system by changing some parameters such as temperature. He and Chen (2007) showed that the absorption refrigeration system, driven by low-potential thermal power such as solar energy gives potential of energy saving. It also have the benefits of using ecofriendly working pair, H₂O/LiBr and NH₃/H₂O. Vereda et al. (2012) said that the potential of the absorption cycle for low-temperature waste heat recovery has been of good extent. It has application to solar cooling which enables this for the benefit due to the appreciative combination between solar energy and air-conditioning demand. Single-effect absorption cycle can operate with low driving temperatures, which supports the use of flat plate collectors. But it should not be lower than about 70°C for air-conditioning. Stitou et al. (2000) observed that increase in the driving temperature for the process provides a comparatively better exploitation of the thermal power of heat source. The amount of heat at the top temperature can be degraded many times before being rejected to the sink, shows the way for possibility of cooling or heating from the machine. Tozer and James (1998) have said that two single stage cycles with one operating at a higher driving temperature can be considered equivalent to double stage

cycle. They also showed that heat rejected from condenser must be equal to the heat absorbed by the low temperature generator.

2. SYSTEM DESCRIPTION

Fig.1 shows the single-effect LiBr-H₂O absorption refrigeration cycle. It consists of an absorber (A) and generator (G) which form the part of solution circuit. Condenser (C) and evaporator (E) are the parts of refrigeration circuit which produces cooling. Strong solution of refrigerant from heat exchanger (HE) enters into the generator and refrigerant water vapour sent to the condenser. The remaining part of the solution strong in LiBr reaches to the absorber. The absorber and evaporator are at low pressure levels while generators and condenser are at higher pressure level.

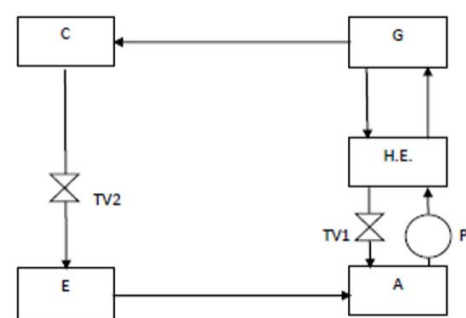


Fig. 1: Single-effect absorption cycle

Table 1: Main parameters considered for the analysis

Environment Temperature (K)	298
Environment pressure (MPa)	0.10135
Absorber Temperature (K)	311
Heat exchanger effectiveness	0.60
Condenser temperature (K)	313
Evaporator temperature (K)	283
Generator temperature (K)	363
Mass flow rate of refrigerant vapour (kg/s)	1

3. THERMODYNAMIC ANALYSIS

The thermodynamic behavior of the absorption refrigeration system and its components have been studied. Part of the exergy supplied to an actual thermal system is destroyed due to irreversibility within the system. The exergy destruction is equal to the product of entropy generation within the system and the temperature of the reference environment.

The coefficient of performance of the cycle is given as:

$$COP = Q_c / Q_g \# \quad (1)$$

The exergetic coefficient of performance is given as:

$$ECOP = Q_c \{1 - (T_o / T_c)\} / [Q_g \{1 - (T_o / T_g)\}] \quad (2)$$

The circulation ratio of EARS is given as:

$$f = m_r / m_s \# \quad (3)$$

To find the steady-state performance of the system from these equations, the operating temperatures, weak and strong solution concentrations, effectiveness of heat exchanger and the refrigeration capacity. It is assumed that the solution at the exit of absorber and generator is at equilibrium so that P-T- ξ and h-T- ξ charts can be used for evaluating solution property data.

4. RESULTS AND DISCUSSION

A thermodynamic analysis has been done to observe the effect of temperature variation of various components of single-effect absorption system.

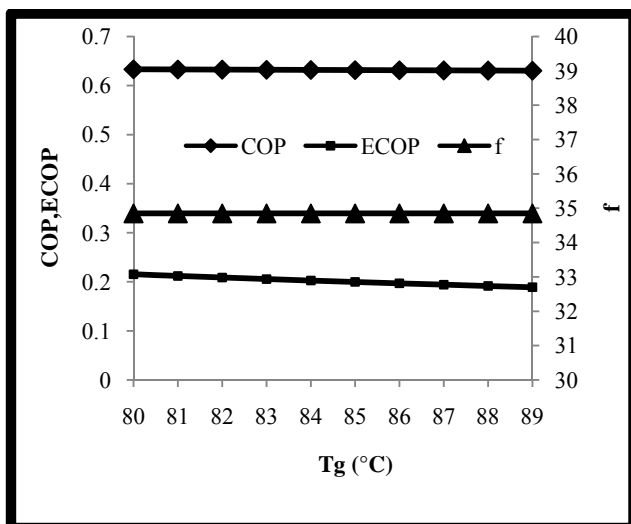


Fig. 2: Effect of generator temperature variation

Fig. 2, 3, 4 and 5 shows the effect on COP, ECOP and circulation ratio with temperature variation in generator, absorber, condenser and evaporator. The circulation ratio (f) remains the same as the temperature increases in case of condenser, evaporator and generator. It varies non-linearly in

case of absorber. The COP increases in case of evaporator temperature but it decreases in other components like absorber, condenser and generator.

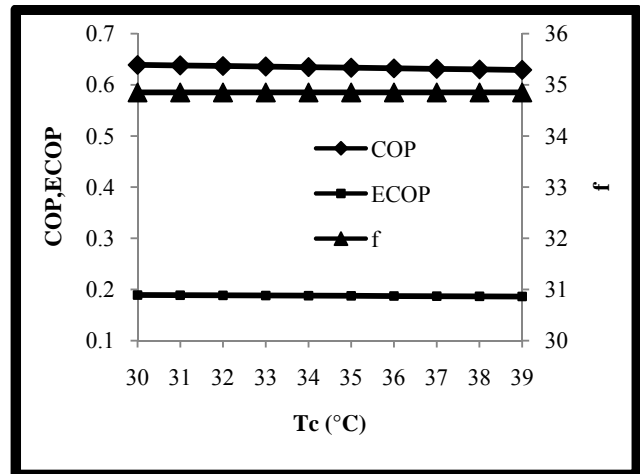


Fig. 3: Effect of condenser temperature variation

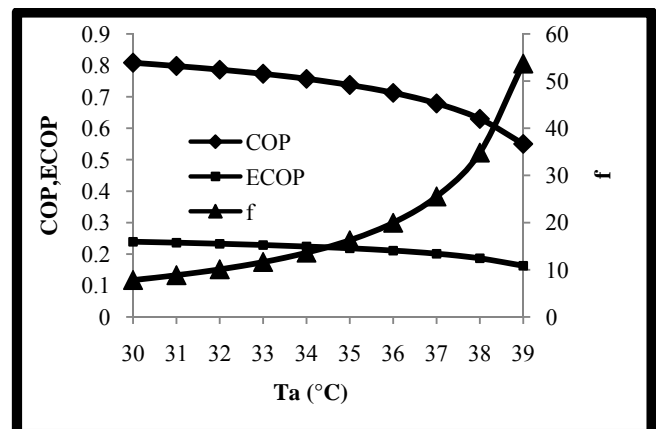


Fig. 4: Effect of absorber temperature variation

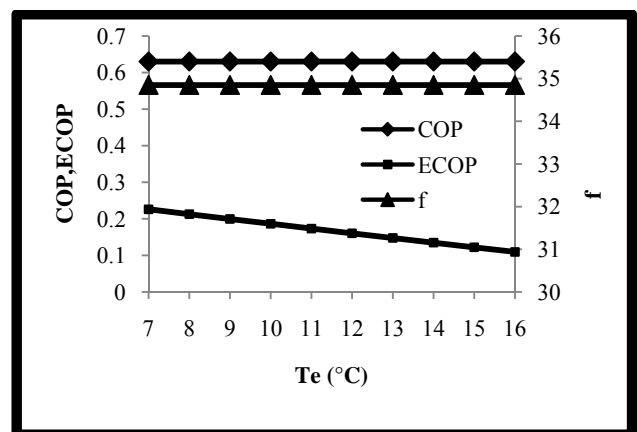


Fig. 5: Effect of evaporator temperature variation

The ECOP decreases with increase in the temperature of all these components. The results of this analysis also indicate that the designing of the absorption refrigeration system should be on the basis of thermodynamic point of view. In the residential and industrial locations, installation of the system is of major concern. The components of absorption refrigeration cycle like absorber, condenser, evaporator and generator are significant in the real world applications.

For commercial applications the above study can be considered a better tool and also for the cooling load and other parameters. From this discussion we see the essential and avoidable parameters of the cycle.

5. CONCLUSION

This study deals with the LiBr-H₂O absorption refrigeration system for cooling and air-conditioning. The effect of temperature variation has been observed on the performance with the help of first law and second law equations of the cycle.

From this useful discussion, it can be concluded that

- As the temperature varies in absorber, the circulation ratio increases while COP and ECOP decrease.
- As the temperature varies in evaporator, the circulation ratio remains same and ECOP decrease while COP increases.
- As the temperature varies in condenser, the circulation ratio remains the same, COP and ECOP decrease.
- As the temperature varies in the generator, the circulation ratio remains, COP and ECOP decrease.

REFERENCES

- [1] He Yijian, ChenGuangming, "Experimental study on an absorption refrigeration system at low temperatures", *International Journal of Thermal Sciences*, 46, 2007, pp. 294–299.
- [2] Vereda C., Ventas R., Lecuona A., Venegas M., "Study of an ejector-absorption refrigeration cycle with an adaptable ejector nozzle for different working conditions", *Applied Energy*, 97, 2012, pp. 305–312.
- [3] Stitou D., Spinnera B., Satzger P., Ziegler F., "Development and comparison of advanced cascading cycles coupling a solid/gas thermochemical process and aliquid/gas absorption process", *Applied Thermal Engineering*, 20, 2000, pp. 1237–1269.
- [4] Tozer Robert, James Ron W, "Heat powered refrigeration cycles", *Applied Thermal Engineering*, 18, 1998, pp. 731–743.